The tectonic evolution of the Hoh Xil Basin and Kunlun Shan: implications for the uplift history of the northern Tibetan Plateau

by

Lydia M. Staisch

A dissertation submitted in partial fulfillment
of requirements of the degree of
Doctor of Philosophy
(Geology)
In the University of Michigan
2014

Doctoral Committee:

Associate Professor Nathan A. Niemi, Chair
Assistant Professor Sarah Aciego
Assistant Professor Adda Athanasopoulos-Zekkos
Associate Professor Marin K. Clark
Assistant Professor Eric Hetland

Dedication

Ich widme diese Dissertation meinem Vater, der meine Ausbildung und Neugier gefördert hat. Ich werde dich in den hohen Bergen treffen, wo der Himmel die Stirn der Erde küsst.

Acknowledgements

First and foremost, I would like to acknowledge my advisor, Nathan Niemi, for his invaluable support during my time at the University of Michigan. This thesis would not have been possible without his guidance. During the Ph.D. process, Nathan and my committee member, Marin Clark, patiently encouraged me to critically examine previous work, thoughtfully analyze my data, and to always return to the big picture. I have learned a great many skills and lessons from Nathan and Marin, and will keep these lessons in mind throughout my career. I would also like to extend thanks to my other committee members, Eric Hetland, Sarah Aciego, and Adda Athanasopoulos-Zekkos, for their insight and constructive criticism of my work. I thank all the members of the CD NSF Grant "Collaborative Research: Growth of the Tibetan Plateau and Eastern Asia Climate: Clues to Understanding the Hydrological Cycle" project, including Peter Molnar, Nathan Niemi, Marin Clark, Carmala Garzione, Hai Cheng, Gerard Roe, David Battisti, Inez Fung, John Chiang, Larry Edwards, Jung-Eun Lee, Warren Beck, John Kutzbach, Zhengyu Liu, and Alex Pullen, as well as our Chinese colleagues, Chang Hong, An Zhisheng, Cai Yanjun, Guangshan Chen, Liu Xiaodong, Wang Xulong, Zhang Peizhen, and Zhou Weihian. All have contributed to my work and growth as a young scientist. I would especially like to thank Chang Hong, Petr Yakovlev, Jiang Yi, Zhang Peng, and Shugang Kang for their help in the field. I was able to visit China four times for field work. Their logistical and scientific assistance in the field made everything in this dissertation possible. I owe thanks to Amanda Carey, Alison Duvall, and Boris Avdeev for their help with apatite (U-Th)/He dating, to those who helped me with fault gouge dating: Ben van der Pluijm, Anja Schleicher, Alison Duvall, Tim O'Brien, and especially to Chris Hall, who also helped with $^{40}Ar/^{39}Ar$ dating of volcanic samples. I'd like to thank John Geissman and Catherine Badgley for their help with magnetostratigraphic and biostratigraphic interpretation, and David Rowley for access to important samples. I owe a great deal to the University of Michigan Department of Earth and Environmental Sciences (nee Geological Sciences) staff, especially Anne Hudon and Nancy Kingsbury. I'd like to thank all of the graduate students in the Department of Geological Sciences for being good friends and colleagues, especially Laura "Gingey" Waters, my friend, roommate, and

role model. A big thanks to my lab family: Alison Duvall, Alex Lechler, Boris Avdeev, Nora Lewandowski, Petr Yakovlev, and Alyssa Abbey for being wonderful friends and colleagues. And speaking of family, I thank and give a lot of credit to my amazing husband, Richard Styron, who helped me scientifically, emotionally, mentally, and lovingly, as well as to my mother and sister for their support. And of course, my fuzz-monster, Jura, the best dog of all time, has helped me with wet-nose-kisses and unadulterated silliness. Lastly, I thank my funding sources, NSF Continental Dynamics grants EAR-0908711 and EAR-1211434 and an NSF Graduate Research Fellowship awarded at the beginning of my graduate student career. The GSA Graduate Student Research Award and two University of Michigan Turner Awards awarded to me helped with field work and analytical costs. NSFC grant 40921120406 to An Zhisheng supported both our Chinese colleagues at the Institute for Earth Environment and our joint fieldwork in Tibet.

TABLE OF CONTENTS

LIST OF FIGURES

FIGURE

LIST OF TABLES

TABLE

Chapter I

Introduction

1.1. Motivation

As the highest and most laterally extensive orogenic system on Earth (Figure 1.1), the Tibetan Plateau has been a long-standing paradigm of extreme lithospheric deformation and topographic growth due to rapid and enduring continental convergence. With an average elevation above 5 km and a crustal thickness that is near-double the average for continental lithosphere, this exceptional geologic feature provides a unique setting for earth systems exploration. For many decades, extensive shortening and thickening of the Tibetan lithosphere was ascribed to be entirely the result of the Indo-Asian collision at ~50 Ma and early models of Cenozoic plateau evolution commonly suggest a northward propagation of crustal shortening and surface uplift (Argand, 1924; England and McKenzie, 1982; England and Houseman, 1986; Powell, 1986; Zhao and Morgan, 1987; Tapponnier et al., 2001). To test whether these models are able to predict the geologic history of the Tibetan Plateau requires a spatially and temporally comprehensive set of geologic observations, which were scarce for some time due to the political and logistical issues associated with field work in Tibet.

As the decades have passed and geologic observations have accumulated, there has been substantial clarification of the deformation history of the Tibetan Plateau. It has become increasingly clear that the southern and central portions of the Tibetan Plateau were extensively deformed and potentially uplifted to near-modern elevation prior to collision between India and Eurasia, and that little crustal shortening has occurred within these regions since (Burg et al., 1983; England and Searle, 1986; Murphy et al., 1997; Kapp et al., 2005, 2007a, 2007b; DeCelles et al., 2007a; Hetzel et al., 2011; Rohrmann et al., 2012; Ding et al., 2014). Additionally, studies along the present northern margin of the Tibetan Plateau suggest that the northern plateau boundary was establish at or very soon after the initial collision between India and Eurasia (Yin et al., 2002; Clark et al., 2010; Duvall et al., 2011). These temporal constraints on deformation challenge the older models of plateau

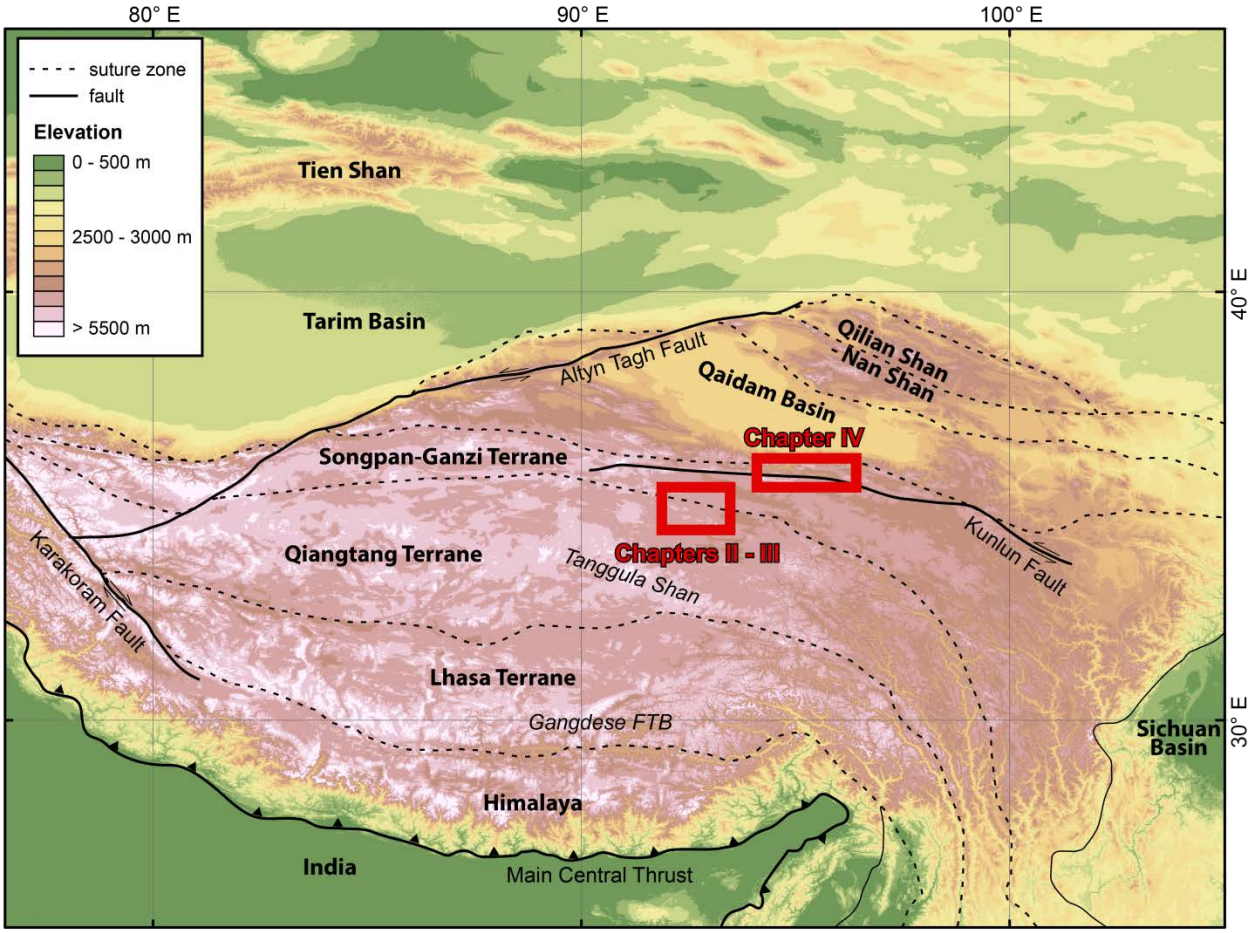

Figure 1.1. Topographic map of the Tibetan Plateau. Tibetan terranes and important geographic features are labeled in bold text and terrane bounding faults are labeled in plain text. The Gangdese Fold and Thrust Belt (FTB) and Tanggula Shan are labeled in italicized text. The field locations of Chapter II-IV are outlines in red.

development and, in so, raise several unanswered questions of pre- and post-collisional topographic uplift of the remainder of the Tibetan Plateau. As the majority of geologic studies within the Tibetan Plateau have been concentrated in the central and southern regions, the northern plateau remains largely unexplored and unexplained owing to its remote nature, harsh weather conditions, and limited access due to permafrost features (Figure 1.2). Thus, the northern Tibetan Plateau presents a frontier in our understanding of the geologic evolution of the orogen and is the focus of many outstanding questions in plateau development. In the following thesis outline, I identify several key questions of Tibetan Plateau evolution, explain the means in which this thesis has approached these questions, and summarize conclusions from each chapter.

1.2. Thesis Outline

To address outstanding questions of Tibetan Plateau evolution, I have employed a variety of analytical and computational techniques, including biostratigraphic and magnetostratigraphic data interpretation, U-Pb geochronology, $^{40}Ar/^{39}Ar$ geochronology, detrital U-Pb zircon provenance analysis, geologic mapping, low-temperature thermochronology and modeling of thermochronologic data, $^{40}Ar/^{39}Ar$ fault gouge dating, cross section construction and retrodeformation, and calculations of isostatic uplift. This thesis is centered around two locales within the northern Tibetan Plateau; Chapters II and III are focused on the sedimentary and deformation histories of the Hoh Xil Basin, and Chapter IV is focused on the deformation history of the central Kunlun Shan (Figure 1.1).

1.2.1. Chapter II

As mentioned above, the majority of crustal shortening, and potentially elevation gain, within the southern and central Tibetan Plateau occurred prior to the Indo-Asian collision at 50 Ma (Burg et al., 1983; England and Searle, 1986; Murphy et al., 1997; Kapp et al., 2005, 2007a, 2007b; DeCelles et al., 2007a; Hetzel et al., 2011; Rohrmann et al., 2012; Ding et al., 2014). However, the northern margin of the pre-collisional deformation belt is not well established and is central to understanding how, when and in what manner did the Tibetan Plateau evolve to its modern dimensions. Previous work in the Hoh Xil Basin, located in north-central Tibet, has suggested that deposition of terrestrial sedimentary units, which suggest deformation, uplift and erosion of the source terrane, initiated in the Eocene (Liu et al., 2001, 2003). In addition, studies suggest that deformation did not progress into this region until the late Eocene – early Oligocene, well after

Figure 1.2. The perils of traveling off road over soupy terrain.

initial collision between India and Eurasia (Liu et al., 2001, 2003; Wang et al., 2008). Based on these interpretations, the Hoh Xil Basin has been used as an important marker for conceptual models of northward growth of the Tibetan Plateau (Dewey et al., 1988; Tapponnier et al., 2001; Wang et al., 2002, 2008). However, previous interpretations from the Hoh Xil Basin rely almost entirely on poorly constrained stratigraphic ages from terrestrial red bed and lacustrine carbonate units (Liu et al., 2001, 2003). Chapter II revisits the depositional ages and stratigraphy of the Hoh Xil Basin by presenting an extensive compilation and analysis of existing biostratigraphic data, new high-precision U-Pb LA-ICPMS and CA-TIMS zircon tuff ages, and new $^{40}Ar/^{39}Ar$ geochronologic age dating of variably deformed volcanic units. These age constraints have been used to reinterpret the magnetostratigraphic data originally published by Liu et al. (2001). Additionally, existing detrital zircon U-Pb age spectra from Tibetan Terranes and Mesozoic sedimentary units are compared to zircon U-Pb age spectra of the Fenghuoshan Group, the oldest terrestrial sequence in Hoh Xil Basin, to finger print the source terrane for sediments shed into the Hoh Xil Basin and identify whether other similar-aged sedimentary units in the Tibetan Plateau have a common source.

This work reveals that deposition of the Fenghuoshan Group initiated at 85 Ma and ceased by 51 Ma, shifting the depositional age over 30 million years earlier than previously recognized. Provenance analysis and sedimentary characteristics of the Fenghuoshan Group indicates that the source terrane is likely the Tanggula Shan, located immediately to the south of the Hoh Xil Basin. These results, along with previous work from central and southern Tibet (Burg et al., 1983; England and Searle, 1986; Murphy et al., 1997; Kapp et al., 2005, 2007a, 2007b), suggest that pre-collisional crustal shortening, uplift, and deformation of the Tibetan Plateau spanned from the Gangdese Fold and Thrust Belt in the south to the Tanggula Shan in the north (Figure 1.1). The north-south extent of the pre-collisional deformation belt in the Tibetan Plateau is comparable in east-west extent to the modern Altiplano-Puna Plateau in South America, suggesting that the western margin of South America may be an appropriate present-day analogue to the Tibetan Plateau prior to the Indo-Asian collision. However, the Tibetan Plateau is currently nearly twice the size of the Altiplano-Puna Plateau, suggesting a doubling in north-south extent following the Indo-Asian collision. The depositional age of the Fenghuoshan Group and results from geochronologic dating of volcanic rocks in the Hoh Xil Basin suggest that deformation initiated after 51 Ma and ceased between 34 and 27 Ma, indicating that crustal shortening may have progressed into north-central Tibet soon after the onset of the Indo-Asian collision. This work was published in the March 2014 issue of *Tectonics*.

1.2.2. Chapter III

Building upon Chapter II, Chapter III focuses on how and when the Tibetan Plateau expanded from its pre-collisional to modern extent by constraining the timing and magnitude of crustal shortening within the Fenghuoshan Fold and Thrust Belt (FFTB), located in central Hoh Xil Basin, and calculating the isostatic uplift response to shortening and thickening. The timing of deformation within the FFTB is addressed with new apatite (U-Th)/He thermochronology, new $^{40}Ar/^{39}Ar$ fault gouge dating, and geochronologic ages from Chapter II. The magnitude of deformation is measured from a balanced cross section, which is based on new and existing geologic mapping (Qinghai Bureau of Geology and Mineral Resources (QBGMR), 1989a, 1989b), measured bedding orientations throughout the FFTB, structural observations, and the stratigraphy of the Hoh Xil Basin. To assess whether the modern crustal thickness and Miocene paleoelevation (Polissar et al., 2009) can be obtained via measured crustal shortening of the Hoh Xil Basin or whether additional mechanisms of crustal thickening and uplift are necessary, the isostatic uplift in response to pure shear deformation is calculated.

The results from low-temperature thermochronologic data modeling and fault gouge dating independently suggest that the Fenghuoshan Fold and Thrust Belt began deforming between 49 and 44 Ma, coincident with or soon after the onset of Indo-Asian collision, and geochronologic constraints suggest that deformation continued until at most 27 Ma. The FFTB was shortened by 28.0 ± 7.2%, which is similar to estimates of Cenozoic shortening throughout the northern Tibetan Plateau (~25%; Yakovlev and Clark, 2014). Isostatic calculations indicate that the high plateau elevations cannot be attained from shortening alone, nor can the modern crustal thickness of 65 – 75 km (Braitenberg et al., 2000; Vergne et al., 2002; Wittlinger et al., 2004; Karplus et al., 2011). Palynological and paleoelevation data suggests that additional surface uplift of the Hoh Xil Basin occurred after crustal shortening ceased, and thus in the absence of observable upper crustal deformation (Duan et al., 2007, 2008; Polissar et al., 2009). Several mechanisms of surface uplift in the absence of upper crustal shortening have been proposed, including lower crustal flow (Clark et al., 2005a; Karplus et al., 2011), preferential thickening of the lower crust and mantle lithosphere (Isacks, 1988; Gubbels et al., 1993) and removal of the mantle lithospheric root (Molnar et al., 1993). Isostatic calculations for thickening and/or surface uplift from these proposed mechanisms suggest that either thickening mechanism is possible, and that mantle root loss may accompany either mechanism. However, lower crustal flow and removal of the mantle root are more likely to explain Neogene magmatism and geophysical observations from the Hoh Xil Basin (McKenna and Walker,

1990; Owens and Zandt, 1997; Ding et al., 2003; Lai et al., 2003; Williams et al., 2004; Chung et al., 2005; Wang et al., 2005; Guo et al., 2006; Klemplerer, 2006; Jiang et al., 2006; Karplus et al., 2011; Chen et al., 2012).

1.2.3. Chapter IV

The timing of northern Tibetan Plateau surface uplift to modern elevation remains vague due to the scarcity of suitable rock samples and precise age constraints for paleoaltimetric estimates. However the attainment of high gravitational potential energy, as a proxy for high elevation, can be discerned from the structural evolution of northern Tibet, namely the transition from pure shear to simple shear dominated deformation along the Kunlun Shan, located at the northern plateau margin (Figure 1.1). Chapter IV concentrates on temporally constraining the shift in principal stress orientation within the Kunlun Shan from crustal shortening, which may have initiated between 28 and 35 Ma (Yin et al., 2008; Clark et al., 2010), to modern left-lateral faulting using low-temperature thermochronology and $^{40}Ar/^{39}Ar$ fault gouge dating. Both thrust and strike-slip faulting result in exhumation and so untangling the complex and multi-stage deformation history of the Kunlun Shan requires detailed structural analysis in addition to the timing of exhumation.

While the Kunlun Shan are over 1000 km in east-west extent, Chapter IV is limited to the Dongdatan Valley, East Wenquan Basin, and East Deshuiwai Mountains, located within the central Kunlun Shan. Here, left-lateral motion along the Kunlun Fault has caused localized basin subsidence in rhombochasms, where strike-slip related exhumation is suppressed, and uplift along restraining bends and fault junctions, where strike-slip related exhumation is concentrated. Results from thermochronologic and fault gouge dating, structural analysis, and stratigraphic observations indicate that exhumation due to thrust fault activity occurred between 47 – 24 Ma and resulted in the syntectonic deposition of terrestrial red bed strata. The initiation of strike-slip related exhumation Kunlun Fault Zone may have initiated as early as 20 Ma and continues today, suggesting that lateral shear initiated after the cessation of crustal shortening, and that the temporal gap between these episodes of deformation was relatively short. The data presented in this chapter, along with other studies of fault motion along the Kunlun Fault, indicates that left-lateral faulting initiated in the western Kunlun Shan by 20 – 15 Ma and propagated to the eastern fault segment by 8 Ma (Jolivet et al., 2003; Duvall et al., 2013). The onset of left-lateral fault motion is roughly coincident with the initiation of normal faulting in southern Tibet (Blisniuk et al., 2001; Garzione et al., 2003; Murphy et al., 2002; Lee et al., 2011; Ratschbacher et al., 2011; McCallister et al., 2013; Sundell et al., 2013;

Styron et al., 2013) and eastward expansion of the Tibetan Plateau via lower crustal flow (Clark and Royden, 2000; Clark et al., 2005a, 2005b), suggesting a plateau-wide attainment of high gravitational potential energy by 20 – 15 Ma required to initiate east-west expansion within an overall compressional environment.

1.2.4. Chapter V

Chapter V summarizes the interpretations and main conclusions from each chapter in a synthesis of the sedimentary, deformation and uplift history of the northern Tibetan Plateau. The summary highlights the key contributions of this thesis to understanding the timing and mechanisms involved in the evolution of the Tibetan Plateau. Each chapter is flanked by an appendix with additional figures, data tables and explanation of methods utilized.

1.3. References

Argand, E., 1924, La Tectonique de l'Asie: Proc. Int. Geol. Congr., v. 7, p. 170–372.

Blisniuk, P. M., Hacker, B.R., Glodny, J., Ratschbacher, L., Bi, S., Wu, Z., McWilliams, M.O., and Calvert, A., 2001, Normal faulting in central Tibet since at least 13.5 Myr ago.: Nature, v. 412, no. 6847, p. 628–32, doi:10.1038/35088045.

Braitenberg, C., Zadro, M., Fang, J., Wang, Y., and Hsu, H.T., 2000, The gravity and isostatic Moho undulations in Qinghai–Tibet plateau: Journal of Geodynamics, v. 30, no. 5, p. 489–505, doi: 10.1016/S0264-3707(00)00004-1.

Burg, J.P., Proust, F., Tapponnier, P., and Chen, G.M., 1983, Deformation phases and tectonic evolution of the Lhasa block: Eclogae Geol. Helv, v. 76, no. 3, p. 643–683.

Chen, J.-L., Xu, J.-F., Wang, B.-D., and Kang, Z.-Q., 2012, Cenozoic Mg-rich potassic rocks in the Tibetan Plateau: Geochemical variations, heterogeneity of subcontinental lithospheric mantle and tectonic implications: Journal of Asian Earth Sciences, v. 53, p. 115–130, doi: 10.1016/j.jseaes.2012.03.003.

Chung, S.-L., Chu, M.-F., Zhang, Y., Xie, Y., Lo, C.-H., Lee, T.-Y., Lan, C.-Y., Li, X., Zhang, Q., and Wang, Y., 2005, Tibetan tectonic evolution inferred from spatial and temporal variations in post-collisional magmatism: Earth-Science Reviews, v. 68, p. 173–196, doi: 10.1016/j.earscirev.2004.05.001.

Clark, M.K., and Royden, L.H., 2000, Topographic ooze : Building the eastern margin of Tibet by lower crustal flow: Geology, v. 28, no. 8, p. 703–706.

Clark, M.K., Bush, J.W.M., and Royden, L.H., 2005a, Dynamic topography produced by lower crustal flow against rheological strength heterogeneities bordering the Tibetan Plateau: Geophysical Journal International, v. 162, no. 2, p. 575–590, doi: 10.1111/j.1365-246X.2005.02580.x.

Clark, M.K., House, M.A., Royden, L.H., Whipple, K., Burchfiel, B.C., Zhang, X., and Tang, W., 2005b, Late Cenozoic uplift of southeastern Tibet: Geology, v. 33, no. 6, p. 525–528, doi: 10.1130/G21265.1.

Clark, M.K., Farley, K.A., Zheng, D., Wang, Z., and Duvall, A.R., 2010, Early Cenozoic faulting of the northern Tibetan Plateau margin from apatite (U–Th)/He ages: Earth and Planetary Science Letters, v. 296, no. 1-2, p. 78–88, doi: 10.1016/j.epsl.2010.04.051.

DeCelles, P.G., Quade, J., Kapp, P., Fan, M., Dettman, D.L., and Ding, L., 2007a, High and dry in central Tibet during the Late Oligocene: Earth and Planetary Science Letters, v. 253, no. 3-4, p. 389–401, doi: 10.1016/j.epsl.2006.11.001.

Dewey, J.F., Shackleton, R.M., Chang, C., and Yiyin, S., 1988, The tectonic evolution of the Tibetan Plateau: Philosophical Transactions of the Royal Society of London. Series A, Mathematical and Physical Sciences, v. 327, no. 1594, p. 379–413.

Ding, L., Kapp, P., Zhong, D., Deng, W., 2003, Cenozoic Volcanism in Tibet: Evidence for a Transition from Oceanic to Continental Subduction: Journal of Petrology, v. 44, p. 1833–1865.

Ding, L., Xu, Q., Yue, Y., Wang, H., Cai, F., and Li, S., 2014, The Andean-type Gangdese Mountains: Paleoelevation record from the Paleocene–Eocene Linzhou Basin: Earth and Planetary Science Letters, v. 392, p. 250–264, doi: 10.1016/j.epsl.2014.01.045.

Duan, Z., Li, Y., Shen, Z., Zhu, X., and Zhong, C., 2007, Analysis of the evolution of the Cenozoic ecological environment and process of plateau surface uplift in the Wenquan area in the interior of the Qinghai-Tibet Plateau: Geology in China, v. 34, no. 4, p. 688–696.

Duan, Q., Zhang, K., Wang, J., Yao, H., and Niu, Z., 2008, Oligocene Palynoflora, Paleovegetation and Paleoclimate in the Tanggula Mountains, northern Tibet: Acta Micropalaeontologica Sinica, v. 25, no. 2, p. 185–195.

Duvall, A.R., Clark, M.K., Van der Pluijm, B.A., and Li, C., 2011, Direct dating of Eocene reverse faulting in northeastern Tibet using Ar-dating of fault clays and low-temperature thermochronometry: Earth and Planetary Science Letters, v. 304, no. 3-4, p. 520–526, doi: 10.1016/j.epsl.2011.02.028.

Duvall, A.R., Clark, M.K., Kirby, E., Farley, K.A., Craddock, W.H., Li, C., and Yuan, D., 2013, Low-temperature thermochronometry along the Kunlun and Haiyuan Faults, NE Tibetan Plateau: Evidence for kinematic change during late-stage orogenesis: Earth and Planetary Science Letters, v. 32, no. 5, p. 1190–1211.

England, P., and Houseman, G., 1986, Finite strain calculations of continental deformation: 2. Comparison with the India-Asia Collision Zone: Journal of Geophysical Research: Solid Earth, v. 91, no. B3, p. 3664–3676.

England, P., and McKenzie, D., 1982, A thin viscous sheet model for continental deformation: Geophysical Journal International, v. 70, no. 2, p. 295–321, doi: 10.1111/j.1365-246X.1982.tb04969.x.

England, P., and Searle, M., 1986, The Cretaceous-tertiary deformation of the Lhasa Block and its implications for crustal thickening in Tibet: Tectonics, v. 5, no. 1, p. 1–14.

Garzione, C. N., DeCelles, P.G., Hodkinson, D.G., Ojha, T.P., Upreti, B.N., 2003, East-west extension and Miocene environmental change in the southern Tibetan plateau: Thakkhola graben, central Nepal: Geol. Soc. Am. Bull., v. 115, no. 1, p. 3–20.

Gubbels, T.L., Isacks, B.L., and Farrar, E., 1993, High-level surfaces, plateau uplift, and foreland development, Bolivian central Andes: Geology, v. 21, p. 695–698, doi: 10.1093/petrology/egl007.

Guo, Z., Wilson, M., Liu, J., and Mao, Q., 2006, Post-collisional, Potassic and Ultrapotassic Magmatism of the Northern Tibetan Plateau: Constraints on Characteristics of the Mantle Source, Geodynamic Setting and Uplift Mechanisms: Journal of Petrology, v. 47, p. 302–310.

Hetzel, R., Dunkl, I., Haider, V., Strobl, M., Von Eynatten, H., Ding, L., and Frei, D., 2011, Peneplain formation in southern Tibet predates the India-Asia collision and plateau uplift: Geology, v. 39, no. 10, p. 983–986, doi: 10.1130/G32069.1.

Isacks, B.L., 1988, Uplift of the central Andean plateau and bending of the Bolivian orocline: Journal of Geophysical Research, v. 93, p. 3211-3231.

Jiang, Y.-H., Jiang, S.-Y., Ling, H.-F., and Dai, B.-Z., 2006, Low-degree melting of a metasomatized lithospheric mantle for the origin of Cenozoic Yulong monzogranite-porphyry, east Tibet: Geochemical and Sr–Nd–Pb–Hf isotopic constraints: Earth and Planetary Science Letters, v. 241, p. 617–633, doi: 10.1016/j.epsl.2005.11.023.

Jolivet, M., Brunel, M., Seward, D., Xu, Z., Yang, J., Malavieille, J., Roger, F., Leyreloup, A., Arnaud, N., and Wu, C., 2003, Neogene extension and volcanism in the Kunlun Fault Zone,

northern Tibet: New constraints on the age of the Kunlun Fault: Tectonics, v. 22, p. 1–23, doi: 10.1029/2002TC001428.

Kapp, P., Yin, A., Harrison, T.M., and Ding, L., 2005, Cretaceous-Tertiary shortening, basin development, and volcanism in central Tibet: Geological Society of America Bulletin, v. 117, no. 7, p. 865–878, doi: 10.1130/B25595.1.

Kapp, P., DeCelles, P.G., Leier, A.L., Fabijanic, J.M., He, S., Pullen, A., and Gehrels, G.E., 2007a, The Gangdese retroarc thrust belt revealed: GSA Today, v. 17, no. 7, p. 4–9.

Kapp, P., DeCelles, P.G., Gehrels, G.E., Heizler, M., and Ding, L., 2007b, Geological records of the Lhasa-Qiangtang and Indo-Asian collisions in the Nima area of central Tibet: Geological Society of America Bulletin, v. 119, no. 7-8, p. 917–933, doi: 10.1130/B26033.1.

Karplus, M.S., Zhao, W., Klemperer, S.L., Wu, Z., Mechie, J., Shi, D., Brown, L.D., and Chen, C., 2011, Injection of Tibetan crust beneath the south Qaidam Basin: Evidence from INDEPTH IV wide-angle seismic data: Journal of Geophysical Research, v. 116, p. 1–23, doi: 10.1029/2010JB007911.

Klemperer, S.L., 2006, Crustal flow in Tibet: geophysical evidence for the physical state of Tibetan lithosphere, and inferred patterns of active flow: Geological Society, London, Special Publications, v. 268, p. 39–70, doi: 10.1144/GSL.SP.2006.268.01.03.

Lai, S.-C., Liu, C.-Y., and Yi, H.-S., 2003, Geochemistry and Petrogenesis of Cenozoic Andesite-Dacite Associations from the Hoh Xil Region, Tibetan Plateau: International Geology Review, v. 45, p. 998–1019, doi: 10.2747/0020-6814.45.11.998.

Lee, J., Hager, C., Wallis, S.R., Stockli, D.F., Whitehouse, M.J., Aoya, M., Wang, Y., 2011, Middle to late Miocene extremely rapid exhumation and thermal reequilibration in the Kung Co rift, southern Tibet: Tectonics, v. 30, no. TC2007, doi:10.1029/2010TC002745.

Liu, Z., Wang, C., and Yi, H., 2001, Evolution and mass accumulation of the Cenozoic Hoh Xil Basin, Northern Tibet: Journal of Sedimentary Research, v. 71, no. 6, p. 971 – 984.

Liu, Z., Zhao, X., Wang, C., Liu, S., and Yi, H., 2003, Magnetostratigraphy of Tertiary sediments from the Hoh Xil Basin: implications for the Cenozoic tectonic history of the Tibetan Plateau: Geophysical Journal International, v. 154, no. 2, p. 233–252, doi: 10.1046/j.1365-246X.2003.01986.x.

McCallister, A.T., Taylor, M.H., Murphy, M.A., Styron, R.H., & Stockli, D.F., 2013, Thermochronologic constraints on the late Cenozoic exhumation history of the Gurla

Mandhata metamorphic core complex, Southwestern Tibet: Tectonics, v. 33, p. 27-52.

McKenna, L.W., and Walker, J.D., 1990, Geochemistry of Crustally Derived Leucocratic Igneous Rocks From the Ulugh Muztagh Area, Northern Tibet and Their Implications for the Formation of the Tibetan Plateau: Journal of Geophysical Research, v. 95, p. 21483 – 21502.

Molnar, P., England, P., and Martinod, J., 1993, Mantle dynamics, uplift of the Tibetan Plateau, and the Indian Monsoon: Reviews in Geophysics, v. 31, no. 4, p. 357–396.

Murphy, M.A., Yin, A., Harrison, T.M., Dürr, S.B., Z, C., Ryerson, F.J., Kidd, W.S.F., X, W., and X, Z., 1997, Did the Indo-Asian collision alone create the Tibetan plateau?: Geology, v. 25, no. 8, p. 719–722, doi: 10.1130/0091-7613(1997)025<0719:DTIACA>2.3.CO;2.

Murphy, M. a., Yin, A., Kapp, P., Harrison, T.M., Manning, C.E., Ryerson, F.J., Lin, D., and Jinghui, G., 2002, Structural evolution of the Gurla Mandhata detachment system, southwest Tibet: Implications for the eastward extent of the Karakoram fault system: Geological Society of America Bulletin, v. 114, no. 4, p. 428–447, doi: 10.1130/0016-7606(2002)114<0428:SEOTGM>2.0.CO;2.

Owens, T.J., and Zandt, G., 1997, Implications of crustal property variations for models of Tibetan plateau evolution: Nature, v. 387, p. 37 – 43.

Polissar, P.J., Freeman, K.H., Rowley, D.B., McInerney, F.A., and Currie, B.S., 2009, Paleoaltimetry of the Tibetan Plateau from D/H ratios of lipid biomarkers: Earth and Planetary Science Letters, v. 287, p. 64–76, doi: 10.1016/j.epsl.2009.07.037.

Powell, C. M., 1986, Continental underplating model for the rise of the Tibetan Plateau: Earth Planet. Sci. Lett., v. 81, no. 1, p. 79–94.

QBGMR (Qinghai Bureau of Geology and Mineral Resources), 1989a, Geologic map of the Cuorendejia region, scale 1:200,000.

QBGMR (Qinghai Bureau of Geology and Mineral Resources), 1989b, Geologic map of the Tuotuohe region, scale 1:200,000.

Ratschbacher, L., Krumrei, I., lumenwitz, M., Staiger, M., Gloaguen, R., Miller, B.V., Samson, S.D., Edwards, M.A., Appel, E., 2011, Rifting and strike-slip shear in central Tibet and the geometry, age and kinematics of upper crustal extension in Tibet: Geol. Soc. Spec. Publ., v. 353, no. 1, p. 127–163, doi:10.1144/SP353.8.

Rohrmann, A., Kapp, P., Carrapa, B., Reiners, P.W., Guynn, J., Ding, L., and Heizler, M., 2012, Thermochronologic evidence for plateau formation in central Tibet by 45 Ma: Geology, v. 40, no. 2, p. 187–190, doi: 10.1130/G32530.1.

Styron, R.H., Taylor, M.H., Sundell, K.E., Stockli, D.F., Oalmann, J.A., Möller, A., Liu, D., Ding, L., 2013, Miocene initiation and acceleration of extension in the South Lunggar rift, western Tibet: Evolution of an active detachment system from structural mapping and (U-Th)/He thermochronology: Tectonics, v. 32, no. 4, p. 880-907.

Sundell, K.E., Taylor, M.H., Styron, R.H., Stockli, D.F., Kapp, P., Hager, C., Liu, D., Ding, L., 2013, Evidence for constriction and Pliocene acceleration of east-west extension in the North Lunggar rift region of west central Tibet: Tectonics, v. 32, no. 5, p. 1454-1479.

Tapponnier, P., Shu, Z., Roger, F., Meyer, B., Arnaud, N., Wittlinger, G., and Jingsui, Y., 2001, Oblique stepwise rise and growth of the Tibet Plateau: Science, v. 294, p. 1671–1677, doi: 10.1126/science.105978.

Vergne, J., Wittlinger, G., Hui, Q., Tapponnier, P., Poupinet, G., Mei, J., Herquel, G., and Paul, A., 2002, Seismic evidence for stepwise thickening of the crust across the NE Tibetan plateau: Earth and Planetary Science Letters, v. 203, p. 25–33, doi: 10.1016/S0012-821X(02)00853-1.

Wang, C.S., Liu, Z.F., Yi, H.S., Liu, S., and Zhao, X.X., 2002, Tertiary crustal shortenings and peneplanation in the Hoh Xil region: implications for the tectonic history of the northern Tibetan Plateau: Journal of Asian Earth Sciences, v. 20, p. 211–223.

Wang, Q., McDermott, F., Xu, J., Bellon, H., and Zhu, Y., 2005, Cenozoic K-rich adakitic volcanic rocks in the Hohxil area, northern Tibet: Lower-crustal melting in an intracontinental setting: Geology, v. 33, no. 6, p. 465–468, doi: 10.1130/G21522.1.

Wang, C.S., Zhao, X., Liu, Z., Lippert, P.C., Graham, S.A, Coe, R.S., Yi, H., Zhu, L., Liu, S., and Li, Y., 2008, Constraints on the early uplift history of the Tibetan Plateau.: Proceedings of the National Academy of Sciences of the United States of America, v. 105, no. 13, p. 4987–4992, doi: 10.1073/pnas.0703595105.

Williams, H.M., Turner, S.P., Pearce, J.A., Kelley, S.P., and Harris, N.B.W., 2004, Nature of the Source Regions for Post-collisional, Potassic Magmatism in Southern and Northern Tibet from Geochemical Variations and Inverse Trace Element Modelling: Journal of Petrology, v. 45, p. 555–607, doi: 10.1093/petrology/egg094.

Wittlinger, G., Vergne, J., Tapponnier, P., Farra, V., Poupinet, G., Jiang, M., Su, H., Herquel, G., and Paul, A., 2004, Teleseismic imaging of subducting lithosphere and Moho offsets beneath western Tibet: Earth and Planetary Science Letters, v. 221, p. 117–130, doi: 10.1016/S0012-821X(03)00723-4.

Yakovlev, P. V, and Clark, M.K., 2014, Conservation and redistribution of crust during the Indo-

Asian collision: Tectonics, v. 33, p. 1016–1027, doi: 10.1002/2013TC003469.Received.

Yin, A., Harrison, T.M., Ryerson, F.J., Wenji, C., Kidd, W.S.F., and Copeland, P., 1994, Tertiary structural evolution of the Gangdese Thrust System, southeastern Tibet: Journal of Geophysical Research, v. 99, p. 18175–18201, doi: 10.1029/94JB00504.

Yin, A., Rumelhart, P.E., Butler, R., Cowgill, E., Harrison, T.M., Foster, D. a., Ingersoll, R.V., Qing, Z., Xian-Qiang, Z., Xiao-Feng, W., Hanson, A., and Raza, A., 2002, Tectonic history of the Altyn Tagh fault system in northern Tibet inferred from Cenozoic sedimentation: Geological Society of America Bulletin, v. 114, p. 1257–1295, doi: 10.1130/0016-7606(2002)114<1257:THOTAT>2.0.CO;2.

Yin, A., Dang, Y.Q., Wang, L.-C., Jiang, W.-M., Zhou, S.-P., Chen, X.-H., Gehrels, G.E., and McRivette, M.W., 2008, Cenozoic tectonic evolution of Qaidam basin and its surrounding regions (Part 1): The southern Qilian Shan-Nan Shan thrust belt and northern Qaidam basin: Geological Society of America Bulletin, v. 120, p. 813–846, doi: 10.1130/B26180.1.

Zhang, P.-Z., Shen, Z., Wang, M., Gan, W., Bürgmann, R., Molnar, P., Wang, Q., Niu, Z., Sun, J., Wu, J., Hanrong, S., and Xinzhao, Y., 2004, Continuous deformation of the Tibetan Plateau from global positioning system data: Geology, v. 32, no. 9, p. 809, doi: 10.1130/G20554.1.

Zhao, W. and Morgan, W.J., 1987, Injection of Indian crust into Tibetan lower crust: A two-dimensional finite element model study: Tectonics, v. 6, no. 4, p. 489–504.

Chapter II

A Cretaceous-Eocene depositional age for the Fenghuoshan Group, Hoh Xil Basin: Implications for the tectonic evolution of the northern Tibetan Plateau[1]

Abstract

The Fenghuoshan Group marks the initiation of terrestrial deposition in the Hoh Xil Basin and preserves the first evidence of uplift above sea level of northern Tibet. The depositional age of the Fenghuoshan Group is debated as are the stratigraphic relationships between the Fenghuoshan Group and other terrestrial sedimentary units in the Hoh Xil Basin. We present new radiometric dates and a compilation of published biostratigraphic data which are used to reinterpret existing magnetostratigraphic data from the Fenghuoshan Group. From these data, we infer an 85 – 51 Ma depositional age range for the Fenghuoshan Group. U-Pb detrital zircon age spectra from this unit are compared to age spectra from Tibetan terranes and Mesozoic sedimentary sequences to determine a possible source terrane for Fenghuoshan Group strata. We propose that these strata were sourced from the Qiangtang Terrane and may share a common sediment source with Cretaceous sedimentary rocks in Nima Basin. Field relationships and compiled biostratigraphic data indicate that the Fenghuoshan and Tuotuohe Groups are temporally distinct units. We report late Oligocene ages for undeformed basalt flows that cap tilted Fenghuoshan Group strata. Together, our age constraints and field relationships imply exhumation of the central Qiangtang Terrane from the Late Cretaceous to earliest Eocene, followed by Eocene-Oligocene deformation, and shortening of the northern Qiangtang and southern Songpan-Ganzi terranes. Crustal shortening within the Hoh Xil Basin ceased by late Oligocene time as is evident from flat-lying basaltic rocks, which cap older, deformed strata.

[1] Citation: Staisch, L. M., N. A. Niemi, C. Hong, M. K. Clark, D. B. Rowley, and B. Currie (2014), A Cretaceous-Eocene depositional age for the Fenghuoshan Group, Hoh Xil Basin: Implications for the tectonic evolution of the northern Tibet Plateau, Tectonics, 33, 281–301, doi:10.1002/2013TC003367.

2.1. Introduction

For decades, the Tibetan Plateau has been studied as an example of Cenozoic continental collision and associated crustal thickening and topographic growth. Numerical and conceptual models have generally considered the Indo-Asian collision to be a single, ongoing tectonic event that has led to the growth of the Tibetan Plateau. Such models have invoked a variety of mechanisms to build Tibet, including continental underplating of India (Argand, 1924; Powell, 1986; Zhao and Morgan, 1987), distributed shortening and thickening of the Eurasian lithosphere (England and McKenzie, 1982; Dewey et al., 1988; England and Houseman, 1986), progressive stepwise uplift along discrete lithospheric blocks (Tapponnier et al., 2001), or removal of the mantle lithosphere followed by replacement with hot, buoyant asthenosphere (Molnar et al., 1993). The southern margin of Eurasia, however, has been the site of active subduction and continental accretion since the early Mesozoic (Dewey et al., 1988; Şengör and Natal'in, 1996; Yin and Harrison, 2000), and the transition from oceanic subduction to continental collision in any such Alpine-style orogeny may include events such as accretion of small island arcs or continental fragments, rifting and closure of interarc basins, and orogenesis during the subduction phase. These processes affect the rheology and elevation of the continental margin prior to continental collision (Cloos, 1993; Boutelier et al., 2003) and may give rise to a unique deformation pattern within the orogen itself (Royden and Burchfiel, 1989; Dilek, 2006).

It has been proposed that much of the ~2500 – 3000 km convergence of India with Eurasia since the widely accepted ~50 Ma age of Indo-Asian collision (Rowley, 1996; Molnar and Stock, 2009; Dupont-Nivet et al., 2010; Najman et al., 2010) was accommodated via crustal shortening (Dewey et al., 1988; England and Houseman, 1986; Dupont-Nivet et al., 2004; Najman et al., 2010). However, the amount of crustal shortening required to accommodate postcollisional Indo-Asian convergence is difficult to reconcile, particularly since there is relatively little evidence for large-scale crustal shortening in the Lhasa and southern Qiangtang terranes since 50 Ma (Burg et al., 1983; England and Searle, 1986; Murphy et al., 1997; Kapp et al., 2005, 2007a, 2007b; DeCelles et al., 2007a; Hetzel et al., 2011; Rohrmann et al., 2012). The formation of a thick continental margin by the Late Cretaceous may have preconditioned the Asian lithosphere's response to further deformation, such that high gravitational potential energy in southern Tibet would inhibit further thickening and elevation gain (England and Searle, 1986; Kong et al., 1997). Instead, a precollisional thick continental margin may favor syncollisional and postcollisional crustal thickening in regions to the north, more distal to the plate boundary and may explain limited surface deformation observed

within the Lhasa and southern Qiangtang terranes during the early to mid-stages of continental collision.

The Hoh Xil Basin, located in north central Tibet, contains a generally complete stratigraphic sequence that ranges from Late Cretaceous to Miocene in age. This locale potentially records the far-field lithospheric response of the transition from subduction to collision at the Indo-Asian plate boundary. Tectonic interpretation of geologic and geochemical data derived from sedimentary strata within the Hoh Xil Basin relies heavily on the depositional age of these strata. However, the timing of deposition in the Hoh Xil Basin, as well as the division of lithostratigraphic units, their depositional relationships, and stratigraphic nomenclature are subject to debate (Yin et al., 1988; Zhong, 1989; Li and Yuan, 1990; Ji, 1994; Liu et al., 2001, 2003; An et al., 2004; Yi et al., 2004; Li et al., 2012). In this study, we redefine the depositional age of nonmarine strata in the Hoh Xil Basin based on new radiometric ages from volcanic units and reinterpretation of biostratigraphic and magnetostratigraphic records. Based on our revised depositional ages for nonmarine strata and field observations, we reevaluate the stratigraphy of the Hoh Xil Basin and its significance for understanding the tectonic evolution of the Tibetan Plateau.

2.2. Geologic Setting

The Fenghuoshan Group (风火山群) is a sedimentary sequence that was deposited within the Hoh Xil Basin, an 83,000 km2 region in the north central Tibetan Plateau that extends from the Tanggula Shan northward to the Kunlun Shan (Figure 2.1). The sedimentary sequence overlies and obscures the Jinsha Suture; thus, the Fenghuoshan Group was deposited within the northernmost Qiangtang and southernmost Songpan-Ganzi terranes. The main subbasin in which the Fenghuoshan Group was deposited is located near the town of Erdaguo, in what is now the Fenghuoshan Range (Figure 2.1). The Fenghuoshan Range extends roughly 35 km north to south and reaches elevations of ~5300m. Postdepositional deformation of the Fenghuoshan Range has resulted in the exposure of ~5.8 km of the Fenghuoshan Group (Zhong, 1989) in the hanging wall of a regionally extensive thrust fault (Figure 2.1), one of the most stratigraphically extensive sections known for this sedimentary unit.

The Fenghuoshan Group is terrestrial in origin and is largely composed of mudstone, siltstone, sandstone, and conglomerate as well as subordinate limestone and evaporite layers (Leeder unconformably over the Triassic Jieza (结扎群), Triassic Batang (巴颜喀拉山群), and

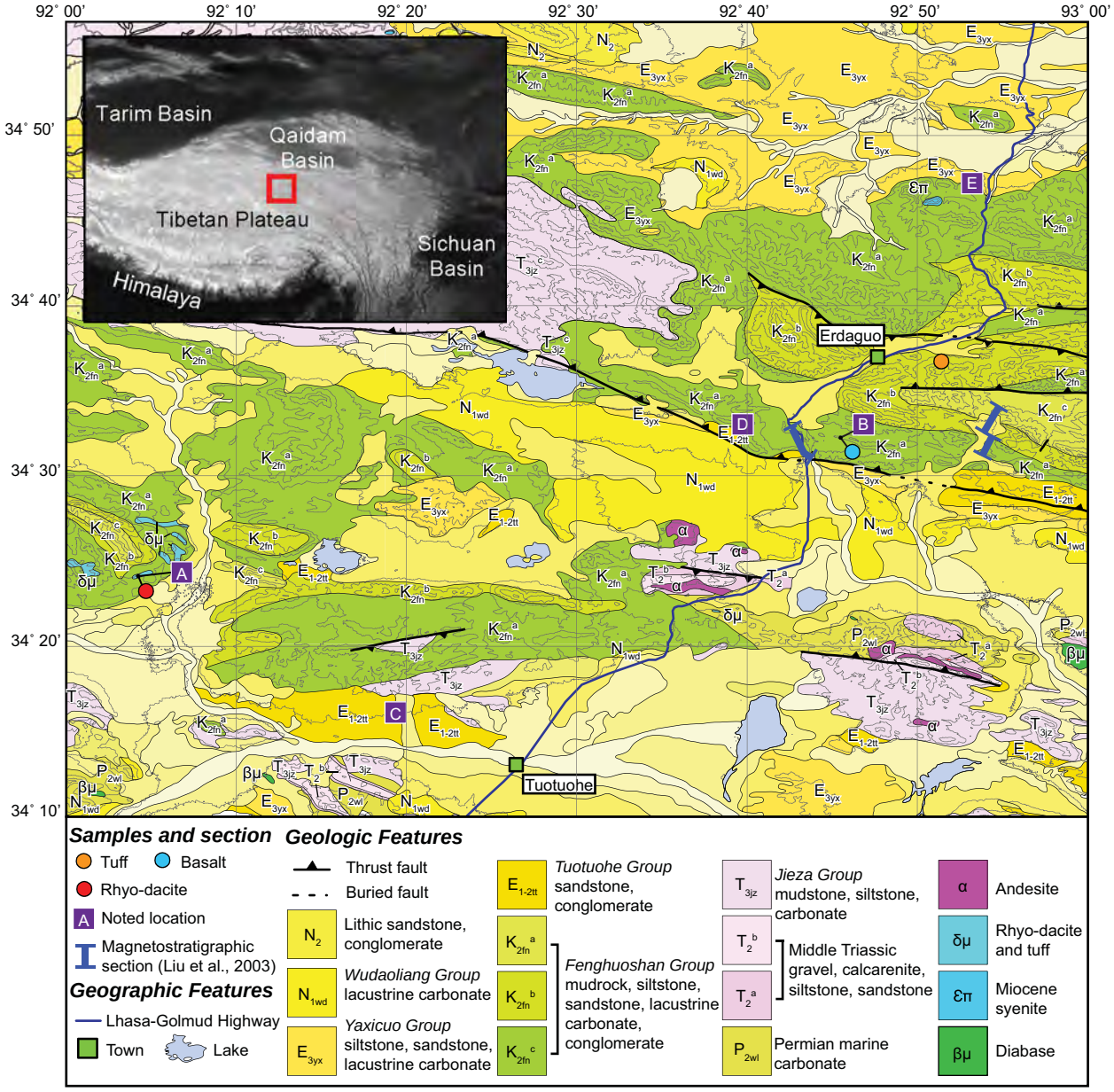

Figure 2.1. Geologic map of the area around the Fenghuoshan Range, Hoh Xil Basin (modified from Qinghai Bureau of Geologic and Mineral Resources (QBGMR) (1989a, 1989b)), showing sample locations and published magnetostratigraphic section (Liu et al., 2001, 2003). Inset map of the Tibetan orogen shows location of geologic map. Chronostratigraphic divisions indicated on geologic units are N2: Pliocene, N1: Miocene, E3: Oligocene, E1-2: Paleocene-Eocene, K2: Upper Cretaceous, T3: Late Triassic, T2: Middle Triassic, P2: Guadalupian. Lettered locations in purple boxes correspond to photographs in Figure 2.4, except for location F which has no corresponding photo.

Jurassic Yanshiping (雁石坪群) Groups (Kidd et al., 1988; Qinghai Bureau of Geology and Mineral Resources (QBGMR), 1989a, 1989b; An et al., 2004). The depositional environment of the Fenghuoshan Group is predominantly fluvial and fan delta, with a minor distal lacustrine component (Leeder et al., 1988; Liu and Wang, 2001a; Liu et al., 2001). Paleocurrent directions suggest that the Fenghuoshan Group was sourced predominantly from the south (Leeder et al., 1988; Liu and Wang, 2001b; Liu et al., 2001; Yi et al., 2008; Li et al., 2012). The sedimentary rocks of the Fenghuoshan Group are characteristically deep brick red to purple in color, with occasional copper-bearing green sandstone (Yin et al., 1988; Li et al., 2005), indicating considerable oxidation. Fossils present in the Fenghuoshan Group include ostracods, gastropods, charophytes, pollen, and plant material (Leeder et al., 1988; Yin et al., 1988; QBGMR, 1989a, 1989b; Zhong, 1989; Li and Yuan, 1990; Liu et al., 2001; An et al., 2004; Cyr et al., 2005).

Overlying the Fenghuoshan Group are the fluvial and lacustrine Tuotuohe (沱沱河群) and Yaxicuo (雅西措群; also published as the Chabaoma) Groups (Yin et al., 1988; QBGMR, 1989a, 1989b; An et al., 2004). These strata exhibit relatively moderate syndepositional to postdepositional deformation. The Miocene Wudaoliang Group (五道梁群), which is composed of lacustrine carbonate and unconformably overlies the Yaxicuo Group, exhibits only mild deformation (Liu and Wang, 2001a; Liu et al., 2001, 2003; Z. Duan et al., 2007; Li et al., 2012). The stratigraphic relationships between the Fenghuoshan, Tuotuohe, and Yaxicuo Groups are a subject of debate, discussed more thoroughly below.

Subordinate volcanic deposits are preserved within, and depositionally on, the Fenghuoshan Group throughout the central Hoh Xil Basin. Within the Fenghuoshan Range, volcanic tuff layers interbedded within the Fenghuoshan Group are rare but present. Tuff and rhyodacitic (?) lava flows, which are interbedded within deformed fluvial red beds mapped as the lower Fenghuoshan Group, are exposed in an ~15 km wide syncline to the southwest of the Fenghuoshan Range (Figure 2.1) (QBGMR, 1989b). Near the southern margin of the Fenghuoshan Range, subhorizontal basalt flows and associated ash layers are locally exposed and unconformably overlie steeply dipping beds of the Fenghuoshan Group (Figure 2.1). In addition to volcanic deposits, syenitic and granitic plutonic bodies are interpreted to have intruded into previously deformed Fenghuoshan and Yaxicuo Group strata (Wu et al., 2007; unpublished data cited in Cyr et al., 2005). The age constraints provided by these intrusive bodies are discussed below.

2.3. New Age Constraints

2.3.1. Biostratigraphy

Biostratigraphic data can provide useful constraints on the depositional age of sedimentary strata; however, the robustness of age constraints is dependent on the level of detail and completeness of the data collected. Within the Hoh Xil Basin, detailed biostratigraphic studies of the Tuotuohe, Yaxicuo, and Wudaoliang Groups provide fossil identification, stratigraphic position, and relative abundance of 252 unique taxa, yielding reliable age control. These studies suggest depositional ages for the Tuotuohe, Yaxicuo, and Wudaoliang Groups of Paleocene to early Oligocene, Oligocene, and early Miocene, respectively (Liu and Wang, 2001a; Liu et al., 2001, 2003; Z. Duan et al., 2007; Q. Duan et al., 2007; Q. Duan et al., 2008; Li et al., 2012). Biostratigraphic data available for the Fenghuoshan Group, however, are less complete, and derived interpretations of its depositional age are subject to debate. Several studies interpret the flora and fauna as suggesting a Late Cretaceous depositional age (Zhong, 1989; Li and Yuan, 1990; Ji; 1994; An, 2004), while others infer a Paleocene-Oligocene depositional age (Smith and Xu, 1988). Here we compile published biostratigraphic data collected from the Fenghuoshan Group to reevaluate its potential for providing robust age control (Zhong, 1989; QBGMR, 1989a, 1989b; Li and Yuan, 1990; Ji, 1994; Liu et al., 2003; An, 2004).

Compiled biostratigraphic data from the Fenghuoshan Group include 68 taxa identified throughout the unit. Stratigraphic information of fossil occurrences throughout the section is reported and plotted in Figure 2.2a. The detail of stratigraphic localities reported for each identified fossil varies between studies, ranging from tens to thousands of meters, and relative abundances of individual taxa are not reported. Most studies from which we compile biostratigraphic data do not span the entire stratigraphic thickness of the Fenghuoshan Group but rather focus on the lower ~1700m of the unit. Therefore, the stratigraphic range over which taxa exist may not be fully realized. Age ranges for each individual fossil lineage identified in Fenghuoshan Group strata, as well as fossils identified in overlying Tuotuohe, Yaxicuo, and Wudaoliang Group strata, were determined from published global accounts of fossil occurrences (Figure 2.2b; Tables A2.1 – A2.5 in the supporting information). For any individual fossil that was ascribed two or more noncontiguous age ranges, the range used in this study is the inclusive span of all of the age ranges.

The lack of published fossil abundances and the coarse stratigraphic information available for many of the fossils identified within the Fenghuoshan Group limits our ability to construct detailed biozones throughout the stratigraphic unit to assess the depositional age and would

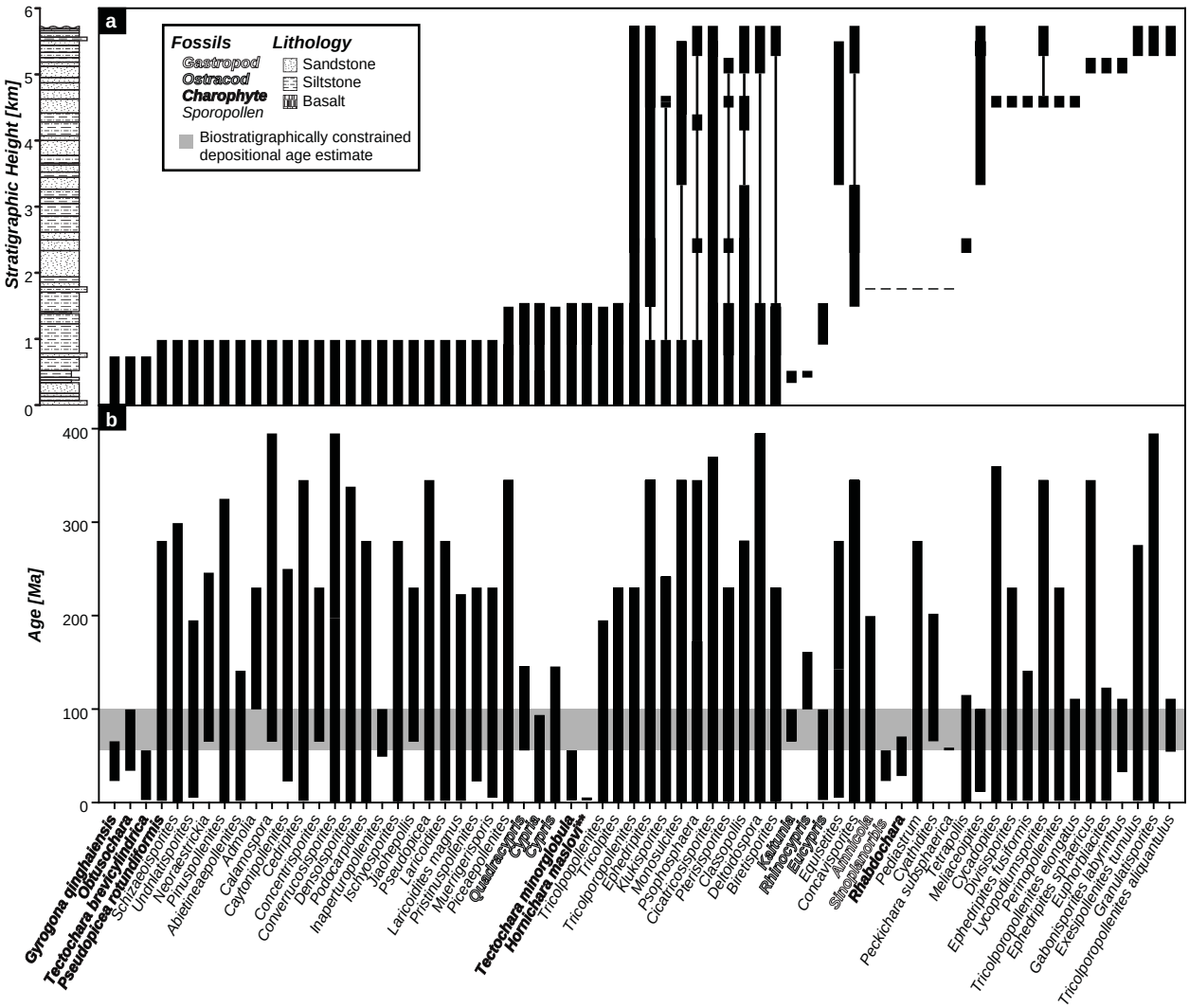

Figure 2.2. Biostratigraphic data ranked by earliest occurrence in the Fenghuoshan Group (QBGMR, 1989a; 1989b; Zhong, 1989; Liu and Yuan, 1990; Ji, 1994; Liu et al., 2003; An, 2004). (a) Stratigraphic column on the left (Zhong, 1989), along with individual taxa and their reported stratigraphic occurrences. Thick lines indicate stratigraphic ranges over which the fossils have been identified. Thin lines indicate the intervening statigraphic range between reported fossil occurrences. (b) Global age ranges for individual fossil lineages are shown as vertical black lines. Lineage age ranges are from published accounts of fossil occurrences (citations and lineage age ranges provided in Supplementary Data, Tables A2.1 – A2.5). Horizontal grey bar indicates the biostratigraphically constrained age range of 56 to 100 Ma from these fossils by the overlap of the oldest last occurrence and the youngest first occurrence.

potentially result in misconstrued fossil assemblages that either omit important taxa for which there is limited stratigraphic information or place emphasis on taxa that are relatively scarce. Instead, we consider the depositional age range of the Fenghuoshan Group to span from the youngest first occurrence to the oldest last occurrence of all fossils identified. Using this approach, the depositional age range for the Fenghuoshan Group lies between 100 and 56 Ma (Cenomanian-Ypresian; Figure 2.2b). All fossils are equally weighted, which potentially broadens our assessment of the depositional age range of the Fenghuoshan Group. One fossil, Hornichara maslovi, does not lie within this age range and is identified as Pliocene in age. Possible explanations for this misfit include fossil misidentification or that Hornichara maslovi has a broader age range than previously recognized.

We attempt to further refine the depositional age of the Fenghuoshan Group by identifying index fossils that are known regionally and globally to be age restrictive and by comparing fossil taxa of the Fenghuoshan Group with the overlying Tuotuohe, Yaxicuo, and Wudaoliang Groups (Figure A2.1). Ostracods Eucypris and Quadracypris were identified in the lower Fenghuoshan Group (Figure 2.2a) and are also found together in Cenomanian-Santonian (99.6 – 83.6 Ma) fossil assemblages from southern China (Ye, 1994). Similarly, ostracod Kaitunia and pollen fossil Schizaeoisporities were both identified in lower the Fenghuoshan Group (Figure 2.2a) and are known to occur coevally in Upper Cretaceous strata from the Hengyang and Songliao basins (Mateer and Chen, 1992; Zhang et al., 2007). Sporopollen fossils Jiaohepollis, Pristinuspollenites, Pseudopicea, Biretisporites, Concavisporites, and Converrucosisporites were identified within the Fenghuoshan Group and are reportedly Cretaceous taxa that disappear after the Maastrichtian (< 65 Ma) (Chen, 1988; Li and Liu, 1994; Li et al., 2011). In the Jiansu Basin, Schizaeoisporites is identified as an index fossil for the Upper Cretaceous Tiazhou Formation and occurs along with sporopollen taxa Gabonisporis, Pterisisporites, Deltoidospora, Classopollis, Exesispollenites, Ephedripites, Podocarpidites, Cedripides, Pinuspollenites, and Inaperturopollenites (Mateer and Chen, 1992; Song et al., 1995) all of which have been identified within the Fenghuoshan Group. Furthermore, Densoisporities, Gabonisporites, and Exesipollenites, which are present in the Fenghuoshan Group but absent from Tuotuohe and Yaxicuo Groups (Q. Duan et al., 2007; Z. Duan et al., 2007; Duan et al., 2008), are common in Upper Cretaceous strata but absent from Tertiary strata from southeast China (Song and Huang, 1997). Charophyte taxa Peckichara is found in Upper Cretaceous to Eocene strata (Van Itterbeeck et al., 2007), and fossils Peckichara subsphaerica, Rhabdochara, Gyrongona, and Obtusochara found in the Fenghuoshan Group are similar to assemblages of Paleocene and early Eocene strata in the Sanshui Basin (Chen and Xie, 2011). Juglans, Betula,

Ostrya, and Alnus pollen, which evolved in middle Eocene time (Crane and Stockey, 1987; Manchester, 1987), are absent in the Fenghuoshan Group but are present in the overlying Tuotuohe, Yaxicuo, and Wudaoliang Groups. This may suggest that deposition of the Fenghuoshan Group ceased before the middle Eocene. Overall, biostratigraphic data from the Fenghuoshan Group share many taxa with Upper Cretaceous nonmarine strata in China, as well as some similarities with nonmarine Paleocene and early Eocene strata.We suggest that our biostratigraphically constrained Cenomanian- Ypresian depositional age for the Fenghuoshan Group is relatively accurate and at the very least provides a rough depositional age constraint for more precise age dating, discussed below.

2.3.2. Uranium-Lead Methods

High-precision U-Pb dates were acquired from a volcanic tuff interbedded in the Fenghuoshan Group (Figure 2.1) using chemically abraded thermal ionization mass spectrometry (CA-TIMS) at the Boise State University Isotope Geology Laboratory. Zircon separates were obtained using standard magnetic and density techniques, mounted in epoxy, and polished to expose crystal cores. Because cathodoluminescence (CL) images of the zircon crystals suggested the possibility of crystal zonation and inherited cores (Figure A2.2), 56 zircon grains were dated using laser ablation inductively coupled plasma mass spectrometry (LA-ICPMS) prior to high-precision CA-TIMS analysis.

U-Pb spot analyses were completed using a ThermoElectron X-Series II quadrupole ICPMS and New Wave Research UP-213 Nd: YAG UV LA system with a spot diameter of 25 μm. Background count rates, which were measured before individual spot analyses, were subtracted from raw count rates. U-Pb dates were corrected for instrumental $^{206}Pb/^{238}U$ and $^{207}Pb/^{206}Pb$ ratio fractionation and calibrated using isotopic ratio measurements of a Plešovice zircon standard (Sláma et al., 2008). U-Pb age error includes counting statistic and background subtraction uncertainty. U-Pb dates and associated errors (2σ) are reported in Table A2.6 and compared to detrital U-Pb zircon ages from the Fenghuoshan Group (Figure 2.3a) (Dai et al., 2012). LA-ICPMS $^{206}Pb/^{238}U$ zircon dates are taken to give the best estimate of crystallization age for these relatively young zircons and range between 107 ± 7 and 56 ± 3 Ma. The faceted appearance of zircon crystals (Figure A2.2), similarity in zircon chemistry, exhibited by low Th/Y ratios and uniform steepness of middle to heavy rare earth element slopes (Figure A2.4 and Table A2.6) (e.g., Rivera et al., 2013), and lack of overlap with detrital U-Pb zircon ages from the Fenghuoshan Group (Figure 2.3a) (Dai et al., 2012) indicate that the U-Pb zircon ages from the tuff are from a single eruptive event and are unlikely to

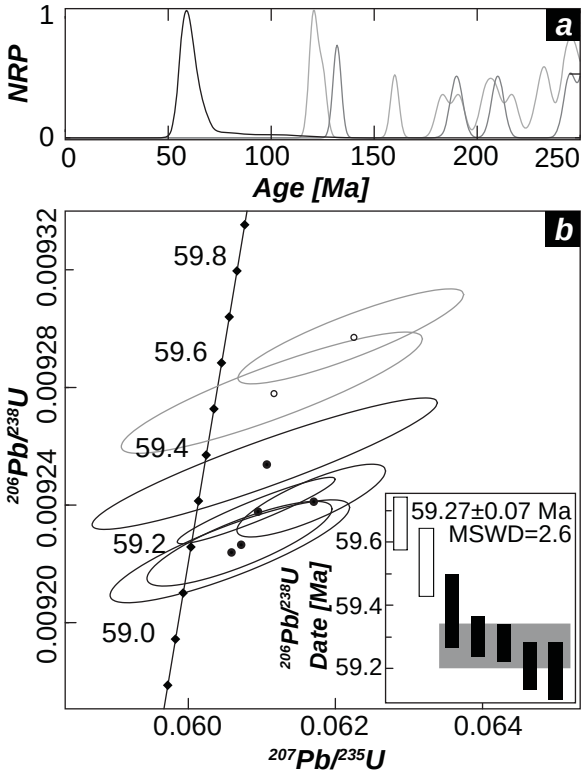

Figure 2.3. U-Pb zircon geochronologic constraints on the depositional age of the Fenghuoshan Group. (a) Normalized relative probability (NRP) plot of Fenghuoshan Group detrital zircon dates (grey; n=78) (Dai et al., 2012) and LA-ICPMS U-Pb zircon dates (black; n=56; this study) from a tuff interbedded within the Fenghuoshan Group. (b) Concordia diagram of zircons from the same tuff. Inset is a ranked age plot showing agreement between five youngest dates with a mean CA-TIMS zircon date of 59.27 Ma. Grey bar indicates overlap of five youngest zircon dates.

have experienced reworking postdeposition. The distribution in ages observed in LA-ICPMS analysis may be explained by xenocrystic contamination during eruption or loss of radiogenic Pb after zircon crystallization (Schoene et al., 2010), and we note that the range in zircon U-Pb ages present in the tuff is consistent with the duration of magmatism in the Gangdese arc (Figure A2.5) (Wen et al., 2008), suggesting a possible eruptive source. On the basis of zircon morphology and zonation based on CL images (Figure A2.2), 38 grains were determined to be autocrystic, while the remaining 18 were assumed to be xenocrystic. The weighted mean LA-ICPMS U-Pb age of the 38 autocrystic zircon grains is 58.8± 0.6 Ma (mean square weighted deviation (MSWD) = 2.4; Figure A2.3 and Table A2.6).

CA-TIMS U-Pb analyses were performed on the seven youngest zircon grains determined by LA-ICPMS analysis because the younger zircons are most likely to record the age of eruption (Schoene et al., 2010). The analyses were obtained using a methodology modified from Mattinson (2005) on a GV Isoprobe-Tmulticollector TIMS equipped with an ion-counting Daly detector. The zircon grains analyzed were removed from the epoxy mount for analysis and were heated to 900°C for 60 h and partially dissolved in 29M HF at 180°C for 12 h. Grains were then placed in 3.5M HNO3 and ultrasonically cleaned. Each crystal grain was spiked with EARTHTIME mixed ^{233}U-^{235}U-^{205}Pb tracer solution (ET535) and dissolved. U and Pb isotopes were separated from the zircon matrix (Krogh, 1973) and loaded onto single outgassed Re filaments and loaded for TIMS measurement (Gerstenberger and Haase, 1997). U and Pb mass fractions were corrected using ^{233}U-^{235}U and ^{202}Pb-^{205}Pb isotopic ratios of the ET535 tracer solution, respectively. U-Pb dates and associated errors were calculated using procedures of Schmitz and Schoene (2007), ET535 tracer solution (Condon et al., 2007), and U decay constants (Jaffey et al., 1971) and corrected for initial ^{230}Th disequilibrium (Crowley et al., 2007). Ages with 2σ uncertainties are reported in Table A2.7 and illustrated in Figure 2.3b. ^{206}Pb/^{238}U zircon dates range between 59.66 ± 0.08 and 59.19 ± 0.09 Ma, with the five youngest dates obtained using CA-TIMS methodology yield a weighted mean date of 59.27 ± 0.07 Ma (MSWD = 2.4; Figure 2.3b and Table A2.7). We interpret this date to reflect the timing of volcanic tuff deposition.

2.3.3. Argon-Argon Methods

Existing constraints for the depositional age of the Fenghuoshan Group include syenite stocks and a granite porphyry that are interpreted to have intruded the previously deformed Fenghuoshan Group and Yaxicuo Group strata and are dated using ^{40}Ar/^{39}Ar methods at 28.6 ± 0.3

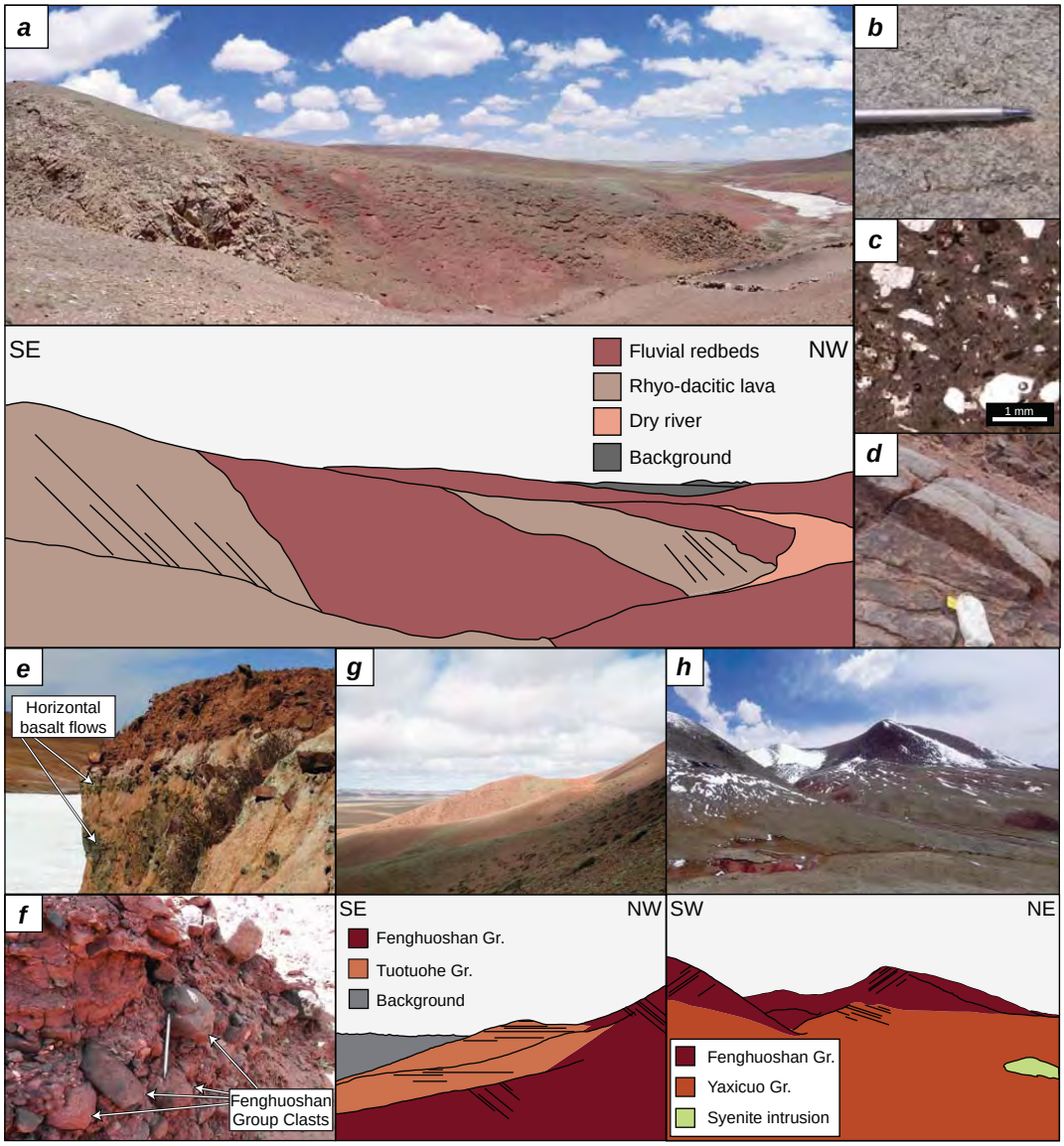

Figure 2.4. Field photographs, thin section photographs, and interpretive sketches of key geologic relationships of both extrusive volcanic rocks and between the Fenghuoshan Group and other Cenozoic sedimentary units. (a) Rhyo-dacitic lava flow interbedded with fluvial redbeds, which have been mapped as the lower Fenghuoshan Group (Figure 2.1, location A) (QBGMR, 1989b). Approximate bedding orientation is shown by horizontal lines. (b) Field photo of rheomorphic banding observed in rhyo-dacitic lava flow. (c) Thin section photograph of rhyo-dacite showing a large percentage of finely crystalline groundmass. (d) Field photo of eutaxitic foliation observed in rhyo-dacite that is sub-parallel to surrounding sedimentary bedding orientation (e) Horizontal basalt lava flows that overlie deformed Fenghuoshan Group strata near Erdagou (Figure 2.1, location B). (f) Tuotuohe Group conglomerate containing a large proportion of rounded cobbles of the Fenghuoshan Group (Figure 2.1, location C). (g) Angular unconformity between the Fenghuoshan and Tuotuohe groups along the southern margin of the Fenghuoshan Range with bedding orientations indicated by straight lines (Figure 2.1, location D). (h) Angular unconformity between the Fenghuoshan and Yaxicuo groups along the northern margin of the Fenghuoshan Range (bedding orientations indicated by straight lines; Figure 2.1, location E).

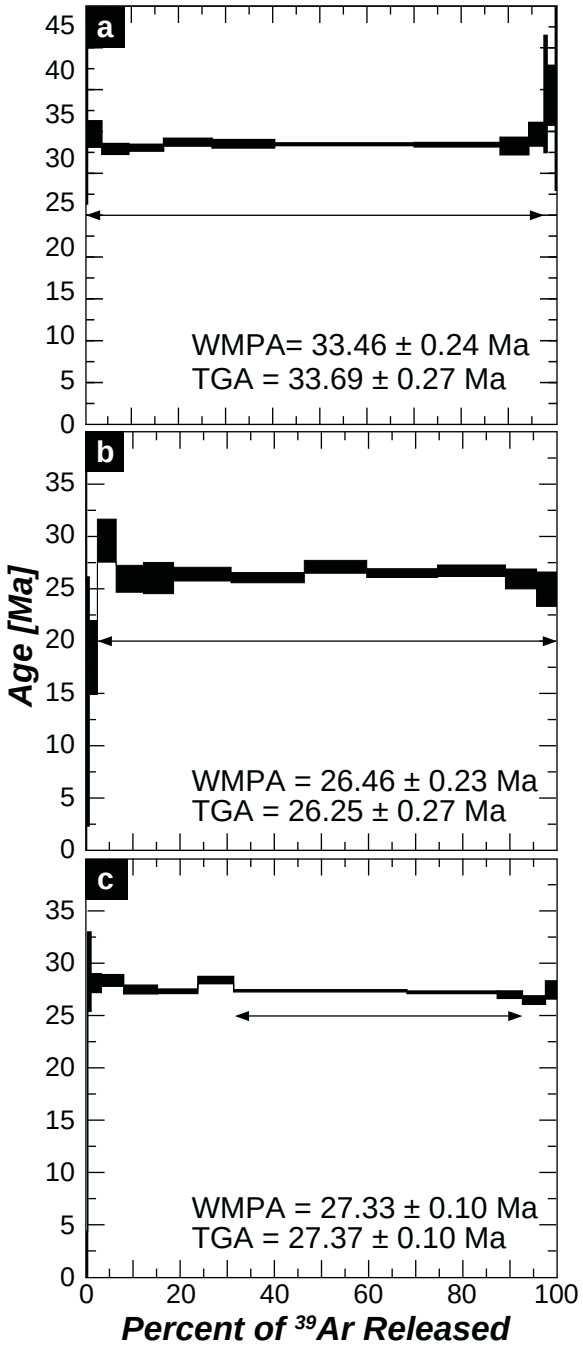

Figure 2.5. $^{40}Ar/^{39}Ar$ geochronologic constraints on the depositional age of the Fenghuoshan Group. (a) $^{40}Ar/^{39}Ar$ spectra for biotites separated from a rhyo-dacite lava flow interbedded within redbeds that are mapped as the lower Fenghuoshan Group (Figure 2.1). (b) and (c) $^{40}Ar/^{39}Ar$ release spectra from biotite separated from horizontal basalt lava flows that unconformably overlie the Fenghuoshan Group near Erdaguo. (b) Sample 11UMT17-A and (c) sample 11UMT17-B. TGA: Total gas age. WMPA: weighted mean plateau age.

and U-Pb zircon methods at 27.6 ± 0.5 Ma, respectively (Wu et al., 2007; D. B. Rowley, unpublished data). We sampled a rhyodacite, which we interpret as a lava flow, interbedded with fluvial red beds that are mapped as the lower Fenghuoshan Group (unit K_{2fn}^{a}) (QBGMR, 1989b), for syndepositional age control (Figures 2.1 and 2.4a). Additionally, two undeformed basalt flows that overlie steeply dipping Fenghuoshan Group beds were collected near the southern margin of the Fenghuoshan Range for postdepositional age control (Figures 2.1 and 2.4e). Ages were measured using biotite $^{40}Ar/^{39}Ar$ dating techniques at the University of Michigan Argon Geochronology Laboratory. Bedrock samples were crushed and sieved to a particle size range of 250 – 1000 μm. The magnetic mineral fraction of the crushed sample was obtained using a Frantz magnetic separator and then shaken manually over a Mylar plastic sheet to concentrate biotite by static force. Biotite crystals for each sample were handpicked under a microscope from the concentrate to ensure purity. The biotite was then packed into pure Al foil and subjected to irradiation for 30 h at the McMaster Nuclear Reactor at McMaster University in packages mc35 and mc40. MMHb-1 was used as a standard with an assumed age of 520.4 Ma (Samson and Alexander, 1987). Biotite was extracted from packets after irradiation and step heated with a Coherent Innova 5W continuous argon ion laser. A VG1200S mass spectrometer with a Daly detector was used for Ar isotope measurement. Fusion system blanks were run every five fusion steps, and blank levels from ^{36}Ar through ^{40}Ar were subtracted from gas fractions. Corrections were made for the decay of ^{37}Ar and ^{39}Ar, K, Ca, and Cl interfering nucleogenic reactions and the production of ^{36}Ar from ^{36}Cl decay. A zero-aged artificial glass sample was used to correct for interfering reactions producing ^{40}Ar. We use the error-weighted average of the plateau age, which corresponds to the flattest portion of the apparent age spectrum, as the best estimate for timing of emplacement. $^{40}Ar/^{39}Ar$ analysis of the rhyodacitic lava yielded a date of 33.46 ± 0.24 Ma (Figure 2.5a; MSWD= 0.39). The upper and lower basalt flows are dated at 26.46 ± 0.23 Ma (MSWD = 0.63) and 27.33 ± 0.1 (MSWD = 0.76), respectively (Figures 2.5b and 2.5c).

2.4. Chronological Interpretations

2.4.1. Revised Age of the Fenghuoshan Group

As previously discussed, the depositional age of the Fenghuoshan Group is debated. Biostratigraphic studies have led to the interpretation that the Fenghuoshan Group is Late Cretaceous (Zhong, 1989; Li and Yuan, 1990; Ji; 1994; An, 2004) or Paleocene to early Eocene in age (Smith and Xu, 1988), based largely on pollen, ostracod, gastropod, and charophyte fossils.

Conversely, magnetostratigraphic studies suggest an Eocene to Oligocene (51 – 31 Ma) age for the Fenghuoshan Group (Liu et al., 2001, 2003). This latter interpretation has been principally adopted by studies over the last decade as the depositional age of the Fenghuoshan Group (Harrison et al., 1992; Cyr et al., 2005; C. Wang et al., 2008; Quade et al., 2011; Dai et al., 2012).

Interpreting the age of the Fenghuoshan Group is also complicated by a lack of consensus on the lateral distribution of the Fenghuoshan Group, and its stratigraphic relationship with the lithologically similar Tuotuohe Group. One interpretation of these two units is that they were deposited synchronously in two adjacent depositional basins (the Fenghuoshan subbasin and Tuotuohe subbasin of the Hoh Xil Basin) and thus are age equivalent (Liu et al., 2005; Li et al., 2012). An alternate interpretation is that the Tuotuohe Group is younger than, and unconformably overlies, the Fenghuoshan Group (Zhong, 1989; QBGMR, 1989a, 1989b; Ji, 1994; An et al., 2004). We will address the stratigraphic relationship between these two units below but focus here on the age of the Fenghuoshan Group from observations that are solely derived from exposures in the Fenghuoshan Range, with the exception of one set of biostratigraphic constraints that were taken from exposures both in and to the south of the Fenghuoshan Range (Ji, 1994).

2.4.1.1. Age of the Fenghuoshan Group in the Fenghuoshan Range

Our new 59.27 Ma U-Pb zircon age from a tuff interbedded with the Fenghuoshan Group strata require that the deposition of these strata is, at least in part, Paleocene in age. The Oligocene ages we have determined of basalt flows overlying the Fenghuoshan Group, combined with existing detrital zircon age spectra (Dai et al., 2012), are used as absolute upper and lower constraints on the depositional age of the Fenghuoshan Group. These constraints place deposition of the Fenghuoshan Group at 121 – 27 Ma. The compiled biostratigraphic data set suggests a more narrow depositional age range of 100 – 56 Ma (Figure 2.2).

Based on these depositional age constraints, we provide a revised correlation of the published magnetostratigraphic record to the geomagnetic polarity timescale (Figure 2.6) (Zhong, 1989; QBGMR, 1989a, 1989b; Li and Yuan, 1990; Ji, 1994; Liu et al., 2001; An, 2004; Dai et al., 2012). The magnetostratigraphic polarity pattern published by Liu et al. (2003) combined sedimentary sections of the Fenghuoshan and Yaxicuo Groups. In our revision, we chose not to include magnetostratigraphic data from the Yaxicuo Group in our reinterpretation. Field evidence from the Fenghuoshan Range indicates an unconformable contact between the Fenghuoshan Group and the overlying Yaxicuo Group. Additionally, magnetostratigraphic samples for the Fenghuoshan

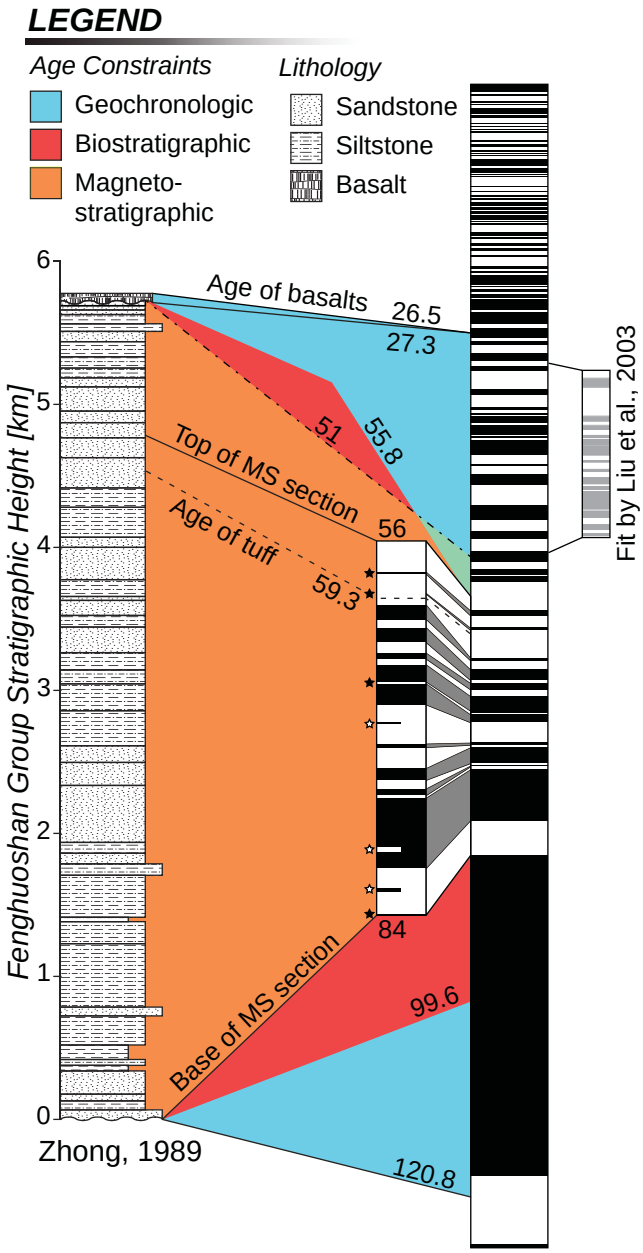

Figure 2.6. Compiled biostratigraphic and radiometric age constraints for the Fenghoshan Group, along with a revised magnetostratigraphic fit and stratigraphic column (as measured by Zhong, (1989)). The possible depositional age range for Fenghuoshan Group strata, constrained by detrital zircon U-Pb age spectra (Dai et al., 2012) and unconformably overlying basaltic lava flows (this study) is shown in cyan. The depositional age constraints inferred from the biostratigraphic compilation (Figure 2.2) is shown in red. The depositional age as constrained from magnetostratigraphy is shown by solid lines. The inferred complete depositional age range of the Fenghuoshan Group, as extended by sediment accumulation rate (Figure 2.8), is shown in orange. The radiometrically dated interbedded volcanic tuff is shown as a dashed line. A previous magnetostratigraphic fit, as published by Liu et al. (2003) is shown to the right of the geomagnetic timescale (Gradstein et al., 2012).

and Yaxicuo Groups were collected from different locations within the Hoh Xil Basin (Liu et al. 2003). Since conformable deposition between these two magnetostratigraphic sections cannot be verified, we argue that the Yaxicuo Group magnetostratigraphy must be correlated to the geomagnetic polarity timescale independent of any correlations made for the Fenghuoshan Group. Because the Yaxicuo Group magnetostratigraphic data contain few magnetic reversals and no precise independent age constraints (Liu et al. 2003), unique correlation with the geomagnetic polarity timescale (GPTS) is not possible at this time.

A revised polarity zonation for the Fenghuoshan Group magnetostratigraphic polarity pattern was devised from paleomagnetic data published by Liu et al. (2003) (Figures 2.6 and A2.6). Polarity zones were defined by two or more samples with sequential characteristic remnant magnetization (ChRM) directions that are clearly normal or reverse in polarity. Published magnetostratigraphic data from the Fenghuoshan Group are correlated to the Gradstein et al. (2012) GPTS using our new age constraints as depositional bounds. We find that the Fenghuoshan Group magnetostratigraphic polarity pattern is best correlated to the GPTS pattern between magnetozones C34n and C24r (Figures 2.6 and A2.6). Four individual magnetozones in the GPTS pattern are not resolved in our revised polarity zonation for the Fenghuoshan Group. By revisiting the Fenghuoshan Group paleomagnetic data, we find that the unresolved GPTS magnetozones are, in fact, recorded, but only with one datum. We include these four magnetozones in the analysis of the Fenghuoshan polarity pattern on the basis that paleomagnetic sampling was conducted at 10 – 12 meter intervals, depending on lithology (Liu et al., 2003), and may have been coarse enough to capture short polarity intervals with only a single sample. Single datum magnetozones included in the Fenghuoshan Group polarity pattern are denoted in Figures 2.6 and A2.6 with black stars. In addition to magnetozones that may be represented by single ChRM measurements, we find that three magnetozones in our reinterpreted polarity pattern are not present in the GPTS. All three uncorrelated magnetozones are defined by two data points that may constrain short intervals and are denoted with white-filled stars in Figures 2.6 and A2.6. Several explanations for minor polarity pattern mismatch are that thin magnetozones observed in the Fenghuoshan Group paleomagnetic data represent short-interval subchrons that are not published in the Gradstein et al. (2012) GPTS, that the primary ChRM directions are fully overprinted such that the recorded paleomagnetic signal does not reflect the true geomagnetic field direction at the time of deposition, or that these specific samples and results are of lesser quality. Without first-hand knowledge of sample quality, resolution, and rock magnetic properties, it is difficult to determine which explanation is likely for mismatched

polarity zones; however, we note that these mismatches are relatively minor compared to the overall magnetic polarity stratigraphy correlation and that the revised correlation satisfies the new age constraints required for correlation and age interpretation. We exclude the three unmatched magnetozones from further analysis.

The base of Liu et al.'s (2003) magnetostratigraphic section was measured ~184m below the oldest reversal (C34n to C33r), and the top of the section was measured ~380m above the youngest reversal (C25n to C24r); thus, the depositional age range of the Fenghuoshan Group extends above and below chrons C25n and C33n, respectively. Furthermore, while the base of the Fenghuoshan Group corresponds to the lowest sample collected for magnetostratigraphic analysis, the full stratigraphic extent of the Fenghuoshan Group extends over 900m beyond the highest magnetostratigraphic sample collected (Zhong, 1989). Therefore, the upper bound of the Fenghuoshan Group depositional age range lies ~1291m above the youngest polarity reversal recorded by paleomagnetic data (Liu et al., 2003). Using a sediment accumulation rate derived from linear regression through our reinterpretation of the magnetostratigraphic data (Figure 2.7), we extrapolate the depositional age of the base (~184m below the oldest recorded reversal) and of the top (~1291m above the youngest recorded reversal) of the Fenghuoshan Group strata. This extrapolation provides a depositional age range for the Fenghuoshan Group of 85 to 51 Ma (Figures 2.6 and 2.7). We therefore propose that the Fenghuoshan Group was deposited from Late Cretaceous (~Santonian/Campanian boundary) to early Eocene (late Ypresian) time.

2.4.1.2. Age of the Fenghuoshan Group (?) in the Tuotuohe Region

In the Tuotuohe region, we collected a rhyodacite lava flow interbedded within deformed red beds in order to constrain the depositional age of those units. Regional geologic maps (QBGMR, 1989a) indicate that the rhyodacite lava is interbedded within the lower Fenghuoshan Group (unit K_{2fn}^{a}; Figures 2.1 and 2.4a). The $^{40}Ar/^{39}Ar$ age determined for the rhyodacite is 33.47 Ma, thus implying that map unit K_{2fn}^{a} is not the same age in the Tuotuohe Basin as in the Fenghuoshan Range. The radiometric age from the rhyodacite lava more closely reflects the biostratigraphic age constraints from strata identified as the Tuotuohe and Yaxicuo Groups. Three possibilities arise from this age: (1) the depositional age range of the Fenghuoshan Group extends from the Late Cretaceous into at least the earliest Oligocene and that the stratigraphy of the Hoh Xil Basin exhibits considerable lateral variation; (2) Fenghuoshan Group strata (as defined from localities in the Fenghuoshan Range) are not exposed in the Tuotuohe subbasin and that the rhyodacitic flow was

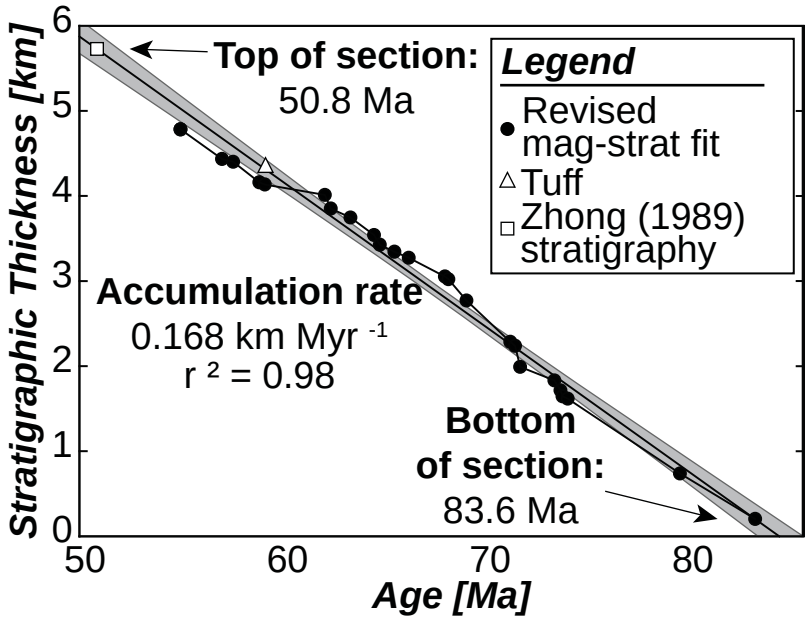

Figure 2.7. Sediment accumulation rate of the Fenghuoshan Group, based on stratigraphic thickness and revised magnetostratigraphic age (black dots; Figure 2.6). The sediment accumulation rate is calculated using linear least squares regression, with 95% confidence interval shaded in grey. White squares are the top and bottom of the Fenghuoshan Group stratigraphic section measured by Zhong (1989), which documents over 5.7 kilometers of continuously deposited Fenghuoshan Group strata. The grey triangle shows the age and assumed stratigraphic thickness of the radiometrically dated volcanic tuff (Figures 2.3 and 2.6).

collected from lithologically similar Tuotuohe Group strata; or (3) we have misinterpreted the rhyodacite as an extrusive lava flow, when it is instead intruded into Fenghuoshan Group strata.

In the third possibility, the rhyodacite may be a sill that has intruded the Fenghuoshan Group, an interpretation that would be in agreement with regional geologic mapping (QBGMR, 1989a). However, the rhyodacite displays a number of characteristics that are indicative of a lava flow, including rheomorphic banding (Figure 2.4b), autobrecciation at the flow margins, and a large percentage (71.2%) of groundmass (Figure 2.4c), which is based on a point count of 1000 points. Although such features are not unique to extrusive flows, they are rarely reported in igneous intrusions, even those known to be hypabyssal (e.g., Orth and McPhie, 2003). The agreement between the orientation of eutaxitic foliation in the rhyodacite (Figure 2.4d) and the orientation of local bedding is also suggestive of an extrusive origin. Nonetheless, if this igneous body is, in fact, intrusive, then the $^{40}Ar/^{39}Ar$ age provides only a minimum depositional age for these red bed strata and does not constrain the timing of deformation in this region. Regardless, the biostratigraphic, geochronologic, and reinterpreted magnetostratigraphic data, described above, imply that the Fenghuoshan Group in the Fenghuoshan Range was deposited in Late Cretaceous to early Eocene time, and the stratigraphic relationships between the Tuotuohe and Fenghuoshan Groups, described below, imply that they are separate geologic units. All of these data underscore the difficulty in constraining absolute depositional age of continental strata on the Tibetan Plateau and the need for additional work to better define the relationships between Cenozoic units in the Hoh Xil region.

2.5. Stratigraphy of the Hoh Xil Basin

Previous studies conducted in the Hoh Xil Basin have inferred several contradictory possibilities for the stratigraphic relationships of the nonmarine sedimentary units. One argument, briefly mentioned above, revolves around whether the Fenghuoshan Group and Tuotuohe Group are lithostratigraphically and chronostratigraphically equivalent. Geologic maps at a scale of 1:200,000 in the Fenghuoshan Range and Tuotuohe region divide Late Cretaceous to Miocene nonmarine sedimentary rocks into four distinct lithologic units: the Fenghuoshan, Tuotuohe, Yaxicuo, and Wudaoliang Groups (QBGMR, 1989a, 1989b). This interpretation of the regional geology of the Hoh Xil Basin contrasts with several local lithostratigraphic and magnetostratigraphic studies of these rocks that consider the Fenghuoshan Group and Tuotuohe Group to be the same stratigraphic unit (Liu et al., 2005; C. Wang et al., 2008; Li et al., 2012). Furthermore, there is disagreement on the depositional boundaries between lithostratigraphic units. The regional geologic

maps and stratigraphic studies that consider the Fenghuoshan and Tuotuohe Groups to be distinct units also consider the Tuotuohe and Yaxicuo Groups to be unconformably deposited on Fenghuoshan Group strata (Figure 2.8a) (Zhong, 1989; Li and Yuan, 1990; Ji, 1994; An, 2004). Conversely, magnetostratigraphic and lithostratigraphic studies from both the Fenghuoshan Range and Tuotuohe Basin report that Yaxicuo strata conformably overlie the Fenghuoshan Group (Figure 2.8b) (Liu et al., 2001, 2003, 2005; Li et al., 2012). Resolving these contradictions in stratigraphic relationships is crucial, as the magnetostratigraphic age interpretations of the Tuotuohe and Yaxicuo Groups rely on stratigraphic correlation with magnetostratigraphic record from the Fenghuoshan Range and the interpretation of depositional contacts between stratigraphic units. Our observations, discussed below, support the interpretation that the Fenghuoshan, Tuotuohe, Yaxicuo, and Wudaoliang Groups are distinct stratigraphic units and that the Tuotuohe and Yaxicuo Groups are unconformably deposited on Fenghuoshan Group strata.

2.5.1. Tuotuohe Group

The Tuotuohe Group is composed of sandstone and conglomerate and shows evidence for moderate postdepositional deformation (Li et al., 2012). The Tuotuohe and Fenghuoshan Groups are lithostratigraphically similar in many locales. However, to the south of the Fenghuoshan Range, clasts of the Fenghuoshan Group are incorporated within gently tilted Tuotuohe Group conglomerate (Figure 2.1, location C; Figure 2.4f). Along the southern margin of the Fenghuoshan Range, the Tuotuohe Group is deposited in angular unconformity on the lower Fenghuoshan Group, which is dipping steeply relative to Tuotuohe Group strata (Figure 2.1, location D; Figure 2.4g). Both units are uplifted along a north dipping thrust fault. These observations suggest that the Tuotuohe and Fenghuoshan Groups are distinct stratigraphic units and that the Tuotuohe Group was deposited after the Fenghuoshan Group was deformed, but before deformation within the Hoh Xil Basin ceased.

2.5.2. Yaxicuo Group

The Yaxicuo Group is exposed on either side of the Fenghuoshan Range as moderately deformed orange buff- colored strata composed of fluvial-lacustrine mudstone, siltstone, and sandstone with interbedded gypsum and lacustrine carbonate (Figure 2.1) (Liu and Wang, 2001a; Liu et al., 2005; Li et al., 2012). On either side of the Fenghuoshan Range, the Yaxicuo Group comes in contact with the lower unit of the Fenghuoshan Group (Figure 2.1). To the north of the

Fenghuoshan Range, an angular unconformity between the Fenghuoshan and Yaxicuo Groups is evidenced by strikingly different bedding orientations between these units (Figure 2.1, location E; Figure 2.4h). The northern margin of the Fenghuoshan Range (Figure 2.1, location E) is marked by an abrupt geomorphic change from steep slopes, in which the lower Fenghuoshan Group strata are exposed, to low-angle slopes, in which the Yaxicuo Group is exposed. Bedding orientations in either unit do not support conformable deposition, but outcrop quality is poor, the contact is obscured, and it is possible that the northern margin of the Fenghuoshan Range is a thrust fault, in which lower Fenghuoshan Group strata is thrust northward over the Yaxicuo Group. A study in the Tuotuohe subbasin, to the south of the Fenghuoshan Range, describes Yaxicuo strata conformably overlying the Fenghuoshan Group (Liu et al., 2005). However, detailed regional geologic maps that differentiate between the Fenghuoshan and Tuotuohe Groups indicate that the Yaxicuo Group is deposited on Tuotuohe Group strata at the study locality. These observations suggest that at least locally, the Yaxicuo Group is conformable with the underlying Tuotuohe Group but is regionally deposited unconformably over the Fenghuoshan Group.

2.5.3. Stratigraphic Interpretation

As mentioned above, previous studies have suggested two stratigraphic interpretations for nonmarine units in the Hoh Xil Basin (Figures 2.8a and 2.8b) (Zhong, 1989; Li and Yuan, 1990; Ji, 1994; Liu et al., 2001, 2003, 2005; An, 2004; Li et al., 2012). However, based on our observed stratigraphic relationships and the biostratigraphically constrained depositional ages of the Tuotuohe and Yaxicuo Groups (Z. Duan et al., 2007; Q. Duan et al., 2007; Duan et al., 2008), which suggest that there may be some chronological overlap between these units in early Oligocene time, we suggest two additional interpretations of the stratigraphy of the Hoh Xil Basin (Figures 2.8c and 2.8d). The first possibility is that the Tuotuohe and Fenghuoshan Groups are distinct stratigraphic units, that the Fenghuoshan Group is unconformably overlain by the Yaxicuo and Tuotuohe Groups, and that the lower Yaxicuo and the upper Tuotuohe Groups were synchronously deposited and represent lateral variability in depositional facies (Figure 2.8c). Alternatively, the Tuotuohe Group may represent continued, syndeformational deposition of the Fenghuoshan Group, in which growth strata produced the angular unconformities we observe along the northern and southern margins of the Fenghuoshan Range, while the Yaxicuo Group was synchronously deposited with the upper member of the Fenghuoshan Group (Figure 2.8d).

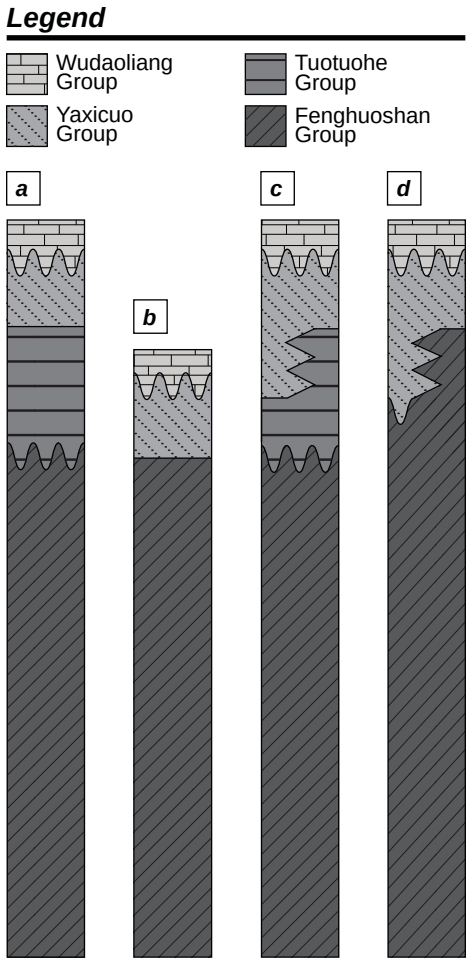

Figure 2.8. Stratigraphic relationships of the Fenghuoshan, Tuotuohe, Yaxicuo, and Wudaoliang groups proposed by (a) Zhong (1989), Li and Yuan (1990), Ji (1994), An (2004) (b) Liu et al., (2001, 2003, 2005), Li et al.(2011); (c) and (d) this study.

Of the four stratigraphic possibilities proposed in Figure 2.8, we favor the interpretation in which the Fenghuoshan Group and Tuotuohe Group are distinct stratigraphic units (Figure 2.8c). While the Fenghuoshan and Tuotuohe Groups are generally lithostratigraphically similar, several observations have led us to distinguish these groups as separate units. To the south of the Fenghuoshan Range, we have observed Tuotuohe Group conglomerate clasts composed of Fenghuoshan Group sandstone (Figure 2.4f). Along the southern margin of the Fenghuoshan Range, the Tuotuohe Group is composed of beige coarse-grained sandstone and is angularly unconformable with deep red fine- to medium-grained sandstone of the Fenghuoshan Group (Figure 2.4g). These observations imply that the Tuotuohe Group is a syntectonic unit that was deposited after the Late Cretaceous to earliest Eocene Fenghuoshan Group, from Eocene to early Oligocene time. While the Yaxicuo Group is reportedly conformable with the Tuotuohe Group in the Tuotuohe subbasin (Li et al., 2011), the overlap of the Yaxicuo Group and Tuotuohe Group biostratigraphically determined age ranges (Z. Duan et al., 2007; Q. Duan et al., 2007; Duan et al., 2008) may suggest coeval deposition and laterally shifting depositional facies in the early Oligocene. Finally, the Miocene Wudaoliang Group is unconformable with underlying stratigraphic units within the Hoh Xil Basin, according to our field observations, as well as observations made by others (Liu et al., 2001, 2003; Wu et al., 2008; Li et al., 2012).

2.6. Source of the Fenghuoshan Group

To constrain possible source terranes for the Fenghuoshan Group, published detrital zircon U-Pb age spectra from the Fenghuoshan Group (Dai et al., 2012) were compared to spectra from 10 Mesozoic sedimentary units from across the Tibetan Plateau (Leier et al., 2007b; Kapp et al., 2007a; Gehrels et al., 2011), as well as detrital zircon age compilations from the Lhasa, southern Qiangtang, northern Qiangtang, and Songpan-Ganzi terranes (Bruguier et al., 1997; Weislogel et al., 2006, 2010; Gehrels et al., 2011). We used three statistical methods in this analysis: (1) measurement of overlap, which considers the age range overlap between two samples; (2) measurement of similarity, in which the proportions of overlapping ages are compared; and (3) the Kolmogorov-Smirnov test (K-S test) to determine the probability that detrital zircon age distributions are derived from the same parent population. For the first two tests, a value of 1.0 suggests perfect overlap and similarity, whereas a value of 0.0 suggests no overlap or similarity (Gehrels, 2000). For the K-S test, a p value of <0.05 indicates, within 95% confidence, that the two age spectra are from different sources (Press et al., 1986).

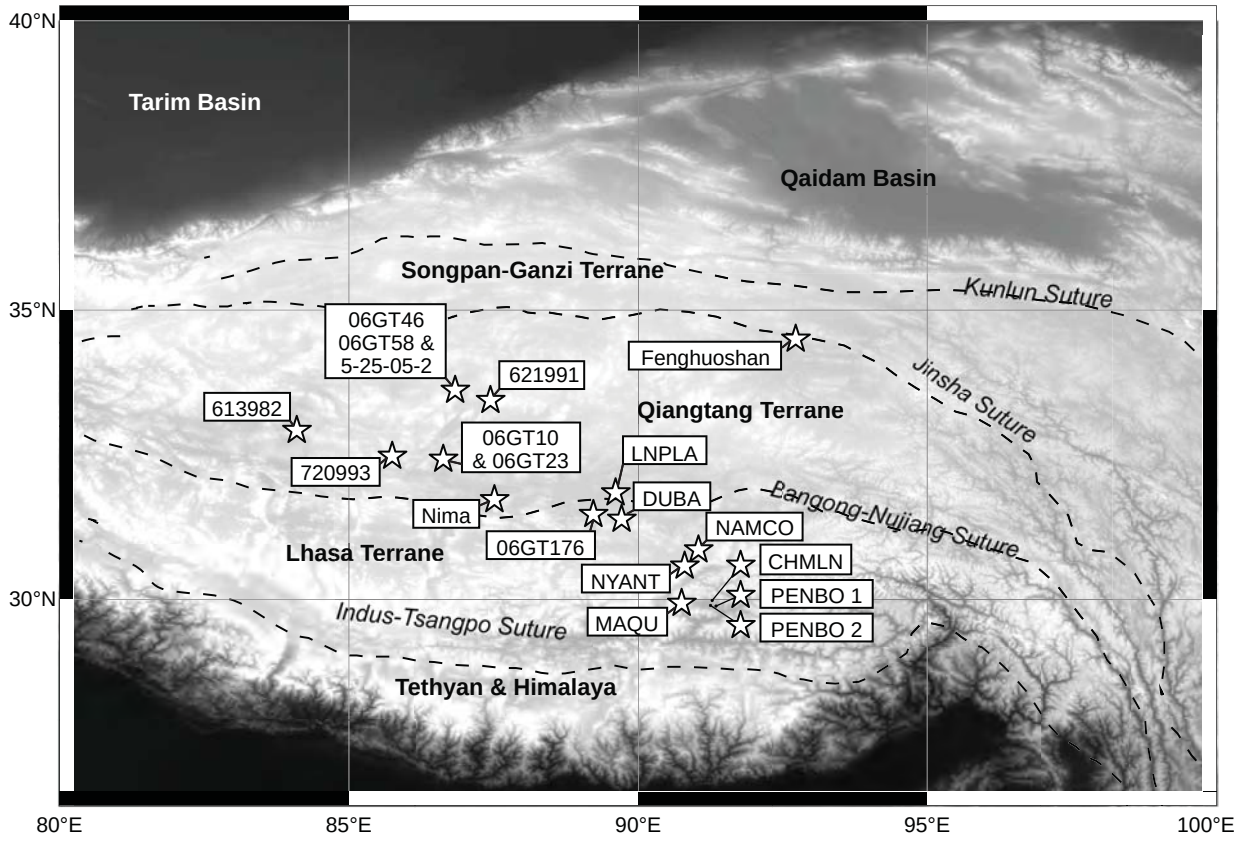

	Terranes				Mesozoic Sedimentary Sequences														
	Songpan-Ganzi	N. Qiangtang	S. Qiangtang	Lhasa	720993	06GT10	06GT23	613982	621991	5-25-02-5	06GT58	06GT46	06GT176	Nima Basin	Takena Fm.	Duoba Fm.	Chomulong Fm.	Lunpola Basin	Nam Co
Overlap	0.362	0.650	0.669	0.560	0.664	0.595	0.632	0.598	0.247	0.584	0.615	0.625	0.608	0.659	0.628	0.475	0.487	0.701	0.540
Similarity	0.537	0.587	0.580	0.497	0.631	0.623	0.613	0.652	0.370	0.545	0.566	0.535	0.568	0.691	0.547	0.313	0.357	0.708	0.464
K-S test					0.001	0.004	0.000	0.000	0.000	0.000	0.002	0.005	0.000	0.452	0.003	0.000	0.026	0.007	0.000
					N. Qiangtang				S. Qiangtang				Lhasa						

Figure 2.9. Comparison between detrital U-Pb zircon age spectra for the Fenghuoshan Group (Dai et al., 2012) with four possible source terranes on the Tibetan Plateau (Lhasa, northern and southern Qiangtang, and Songpan-Ganzi) and ten Mesozoic sedimentary sequences deposited across the Tibetan Plateau (Bruguier, 1997; Weislogel et al., 2006; 2010; Leier et al., 2007b; Kapp et al., 2007a; Gehrels et al., 2011). The map shows locations and sample names of Mesozoic sedimentary units compared to the Fenghuoshan Group (white stars). The table below shows the overlap, similarity, and K-S test values derived from comparison of the Fenghuoshan Group with each Tibetan terrane and Mesozoic sedimentary unit. Sutures delineate the terrane boundaries, and are marked as dashed black lines (Styron et al., 2010).

Of the compiled zircon age spectra from Tibetan terranes compared to the Fenghuoshan Group, the northern and southern regions of the Qiangtang Terrane have the highest values of similarity and overlap, respectively (Figure 2.9). This provenance analysis suggests that the Qiangtang Terrane is the source of Fenghuoshan Group sedimentary rocks. This is consistent with paleocurrent indicators from the Fenghuoshan Group, which suggest northward flow directions (Leeder et al., 1988; Liu and Wang, 2001b; Liu et al., 2001; Yi et al., 2008; Li et al., 2012). While we cannot statistically distinguish between the northern and southern sections of the Qiangtang Terrane, we interpret the presence of conglomerates in the Fenghuoshan Group as indicative of a proximal sedimentary source and thus infer that the Qiangtang Terrane is a more likely source than the Lhasa or Songpan-Ganzi terranes.

Overlap and similarity tests between the Fenghuoshan Group and all Mesozoic sedimentary units within the Tibetan Plateau are generally high but do not identify a specific sedimentary unit that may share a source terrane with the Fenghuoshan Group (Figure 2.9). However, when the K-S test is used to compare detrital zircon age spectra, we find that the null hypothesis is not rejected for a Lower Cretaceous sandstone collected in the Nima Basin (Figures 2.1, 2.9, and A2.7) (Kapp et al., 2007a), indicating that the Nima Basin and Fenghuoshan Group samples may share a common source. Paleocurrent indicators for the Early Cretaceous sandstone in the Nima Basin are not reported, but paleocurrent directions from overlying Late Cretaceous volcaniclastic strata indicate southward flow (Kapp et al., 2007b; DeCelles et al., 2007a). We also note that a strong detrital age peak near ~125 – 120 Ma is present in the detrital zircon age spectra from the Nima Basin and Fenghuoshan Group samples (Figure A2.7). Few of the other Mesozoic sedimentary basins analyzed for provenance have zircons of this age. Of the units compared, we consider the Nima Basin sandstone to be the one most similar to the Fenghuoshan Group based on the young zircon age peak, high values of similarity and overlap, and the results of the K-S test. Assuming paleoflow did not change in the Nima Basin between the Early and Late Cretaceous, this may suggest that the Nima Basin and Fenghuoshan Group shared a common sediment source located in the Qiangtang Terrane.

2.7. Discussion

2.7.1. Timing and Extent Deformation in Tibet Prior to the Onset of Indo-Asian Collision

The timing of nonmarine deposition within the Hoh Xil Basin places important constraints on the deformation history of the north central Tibetan Plateau by providing temporal and spatial

information on the deformation of the source terrane. Controversy over the depositional age of the Fenghuoshan Group, in particular, has led to various interpretations of plateau evolution. For example, the magnetostratigraphically determined Eocene-Oligocene depositional age for the Fenghuoshan Group (Liu et al., 2003) is the most prominently cited and has been used to infer the existence of an Eocene proto-plateau in central Tibet that formed shortly after the Indo-Asian collision (C. Wang et al., 2008; Dai et al., 2012). However, our revised Late Cretaceous to early Eocene depositional age for the Fenghuoshan Group requires deformation of the source terrane for these strata prior to the onset of the Indo-Asian collision.

2.7.1.1. Central Qiangtang Terrane

Coarse sediment accumulation in the Nima Basin (Kapp et al., 2007a) and in the Hoh Xil Basin likely reflects concurrent deformation and erosion of the source terrane. The presence of conglomerates within the Fenghuoshan Group suggests a proximal sediment source, which we infer to be the Tanggula Shan. We suggest that uplift and erosion of the Tanggula Shan provided sediment to the Hoh Xil and Nima Basins and that the Tanggula Shan formed a local topographic high since at least the Late Cretaceous, although whether or not the Tanggula Shan achieved modern elevation at this time is unknown.

While few studies have focused on the deformation history of the Tanggula Shan, low-temperature thermochronologic ages from the Tanggula Shan range between 65 and 39 Ma and may suggest increased cooling rates, and potentially tectonic exhumation, from Late Cretaceous to mid-Eocene time (C. Wang et al., 2008; Rohrmann et al., 2012). In addition, several magmatic bodies within and proximal to the Tanggula Shan have been dated between ~70 and 40 Ma (Roger et al., 2000; Z. Duan et al., 2005; Rohrmann et al., 2012) and overlap with the timing of sedimentation within the Hoh Xil Basin. The genesis of these magmatic bodies remains controversial. Roger et al. (2000) and Q. Wang et al. (2008) propose that southward subduction of the Songpan-Ganzi Terrane along the Jinsha Suture generated these plutonic rocks. However, crustal thickening and uplift of the Qiangtang Terrane may have caused crustal anatexis and magmatic activity at this time (Xu et al., 1985). In either case, the ages of magmatic intrusions within the Tanggula Shan may give insight into the timing of uplift in this region. Along with concurrent sedimentation of the Hoh Xil Basin, thermochronologic data and the timing of magmatism in the central Qiangtang Terrane suggest that this region was uplifted and eroded prior to the onset of Indo-Asian collision, during Late Cretaceous to early Eocene time. Evidence for precollisional deformation, uplift, and erosion has

also been reported farther south, in the Lhasa and southern Qiangtang terranes.

2.7.1.2. Lhasa and Southern Qiangtang Terranes

Prior to the onset of the Indo-Asian collision, the Lhasa Terrane had experienced significant crustal shortening and likely formed part of an elevated deformation belt (Murphy et al., 1997; Kapp et al., 2005; 2007a, 2007b; DeCelles et al., 2007a; Rohrmann et al., 2012). The northernmost Lhasa Terrane, near the Banggong-Nujiang Suture, underwent deformation during Aptian to Albian time (Kapp et al., 2005, 2007a). Subsequently, deformation migrated southward to the Gangdese retroarc, where north directed contractional deformation accommodated up to 55% shortening between 105 and 53 Ma (Kapp et al., 2007b). Widespread magmatism between 69 and 50 Ma has been interpreted as slab steepening and removal of the mantle lithosphere beneath the Lhasa Terrane (DeCelles et al., 2007a; Kapp et al., 2007b). Loss of the mantle lithosphere and associated rapid uplift prior to the Indo-Asian collision (DeCelles et al., 2007a) is consistent with rapid erosion rates inferred by Hetzel et al. (2011) between 69 and 48 Ma. The cessation of large-scale shortening within the Lhasa Terrane by ~55 – 50 Ma, concurrent with the main phase of Linzizong magmatism (Murphy et al., 1997; Kapp et al., 2007b), is consistent with the establishment of low erosion rates by ~54 Ma in northern Lhasa (Rohrmann et al., 2012) and may suggest the establishment of high elevation by this time.

The precollisional crustal shortening recognized in the Lhasa Terrane also extended into the southern Qiangtang Terrane and is far greater than observed Tertiary deformation (Kapp et al., 2005). The deformation history, along with the establishment of low erosion rates in the southern Qiangtang Terrane by ~45 Ma (Rohrmann et al., 2012), suggests that plateau development initiated in southern Tibet before the Indo-Asian collision and may have been largely completed soon after the collision. The evidence we have presented for an elevated and eroding Tanggula Shan (central Qiangtang Terrane) by Late Cretaceous time suggests that precollisional deformation that affected the northern Lhasa and southern Qiangtang terranes also extended several hundred kilometers farther north than previously recognized. This interpretation contradicts previous suggestions for an Eocene uplift of the southern and central Tibetan Plateau due to continental collision with India (e.g., Tapponnier et al., 2001; C. Wang et al., 2008; Dai et al., 2012).

2.7.2. Timing and Distribution of Syncollisional and Postcollisional Deformation and Uplift in Northern Tibet

Our provenance analysis and revised depositional age of the Fenghuoshan Group suggest

that the Hoh Xil Basin was at low elevation relative to the central Qiangtang Terrane from the Late Cretaceous to earliest Eocene. However, the deformation preserved in Late Cretaceous to Oligocene strata and the high modern elevations of the Hoh Xil Basin suggest crustal shortening, thickening, and uplift of the northern Qiangtang and southern Songpan-Ganzi terranes followed Fenghuoshan Group deposition.

2.7.2.1. Cenozoic Deformation of Northern Tibet

In the Hoh Xil Basin, we interpret the stratigraphic relationships and radiometric ages of variably deformed volcanic units to indicate deformation between the early Eocene and late Oligocene. This is consistent with documented syndepositional deformation in the Yushu-Nangqian region to the east (Horton et al., 2002; Spurlin et al., 2005), regional clockwise rotation in the Xining-Lanzhou region (Horton et al., 2004; Dupont-Nivet et al., 2004), and the initiation of widespread deformation of the northern plateau margin soon after the onset of Indo-Asian collision (Yin et al., 2008; Clark et al., 2010; Duvall et al., 2011).

Despite ongoing convergence between the Indian and Eurasian continents, shortening in the Hoh Xil Basin appears to have been largely complete since late Oligocene time, suggesting deformation localized elsewhere. Currently, geodetic data from across the Tibetan Plateau show localized strong gradients in geodetic velocity profiles parallel to plate convergence at its southern and northern margins in the Himalaya and Qilian Shan, respectively (Zhang et al., 2004; Allmendinger et al., 2007; Gan et al., 2007). This is consistent with observed active folding and thrust faulting in those regions (Taylor and Yin, 2009). Within the plateau interior, there are no reliable fault plane solutions that indicate active crustal shortening (Molnar and Lyon-Caen, 1989).

2.7.2.2. Paleoelevation of the Hoh Xil Basin

How early Cenozoic shortening in the Hoh Xil Basin relates to the attainment of high elevations across northern Tibet remains unclear. Palynological studies conducted in the Hoh Xil Basin observe a general shift from an angiosperm-dominated environment recorded in the Eocene to early Oligocene Tuotuohe Group to a gymnosperm-dominated environment, specifically with an increase in high-mountain conifers and broadleaved drought-resistant plants and herbs, recorded in the Oligocene Yaxicuo Group (Q. Duan et al., 2007; Duan et al., 2008). This faunal shift may record tectonic uplift and local elevation-related cooling from Eocene to Oligocene time. However, deep-sea isotopic data show a global decrease in temperature over this time period (Zachos et al., 2001),

which may be a contributing factor in the faunal shift observed in the Hoh Xil Basin.

Oxygen isotope data from lacustrine carbonates in the Fenghuoshan Group have been used to determine paleoelevations (Cyr et al., 2005). However, a range of paleoelevation values have been proposed from this data set, the variance of which results from differences in assumed dependence of $\delta^{18}O$ on elevation across northern Tibet at the time of limestone deposition (Cyr et al., 2005; DeCelles et al., 2007b; Quade et al., 2011; Lechler and Niemi, 2011; Bershaw et al., 2012). Considerable variability in the dependence of $\delta^{18}O$ on elevation across northern Tibet suggests that accurate quantification of paleoelevations from oxygen isotope data is likely to be difficult (Lechler and Niemi, 2011; Bershaw et al., 2012), which is further complicated by the likelihood that lacustrine carbonates from the Fenghuoshan Group were deposited farther south than their present location. More recent work has constrained paleoelevations from lipid biomarkers from both the Fenghuoshan and Wudaoliang Groups (Polissar et al., 2009). These data suggest that the Fenghuoshan Group carbonates used by Cyr et al. (2005) were extensively thermally altered and that measured oxygen isotope values may not reflect primary values. Thermal alteration of Fenghuoshan Group strata is further shown by reset apatite fission track ages reported by C. Wang et al. (2008), which suggest burial to temperatures in excess of 120°C, casting further doubt on the reliability of paleoelevation estimates for the Fenghuoshan Group at the time of deposition.

Despite the lack of reliable paleoelevation estimates from the Fenghuoshan Group, paleoelevation estimates of 3400 – 4200 m have been derived from lipid biomarkers from Wudaoliang Group lacustrine carbonate rocks (Polissar et al., 2009). Together with the lack of deformation observed in Miocene Wudaoliang strata (Liu et al., 2003; C. Wang et al., 2008; Wu et al., 2008) and late Oligocene-aged basalt flows, these data suggest that potentially 800 – 1600m of elevation gain occurred in northern Tibet since the early Miocene, but in the absence of significant surface shortening. Thus, it is debatable whether the cessation of crustal shortening within the Hoh Xil Basin signals the attainment of modern elevation. Other mechanisms for surface uplift of northern Tibet, such as lower crustal flow (Karplus et al., 2011) or loss of a mantle root (Molnar et al., 1993), have been proposed and could have resulted in surface uplift of 1 km or more in the absence of crustal shortening.

2.7.3. Tectonic Interpretation

We propose that the precollisional contractional deformation that extended from the Lhasa to the Tanggula Shan occurred during a period of relatively flat-slab subduction of the Neo-Tethyan

Ocean between ~85 and 70 Ma, coincident to the onset of deposition of the Fenghuoshan Group and magmatism in the central Qiangtang Terrane. We speculate that the initial stages of slab steepening circa 70 Ma and southward expansion of the mantle wedge resulted in small-scale Late Cretaceous to early Eocene magmatism observed in the Tanggula Shan (Roger et al., 2000; Z. Duan et al., 2005; Rohrmann et al., 2012) and may have promoted further uplift and erosion of the central Qiangtang Terrane. Thus, a wide precollisional deformation belt extended from the subduction zone north to the Tanggula Shan. As slab-steepening progressed beneath the Lhasa Terrane (DeCelles et al., 2007a; Wen et al., 2008), there was voluminous, widespread magmatism in southern Tibet between ~69 and 50 Ma, and the cessation of large-scale shortening and rapid erosion of the elevated margin of Eurasia (Murphy et al., 1997; DeCelles et al., 2007a; Kapp et al., 2007b; Rohrmann et al., 2012). During the early stages of Indo-Asian collision, high gravitational potential energy inhibited further thickening and elevation gain between the collision zone and the Tanggula Shan, thus promoting the northward migration of deformation into the Hoh Xil Basin in Eocene-Oligocene time.

Our observations within the Hoh Xil Basin do not uniquely constrain the tectonic mechanisms responsible for the observed syncollisional and postcollisional sedimentation and deformation. Convergence along the Jinsha Suture could have caused flexure within the northern Qiangtang Terrane concurrent with compression localized near the suture zone, thus explaining syndeformational deposition of the Tuotuohe and Yaxicuo Groups in the Hoh Xil Basin from Eocene to late Oligocene time. Post-Early Miocene uplift in the absence of crustal shortening may have been caused by lower crustal flow (Karplus et al., 2011) or the loss of a mantle root (Molnar et al., 1993) beneath northern Tibet. Observed Oligocene-Miocene reactivation of the Banggong-Nujiang Suture (Kapp et al., 2007a) may have been caused by the attainment of moderate to high elevations within the Hoh Xil Basin and the cessation of deformation near the Jinsha Suture. Miocene initiation of strike-slip movement along the Kunlun Fault largely follows cessation of shortening in the Hoh Xil Basin and may also indicated a major kinematic change related to high elevation within the northern plateau (Jolivet et al., 2003; Fu and Awata, 2007; Duvall et al., 2013).

2.8. Conclusions

Late Cretaceous shortening and elevated exhumation rates are documented within the Lhasa and southern to central Qiangtang terranes (e.g., Murphy et al., 1997; Kapp et al., 2007b; DeCelles et al., 2007a; Hetzel et al., 2011; Rohrmann et al., 2012; Dai et al., 2013). However, the persistence of

slow exhumation rates within the Kunlun Shan from ~ 150 Ma until 35 Ma and until ~ 40 Ma farther east suggests that Late Cretaceous deformation did not extend to the modern northern plateau margin (Jolivet et al., 2001; Clark et al., 2010). The history of sedimentation and deformation within the Hoh Xil Basin provides a spatial and temporal link between the Lhasa and southern Qiangtang terranes, which deformed prior to the Indo-Asian collision, and the northern plateau margin, where thrust faults were activated in the Eocene. Thus, this region potentially records how the northern plateau responds as plate boundary forces change as the last of the Neotethys Ocean subducts and the Indian continental lithosphere collides.

In this work, we revise the depositional age range of the Fenghuoshan Group based on new biostratigraphic and radiometric age constraints and reinterpretation of published magnetostratigraphy. The thin interbedded tuff we radiometrically dated at 59.27 Ma provides a critical tie point for correlation with the geomagnetic polarity timescale. We compare detrital zircon age spectra of the Fenghuoshan Group with age spectra from Tibetan terranes and Mesozoic sedimentary sequences from across the Tibetan Plateau. Our results suggest that the Fenghuoshan Group was deposited from 85 to 51 Ma, was sourced from the Qiangtang Terrane, and may share a sediment source with Cretaceous sedimentary rocks in the Nima Basin. Based on age data and field observations, we suggest that the Tuotuohe and Yaxicuo Groups unconformably overlie Fenghuoshan Group strata. Furthermore, we interpret the Tuotuohe and Yaxicuo Groups as coeval sedimentary units during the early Oligocene. The presence of relatively undeformed Miocene lacustrine strata and ~27 Ma flat-lying volcanic rocks in the Hoh Xil Basin suggest that crustal shortening of the northern Tibetan Plateau ceased by late Oligocene time.

2.9 References

Allmendinger, R. W., R. Reilinger, and J. Loveless (2007), Strain and rotation rate from GPS in Tibet, Anatolia, and the Altiplano, Tectonics, 26, TC3013, doi:10.1029/2006TC002030.

An, Y., Z. Deng, and Y. Zhuang (2004), Characteristics of the Fenghuoshan Group's material and its era discussion, Northwestern Geol., 37(1), 63–68.

Argand, E. (1924), La Tectonique de l'Asie, Proc. Int. Geol. Congr., 7, 170–372.

Bershaw, J., S. M. Penny, and C. N. Garzione (2012), Stable isotopes of modern water across the Himalaya and eastern Tibetan Plateau: Implications for estimates of paleoelevation and paleoclimate, J. Geophys. Res., 117, D02110, doi:10.1029/2011JD016132.

Boutelier, D., A. Chemenda, and J. P. Burg (2003), Subduction versus accretion of intra-oceanic

volcanic arcs: Insight from thermo-mechanical analogue experiments, Earth Planet. Sci. Lett., 212(1–2), 31–45, doi:10.1016/S0012-821X(03)00239-5.

Bruguier, O., J. R. Lancelot, and J. Malavielle (1997), U-Pb dating on single detrital zircon grains from the Triassic Songpan-Ganzi flysch (central China): Provenance and tectonic correlations, Earth Planet. Sci. Lett., 152, 217–231, doi:10.1016/S0012-821X(97)00138-6.

Burg, J. P., F. Proust, P. Tapponnier, and G. M. Chen (1983), Deformation phases and tectonic evolution of the Lhasa block (southern Tibet, China), Eclogae Geol. Helv., 76(3), 643–665.

Chen, P. J. (1988), Distribution and migration of the Jehol Fauna with reference to non-marine Jurassic-Cretaceous boundary in China, Acta Palaeontologica Sin., 27, 659–683.

Chen, L., and Y. S. Xie (2011), Discussion of Paleocene-Eocene boundary of SanShui Basin, Adv. Mater. Res., 236, 2487–2490.

Clark, M. K., K. A. Farley, D. Zheng, Z. Wang, and A. R. Duvall (2010), Early Cenozoic faulting of the northern Tibetan Plateau margin from apatite (U–Th)/He ages, Earth Planet. Sci. Lett., 296(1–2), 78–88, doi:10.1016/j.epsl.2010.04.051.

Cloos, M. (1993), Lithospheric buoyancy and collisional orogenesis: Subduction of oceanic plateaus, continental margins, island arcs, spreading ridges, and seamounts, Geol. Soc. Am. Bull., 105(6), 715–737.

Condon, D., B. Schoene, S. Bowring, R. Parrish, N. Mclean, S. Noble, and Q. Crowley (2007), EARTHTIME: Isotopic tracers and optimized solutions for high-precision U-Pb ID-TIMS geochronology, Eos Trans. AGU, 88(52), Fall Meet. Suppl., Abstract V41E–06.

Crane, P. R., and R. A. Stockey (1987), Betula leaves and reproductive structures from the middle Eocene of British Columbia, Canada, Can. J. Bot., 65(12), 2490–2500.

Crowley, J. L., B. Schoene, and S. A. Bowring (2007), U-Pb dating of zircon in the Bishop Tuff at the millennial scale, Geology, 35, 1123–1126.

Cyr, A. J., B. S. Currie, and D. B. Rowley (2005), Geochemical evaluation of Fenghuoshan Group lacustrine carbonates, north-central Tibet: Implications for the paleoaltimetry of the Eocene Tibetan Plateau, J. Geol., 113(5), 517–533, doi:10.1086/431907.

Dai, J., X. Zhao, C. Wang, L. Zhu, Y. Li, and D. Finn (2012), The vast proto-Tibetan Plateau: New constraints from Paleogene Hoh Xil Basin, Gondwana Res., 22(2), 434–446, doi:10.1016/j.gr.2011.08.019.

Dai, J., C. Wang, J. Hourigan, Z. Li, and G. Zhuang (2013), Exhumation history of the Gangdese batholith, southern Tibetan Plateau: Evidence from apatite and zircon (U-Th)/He

thermochronology, J. Geol., 121(2), 155–172, doi:10.1086/669250.

DeCelles, P. G., P. Kapp, L. Ding, and G. E. Gehrels (2007a), Late Cretaceous to middle Tertiary basin evolution in the central Tibetan Plateau: Changing environments in response to tectonic partitioning, aridification, and regional elevation gain, Geol. Soc. Am. Bull., 119(5–6), 654–680, doi:10.1130/B26074.1.

DeCelles, P. G., J. Quade, P. Kapp, M. Fan, D. L. Dettman, and L. Ding (2007b), High and dry in central Tibet during the late Oligocene, Earth Planet. Sci. Lett., 253, 389–401, doi:10.1016/j.epsl.2006.11.001.

Dewey, J. F. (1988), Extensional Collapse of Orogens, Tectonics, 7(6), 1123–1139.

Dilek, Y. (2006), Collision tectonics of the Mediterranean region: Causes and consequences, Geol. Soc. Am. Spec. Pap., 409, 1–13, doi:10.1130/2006.2409(01).

Duan, Z., Y. Li, Y. Zhang, Y. Li, and M. Wang (2005), Zircon U-Pb age, continent dynamics significance and geochemical characteristics of the Mesozoic and Cenozoic granites from the Tanggula Range in the Qinghai-Tibetan Plateau, Acta Geol. Sin., 79(1), 88–97.

Duan, Q., K. X. Zhang, J. Wang, H. Yao, and J. Bu (2007), Sporopollen assemblage from the Totohe Formation and its stratigraphic significance in the Tanggula Mountains, northern Tibet, Earth Sci.-J. China Univ. Geosci., 32(5), 629–637.

Duan, Z., Y. Li, Z. Shen, X. Zhu, and C. Zhong (2007), Analysis of the evolution of the Cenozoic ecological environment and process of plateau surface uplift in the Wenquan area in the interior of the Qinghai-Tibet Plateau, Geol. China, 34(4), 688–696.

Duan, Q., K. Zhang, J. Wang, H. Yao, and Z. Niu (2008), Oligocene Palynoflora, Paleovegetation and Paleoclimate in the Tanggula Mountains, northern Tibet, Acta Micropalaeontol. Sin., 25(2), 185–195.

Dupont-Nivet, G., B. K. Horton, R. F. Butler, J. Wang, J. Zhou, and G. L. Waanders (2004), Paleogene clockwise tectonic rotation of the Xining-Lanzhou region, northeastern Tibetan Plateau, J. Geophys. Res., 109, B04401, doi:10.1029/2003JB002620.

Dupont-Nivet, G., P. C. Lippert, D. J. van Hinsbergen, M. J. Meijers, and P. Kapp (2010), Palaeolatitude and age of the Indo–Asia collision: Palaeomagnetic constraints, Geophys. J. Int., 182(3), 1189–1198.

Duvall, A. R., M. K. Clark, B. A. van der Pluijm, and C. Li (2011), Direct dating of Eocene reverse faulting in northeastern Tibet using Ar-dating of fault clays and low-temperature thermochronometry, Earth Planet. Sci. Lett., 304(3–4), 520–526,

doi:10.1016/j.epsl.2011.02.028.

Duvall, A. R., M. K. Clark, E. Kirby, K. A. Farley, W. H. Craddock, C. Li, and D. Y. Yuan (2013), Low-temperature thermochronometry along the Kunlun and Haiyuan Faults, NE Tibetan Plateau: Evidence for kinematic change during late-stage orogenesis, Tectonics, 32, 1190–1211, doi:10.1002/tect.20072.

England, P., and D. McKenzie (1982), A thin viscous sheet model for continental deformation, Geophys. J. Int., 70(2), 295–321, doi:10.1111/j.1365-246X.1982.tb04969.x.

England, P., and M. Searle (1986), The Cretaceous-Tertiary deformation of the Lhasa block and its implications for crustal thickening in Tibet, Tectonics, 5(1), 1–14.

England, P., and G. Houseman (1986), Finite strain calculations of continental deformation: 2. Comparison with the India-Asia Collision Zone, J. Geophys. Res., 91(B3), 3664–3676.

Fu, B., and Y. Awata (2007), Displacement and timing of left-lateral faulting in the Kunlun fault zone, northern Tibet, inferred from geologic and geomorphic features, J. Asian Earth Sci., 29(2–3), 253–265, doi:10.1016/j.jseaes.2006.03.004.

Gan, W., P. Zhang, Z.-K. Shen, Z. Niu, M. Wang, Y. Wan, D. Zhou, and J. Cheng (2007), Present-day crustal motion within the Tibetan Plateau inferred from GPS measurements, J. Geophys. Res., 112, B08416, doi:10.1029/2005JB004120.

Gehrels, G. E. (2000), Introduction to detrital zircon studies of Paleozoic and Triassic strata in western Nevada and northern California, Geol. Soc. Am., 347, 1–17, doi:10.1130/0-8137-2347-7.1.

Gehrels, G. P., et al. (2011), Detrital zircon geochronology of pre-Tertiary strata in the Tibetan-Himalayan orogen, Tectonics, 30, TC5016, doi:10.1029/2011TC002868.

Gerstenberger, H., and G. Haase (1997), A highly effective emitter substance for mass spectrometric Pb isotope ratio determinations, Chem. Geol., 136, 309–312.

Gradstein, F.M., J. G. Ogg,M. Schmitz, and G. Ogg (2012), Geomagnetic polarity time scale, in The Geologic Time Scale 2012 2-Volume Set, pp. 85–113, Elsevier, B.V.

Harrison, T. M., P. Copeland, W. S. F. Kidd, and A. Yin (1992), Raising Tibet, Science, 255(5052), 1663–1670.

Hetzel, R., I. Dunkl, V. Haider, M. Strobl, H. von Eynatten, L. Ding, and D. Frei (2011), Peneplain formation in southern Tibet predates the India-Asia collision and plateau uplift, Geology, 39(10), 983–986, doi:10.1130/G32069.1.

Horton, B. K., A. Yin, M. S. Spurlin, J. Zhou, and J. Wang (2002), Paleocene–Eocene

syncontractional sedimentation in narrow, lacustrinedominated basins of east-central Tibet, Geol. Soc. Am. Bull., 114(7), 771–786, doi:10.1130/0016-7606(2002)114<0771.

Horton, B. K., G. Dupont-Nivet, J. Zhou, G. L. Waanders, R. F. Butler, and J. Wang (2004), Mesozoic-Cenozoic evolution of the Xining-Minhe and Dangchang basins, northeastern Tibetan Plateau: Magnetostratigraphic and biostratigraphic results, J. Geophys. Res., 109, B04402, doi:10.1029/2003JB002913.

Jaffey, A. H., K. F. Flynn, L. E. Glendenin, W. C. Bentley, and A. M. Essling (1971), Precision measurements of half-lives and specific activities of 235U and 238U, Phys. Rev. C, 4, 1889–1906.

Ji, L. (1994), On the problem of the definition of the Fenghuoshan Group in the Tanggula Mountains area, Qinghai, Reg. Geol. China, 1994(4), 373–380.

Jolivet, M., M. Brunel, D. Seward, Z. Xu, J. Yang, F. Roger, and P. Tapponnier (2001), Mesozoic and Cenozoic tectonics of the northern edge of the Tibetan plateau: Fission-track constraints, Tectonophysics, 343(1–2), 111–134, doi:10.1016/S0040-1951(01)00196-2.

Jolivet,M., M. Brunel,D. Seward, Z. Xu, J. Yang, J.Malavieille, F. Roger, A. Leyreloup,N. Arnaud, and C.Wu (2003), Neogene extensionand volcanism in the Kunlun fault zone, northern Tibet: New constraints on the age of the Kunlun fault, Tectonics, 22(5), 1052, doi:10.1029/2002TC001428.

Kapp, P., A. Yin, T. M. Harrison, and L. Ding (2005), Cretaceous-Tertiary shortening, basin development, and volcanism in central Tibet, Geol. Soc. Am. Bull., 117(7), 865–878, doi:10.1130/B25595.1.

Kapp, P., P. G. DeCelles, G. E. Gehrels, M. Heizler, and L. Ding (2007a), Geological records of the Lhasa-Qiangtang and Indo-Asian collisions in the Nima area of central Tibet, Geol. Soc. Am. Bull., 119(7–8), 917–933, doi:10.1130/B26033.1.

Kapp, P., P. G. DeCelles, A. L. Leier, J. M. Fabijanic, S. He, A. Pullen, and G. E. Gehrels (2007b), The Gangdese retroarc thrust belt revealed, GSA Today, 17(7), 4–9.

Karplus, M. S., W. Zhao, S. L. Klemperer, Z. Wu, J. Mechie, D. Shi, L. D. Brown, and C. Chen (2011), Injection of Tibetan crust beneath the south Qaidam Basin: Evidence from INDEPTH IV wide-angle seismic data, J. Geophys. Res., 116, B07301, doi:10.1029/2010JB007911.

Kidd, W. S. F., Y. Pan, C. Chang, M. P. Coward, J. F. Dewey, A. Gansser, P. Molnar, R. M. Shackleton, and S. Yiyin (1988), Geological mapping of the 1985 Chinese-British Tibetan

(Xizang-Qinghai) Plateau Geotraverse route. Philosophical Transactions of the Royal Society of London. Series A, Math. Phys. Sci., 327(1594), 287–305.

Kong, X., A. Yin, and T. M. Harrison (1997), Evaluating the role of preexisting weaknesses and topographic distributions in the Indo-Asian collision by use of a thin-shell numerical model, Geology, 25, 527–530, doi:10.1130/0091-7613(1997)025<0527.

Krogh, T. E. (1973), A low contamination method for hydrothermal decomposition of zircon and extraction of U and Pb for isotopic age determination, Geochim. Cosmochim. Acta., 37, 485–494.

Lechler, A. R., and N. A. Niemi (2011), Controls on the spatial variability of modern meteoric δ18O: Empirical constraints from the western U.S. and East Asia and implications for stable isotope studies, Am. J. Sci., 311(8), 664–700, doi:10.2475/08.2011.02.

Leeder, M. R., A. B. Smith, and J. Yin (1988), Sedimentology, palaeoecology and palaeoenvironmental evolution of the 1985 Lhasa to Golmud Geotraverse, Phil. Trans. R. Soc. A, 327(1594), 107–143.

Leier, A. L., P. Kapp, G. E. Gehrels, and P. G. DeCelles (2007b), Detrital zircon geochronology of Carboniferous-Cretaceous strata in the Lhasa Terrane, southern Tibet, Basin Res., 19(3), 361–378, doi:10.1111/j.1365-2117.2007.00330.x.

Li, P., and L. Yuan (1990), The Fenghuoshan Group of palynological assemblages and their meaning, Northwestern Geol., 1990(4), 7–9.

Li, W., and Z. Liu (1994), The Cretaceous palynofloras and their bearing on stratigraphic correlation in China, Cretaceous Res., 15(3), 333–365.

Li, W., Z. Song, Z. Liou, C. Li, Z. Li, and H. Li (2005), Geologic characteristics and ore-controls of the Fenghuoshan copper ore deposit, Qinghai province, China, in Mineral Deposit Research: Meeting the Global Challenge, pp. 153–156, Springer, Berlin.

Li, Y., C. Wang, C. Ma, G. Xu, and X. Zhao (2011), Balanced cross-section and crustal shortening analysis in the Tanggula-Tuotuohe area, northern Tibet, J. Earth Sci., 22(1), 1–10, doi:10.1007/s12583-011-0152-2.

Li, Y., C. Wang, X. Zhao, A. Yin, and C. Ma (2012), Cenozoic thrust system, basin evolution, and uplift of the Tanggula Range in the Tuotuohe region, central Tibet, Gondwana Res., 22(2), 482–492, doi:10.1016/j.gr.2011.11.017.

Liu, Z., and C. Wang (2001a), Facies analysis and depositional systems of Cenozoic sediments in the Hoh Xil Basin, northern Tibet, Sediment. Geol., 140(3–4), 251–270, doi:10.1016/S0037-

0738(00)00188-3.

Liu, Z., and C. Wang (2001b), Depositional Environment of the Tertiary Fenghuoshan Group in the Hoh Xil Basin, Northern Tibetan Plateau, Acta Sedimentologica Sin., 19(1), 28–34.

Liu, Z., C. Wang, and H. Yi (2001), Evolution and Mass Accumulation of the Cenozoic Hoh Xil Basin, Northern Tibet, J. Sediment. Res., 71(6), 971–984.

Liu, Z., X. Zhao, C. Wang, S. Liu, and H. Yi (2003), Magnetostratigraphy of Tertiary sediments from the Hoh Xil Basin: Implications for the Cenozoic tectonic history of the Tibetan Plateau, Geophys. J. Int., 154(2), 233–252, doi:10.1046/j.1365-246X.2003.01986.x.

Liu, Z., C. Wang, W. Jin, H. Yi, H. Zheng, X. Zhao, and Y. Li (2005), Oligo-Miocene depositional environment of the Tuotuohe Basin, central Tibetan Plateau, Acta Sediment Sin., 23(2), 210–216.

Manchester, S. R. (1987), The fossil history of the Juglandaceae, Monogr. Syst. Bot. Missouri Bot. Gard, 21, 1–137.

Mateer, N. J., and P. Chen (1992), A review of the nonmarine Cretaceous-Tertiary transition in China, Cretaceous Res., 13(1), 81–90.

Mattinson, J. M. (2005), Zircon U-Pb chemical abrasion (CA-TIMS)method: Combined annealing and multi-step partial dissolution analysis for improved precision and accuracy of zircon ages, Chem. Geol., 220, 47–66.

Molnar, P., and H. Lyon-Caen (1989), Fault plane solutions of earthquakes and active tectonics of the Tibetan Plateau and its margins, Geophys. J. Int., 99(1), 123–154, doi:10.1111/j.1365-246X.1989.tb02020.x.

Molnar, P., and J. Stock (2009), Slowing of India's convergence with Eurasia since 20 Ma and its implications for Tibetan mantle dynamics, Tectonics, 28, TC3001, doi:10.1029/2008TC002271.

Molnar, P., P. England, and J. Martinod (1993), Mantle dynamics, uplift of the Tibetan Plateau, and the Indian Monsoon, Rev. Geophys., 31(4), 357–396.

Murphy, M. A., A. Yin, T. M. Harrison, S. B. Dürr, Z. Chen, F. J. Ryerson, W. S. F. Kidd, X. Wang, and X. Zhou (1997), Did the Indo-Asian collision alone create the Tibetan plateau?, Geology, 25(8), 719–722, doi:10.1130/0091-7613(1997)025<0719:DTIACA>2.3.CO;2.

Najman, Y., et al. (2010), Timing of India-Asia collision: Geological, biostratigraphic, and palaeomagnetic constraints, J. Geophys. Res., 115, B12416, doi:10.1029/2010JB007673.

Orth, K., and J. McPhie (2003), Textures formed during emplacement and cooling of a

Palaeoproterozoic, small-volume rhyolitic sill, J. Volcanol. Geotherm. Res., 128(4), 341–362.

Polissar, P. J., K. H. Freeman, D. B. Rowley, F. A. McInerney, and B. S. Currie (2009), Paleoaltimetry of the Tibetan Plateau from D/H ratios of lipid biomarkers, Earth and Planet. Sci. Lett., 287(1–2), 64–76, doi:10.1016/j.epsl.2009.07.037.

Powell, C. M. (1986), Continental underplating model for the rise of the Tibetan Plateau, Earth Planet. Sci. Lett., 81(1), 79–94.

Press, W. H., B. P. Flannery, S. A. Teukolsky, and W. T. Vetterling (1986), Numerical recipes, in The Art of Scientific Computing, pp. 186, Cambridge Univ. Press, Cambridge.

QBGMR (Qinhai Bureau of Geology and Mineral Resources) (1989a), Geologic map of the Tuotuohe region, scale 1:200,000.

QBGMR (Qinhai Bureau of Geology and Mineral Resources) (1989b), Geologic map of the Cuorendejia region, scale 1:200,000.

Quade, J., D. O. Breecker, M. Daeron, and J. Eiler (2011), The paleoaltimetry of Tibet: An isotopic perspective, Am. J. Sci., 311(2), 77–115, doi:10.2475/02.2011.01.

Rivera, T. A., M. Storey, M. D. Schmitz, and J. L. Crowley (2013), Age intercalibration of $^{40}Ar/^{39}Ar$ sanidine and chemically distinct U/Pb zircon populations from the Alder Creek Rhyolite Quaternary geochronology standard, Chem. Geol., 345, 87–98.

Roger, F., P. Tapponnier, N. Arnaud, U. Scharer, M. Brunel, Z. Xu, and J. Yang (2000), An Eocene magmatic belt across central Tibet: Mantle subduction triggered by the Indian collision?, Terra Nova, 12(3), 102–108.

Rohrmann, A., P. Kapp, B. Carrapa, P. W. Reiners, J. Guynn, L. Ding, and M. Heizler (2012), Thermochronologic evidence for plateau formation in central Tibet by 45 Ma, Geology, 40(2), 187–190, doi:10.1130/G32530.1.

Royden, L., and B. C. Burchfiel (1989), Are systematic variations in thrust belt style related to plate boundary processes? (the western Alps versus the Carpathians), Tectonics, 8(1), 51–61.

Rowley, D. B. (1996), Age of initiation of collision between India and Asia: A review of stratigraphic data, Earth Planet. Sci. Lett., 145(1), 1–13.

Samson, S. D., and E. C. Alexander (1987), Calibration of the interlaboratory $^{40}Ar/^{39}Ar$ dating standard, MMhb-1, Chem. Geol., 66, 27–34.

Schmitz, M. D., and B. Schoene (2007), Derivation of isotope ratios, errors and error correlations for U-Pb geochronology using 205Pb-235U-(233U)- spiked isotope dilution thermal ionization mass spectrometric data, Geochem. Geophys. Geosyst., 8, Q08006,

doi:10.1029/2006GC001492.

Schoene, B., J. Guex, A. Bartolini, U. Schaltegger, and T. J. Blackburn (2010), Correlating the end-Triassic mass extinction and flood basalt volcanism at the 100 ka level, Geology, 38(5), 387–390.

Şengör, A. M. C., and B. A. Natal'in (1996), Paleotectonics of Asia: Fragments of a synthesis, in The Tectonic Evolution of Asia, edited by A. Yin and T. M. Harrison, 486–640, Cambridge Univ. Press, New York.

Sláma, J., et al. (2008), Plešovice zircon—A new natural reference material for U–Pb and Hf isotopic microanalysis, Chem. Geol., 249, 1–35.

Smith, A. B., and J. Xu (1988), Palaeontology of the 1985 Tibet Geotraverse, Lhasa to Golmud, Phil. Trans. R. Soc. A, 327(1594), 53–105.

Song, Z., and F. Huang (1997), Comparison of palynomorph assemblages from the Cretaceous/Tertiary boundary interval in western Europe, northwest Africa and southeast China, Cretaceous Res., 18(6), 865–871.

Song, Z., Y. Zheng, and J. Liu (1995), Palynological assemblages across the Cretaceous/Tertiary boundary in northern Jiangsu, eastern China, Cretaceous Res., 16(4), 465–482.

Spurlin, M. S., A. Yin, B. K. Horton, J. Zhou, and J. Wang (2005), Structural evolution of the Yushu-Nangqian region and its relationship to syncollisional igneous activity, east-central Tibet, Geol. Soc. Am. Bull., 117(9–10), 1293–1317, doi:10.1130/B25572.1.

Styron, R. H., M. Taylor, and K. Okoronkwo (2010), Database of active structures from the Indo-Asian collision, Eos Trans. AGU, 91(20), 181–182, doi:10.1029/2010EO200001.

Tapponnier, P., X. Zhiqin, F. Roger, B. Meyer, N. Arnaud, G. Wittlinger, and Y. Jingsui (2001), Oblique stepwise rise and growth of the Tibet Plateau, Science, 294, 1671–1677.

Taylor, M., and A. Yin (2009), Active structures of the Himalayan-Tibetan orogen and their relationships to earthquake distribution, contemporary strain field, and Cenozoic volcanism, Geosphere, 5(3), 199–214.

Van Itterbeeck, J., P. Missiaen, A. Folie, V. S. Markevich, D. Van Damme, G. Dian-Yong, and T. Smith (2007), Woodland in a fluvio-lacustrine environment on the dry Mongolian Plateau during the late Paleocene: Evidence from the mammal bearing Subeng section (Inner Mongolia, PR China), Palaeogeogr. Palaeoclimatol. Palaeoecol., 243(1), 55–78.

Wang, C., X. Zhao, Z. Liu, P. C. Lippert, S. A. Graham, R. S. Coe, H. Yi, L. Zhu, S. Liu, and Y. Li (2008), Constraints on the early uplift history of the Tibetan Plateau, Proc. Natl. Acad. Sci.

U. S. A., 105(13), 4987–4992, doi:10.1073/pnas.0703595105.

Wang, Q., et al. (2008), Eocene melting of subducting continental crust and early uplifting of central Tibet: Evidence from central-western Qiangtang high-K calc-alkaline andesites, dacites and rhyolites, Earth Planet. Sci. Lett., 272(1–2), 158–171, doi:10.1016/j.epsl.2008.04.034.

Weislogel, A. L., S. A. Graham, E. Z. Chang, J. L.Wooden, G. E. Gehrels, and H. Yang (2006), Detrital zircon provenance of the Late Triassic Songpan–Ganzi complex: Sedimentary record of collision of the north and south China blocks, Geology, 34, 97–100, doi:10.1130/G21929.1.

Weislogel, A. L., S. A. Graham, E. Z. Chang, J. L. Wooden, and G. E. Gehrels (2010), Detrital zircon provenance from three turbidite depocenters of the Middle–Upper Triassic Songpan–Ganzi complex, central China, record of collision tectonics, erosional exhumation, and sediment production, Geol. Soc. Am. Bull., 122, 1969–1990.

Wen, D., D. Liu, S. Chung, M. Chu, J. Ji, Q. Zhang, B. Song, T. Lee, M. Yeh, and C. Lo (2008), Zircon SHRIMP U–Pb ages of the Gangdese batholith and implications for Neotethyan subduction in southern Tibet, Chem. Geol., 252(3–4), 191–201, doi:10.1016/j.chemgeo.2008.03.003.

Wu, Z., P. Ye, D. Hu, W. Zhang, and C. Zhou (2007), U-Pb isotopic dating of zircons from porphyry granite of the Fenghuoshan Mountains, northern Tibetan Plateau and its geological significance, Geoscience, 21(3), 435–442.

Wu, Z., P. J. Barosh, Z. Wu, D. Hu, X. Zhao, and P. Ye (2008), Vast early Miocene lakes of the central Tibetan Plateau, Geol. Soc. Am. Bull., 120(9–10), 1326–1337, doi:10.1130/B26043.1.

Xu, R. H., U. Schärer, and C. J. Allègre (1985), Magmatism and metamorphism in the Lhasa block (Tibet): A geochronological study, J. Geol., 93(1), 41–57.

Ye, C. (1994), Succession of Cypridacea (Ostracoda) and nonmarine Cretaceous stratigraphy of China, Cretaceous Res., 15(3), 285–303.

Yi, H., X. Zhao, J. Lin, Z. Shi, B. Li, and B. Zhao (2004), Magnetostratigraphic studies of tertiary continental redbeds from the Wulanwula lake area of northern Tibetan Plateau and their geologic significance, Acta Geoscientia Sin., 25, 633–638.

Yi, H., C. Wang, Z. Shi, J. Lin, and L. Zhu (2008), Early uplift history of the Tibetan Plateau: Records from paleocurrents and paleodrainage in the Hoh Xil Basin, Acta Geol. Sin., 82(1), 206–213.

Yin, J., J. Xu, C. Liu, and H. Li (1988), The Tibetan Plateau: Regional stratigraphic context and

previous work, Phil. Trans. R. Soc. A, 327(1594), 5–52.

Yin, A., and T. M. Harrison (2000), Geologic Evolution of the Himalayan-Tibetan Orogen, Annu. Rev. Earth Planet. Sci., 28, 211–280.

Yin, A., Y. Q. Dang, L. C. Wang, W. M. Jiang, S. P. Zhou, X. H. Chen, G. E. Gehrels, and M. W. McRivette (2008), Cenozoic tectonic evolution of Qaidam basin and its surrounding regions (Part 1): The southern Qilian Shan-Nan Shan thrust belt and northern Qaidam Basin, Geol. Soc. Am. Bull., 120(7–8), 813–846, doi:10.1130/B26180.1.

Zachos, J., M. Pagani, L. Sloan, E. Thomas, and K. Billups (2001), Trends, rhythms, and aberrations in global climate 65 Ma to present, Science, 292(5517), 686–693.

Zhao, W., and W. J. Morgan (1987), Injection of Indian crust into Tibetan lower crust: A two-dimensional finite element model study, Tectonics, 6(4), 489–504.

Zhang, P. Z., et al. (2004), Continuous deformation of the Tibetan Plateau from Global Positioning System data, Geology, 32(9), 809–812, doi:10.1130/G20554.1.

Zhang, Z., Z. Liu, Z. Wang, Y. Zhang, and D. Ye (2007), Ostracod Biostratigraphy of the Late Cretaceous Qingshankou Formation in the Songliao Basin, Acta Geologica Sinica, 81(5), 727–737.

Zhong, X. (1989), Fenghuoshan Group geological era, Tanggula Qinghai, Northwestern Geol., 1989(6), 1–6.

Appendix: Chapter II

This appendix contains seven figures and eight tables.

Figure A2.1 is a range diagram of flora and fauna identified within the Fenghuoshan, Tuotuohe, Yaxicuo, and Wudaoliang Groups.

Figure A2.2 contains cathadoluminescence images of Fenghuoshan Group tuff zircons. Circles represent the location of 25 um LA-ICPMS spot analyses.

Figure A2.3 is a Ranked age plot of 38 youngest LA-ICPMS U-Pb zircon ages from the Fenghuoshan Tuff. The horizontal line represents the weighted mean U-Pb zircon age. Associated error is indicated from the orange shaded region. Of the 38 youngest U-Pb zircon ages, only one does not overlap with the weighted mean age.

Figure A2.4 Rare earth element values of 56 zircons from the Fenghuoshan tuff sample analyzed using LA-ICPMS. Concentrations are normalized using Boynton (1984) primitive mantle data

Figure A2.5 is a normalized relative probability distribution of LA-ICPMS U-Pb zircon ages of the Fenghuoshan tuff (blue line) compared to SHRIMP U-Pb zircon ages from the Gangdese Batholith (red line; Wen et al., 2008)

Figure A2.6 contains paleomagnetic data from Liu et al., (2003). Polarity pattern interpretation on the left is from Liu et al., (2003). Polarity pattern on the right is from this study. Yellow shaded region is the Yaxicuo Group paleomagnetic data, which is excluded from our analysis

Figure A2.7 contains detrital U-Pb zircon age spectra of the Fenghuoshan Group, Tibetan terranes, and Tibetan Mesozoic sedimentary rocks. OVLP=overlap, SIM=similarity, K-S=K-S test.

Table A2.1 contains detailed data on Wudaoliang Group fossils.

Table A2.2 contains detailed data on Yaxicuo Group fossils.

Table A2.3 contains detailed data on Tuotuohe Group fossils.

Table A2.4 contains detailed data on Fenghuoshan Group fossils.

Table A2.5 contains citation information for fossil age ranges.

Table A2.6 contains detailed LA-ICPMS U-Pb geochronologic data for the Fenghuoshan tuff.

Table A2.7 contains detailed CA-TIMS U-Pb geochronologic data for the Fenghuoshan tuff.

Table A2.8 contains detailed Argon isotopic data for $^{40}Ar/^{39}Ar$ age dating of volcanic rocks.

Figure A2.1. Range diagram of flora and fauna identified within the Fenghuoshan, Tuotuohe, Yaxicuo, and Wudaoliang Groups.

Figure A2.1. continued

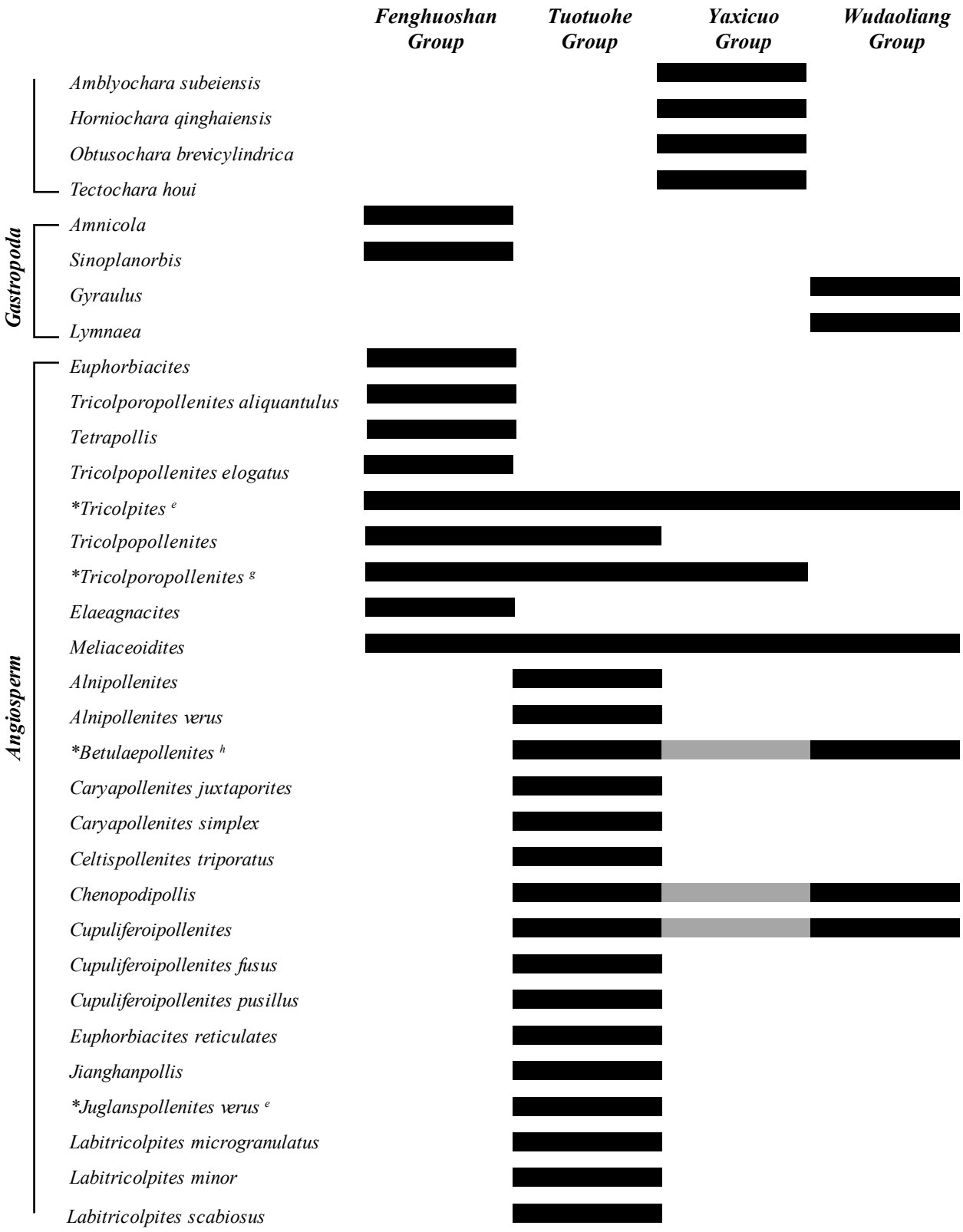

Figure A2.1. continued

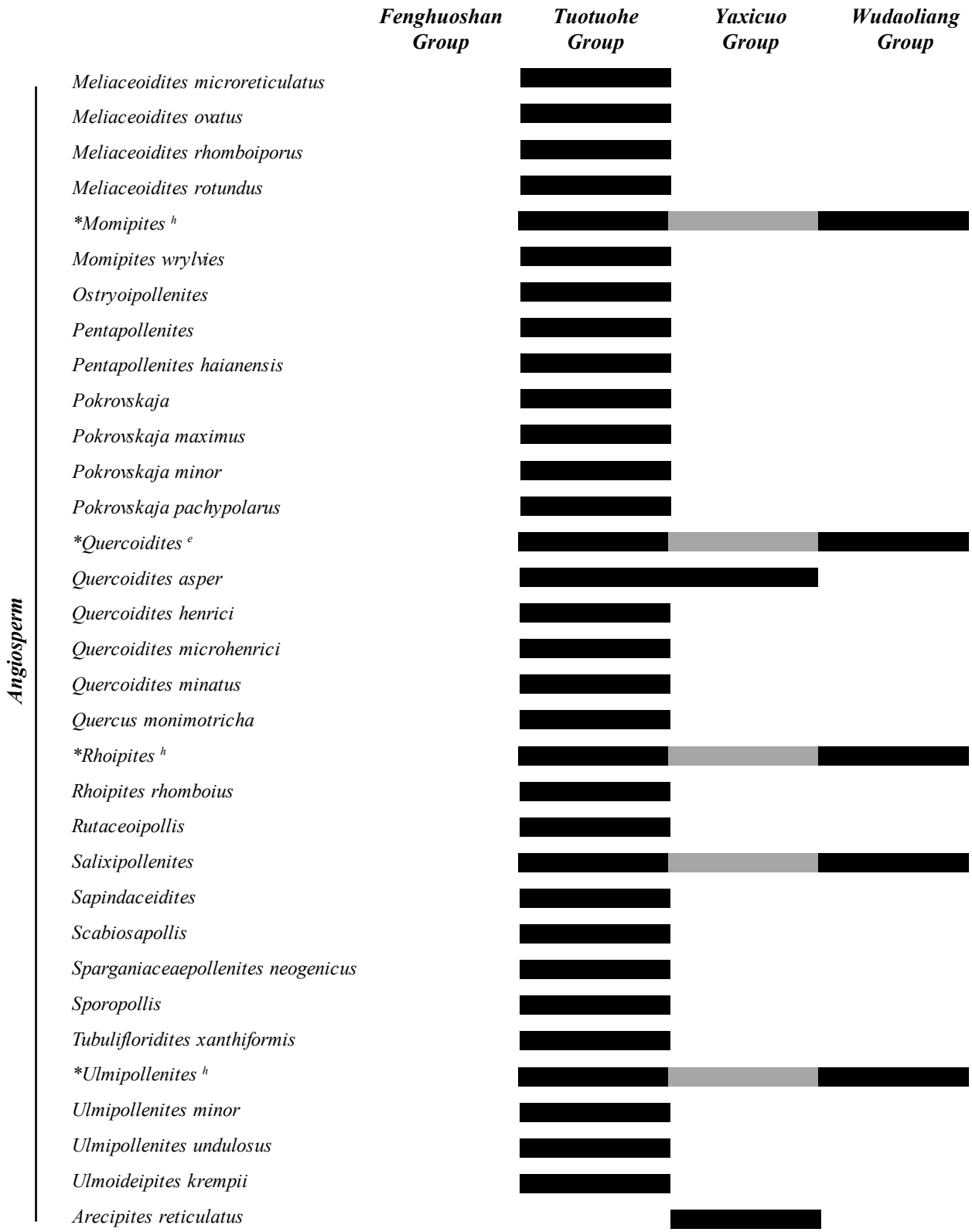

Figure A2.1. continued

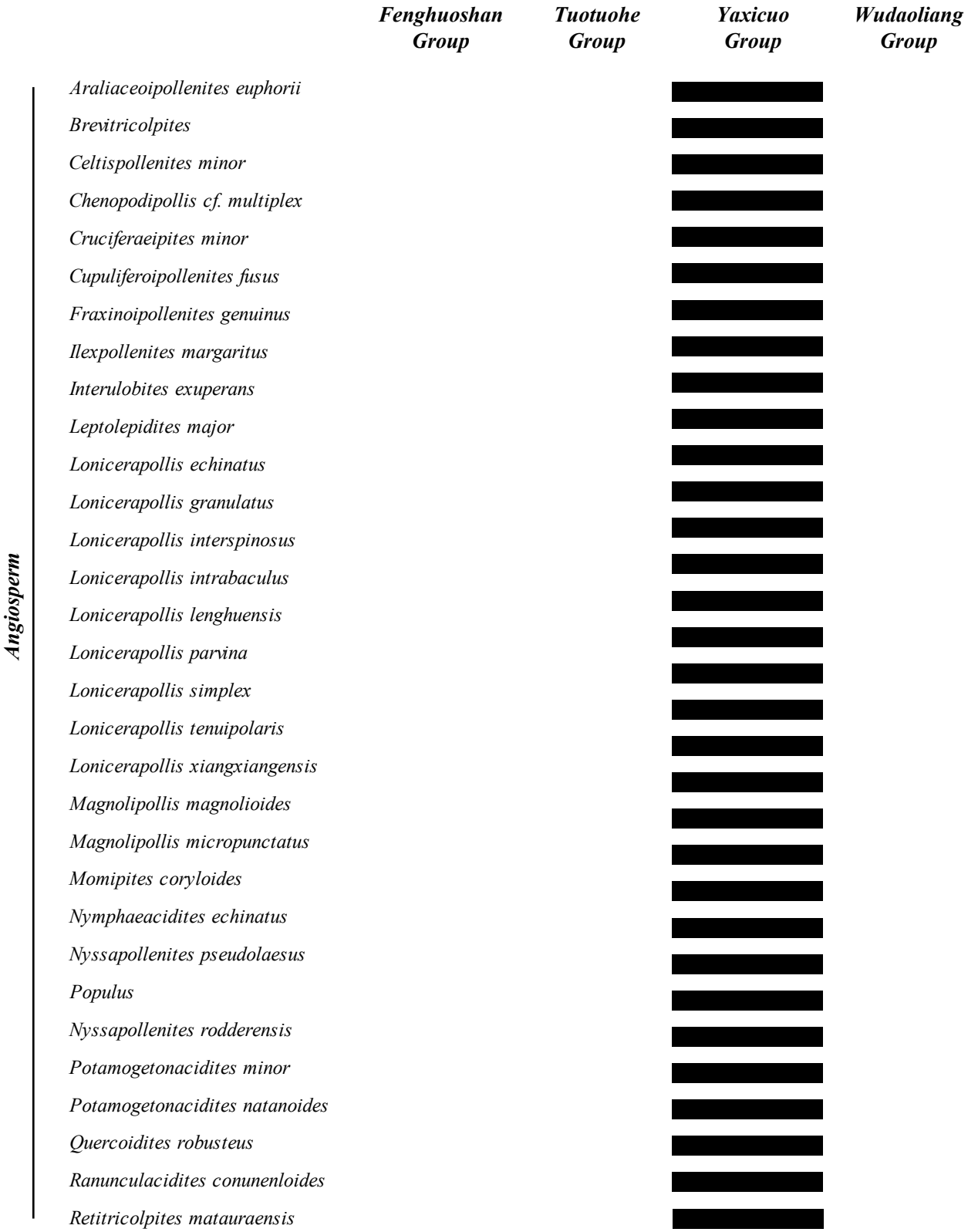

Figure A2.1. continued

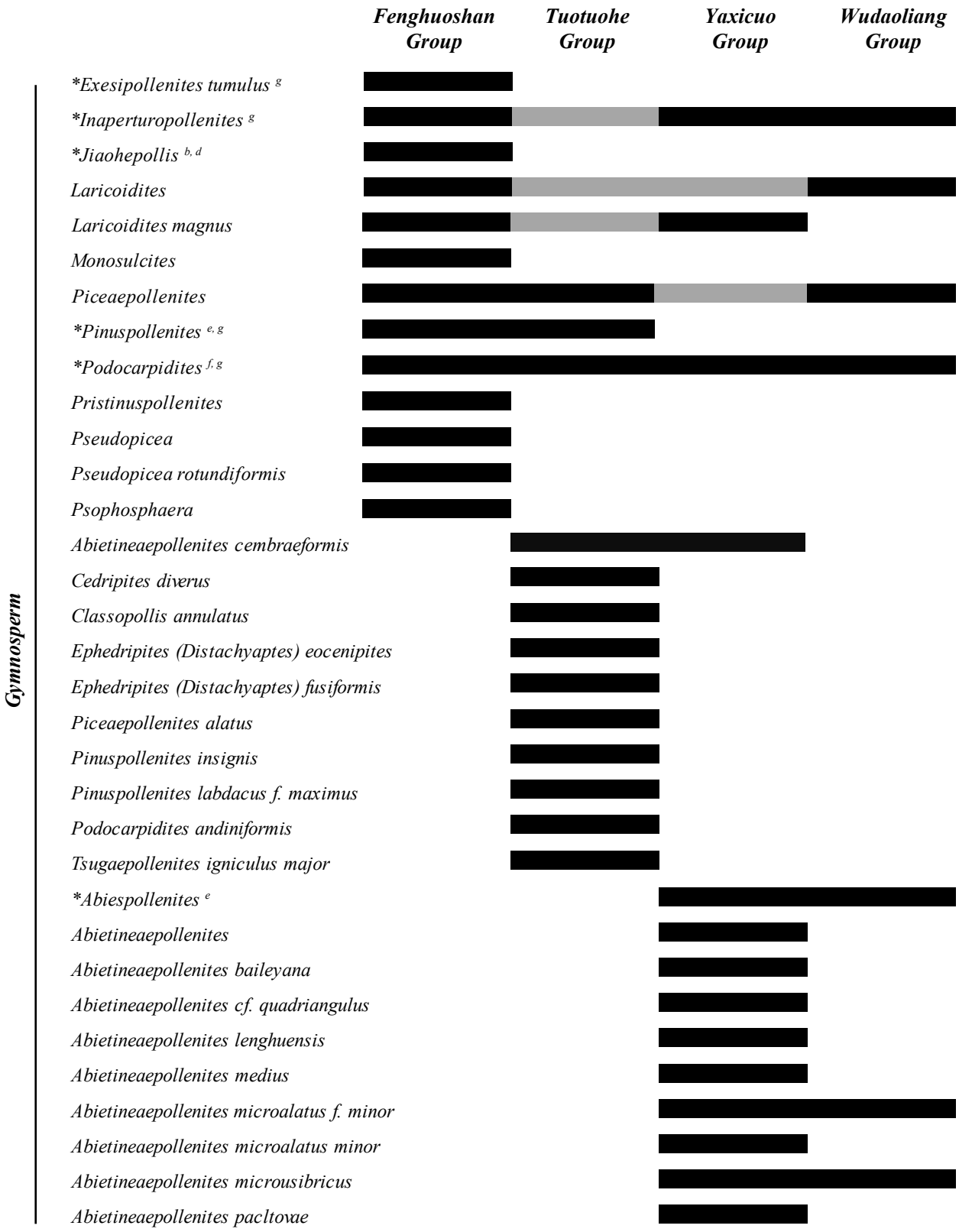

Figure A2.1. continued

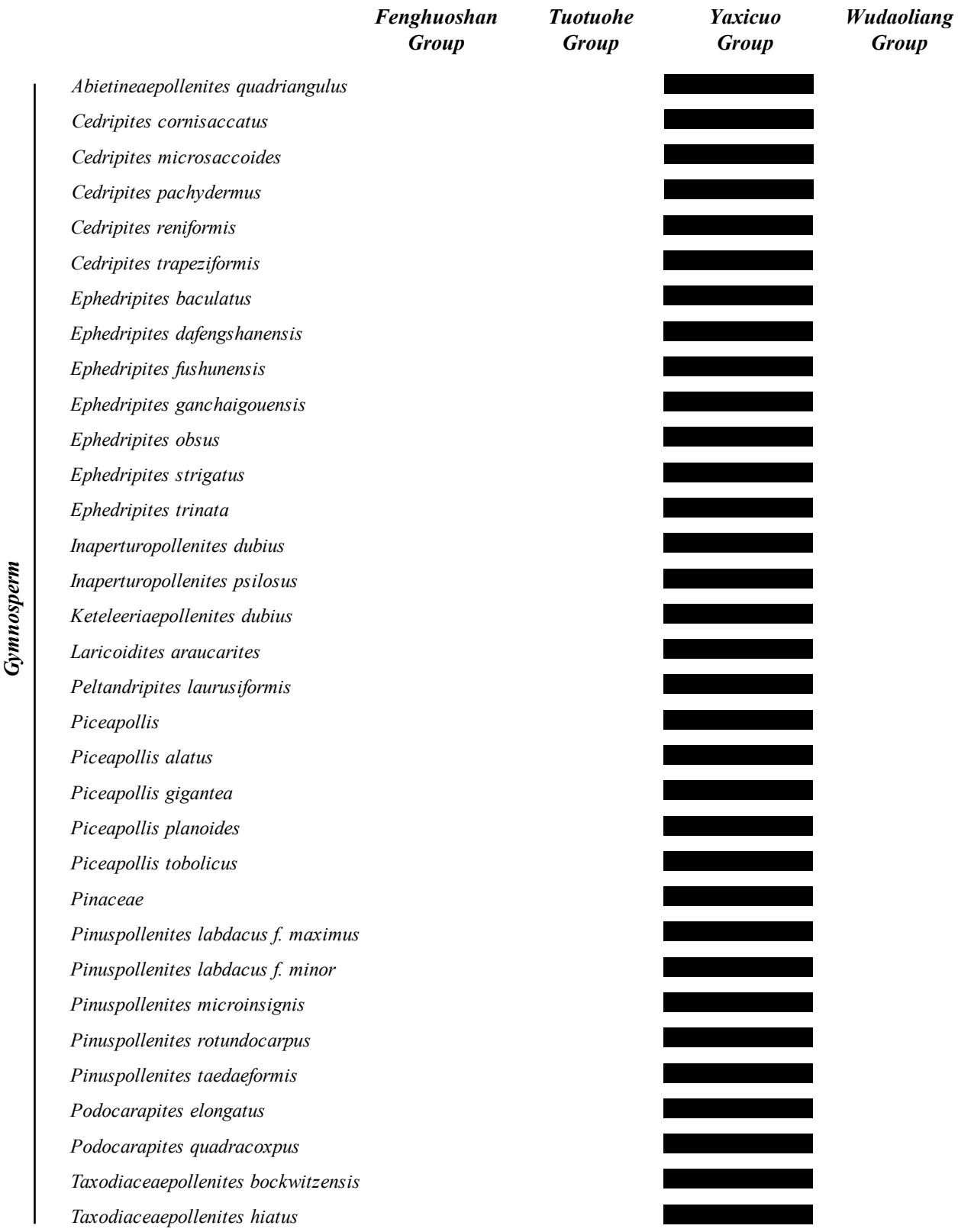

Figure A2.1. continued

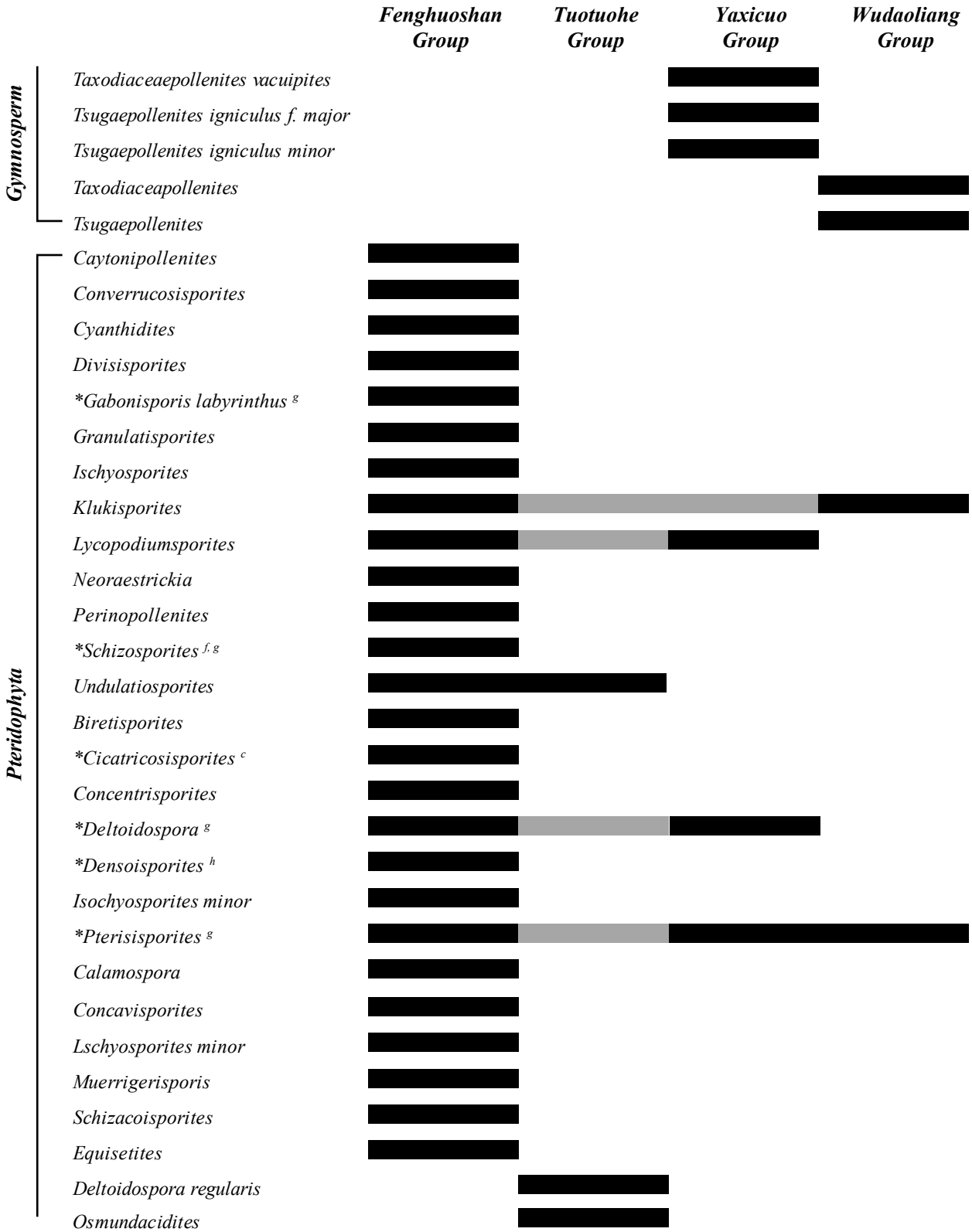

Figure A2.1. continued

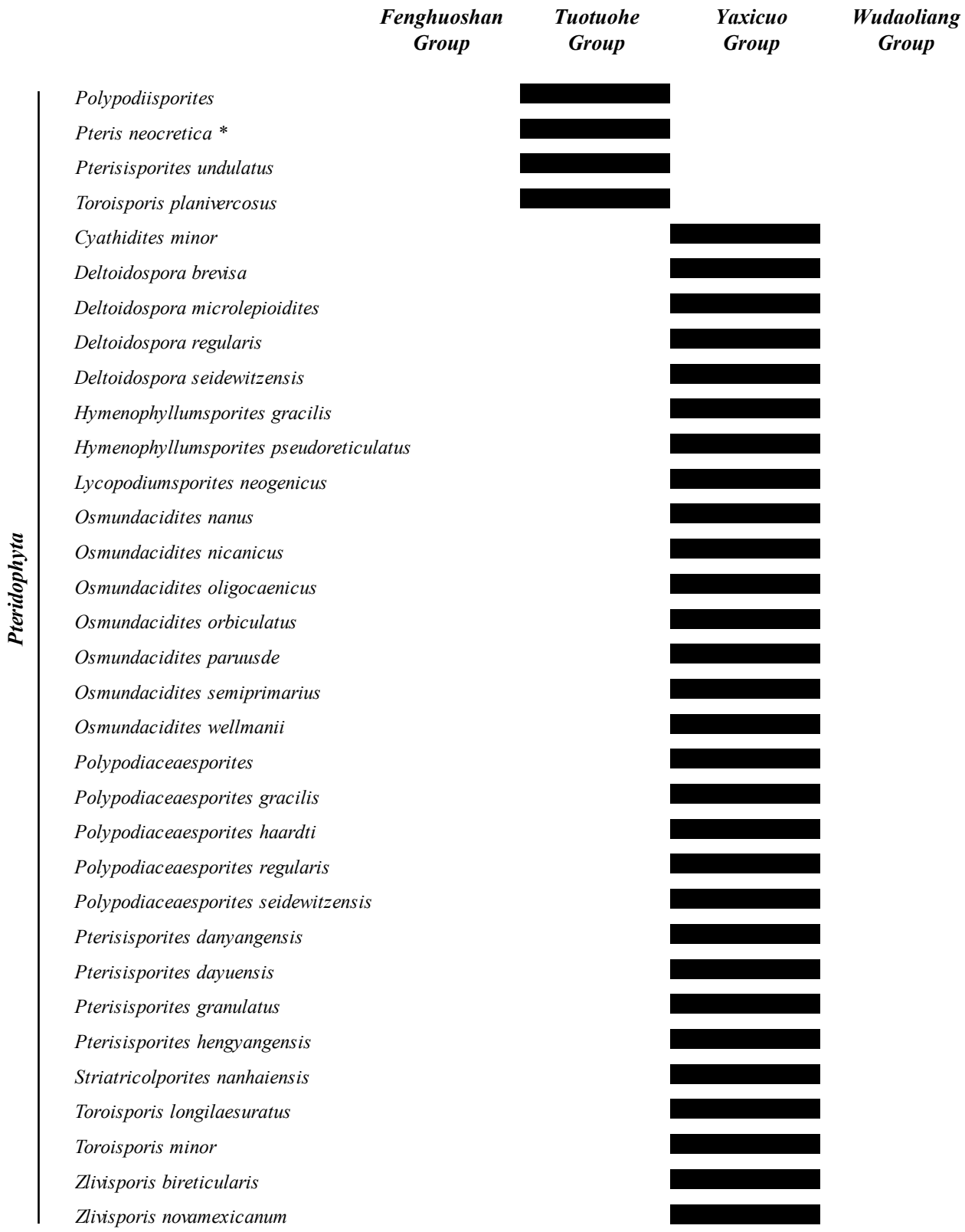

Figure A2.1. continued

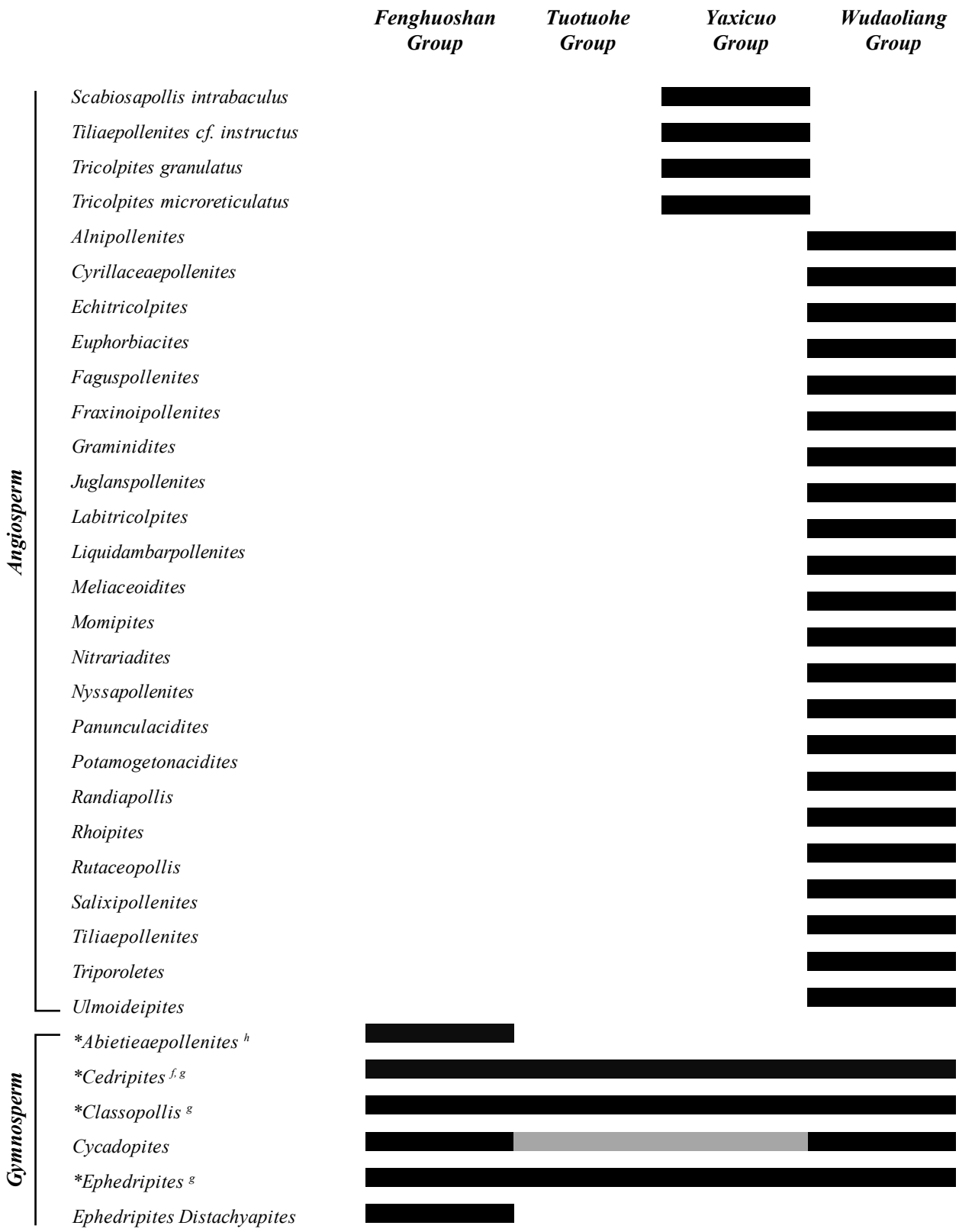

Figure A2.1. continued

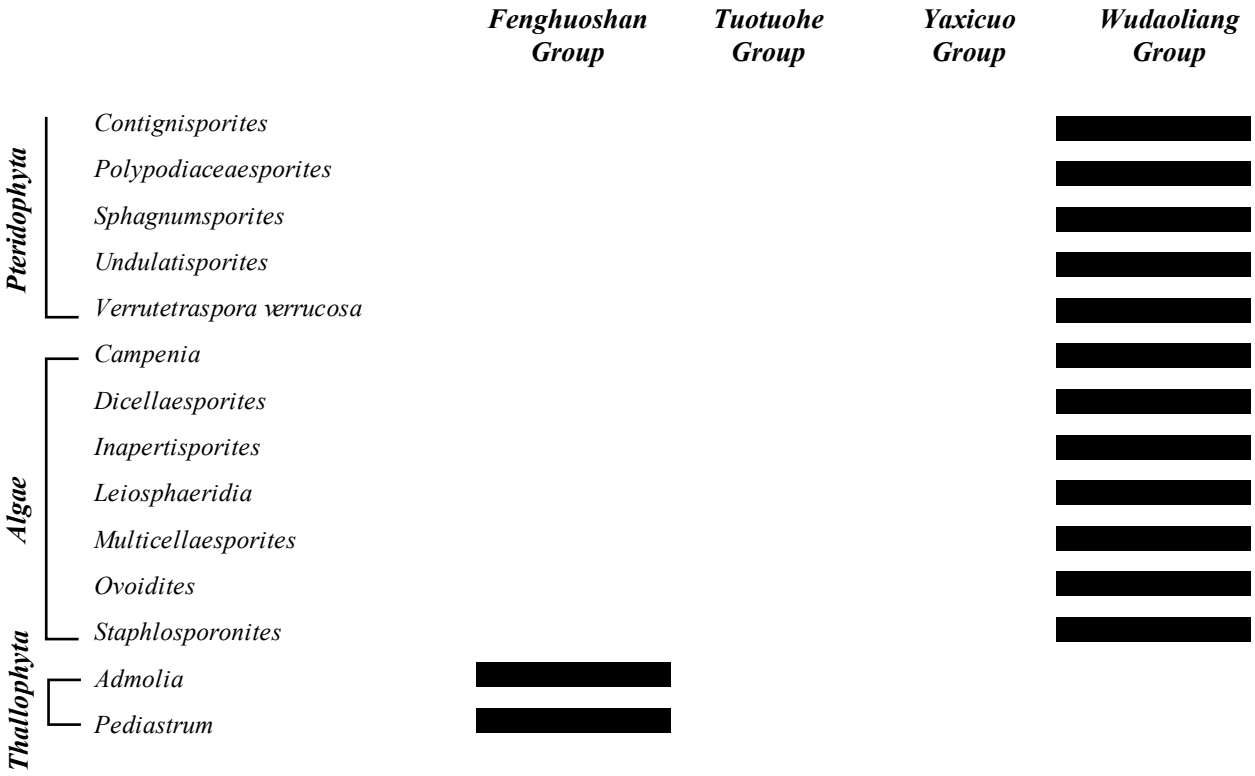

a Chen, L., & Xie, Y. S. (2011). Discussion of Paleocene-Eocene Boundary of SanShui Basin. Advanced Materials Research, 236, 2487-2490.

b Chen, P. J. (1988). Distribution and migration of the Jehol Fauna with reference to non-marine Jurassic-Cretaceous boundary in China. Acta Palaeontologica Sinica, 27, 659-683.

c He, J. D., Van Nieuwenhuise, D. S., & Swain, F. M. (1988). Biostratigraphy of Paleogene non-marine Ostracoda from east China. Developments in Palaeontology and Stratigraphy, 11, 1153-1161.

d Li, W., & Liu, Z. (1994). The Cretaceous palynofloras and their bearing on stratigraphic correlation in China. Cretaceous Research,15(3), 333-365.

e Li, J., Batten, D. J., & Zhang, Y. (2011). Palynological record from a composite core through Late Cretaceous–early Paleocene deposits in the Songliao Basin, Northeast China and its biostratigraphic implications. Cretaceous Research, 32(1), 1-12.

f Mateer, N. J., & Pei-ji, C. (1992). A review of the nonmarine Cretaceous-Tertiary transition in China. Cretaceous research, 13(1), 81-90.

g Song, Z., & Huang, F. (1997). Comparison of palynomorph assemblages from the Cretaceous/Tertiary boundary interval in Western Europe, northwest Africa and southeast China. Cretaceous Research, 18(6), 865-871.

h Zhichen, S., Yahui, Z., & Jinling, L. (1995). Palynological assemblages across the Cretaceous/Tertiary boundary in northern Jiangsu, eastern China. Cretaceous Research, 16(4), 465-482.

i Van Itterbeeck, J., Missiaen, P., Folie, A., Markevich, V. S., Van Damme, D., Dian-Yong, G., & Smith, T. (2007). Woodland in a fluvio-lacustrine environment on the dry Mongolian Plateau during the late Paleocene: Evidence from the mammal bearing Subeng section (Inner Mongolia, PR China). Palaeogeography, Palaeoclimatology, Palaeoecology, 243(1), 55-78.

j Ye, C. (1994). Succession of Cypridacea (Ostracoda) and nonmarine Cretaceous stratigraphy of China. Cretaceous Research, 15(3), 285-303.

k Zhang, Z., Liu, Z., Wang, B., Xhang, Y., Ye & D. (2007). Ostracod biostratigraphy of the Late Cretaceous Qingshankou formation in the Songliao Basin. Acta Geologica Sinica-English Edition, 81(5), 727-738.

Figure A2.2. Cathadoluminescence images of Fenghuoshan Group tuff zircons. Circles represent the location of 25 um LA-ICPMS spot analyses.

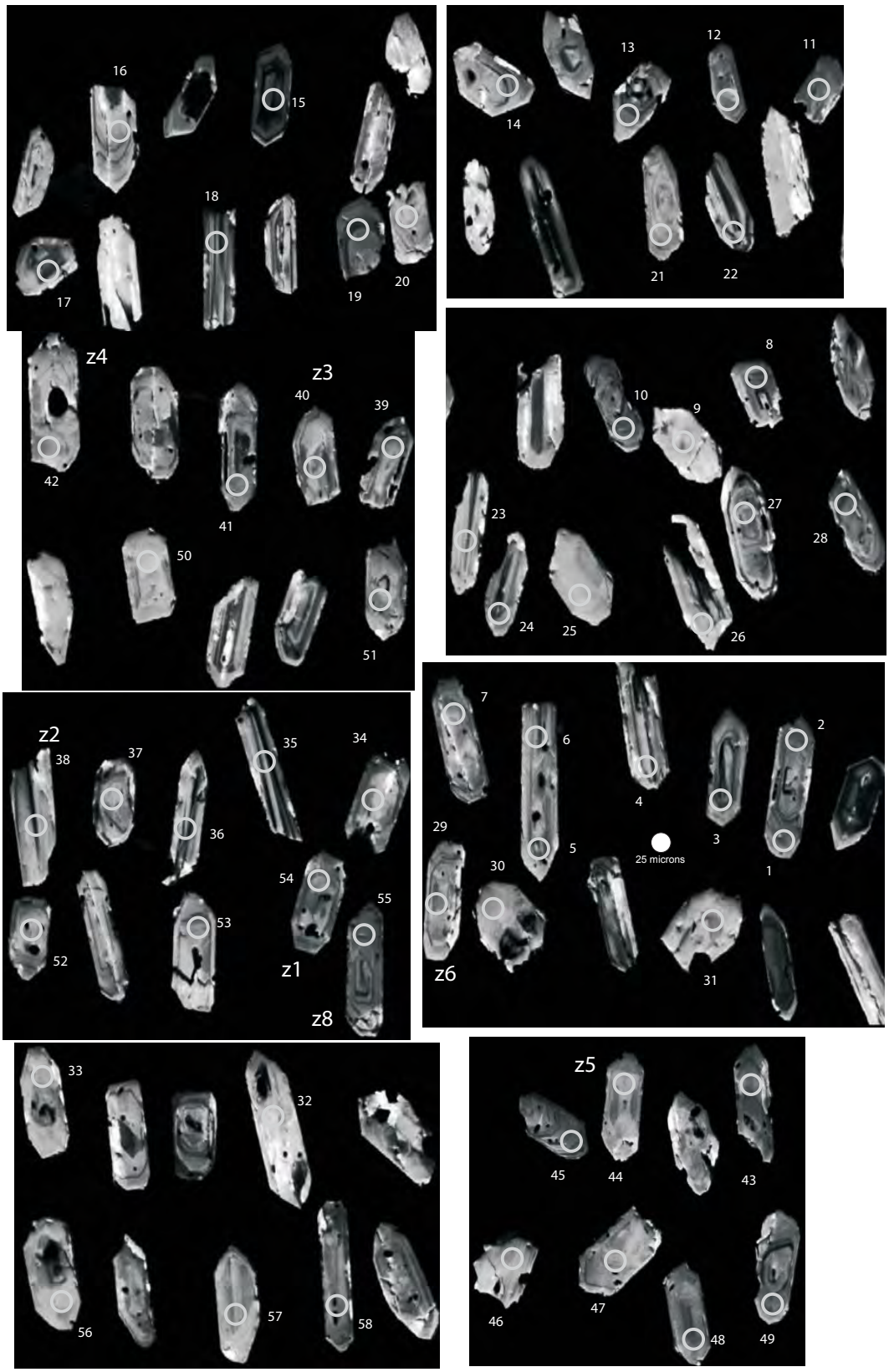

Figure A2.3. Ranked age plot of 38 youngest LA-ICPMS U-Pb zircon ages from the Fenghuoshan Tuff. The horizonal line represents the weighted mean U-Pb zircon age. Associated error is indicated from the orange shaded region. Of the 38 youngest U-Pb zircon ages, only one does not overlap with the weighted mean age.

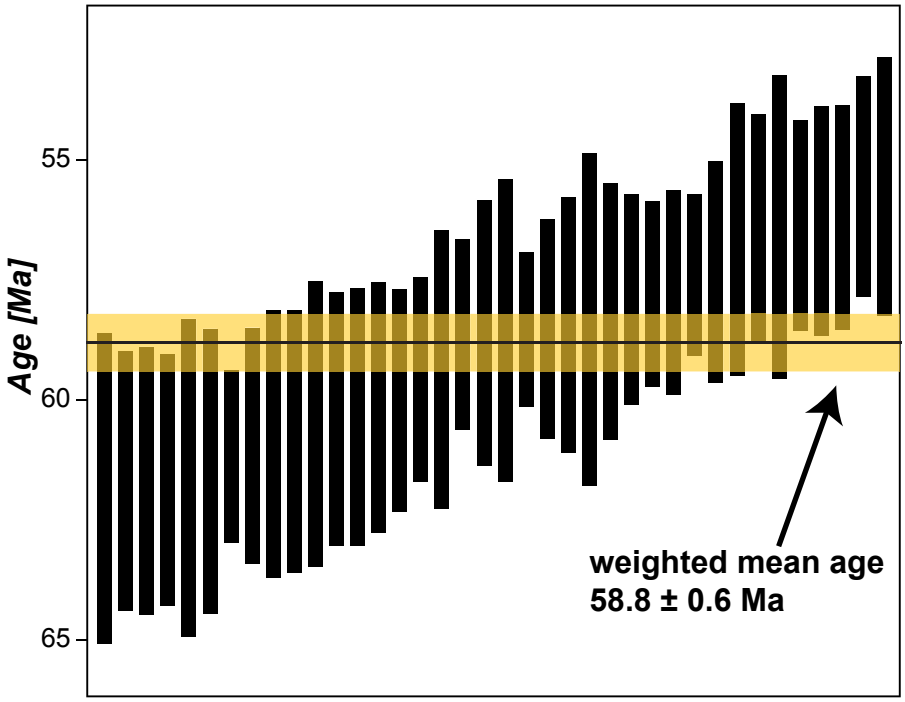

Figure A2.4. Rare earth element values of 56 zircons from the Fenghuoshan tuff sample analysed using LA-ICPMS. Concentrations are normalized using Boynton (1984) primitive mantle data.

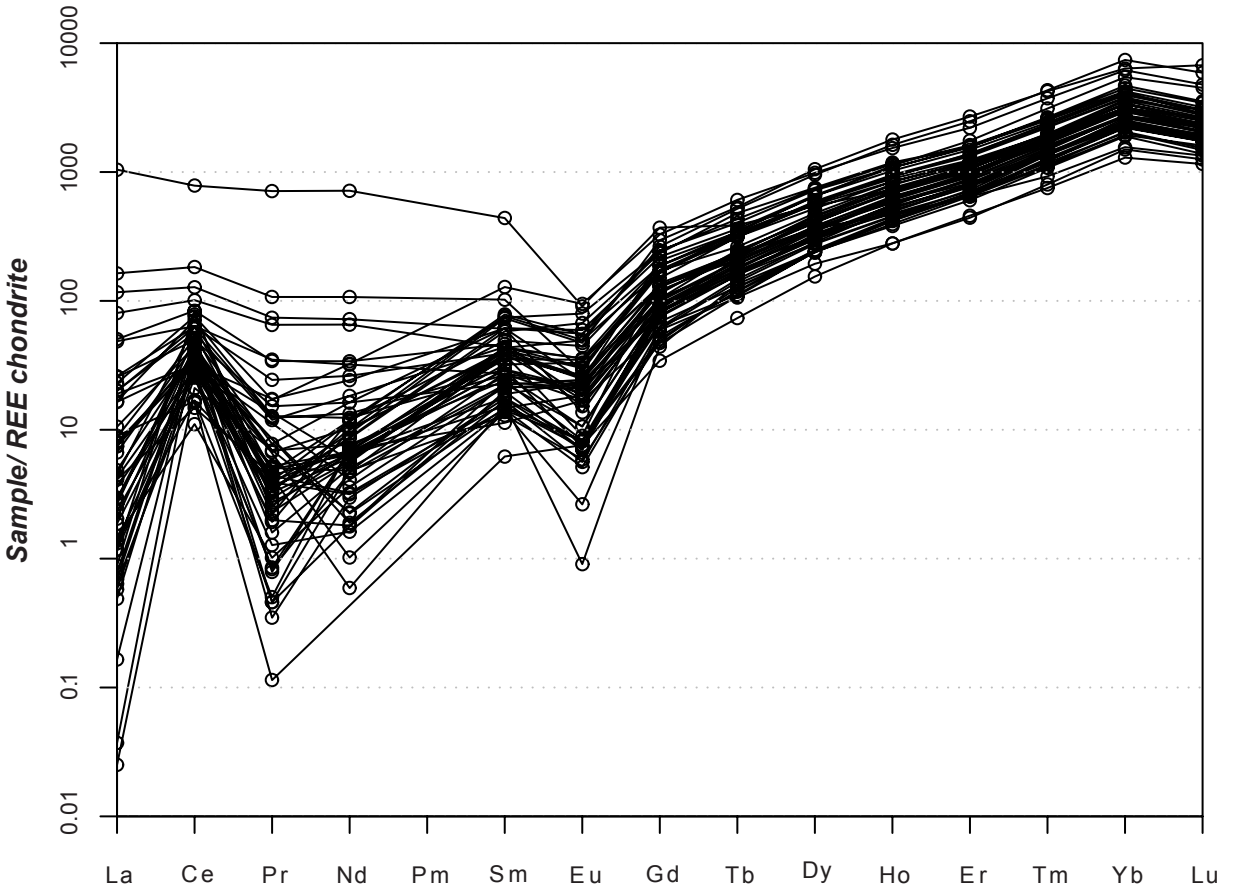

Boynton, W.V. (1984), Cosmochemistry of the rare elements: meteorite studies, in Rare Earth Element Geochemistry, edited by P. Henderson, Elsevier, pp. 63-114.

Figure A2.5. Normalized relative probability distribution of LA-ICPMS U-Pb zircon ages of the Fenghuoshan tuff (blue line) compared to SHRIMP U-Pb zircon ages from the Gangdese Batholith (red line; Wen et al., 2008)

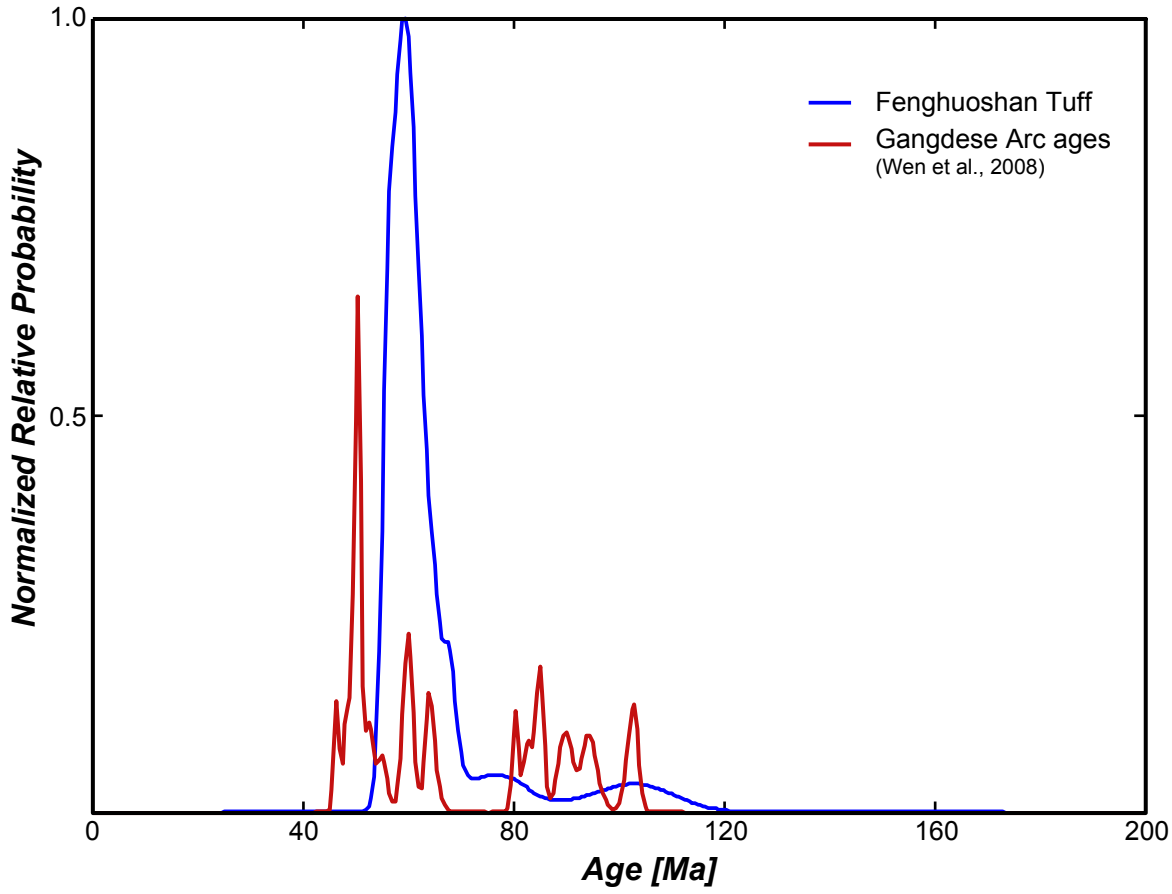

Figure A2.6. Paleomagnetic data from Liu et al., [2003]. Polarity pattern interpretation on the left is from Liu et al., [2003]. Polarity pattern on the right is from this study. Yellow shaded region is the Yaxicuo Group paleomagnetic data, which is excluded from our analysis.

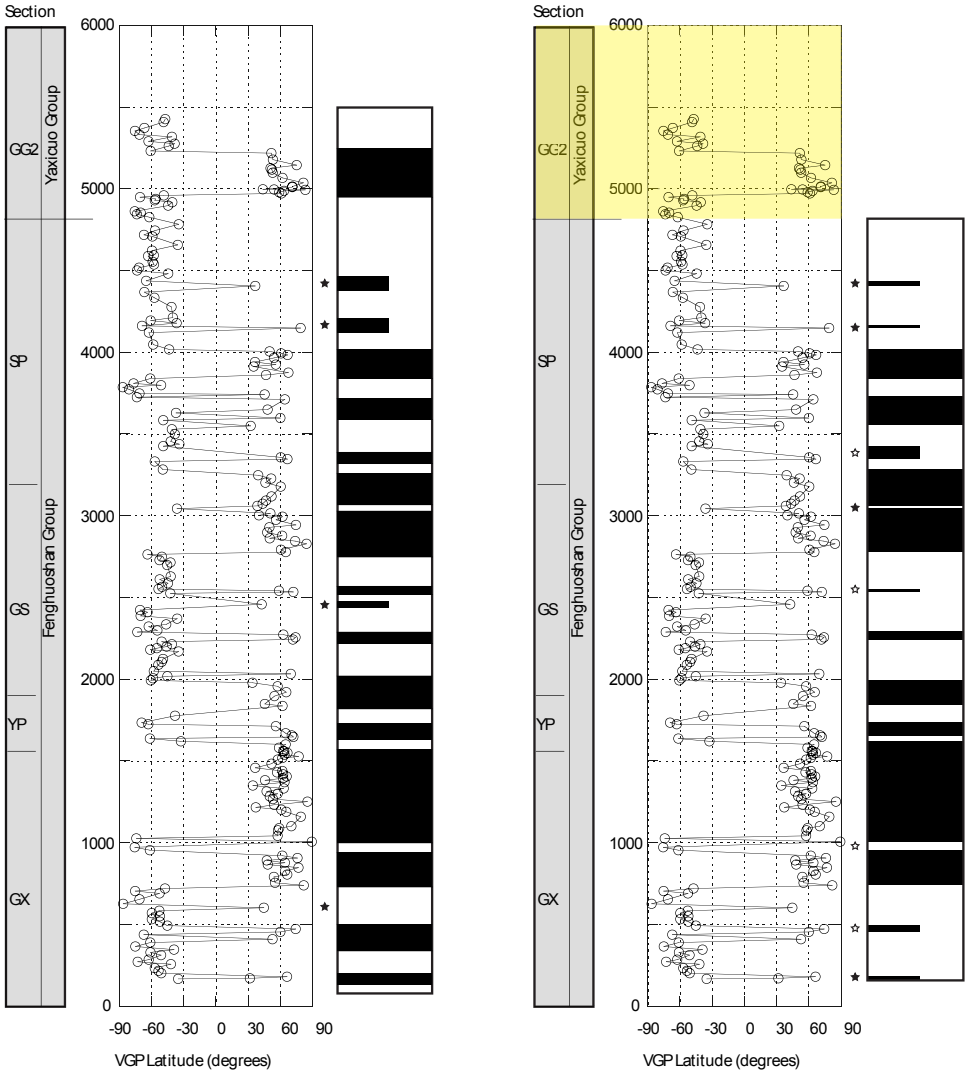

Figure A2.7. Detrital U-Pb zircon age spectra of the Fenghuoshan Group, Tibetan terranes, and Tibetan Mesozoic sedimentary rocks. OVLP=overlap, SIM=similarity , K-S=K-S test.

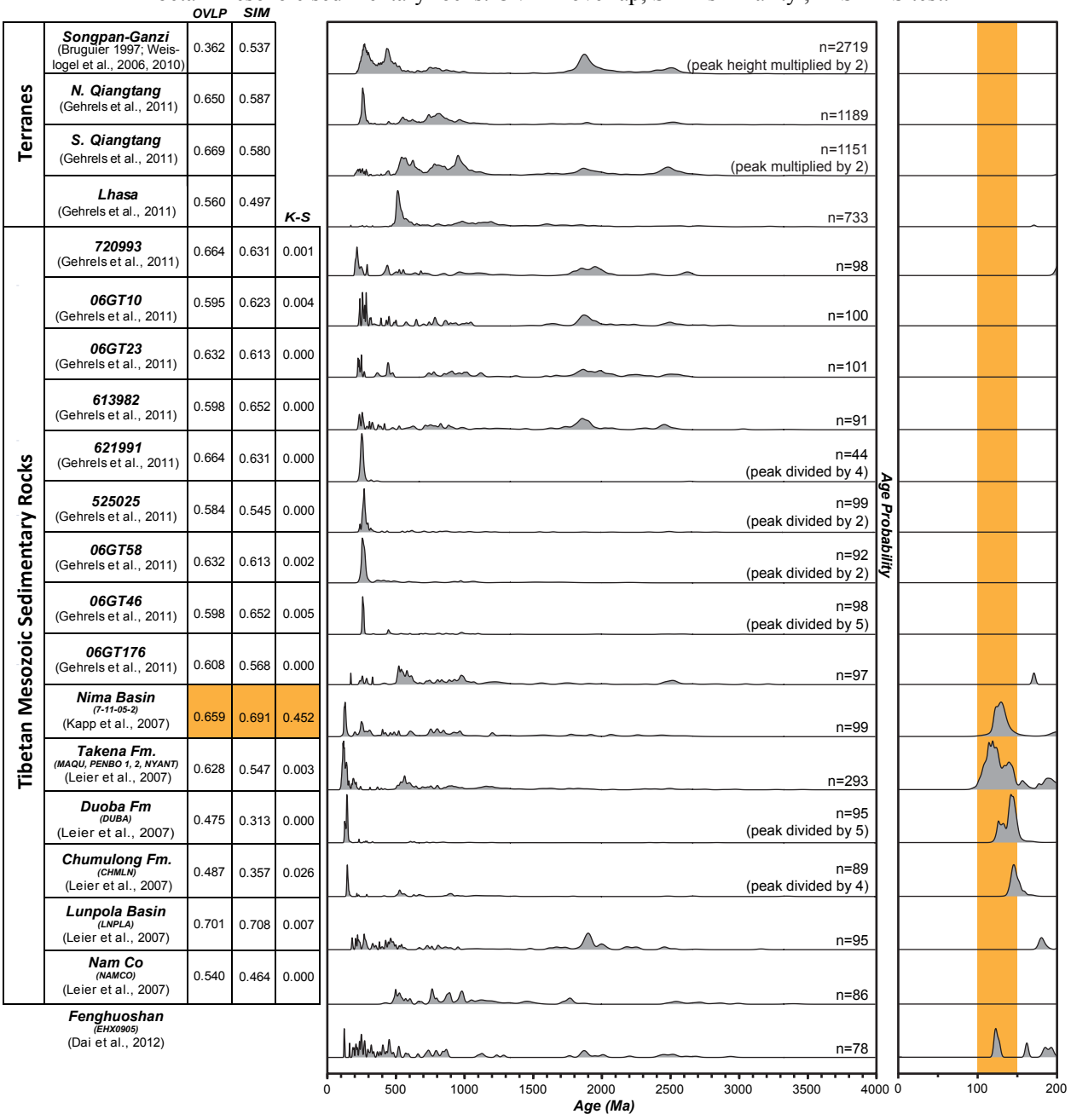

Table A2.1. Wudaoliang Fossils

Fossil Type	*Fossil*	*First appearance (Ma)*	*Last appearance (Ma)*	*Citations*
Ostracod	Candona	196.5	0.021	26; 27
	Candoniella marcida	33.9	16.0	42
	Cyclocypris	0.126	0.012	36; 40
	Cyprinotus	33.9	0.1	1; 22; 28
	Candoniella	99.6	0.012	26; 29
	Eucypris	99.6	2.6	6; 14; 22; 46
	Eucypris mutilis	40.4	23.0	29; 45
	Youshashania	22	8.5	37
Gastropod	Gyraulus	171.6	0	13
	Lymnaea	70.6	0	12
Sporopollen	Alnipollenites	141	0	25
	Betulaepollenites	345	0	25
	Chenopodipollis	111	0	25
	Cupuliferoipollenites	141	0.01	25
	Cyrillaceaepollenites	100	0.0	25
	Echitricolpites	65	0	25
	Euphorbiacites	90.3	1.8	25
	Faguspollenites	141	1.8	25
	Fraxinoipollenites	105	22.5	25
	Graminidites	150	0.01	25
	Juglanspollenites	141	0.0	25
	Labitricolpites	65	1.8	25
	Liquidambarpollenites	100	0	25
	Meliaceoidites	65	0	25
	Momipites	183	0	25
	Nitrariadites	58	1.8	25
	Nyssapollenites	345	0	25
	Potamogetonacidites	65	1.8	25
	Quercoidites	345	0	25
	Randiapollis	58	22.5	25
	Rhoipites	141	0	25
	Rutaceopollis	117	0	25
	Salixipollenites	141	1.2	25
	Tiliaepollenites	68.5	1.8	25
	Tricolpites	230.0	0.0	25
	Tricolporopollenites	230	0.01	25
	Triporoletes	230	1.8	25
	Ulmipollenites	141	0	25
	Ulmoideipites	141	0	25
	Abiespollenites	345	0.0	25
	Abietineaepollenites	345	0.0	25
	Abietineaepollenites microalatus f. minor	195	0.01	25
	Abietineaepollenites microsibiricus	65	0.01	25
	Cedripites	345	1.8	25
	Classopollis	280	0	25
	Cycadopites	360	0.00	25
	Ephedripites	345	0	25
	Inaperturopollenites	345	0	25

Table A2.1. Wudaoliang Fossils continued

Fossil Type	*Fossil*	*First appearance (Ma)*	*Last appearance (Ma)*	*Citations*
Sporopollen	Laricoidites	280.0	1.80	25
	Piceaepollenites	345.0	0.0	25
	Piceaepollenites giganteus	141	1.8	25
	Pinuspollenites	325	0	25
	Podocarpidites	280	0	25
	Taxodiaceapollenites	195	1.8	25
	Tsugaepollenites	289	0	25
	Contignisporites	223	43.9	25
	Klukisporites	242.0	0.00	25
	Polypodiaceaesporites	195	0	25
	Pterisisporites	230	0.01	25
	Rutaceoipollis	117	0	25
	Sphagnumsporites	230	1.8	25
	Undulatisporites	369	0	25
	Verrutetraspora verrucosa	90.3	11.5	25
	Campenia	195	1.8	25
	Dicellaesporites	100	1.8	25
	Inapertisporites	160	0.01	25
	Leiosphaeridia	570	0.01	25
	Multicellaesporites	100	11.5	25
	Ovoidites	199	0.01	25
	Staphlosporonites	65	5	25

Table A2.2. Yaxicuo Fossils

Fossil Type	*Fossil*	*First appearance (Ma)*	*Last appearance (Ma)*	*Citations*
Ostracod	Eucypris	99.6	2.6	6; 14; 22; 46
	Cyprinotus	33.9	0.01	1; 22
	Candoniella albicaus	65	0	30; 32
	Candoniella suzini	65	2.6	30
	Darwinula	164.7	0	7; 31
Charophyte	Amblyochara subeiensis	83.5	2.6	4; 32
	Obtusochara	99.6	33.90	20
	Obtusochara brevicylindrica	55.8	33.9	5
	Tectochara houi	23	2.6	3
Sporopollen	Classopollis	280	0	25
	Ephedripites	345	0	25
	Tricolporopollenites	230	0.01	25
	Meliaceoidites	65	0	25
	Pinaceae	345	0	25
	Lycopodiumsporites	345	0	25
	Lycopodiumsporites neogenicus	65	1.8	25
	Osmundacidites wellmanii	280	0	25
	Osmundacidites nanus	100	1.8	25
	Osmundacidites orbiculatus	230	40.25	25
	Osmundacidites semiprimarius	100	16.5	25
	Osmundacidites nicanicus	230	32.5	25
	Osmundacidites oligocaenicus	37.5	5	25
	Pterisisporites	230.0	1.80	25
	Pterisisporites danyangensis	76	37.5	25
	Pterisisporites hengyangensis	230	37.5	25
	Pterisisporites granulatus	141	5	25
	Pterisisporites dayuensis	76	37.5	25
	Cyathidites minor	280	0	25
	Interulobites exuperans	100	68.5	25
	Deltoidospora	395	0.00	25
	Deltoidospora brevisa	100	40.25	25
	Deltoidospora seidewitzensis	100	16.5	25
	Deltoidospora regularis	230	0.01	25
	Deltoidospora microlepioidites	230	37.5	25
	Polypodiaceaesporites	195	0	25
	Polypodiaceaesporites haardti	176	0	25
	Polypodiaceaesporites gracilis	94	1.8	25
	Toroisporis minor	68.5	22.5	25
	Toroisporis longilaesuratus	230	22.5	25
	Hymenophyllumsporites gracilis	100	94	25
	Hymenophyllumsporites pseudoreticulatus	105	11.5	25
	Leptolepidites major	280	11.5	25
	Zlivisporis novamexicanum	100	22.5	25
	Zlivisporis bireticularis	100	22.5	25

Table A2.2. Yaxicuo Fossils continued

Fossil Type	*Fossil*	*First appearance (Ma)*	*Last appearance (Ma)*	*Citations*
Sporopollen	Pinuspollenites	325	0	25
	Pinuspollenites labdacus f. minor	230	0.01	25
	Pinuspollenites microinsignis	100	0.01	25
	Pinuspollenites taedaeformis	111	27.5	25
	Pinuspollenites labdacus f. maximus	230	0.01	25
	Abietineaepollenites	345	0.0	25
	Abietineaepollenites medius	65	3.9	25
	Abietineaepollenites microalatus minor	195	0.01	25
	Abietineaepollenites microalatus f. minor	195	0.01	25
	Abietineaepollenites quadriangulus	54.5	1.8	25
	Abietineaepollenites cf. quadriangulus	54.5	1.8	25
	Abietineaepollenites lenghuensis	65	3.9	25
	Abietineaepollenites baileyana	40.25	3.9	25
	Abietineaepollenites cembraeformis	65	0.01	25
	Abietineaepollenites pacltovae	65	11.5	25
	Cedripites	345	1.8	25
	Cedripites pachydermus	230	3.9	25
	Cedripites microsaccoides	174	1.8	25
	Cedripites reniformis	40.25	3.9	25
	Cedripites trapeziformis	40.25	3.9	25
	Cedripites cornisaccatus	100	1.8	25
	Abiespollenites	345	0.0	25
	Keteleeriaepollenites dubius	100	0.01	25
	Piceapollis	103	5	25
	Piceapollis gigantea	100	22.5	25
	Piceapollis planoides	68.5	3.9	25
	Piceapollis tobolicus	100	3	25
	Tsugaepollenites igniculus minor	134	0	25
	Tsugaepollenites igniculus f. major	134	0	25
	Laricoidites magnus	230	0.01	25
	Laricoidites araucarites	141	22.5	25
	Podocarapites	289	0.01	25
	Taxodiaceaepollenites vacuipites	100	5	25
	Taxodiaceaepollenites hiatus	370	0.01	25
	Inaperturopollenites	345	0	25
	Inaperturopollenites dubius	370	0.01	25
	Inaperturopollenites psilosus	230	27.5	25
	Ephedripites	345	0	25
	Ephedripites trinata	123	1.8	25
	Ephedripites obsus	230	22.5	25
	Ephedripites fushunensis	100	1.8	25
	Ephedripites baculatus	54.5	1.8	25

Table A2.2. Yaxicuo Fossils continued

Fossil Type	*Fossil*	*First appearance (Ma)*	*Last appearance (Ma)*	*Citations*
Sporopollen	Ephedripites dafengshanensis	100	1.8	25
	Ephedripites strigatus	174	3.9	25
	Ephedripites ganchaigouensis	40.25	11.5	25
	Momipites coryloides	141	0.01	25
	Cupuliferoipollenites fusus	123	3.9	25
	Quercoidites asper	123	1.8	25
	Quercoidites robusteus	68.5	15	25
	Celtispollenites minor	100	0.01	25
	Magnolipollis magnolioides	230	1.8	25
	Magnolipollis micropunctatus	100	7.5	25
	Ilexpollenites margaritus	100	0.01	25
	Tiliaepollenites cf. instructus	27.5	1.8	25
	Lonicerapollis intrabaculus	100	22.5	25
	Lonicerapollis lenghuensis	68.5	11.5	25
	Lonicerapollis granulatus	68.5	11.5	25
	Lonicerapollis interspinosus	68.5	1.8	25
	Lonicerapollis xiangxiangensis	68.5	37.5	25
	Lonicerapollis simplex	68.5	22.5	25
	Lonicerapollis parvina	68.5	37.5	25
	Lonicerapollis tenuipolaris	68.5	22.5	25
	Lonicerapollis echinatus	65	3.9	25
	Araliaceoipollenites euphorii	195	0.01	25
	Populus	65	5	25
	Fraxinoipollenites genuinus	55.8	5	25
	Aceripites reticulatus	100	5	25
	Peltandripites laurusiformis	100	22.5	25
	Nyssapollenites rodderensis	100	5	25
	Nyssapollenites pseudolaesus	100	5	25
	Chenopodipollis cf. multiplex	195	5	25
	Scabiosapollis intrabaculus	100	22.5	25
	Potamogetonacidites natanoides	100	22.5	25
	Potamogetonacidites minor	100	22.5	25
	Nymphaeacidites echinatus	100	3.9	25
	Retitricolpites matauraensis	100	5	25
	Tricolpites	230	0.01	25
	Tricolpites granulatus	90.3	54.5	25
	Tricolpites microreticulatus	88	5	25
	Brevitricolpites	100	5	25
	Tricolporopollenites	141	0.01	25
	Cruciferaeipites minor	100	22.5	25
	Triporopollenites	160	0.01	25

Table A2.3. Tuotuohe Fossils

Fossil Type	*Fossil*	*First appearance (Ma)*	*Last appearance (Ma)*	*Citations*
Ostracod	Candoniella albicans	65	2.6	19; 29
	Darwinula	164.7	0.0	7; 31
	Cypris decaryi	55.8	0.0	16
Charophyte	Pekichara serialis	83.5	55.8	33
Sporopollen	Pteris neocretica	8.7	1.8	25
	Sparganiaceaepollenites neogenicus	100	1.8	25
	Tricolpites	230	0	25
	Salixipollenites	141	1.2	25
	Quercus monimotricha	8.7	1.8	25
	Chenopodipollis	111	0	25
	Deltoidospora regularis	223	3.9	25
	Osmundacidites	404	0	25
	Polypodiisporites	289	0	25
	Pterisisporites undulatus	230	1.8	25
	Toroisporis planivercosus	145	2.6	9; 25; 37
	Undulatiosporites	369	0	25
	Abietineaepollenites cembraeformis	111	0.01	25
	Cedripites	345	1.8	25
	Cedripites diverus	111	2.86	25
	Classopollis	280	0	25
	Classopollis annulatus	230	1.8	25
	Ephedripites	345	0	25
	Ephedripites (Distachyaptes) eocenipites	150	1.8	25
	Ephedripites (Distachyaptes) fusiformis	141	1.8	25
	Piceaepollenites	345.0	0.0	25
	Piceaepollenites alatus	223	0.01	25
	Pinuspollenites	325	0	25
	Pinuspollenites insignis	230	1.8	25
	Pinuspollenites labdacus f. maximus	230	0.01	25
	Podocarpidites	280	0	25
	Podocarpidites andiniformis	230	1.8	25
	Tsugaepollenites igniculus major	141	0	25
	Alnipollenites	141	0	25
	Alnipollenites verus	141	0	25
	Betulaepollenites	345	0	25
	Caryapollenites juxtaporites	65	22.5	25
	Caryapollenites simplex	195	0	25
	Celtispollenites triporatus	100	11.5	25
	Cupuliferoipollenites	141	0.01	25
	Cupuliferoipollenites fusus	141	1.8	25
	Cupuliferoipollenites pusillus	141	0.01	25
	Elaeagnacites	100	1.8	25
	Euphorbiacites reticulates	195	1.8	25
	Jianghanpollis	90.3	37.5	25
	Juglanspollenites verus	40.4	5.3	11; 17; 23
	Labitricolpites microgranulatus	65	1.8	25
	Labitricolpites minor	65	16.5	25

Table A2.3. Tuotuohe Fossils continued

Fossil Type	*Fossil*	*First appearance (Ma)*	*Last appearance (Ma)*	*Citations*
Sporopollen	Labitricolpites scabiosus	65	1.8	25
	Meliaceoidites microreticulatus	58	3.9	25
	Meliaceoidites ovatus	54.5	1.8	25
	Meliaceoidites rhomboiporus	141	1.8	25
	Meliaceoidites rotundus	65	3.9	25
	Meliaceoidites	65	0	25
	Momipites	183	0	25
	Ostryoipollenites	141	0.9	25
	Pentapollenites	141	1.8	25
	Pokrovskaja	65	22.5	25
	Pokrovskaja maximus	54.5	32.5	25
	Pokrovskaja minor	54.5	5	25
	Pokrovskaja pachypolarus	54.5	32.5	25
	Quercoidites	345	0	25
	Quercoidites asper	141	0.01	25
	Quercoidites henrici	195	0.01	25
	Quercoidites microhenrici	195	0.01	25
	Quercoidites minatus	115	1.8	25
	Rhoipites	141	0	25
	Rhoipites rhomboius	141	1.8	25
	Rutaceoipollis	117	0	25
	Sapindaceidites	90.3	1.8	25
	Scabiosapollis	100	5	25
	Sporopollis	141	1.8	25
	Tricolpopollenites	195	0.01	25
	Tricolporopollenites	230	0.01	25
	Tubulifloridites xanthiformis	100	1.8	25
	Ulmipollenites	141	0	25
	Ulmipollenites minor	141	1.8	25
	Ulmipollenites undulosus	141	0.01	25
	Ulmoideipites krempii	141	1.8	25

Table A2.4. Fenghuoshan Fossils

Fossil Type	*Fossil*	*First appearance (Ma)*	*Last appearance (Ma)*	*Citations*
Ostracod	Cypria	93.5	0.00	6; 26
	Cypris	145.5	0.01	10; 15; 24; 33
	Eucypris	99.6	2.60	6; 17; 22; 46
	Kaitunia	99.6	65.50	46
	Quadracypris	145.5	55.80	18
	Rhinocypris	161.2	99.60	44
Gastropod	Amnicola	199.6	0.00	33; 46
	Sinoplanorbis	55.8	23.03	30; 38
Charophyte	Gyrogona qinghaiensis	65.5	23.03	45
	Obtusochara	99.6	33.90	20
	Peckichara subsphaerica	58.7	55.80	33
	Rhabdochara	70.6	28.40	21
Sporopollen	Admolia	230	99.6	2
	Biretisporites	230	1.8	25
	Caytonipollenites	250	61.5	25
	Cedripites	345	1.8	25
	Cicatricosisporites	370.0	0	25
	Classopollis	280	0	25
	Concavisporites	345.0	0	25
	Concentrisporites	230.0	65	25
	Converrucosisporites	395	0.01	25
	Cyanthidites	202	65.5	25
	Cycadopites	360	0	25
	Deltoidospora	395	0	25
	Densoisporites	338.0	0	25
	Divisisporites	230.0	1.8	25
	Ephedripites	345	0	25
	Ephedripites Distachyapites	345	0	25
	Equisetites	280.0	54	25
	Exesipollenites tumulus	275.6	1.8	25
	Granulatisporites	395.0	0	25
	Ischyosporites	280.0	1	25
	Jiaohepollis	230.0	65	25
	Klukisporites	242.0	0	25
	Laricoidites	280.0	1.8	25
	Laricoidites magnus	223.0	1.8	25
	Lycopodiumsporites	345.0	0	25
	Monosulcites	345	0	25
	Muerrigerisporis	230	5	25
	Pediastrum	280	0	25

Table A2.4. Fenghuoshan Fossils continued

Fossil Type	*Fossil*	*First appearance (Ma)*	*Last appearance (Ma)*	*Citations*
Sporopollen	Perinopollenites	230	1.8	25
	Piceaepollenites	345.0	0.01	25
	Pinuspollenites	325	0	25
	Podocarpidites	280	0	25
	Pristinuspollenites	230	22.5	25
	Pseudopicea	345	1.8	25
	Pseudopicea rotundiformis	280.0	1.8	25
	Psophosphaera	345	0.01	25
	Pterisisporites	230.0	1.8	25
	Schizacoisporites	299.0	0.01	25
	Schizosporites	242.0	37.5	25
	T. aliquantulus	111.0	54.5	25
	Tricolpites	230.0	0	25
	Tricolpopollenites	195.0	0.01	25
	Tricolporopollenites	230.0	0.01	25

Table A2.5. Citations for fossil age ranges

Reference Number	Citations
1	Alberdi, M. T. and Sanchez-Chillon, B., 1998, The Cullar Baza 1 site. In Agusti, J., Oms, O. and Martin-Suarez, E., 1998, The Plio-Pleistocene vertebrate succession of the Guadix-Baza Basin (SE Spain), *European Quaternary Mammal Research Association (INQUA-SEQS)* 33-35
2	Batten, D.J., 1973, Palynology of early Cretaceous soil beds and associated strata, *Paleontology*, **16**(2), p 399-424
3	Bovet, P. M., Ritts, B. D., Gehrels, G., Abbink, A. O., Darby, B., & Hourigan, J., 2009, Evidence of Miocene crustal shortening in the north Qilian Shan from Cenozoic stratigraphy of the western Hexi Corridor, Gansu Province, *China.American Journal of Science,* **309**(4), 290-329.
4	Buffetaut, E.,Marandat, B., and Sigé, B., 1986, Découverte de dents de deinonychosaures (Saurischia, Theropoda) dans le Crétacé superieur du Sud de la France [Discovery of deinonychosaur teeth (Saurischia, Theropoda) in the Upper Cretaceous of southern France]**.** *Comptes Rendus de l'Académie des Sciences à Paris, Série II* **303**:1393-1396
5	Chen, L., and Y. Xie, 2011, Discussion of the Paleocene-Eocene boundary of SanShui Basin, *Advanced Materials Research,* **236-238**, p 2487-2490
6	Currie, P.J. and D.A. Eberth, 1994, Palaeontology, sedimentology and palaeoecology of the Iren Dabasu Formation (Upper Cretaceous), Inner Mongolia, People's Republic of China, *Cretaceous Research,* **14**, p 127-144
7	Deng, T., Wang, S., Xie, G., Li, Q., Hou, S., & Sun, B., 2012, A mammalian fossil from the Dingqing Formation in the Lunpola Basin, northern Tibet, and its relevance to age and paleo-altimetry, *Chinese Science Bulletin,* **57**(2), 261-269
8	Ding, Q.h. and L.j. Zhang, 2005, The lower Triassic series and its palynological assemblages in southwestern Songliao Basin, NE China, *Acta Micropalaeontologica Sinica*, (1), p 107-114
9	Fang, A., Liu, X., Wang, W., Yu L., Li, X., Huang, F., Premilimary study on the spore-pollen assemblages found in the Cenozoic sedimentary rocks in Grove Mountains, East Antarctica, *Quaternary Research*, 2004, **24**(6): 645-653
10	Forbes, E., 1856, On the Tertiary fluvio-marine formation of the Isle of Wight, *Memoirs of the Geological Survey of Great Britain, and of the Museum of Practical Geology,* p. 1-162
11	Gengwu, L., & Rongyu, Y. (1999). Pollen assemblages of the late Eocene Nadu Formation from the Bose basin of Guangxi, southern China. *Palynology*, **23**(1), 97-114.
12	Grigorescu, D., Venczel, M., Csiki, Z., and Limberea, R., 1999, New latest Cretaceous microvertebrate fossil assemblages from the Hateg Basin (Romania). *Geologie en Mijnbouw* **78**:301-314
13	Gründel, J., Pelissie, T., and Guerin, M., 2000, Brackwasser-Gastropoden des mittleren Doggers von La Balme (Causses du Quercy, Südfrankreich). *Berliner geowissenschaftliche Abhandlungen*, Reihe E **34**:185-203
14	Guernet, C., 1994, Ostracods from Nkondo Formation,upper Miocene,lake Albert Basin,Uganda, *.Int.Cent.Train.Exch.in the Geosci.,* 29, p. 59-63
15	Harris, J.M, 1983, Koobi Fora Research Project The Fossil Ungulates: Proboscidea, Perissodactyla, Suidae. *Clarendon Press, Oxford, United Kingdom* 2
16	Holmes, J. A. (1997). Recent non-marine Ostracoda from Jamaica, West Indies, *Journal of Micropalaeontology*, **16**(2), 137-143.
17	Hoorn, C., Straathof, J., Abels, H. A., Xu, Y., Utescher, T., & Dupont-Nivet, G. (2012). A late Eocene palynological record of climate change and Tibetan Plateau uplift (Xining Basin, China). *Palaeogeography, Palaeoclimatology, Palaeoecology*, **344–345**, 16–38
18	Hou, Y., T. Chen, H. Yang, J. Ho, 1982, Cretaceous-Quaternary ostracode fauna from Jiangsu,Beijing,*Geological Publishing House*, p 386 (in Chinese with English abstract)
19	Huang, B., Guo, S., Wu, R., & Guo, S., 1992, Late Cenozoic Stratigraphy and Sedimentary Environments of Central Shanxi Province.
20	Huang, R.J., 1985, Cretaceous and early Tertiary charophytes from Sichuan, *Acta Micropaleontologica Sinica*, (2), p 77-89
21	Jaillard, E., Grambast-Fessard, N., Feist, M., & Carlotto, V., 1994, Senonian-Paleocene charophyte succession of the Peruvian Andes, Cretaceous Research, ***15***(4), 445-456.
22	Kadolsky, D., 1975, Zur Palaeontologie und Biostratigraphie des Tertiärs im Neuwieder Becken; I. Taxonomie und stratigraphische Bedeutung von Mollusken. *Decheniana* **128**:113-137
23	Li, J. G., Guo, Z. Y., Batten, D. J., Cai, H. W., & Zhang, Y. Y. (2010). Palynological stratigraphy of the Late Cretaceous and Cenozoic collision-related conglomerates at Qiabulin, Xigaze, Xizang (Tibet) and its bearing on palaeoenvironmental development. *Journal of Asian Earth Sciences*, **38**(3), 86-95.
24	Owen, R., 1861, Monograph on the fossil Reptilia of the Wealden and Purbeck formations. Part V. Lacertilia (Nuthetes, etc.), *The Palaeontological Society, London,* 1858, p. 31-39
25	Palynodata Inc. and J.M. White, 2008. Palynodata Datafile: 2006 version, with Introduction by J. M. White. *Geological Survey of Canada Open File 5793*, 1 CD-ROM.
26	Pu, Q. and F. Qian ,1977,Identification of the Yuanmou fossil-man strata; study of the Yuanmou Formation, *Acta Geologica Sinica*, (1), p 89-100
27	Rao, C.N. and S.C. Shah, 1963, On the occurrence of pterosaur from the Kota-Maleri beds of Chanda District, Maharashtra, *Records of the Geological Survey of India*, 92, 315-318
28	Schultz, G.E., 1969, Geology and paleontology of a late Pleistocene basin in southwest Kansas, *Geological Society of America Special Paper* **105**:1-85
	Shen, Y.B. and N. J. Mateer, 1992, An outline of the Cretaceous System in northern Xinjiang, western China. In N. J. Mateer, P.-j. Chen (eds.), *Aspects of Nonmarine Cretaceous Geology*, China Ocean Press, Beijing, 50-77.
29	Shen, Z. (1995). Cretaceous-Eogene Ostracod Assemblages in Henan and Their Evolutionary Features. Acta Geologica Sinica-English Edition, 8(1), 99-110.
30	Smith, A.B.,& Xu, J., 1988, Palaeontology of the 1985 Geotraverse, Lhasa to Golmud. *Phil. Trans. R. Soc. Lond. A* **327**:53-105
31	Sun, Z., Feng, X., Li, D., Yang, F., Qu, Y., & Wang, H., 1999, Cenozoic Ostracoda and palaeoenvironments of the northeastern Tarim Basin, western China, *Palaeogeography, Palaeoclimatology, Palaeoecology,* **148**(1), 37-50.
32	Van Itterbeeck, J., P. Missiaen, A. Folie, V.S. Markevich, D. Van Damme, D.y. Guo, T. Smith, 2007, Woodland in a fluvio-lacustrine environment on the dry Mongolian Plateau during the late Paleocene: Evidence from the mammal bearing Subeng section (Inner Mongolia, P.R. China), *Palaeogeography, Palaeoclimatology, Palaeoecology*, **243**(1-2), p 55-78
33	Wang, W.m., 2006, Correlation of pollen sequences in the Neogene palynofloristic regions of China, *Palaeoworld*, **15**(1), p 77-99
34	Wang, W.t., Zhang, P.z., Kirby, E., Wang, L.h., Zhang, G.l., Zheng, D.w., Chai, C.Z., 2011, A revised chronology for Tertiary sedimentation in the Sikouzi basin: Implications for the tectonic evolution of the northeastern corner of the Tiebetan Plateau, *Tectonophysics,* **505**(1-4), p 100-114

Table A2.6. LA-ICPMS U-Pb geochronologic analysis

677-187 Fenghuoshan Tuff

92.85386° E, 34.611° N

						Corrected isotope ratios														*Apparent ages (Ma)*							
Spot #	U ppm	Th ppm	Pb* ppm	Th/U	$^{206}Pb/^{204}Pb$	$^{208}Pb^*/^{232}Th$	±2σ (%)	$^{206}Pb^*/^{207}Pb^*$	±2σ (%)	$^{207}Pb^*/^{235}U^*$	±2σ (%)	$^{206}Pb^*/^{238}U^*$	±2σ (%)	error corr.	$^{238}U^*/^{206}Pb^*$	±2σ (%)	$^{207}Pb^*/^{206}Pb^*$	±2σ (%)	$^{208}Pb^*/^{232}Th$	±2σ (%)	$^{207}Pb^*/^{206}Pb^*$	±2σ (%)	$^{207}Pb^*/^{235}U^*$	±2σ (%)	$^{206}Pb^*/^{238}U^*$	±2σ (%)
1	350.63	301.17	0.83	0.86	61.20	0.00	8.33	20.52	10.96	0.06	11.47	0.01	3.36	0.29	111.06	3.36	0.05	10.96	70	6	135	258	60	7	58	2
2	517.86	944.77	3.31	1.82	113.05	0.00	6.78	19.81	10.05	0.06	11.68	0.01	5.97	0.51	110.05	5.97	0.05	10.05	69	5	217	233	62	7	58	3
3	137.03	134.12	2.49	0.98	164.13	0.03	36.12	4.84	18.00	0.45	25.38	0.02	17.89	0.70	64.02	17.89	0.21	18.00	567	202	2880	292	374	79	100	18
4	127.43	136.48	0.46	1.07	65.58	0.00	10.72	21.15	25.01	0.06	25.40	0.01	4.46	0.18	106.30	4.46	0.05	25.01	69	7	63	596	60	15	60	3
5	446.43	639.15	4.34	1.43	325.89	0.00	6.72	15.28	17.67	0.09	17.97	0.01	3.30	0.18	101.09	3.30	0.07	17.67	94	6	789	371	87	15	63	2
6	219.93	213.41	-2.07	0.97	22.04	0.00	10.89	23.90	18.98	0.06	19.69	0.01	5.24	0.27	100.06	5.24	0.04	18.98	83	9	-236	479	57	11	64	3
7	282.26	251.96	2.33	0.89	297.13	0.00	8.77	21.50	10.82	0.06	11.51	0.01	3.91	0.34	113.87	3.91	0.05	10.82	68	6	25	260	56	6	56	2
8	208.52	263.90	1.87	1.27	664.86	0.00	6.40	21.60	16.77	0.06	17.38	0.01	4.57	0.26	109.80	4.57	0.05	16.77	69	4	14	403	57	10	58	3
9	64.45	65.95	0.12	1.02	33.12	0.01	16.19	6.18	51.94	0.22	52.34	0.01	6.49	0.12	100.20	6.49	0.16	51.94	146	24	2475	877	204	97	64	4
10	301.83	271.33	2.89	0.90	233.14	0.01	12.88	12.41	23.87	0.12	24.74	0.01	6.51	0.26	96.00	6.51	0.08	23.87	112	14	1211	470	111	26	67	4
11	185.27	168.08	0.69	0.91	52.55	0.00	9.36	21.75	21.78	0.06	22.11	0.01	3.80	0.17	110.84	3.80	0.05	21.78	79	7	-4	525	56	12	58	2
12	142.24	137.69	0.35	0.97	36.34	0.00	14.32	12.88	16.31	0.10	16.77	0.01	3.88	0.23	106.92	3.88	0.08	16.31	90	13	1138	325	97	15	60	2
13	305.11	224.42	1.67	0.74	64.82	0.00	8.67	16.81	10.69	0.08	11.54	0.01	4.35	0.38	106.67	4.35	0.06	10.69	88	8	586	232	75	8	60	3
14	176.64	279.13	0.32	1.58	37.64	0.00	9.28	20.07	17.79	0.07	18.36	0.01	4.54	0.25	104.03	4.54	0.05	17.79	81	7	186	414	65	12	62	3
16	245.71	179.99	0.88	0.73	40.22	0.00	9.93	21.84	13.36	0.06	14.17	0.01	4.74	0.33	109.51	4.74	0.05	13.36	66	7	-13	323	57	8	59	3
17	251.95	497.24	1.60	1.97	263.08	0.00	7.37	20.73	13.12	0.06	13.90	0.01	4.60	0.33	105.32	4.60	0.05	13.12	76	6	111	310	62	8	61	3
18	285.85	381.73	1.69	1.34	87.04	0.00	8.52	22.06	20.93	0.06	21.39	0.01	4.39	0.21	106.23	4.39	0.05	20.93	70	6	-	-	58	12	60	3
19	615.51	515.89	4.77	0.84	257.66	0.00	5.71	20.09	7.84	0.06	8.67	0.01	3.71	0.43	111.12	3.71	0.05	7.84	74	4	184	182	61	5	58	2
20	138.54	103.20	0.47	0.74	25.16	0.00	12.76	18.36	20.02	0.07	20.74	0.01	5.41	0.26	109.59	5.41	0.05	20.02	77	10	390	449	67	14	59	3
21	156.17	129.69	1.19	0.83	279.20	0.00	11.06	23.49	19.73	0.05	20.17	0.01	4.18	0.21	114.23	4.18	0.04	19.73	67	7	-192	494	51	10	56	2
22	127.19	163.33	0.79	1.28	69.96	0.01	10.10	12.57	30.77	0.12	30.98	0.01	3.65	0.12	94.40	3.65	0.08	30.77	115	12	1185	608	112	33	68	2
23	244.37	253.43	1.70	1.04	103.70	0.00	7.75	17.16	11.77	0.08	12.44	0.01	4.05	0.33	105.27	4.05	0.06	11.77	86	7	540	257	75	9	61	2
24	185.11	190.80	1.20	1.03	33.22	0.00	16.33	14.78	35.98	0.11	37.87	0.01	11.82	0.31	87.87	11.82	0.07	35.98	96	16	858	747	102	37	73	9
25	147.22	136.17	1.14	0.92	545.80	0.00	9.25	19.87	50.73	0.06	50.85	0.01	3.40	0.07	109.46	3.40	0.05	50.73	70	6	210	1176	62	31	59	2
26	109.56	338.37	3.53	3.09	14.79	0.01	16.99	5.75	30.63	0.38	35.50	0.02	17.94	0.51	63.15	17.94	0.17	30.63	109	18	2595	511	327	99	101	18
27	169.63	131.20	1.37	0.77	5373.65	0.00	10.37	17.91	18.50	0.07	18.98	0.01	4.27	0.23	104.04	4.27	0.06	18.50	96	10	446	411	72	13	62	3
28	264.94	198.64	1.81	0.75	54.15	0.00	9.16	20.56	11.46	0.06	12.15	0.01	4.05	0.33	111.95	4.05	0.05	11.46	74	7	130	270	59	7	57	2
29	196.90	213.58	1.47	1.08	191.48	0.00	10.03	26.26	17.09	0.05	17.65	0.01	4.41	0.25	104.00	4.41	0.04	17.09	69	7	-480	453	50	9	62	3
30	138.80	88.46	1.22	0.64	1643.00	0.00	15.47	17.26	33.22	0.08	33.66	0.01	5.40	0.16	104.12	5.40	0.06	33.22	82	13	528	728	75	24	62	3
31	129.03	137.89	0.87	1.07	24.98	0.00	9.46	23.79	35.31	0.06	35.72	0.01	5.38	0.15	100.42	5.38	0.04	35.31	76	7	-224	889	57	20	64	3
33	652.95	931.86	3.61	1.43	85.91	0.00	4.80	22.23	9.00	0.06	9.42	0.01	2.76	0.29	109.65	2.76	0.04	9.00	78	4	-56	219	56	5	59	2
34	204.23	181.76	1.68	0.89	48.91	0.01	21.31	18.42	22.61	0.08	23.38	0.01	5.92	0.25	94.72	5.92	0.05	22.61	116	25	383	508	77	17	68	4
35	348.42	497.79	3.09	1.43	83.15	0.00	23.62	21.18	21.63	0.08	23.49	0.01	9.17	0.39	79.92	9.17	0.05	21.63	94	22	60	515	80	18	80	7
36	66.93	96.16	-0.07	1.44	354.14	0.02	33.10	4.34	19.61	0.53	22.55	0.02	11.14	0.49	59.49	11.14	0.23	19.61	439	144	3055	314	434	80	107	12
37	160.65	151.71	1.31	0.94	108.38	0.00	13.87	23.80	18.76	0.05	19.29	0.01	4.51	0.23	105.43	4.51	0.04	18.76	65	9	-226	472	54	10	61	3
38	558.06	447.93	4.24	0.80	127.12	0.00	6.01	22.47	7.52	0.06	8.49	0.01	3.92	0.46	109.68	3.92	0.04	7.52	70	4	-83	184	55	5	59	2
39	235.49	205.67	1.73	0.87	40.25	0.00	8.64	17.85	13.74	0.07	14.39	0.01	4.27	0.30	114.06	4.27	0.06	13.74	79	7	453	305	67	9	56	2
40	181.68	178.23	1.29	0.98	24.46	0.00	7.62	25.67	22.04	0.05	22.24	0.01	2.95	0.13	104.89	2.95	0.04	22.04	74	6	-420	577	51	11	61	2
41	238.99	239.63	2.46	1.00	136.75	0.00	15.86	18.15	25.12	0.10	30.54	0.01	17.37	0.57	79.35	17.37	0.06	25.12	79	12	417	561	93	27	81	14
42	107.16	135.82	0.72	1.27	35.55	0.00	11.92	19.61	22.43	0.07	22.96	0.01	4.91	0.21	108.12	4.91	0.05	22.43	76	9	240	517	64	14	59	3
43	252.46	152.99	2.05	0.61	83.39	0.00	7.84	24.53	22.66	0.05	23.19	0.01	4.95	0.21	106.07	4.95	0.04	22.66	75	6	-303	579	52	12	60	3
44	127.80	75.30	1.19	0.59	164.77	0.00	14.40	28.35	27.32	0.05	27.96	0.01	5.98	0.21	99.92	5.98	0.04	27.32	84	12	-687	756	48	13	64	4
45	390.88	291.19	2.92	0.74	91.14	0.00	6.36	22.44	9.56	0.05	10.01	0.01	2.95	0.29	111.83	2.95	0.04	9.56	69	4	-80	234	54	5	57	2
46	96.65	169.38	0.77	1.75	25.24	0.01	10.72	3.94	19.14	0.55	22.71	0.02	12.21	0.54	63.19	12.21	0.25	19.14	253	27	3209	302	448	82	101	12
47	222.11	174.43	1.53	0.79	31.21	0.00	11.45	27.43	16.38	0.04	16.89	0.01	4.14	0.25	115.55	4.14	0.04	16.38	73	8	-597	445	43	7	56	2
48	111.04	91.92	1.21	0.83	44.33	0.00	15.44	16.39	27.78	0.08	28.27	0.01	5.25	0.19	103.75	5.25	0.06	27.78	85	13	639	598	79	22	62	3
49	246.30	166.08	1.84	0.67	82.68	0.00	8.96	22.58	14.21	0.06	14.94	0.01	4.61	0.31	110.36	4.61	0.04	14.21	81	7	-95	349	55	8	58	3
50	111.37	115.00	0.73	1.03	57.49	0.00	13.08	20.35	18.80	0.06	19.62	0.01	5.62	0.29	113.80	5.62	0.05	18.80	79	10	155	440	59	11	56	3
51	168.59	163.20	1.12	0.97	71.14	0.01	9.05	8.09	12.45	0.18	13.32	0.01	4.74	0.36	95.56	4.74	0.12	12.45	151	14	2009	221	167	20	67	3
52	142.82	151.28	0.95	1.06	268.84	0.00	28.34	16.17	24.56	0.07	24.93	0.01	4.26	0.17	113.72	4.26	0.06	24.56	98	28	669	526	73	18	56	2
53	192.18	157.46	1.31	0.82	41.37	0.00	11.06	17.99	24.16	0.07	24.43	0.01	3.60	0.15	107.72	3.60	0.06	24.16	97	11	436	538	70	16	60	2
54	449.20	479.16	3.52	1.07	599.19	0.01	5.80	11.99	11.44	0.12	12.02	0.01	3.68	0.31	98.52	3.68	0.08	11.44	101	6	1278	223	112	13	65	2
55	203.51	155.46	1.44	0.76	143.72	0.00	11.24	29.44	23.21	0.04	23.71	0.01	4.87	0.21	115.56	4.87	0.03	23.21	74	8	-793	657	40	9	56	3
56	150.41	138.20	0.83	0.92	40.63	0.00	9.82	25.21	25.24	0.05	25.74	0.01	5.03	0.20	113.30	5.03	0.04	25.24	72	7	-373	655	48	12	57	3
57	135.37	197.37	0.91	1.46	217.71	0.00	9.27	21.23	22.94	0.06	23.45	0.01	4.85	0.21	104.35	4.85	0.05	22.94	76	7	54	547	61	14	61	3
58	336.63	70.29	4.33	0.21	96.02	0.00	25.66	13.58	80.17	0.12	80.86	0.01	10.52	0.13	86.06	10.52	0.07	80.17	85	22	1032	1620	113	87	74	8

Table A2.6. LA-ICPMS U-Pb geochronologic analysis
677-187 Fenghuoshan Tuff

Concentrations (ppm)

P	Ti	Y	Zr	Nb	La	Ce	Pr	Nd	Sm	Eu	Gd	Tb	Dy	Ho	Er	Tm	Yb	Lu	Hf	Ta	Th	U
191.48	75.73	622.97	356141.09	2.64	2.78	13.46	0.49	4.22	2.21	1.24	15.40	5.04	62.47	20.08	96.34	24.35	270.06	37.15	5784.87	0.50	96.16	66.93
207.83	62.62	897.35	353119.92	2.78	0.73	21.47	0.64	4.04	8.50	2.63	34.09	9.75	117.17	33.90	135.11	30.00	325.94	43.18	6132.95	0.47	338.37	109.56
219.03	22.29	1117.63	391860.49	2.00	0.41	13.64	0.06	4.37	6.87	2.57	33.74	10.84	118.05	41.52	171.89	45.04	498.50	58.55	5677.03	0.49	169.38	96.65
221.48	111.84	1174.42	297004.72	5.87	5.88	25.76	0.82	6.14	7.71	1.82	31.16	10.06	119.85	41.93	182.13	46.24	490.39	60.26	4912.17	1.50	134.12	137.03
371.65	35.18	998.04	456033.00	8.75	7.95	39.95	1.86	9.77	4.43	0.78	21.93	7.78	96.91	35.26	163.65	44.65	503.94	63.12	8413.85	3.74	239.63	238.99
383.73	9.67	3623.58	395847.69	4.01	0.24	38.34	0.47	5.61	14.31	3.47	76.65	25.32	338.82	128.14	565.31	137.24	1328.69	217.00	5556.61	1.13	497.79	348.42
426.87		752.97	489739.03	1.59	1.27	11.98	0.54	1.94	3.15	0.07	11.47	6.42	77.85	27.39	126.89	34.87	395.44	44.51	7777.35	0.60	70.29	336.63
380.57	9.98	1802.46	452546.37	6.70	0.21	38.32	0.10	4.17	6.26	2.44	43.57	14.78	186.68	67.27	284.56	73.04	794.10	91.34	8076.90	2.29	190.80	185.11
280.57	6.55	1642.25	473059.41	2.08		23.05	0.43	5.24	11.98	4.09	48.36	15.50	179.86	60.51	250.89	63.87	709.62	82.42	6866.04	0.72	163.33	127.19
412.16	23.88	1683.47	462665.49	2.59	5.10	25.52	2.12	14.55	11.95	1.79	53.15	16.11	186.58	63.78	259.74	62.93	649.56	69.91	7632.45	1.21	181.76	204.23
397.35	24.58	1437.42	442913.16	5.33	2.07	36.60	0.36	4.03	5.04	1.70	26.96	11.38	144.58	54.03	231.48	59.56	636.66	75.36	8212.45	2.24	163.20	168.59
11703.50	8.61	1468.29	460803.01	6.73	323.39	633.19	86.78	429.50	85.61	6.67	95.91	18.30	176.01	52.35	212.36	52.10	566.67	76.47	7915.10	2.94	271.33	301.83
309.34	34.73	1624.65	431539.87	6.19	1.32	24.06	0.33	3.41	7.47	0.66	38.90	14.88	167.90	60.55	251.52	61.43	646.69	76.59	7719.26	2.78	479.16	449.20
310.57	2.32	867.51	450893.73	6.25		25.65		0.35	2.92	0.54	17.83	6.09	76.67	30.22	139.24	36.95	429.80	49.19	8586.00	2.70	75.30	127.80
298.35		1417.07	478248.98	3.18	0.58	22.05	0.06	2.85	7.31	1.87	29.43	11.71	137.61	49.67	227.96	59.50	708.59	83.12	7225.04	1.41	213.41	219.93
219.48	27.41	869.23	439528.06	1.56	0.46	8.94	0.12	2.15	4.21	1.53	19.93	7.54	90.10	32.80	135.97	35.83	404.88	51.69	5594.71	0.44	65.95	64.45
326.67	10.74	1068.65	488121.32	2.72		25.41	0.24	1.08	4.56	1.55	21.64	7.91	100.54	37.72	168.68	45.69	527.75	62.41	7612.02	1.42	137.89	129.03
853.16	55.85	3061.20	398135.51	7.26	7.13	61.18	2.08	19.49	24.98	6.97	84.83	28.82	317.03	110.22	462.47	120.83	1287.94	153.77	5703.62	2.19	639.15	446.43
488.01	10.37	1207.85	463204.40	2.37	0.01	17.03		1.37	3.69	1.72	24.49	9.18	116.55	44.31	200.01	54.25	630.73	72.45	7266.79	1.12	91.92	111.04
678.38	9.72	1877.59	483746.06	4.42	6.24	45.68	1.46	10.99	8.55	2.25	45.12	15.24	190.74	68.22	288.36	76.45	827.72	96.10	8349.53	1.94	213.58	196.90
653.61	13.91	2066.34	476394.82	3.73	2.72	41.35	0.95	9.79	11.97	4.36	56.94	17.17	212.82	77.76	326.59	84.84	932.60	110.64	7123.45	1.45	279.13	176.64
1517.94	5.36	1005.50	472152.83	4.17	15.07	51.48	4.27	19.24	5.29	1.25	23.70	7.70	96.53	35.79	163.53	44.52	515.01	62.89	8111.47	1.85	131.20	169.63
161.94	11.07	562.49	470233.83	2.60		13.09	0.01		1.21	0.56	8.90	3.48	49.73	20.07	92.72	25.93	312.85	40.36	7916.01	1.29	88.46	138.80
389.17	9.21	2183.55	483807.64	2.88	0.01	36.47	0.27	7.18	14.50	5.86	63.19	20.47	238.27	82.50	339.15	83.91	883.86	102.48	7496.15	1.33	197.37	135.37
473.18		1375.80	475759.96	3.81	0.85	35.32	0.45	3.83	5.73	1.56	32.96	10.82	131.18	49.54	222.72	58.11	650.81	75.70	8492.98	2.31	178.23	181.68
398.30	7.00	1382.46	470158.06	4.12	0.92	24.87		2.46	5.35	1.57	30.17	10.71	129.69	51.00	220.88	61.28	697.84	83.70	7638.79	1.72	253.43	244.37
572.24	17.58	2201.85	478630.93	6.58	0.37	63.47	0.42	5.15	11.31	4.94	60.80	22.75	243.27	85.18	330.62	81.85	868.40	90.88	6850.70	2.50	497.24	251.95
372.35	10.64	1429.58	488764.31	3.63	2.31	26.94	0.24	6.00	8.06	1.87	35.39	11.08	148.43	52.24	226.60	56.42	623.39	74.63	8172.18	1.63	151.71	160.65
253.56	6.03	911.26	458620.94	6.07	0.43	22.12	0.16	0.97	2.77	0.60	13.10	5.68	80.11	31.33	145.52	44.04	547.97	66.35	7481.43	3.02	152.99	252.46
470.44	7.85	2147.20	473002.34	5.76		44.98	0.49	6.92	15.28	4.04	63.93	19.11	232.51	77.64	331.39	86.14	978.81	113.79	6522.05	1.83	381.73	285.85
418.38	3.45	1536.25	481938.76	3.13	0.20	20.49	0.10	4.14	8.34	2.63	44.45	12.44	154.18	57.73	240.26	63.46	700.34	81.15	7682.34	1.17	136.48	127.43
289.26	5.44	849.37	467926.23	6.54	1.51	31.77	0.48	1.90	2.79	0.38	13.72	5.60	77.31	30.71	140.94	39.56	460.85	55.68	8557.00	4.21	224.42	305.11
421.87	5.16	1552.99	481481.80	6.28	0.91	35.31	0.31	3.96	5.68	1.40	33.92	11.27	145.58	56.90	246.17	64.41	652.39	85.67	9136.95	2.62	137.69	142.24
1239.39	7.85	1019.66	477594.68	6.49	24.98	81.85	7.95	39.31	8.52	1.12	23.21	8.13	97.30	36.23	160.68	43.66	506.70	60.83	9025.14	2.49	157.46	192.18
382.11	13.67	1789.59	461397.14	2.77		25.75		3.48	8.44	3.62	43.08	14.99	182.13	66.71	277.78	71.81	780.26	88.76	6404.61	1.08	135.82	107.16
427.93	8.23	1361.65	471795.66	3.89	1.11	21.97	0.40	3.63	7.62	1.94	33.94	10.46	137.02	48.91	212.75	55.09	614.95	71.61	7277.72	1.37	136.17	147.22
261.02	8.33	922.05	458678.41	6.60		30.53		1.14	3.28	0.41	15.56	6.66	88.84	32.37	152.82	44.37	507.71	59.27	8147.31	2.85	179.99	245.71
320.63	4.96	857.17	475300.04	4.92	2.45	28.70	0.54	4.00	3.45	0.60	12.21	5.16	77.50	30.64	140.19	40.36	464.66	55.85	9251.09	2.32	103.20	138.54
400.34	5.31	2268.02	479045.66	14.62	0.27	67.06	0.28	3.33	8.08	2.21	42.54	16.50	208.26	80.37	367.68	100.70	1138.01	144.98	7980.14	5.74	931.86	652.95
726.35	7.04	3259.27	481404.03	10.98	0.18	25.35	0.41	6.08	14.86	3.65	68.55	24.58	306.80	116.56	519.30	139.59	1547.73	189.83	6028.53	3.59	447.93	558.06
507.53	11.29	2030.27	470531.79	5.89	1.38	51.44	0.58	7.07	9.60	3.28	48.42	16.35	210.67	73.47	312.48	78.51	856.16	98.05	8496.59	2.47	263.90	208.52
1800.77	7.72	1830.51	482124.63	15.28	50.76	147.90	13.09	64.32	19.93	2.09	48.65	15.62	186.22	65.76	292.34	75.11	830.53	97.10	8657.01	4.47	944.77	517.86
355.55	7.41	841.21	465043.52	3.93	2.51	25.62	0.60	3.82	2.97	0.61	16.51	5.30	76.99	28.38	136.28	39.52	473.72	57.00	8013.37	2.13	166.08	246.30
1031.61	11.61	1214.63	477398.49	6.68	15.64	67.84	4.17	20.40	9.01	1.33	27.46	8.57	114.20	43.91	192.25	51.39	561.47	65.63	8971.48	2.95	168.08	185.27
1164.58	3.23	1302.87	482381.18	8.71	36.17	103.33	9.04	43.22	11.84	1.00	26.50	9.64	122.21	45.56	206.81	58.93	662.48	80.05	8570.68	3.98	301.17	350.63
667.35		1440.16	479692.70	16.01	5.15	57.13	1.56	7.41	5.19	0.78	22.25	10.18	133.55	49.96	227.10	63.86	762.45	92.44	8343.56	7.44	515.89	615.51
750.93	4.09	1204.39	468734.19	9.01	6.19	50.12	1.51	8.02	5.73	0.54	23.37	8.33	110.68	43.51	195.59	56.92	661.88	75.95	8096.36	4.77	291.19	390.88
263.13	4.90	1022.91	488355.94	8.38	0.05	34.09		0.61	2.68	0.19	16.20	6.97	91.76	37.27	170.79	47.99	572.29	67.41	9251.15	4.24	198.64	264.94
318.99	4.52	1046.58	483489.10	3.67		26.12		1.34	2.87	1.36	21.12	7.46	102.92	38.39	164.99	43.95	481.82	57.03	8014.06	1.75	138.20	150.41
302.86	14.65	1183.50	488437.25	4.71	0.36	21.98	0.10	2.80	4.17	1.65	25.66	9.50	121.99	46.49	200.25	54.07	614.95	70.35	8027.17	1.58	151.28	142.82
610.65	13.98	964.35	476599.30	3.64	8.08	50.91	2.97	15.72	7.65	1.26	23.90	8.71	101.90	34.12	149.15	38.20	421.90	47.63	8043.06	1.70	115.00	111.37
230.30	9.08	1105.30	480800.26	6.11	0.63	34.85	0.04	1.78	3.41	0.51	19.44	7.50	106.39	39.45	187.23	51.74	576.67	70.71	8808.84	3.49	251.96	282.26
322.29	4.50	1252.70	473693.00	4.06	3.27	35.74	0.84	4.60	4.69	0.61	21.22	9.08	114.10	45.60	202.89	56.53	640.89	76.34	8811.91	2.70	205.67	235.49
386.62	3.60	1479.86	465163.47	8.39	0.82	41.58	0.19	3.04	4.36	1.80	30.85	10.45	139.92	52.73	238.13	62.79	742.19	85.60	7246.32	2.56	129.69	156.17
330.20	4.44	1107.42	469086.66	7.66	0.15	35.85	0.06	1.07	3.87	0.52	21.05	7.96	99.33	40.28	180.03	49.71	558.30	65.21	8781.53	3.27	174.43	222.11
309.60	7.15	863.00	475643.26	6.92	2.30	30.73	0.62	2.89	2.52	0.43	12.61	6.03	76.47	29.89	142.09	41.39	471.54	59.02	9015.82	3.41	155.46	203.51

Table A2.6. LA-ICPMS U-Pb geochronologic analysis

677-187 Fenghuoshan Tuff

Chondrite normalizing values from Sun & McDonough

La	Ce	Pr	Nd	Sm	Eu	Gd	Tb	Dy	Ho	Er	Tm	Yb	Lu	Ti-in-zircon T(°C)	Ce/Ce*	Eu/Eu*	(Sm/Nd)cn	(Lu/Nd)cn
11.74	22.00	5.11	9.03	14.44	21.36	74.93	134.89	245.93	354.70	582.14	954.83	1588.59	1462.59	1012.20	2.61	0.48	1.60	161.93
3.08	35.08	6.70	8.65	55.57	45.31	165.90	260.64	461.31	598.93	816.40	1176.63	1917.32	1699.94	984.41	7.18	0.41	6.42	196.51
1.72	22.30	0.65	9.35	44.90	44.26	164.17	289.81	464.74	733.54	1038.59	1766.23	2932.36	2305.27	852.20	18.84	0.42	4.80	246.43
24.82	42.08	8.61	13.16	50.37	31.32	151.63	269.09	471.86	740.77	1100.49	1813.50	2884.66	2372.32	1073.24	2.52	0.31	3.83	180.29
33.54	65.28	19.54	20.92	28.96	13.45	106.74	208.04	381.54	622.96	988.80	1750.89	2964.37	2484.92	907.00	2.46	0.20	1.38	118.80
1.02	62.64	4.93	12.02	93.50	59.89	373.02	676.99	1333.95	2263.98	3415.79	5382.07	7815.83	8543.43	764.03	21.07	0.26	7.78	710.72
5.38	19.57	5.67	4.15	20.57	1.15	55.82	171.60	306.51	483.88	766.70	1367.30	2326.14	1752.30		3.54	0.03	4.96	422.53
0.90	62.61	1.01	8.94	40.93	41.99	212.03	395.08	734.97	1188.59	1719.41	2864.45	4671.17	3596.21	767.12	65.40	0.33	4.58	402.38
0.11	37.66	4.49	11.22	78.31	70.48	235.33	414.31	708.10	1069.04	1515.93	2504.83	4174.26	3244.75	727.41	16.38	0.45	6.98	289.32
21.51	41.70	22.31	31.16	78.12	30.86	258.65	430.75	734.55	1126.81	1569.45	2467.88	3820.94	2752.24	860.15	1.90	0.18	2.51	88.32
8.73	59.80	3.79	8.63	32.91	29.27	131.18	304.29	569.20	954.60	1398.69	2335.54	3745.08	2967.02	863.50	9.56	0.36	3.81	343.75
1364.52	1034.63	913.49	919.69	559.54	114.94	466.70	489.28	692.96	924.96	1283.13	2043.09	3333.38	3010.73	752.83	0.91	0.22	0.61	3.27
5.56	39.32	3.50	7.31	48.82	11.37	189.28	397.82	661.01	1069.73	1519.77	2409.13	3804.03	3015.21	905.37	8.68	0.10	6.68	412.60
	41.90	0.17	0.76	19.09	9.28	86.76	162.90	301.87	533.93	841.36	1448.95	2528.24	1936.50	641.68		0.18	25.13	2549.58
2.45	36.02	0.59	6.10	47.75	32.32	143.21	313.20	541.79	877.52	1377.39	2333.21	4168.15	3272.47		23.70	0.34	7.82	536.12
1.96	14.60	1.30	4.61	27.52	26.36	96.97	201.61	354.71	579.52	821.54	1405.26	2381.65	2034.89	876.37	8.96	0.42	5.97	441.18
0.06	41.52	2.55	2.32	29.81	26.73	105.30	211.61	395.82	666.49	1019.22	1791.60	3104.40	2457.23	774.30	31.74	0.40	12.85	1059.36
30.07	99.98	21.90	41.72	163.28	120.09	412.81	770.48	1248.13	1947.34	2794.38	4738.40	7576.13	6054.10	968.25	3.85	0.42	3.91	145.10
0.03	27.83	0.66	2.94	24.08	29.66	119.18	245.51	458.88	782.88	1208.49	2127.62	3710.15	2852.39	770.88	80.78	0.41	8.20	971.19
26.32	74.64	15.32	23.53	55.90	38.87	219.56	407.52	750.93	1205.25	1742.37	2998.15	4868.93	3783.38	764.53	3.58	0.28	2.38	160.82
11.47	67.56	9.97	20.96	78.23	75.25	277.09	459.15	837.89	1373.81	1973.32	3327.19	5485.87	4355.91	800.61	6.30	0.42	3.73	207.80
63.60	84.12	44.93	41.20	34.60	21.60	115.31	206.01	380.03	632.33	988.08	1745.75	3029.49	2475.97	709.67	1.55	0.29	0.84	60.10
0.00	21.40	0.15	0.81	7.90	9.62	43.32	93.14	195.77	354.57	560.24	1016.85	1840.31	1588.97	777.34	284.76	0.38	9.77	1964.40
0.05	59.60	2.84	15.38	94.74	100.97	307.48	547.28	938.07	1457.55	2049.24	3290.70	5199.17	4034.80	759.29	41.30	0.50	6.16	262.27
3.60	57.72	4.70	8.21	37.48	26.82	160.38	289.20	516.45	875.22	1345.72	2278.91	3828.31	2980.17		13.90	0.27	4.57	363.18
3.89	40.64	1.18	5.27	34.97	27.08	146.81	286.40	510.61	901.02	1334.63	2403.25	4104.94	3295.39	733.51	16.05	0.30	6.64	625.53
1.55	103.71	4.37	11.02	73.93	85.25	295.89	608.30	957.76	1504.95	1997.69	3209.73	5108.21	3578.12	825.65	35.03	0.46	6.71	324.58
9.76	44.02	2.47	12.85	52.70	32.31	172.20	296.33	584.36	922.96	1369.20	2212.59	3667.01	2938.02	773.38	7.19	0.29	4.10	228.63
1.81	36.14	1.63	2.08	18.08	10.38	63.74	151.87	315.38	553.56	879.28	1726.95	3223.33	2612.26	719.95	21.00	0.25	8.70	1256.64
0.13	73.49	5.17	14.81	99.86	69.69	311.08	510.94	915.40	1371.66	2002.37	3377.95	5757.72	4479.74	744.17	27.73	0.34	6.74	302.54
0.84	33.49	1.10	8.86	54.53	45.35	216.32	332.73	607.02	1019.95	1451.70	2488.82	4119.67	3194.88	672.66	34.65	0.33	6.15	360.47
6.36	51.91	5.02	4.06	18.23	6.50	66.77	149.68	304.38	542.52	851.61	1551.19	2710.89	2192.27	710.97	9.12	0.15	4.49	539.75
3.82	57.69	3.29	8.48	37.11	24.07	165.08	301.44	573.14	1005.35	1487.42	2525.94	3837.61	3372.73	706.28	16.22	0.24	4.38	397.83
105.39	133.74	83.73	84.18	55.68	19.34	112.97	217.37	383.09	640.09	970.89	1712.14	2980.58	2394.75	744.13	1.41	0.23	0.66	28.45
	42.08	1.66	7.44	55.13	62.47	209.64	400.82	717.06	1178.66	1678.42	2815.91	4589.79	3494.66	798.85		0.47	7.41	469.47
4.68	35.90	4.20	7.78	49.82	33.38	165.15	279.60	539.45	864.13	1285.49	2160.38	3617.37	2819.13	748.52	8.09	0.31	6.41	362.52
	49.89	0.54	2.43	21.43	7.12	75.71	178.19	349.76	571.90	923.41	1740.08	2986.55	2333.41	749.68		0.15	8.81	959.31
10.33	46.89	5.68	8.57	22.54	10.29	59.43	138.06	305.11	541.29	847.06	1582.57	2733.27	2198.82	702.83	5.86	0.25	2.63	256.53
1.15	109.58	2.97	7.14	52.79	38.06	207.01	441.31	819.93	1419.94	2221.64	3948.99	6694.15	5707.89	708.85	53.18	0.29	7.40	799.87
0.76	41.42	4.27	13.02	97.12	63.01	333.60	657.34	1207.89	2059.39	3137.79	5473.97	9104.30	7473.80	734.06	16.47	0.29	7.46	573.90
5.81	84.05	6.05	15.14	62.75	56.58	235.61	437.08	829.39	1298.14	1888.08	3079.01	5036.22	3860.08	779.32	14.16	0.38	4.14	254.97
214.18	241.66	137.77	137.72	130.25	36.04	236.72	417.76	733.15	1161.89	1766.39	2945.44	4885.46	3822.67	742.51	1.37	0.20	0.95	27.76
10.59	41.86	6.36	8.19	19.40	10.45	80.35	141.69	303.10	501.45	823.44	1549.95	2786.56	2244.10	738.77	4.94	0.21	2.37	274.11
65.98	110.85	43.87	43.69	58.89	22.88	133.64	229.15	449.60	775.71	1161.62	2015.39	3302.74	2583.96	782.10	2.02	0.24	1.35	59.15
152.63	168.85	95.21	92.54	77.40	17.32	128.94	257.74	481.16	804.89	1249.63	2310.95	3896.93	3151.65	667.16	1.36	0.17	0.84	34.06
21.72	93.35	16.42	15.88	33.91	13.44	108.28	272.30	525.77	882.73	1372.22	2504.12	4485.01	3639.36		4.90	0.19	2.14	229.24
26.13	81.89	15.89	17.17	37.46	9.31	113.73	222.86	435.76	768.81	1181.83	2232.12	3893.39	2990.19	686.59	3.90	0.12	2.18	174.20
0.22	55.70	0.29	1.31	17.53	3.34	78.84	186.37	361.25	658.46	1031.98	1882.14	3366.39	2653.97	701.81	219.14	0.07	13.37	2024.55
	42.67	0.64	2.88	18.77	23.40	102.78	199.56	405.21	678.34	996.91	1723.69	2834.22	2245.11	694.93		0.38	6.52	779.98
1.52	35.91	1.07	5.99	27.26	28.43	124.86	254.14	480.29	821.40	1209.96	2120.52	3617.35	2769.73	806.04	27.82	0.37	4.55	462.36
34.11	83.19	31.28	33.67	49.98	21.71	116.31	233.02	401.17	602.75	901.19	1498.18	2481.77	1875.17	801.20	2.54	0.26	1.48	55.70
2.67	56.95	0.45	3.82	22.30	8.84	94.58	200.43	418.87	696.96	1131.31	2029.21	3392.16	2783.84	757.93	36.52	0.15	5.84	728.91
13.79	58.39	8.87	9.85	30.63	10.50	103.24	242.84	449.21	805.60	1225.95	2216.99	3769.93	3005.43	694.48	5.15	0.16	3.11	305.17
3.46	67.94	2.05	6.50	28.46	30.95	150.14	279.38	550.86	931.57	1438.86	2462.18	4365.83	3370.20	675.93	24.68	0.35	4.38	518.57
0.64	58.58	0.59	2.28	25.26	8.98	102.43	212.95	391.08	711.67	1087.78	1949.28	3284.13	2567.35	693.50	95.30	0.14	11.07	1124.63
9.70	50.21	6.49	6.18	16.48	7.47	61.36	161.20	301.07	528.01	858.56	1622.98	2773.76	2323.63	735.51	6.20	0.19	2.67	376.06

Sun, S.S., & McDonough, W. (1989), Chemical and isotopic systematics of oceanic basalts: implications for mantle composition and processes, Geological Society, London, Special Publications, 42(1), 313-345.

Table A2.7. CA-TIMS U-Pb geochronologic analysis
677-187 Fenghuoshan Tuff
92.85386° E, 34.611° N

							Radiogenic Isotope Ratios								Isotopic Dates					
Sample	Th/U	$^{206}Pb^*$ x10^{-13} mol	mol % $^{206}Pb^*$	Pb^*/Pb_c	Pb_c (pg)	$^{206}Pb/^{204}Pb$	$^{208}Pb/^{206}Pb$	$^{207}Pb/^{206}Pb$	% err	$^{207}Pb/^{235}U$	% err	$^{206}Pb/^{238}U$	% err	corr. coef.	$^{207}Pb/^{206}Pb$	±	$^{207}Pb/^{235}U$	±	$^{206}Pb/^{238}U$	±
(a)	(b)	(c)	(c)	(c)	(c)	(d)	(e)	(e)	(f)	(e)	(f)	(e)	(f)		(g)	(f)	(g)	(f)	(g)	(f)
z1	0.800	0.1590	97.13%	11	0.39	640	0.259	0.047710	1.589	0.060696	1.693	0.009227	0.128	0.821	84.9	37.7	59.83	0.98	59.21	0.08
z2	0.687	0.1230	96.28%	8	0.39	493	0.222	0.047621	2.066	0.060566	2.196	0.009224	0.155	0.854	80.5	49.0	59.71	1.27	59.19	0.09
z3	0.999	0.0987	95.37%	7	0.40	396	0.324	0.047790	2.575	0.061137	2.735	0.009278	0.182	0.888	88.9	61.0	60.25	1.60	59.54	0.11
z4	0.805	0.1152	96.46%	9	0.35	518	0.265	0.048528	1.892	0.062210	2.015	0.009297	0.142	0.879	125.1	44.5	61.28	1.20	59.66	0.08
z5	0.747	0.0747	94.76%	6	0.34	350	0.243	0.047839	2.959	0.061040	3.141	0.009254	0.197	0.929	91.3	70.1	60.16	1.83	59.38	0.12
z6	0.830	0.1855	97.22%	12	0.44	660	0.270	0.047830	1.346	0.060924	1.439	0.009238	0.100	0.942	90.9	31.9	60.05	0.84	59.28	0.06
z8	0.850	0.2025	97.03%	11	0.51	620	0.279	0.048399	1.251	0.061671	1.339	0.009242	0.109	0.816	118.8	29.5	60.77	0.79	59.30	0.06

(a) z1, z2 etc. are labels for fractions composed of single zircon grains or fragments. Fractions were annealed and chemically abraded after Mattinson (2005). Fraction labels in bold are used in the weighted mean calculations.

(b) Model Th/U ratio calculated from radiogenic $^{208}Pb/^{206}Pb$ ratio and $^{207}Pb/^{235}U$ date.

(c) Pb* and Pbc are radiogenic and common Pb, respectively. mol % $^{206}Pb^*$ is with respect to radiogenic and blank Pb.

(d) Measured ratio corrected for spike and fractionation only. Fractionation correction is 0.15 ± 0.03 (1 sigma) %/amu (atomic mass unit) for single-collector Daly analyses, based on analysis of the $^{202}Pb/^{205}Pb$ in ET2535 tracer solution.

(e) Corrected for fractionation, spike, common Pb, and initial disequilibrium in $^{230}Th/^{238}U$. Common Pb is assigned to procedural blank with composition of $^{206}Pb/^{204}Pb$ = 18.35 ± 1.50%; $^{207}Pb/^{204}Pb$ = 15.60 ± 0.75%; $^{208}Pb/^{204}Pb$ = 38.53 ± 1.00% (1 sigma). $^{206}Pb/^{238}U$ and $^{207}Pb/^{206}Pb$ ratios corrected for initial disequilibrium in $^{230}Th/^{238}U$ using Th/U [magma] = 3.

(f) Errors are 2 sigma, propagated using algorithms of Schmitz and Schoene (2007) and Crowley et al. (2007).

(g) Calculations based on the decay constants of Jaffey et al. (1971). $^{206}Pb/^{238}U$ and $^{207}Pb/^{206}Pb$ dates corrected for initial disequilibrium in $^{230}Th/^{238}U$ using Th/U [magma] = 3.

Table A2.8 continued. Argon isotopic data for 40Ar/39Ar age dating

F39	Laser Power [mW]	Volume [ccSTP] ^{36}Ar	^{37}Ar	^{38}Ar	^{39}Ar	^{40}Ar	Age [Ma]
11UMT17B (mc35-a29b) Biotite (J=0.00393655) Total gas age = 27.369 ± 0.104 Ma (34.5352816667° N, 92.7533433333° E)							
0.003	200	5.171 ± 0.125	28.970 ± 0.555	20.786 ± 0.090	31.554 ± 0.197	1510.368 ± 1.447	-3.96 ± 8.37
0.011	400	3.750 ± 0.120	51.124 ± 0.771	59.960 ± 0.303	65.250 ± 0.394	1378.777 ± 1.621	29.23 ± 3.80
0.033	600	4.084 ± 0.086	51.585 ± 0.523	89.829 ± 0.487	199.435 ± 0.890	2003.148 ± 2.486	28.14 ± 0.90
0.080	800	4.782 ± 0.115	60.542 ± 0.559	100.054 ± 0.391	431.948 ± 1.199	3153.996 ± 2.412	28.40 ± 0.56
0.152	1000	6.363 ± 0.131	31.336 ± 0.320	96.934 ± 0.325	650.436 ± 0.906	4420.776 ± 2.671	27.53 ± 0.42
0.237	1200	5.583 ± 0.077	30.863 ± 0.421	81.036 ± 0.262	781.139 ± 1.427	4682.364 ± 5.312	27.36 ± 0.22
0.313	1600	4.162 ± 0.115	79.207 ± 0.740	28.762 ± 0.282	690.700 ± 1.290	4016.783 ± 3.039	28.43 ± 0.35
0.681	2400	14.582 ± 0.158	539.349 ± 0.945	188.640 ± 0.493	3345.978 ± 2.615	17320.046 ± 14.154	27.41 ± 0.10
0.873	2800	4.804 ± 0.099	433.832 ± 1.157	66.260 ± 0.421	1743.262 ± 1.968	8162.424 ± 6.695	27.26 ± 0.13
0.926	3200	0.806 ± 0.082	105.497 ± 0.812	17.837 ± 0.218	486.661 ± 1.112	2104.898 ± 2.854	27.04 ± 0.36
0.975	3600	0.806 ± 0.086	134.216 ± 0.988	12.509 ± 0.219	444.537 ± 0.926	1910.244 ± 3.361	26.52 ± 0.41
1.000	4000	0.243 ± 0.094	47.890 ± 0.603	5.460 ± 0.135	226.288 ± 0.553	954.185 ± 3.005	27.49 ± 0.87
12FGS10 (mc40-r0a) Biotite (J=0.00236596) Total gas age = 33.482 ± 0.254 Ma (34.3995° N, 92.068583° E)							
0.001	200	2.563 ± 0.116	0.480 ± 0.114	0.967 ± 0.084	3.065 ± 0.087	750.365 ± 1.143	-9.72 ± 48.20
0.011	400	1.434 ± 0.098	0.545 ± 0.170	4.285 ± 0.087	29.720 ± 0.259	662.740 ± 0.907	34.01 ± 4.09
0.043	600	1.128 ± 0.122	0.512 ± 0.171	12.445 ± 0.184	93.280 ± 0.220	1022.656 ± 1.550	31.27 ± 1.63
0.083	800	0.850 ± 0.117	0.487 ± 0.332	15.368 ± 0.172	115.088 ± 0.584	1108.927 ± 1.343	31.53 ± 1.27
0.142	1000	0.631 ± 0.116	0.393 ± 0.124	23.551 ± 0.166	174.785 ± 0.711	1549.381 ± 2.050	32.98 ± 0.84
0.233	1200	0.545 ± 0.122	0.669 ± 0.250	34.793 ± 0.255	263.046 ± 0.702	2231.719 ± 2.248	33.29 ± 0.58
0.369	1600	0.505 ± 0.072	0.877 ± 0.271	52.353 ± 0.249	397.836 ± 0.800	3482.546 ± 3.456	35.41 ± 0.24
0.450	2000	0.181 ± 0.070	0.895 ± 0.281	32.198 ± 0.194	236.721 ± 0.605	1933.819 ± 2.062	33.59 ± 0.38
0.541	2400	0.174 ± 0.074	3.482 ± 0.280	36.104 ± 0.241	266.732 ± 0.569	2158.516 ± 1.885	33.41 ± 0.35
0.764	2800	0.410 ± 0.101	48.929 ± 0.379	91.056 ± 0.466	651.543 ± 0.627	5292.526 ± 4.953	33.56 ± 0.20
0.910	3200	0.297 ± 0.058	2.272 ± 0.330	55.523 ± 0.319	423.666 ± 1.446	3429.351 ± 2.821	33.36 ± 0.21
0.987	3600	0.230 ± 0.057	0.318 ± 0.176	29.587 ± 0.224	225.279 ± 1.106	1853.454 ± 2.336	33.52 ± 0.36
1.000	4000	0.211 ± 0.090	-0.044 ± 0.188	4.835 ± 0.121	38.884 ± 0.317	346.201 ± 1.236	30.90 ± 2.88
12FGS10 (mc40-r0b) Biotite (J=0.00236596) Total gas age = 33.69 ± 0.27 Ma (34.3995° N, 92.068583° E)							
0.003	200	1.649 ± 0.056	0.703 ± 0.267	1.149 ± 0.071	6.545 ± 0.087	544.634 ± 1.280	37.00 ± 10.65
0.034	400	1.178 ± 0.075	0.919 ± 0.185	8.068 ± 0.129	59.951 ± 0.464	840.500 ± 1.750	34.72 ± 1.58
0.091	600	0.868 ± 0.058	0.256 ± 0.170	15.512 ± 0.166	112.880 ± 0.354	1135.400 ± 1.157	32.93 ± 0.64
0.165	800	0.576 ± 0.046	0.262 ± 0.185	19.831 ± 0.242	145.345 ± 0.415	1306.937 ± 2.019	33.08 ± 0.41
0.268	1000	0.506 ± 0.073	0.009 ± 0.238	27.262 ± 0.268	202.817 ± 0.780	1767.704 ± 1.898	33.74 ± 0.47
0.400	1200	0.499 ± 0.105	-0.177 ± 0.274	35.343 ± 0.310	261.430 ± 0.399	2221.416 ± 2.266	33.55 ± 0.50
0.697	1600	0.969 ± 0.057	0.680 ± 0.261	78.804 ± 0.345	584.039 ± 1.665	4911.841 ± 6.483	33.49 ± 0.16
0.879	2000	0.440 ± 0.069	5.247 ± 0.340	48.742 ± 0.273	359.294 ± 1.026	2970.701 ± 2.410	33.44 ± 0.26
0.940	2400	0.193 ± 0.100	1.816 ± 0.275	16.417 ± 0.113	119.733 ± 0.452	999.325 ± 1.210	33.28 ± 1.04
0.973	2800	0.065 ± 0.073	1.010 ± 0.247	8.900 ± 0.132	64.030 ± 0.250	544.535 ± 0.676	34.69 ± 1.41
0.979	3200	-0.056 ± 0.071	-0.121 ± 0.129	1.648 ± 0.079	12.502 ± 0.090	100.508 ± 1.034	39.50 ± 7.00
0.996	3600	-0.136 ± 0.100	-0.001 ± 0.170	4.809 ± 0.070	34.632 ± 0.332	282.636 ± 1.076	39.35 ± 3.58
1.000	4000	-0.042 ± 0.065	-0.115 ± 0.148	0.802 ± 0.055	6.897 ± 0.164	52.292 ± 0.713	39.60 ± 11.60

Table A2.8. Argon isotopic data for 40Ar/39Ar age dating

F39	Laser Power [mW]	Volume [ccSTP] ^{36}Ar	^{37}Ar	^{38}Ar	^{39}Ar	^{40}Ar	Age [Ma]
11UMT17A (mc35-a28a) Biotite (J=0.00393559) Total gas age = 26.77 ± 0.79 Ma (34.5352816667° N, 92.7533433333° E)							
0.001	100	0.160 ± 0.073	0.806 ± 0.213	0.505 ± 0.085	0.581 ± 0.091	48.744 ± 0.448	18.44 ± 261.17
0.001	150	0.019 ± 0.070	0.522 ± 0.215	0.451 ± 0.082	0.800 ± 0.094	34.574 ± 0.594	239.41 ± 163.64
0.002	200	0.079 ± 0.074	0.610 ± 0.253	0.399 ± 0.061	0.784 ± 0.076	26.840 ± 0.464	30.55 ± 195.40
0.003	250	0.041 ± 0.065	0.403 ± 0.220	0.535 ± 0.059	1.227 ± 0.093	26.755 ± 0.370	82.70 ± 106.05
0.005	300	0.097 ± 0.063	0.347 ± 0.210	0.866 ± 0.042	1.326 ± 0.095	42.027 ± 0.415	70.43 ± 96.75
0.007	400	0.068 ± 0.067	0.936 ± 0.265	1.717 ± 0.070	2.152 ± 0.100	33.847 ± 0.394	44.84 ± 64.21
0.010	500	0.089 ± 0.067	0.657 ± 0.272	2.344 ± 0.070	2.942 ± 0.082	49.369 ± 0.559	55.05 ± 46.11
0.014	600	-0.014 ± 0.069	0.759 ± 0.136	2.770 ± 0.080	3.774 ± 0.073	43.104 ± 0.739	86.50 ± 36.50
0.025	800	0.174 ± 0.073	1.533 ± 0.194	4.674 ± 0.103	11.160 ± 0.173	99.391 ± 0.645	30.18 ± 13.55
0.048	1000	0.366 ± 0.115	1.460 ± 0.193	4.479 ± 0.076	22.926 ± 0.110	163.687 ± 0.642	17.12 ± 10.46
0.083	1200	0.478 ± 0.109	1.433 ± 0.221	3.410 ± 0.088	35.552 ± 0.185	241.498 ± 0.784	19.94 ± 6.38
0.177	1600	1.239 ± 0.108	3.803 ± 0.233	5.403 ± 0.162	92.917 ± 0.304	686.727 ± 0.863	24.34 ± 2.40
0.305	2000	1.906 ± 0.118	4.416 ± 0.398	4.757 ± 0.147	127.862 ± 0.382	994.362 ± 1.658	23.78 ± 1.92
0.496	2600	1.339 ± 0.159	7.264 ± 0.374	5.494 ± 0.083	191.275 ± 0.343	1110.730 ± 1.090	26.34 ± 1.72
0.706	3200	0.860 ± 0.099	12.020 ± 0.394	5.638 ± 0.101	209.555 ± 0.468	1058.245 ± 1.328	27.04 ± 0.98
1.000	4000	1.607 ± 0.124	26.721 ± 0.579	8.434 ± 0.183	292.934 ± 0.428	1573.979 ± 1.661	26.45 ± 0.87
11UMT17A (mc35-a28b) Biotite (J=0.00393559) Total gas age = 26.248 ± 0.272 Ma (34.5352816667° N, 92.7533433333° E)							
0.002	200	1.336 ± 0.078	3.744 ± 0.246	2.262 ± 0.081	5.315 ± 0.125	401.392 ± 1.182	8.69 ± 30.68
0.007	400	0.584 ± 0.075	3.262 ± 0.230	3.241 ± 0.104	13.191 ± 0.137	198.980 ± 1.201	14.23 ± 11.92
0.025	600	1.038 ± 0.073	9.389 ± 0.377	3.396 ± 0.115	43.009 ± 0.289	418.854 ± 1.073	18.43 ± 3.54
0.064	800	0.725 ± 0.098	3.686 ± 0.199	3.807 ± 0.096	99.143 ± 0.331	630.881 ± 1.916	29.60 ± 2.06
0.122	1000	0.807 ± 0.089	2.944 ± 0.207	4.267 ± 0.117	144.175 ± 0.526	769.212 ± 1.170	25.96 ± 1.29
0.186	1200	0.841 ± 0.115	2.459 ± 0.296	4.327 ± 0.115	159.525 ± 0.517	837.408 ± 1.104	26.03 ± 1.49
0.308	1600	1.831 ± 0.095	6.680 ± 0.486	7.498 ± 0.145	304.239 ± 0.986	1680.433 ± 1.147	26.40 ± 0.66
0.464	2000	1.380 ± 0.090	9.448 ± 0.299	9.717 ± 0.198	387.251 ± 0.960	1839.557 ± 3.099	26.06 ± 0.49
0.596	2400	0.866 ± 0.097	10.050 ± 0.251	7.867 ± 0.189	330.281 ± 0.786	1525.982 ± 2.322	27.10 ± 0.62
0.746	2800	0.918 ± 0.074	28.255 ± 0.586	9.786 ± 0.100	374.346 ± 0.710	1678.680 ± 3.981	26.50 ± 0.42
0.891	3200	0.910 ± 0.095	22.454 ± 0.283	8.512 ± 0.163	359.393 ± 0.703	1631.781 ± 2.084	26.73 ± 0.55
0.957	3600	0.472 ± 0.075	6.594 ± 0.382	4.028 ± 0.095	164.550 ± 0.363	745.100 ± 1.605	25.94 ± 0.95
1.000	4000	0.597 ± 0.086	11.395 ± 0.236	2.881 ± 0.114	108.103 ± 0.178	558.972 ± 0.889	24.96 ± 1.64
11UMT17B (mc35-a29a) Biotite (J=0.00393655) Total gas age = 25.757 ± 0.57 Ma (34.5352816667° N, 92.7533433333° E)							
0.001	100	0.172 ± 0.107	0.977 ± 0.174	0.607 ± 0.086	1.036 ± 0.076	88.589 ± 0.899	241.79 ± 190.41
0.002	150	0.151 ± 0.105	0.331 ± 0.225	0.730 ± 0.039	0.814 ± 0.057	56.381 ± 0.872	99.89 ± 256.90
0.002	200	0.315 ± 0.100	0.576 ± 0.274	1.165 ± 0.051	0.846 ± 0.097	62.100 ± 0.683	-280.94 ± 291.40
0.003	250	0.057 ± 0.103	0.233 ± 0.191	1.435 ± 0.095	1.123 ± 0.049	44.077 ± 0.694	164.61 ± 175.55
0.004	300	0.366 ± 0.074	0.716 ± 0.219	1.617 ± 0.085	1.234 ± 0.077	64.411 ± 0.788	-271.30 ± 148.33
0.007	400	0.348 ± 0.066	1.025 ± 0.237	3.039 ± 0.102	3.017 ± 0.083	81.315 ± 0.847	-51.65 ± 47.08
0.011	500	0.239 ± 0.071	1.511 ± 0.252	4.005 ± 0.134	5.302 ± 0.177	77.810 ± 0.658	9.69 ± 28.00
0.018	600	0.166 ± 0.061	1.226 ± 0.318	4.461 ± 0.113	8.674 ± 0.123	71.235 ± 0.812	18.00 ± 14.70
0.043	800	0.465 ± 0.084	2.202 ± 0.270	8.565 ± 0.115	29.289 ± 0.343	191.855 ± 0.973	13.18 ± 6.01
0.096	1000	0.300 ± 0.074	2.782 ± 0.311	13.057 ± 0.217	64.926 ± 0.160	363.717 ± 1.310	29.84 ± 2.36
0.169	1200	0.350 ± 0.052	3.171 ± 0.270	14.266 ± 0.245	87.860 ± 0.309	456.970 ± 0.708	28.36 ± 1.23
0.345	1600	1.016 ± 0.063	8.032 ± 0.377	28.077 ± 0.178	212.491 ± 0.668	1094.207 ± 1.592	26.34 ± 0.62
0.498	2000	0.689 ± 0.070	15.632 ± 0.356	19.299 ± 0.224	184.531 ± 0.741	908.299 ± 0.697	26.92 ± 0.79
0.665	2600	0.529 ± 0.068	26.307 ± 0.349	12.948 ± 0.122	201.264 ± 0.403	951.965 ± 1.158	27.86 ± 0.70
0.844	3200	0.730 ± 0.082	20.006 ± 0.569	8.921 ± 0.249	215.557 ± 0.685	978.118 ± 4.229	24.94 ± 0.80
1.000	4000	0.754 ± 0.107	22.466 ± 0.542	6.485 ± 0.174	188.221 ± 0.694	878.969 ± 2.063	24.59 ± 1.19

Chapter III

Eocene – late Oligocene history of crustal shortening within the Hoh Xil Basin, north-central Tibetan Plateau[2]

Abstract

The timing and magnitude of deformation within the Hoh Xil Basin provides constraints on the progression of deformation of the northern Tibetan Plateau following the Indo-Asian collision. Here we present new $^{40}Ar/^{39}Ar$ fault gouge ages, modeled low-temperature thermochronologic data, and a balanced cross section from the FFTB to constrain the timing and magnitude of deformation in the central Hoh Xil Basin. Apatite fission-track and (U-Th)/He ages were obtained from deeply exhumed sandstone samples from the FFTB and modeled using HeFTy software. The modeled cooling history of the FFTB is consistent with $^{40}Ar/^{39}Ar$ fault gouge ages and suggests that deformation of the thrust belt took place from mid-Eocene to early Oligocene time, consistent with previous studies. Published geochronologic constraints indicate that upper crustal shortening within the Hoh Xil Basin ceased by ~27 Ma. Together with constraints on the timing of crustal shortening throughout the northern Tibetan Plateau, our work suggests that deformation initiated throughout the northern plateau near the onset of Indo-Asian collision.

We construct a balanced geologic cross section across the FFTB and derive a shortening estimate of 40 ± 10 km (28.0 ± 7.2%). We test whether Eocene – Oligocene shortening of the Hoh Xil Basin can account for published Miocene paleoelevations (3.4 – 4.2 km) by calculating isostatic uplift in response to shortening and thickening of the lithosphere. Our results indicate that ~28.0% crustal shortening and associated thickening produced surface uplift between 0.6 and 1.7 km and crustal thickness values up to 52 km, assuming that the initial elevation of the Hoh Xil Basin was between 0 and 1 km. These results cannot account for Miocene paleoelevations or modern crustal thicknesses (65 – 70 km). Attainment of high elevation and modern crustal thickness require

[2] Citation: Staisch, L. M., N. A. Niemi, M. K. Clark, H. Chang, *in prep*, Eocene – late Oligocene history of crustal shortening within the Hoh Xil Basin, north-central Tibetan Plateau.

further mechanisms of crustal thickening and surface uplift, such as lower crustal flow or distributed thickening of the lower crust, and possibly removal of the mantle lithosphere.

3.1. Introduction

Resolving the timing and magnitude of deformation throughout the Tibetan Plateau is essential for understanding the lithospheric response to continental collision and addressing proposed models of plateau formation. While early models of Tibetan Plateau growth generally assumed that the Indo-Asian collision was the main driver in crustal thickening and inferred that deformation progressed northward from the collision boundary (England and McKenzie, 1982; Dewey et al., 1988; England and Houseman, 1986; Tapponnier et al., 2001), more recent geologic studies throughout the Himalaya and Tibetan Plateau reveal a more complicated picture of the tectonic evolution of Tibet. In particular, the concept that the southern margin of Eurasia had formed a wide and elevated deformation belt prior to collision has gained considerable traction over the past several decades (Burg et al., 1983; Murphy et al., 1997; Rohrmann et al., 2012; Ding et al., 2014).

Studies conducted in the Lhasa and Qiangtang Terranes report extensive Mesozoic and early Cenozoic crustal shortening and only modest crustal shortening since ~50 Ma, suggesting that central Tibet was thickened to near modern values prior to the onset of continental collision and has been little deformed since (Figure 3.1; Burg et al., 1983; England and Searle, 1986; Rowley, 1996; Murphy et al., 1997; Kapp et al., 2003, 2005, 2007a, 2007b; DeCelles et al., 2007b; Molnar and Stock, 2009; Dupont-Nivet et al., 2010; Najman et al., 2010). Paleoelevation estimates in the central Tibetan Plateau have been used to infer that near modern elevations were established by ~48 Ma in the Lhasa Terrane, by 51 – 28 Ma in the Qiangtang Terrane, and by 40 – 26 Ma along the Bangong-Nujiang Suture Zone (Rowley and Currie, 2006; DeCelles et al., 2007a, 2007b; Polissar et al., 2009; Xu et al., 2013; Ding et al., 2014). The northern extent of pre-collisional deformation and uplift is inferred to be the Tanggula Shan, based on the Cretaceous to early Eocene record of continuous deposition in Hoh Xil Basin, located immediately to the north (Figure 3.1 and 3.2; Staisch et al., 2014). Together, these studies suggest that a high-elevation pre-collisional deformation belt spanned from the Gangdese Fold and Thrust Belt, located just north of the Indus Yarlung Suture, to the Tanggula Shan (Figures 3.1 and 3.2). Currently, this region is roughly 500 – 600 km in north-south extent and encompasses ~45 – 50% of the modern latitudinal width of the Tibetan Plateau, indicating that the orogen has roughly doubled in size since collision. Several similarities can be

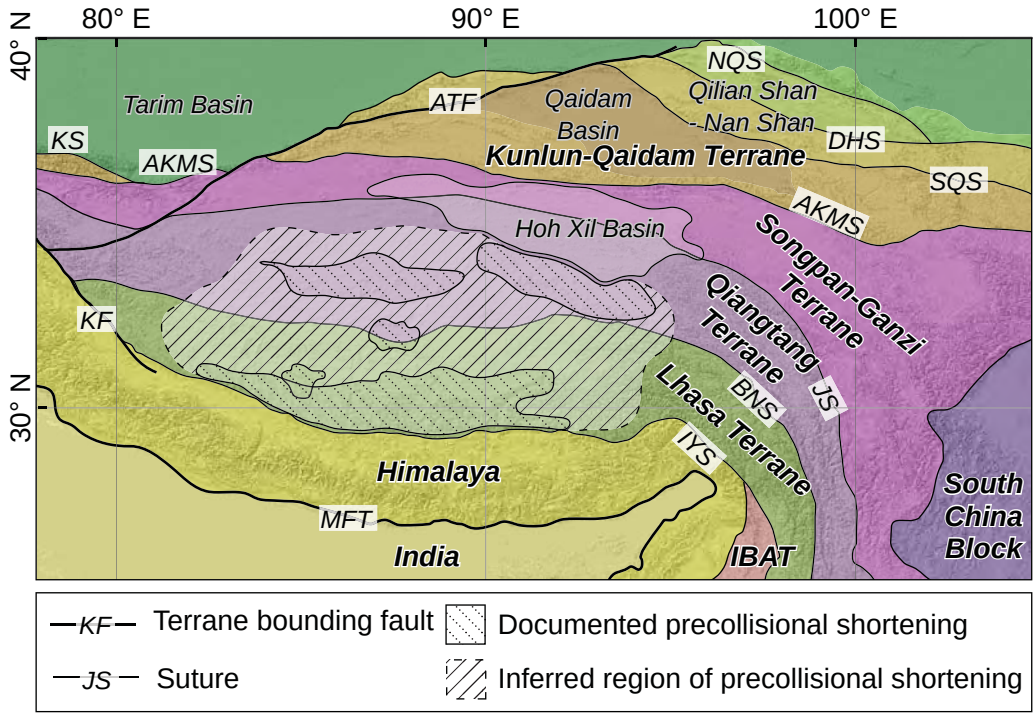

Figure 3.1. Map of the Tibetan Plateau delineating regions of documented and inferred precollisional deformation. Terranes are colored and labeled, as well as the location of the Hoh Xil Basin. Terrane, suture and terrane bounding fault names are abbreviated as follows; IBAT: Indo Burman Andaman Terrane, KS: Kudi Suture, AKMS: Ayimaqin-Kunlun-Mutztagh Suture, NQS: North Qilian-Shan Suture, DHS: Danghe Nan-Shan Suture, SQS: South Qilian-Shan Suture, JS: Jinsha Suture, BNS: Bangong-Nujiang Suture, IYS: Indus-Yarlung Suture, ATF: Altyn Tagh Fault, KF: Karakoram Fault, MFT: Main Frontal Thrust.

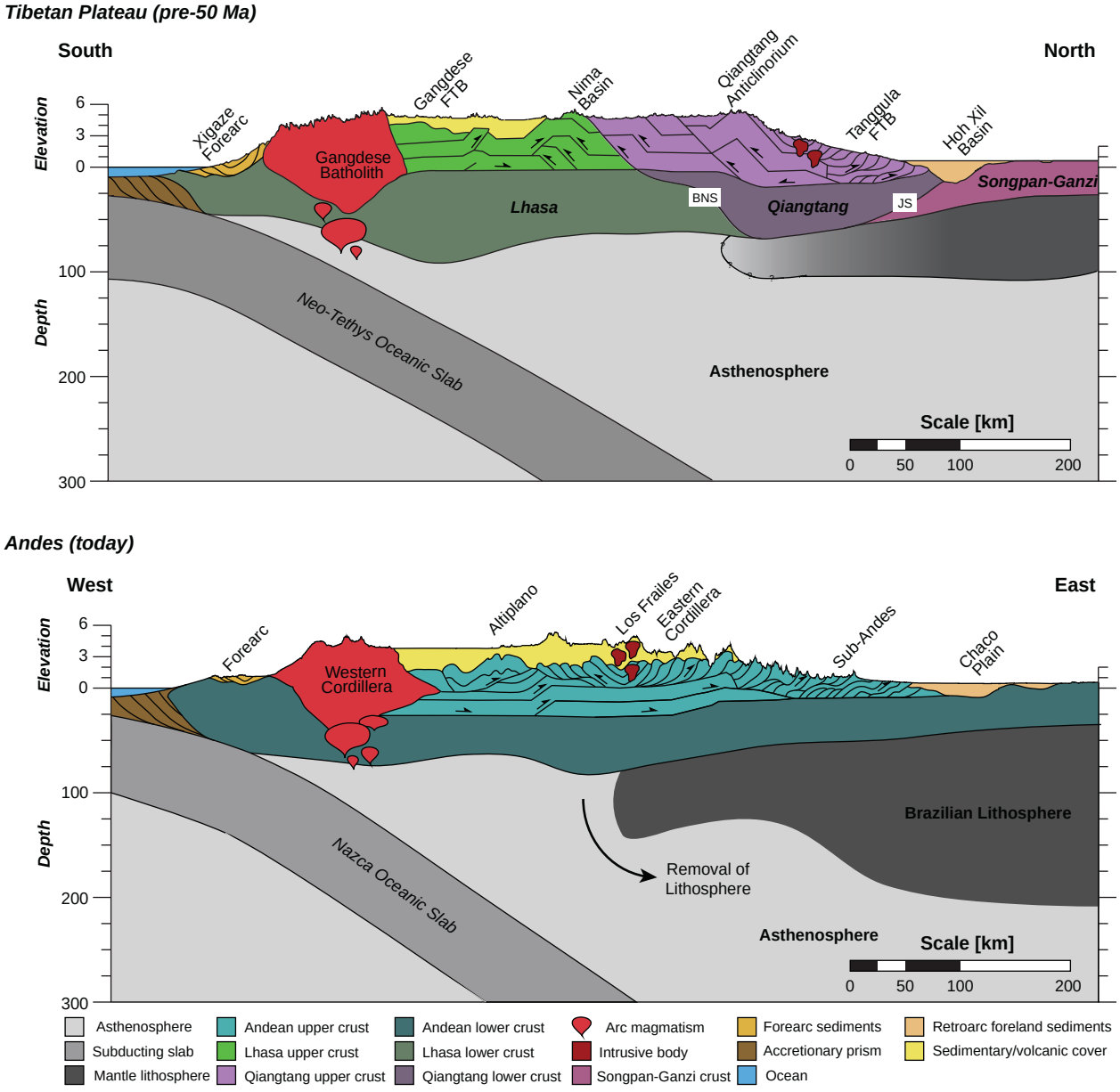

Figure 3.2. Comparison of schematic cross sections of the pre-collisional Tibetan Plateau (top) and the modern Andes. The cross section for the Tibetan Plateau was constructed based on cross sections of the Gangdese Fold and Thrust Belt (Kapp et al., 2007b), the Nima Basin (Kapp et al., 2007a), the Qiangtang Anticlinorium (Kapp et al., 2005), the Tanggula Shan (Li et al., 2012), and Hoh Xil Basin (Liu et al., 2001). The yellow shaded region above the deformed Lhasa Terrane represents the relatively undeformed Linzizong volcanic cover. The mantle lithosphere shown beneath the Songpan-Ganzi and Qiangtang Terranes is based on modern geophysical data (Owens and Zandt, 1997) and is speculative. The Andean cross section is modified from McQuarrie et al. (2005) and is taken as an east-west transect across central Bolivia.

drawn between the pre-collisional tectonic setting of the Tibetan Plateau and of the modern Altiplano-Puna Plateau (England and Searle, 1986), where eastward subduction of the Nazca Plate has resulted in thickened South American lithosphere and an associated high-elevation mountain belt and plateau (Figure 3.2). Similarities include the width of the deformed margin normal to the direction of convergence, the relative locations and extent of arc magmatism, the width and depth of retroarc foreland basin sedimentation, and volcanic cover in the central plateau regions (Figure 3.2).

If an Andean-style margin was established across the Lhasa and Qiangtang terranes prior to continental collision, one may ask how and when this margin evolved into the modern Tibetan Plateau. Extensive work in the Himalayan Fold and Thrust Belt (HFTB), located to the south of the pre-collisional deformation, shows that crustal shortening initiated in the Tethyan Himalaya near 50 Ma and propagated southward in time and that southward foreland basin migration initiated between 60 and 50 Ma (Ratschbacher et al., 1994; DeCelles et al., 2001; Searle et al., 2003; Murphy and Yin, 2003; Yin et al., 2005; Aikman et al., 2008, DeCelles et al., 2014). The spatiotemporal pattern of deformation south of the Indus-Yarlung Suture suggests that continental collision drove southward expansion of the extent of thickened lithosphere and possibly of high topography. Spatially, the HFTB represents ~20 – 25% of the present-day north-south width of the Himalayan-Tibetan orogen and, while the tectonic evolution of this region provides key insight into the timing and pattern of crustal shortening and plateau expansion, it encompasses just under half of the post-collisional shortening history of the orogen. The remaining history of post-collisional plateau evolution lies to the north of the Tanggula Shan.

Compared to the tectonic evolution of the Himalaya and central Tibetan Plateau, the deformation history of northern Tibet is significantly less well understood. Recent work along much of the modern northern and northeastern plateau margin has convincingly documented initial crustal shortening and exhumation during or soon after the ~50 Ma onset of collision, which suggests that the northern boundary of the plateau was established at the onset of the Indo-Asian collision and challenges the concept of northward propagation of deformation (Yin et al., 2002; Clark et al., 2010; Duvall et al., 2011). Deformation of the modern northern plateau boundary early in the collision history has been used to infer that heterogeneities in lithospheric strength play an important role in localizing deformation, and that the plateau margin may have a separate deformation history from the remainder of the plateau (Dayem et al., 2009). However, the timing of deformation across the northern Tibetan Plateau is only broadly constrained and several possible post-collisional deformation histories are viable. Potential deformation scenarios include (a) distributed crustal

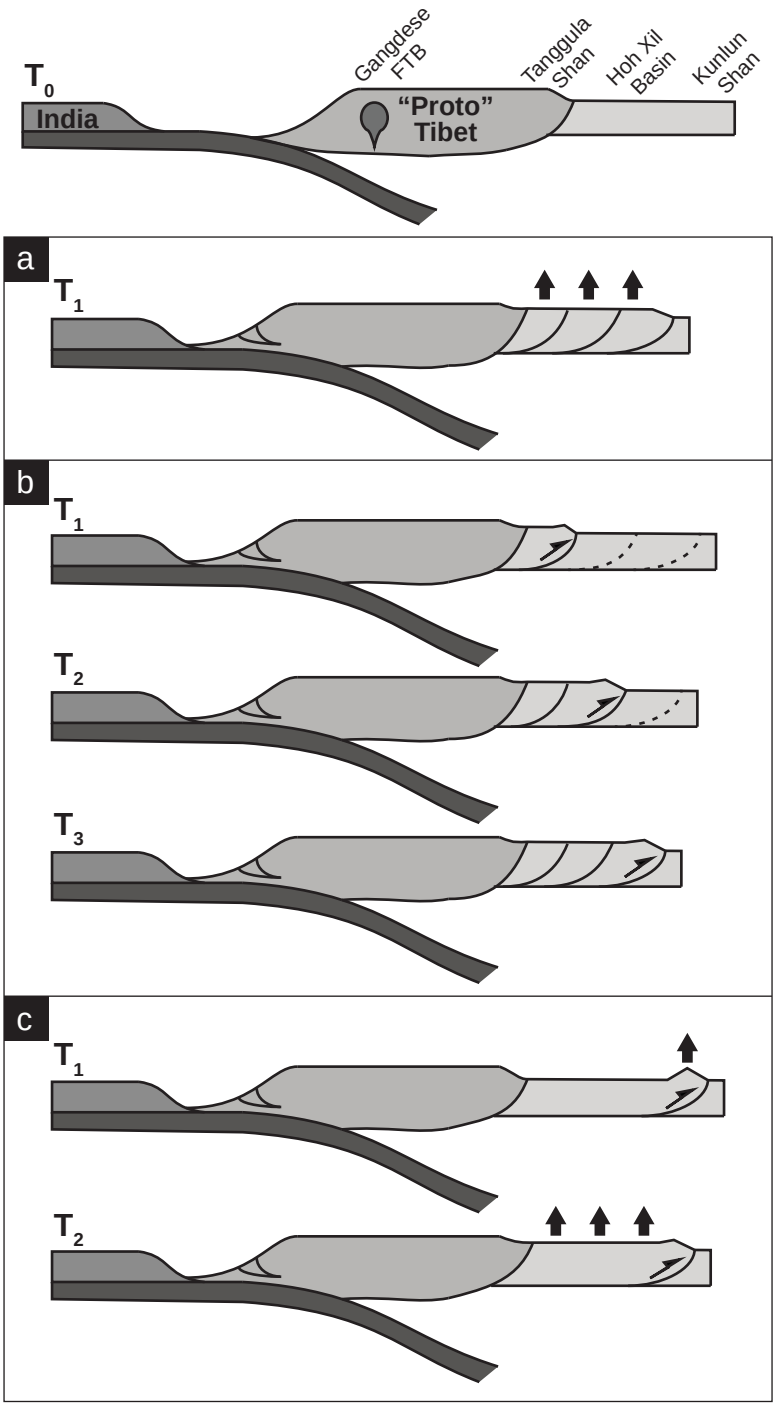

Figure 3.3. Schematic cross sections of possible post-collisional deformation scenarios of the Tibetan Plateau. The top panel shows Tibet at time T0 prior to collision, with a pre-collisional Andean-type margin, "Proto-Tibet". (a) This scenario shows distributed uplift across the northern Tibetan Plateau at the onset of Indo-Asian collision. (b) This scenario shows several time periods in which deformation in northern Tibet progresses northward in time (e.g. Wang et al., 2008). (c) This scenario shows initial deformation in response to continental collision localized along the modern northern margin, followed by a separate deformation history of the remainder of the northern Tibetan Plateau (e.g. Dayem et al., 2009).

shortening throughout the northern plateau (Figure 3.3a; Clark, 2012), (b) a northward propagating deformation front (Figure 3.3b; e.g., Wang et al., 2008), or (c) concentrated shortening along the northern plateau boundary due to rheological heterogeneity soon after collision that is separate from and precedes the shortening history of the remainder of northern Tibet (Figure 3.3c; e.g., Dayem et al., 2009). Resolution of the spatiotemporal deformation history of northern Tibet affords potential insight into the Eurasian lithospheric response to continental collision, stress transmission through the crust, and the relative importance of crustal heterogeneities in strain localization.

The Hoh Xil Basin, located between the Tanggula Shan and Kunlun Shan (Figure 3.1), contains strata that span the late Cretaceous to Miocene and thus record the pre- and post-collisional deformational history of the northern Tibetan Plateau (Liu et al., 2001, 2003; Wang et al., 2008; Staisch et al., 2014). Stratigraphic relationships and radiometric dating of variably deformed volcanic units within the Hoh Xil Basin suggest that deformation occurred sometime between ~51 and 27 Ma (Staisch et al., 2014), however a detailed chronology of deformation in this region has not been established. In this study, we focus on refining the deformation history of the Fenghuoshan Fold and Thrust Belt (FFTB), located in central Hoh Xil Basin, in order to address possible growth histories of the northern Tibetan Plateau. We investigate the deformation history of this region by $^{40}Ar/^{39}Ar$ dating of fault-grown illite and modeling of low-temperature thermochronologic data. The magnitude of deformation is estimated by balancing a structural cross section across the FFTB. We combine our results with a compilation of data on Cenozoic deformation and exhumation throughout the Tibetan Plateau to evaluate the spatiotemporal pattern of deformation, discuss shortening in northern Tibet in context of alternative descriptions of continental collision, and investigate possible mechanisms for crustal thickening throughout the orogen.

3.2. Geologic Setting

3.2.1. Stratigraphy of the Hoh Xil Basin

The Hoh Xil Basin is located in the north-central Tibetan Plateau, bounded to the south by the Tanggula Shan and to the north by the Kunlun Shan. The basin is roughly 83,000 km^2 in area and has an average elevation of ~4800 meters above sea level. The Jinsha Suture trends east-west near the center of the Hoh Xil Basin, thus dividing it between the Qiangtang and Songpan-Ganzi terranes (Figure 3.1). Terrestrial sedimentary rocks exposed within the Hoh Xil Basin range from late Cretaceous to Miocene in age (Yin et al., 1988; Zhong, 1989; Li and Yuan, 1990; Ji, 1994; Liu et al., 2001; 2003; An et al., 2004; Yi et al., 2004; Li et al., 2012; Staisch et al., 2014) and exhibit varying

degrees of deformation, such that the basin records a nearly continuous depositional history over this time period.

The Fenghuoshan Range is located in the center of the Hoh Xil Basin, near the town of Erdaguo (二道溝), and is roughly 35 km in north-south extent (Figure 3.4a; map units are described in Appendix A). The rocks exposed within the Fenghuoshan Range are almost entirely composed of the Fenghuoshan Group (风火山群) terrestrial red bed sequence, in addition to limited outcroppings of the late Triassic Jieza Group (结扎群), the Paleocene – early Oligocene Tuotuohe Group (沱沱河群), the Oligocene Yaxicuo Group (雅西措群), the Miocene Wudaoliang Group (五道梁群), and small volume late Oligocene intrusions and lava flows (Qinghai Bureau of Geology and Mineral Resources (QBGMR), 1989a, 1989b; Duan et al., 2005; Staisch et al., 2014).

The Fenghuoshan Group records the earliest terrestrial sedimentation in the Hoh Xil Basin and thus provides the first evidence of uplift above sea level within the region. Reinterpretation of magnetostratigraphic data from the Fenghuoshan Group (Liu et al., 2001, 2003; Staisch et al., 2014) suggests that deposition initiated in the late Cretaceous and ceased in the early Eocene, ca. 85 – 51 Ma. Paleocurrent data (Leeder et al., 1988; Liu and Wang, 2001; Liu et al., 2001; Yi et al., 2008; Wang et al., 2008; Li et al., 2012) and U-Pb zircon provenance data (Dai et al., 2012) and analysis (Staisch et al., 2014), suggest that the Fenghuoshan Group strata were sourced from the south, likely the Tanggula Shan in the central Qiangtang Terrane. This is consistent with thermochronologically constrained ~60 – 50 Ma rapid unroofing (Wang et al., 2008) and the timing of magmatic intrusion (Roger et al., 2000; Duan et al., 2005) in the Tanggula Shan. Basin development and deposition of the Fenghuoshan Group was likely caused by thrust loading and erosion of the Tanggula Fold and Thrust Belt (TFTB; Figure 3.5), and suggests that the Tanggula Shan was a local topographic high since the late Cretaceous. Flat-lying volcanic rocks dated at ~44.6 – 40.2 Ma that overlie strongly deformed strata in the TFTB (Wang et al., 2008) combined with evidence for the onset of slow cooling of this region by ~45 Ma (Rohrmann et al., 2012) suggest that N-S oriented contraction and rapid erosion of the TFTB ceased by the early Eocene. No evidence for syn-depositional deformation of the Fenghuoshan Group has been recognized, suggesting that crustal shortening did not progress into the Hoh Xil Basin until after ~51 Ma.

3.2.2. Structural Geology of the Fenghuoshan Fold and Thrust Belt

East-west striking folds and thrust faults are exposed within the Fenghuoshan Fold and Thrust Belt and postdate deposition of the Fenghuoshan Group (Staisch et al., 2014). Three major

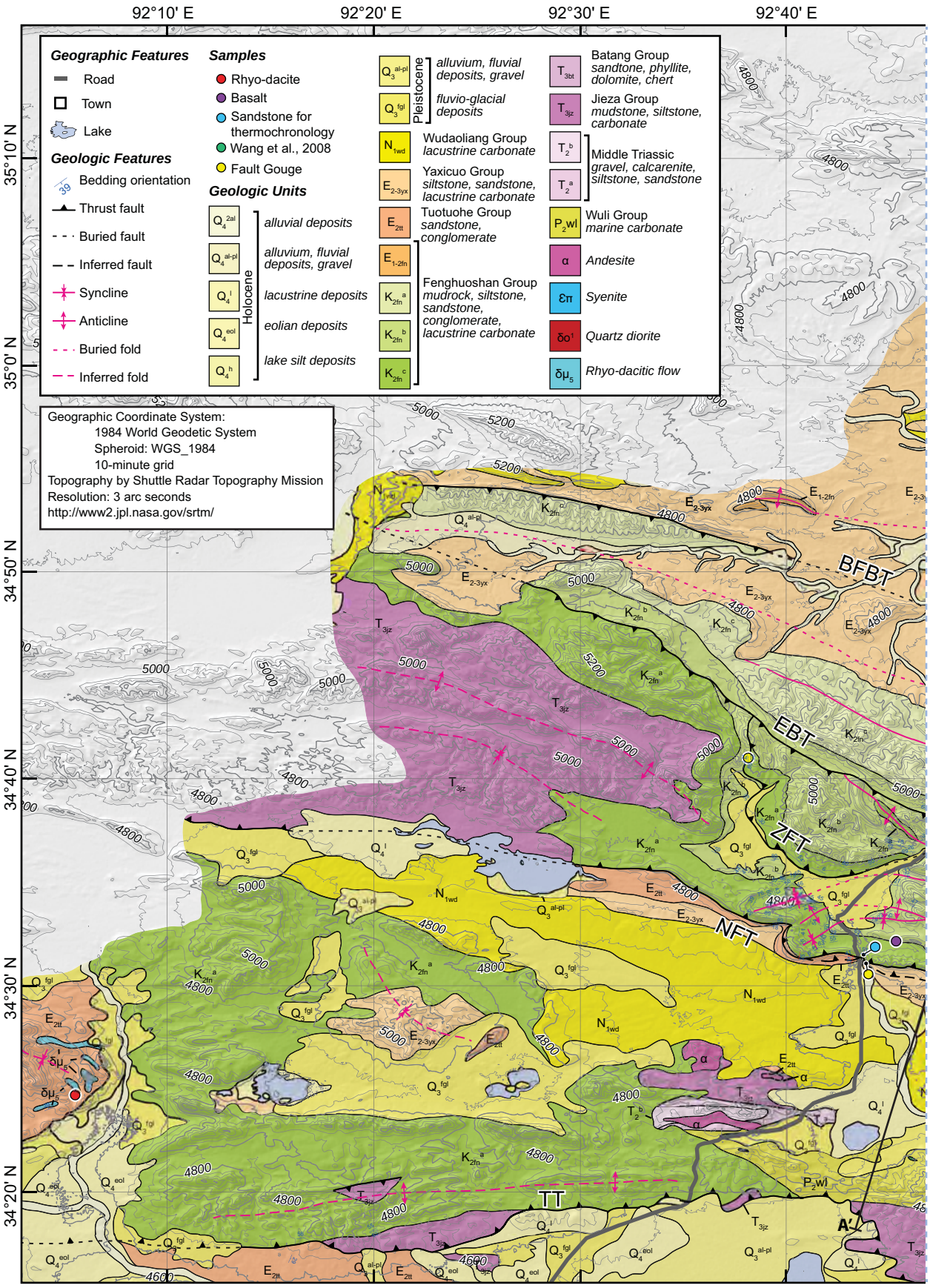
92°10' E
92°20' E
92°30' E
92°40' E
35°10' N
35°0' N
34°50' N
34°40' N
34°30' N
34°20' N
Geographic Features
Road
Town
Lake
Geologic Features
Bedding orientation
Thrust fault
Buried fault
Inferred fault
Syncline
Anticline
Buried fold
Inferred fold
Samples
Rhyo-dacite
Basalt
Sandstone for thermochronology
Wang et al., 2008
Fault Gouge
Geologic Units
Holocene
alluvial deposits
alluvium, fluvial deposits, gravel
lacustrine deposits
eolian deposits
lake silt deposits
Pleistocene
alluvium, fluvial deposits, gravel
fluvio-glacial deposits
Wudaoliang Group lacustrine carbonate
Yaxicuo Group siltstone, sandstone, lacustrine carbonate
Tuotuohe Group sandstone, conglomerate
Fenghuoshan Group mudrock, siltstone, sandstone, conglomerate, lacustrine carbonate
Batang Group sandtone, phyllite, dolomite, chert
Jieza Group mudstone, siltstone, carbonate
Middle Triassic gravel, calcarenite, siltstone, sandstone
Wuli Group marine carbonate
Andesite
Syenite
Quartz diorite
Rhyo-dacitic flow
Geographic Coordinate System:
1984 World Geodetic System
Spheroid: WGS_1984
10-minute grid
Topography by Shuttle Radar Topography Mission
Resolution: 3 arc seconds
http://www2.jpl.nasa.gov/srtm/
BFBT
EBT
ZFT
NFT
TT
A'

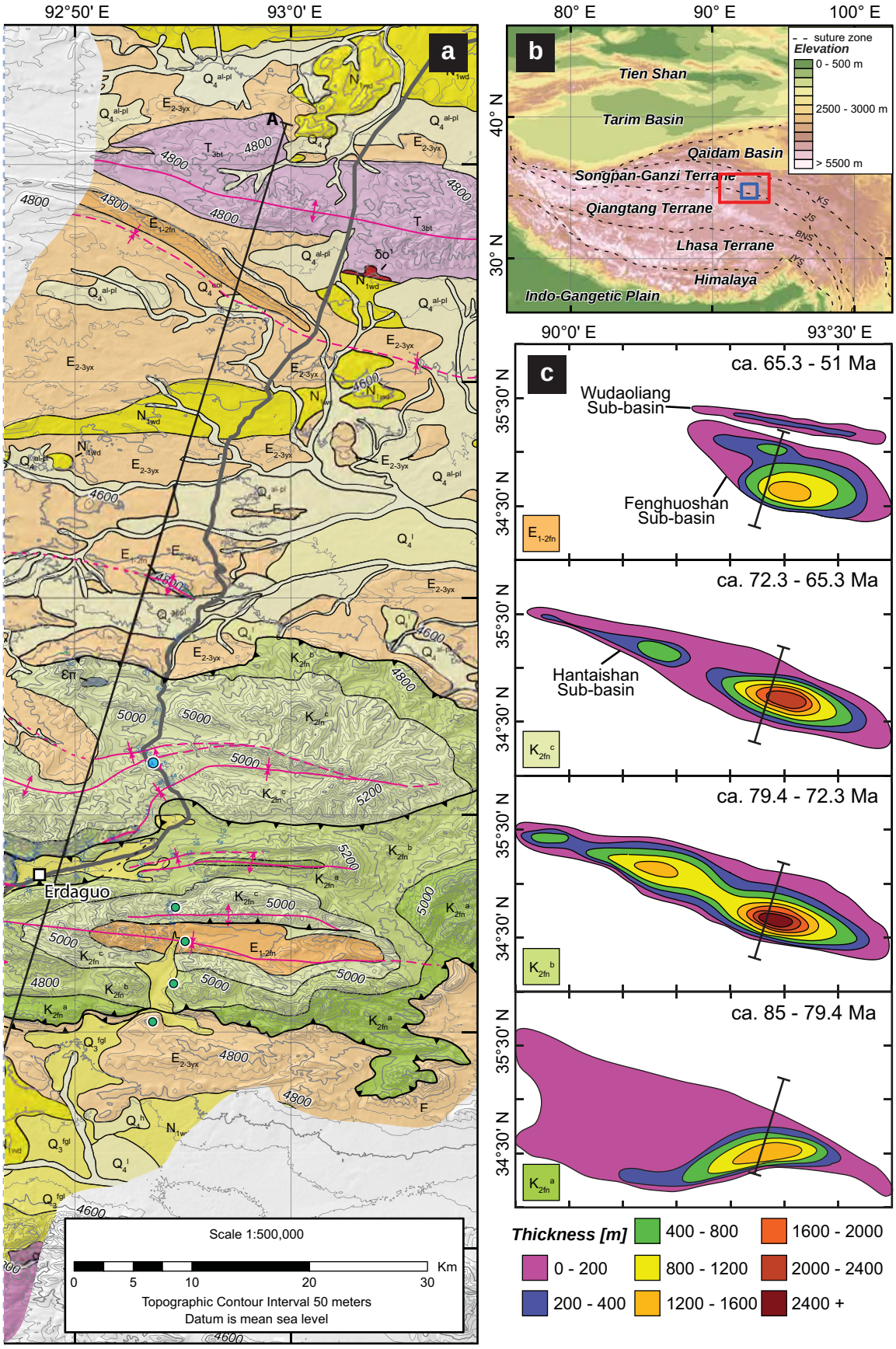
92°50' E
93°0' E
a
Erdaguo
Scale 1:500,000
0 5 10 20 30 Km
Topographic Contour Interval 50 meters
Datum is mean sea level
80° E
90° E
100° E
40° N
30° N
b
suture zone
Elevation
0 - 500 m
2500 - 3000 m
> 5500 m
Tien Shan
Tarim Basin
Qaidam Basin
Songpan-Ganzi Terrane
Qiangtang Terrane
Lhasa Terrane
Himalaya
Indo-Gangetic Plain
KS
JS
BNS
IYS
90°0' E
93°30' E
35°30' N
34°30' N
c
ca. 65.3 - 51 Ma
Wudaoliang Sub-basin
Fenghuoshan Sub-basin
ca. 72.3 - 65.3 Ma
Hantaishan Sub-basin
ca. 79.4 - 72.3 Ma
ca. 85 - 79.4 Ma
Thickness [m]
0 - 200
200 - 400
400 - 800
800 - 1200
1200 - 1600
1600 - 2000
2000 - 2400
2400 +

Figure 3.4. (a) Geologic map of the Fenghuoshan Fold and Thrust Belt (FFTB), based on original mapping, satellite imagery, and published geologic maps (QBGMR, 1989a, 1989b). Sample locations are noted by colored circles. Abbreviated fault names: Beifeng Fenghuoshan Back Thrust Fault, BFBT; Erdaguo Back Thrust Fault, EBT; Zhong Fenghuoshan Thrust Fault, ZFT; Nan Fenghuoshan Thrust Fault, NFT. Hillshade and topographic contours are obtained from Satellite Radar Topography Mission (SRTM) data (http://www2.jpl.nasa.gov/srtm/). Cross section for the transect from A-A′ is shown in Figure 3.9. (b) Topographic map of the Tibetan Plateau and adjacent regions from SRTM data. Suture zones are shown as dotted lines (Styron et al., 2010). The red box indicates the geologic map location. The blue box indicates the isopach map location (c) Isopach maps for various stages of Fenghuoshan Group deposition, modified from Liu et al. (2001). Sub-basins are labeled, and transect A-A′ corresponds to the geologic map and cross section in Figure 3.9.

thrust faults and two back thrusts cross cut the Fenghuoshan Fold and Thrust Belt (Figure 3.4a). Most faults are located within the Fenghuoshan Range proper, however the southernmost thrust fault is located to the south of the range. Here, we name the thrust faults, from north to south, the Zhong Fenghuoshan Thrust Fault (ZFT, 中風火山逆斷裂), the Nan Fenghuoshan Thrust Fault (NFT; 南風火山逆斷裂), and the Tuotuohe Thrust Fault (TT; 沱沱河逆斷裂). We name the two back thrusts, from north to south, the Beifang Fenghuoshan Back Thrust (BFBT; 北方風火山反冲斷裂) and the Erdaguo Back Thrust (EBT; 二道溝反冲斷裂).

Along the southern margin of the Fenghuoshan Range, the south-directed Nan Fenghuoshan Thrust Fault places lower Fenghuoshan Group and unconformably overlying Tuotuohe Group strata over the Yaxicuo Group, suggesting that deformation within the Hoh Xil Basin occurred during and after deposition of the Tuotuohe and Yaxicuo Groups (Staisch et al., 2014). Roughly 20 km south of the Fenghuoshan Range, deformation of a 33.5 Ma rhyo-dacite suggests that crustal shortening continued after this time (Figure 3.4a; Staisch et al., 2014). Sub-horizontal late Oligocene basalt flows and only mild tilting of the Miocene Wudaoliang strata indicate that crustal shortening within the Hoh Xil Basin was largely complete by 27.4 Ma. Together, these constraints suggest that northeast-southwest compression of the Hoh Xil Basin took place between the early Eocene and late Oligocene. However, the 51 – 27 Ma duration of deformation is constrained solely by depositional ages of deformed strata and flat-lying volcanic units and only represents a maximum duration of deformation.

3.3. Timing of Deformation in the Fenghuoshan Fold and Thrust Belt

In order to address the timing of deformation within the Fenghuoshan Fold and Thrust Belt,

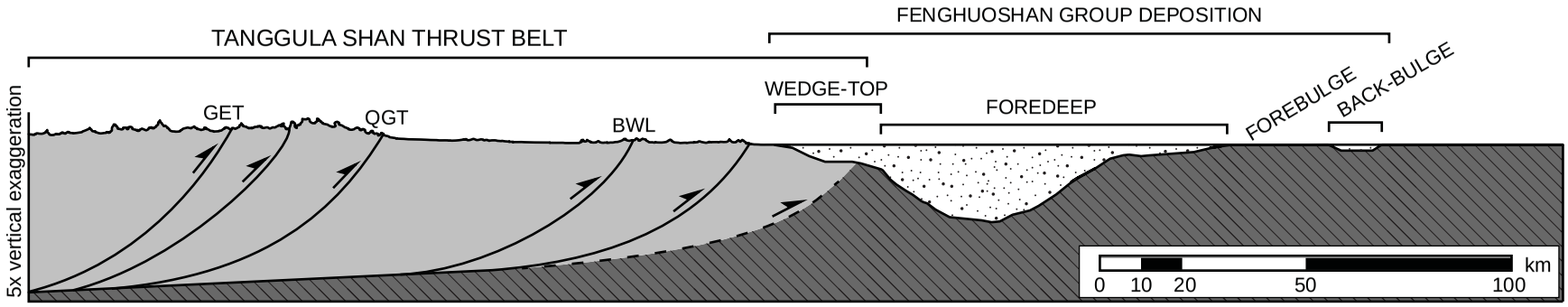

Figure 3.5. An idealized cross section across the Tanggula Shan and Hoh Xil Basin, prior to FFTB deformation showing the relationship between uplift and erosion of the Tanggula Fold and Thrust Belt (TFTB), thrust loading within Hoh Xil Basin, and deposition of the Fenghuoshan Group. Thrust faults within the TFTB are mapped by Li et al. (2011): GET, Geraddong-Esuima Thrust; QGT, Quemocuo-Gaina Thrust; BWL, Baqing-Wulwl Lake Thrust. Inferred subsurface geometries and sedimentological nomenclature adapted from DeCelles and Giles (1996).

we employ $^{40}Ar/^{39}Ar$ fault gouge dating and low-temperature thermochronology. Fault gouge dating directly dates minerals formed during faulting, whereas modeled low-temperature thermochronologic ages provide information on the onset, duration, and rate of exhumation. With these two techniques, we provide new constraints on the deformation history of the Fenghuoshan Fold and Thrust Belt.

3.3.1. $^{40}Ar/^{39}Ar$ Fault Gouge Dating

Fault gouge dating is a method based on radiometric dating of potassium-bearing clay minerals that are authigenically grown within the fault zone during active faulting. Clay-rich fault gouge often contains detrital and authigenically-grown illite, the $2M_1$ and $1M_d$ polytypes, respectively, which are assumed to be the only potassium-bearing clay phases within the gouge (van der Pluijm et al., 2006). Because extraction of 100% authigenic illite from a sample is rarely possible, the authigenic illite age is estimated from a two end-member mixing model between $2M_1$ and $1M_d$ illite polytypes. The fault gouge sample is separated into several aliquots by gravitational separation in a centrifuge, which varies the clay crystal size in each separate. Because authigenic ($1M_d$) illite crystals tend to be smaller in size than detrital ($2M_1$) illite crystals, gravitational separation also varies relative proportions of authigenic and detrital illite in each aliquot. The proportions of authigenic and detrital illite are estimated using X-Ray Diffractometry in each aliquot. The age of each aliquot is measured using $^{40}Ar/^{39}Ar$ geochronology. The end member authigenic and detrital illite ages are traditionally obtained by linear regression using a York least-squares method (York, 1968). Below we use a Bayesian regression technique to obtain end member ages.

3.3.1.1. Sample collection

Samples for fault gouge age analysis are collected from clay-rich horizons within fault zones. In this study, two fault gouge samples were collected from the Fenghuoshan Range. The first sample was collected from the south-southwest-directed Zhong Fenghuoshan Thrust Fault (ZFT), which is internal to the Fenghuoshan Range (Figures 3.4a and 3.6a). This fault places the Fenghuoshan Group over stratigraphically lower portions of the same unit. The second sample was collected along the north-dipping, south-directed range bounding Nan Fenghuoshan Thrust Fault (NFT), which places the lower Fenghuoshan Group strata over younger Tuotuohe and Yaxicuo Group strata (Figures 3.4a and 3.6b). Sample preparation is described in Appendix B.

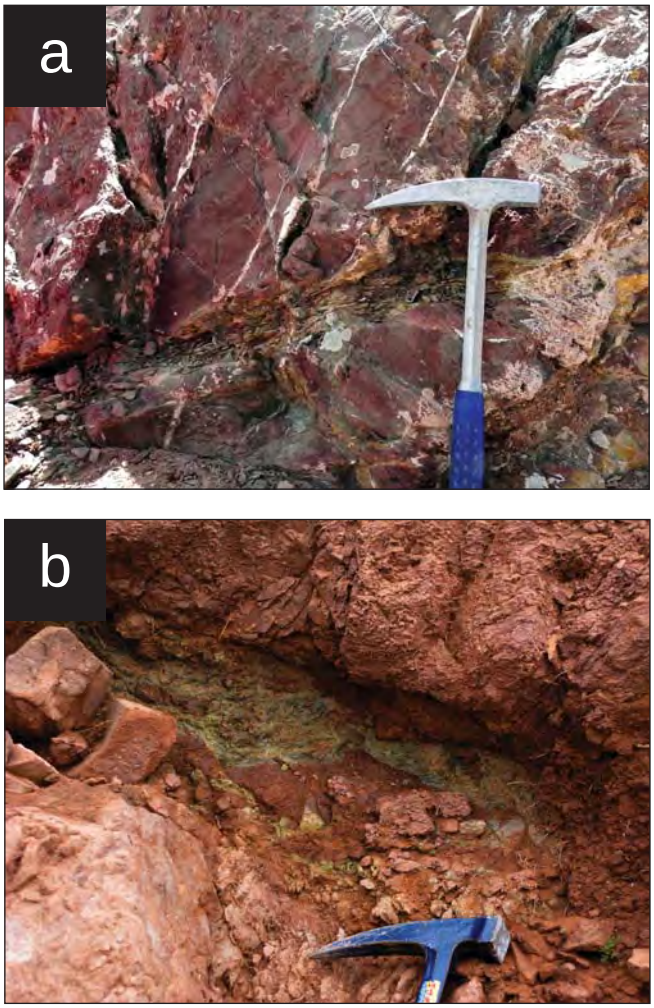

Figure 3.6. Field photographs of fault gouge. (a) Photograph of fault gouge sample 12FHS12 with rock hammer for scale. (b) Field photograph of fault gouge sample 10UMT09 with rock hammer for scale.

Table 3.1. Fault gouge age and illite concentrations for samples 10UMT09 and 12FHS12. Total gas ages are used in the linear regression.

Sample	Size fraction	Concentration $2M_1$ illite [%]	$^{40}Ar/^{39}Ar$ Total gas age * [Ma]	$^{40}Ar/^{39}Ar$ Retention age [Ma]
10UMT09				
	Coarse	75 ± 4	127.60 ± 1.20	138.43 ± 1.27
	Medium	55 ± 4	96.91 ± 0.40	111.50 ± 0.46
	Fine	39 ± 4	84.69 ± 0.56	101.75 ± 0.65
	Ultra fine	15 ± 4	64.65 ± 1.03	93.11 ± 2.88
12FGS12				
	Coarse	64 ± 4	92.79 ± 0.54	106.72 ± 0.62
	Medium-coarse	40 ± 4	70.89 ± 0.36	88.82 ± 0.45
	Fine	21 ± 4	61.86 ± 0.22	78.28 ± 0.28
	Ultra fine	12 ± 4	52.20 ± 0.50	74.80 ± 0.65

* Total gas age errors were increased to 3% of the age in the linear regression to account for external errors.

3.3.1.2. XRD analysis

For each size fraction, XRD powder patterns were obtained in order to estimate the proportion of detrital ($2M_1$) to authigenic ($1M_d$) illite. Each size fraction was mounted on a metal sample plate using an end-packer device to obtain near-random crystal orientation, and placed in a Scintag X1 Powder X-Ray Diffractometer (PXRD) at the University of Michigan Electron Microbeam Analysis Laboratory (EMAL). Powder patterns were measured between 16 and 44 degrees (2Θ) at 0.05° step size for 30 seconds. We estimated the relative concentration of $2M_1$ and $1M_d$ for each size fraction using PXRD patterns generated from mineral standards. For the $2M_1$ component, we used patterns generated from the Owl Creek pegmatite in the Wind Rivers Range, WY, and for the $1M_d$ component, we used the IMt-1 standard from Silver Hill, MT (Hower and Mowatt, 1966; Haines and van der Pluijm, 2008). Modeled $2M_1$ and $1M_d$ powder patterns were combined in varying proportions to obtain a modeled mixed illite powder pattern. Modeled powder patterns were iteratively compared to measured PXRD patterns until the modeled and measured patterns matched. The error in the estimated proportion of $2M_1$ and $1M_d$ illite using polytype pattern matching is generally between 3 and 5% (Haines and van der Pluijm, 2008), which we average to a 4% error for each aliquot in our analysis.

3.3.1.3. Illite age analysis

Illite ages for each fault gouge size fraction were measured using $^{40}Ar/^{39}Ar$ dating techniques at the University of Michigan Argon Geochronology Laboratory. In order to avoid recoil loss of argon gas during irradiation, the clay samples were spun into small pellets and encapsulated in fused silica tubes at high vacuum such that any recoil ^{39}Ar remained within the glass capsule (van der Pluijm et al., 2001). Samples were irradiated at the McMaster Nuclear Reactor at McMaster University in packages mc32, mc33, and mc42. Silica capsules were cracked under high vacuum to measure recoil argon, and then step heated with a Coherent Innova 5 W continuous argon-ion laser. Argon isotope measurement was done using a VG1200S mass spectrometer with a Daly detector and fusion system blanks were run every five fusion steps. Blank levels from ^{36}Ar through ^{40}Ar were subtracted from gas fractions. Correction for interfering reactions producing ^{40}Ar was obtained using a zero-aged artificial glass sample. Further corrections were made for the decay of ^{37}Ar and ^{39}Ar, K, Ca, and Cl interfering nucleogenic reactions, as well as the production of ^{36}Ar from ^{36}Cl decay. The resulting argon age spectra do not exhibit age plateaus typical of $^{40}Ar/^{39}Ar$ geochronologic analysis because clay size fractions contain a mixture of detrital and authigenic illite

ages, and because of argon recoil. For this analysis, we use total gas ages to determine the age of authigenic illite. The age of fault motion is inferred from the authigenic illite age.

3.3.1.4. Results

Coarse, medium-coarse, fine and ultrafine size fractions were analyzed from the ZFT (12FHS12; Figure 3.6a). XRD powder pattern analysis suggests that these clay size fractions contain 65%, 40%, 21%, and 12% (±4%) detrital illite, respectively (Table 3.1; Figure A3.1). Total gas ages and analytical errors (2σ) for these size fractions are 92.79 ± 1.02, 70.89 ± 0.72, 61.86 ± 0.44, and 52.20 ± 1.00 Ma, respectively (Tables 3.1 and A3.1; Figure A3.2).

For the fault gouge sample collected along the NFT (10UMT09; Figure 3.6b), we analyzed the coarse, medium, fine, and ultrafine size fractions. XRD powder pattern analysis suggests that these clay size fractions contain 75%, 55%, 39%, and 15% (±4%) detrital illite, respectively (Table 3.1; Figure A3.3). Total gas ages for these size fractions are 127.60 ± 2.40, 96.91 ± 0.80, 84.69 ± 1.12, and 64.65 ± 2.06 Ma, respectively (Tables 3.1 and A3.1; Figure A3.2).

3.3.1.5. Bayesian linear regression and fault gouge age interpretation

To estimate the authigenic and detrital illite end-member ages, we use a Bayesian method for linear regression through measured size fraction ages and polytype concentrations (Figure 3.7). We consider the Bayesian method used in this study to be advantageous over the more traditionally used York least-squares linear regression for data with errors in x- and y-values (York, 1968). In York least-squares linear regression, the slope and intercept values are assumed to be Gaussian, independent, and uncorrelated. This may misrepresent the values and errors of the modeled slope or intercept if there is correlation between slope and intercept values (Figure A3.4). The Bayesian method, on the other hand, tests the likelihood of modeled linear fits to the observed data and is able to resolve correlation between parameters. The resulting posterior probability density functions of slope and intercept values are used to calculate the range of possible authigenic and detrital illite ages and provides a more statistically meaningful assessment of uncertainty. A more thorough description of the Bayesian linear regression is provided in Appendix C.

For the Bayesian linear regression, we input observed age and illite concentrations for each sample aliquot, associated uncertainty, and prior bounds on parameter values. In this study, we increased the uncertainty of $^{40}Ar/^{39}Ar$ age to 3% of the measured age in order to account for external errors. We chose a value of 3% based on previous work which indicates that sample quality,

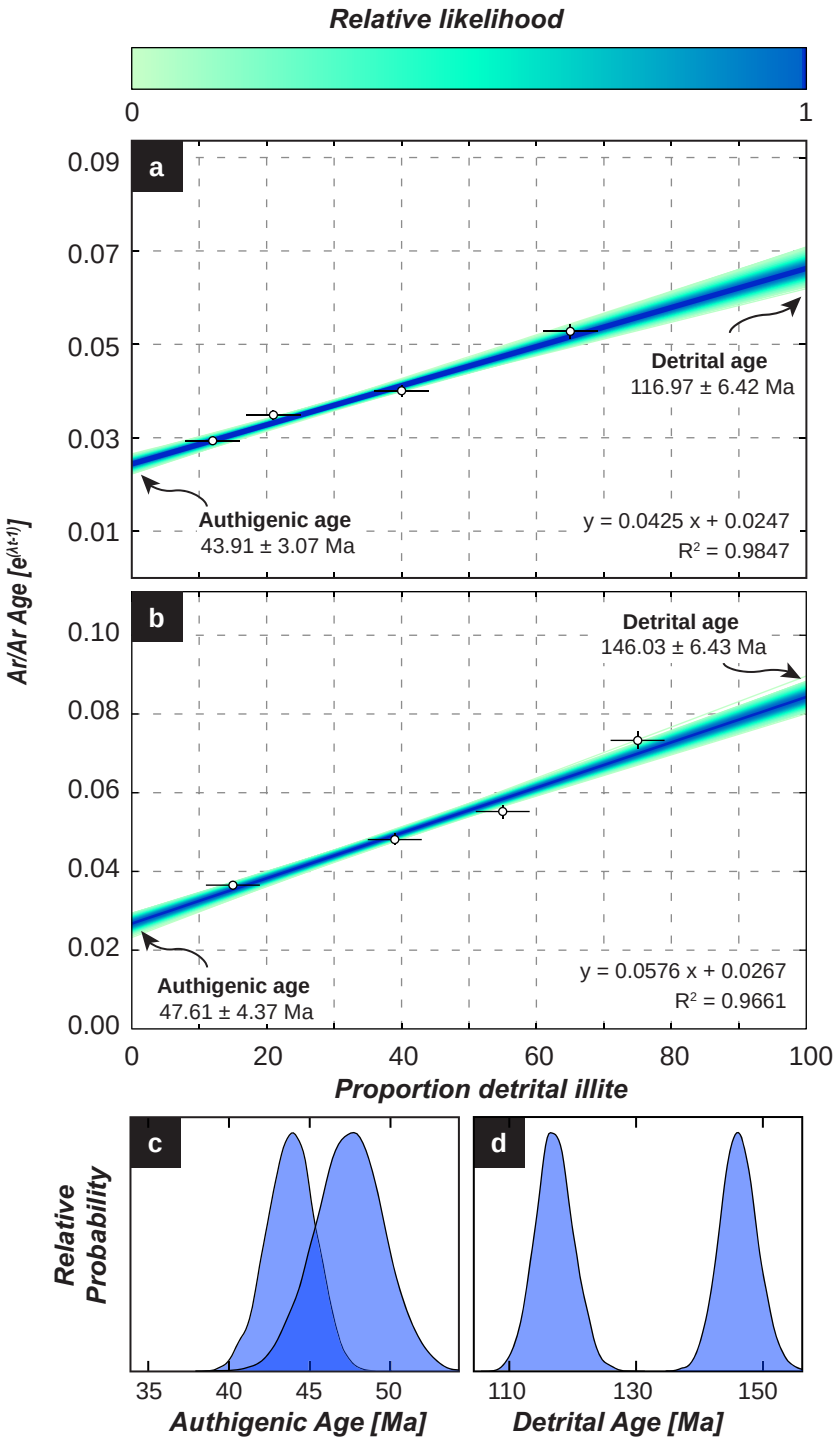

Figure 3.7. Fault gouge age and illite concentrations for samples 12FHS12 and 10UMT09. (a) Age-illite plot for sample 12FHS12 with Bayesian linear regression (dark blue line) and associated error (shaded region). (b) Age-illite plot for sample 10UMT09 with Bayesian linear regression (dark blue line) and associated error (shaded region). (c) Relative probability plot of modeled authigenic illite age for sample 12FHS12 and 10UMT09. (d) Relative probability plot of modeled detrital illite age for sample 12FHS12 and 10UMT09.

inhomogeneity in standards, and variations in interlaboratory and analytical conditions can account for up to 2 – 4% uncertainty in $^{40}Ar/^{39}Ar$ ages (Renne et al., 1998; Karner and Renne, 1998; Dazé et al., 2003). Loose prior bounds on slope and intercept were chosen to limit the model search of parameter values without restricting the sampling of likely regression parameters. This was done by ensuring that prior bounds were not within the 5% bound of posterior ranges in slope and intercept, once posteriors were established. The best-fit linear regression is represented by the modeled slope and intercept combination with the highest likelihood (Figures 3.7 and A3.5). The errors in slope and intercepts are reported at 2σ.

The Bayesian linear regression through $^{40}Ar/^{39}Ar$ age and illite concentration data for sample 12FHS12 gives an authigenic illite age of 43.91 ± 3.07 Ma and a detrital illite age of 116.97 ± 6.42 Ma with an R^2 value of 0.98 (Figure 3.7a). Probability distribution functions (PDFs) for the authigenic and detrital illite ages are shown in Figures 3.7c and 3.7d. We interpret these data to mean that the Zhong Fenghuoshan Thrust was active at ~44 Ma and that the sedimentary units within the hanging and footwall of this thrust fault have a sediment source containing late Cretaceous illite ages. For sample 10UMT09, a Bayesian linear fit through $^{40}Ar/^{39}Ar$ age and illite concentration data resulted in an authigenic illite age of 47.61 ± 4.37 Ma and a detrital illite age of 146.03 ± 6.43 Ma with an R^2 value of 0.97 (Figure 3.7b). We interpret this fault gouge age to mean that the Nan Fenghuoshan Thrust Fault was active at ~48 Ma and that the sedimentary units within the hanging and foot wall of this thrust fault have a sediment source containing early Cretaceous illite ages.

Comparison of authigenic age probability distribution functions (PDFs) for 10UMT09 and 12FHS12 gouge samples shows that there is overlap in authigenic illite age (Figure 3.7c). The amount of overlap may suggest that the ZFT and NFT faults were active at roughly the same time. There is no apparent overlap in detrital ages for fault gouge samples (Figure 3.7d). This may suggest that the source of detrital illite from the wall rock of either thrust is different. The hanging and foot walls of the ZFT and NFT are both composed of the Fenghuoshan Group, however the Fenghuoshan Group was not deposited to great enough depths to reset detrital illite ages. The detrital ages are therefore likely controlled by the age of Fenghuoshan Group source material, which is the lithologically heterogeneous Tanggula Shan (Pan et al., 2004). Because the wall rock of the ZFT is composed of stratigraphically younger material than of the NFT wall rock, we attribute the mismatch in $2M_1$ illite ages to the possibility of a variable detrital illite source throughout the depositional history of the Fenghuoshan Group.

3.3.2. Low-Temperature Thermochronology

3.3.2.1. Sample collection and processing

In order to constrain the exhumation history of the Fenghuoshan Range, two medium-coarse grained sandstone samples were analyzed from the Fenghuoshan Group for low-temperature thermochronologic analysis. The southernmost sample, 11UMT16, was collected from the hanging wall of the NFT, near the fault trace. A second sample, 11UMT22, was collected near the core of an anticline in the northern portion of the Fenghuoshan Range (Figure 3.4a). Other samples were collected for low-temperature thermochronology, however the material was too fine-grained and apatite-poor to provide suitable material for analysis. Apatite crystals were separated and picked using standard magnetic and density separation techniques, further outlined in Appendix B. For (U-Th)/He dating, apatite aliquots were outgassed using the AlphaChron at the University of Michigan He Laboratory and U, Th, Sm and Ca concentrations were measured by ICP-MS at the University of Arizona LaserChron Center following standard procedures (Farley and Stockli, 2002). For apatite fission-track dating, samples were analyzed at Apatite to Zircon, Inc.

3.3.2.2. Apatite (U-Th)/He results

Apatite (U-Th)/He ages for the north sample (11UMT22) range between 26.7 and 29.3 Ma, with the exception of a single grain that was dated at 10.1 Ma (Table A3.2). This grain was considered an outlier based on Dixon's Q-test and removed from further analysis (Dean and Dixon, 1951). The mean age and 2σ standard deviation of the remaining single-grain analyses for this sample is 28.1 ± 2.2 Ma (Table 3.2). The southern sample (11UMT16) apatite (U-Th)/He ages range between 23.1 and 26.2 Ma (Table A3.2) with a mean and 2σ standard deviation of 26.0 ± 6.1 Ma (Table 3.2).

3.3.2.3. Apatite fission-track results

We analyzed samples 11UMT22 and 11UMT16 for apatite fission-track (AFT) age and track length data (Tables A3.3 – A3.6) and evaluated whether single-crystal apatite fission-track ages are derived from the same population using the standard χ^2 criterion (Galbraith, 1981; Green, 1981). In both sample, the results from the χ^2 test indicate that single-grain AFT ages are not derived from the same population which, along with the variation in measured kinetic parameters (D_{par} and r_{mr0}), suggests that samples are composed of multiple kinetic populations (Ketcham et al., 1999; 2007). We identified two kinetic populations per sample using HeFTy, a program for thermochronologic data

Table 3.2. Apatite (U-Th)/He (AHe) and fission-track (AFT) ages and sample locations from this study and from published data in Wang et al. (2008).

Sample	*Latitude*	*Longitude*	*Elevation*	*Apatite (U-Th)/He*		*Apatite Fission-Track*				
	[°N]	*[°E]*	*[m]*	*No. grains*	*Age [Ma]*	*Population*	*No. grains*	*Age [Ma]*	*Mean r_{mr0}*	*Mean Track Length*
11UMT16	34.525	92.729	4614	5	26.0 ± 6.1	1	4	41.9 ± 9.7	0.53	14.24 ± 1.18
						2	13	31.0 ± 9.8	0.80	14.17 ± 1.28
11UMT22	34.708	92.894	4848	4	28.1 ± 2.2	1	7	30.4 ± 11.4	0.84	14.42 ± 0.98
						2	7	29.2 ± 9.3	0.79	14.10 ± 0.92
SQ22 *	34.536	92.910	4743	-	-	-	-	36.0 ± 4.3	-	14.10 ± 0.47
SQ16 *	34.568	92.919	4780	-	-	-	-	39.0 ± 4.2	-	13.90 ± 0.51
SP19-1 *	34.594	92.912	4805	-	-	-	-	37.0 ± 4.5	-	12.90 ± 0.51

* sample locations are estimated from georeferenced location figure in Wang et al., 2008

analysis and modeling (Ketcham, 2005). Kinetic populations are defined by the annealing behavior of apatite crystals, which can vary widely within detrital populations (Ketcham et al., 1999; 2007). Thus, it is not unusual for sedimentary rocks to contain apatites with a wide range in annealing behaviors and closure temperatures (Ketcham et al., 1999; 2007). The identification of multiple kinetic populations allows for more robust fission-track age interpretation and improved inverse modeling of fission-track data by associating variations in apatite annealing behavior with multiple closure temperatures.

We defined kinetic populations by the parameter r_{mr0}, which is a measure of the reduced fission-track length of an apatite with higher resistance to annealing at the time-temperature conditions for which a less resistant apatite is completely annealed (Ketcham et al., 1999). Thus apatite crystals with a high r_{mr0} value are typically less resistant to annealing, and are therefore likely to have a lower closure temperature than apatites with low r_{mr0} values (Ketcham et al., 1999). According to laboratory experiments, variations in r_{mr0} characterize apatite annealing behavior particularly well relative to other parameters (Ketcham et al., 1999). For sample 11UMT16, we identified two kinetic populations with pooled ages of 41.9 ± 9.7 and 31.0 ± 9.8 Ma, mean fission-track lengths of 14.24 ± 1.18 and 14.17 ± 1.28 μm, and r_{mr0} values of 0.53 and 0.80, respectively (Tables 3.2 and A3.3). We identified two kinetic populations in sample 11UMT22 with pooled ages of 30.4 ± 11.4 and 29.2 ± 9.3 Ma, mean track-lengths of 14.42 ± 0.98 and 14.1 ± 0.92 μm, and r_{mr0} values of 0.84 and 0.79, respectively (Tables 3.2 and A3.4). Track length data for samples 11UMT16 and 11UMT22 is available in Tables A3.5 and A3.6, respectively.

3.3.2.4. HeFTy inverse modeling of low-temperature thermochronologic data

Single grain apatite (U-Th)/He ages for each sample, along with apatite fission-track age and length data for multiple kinetic populations, were modeled using the HeFTy program for time-temperature histories (Ketcham, 2005). We used the RDAAM helium diffusion model for apatite (U-Th)/He data (Flowers et al., 2009) and the Ketcham et al. (2007) model for fission-track annealing behavior. Three geologic constraints from Staisch et al. (2014) were placed on each model run: (1) samples collected from the lower Fenghuoshan Group were at the surface, and thus between 0 – 20 °C, within the interval of 85 – 60 Ma based on the depositional age of the Fenghuoshan Group, (2) samples were buried to depth and at temperatures that exceed 40 °C within the interval of 75 – 35 Ma, and (3) based on unconformably overlying late Oligocene aged volcanic rocks, the southern sample (11UMT16) was at the surface (0 – 20 °C), between 30 and 25 Ma. We

tested HeFTy model runs for the southern thermochronologic sample that both included and excluded the third geologic constraint. For all HeFTy models, we also emplaced the constraint that each sample was reset (at depth) sometime prior to sedimentary deposition. In the models presented here, this appears as a constraint from 120 – 200 °C from 150 – 130 Ma. We explored other models in which the early resetting constraint was 100 – 90 Ma. This exercise confirmed that the Cenozoic exhumation histories were not sensitive to the early resetting history.

Goodness of fit is determined by comparing modeled apatite fission track and (U-Th)/He ages for each thermal history to measured data for each grain. Kuiper's statistic was used to define the goodness of fit of modeled and measured track length distributions for each kinetic population (Kuiper, 1960). To constrain "good" and "acceptable" model fits, we chose standard values of 0.5 and 0.05, respectively (Ketcham, 2005). We ran each model until at least 10,000 time-temperature paths were generated and at least 100 good-fit model paths were obtained.

3.3.2.5. Modeling results

The model results for samples 11UMT16 and 11UMT22 reveal an Eocene onset of cooling, followed by very rapid cooling to near-surface temperatures in the Oligocene (Figure 3.8). For sample 11UMT16, the two models run with and without the late Oligocene basalt constraints both require Oligocene rapid cooling and show only minor differences (Figures 3.8b and 3.8c).

The best fit time-temperature history modeled for the northernmost sample collected in the Fenghuoshan Range (11UMT22; Figure 3.8a) indicates that this sample remained at the surface until 73 Ma, followed by burial to a maximum temperature of 133 °C at 49 Ma. Between 49 and 29 Ma, the sample was slowly cooled at a rate of 1.2 °C Ma^{-1}.Between 29 and 27 Ma, the sample was cooled at a rate of 36.5 °C Ma^{-1}, after which it remained at near-surface temperatures (Figure 3.8a). This cooling rate translates to an apparent erosion rate of ~1.2 – 1.5 mm yr^{-1}, assuming a geothermal gradient of 25 – 30 °C km^{-1}.

The best fit time-temperature history modeled for the southernmost sample collected from the Fenghuoshan Range (11UMT16) that includes the basalt constraint (Figure 3.8b) indicates that this sample was at the surface at 66 Ma and was buried to a maximum temperature of 136 °C by 43 Ma. Rapid exhumation of this sample initiated ca. 35 Ma and continued until 25 Ma, during which time the average cooling rate is modeled at 12.4 °C Ma^{-1}. After this time, the sample remained at surface temperatures (Figure 3.8b). This cooling rate translates to an apparent erosion rate of 0.4 – 0.5 mm yr^{-1}, assuming a geothermal gradient of 25 – 30 °C km^{-1}.

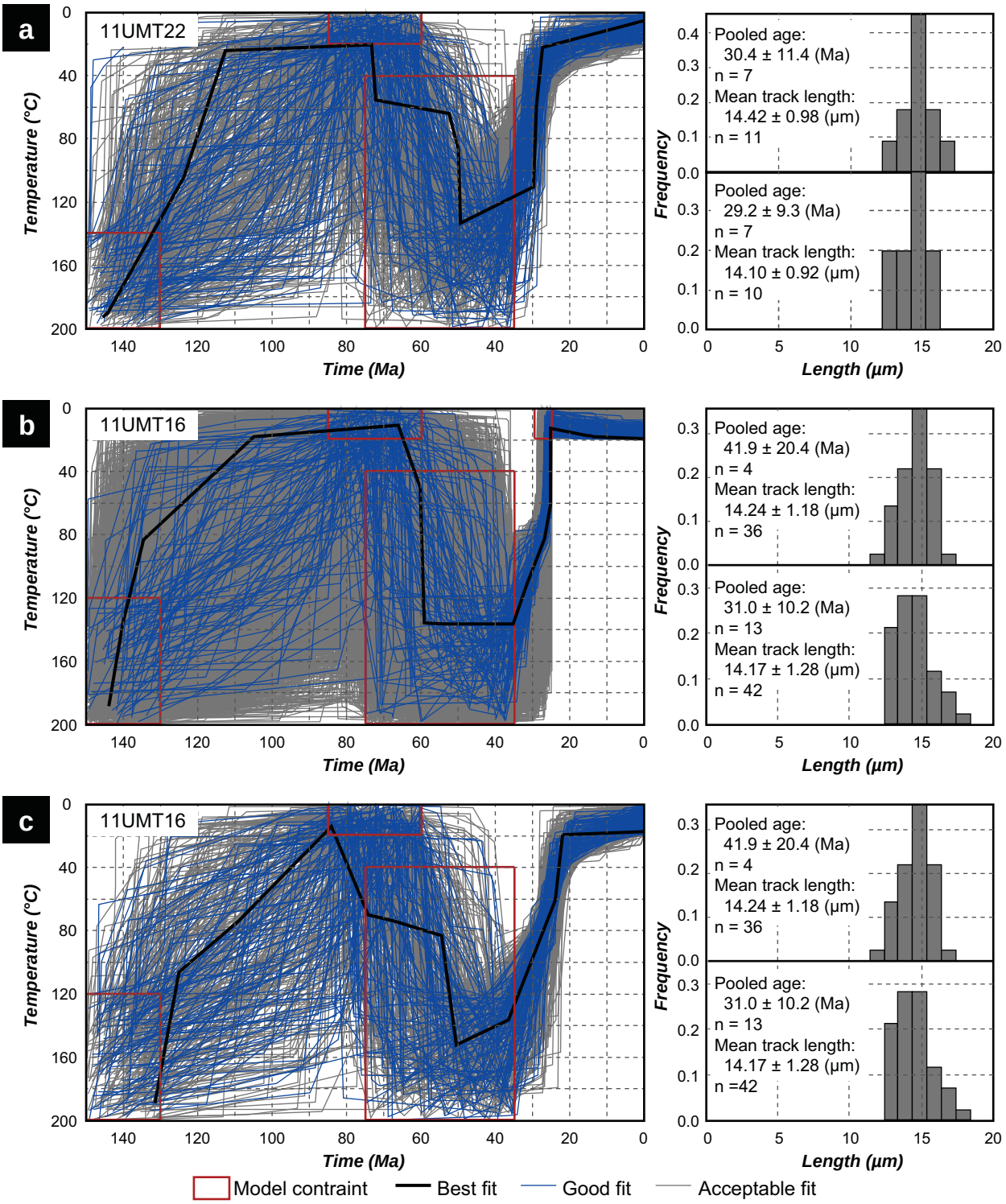

Figure 3.8. Modeled time-temperature paths for exhumation of the FFTB. Grey, blue, and black lines represent acceptable, good, and best fit models for each sample. Red boxes represent geologic constraints, explained in the text. Fission-track length distributions and are shown to the right of each sample modeled. (a) Modeled AHe and AFT data for sample 11UMT22. (b) Modeled AHe and AFT data for sample 11UMT16 including late Oligocene basalt constraint. (c) Modeled AHe and AFT data for sample 11UMT16 excluding late Oligocene basalt constraint.

The best fit time-temperature history modeled for the southernmost sample collected from the Fenghuoshan Range (11UMT16) that does not include the basalt constraint (Figure 3.8c) shows a similar cooling history to that modeled for sample 11UMT22. The best-fit model indicates that the sample was buried to 152 °C by 51 Ma, followed by an episode of rapid exhumation from 36 to 22 Ma, during which the sample cooled at a rate of 7.9 °C Ma^{-1}. This cooling rate translates of an apparent erosion rate of ~ 0.3 mm yr^{-1}. We suggest that the similarity in these models indicates that the onset of exhumation at 49 – 35 Ma is likely. Of the two models for sample 11UMT16 (Figure 3.8b-c), we prefer the model that includes the surface constraint of the basalt (Figure 3.8b) because the age and geologic context of the late Oligocene flat-lying basalt clearly suggests the hanging wall of the Nan Fenghuoshan Thrust Fault was uplifted and eroded prior to basaltic eruption.

The HeFTy modeled cooling histories for both samples suggest that deformation of the Fenghuoshan Fold and Thrust Belt initiated by in the Eocene, subsequent to the ~51 Ma cessation of Fenghuoshan Group deposition (Staisch et al., 2014). These models suggest that exhumation continued into late Eocene – Oligocene time and that the samples cooled below temperatures resolved from thermochronologic data by ~27 – 25 Ma.

3.4. Balanced Cross Section

3.4.1. Data collection and field observations

A balanced cross section for the Fenghuoshan Range was constructed along a N17°E transect (Figure 3.4a; A-A'). The cross section has a present-day length of ~103 km, strikes perpendicular to the inferred direction of maximum convergence, and was chosen to maximize nearness to structural measurements and observations. The structural interpretations of this cross section are guided by new geologic mapping of the area (Figure 3.4a), which is based on new field observations and measured bedding orientations (Table A3.7), and supplemented by existing 1:200,000 scale geologic mapping (QBRMR 1989a; 1989b).

The stratigraphic thickness of the Fenghuoshan Group is based on isopach data from Liu et al. (2001) (Figure 3.4c). The thicknesses of the overlying Tuotuohe and Yaxicuo Groups and the underlying Wuli, Jieza, Batang, and Bayan Groups are based on existing geologic maps and stratigraphic columns (QBGMR 1989a; 1989b). Angular unconformities observed between the Fenghuoshan Group and the Tuotuohe and Yaxicuo Groups suggest that the deposition of these overlying strata occurred during or after deformation of the Fenghuoshan Range. The underlying Triassic and Permian strata appear to vary significantly in stratigraphic thickness along the cross

section, which may be due to lateral variation in sediment accumulation or subsequent erosion. An observed depositional contact between the lower Fenghuoshan Group and the Triassic Jieza Group at the southern limit of the cross section, and the presence of the intervening Triassic Batang and Bayan Groups to the north, indicate that the variations in along-strike sedimentary thickness of pre-Cretaceous strata were established before deposition of the Fenghuoshan Group.

While several cross sections constructed in the region have been previously published (Coward et al., 1988; Wang et al., 2002), these lines of section did not incorporate variations in stratigraphic unit thicknesses, which is a potentially large source of uncertainty in estimates of crustal shortening (Judge and Allmendinger, 2011). Here, we incorporate variations in unit thicknesses from published isopach data and stratigraphic columns (QBGMR 1989a; 1989b; Liu et al., 2001) and formally propagate uncertainty in stratigraphic thickness, eroded hanging wall cut offs, and depth to décollement into the final assessment of crustal shortening within the Fenghuoshan Fold and Thrust Belt. Additionally, fault gouge dating and low-temperature thermochronologic constraints allow us to include the timing and progression of deformation into a kinematic reconstruction of crustal shortening within the Hoh Xil Basin. The inclusion of timing and uncertainty in magnitude of shortening in the Hoh Xil Basin allows us to more quantitatively assess the viability of various descriptions of Tibetan crustal shortening and thickening.

3.4.2. Methods and Error Propagation

The cross section along transect A-A' (Figures 3.4a and 3.9a) was constructed based on bedding orientation measurements (Figure 3.4a and Table A3.7) and field observations. We retrodeformed the cross section to estimate the original width and to constrain the amount of shortening. For line balancing, we use the sinuous bed method (Dahlstrom, 1969), in which bedding thickness is maintained while the length of the top and bottom of each unit and the lengths of fault ramps and flats are matched in the deformed and undeformed cross sections. For area balancing, we match the area encompassed by deformed and sequentially retrodeformed units using the AreaErrorProp program presented in Judge and Allmendinger (2011). To calculate the retrodeformed width, amount of shortening, and to propagate errors in our shortening estimate, we slightly modified equations presented in Judge and Allmendinger (2011). These modifications were necessary to account for the more complicated décollement geometry in the FFTB. Modified equations are available in Appendix D. The calculated values of shortening and associated errors are shown in Table 3.4.

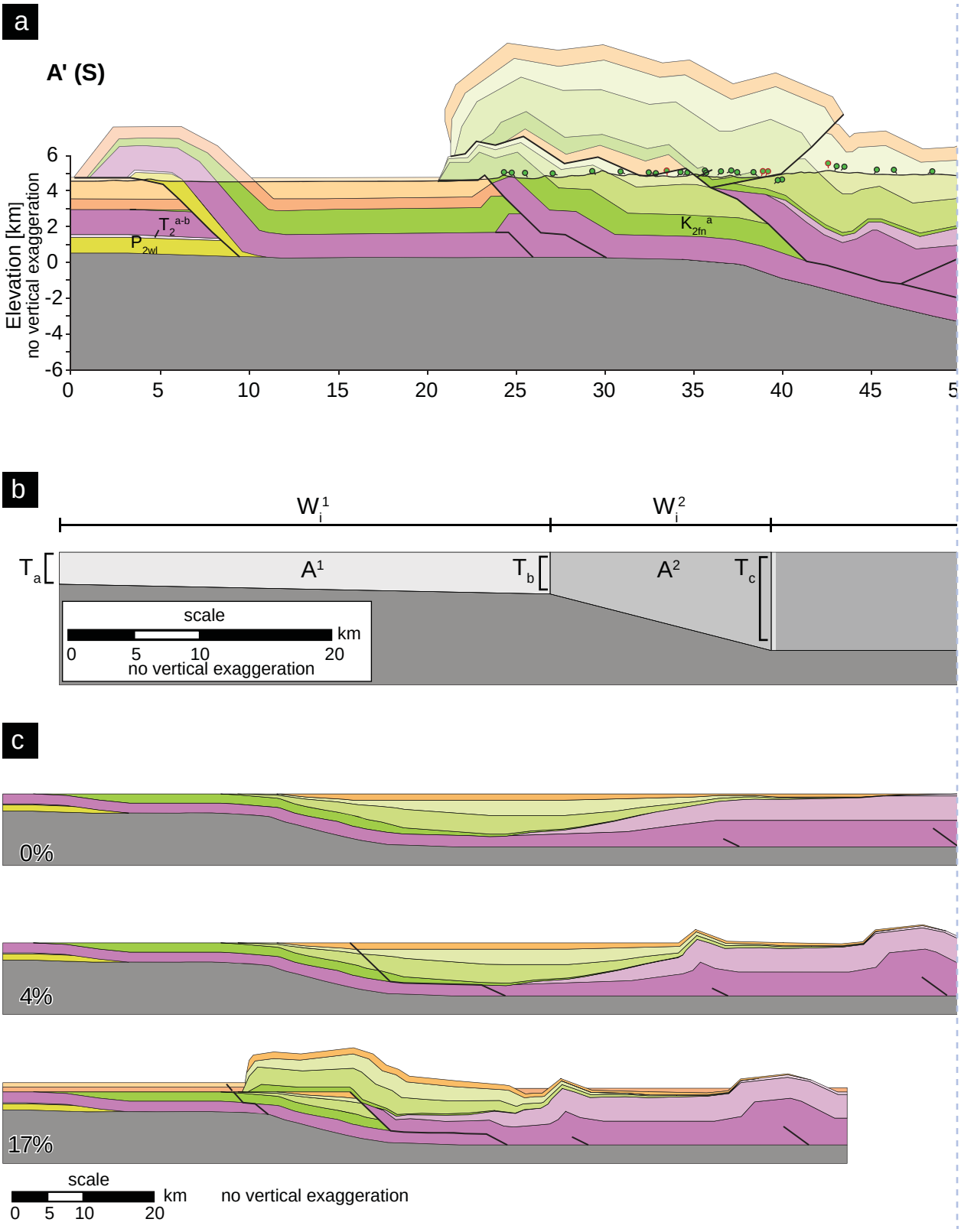

Figure 3.9. Balanced cross section across the Fenghuoshan Fold and Thrust Belt, along transect A-A' in Figure 3.4. (a) Fully deformed cross section shown with dip-tick marks for bedding orientations measurements. Unit colors correlate to the geologic map (Fig. 3.4). (b) Geometric considerations

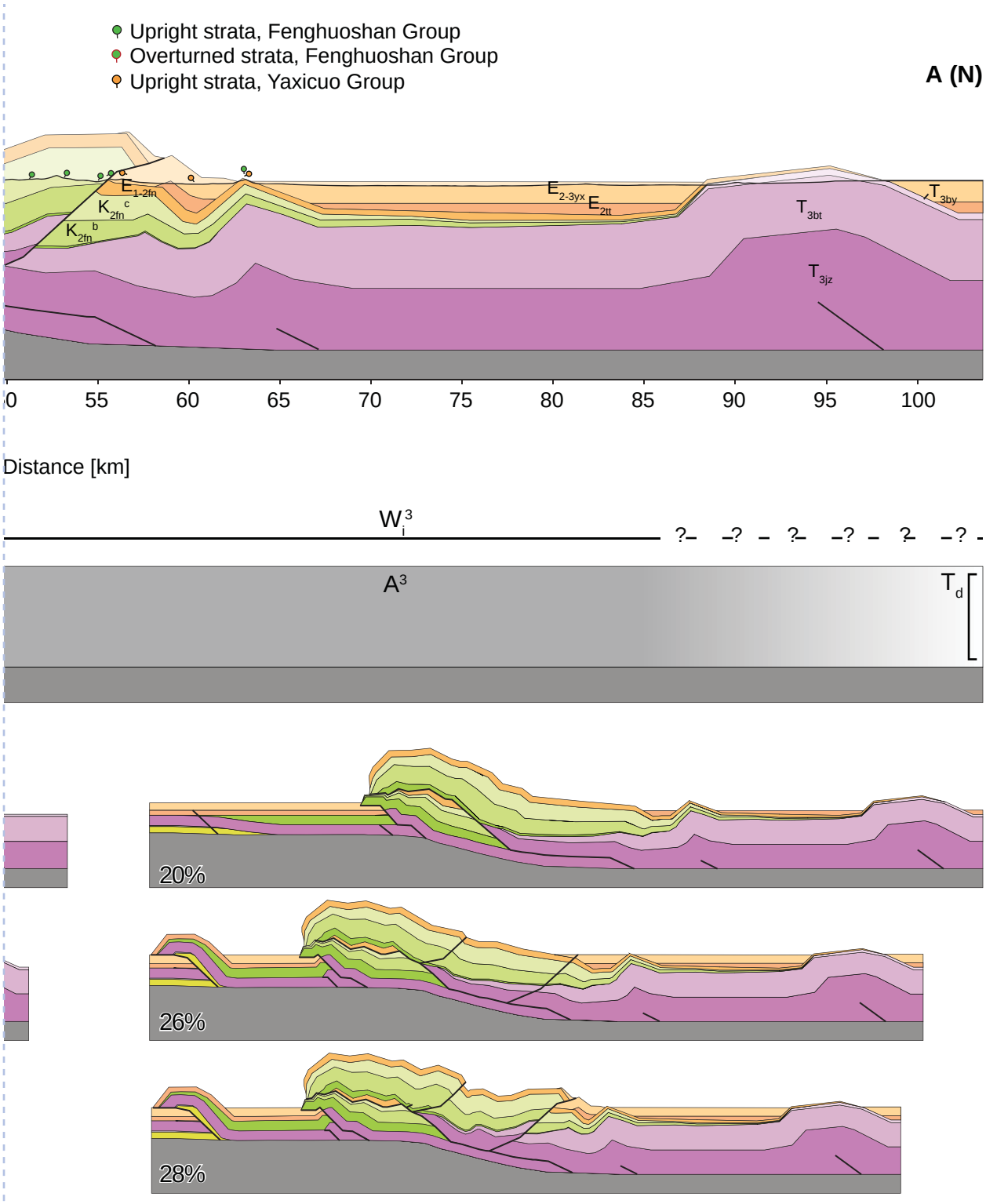

Figure 3.9 continued. taken into account for calculation of shortening and associated error, explained in the text and in Appendix D. (c) Sequentially retrodeformation of cross section, from fully undeformed (0% shortening) to fully deformed (28% shortening).

3.4.3. Results

Retrodeformation of the Fenghuoshan Fold and Thrust Belt cross section (Figures 3.4a and 3.9a-c) results in an original width of 143 ± 10 km and suggests that the FFTB was shortened by 40 ± 10 km (28.0 ± 7.2%). When compared to previous estimates of shortening within the Fenghuoshan Fold and Thrust Belt, our shortening amount of 40 ± 10 km compares with the 50 km and ~43 km estimates from Coward et al. (1988) and Wang et al. (2002), respectively. We present a series of sequentially retrodeformed cross sections (Figure 3.9c) to illustrate how the FFTB may have been deformed over time. The relative timing of fold and fault motion of the Fenghuoshan Range is based in part on our $^{40}Ar/^{39}Ar$ fault gouge ages sampled from the Zhong Fenghuoshan and Nan Fenghuoshan Thrust Faults and modeled apatite fission-track and (U-Th)/He data. Additionally, a deformed 33.5 Ma rhyo-dacitic lava flow to the south of the Fenghuoshan Range (Staisch et al., 2014) was used to constrain deformation along the Tuotuohe Fault. While not directly on our line of section, this lava flow was deformed during formation of a syncline in the hanging wall of the Tuotuohe Fault, and thus bears on the timing of motion along this structure.

3.4.4. Distribution of shortening across structures

Within the Fenghuoshan Fold and Thrust Belt, several structures are principally responsible for the accommodation of shortening (Figures 3.4a and 3.9). From north to south, these structures are the Zhong Fenghuoshan Thrust Fault, the Nan Fenghuoshan Thrust Fault, and the Tuotuohe Thrust Fault (Nan and Zhong mean south and central in Chinese, respectively). The Zhong Fenghuoshan Thrust Fault accommodates as much as ~19.5 km of displacement, placing the lowermost Fenghuoshan Group strata (K_{2fn}^{a}) over stratigraphically younger Fenghuoshan Group strata (K_{2fn}^{b-c}). Along the southern margin of the Fenghuoshan Range, the Nan Fenghuoshan Thrust Fault places lowermost Fenghuoshan Group strata (K_{2fn}^{a}) over the overlying Tuotuohe and Yaxicuo Groups and accommodates ~4 km of offset (Figures 3.4a and 3.9a). To the west, the depositional contact between the Fenghuoshan and underlying Jieza Groups is exposed, and the Nan Fenghuoshan Thrust Fault places Jieza Group strata over Oligocene strata. This along-strike variation in lithostratigraphic levels exposed in the hanging wall may be due to a westward decrease in Fenghuoshan Group sedimentary thickness (Figure 3.4c; Liu et al., 2001) or an increase in along-strike exhumation of the Nan Fenghuoshan Thrust Fault. To the southwest, the Tuotuohe Group is locally exposed at the core of a broad syncline, which may have formed during hanging wall exhumation along the Tuotuohe Thrust. The Tuotuohe Thrust places Cretaceous – Permian strata

Table 3.3. Parameters used for the area balancing and propagation of uncertainty for the balanced cross section presented in Figure 3.9.

Variable	Value
W_f [km]	103.51 ± 0.35
T_a [km]	2.44 ± 1.39
T_b [km]	3.27 ± 0.48
T_c [km]	6.96 ± 0.48
T_d [km]	7.51 ± 0.48
A [km^2]	840.45 ± 21.35
$W^1{}_i$ [km]	37.49 ± 5.00
$W^2{}_i$ [km]	16.88 ± 5.00
A^1 [km^2]	107.09 ± 29.40
A^2 [km^2]	86.38 ± 20.06

Table 3.4. Values obtained from area balancing and error propagation using parameters values in Table 3.3 and equations in Appendix D.

Variable	Value
W^3_i [km]	89.39 ± 7.10
A^3 [km^2]	646.98 ± 41.50
W_i [km]	143.77 ± 10.02
S [km]	40.26 ± 10.03
S %	0.28 ± 0.07

over Oligocene strata, and the hanging wall of this thrust fault exhumes the southernmost mapped exposure of the Fenghuoshan Group. The Tuotuohe Thrust fault may accommodate as much as ~6.5 km of displacement.

Several back thrusts accommodate small to moderate amounts of shortening within the Fenghuoshan Fold and Thrust Belt (Figures 3.4a and 3.9a). The Erdaguo Back Thrust, which cuts across much of the Fenghuoshan Range, cross-cuts the Zhong Fenghuoshan Thrust near the town of Erdaguo (Figure 3.4a) and accommodates ~0.7 km of offset. To the east and west of the Lhasa-Golmud Highway, the Erdaguo Back Thrust may reactivate portions of the Zhong Fenghuoshan Thrust, however this is speculative and is based largely on the lack of Zhong Fenghuoshan Thrust exposure east of the Lhasa-Golmud Highway. To the north, the Fenghuoshan Range is bounded by the Beifang Fenghuoshan Back Thrust (Beifang means north in Chinese), which places the Fenghuoshan Group over Yaxicuo Group strata (Figure 3.4a). This fault may accommodate ~2.5 km of displacement. The cross cutting relationships between north and south-directed faulting suggests that the back thrusts were active more recently than the south-directed thrust faults. From this we infer that, as deformation progressed to the south, the deforming thrust wedge toe above the basal décollement thinned and became subcritical, such that the frontal ramp could no longer propagate southward (Dahlen, 1990). Subsequently, north-south contraction continued and the FFTB shortened internally in attempt to obtain critical taper, at which point underthrusting beneath the Nan Fenghuoshan and Zhong Fenghuoshan Thrust Faults caused backthrusting along the Erdaguo and Beifang Fenghuoshan Back Thrusts (e.g. Gutscher and Kukowski, 1998).

Across the structural transect, we observe a correlation between the variability in Fenghuoshan Group stratigraphic thickness, syntectonic sediment accumulation, and the style and magnitude of shortening. Several regions along the structural transect are characterized by broad expanses of syntectonic Tuotuohe Group and Yaxicuo Group strata with few outcrops of Fenghuoshan Group strata. For example, along the northern portion of the transect, the Fenghuoshan Group and underlying strata are generally obscured by the overlying deformed Yaxicuo Group, except near the axial trace of anticlines (Figure 3.9a). We posit that this region is characterized by a broad syncline where deposition of syntectonic strata was concentrated. Similarly, to the south, the region between the Nan Fenghuoshan and Tuotuohe Thrust Faults is characterized by a broad expanse of moderately to mildly deformed Tuotuohe and Yaxicuo Group sedimentary cover, which we interpret as a flat at depth where material eroded from the hanging walls of the Nan Fenghuoshan and Tuotuohe Thrust Faults was accumulated during shortening of the southern

FFTB. Within the central portion of the cross section, the wavelength between fold axes decreases and we observe exposure of the lower Fenghuoshan Group, possibly due to a step in the décollement geometry, duplexing, and increased displacement along south-directed thrust faults (Figure 3.9a). These observations illustrate how the percentage of shortening in the Hoh Xil Basin may be overestimated if structural measurements are concentrated in the central Fenghuoshan Range, where tectonic exhumation and fault displacement is greatest, and underscores the importance of expanding cross sections over larger regions in order to obtain a more integrated shortening estimate. As a result, our estimate of the total amount of shortening measured across the FFTB (40 km) is similar to previously published estimates (43 – 50 km) but the extended length of our cross section results in a lower percentage of shortening (~28%) versus percentage of shortening reported by Coward et al. (1988) and Wang et al. (2002) (40 – 43%) for shorter cross sections limited to the central FFTB.

3.5. Discussion

It is commonly recognized that the Lhasa and Qiangtang Terranes were not only deformed prior to collision, but may have also uplifted to near-modern elevations by ~50 Ma, somewhat analogous to the modern Altiplano-Puna Plateau in South America (Figure 3.2; Burg et al., 1983; England and Searle, 1986; Murphy et al., 1997; Kapp et al., 2005, 2007a, 2007b; Rowley and Currie, 2006; DeCelles et al., 2007a, 2007b; Polissar et al., 2009; Rohrmann et al., 2012; Xu et al., 2013; Ding et al., 2014). Structural and stratigraphic data suggests that the Andean-type margin may have extended from the Gangdese Fold and Thrust Belt in the south to the Tanggula Shan in the north (Figures 3.1 and 3.2; Kapp et al., 2007b; Wang et al., 2008; Staisch et al., 2014). However, the modern Tibetan Plateau is roughly double the width of this proposed pre-collisional deformation belt and a significant fraction of post-collisional plateau expansion took place north of the Tanggula Shan. In the following discussion, we focus on how and when the Tibetan Plateau evolved from pre-collisional to modern dimensions, and pay specific attention to the northern plateau.

3.5.1. The deformation history of the Fenghuoshan Fold and Thrust Belt

3.5.1.1. Initiation

The cessation of Fenghuoshan Group deposition at 51 Ma (Staisch et al., 2014), initiation of rapid cooling in the Eocene, and the fault gouge ages from the ZFT and NFT between 44 and 48 Ma independently constrain the initiation of crustal shortening in Hoh Xil Basin soon after the ~50

Ma onset of the Indo-Asian collision. The timing of deformation we infer from fault gouge and thermochronologic analyses differs from previous interpretations for the timing of shortening in the Hoh Xil Basin (Wang et al., 2008), in which deformation is suggested to be primarily late Oligocene in age (~30 – 22 Ma). This interpretation was based on the observation, with which we concur, that deformation is younger than the depositional age of the Fenghuoshan Group. Previous estimates placed the deposition of the Fenghuoshan Group from 52 – 31 Ma (Liu et al., 2001, 2003). Recently, however, the depositional history of the Hoh Xil Basin has been revised based on absolute age control, and refines the depositional age of the Fenghuoshan Group to be Late Cretaceous to earliest Eocene (Staisch et al., 2014). In this context, the apatite fission track ages reported by Wang et al. (2008), which range between 47 and 36 Ma, are younger than the depositional age of the Fenghuoshan Group and therefore record tectonic exhumation in Eocene time, consistent with our thermochronologic and fault gouge data.

3.5.1.2. Cessation

The youngest absolute age control on crustal shortening in the Hoh Xil Basin is a deformed rhyo-dacitic flow dated at 33.5 Ma (Staisch et al., 2014). This, along with ~27 Ma flat-lying basalts (Staisch et al., 2014) and widespread deposition of Miocene lacustrine carbonates that show little to no post-depositional deformation (Wu et al., 2008), constrains the cessation of deformation within the Hoh Xil Basin to be between 33.5 and 27 Ma. The thermal histories of the north and south FFTB constrained by modeling of apatite fission-track and (U-Th)/He data presented above are consistent with the cessation of deformation by late Oligocene time.

3.5.2. Comparison to deformation throughout northern Tibet

Our new data on the timing of deformation in the Fenghuoshan Fold and Thrust Belt, combined with existing observations of deformation in northern Tibet, suggest that the initiation of crustal shortening at ~50 Ma was distributed over a large portion of the northern Tibetan Plateau, from the Hoh Xil Basin to the southern Qilian Shan (Figures 3.3a and 3.10; Horton et al., 2002; Spurlin et al., 2005; Yin et al., 2008; Clark et al., 2010; Duvall et al., 2011; Zhuang et al., 2011).

Widespread, flat-lying Miocene carbonates in northern Tibet provide strong evidence for the cessation of upper crustal shortening prior to 24 – 14 Ma lacustrine deposition (Figure 3.10; Wu et al., 2008), in agreement with dating of undeformed basalts at 27 Ma in the Hoh Xil Basin (Staisch et al., 2014). These age constraints, along with minimal post-collisional deformation observed in the

Lhasa and Qiangtang Terranes (Burg et al., 1983; Murphy et al., 1997; Kapp et al., 2003; 2005; 2007a; 2007b), suggest that deformation of the Tibetan Plateau ceased in the Miocene and that continued convergence between India and Eurasia must have been accommodated either outboard of the Tibetan Plateau proper or by underthrusting of India beneath Asia. The former possibility is consistent with the documented Miocene crustal shortening in the Himalaya, the Qilian Shan-Nan Shan, and the western Qaidam Basin (Figure 3.10 and Table A3.8; DeCelles et al., 2001; Murphy et al., 2003; Searle et al., 2003; Yin et al., 2008; Zheng et al., 2010; Craddock et al., 2011; Zhuang et al., 2011), while evidence for the extent to which India has underthrust Asia is controversial (e.g. Owens and Zandt, 1997; Zhou and Murphy, 2005; Nábelek et al., 2009).

3.5.3. Uplift of the Hoh Xil Basin

The quantification of surface uplift in the Hoh Xil Basin is essential for understanding how and when the northern Tibetan Plateau reached its modern elevation. As mentioned above, upper crustal shortening in the Hoh Xil Basin ceased between 33.5 and 27.4 Ma (Staisch et al., 2014) after a period of ~28% shortening. One may infer that this cessation of deformation implies the attainment of near-modern elevation by the late Oligocene; however palynological and paleoaltimetric data from the Hoh Xil Basin are suggestive of post-Oligocene surface uplift (Duan et al., 2007; 2008; Wu et al., 2008; Polissar et al., 2009). These observations, when combined with the lack of deformation of late Oligocene basalts (Staisch et al., 2014) and Miocene lacustrine carbonates (Wu et al., 2008), indicates that post-Oligocene uplift occurred in the absence of upper crustal shortening. Several mechanisms have been proposed to cause the uplift of orogenic plateaux in the absence of upper crustal shortening, including lower crustal flow (Clark et al., 2005; Karplus et al., 2011), decoupling at mid-crustal levels and preferential thickening of the lower crust (Isacks, 1988; Gubbels et al., 1993), and removal of the mantle lithospheric root (Molnar et al., 1993).

3.5.3.1. Shortening-related crustal thickening and surface uplift

To test whether the timing and magnitude of shortening measured in the Fenghuoshan Fold and Thrust Belt are compatible with the modern crustal thickness and uplift history of the Hoh Xil Basin inferred from paleoelevation and palynological data, we calculate the isostatic response to crustal shortening and thickening. In our calculations of surface uplift and crustal thickening, we assume that the measured upper crustal shortening is representative of shortening throughout the lithospheric column (Houseman et al., 1981) and that volume is conserved, such that the volume of

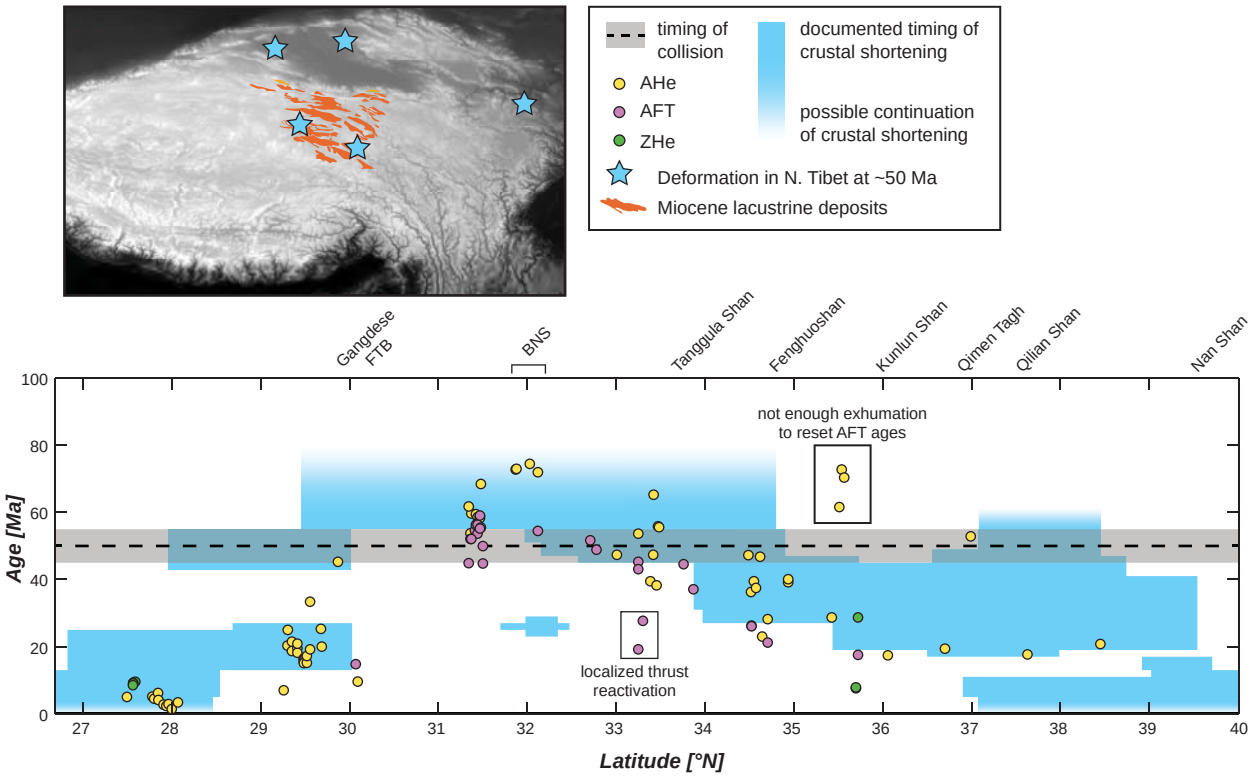

Figure 3.10. Inset map showing documented deformation in northern Tibet initiating ca. 50 Ma (Horton et al., 2002; Spurlin et al., 2005; Yin et al., 2008; Clark et al., 2010; Duvall et al., 2011; Zhuang et al., 2011; this study). Latitudinal extent of crustal shortening as a function of time (blue regions) plotted along with low-temperature thermochronologic ages (colored dots), showing a general covariance in timing of north-south oriented contraction and cooling ages. Thermochronologic ages are compiled from Copeland et al. (1995), Jolivet et al. (2001), Yuan et al. (2006), Wang et al. (2008), Hetzel et al. (2011), Rohrmann et al. (2012), and Duvall et al. (2013). The timing of thrust fault activity is compiled from several sources, detailed in Table A3.6.

material displaced from crustal shortening is translated directly into an increase in crustal thickness (pure shear). The amount of surface uplift is quantified from equations of isostatic compensation (Heiskanen and Moritz, 1967; England and Houseman, 1989). Several key assumptions in our calculations influence the predicted elevation gain due to crustal shortening and thickening. First, we assume that the elevation of the Hoh Xil Basin was similar to modern foreland basin systems prior to crustal shortening and thus between 0 and 1 km above sea level (asl). Modern foreland basins that we used as analogues include the Chaco Plain east of the central Andes (0.35 – 0.5 km asl), the Mesopotamian foreland basin west of the Zagros Mountains (0.0 – 0.4 km asl), and the Western Canadian Basin located to the east of the Canadian Rocky Mountains (0.6 – 1.0 km asl). Palynological data from the late Cretaceous – early Eocene Fenghuoshan Group suggests that sediments were deposited in a warm, arid climate and provides support for our assumption of low initial elevation (Li and Yuan, 1990).

We also assume that the initial crustal thickness of the Hoh Xil Basin was no thicker than the average crustal column because it has been proposed that that the Songpan-Ganzi Terrane is underlain by oceanic crust (Şengör and Hsü, 1984; Şengör, 1984; Bruguier et al., 1997) or extended continental crust (Burchfiel et al., 1995). Furthermore, an anomalously thick continental lithosphere in northern Tibet prior to deformation exacerbates outstanding issues with mass balance in the Himalayan-Tibetan orogen (Clark, 2012; Yakovlev and Clark, 2014; Lippert et al., 2014). Thus, we limit the initial crustal thickness to be less than or equal to the global average (41 km; Christensen and Mooney, 1995), between 20 and 41 km.

The third key assumption is that the shortening measured in the FFTB is representative of shortening throughout the northern Tibetan Plateau. We suggest that the shortening estimated from our cross section in the FFTB is an improvement from previous estimates of shortening in the Hoh Xil Basin (Coward et al., 1988; Wang et al., 2002) because our measurements are not only concentrated in the tightly-folded Fenghuoshan Range, but also account for the broader, low-frequency structures to the north and south of the central range, and thus give a more integrated shortening estimate for the region. Furthermore, compiled Cenozoic shortening estimates from the orogen suggest that the average percentage crustal shortening north of the Tanggula Shan is 25.0 ± 10.7%, and thus comparable to our estimates from the FFTB (Yakovlev and Clark, 2014). Additional assumptions and parameter values are described in Appendix E.

We included a broad range of initial values of lithospheric thickness, from 20 – 140 km, and limit the post-shortened lithospheric thickness to the modern 80 – 120 km thickness of the north

Tibetan lithosphere (Vozar et al., *in press*). We find lithospheric thickness is somewhat limited within the range explored by our assumptions of initial low elevation (0 – 1 km) and thin to average crust (20 – 41 km; Figure 3.11; Table 3.5). Given our assumed initial values of crustal thickness, we find that 28.0 ± 7.2 % shortening results in a 31.6 – 52.1 km thick crust and surface uplift between 0.6 and 1.7 km, leading to a post-shortening elevation estimated between 0.6 and 2.7 km (Figure 3.11; Table 3.5). Our results indicate that the modern elevation (4.5 – 5.5 km) and crustal thickness of the Hoh Xil Basin (65 – 75 km; Braitenberg et al., 2000; Vergne et al., 2002; Wittlinger et al., 2004; Karplus et al., 2011) cannot be attained via ~28% upper crustal shortening of the Hoh Xil Basin alone, and that additional mechanisms of surface uplift and crustal thickening are required, such as lower crustal flow (Clark et al., 2005; Karplus et al., 2011), preferential shortening and thickening of the lower crust and mantle lithosphere (Isacks, 1988; Gubbels et al., 1993), and mantle root loss (Molnar et al., 1993).

We quantify the amount of elevation gain due to these proposed mechanisms of crustal thickening and surface uplift by calculating the isostatic response to each process. Methods and assumptions are further explained in Appendix E and results are plotted in Figure A3.6. The results from these calculations indicate that lower crustal flow and preferential thickening of the lower crust and mantle lithosphere are both viable mechanisms capable of reproducing the modern elevation and crustal thickness of the Hoh Xil Basin. We also find that mantle root loss may accompany either crustal thickening mechanism and reproduce the modern elevation and crustal thickness of the Hoh Xil Basin, but is not explicitly required to attain modern plateau elevation.

3.5.3.2. The timing of surface uplift

The timing of surface uplift in Hoh Xil Basin is not easily determined as elevation gain need not leave surficial evidence and could therefore occur before, during, or after Eocene – late Oligocene upper crustal shortening. However, fossil plants in the Hoh Xil Basin show a floral shift from mixed vegetation in the Oligocene, including coniferous, broad-leaved deciduous and subtropical tree species, to an environment dominated by drought- and cold- tolerant species in the Miocene (Duan et al., 2007; 2008; Wu et al., 2008). These data, along with our calculations of shortening-related surface uplift, suggest that only moderate elevations were attained via crustal shortening by ~27 Ma, and that uplift to high elevation occurred after the cessation of upper crustal shortening, in the Miocene. The attainment of high elevation in the Miocene is further supported by paleoaltimetric data, but Miocene elevation estimates (3.4 – 4.2 km) also suggest moderate uplift to

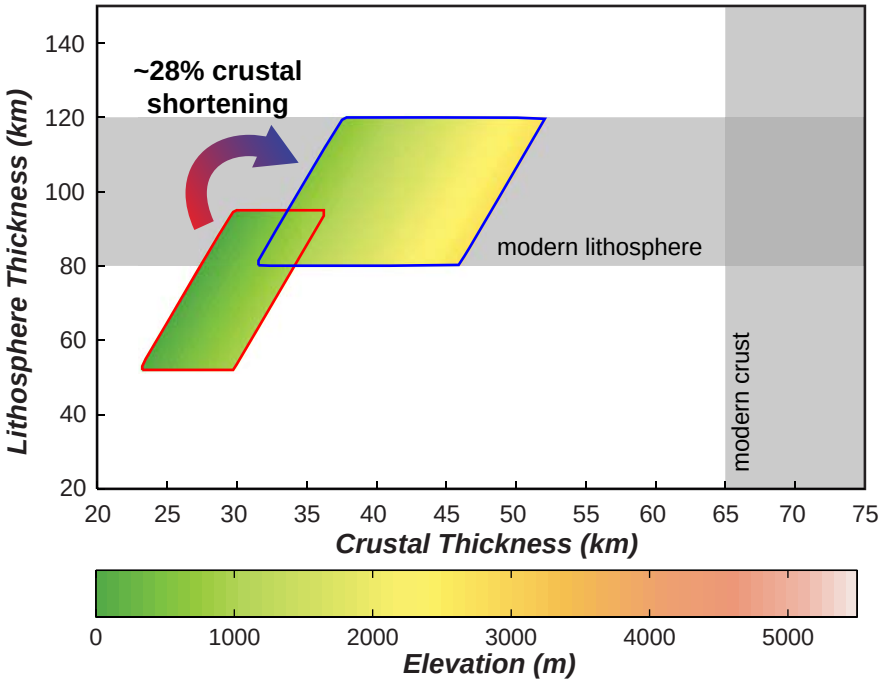

Figure 3.11. Results of surface uplift due to isostatic compensation of crustal and lithospheric thickening are plotted as crustal versus lithospheric thickness, and colored by elevation. The modern crustal thickness is indicated by a grey bar. Initial values lithospheric thickness are dependent on the assumptions that the Hoh Xil Basin was between 0 – 1 km elevation and that the crustal thickness was between 20 and 40 km prior to shortening and thickening. Initial crustal and lithospheric thicknesses are outlined in red and post-28% pure shear crustal and lithospheric thicknesses are outlined in blue.

Table 3.5. Isostatic results for shortening and thickening of the Hoh Xil Basin. Results are plotted in Figure 3.11.

	Initial	***Post-shortening***
Uniform ~28% pure shear (Fig. 3.11)		
H_C (km)	23.3 - 36.3	31.6 - 52.1
H_L (km)	52.0 - 95.0	80.0 - 119.9
E (m)	0.0 - 999.0	580.0 - 2741.0
ΔE (m)	~	580.0 - 1742.0

H_C and H_L are values of crustal and lithospheric thickness, respectively.
E and ΔE are values of elevation and elevation change, respectively.

reach modern elevations may have continued into Pliocene – Quaternary time (Polissar et al., 2009). Thus, on the basis of palynological and paleoelevation data, along with the results of our isostatic calculations (Figure 3.11), suggest that as much as 50% of the modern elevation of the Hoh Xil Basin was attained after the late Oligocene cessation of crustal shortening (Duan et al., 2007; 2008; Wu et al., 2008; Polissar et al., 2009).

3.5.3.3. Causal mechanisms for post-Oligocene surface uplift

While our isostatic results and the uplift history of the Hoh Xil Basin suggest that crustal thickening and surface uplift continued in the absence of upper crustal shortening, the mechanisms responsible for building the northern Tibetan Plateau to its modern height and thickness are not currently well understood and the proposed mechanisms are not necessarily mutually exclusive. However, geophysical observations show low shear wave velocities and high Poisson ratios in northern Tibet, which are indicative of partial melt of the middle to lower crust. Additionally, high Poisson ratios may exist over a depth range of over 30 km (Owens and Zandt, 1997; Klemplerer, 2006; Karplus et al., 2011), and may suggest the presence of a 30 km thick channel of partially molten, and potentially flowing, lower crustal material in the Hoh Xil Basin (Karplus et al., 2011). Our isostatic calculations support the attainment of modern elevation and crustal thickness from ~28% shortening and the addition of 30 km of crustal material via lower crustal flow (Figure A3.6b). These calculations constrain the pre-shortened crustal thickness of Hoh Xil Basin to 23 and 36 km, which overlaps with the range of crustal thicknesses compatible with orogenic mass balance calculations and plateau-wide isostatic balance (Clark, 2012; Yakovlev and Clark, 2014). We note that geophysical observations and our isostatic calculations do not exclude the possibility of mantle root loss in addition to lower crustal thickening (Figure A3.6c-d).

3.6. Conclusions

In this study, we constrained the history of deformation and uplift within the Hoh Xil Basin. Our fault gouge dating and thermochronologic modeling results independently agree on an early Eocene onset of crustal shortening within the Hoh Xil Basin, and thermochronologic modeling elucidates the later history of exhumation. Previously published volcanic ages from the Fenghuoshan Fold and Thrust Belt indicate that deformation ceased between 33.5 and 27.4 Ma. We construct and retrodeform a balanced cross section through the Fenghuoshan Range, from which we determine ~28.0% (~40 km) shortening in the Fenghuoshan Fold and Thrust Belt.

Calculations of isostatic uplift indicate that elevation gain and crustal thickening due to ~28% crustal shortening does not account for the modern elevation and crustal thickness of Hoh Xil Basin and that additional mechanisms for crustal thickening in the absence of crustal shortening, are likely. Palynological and paleoelevation data suggest that significant surface uplift in the absence of upper crustal shortening occurred after the Oligocene (Duan et al., 2007; 2008; Polissar et al., 2009). Along with previously published geophysical data in northern Tibet (Owens and Zandt, 1997; Klemplerer, 2006; Karplus et al., 2011), isostatic calculations are supportive of a model in which the modern elevation and crustal thickness of the Hoh Xil Basin was attained via ~28% shortening followed by lower crustal flow.

Together with previous work on the tectonic evolution of the Tibetan Plateau, this work suggests that continental collision between India and Eurasia at ~50 Ma drive distributed northward expansion of crustal shortening throughout northern Tibet (Yin et al., 2002; 2008; Polissar et al., 2009; Clark et al., 2010; Duvall et al., 2011). By ~25 Ma, upper crustal shortening within the modern plateau interior ceased, however elevation gain continued in northern Tibet (Kapp et al., 2005; 2007a; 2007b; Duan et al., 2007; 2008; Polissar et al., 2009).

3.7. References

Aikman, A.B., Harrison, T.M., and Lin, D., 2008, Evidence for Early (>44 Ma) Himalayan Crustal Thickening, Tethyan Himalaya, southeastern Tibet: Earth and Planetary Science Letters, v. 274, no. 1-2, p. 14–23, doi: 10.1016/j.epsl.2008.06.038.

Aitchison, J.C., and Davis, A.M., 2004, Evidence for the multiphase nature of the India-Asia collision from the Yarlung Tsangpo suture zone, Tibet: Geological Society, London, Special Papers, v. 226, no. 1, p. 217–233.

Aitchison, J.C., Ali, J.R., and Davis, A.M., 2007, When and where did India and Asia collide?: Journal of Geophysical Research, v. 112, no. B5, p. 1–19, doi: 10.1029/2006JB004706.

An, Y., Deng, Z., and Zhuang, Y., 2004, Characteristics of the Fenghuoshan Group's material and its era discussion: Northwestern Geology, v. 37, no. 1, p. 63 – 68.

Bird, P., 1991, Lateral extrusion of lower crust from under high topography in the isostatic limit: Journal of Geophysical Research, v. 96, p. 10,275–10,286, doi: 10.1029/91JB00370.

Braitenberg, C., Zadro, M., Fang, J., Wang, Y., and Hsu, H.T., 2000, The gravity and isostatic Moho undulations in Qinghai–Tibet plateau: Journal of Geodynamics, v. 30, no. 5, p. 489–505, doi: 10.1016/S0264-3707(00)00004-1.

Braitenberg, C., Wang, Y., Fang, J., and Hsu, H.T., 2003, Spatial variation of flexure parameters over the Tibetan-Qinghai plateau: Earth and Planetary Science Letters, v. 205, no. 3-4, p. 211–224.

Bruguier, O., Lancelot, J.R., and Malavieille, J., 1997, U-Pb dating on single detrital zircon grains from the Triassic Songpan-Ganze flysch (Central China) : provenance and tectonic correlations: Earth and Planetary Science Letters, v. 152, p. 217–231.

Burchfiel, B.C., Chen, Z., Liu, Y., and Royden, L.H., 1995, Tectonics of the Longmen Shan and Adjacent Regions, Central China: International Geology Review, v. 37, p. 661–735.

Burg, J.P., Proust, F., Tapponnier, P., and Chen, G.M., 1983, Deformation phases and tectonic evolution of the Lhasa block: Eclogae Geol. Helv, v. 76, no. 3, p. 643–683.

Chamoli, A., Lowry, A., and Jeppson, T., 2014, Implications of transient deformation in the northern Basin and Range, western United States: Journal of Geophysical Research: Solid Earth, v. 119, p. 4393–4413, doi: 10.1002/2013JB010605.

Chen, J.-L., Xu, J.-F., Wang, B.-D., and Kang, Z.-Q., 2012, Cenozoic Mg-rich potassic rocks in the Tibetan Plateau: Geochemical variations, heterogeneity of subcontinental lithospheric mantle and tectonic implications: Journal of Asian Earth Sciences, v. 53, p. 115–130, doi: 10.1016/j.jseaes.2012.03.003.

Chung, S.-L., Chu, M.-F., Zhang, Y., Xie, Y., Lo, C.-H., Lee, T.-Y., Lan, C.-Y., Li, X., Zhang, Q., and Wang, Y., 2005, Tibetan tectonic evolution inferred from spatial and temporal variations in post-collisional magmatism: Earth-Science Reviews, v. 68, p. 173–196, doi: 10.1016/j.earscirev.2004.05.001.

Christensen, N.I., and Mooney, W.D., 1995, Seismic velocity structure and composition of the continental crust: A global view: Journal of Geophysical Research, v. 100, no. B7, p. 9761–9788.

Clark, M.K., and Royden, L.H., 2000, Topographic ooze : Building the eastern margin of Tibet by lower crustal flow: Geology, v. 28, no. 8, p. 703–706.

Clark, M.K., Bush, J.W.M., and Royden, L.H., 2005a, Dynamic topography produced by lower crustal flow against rheological strength heterogeneities bordering the Tibetan Plateau: Geophysical Journal International, v. 162, no. 2, p. 575–590, doi: 10.1111/j.1365-246X.2005.02580.x.

Clark, M.K., House, M.A., Royden, L.H., Whipple, K., Burchfiel, B.C., Zhang, X., and Tang, W., 2005b, Late Cenozoic uplift of southeastern Tibet: Geology, v. 33, no. 6, p. 525–528, doi:

10.1130/G21265.1.

Clark, M.K., Farley, K.A., Zheng, D., Wang, Z., and Duvall, A.R., 2010, Early Cenozoic faulting of the northern Tibetan Plateau margin from apatite (U–Th)/He ages: Earth and Planetary Science Letters, v. 296, no. 1-2, p. 78–88, doi: 10.1016/j.epsl.2010.04.051.

Clark, M.K., 2012, Continental collision slowing due to viscous mantle lithosphere rather than topography: Nature, v. 483, p. 74–77, doi: 10.1038/nature10848.

Copeland, P., Harrison, T.M., Yun, P., Kidd, W.S.F., Roden, M., and Zhang, Y., 1995, Thermal evolution of the Gangdese batholith, southern Tibet: A history of episodic unroofing: Tectonics, v. 14, no. 2, p. 223–236.

Coward, M.P., Kidd, W.S.F., Yun, P., Shackleton, R.M., and Zhang, H., 1988, The structure of the 1985 Tibet Geotraverse, Lhasa to Golmud: Philosophical Transactions of the Royal Society of London. Series A, Mathematical and Physical Sciences, v. 327, no. 1594, p. 307–333.

Craddock, W., Kirby, E., and Zhang, H., 2011, Late Miocene-Pliocene range growth in the interior of the northeastern Tibetan Plateau: Lithosphere, v. 3, p. 420–438, doi: 10.1130/L159.1.

Daczko, N.R., Klepeis, K.A., and Clarke, G.L., 2001, Evidence of Early Cretaceous collisional-style orogenesis in northern Fiordland, New Zealand and its effects on the evolution of the lower crust: Journal of Structural Geology, v. 23, p. 693 - 713.

Dahlen, F.A., 1990, Critical Taper Model of Fold-and-Thrust Belts and Accretionary Wedges: Annual Reviews Earth and Planetary Science, v. 18, p. 55–99.

Dahlstrom, C.D.A., 1969, Balanced cross sections: Canadian Journal of Earth Science, v. 6, no. 4, p. 743–757.

Dai, J., Zhao, X., Wang, C., Zhu, L., Li, Y., and Finn, D., 2012, The vast proto-Tibetan Plateau: New constraints from Paleogene Hoh Xil Basin: Gondwana Research, v. 22, no. 2, p. 434–446, doi: 10.1016/j.gr.2011.08.019.

Dayem, K.E., Molnar, P., Clark, M.K., and Houseman, G.A., 2009, Far-field lithospheric deformation in Tibet during continental collision: Tectonics, v. 28, TC6005, doi: 10.1029/2008TC002344.

Dazé, A., Lee, J.K., and Villeneuveb, M., 2003, An intercalibration study of the Fish Canyon sanidine and biotite $^{40}Ar/^{39}Ar$ standards and some comments on the age of the Fish Canyon Tuff: Chemical Geology, v. 199, no. 1–2, p. 111–127.

Dean and Dixon, 1951, Simplified Statistics for Small Numbers of Observations: Analytical Chemistry, v. 23, no. 4, p 636–638.

DeCelles, P.G., Robinson, D.M., Quade, J., Ojha, T.P., Garzione, C.N., Copeland, P., and Upreti, B.N., 2001, Himalayan fold-thrust belt in western Nepal: Tectonics, v. 20, no. 4, p. 487–509.

DeCelles, P.G., Quade, J., Kapp, P., Fan, M., Dettman, D.L., and Ding, L., 2007a, High and dry in central Tibet during the Late Oligocene: Earth and Planetary Science Letters, v. 253, no. 3-4, p. 389–401, doi: 10.1016/j.epsl.2006.11.001.

DeCelles, P.G., Kapp, P., Ding, L., and Gehrels, G.E., 2007b, Late Cretaceous to middle Tertiary basin evolution in the central Tibetan Plateau: Changing environments in response to tectonic partitioning, aridification, and regional elevation gain: Geological Society of America Bulletin, v. 119, no. 5-6, p. 654–680, doi: 10.1130/B26074.1.

DeCelles, P.G., Kapp, P., Gehrels, G.E., and Ding, L., 2014, Paleocene-Eocene foreland basin evolution in the Himalaya of southern Tibet and Nepal: implications for the age of initial India-Asia collision: Tectonics, v. 33, no. 5, p. 824–849, doi: 10.1002/2014TC003522.

Dewey, J.F., Shackleton, R.M., Chang, C., and Yiyin, S., 1988, The tectonic evolution of the Tibetan Plateau: Philosophical Transactions of the Royal Society of London. Series A, Mathematical and Physical Sciences, v. 327, no. 1594, p. 379–413.

Ding, L., 2003, Cenozoic Volcanism in Tibet: Evidence for a Transition from Oceanic to Continental Subduction: Journal of Petrology, v. 44, p. 1833–1865.

Ding, L., Xu, Q., Yue, Y., Wang, H., Cai, F., and Li, S., 2014, The Andean-type Gangdese Mountains: Paleoelevation record from the Paleocene–Eocene Linzhou Basin: Earth and Planetary Science Letters, v. 392, p. 250–264, doi: 10.1016/j.epsl.2014.01.045.

Donelick, R.A., 2005, Apatite Fission-Track Analysis: Reviews in Mineralogy and Geochemistry, v. 58, no. 1, p. 49–94, doi: 10.2138/rmg.2005.58.3.

Duan, Z., Li, Y., Zhang, Y., Li, Y., and Wang, M., 2005, Zircon U-Pb Age, Continent Dynamics Significance and Geochemical Characteristics of the Mesozoic and Cenozoic Granites from the Tanggula Range in the Qinghai-Tibetan Plateau: Acta Geologica Sinica, v. 79, no. 1, p. 88 – 97.

Duan, Q., Zhang, K.-X., Wang, J., Yao, H., and Bu, J., 2007, Sporopollen Assemblage from the Totohe Formation and Its Stratigraphic Significance in the Tanggula Mountains, Northern Tibet: Earth Science-Journal of China University of Geosciences, v. 32, no. 5, p. 629–637.

Duan, Z., Li, Y., Shen, Z., Zhu, X., and Zhong, C., 2007, Analysis of the evolution of the Cenozoic ecological environment and process of plateau surface uplift in the Wenquan area in the interior of the Qinghai-Tibet Plateau: Geology in China, v. 34, no. 4, p. 688 – 696.

Duan, Q., Zhang, K., Wang, J., Yao, H., and Niu, Z., 2008, Oligocene Palynoflora, Paleovegetation and Paleoclimate in the Tanggula Mountains, northern Tibet: Acta Micropalaeontologica Sinica, v. 25, no. 2, p. 185–195.

Dupont-Nivet, G., Horton, B.K., Butler, R.F., Wang, J., Zhou, J., and Waanders, G.L., 2004, Paleogene clockwise tectonic rotation of the Xining-Lanzhou region, northeastern Tibetan Plateau: Journal of Geophysical Research, v. 109, B04401, doi: 10.1029/2003JB002620.

Dupont-Nivet, G., Lippert, P.C., van Hinsbergen, D.J.J., Meijers, M.J.M., and Kapp, P., 2010, Palaeolatitude and age of the Indo-Asia collision: palaeomagnetic constraints: Geophysical Journal International, v. 182, no. 3, p. 1189–1198, doi: 10.1111/j.1365-246X.2010.04697.x.

Duvall, A.R., Clark, M.K., Van der Pluijm, B.A., and Li, C., 2011, Direct dating of Eocene reverse faulting in northeastern Tibet using Ar-dating of fault clays and low-temperature thermochronometry: Earth and Planetary Science Letters, v. 304, no. 3-4, p. 520–526, doi: 10.1016/j.epsl.2011.02.028.

Duvall, A.R., Clark, M.K., Kirby, E., Farley, K.A., Craddock, W.H., Li, C., and Yuan, D., 2013, Low-temperature thermochronometry along the Kunlun and Haiyuan Faults, NE Tibetan Plateau: Evidence for kinematic change during late-stage orogenesis: Earth and Planetary Science Letters, v. 32, no. 5, p. 1190–1211.

England, P., and Houseman, G., 1986, Finite strain calculations of continental deformation: 2. Comparison with the India-Asia Collision Zone: Journal of Geophysical Research: Solid Earth, v. 91, no. B3, p. 3664–3676.

England, P.C., Houseman, G.A., Osmaston, M.F., and Ghosh, S., 1988, The mechanics of the Tibetan Plateau: Philosophical Transactions of the Royal Society of London. Series A, Mathematical and Physical Sciences, v. 326, p. 301–319.

England, P., and Houseman, G., 1989, Extension During Continental Convergence, With Application to the Tibetan Plateau: Journal of Geophysical Research, v. 94, no. B12, p. 17,561 – 17,579.

England, P., and McKenzie, D., 1982, A thin viscous sheet model for continental deformation: Geophysical Journal International, v. 70, no. 2, p. 295–321, doi: 10.1111/j.1365-246X.1982.tb04969.x.

England, P., and Searle, M., 1986, The Cretaceous-tertiary deformation of the Lhasa Block and its implications for crustal thickening in Tibet: Tectonics, v. 5, no. 1, p. 1–14.

England, P., and Thompson, A. B., 1984, Pressure-Temperature-Time Paths of Regional

Metamorphism I. Heat Transfer during the Evolution of Regions of Thickened Continental Crust: Journal of Petrology, v. 25, no. 4, p. 894–928, doi: 10.1093/petrology/25.4.894.

Farley, K.A., and Stockli, D.F., 2002, (U-Th)/He Dating of Phosphates: Apatite, Monazite, and Xenotime: Reviews in Mineralogy and Geochemistry, v. 48, p. 559–577, doi: 10.2138/rmg.2002.48.15.

Flowers, R.M., Ketcham, R. a., Shuster, D.L., and Farley, K. a., 2009, Apatite (U–Th)/He thermochronometry using a radiation damage accumulation and annealing model: Geochimica et Cosmochimica Acta, v. 73, p. 2347–2365, doi: 10.1016/j.gca.2009.01.015.

Fu, B., and Awata, Y., 2007, Displacement and timing of left-lateral faulting in the Kunlun Fault Zone, northern Tibet, inferred from geologic and geomorphic features: Journal of Asian Earth Sciences, v. 29, p. 253–265, doi: 10.1016/j.jseaes.2006.03.004.

Galbraith, R.F., 1981, On Statistical Models for Fission Track Counts: Mathematical Geology, v. 13, p. 471–478.

Gans, P.B., 1987, An open-system, two-layer crustal stretching model for the eastern Great Basin: Tectonics, v. 6, p. 1–12.

Grathoff, G.H., and Moore, D.M., 1996, Illite plytype quantification using Wildfire calculated X-ray diffraction patterns: Clays and Clay Minerals, v. 44, no. 6, p. 835–842.

Green, P.F., 1981, A new look at statistics in fission-track dating: Nuclear Tracks, v. 5, p. 77–86, doi: 10.1016/0191-278X(81)90029-9.

Guo, Z., Wilson, M., Liu, J., and Mao, Q., 2006, Post-collisional, Potassic and Ultrapotassic Magmatism of the Northern Tibetan Plateau: Constraints on Characteristics of the Mantle Source, Geodynamic Setting and Uplift Mechanisms: Journal of Petrology, v. 47, p. 1177–1220, doi: 10.1093/petrology/egl007.

Gutscher, M.A., and Kukowski, N., 1998, Episodic imbricate thrusting and underthrusting: Analog experiments and machanical analysis applied to the Alaskan Accretionary Wedge: Journal of Geophysical Research, v. 103, no. B5, p. 10,161–10,176.

Haines, S.H., and van der Pluijm, B.A., 2008, Clay quantification and Ar–Ar dating of synthetic and natural gouge: Application to the Miocene Sierra Mazatán detachment fault, Sonora, Mexico: Journal of Structural Geology, v. 30, no. 4, p. 525–538, doi: 10.1016/j.jsg.2007.11.012.

Heiskanen, W.A., and Moritz, H., 1967, Physical Geodesy: Bulletin Géodésique (1946-1975), v. 86, no. 1, p. 491–492.

Hetzel, R., Dunkl, I., Haider, V., Strobl, M., Von Eynatten, H., Ding, L., and Frei, D., 2011,

Peneplain formation in southern Tibet predates the India-Asia collision and plateau uplift: Geology, v. 39, no. 10, p. 983–986, doi: 10.1130/G32069.1.

Horton, B.K., Yin, A., Spurlin, M.S., Zhou, J., and Wang, J., 2002, Paleocene – Eocene syncontractional sedimentation in narrow , lacustrine-dominated basins of east-central Tibet: Geological Society of America Bulletin, v. 114, no. 7, p. 771–786, doi: 10.1130/0016-7606(2002)114<0771.

Horton, B.K., Dupont-Nivet, G., Zhou, J., Waanders, G.L., Butler, R.F., and Wang, J., 2004, Mesozoic-Cenozoic evolution of the Xining-Minhe and Dangchang basins, northeastern Tibetan Plateau: Magnetostratigraphic and biostratigraphic results: Journal of Geophysical Research, v. 109, p. 1–15, doi: 10.1029/2003JB002913.

Houseman, G.A., McKenzie, D.P., and Molnar, P., 1981, Convective instability of a thickened boundary layer and its relevance for the thermal evolution of continental convergence belts: Journal of Geophysical Research: Solid Earth, v. 86, no. B7, p. 6115–6132.

Hower, J., and Mowatt, T., 1966, The minerology of illites and mixed-layer illite/montmorillonites: American Minerologist, v. 51, p. 825 – 854.

Ji, L., 1994, On the problem of the definition of the Fenghuoshan Group in the Tanggula Mountains area, Qinghai: Regional Geology of China, , no. 4, p. 373 – 380.

Jiang, Y.-H., Jiang, S.-Y., Ling, H.-F., and Dai, B.-Z., 2006, Low-degree melting of a metasomatized lithospheric mantle for the origin of Cenozoic Yulong monzogranite-porphyry, east Tibet: Geochemical and Sr–Nd–Pb–Hf isotopic constraints: Earth and Planetary Science Letters, v. 241, p. 617–633, doi: 10.1016/j.epsl.2005.11.023.

Jolivet, M., Brunel, M., Seward, D., Xu, Z., Yang, J., Roger, F., and Tapponnier, P., 2001, Mesozoic and Cenozoic tectonics of the northern edge of the Tibetan plateau : fission-track constraints: Tectonophysics, v. 343, p. 111–134, doi: 10.1016/S0040-1951(01)00196-2.

Jolivet, M., Brunel, M., Seward, D., Xu, Z., Yang, J., Malavieille, J., Roger, F., Leyreloup, A., Arnaud, N., and Wu, C., 2003, Neogene extension and volcanism in the Kunlun Fault Zone, northern Tibet: New constraints on the age of the Kunlun Fault: Tectonics, v. 22, p. 1–23, doi: 10.1029/2002TC001428.

Judge, P. A., and Allmendinger, R.W., 2011, Assessing uncertainties in balanced cross sections: Journal of Structural Geology, v. 33, p. 458–467, doi: 10.1016/j.jsg.2011.01.006.

Kapp, P., Murphy, M. a., Yin, A., Harrison, T.M., Ding, L., and Guo, J., 2003, Mesozoic and Cenozoic tectonic evolution of the Shiquanhe area of western Tibet: Tectonics, v. 22, no. 4,

p. 1–24, doi: 10.1029/2001TC001332.

Kapp, P., Yin, A., Harrison, T.M., and Ding, L., 2005, Cretaceous-Tertiary shortening, basin development, and volcanism in central Tibet: Geological Society of America Bulletin, v. 117, no. 7, p. 865–878, doi: 10.1130/B25595.1.

Kapp, P., DeCelles, P.G., Leier, A.L., Fabijanic, J.M., He, S., Pullen, A., and Gehrels, G.E., 2007a, The Gangdese retroarc thrust belt revealed: GSA Today, v. 17, no. 7, p. 4–9.

Kapp, P., DeCelles, P.G., Gehrels, G.E., Heizler, M., and Ding, L., 2007b, Geological records of the Lhasa-Qiangtang and Indo-Asian collisions in the Nima area of central Tibet: Geological Society of America Bulletin, v. 119, no. 7-8, p. 917–933, doi: 10.1130/B26033.1.

Karner, D.B., Renne, P.R., Karner, D.B., and Renne, P.R., 1998, $^{40}Ar/^{39}Ar$ geochronology of Roman volcanic province tephra in the Tiber River valley : Age calibration of middle Pleistocene sea-level changes: Geological Society of America Bulletin, v. 110, p. 740–747, doi: 10.1130/0016-7606(1998)110<0740.

Karplus, M.S., Zhao, W., Klemperer, S.L., Wu, Z., Mechie, J., Shi, D., Brown, L.D., and Chen, C., 2011, Injection of Tibetan crust beneath the south Qaidam Basin: Evidence from INDEPTH IV wide-angle seismic data: Journal of Geophysical Research, v. 116, p. 1–23, doi: 10.1029/2010JB007911.

Ketcham, R. A., 2005, Forward and Inverse Modeling of Low-Temperature Thermochronometry Data: Reviews in Mineralogy and Geochemistry, v. 58, no. 1, p. 275–314, doi: 10.2138/rmg.2005.58.11.

Ketcham, R.A., Donelick, R.A., and Carlson, W.D., 1999, Variability of apatite fission-track annealing kinetics : III . Extrapolation to geological time scales: American Mineralogist, v. 84, p. 1235–1255.

Ketcham, R.A., Carter, A., Donelick, R.A., Barbarand, J., and Hurford, A.J., 2007, Improved modeling of fission-track annealing in apatite: American Mineralogist, v. 92, p. 799–810, doi: 10.2138/am.2007.2281.

Klemperer, S.L., 2006, Crustal flow in Tibet: geophysical evidence for the physical state of Tibetan lithosphere, and inferred patterns of active flow: Geological Society, London, Special Publications, v. 268, p. 39–70, doi: 10.1144/GSL.SP.2006.268.01.03.

Kuiper, N.H., 1960, Tests concerning random points on a circle: Proceedings of the Koninklijke Nederlandse Akademie van Wetenschappen, Series A, v. 63, p. 38–47.

Lai, S.-C., Liu, C.-Y., and Yi, H.-S., 2003, Geochemistry and Petrogenesis of Cenozoic Andesite-

Dacite Associations from the Hoh Xil Region, Tibetan Plateau: International Geology Review, v. 45, p. 998–1019, doi: 10.2747/0020-6814.45.11.998.

Leeder, M.R., Smith, A.B., and Yin, J., 1988, Sedimentology, palaeoecology and palaeoenvironmental evolution of the 1985 Lhasa to Golmud Geotraverse: Philosophical Transactions of the Royal Society of London. Series A, Mathematical and Physical Sciences, v. 327, no. 1594, p. 107–143.

Li, C.Y., Liu, Y., Zhu, B.C., Feng, Y.M., and Wu, H.C., 1978, Structural evolution of Qinling and Qilian Shan, in Scientific Papers in Geology and International Exchange, Beijing: Geologic Publishing House, p. 174–197.

Li, P., and Yuan, L., 1990, The Fenghuoshan Group of palynological assemblages and their meaning: Northwestern Geology, v. 4, p. 7–9.

Li, W., Song, Z., Liou, Z., Li, C., Li, Z., and Li, H., 2005, Geologic characteristics and ore-controls of the Fenghuoshan copper ore deposit , Qinghai province , China, in Mineral Deposit Research: Meeting the Global Challenge, Springer Berlin Heidelberg, p. 153 – 156.

Li, Y., Wang, C., Ma, C., Xu, G., and Zhao, X., 2011, Balanced cross-section and crustal shortening analysis in the Tanggula-Tuotuohe Area, Northern Tibet: Journal of Earth Science, v. 22, p. 1–10, doi: 10.1007/A3.12583-011-0152-2.

Li, Y., Wang, C., Zhao, X., Yin, A., and Ma, C., 2012, Cenozoic thrust system, basin evolution, and uplift of the Tanggula Range in the Tuotuohe region, central Tibet: Gondwana Research, v. 22, p. 482–492, doi: 10.1016/j.gr.2011.11.017.

Lippert, P.C., van Hinsbergen, D.J.J., Dupont-Nivet, G., 2014, The Early Cretaceous to Present latitude of the central proto-Tibetan Plateau: A paleomagnetic synthesis with implications for Cenozoic tectonics, paleogeography and climate of Asia, *in*: Nie, J.S., Hoke, G.D. and Horton, B.K. (editors), Towards an improved understanding of uplift mechanisms and the elevation history of the Tibetan plateau, *Geological Society of America Special Paper,* v. 507, p. 1–21, doi:10.1130/2014.2507

Liu, Z., and Wang, C., 2001a, Depositional Environment of the Tertiary Fenghuoshan Group in the Hoh Xil Basin, Northern Tibetan Plateau: Acta Sedimentologica Sinica, v. 19, no. 1, p. 28 – 34.

Liu, Z., and Wang, C., 2001b, Facies analysis and depositional systems of Cenozoic sediments in the Hoh Xil basin, northern Tibet: Sedimentary Geology, v. 140, no. 3-4, p. 251–270, doi: 10.1016/S0037-0738(00)00188-3.

Liu, Z., Wang, C., and Yi, H., 2001, Evolution and mass accumulation of the Cenozoic Hoh Xil Basin, Northern Tibet: Journal of Sedimentary Research, v. 71, no. 6, p. 971 – 984.

Liu, Z., Zhao, X., Wang, C., Liu, S., and Yi, H., 2003, Magnetostratigraphy of Tertiary sediments from the Hoh Xil Basin: implications for the Cenozoic tectonic history of the Tibetan Plateau: Geophysical Journal International, v. 154, no. 2, p. 233–252, doi: 10.1046/j.1365-246X.2003.01986.x.

Mattauer, M., 1986, Intracontinental subduction, crustal stacking wedge and crustmantle decollement, in Coward, M.P. and Reis, A.C. eds., Collisional Tectonics, Geological Society of London Special Publication, v. 19, no. 1, p. 37–50.

McKenna, L.W., and Walker, J.D., 1990, Geochemistry of Crustally Derived Leucocratic Igneous Rocks From the Ulugh Muztagh Area, Northern Tibet and Their Implications for the Formation of the Tibetan Plateau: Journal of Geophysical Research, v. 95, p. 21,483 – 21,502.

Meng, Q., and Zhang, G.-W., 1999, Timing of collision of the North and South China blocks : Controversy and reconciliation: Geology, v. 27, p. 123–126, doi: 10.1130/0091-7613(1999)027<0123.

Miller, D.S., Duddy, I.R., 1989, Early Cretaceous uplift and erosion of the northern Appalachian Basin, New York, based on apatite fission track analysis: Earth and Planetary Science Letters, v. 93, p. 35–49.

Mock, C., Arnaud, N.O., and Cantagrel, J., 1999, An early unroofing in northeastern Tibet ? Constraints from $^{40}Ar/^{39}Ar$ thermochronology on granitoids from the eastern Kunlun range: Earth and Planetary Science Letters, v. 171, p. 107–122.

Molnar, P., and Stock, J.M., 2009, Slowing of India's convergence with Eurasia since 20 Ma and its implications for Tibetan mantle dynamics: Tectonics, v. 28, p. 1–11, doi: 10.1029/2008TC002271.

Molnar, P., England, P., and Martinod, J., 1993, Mantle dynamics, uplift of the Tibetan Plateau, and the Indian Monsoon: Reviews in Geophysics, v. 31, no. 4, p. 357–396.

Murphy, M.A., Yin, A., Harrison, T.M., Dürr, S.B., Z, C., Ryerson, F.J., Kidd, W.S.F., X, W., and X, Z., 1997, Did the Indo-Asian collision alone create the Tibetan plateau?: Geology, v. 25, no. 8, p. 719–722, doi: 10.1130/0091-7613(1997)025<0719:DTIACA>2.3.CO;2.

Murphy, M.A., and Yin, A., 2003, Structural evolution and sequence of thrusting in the Tethyan fold-thrust belt and Indus-Yalu suture zone, southwest Tibet: Geological Society of America

Bulletin, v. 115, p. 21–34, doi: 10.1130/0016-7606(2003)115<0021.

Nábelek, J., Hetényi, G., Vergne, J., Sapkota, S., Kafle, B., Jiang, M., Su, H., Chen, J., and Huang, B.-S., 2009, Underplating in the Himalaya-Tibet collision zone revealed by the Hi-CLIMB experiment.: Science (New York, N.Y.), v. 325, p. 1371–4, doi: 10.1126/science.1167719.

Najman, Y., Appel, E., Boudagher-Fadel, M., Bown, P., Carter, A., Garzanti, E., Godin, L., Han, J., Liebke, U., Oliver, G., Parrish, R., and Vezzoli, G., 2010, Timing of India-Asia collision: Geological, biostratigraphic, and palaeomagnetic constraints: Journal of Geophysical Research, v. 115, no. B12, p. 1–18, doi: 10.1029/2010JB007673.

Owens, T.J., and Zandt, G., 1997, Implications of crustal property variations for models of Tibetan plateau evolution: Nature, v. 387, p. 37 – 43.

Pan, G., J. Ding, D. Yao, and L. Wang, 2004, Guidebook of 1:1,500,000 geologic map of the Qinghai-Xizang (Tibet) plateau and adjacent areas, Chengdu, China, Chengdu Cartographic Publishing House, p. 48.

Polissar, P.J., Freeman, K.H., Rowley, D.B., McInerney, F.A., and Currie, B.S., 2009, Paleoaltimetry of the Tibetan Plateau from D/H ratios of lipid biomarkers: Earth and Planetary Science Letters, v. 287, p. 64–76, doi: 10.1016/j.epsl.2009.07.037.

QBGMR (Qinghai Bureau of Geology and Mineral Resources), 1989a, Geologic map of the Cuorendejia region, scale 1:200,000.

QBGMR (Qinghai Bureau of Geology and Mineral Resources), 1989b, Geologic map of the Tuotuohe region, scale 1:200,000.

Ratschbacher, L., Frisch, W., and Liu, G., 1994, Distributed deformation in southern and western Tibet during and after the India-Asian collision: Journal of Geophysical Research, v. 99, p. 19,917–19,945.

Reiners, P.W., Farley, K.A., and Hickes, H.J., 2002, He diffusion and (U-Th)/He thermochronometry of zircon : initial results from Fish Canyon Tuff and Gold Butte: Tectonophysics, v. 349, p. 297–308, doi: 10.1016/S0040-1951(02)00058-6.

Renne, P.R., Swisher, C.C., Deino, A.L., Karner, D.B., Owens, T.L., and Depaolo, D.J., 1998, Intercalibration of standards, absolute ages and uncertainties in $^{40}Ar/^{39}Ar$ dating: Chemical Geology, v. 145, p. 117–152.

Reynolds R., Jr., 1994, WILDFIRE©, A Computer Program for the Calculation of Threedimensional Powder X-ray Diffraction Patterns for Mica Polytypes and their Disordered Variations. Hanover, NH: RC Reynolds, Jr, 8 Brook Rd.

Roger, F., Tapponnier, P., Arnaud, N., Scharer, U., Brunel, M., Xu, Z., and Yang, J., 2000, An Eocene magmatic belt across central Tibet: mantle subduction triggered by the Indian collision?: Terra Nova, v. 12, no. 3, p. 102–108.

Rohrmann, A., Kapp, P., Carrapa, B., Reiners, P.W., Guynn, J., Ding, L., and Heizler, M., 2012, Thermochronologic evidence for plateau formation in central Tibet by 45 Ma: Geology, v. 40, no. 2, p. 187–190, doi: 10.1130/G32530.1.

Rowley, D.B., 1996, Age of initiation of collision between India and Asia: A review of stratigraphic data: Earth and Planetary Science Letters, v. 145, p. 1–13.

Rowley, D.B., and Currie, B.S., 2006, Palaeo-altimetry of the late Eocene to Miocene Lunpola basin, central Tibet: Nature, v. 439, p. 677–681, doi: 10.1038/nature04506.

Royden, L., Burchfiel, B., King, R., Wang, E., Chen, Z., Shen, F., and Liu, Y., 1997, Surface Deformation and Lower Crustal Flow in Eastern Tibet: Science, v. 276, p. 788–790.

Sandiford, M., and Powell, R., 1991, Some remarks on high-temperature - low-pressure metamorphism in convergent orogens: Journal of Metamorphic Geology, v. 9, p. 333–340.

Schoenbohm, L.M., Burchfiel, B.C., and Liangzhong, C., 2006, Propagation of surface uplift, lower crustal flow, and Cenozoic tectonics of the southeast margin of the Tibetan Plateau: Geology, v. 34, p. 813–816, doi: 10.1130/G22679.1.

Searle, M.P., Simpson, R.L., Law, R.D., Parrish, R.R., and Waters, D.J., 2003, The structural geometry, metamorphic and magmatic evolution of the Everest massif, High Himalaya of Nepal-South Tibet: Journal of the Geological Society of London, v. 160, p. 345–366.

Şengör, A.M.C., 1984, The Cimmeride orogenic system and the tectonics of Eurasia: Geological Society of America Special Papers, v. 195, p. 1–74.

Şengör, A.M.C., and Hsü, K.J., 1984, The Cimmerides of eastern Asia: history of the eastern end of Palaeo-Tethys: Mem. Soc. Geol. Fr., v. 147, p. 139–167.

Spurlin, M.S., Yin, A., Horton, B.K., Zhou, J., and Wang, J., 2005, Structural evolution of the Yushu-Nangqian region and its relationship to syncollisional igneous activity, east-central Tibet: Geological Society of America Bulletin, v. 117, no. 9-10, p. 1293–1317, doi: 10.1130/B25572.1.

Staisch, L.M., Niemi, N.A., Chang, H., Clark, M.K., Rowley, D.B., and Currie, B.S., 2014, A Cretaceous-Eocene depositional age for the Fenghuoshan Group, Hoh Xil Basin: Implications for the tectonic evolution of the northern Tibetan Plateau: Tectonics, v. 33, p. 281–301, doi: 10.1002/2013TC003367.

Tapponnier, P., Shu, Z., Roger, F., Meyer, B., Arnaud, N., Wittlinger, G., and Jingsui, Y., 2001, Oblique stepwise rise and growth of the Tibet Plateau.: Science, v. 294, p. 1671–1677, doi: 10.1126/science.105978.

Turner, S., Sandiford, M., and Foden, J., 1992, Some geodynamic and compositional constraints on "postorogenic" magmatism: Geology, v. 20, p. 931–934.

van der Pluijm, B.A, Hall, C.M., Vrolijk, P.J., Pevear, D.R., and Covey, M.C., 2001, The dating of shallow faults in the Earth's crust.: Nature, v. 412, p. 172–175, doi: 10.1038/35084053.

van der Pluijm, B.A., Vrolijk, P.J., Pevear, D.R., Hall, C.M., and Solum, J., 2006, Fault dating in the Canadian Rocky Mountains: Evidence for late Cretaceous and early Eocene orogenic pulses: Geology, v. 34, no. 10, p. 837, doi: 10.1130/G22610.1.

van Hinsbergen, D.J.J., Kapp, P., Dupont-Nivet, G., Lippert, P.C., DeCelles, P.G., and Torsvik, T.H., 2011, Restoration of Cenozoic deformation in Asia and the size of Greater India: Tectonics, v. 30, no. 5, TC5003, doi: 10.1029/2011TC002908.

van Hinsbergen, D.J.J., Lippert, P.C., Dupont-Nivet, G., McQuarrie, N., Doubrovine, P. V, Spakman, W., and Torsvik, T.H., 2012, Greater India Basin hypothesis and a two-stage Cenozoic collision between India and Asia.: Proceedings of the National Academy of Sciences of the United States of America, v. 109, no. 20, p. 7659–7664, doi: 10.1073/pnas.1117262109.

Vergne, J., Wittlinger, G., Hui, Q., Tapponnier, P., Poupinet, G., Mei, J., Herquel, G., and Paul, A., 2002, Seismic evidence for stepwise thickening of the crust across the NE Tibetan plateau: Earth and Planetary Science Letters, v. 203, p. 25–33, doi: 10.1016/S0012-821X(02)00853-1.

Vozar, J., Jones, A.G., Fullea, J., Agius, M.R., Lebedev, S., Pape, F. Le, and Wei, W. Integrated geophysical-petrological modeling of lithosphere – asthenosphere boundary in Central Tibet using electromagnetic and seismic data: Geochemistry Geophysics Geosystems.

Wang, C.S., Liu, Z.F., Yi, H.S., Liu, S., and Zhao, X.X., 2002, Tertiary crustal shortenings and peneplanation in the Hoh Xil region: implications for the tectonic history of the northern Tibetan Plateau: Journal of Asian Earth Sciences, v. 20, p. 211–223.

Wang, Q., McDermott, F., Xu, J., Bellon, H., and Zhu, Y., 2005, Cenozoic K-rich adakitic volcanic rocks in the Hohxil area, northern Tibet: Lower-crustal melting in an intracontinental setting: Geology, v. 33, p. 465–468, doi: 10.1130/G21522.1.

Wang, C.S., Zhao, X., Liu, Z., Lippert, P.C., Graham, S.A, Coe, R.S., Yi, H., Zhu, L., Liu, S., and Li, Y., 2008, Constraints on the early uplift history of the Tibetan Plateau.: Proceedings of the

National Academy of Sciences of the United States of America, v. 105, no. 13, p. 4987–4992, doi: 10.1073/pnas.0703595105.

Williams, H.M., Turner, S.P., Pearce, J.A., Kelley, S.P., and Harris, N.B.W., 2004, Nature of the Source Regions for Post-collisional, Potassic Magmatism in Southern and Northern Tibet from Geochemical Variations and Inverse Trace Element Modelling: Journal of Petrology, v. 45, p. 555–607, doi: 10.1093/petrology/egg094.

Wittlinger, G., Vergne, J., Tapponnier, P., Farra, V., Poupinet, G., Jiang, M., Su, H., Herquel, G., and Paul, a, 2004, Teleseismic imaging of subducting lithosphere and Moho offsets beneath western Tibet: Earth and Planetary Science Letters, v. 221, p. 117–130, doi: 10.1016/S0012-821X(03)00723-4.

Wu, Z., Barosh, P.J., Wu, Z., Hu, D., Zhao, X., and Ye, P., 2008, Vast early Miocene lakes of the central Tibetan Plateau: Geological Society of America Bulletin, v. 120, no. 9-10, p. 1326–1337, doi: 10.1130/B26043.1.

Xia, L., Li, X., Ma, Z., Xu, X., and Xia, Z., 2011, Cenozoic volcanism and tectonic evolution of the Tibetan plateau: Gondwana Research, v. 19, p. 850–866, doi: 10.1016/j.gr.2010.09.005.

Xu, Q., Ding, L., Zhang, L., Cai, F., Lai, Q., Yang, D., and Liu-Zeng, J., 2013, Paleogene high elevations in the Qiangtang Terrane, central Tibetan Plateau: Earth and Planetary Science Letters, v. 362, p. 31–42, doi: 10.1016/j.epsl.2012.11.058.

Yakovlev, P. V., Clark, M. K., 2014, Conservation and redistribution of crust during the Indo-Asian collision: Tectonics, v. 33, no. 6, p. 1016–1027, doi: 10.1002/2013TC003469.

Yi, H., Zhao, X., Lin, J., Shi, Z., Li, B., and Zhao, B., 2004, Magnetostratigraphic results of Tertiary continental redbeds from the Wulanwula Lake area of northern Tibetan plateau and its geologic implications: Acta Geosicientia Sinica, v. 6, p. 633–638.

Yi, H., Wang, C., Shi, Z., Lin, J., and Zhu, L., 2008, Early Uplift History of the Tibetan Plateau : Records from Paleocurrents and Paleodrainage in the Hoh Xi1 Basin: Acta Geologica Sinica, v. 82, p. 206–213.

Yin, A., 2005, Cenozoic tectonic evolution of the Himalayan orogen as constrained by along-strike variation of structural geometry, exhumation history, and foreland sedimentation: Earth-Science Reviews, v. 76, p. 1–131, doi: 10.1016/j.earscirev.2005.05.004.

Yin, A., and Harrison, T.M., 2000, Geologic Evolution of the Himalayan-Tibetan Orogen: Annual Reviews Earth and Planetary Science, v. 28, p. 211–280.

Yin, A., and Nie, S., 1993, An indentation model for the North and South China collision and the

development of the Tan-Lu and Honom fault systems, Eastern Asia: Tectonics, v. 12, p. 801–813.

Yin, A., and Nie, S., 1996, A Phanerozoic palinspastic reconstruction of China and its neighboring regions, in Yin, A. and Harrison, T. eds., The Tectonics of Asia, New York:, Cambridge Univeristy Press, p. 442–485.

Yin, A., Harrison, T.M., Ryerson, F.J., Wenji, C., Kidd, W.S.F., and Copeland, P., 1994, Tertiary structural evolution of the Gangdese Thrust System, southeastern Tibet: Journal of Geophysical Research, v. 99, p. 18175–18201, doi: 10.1029/94JB00504.

Yin, A., Rumelhart, P.E., Butler, R., Cowgill, E., Harrison, T.M., Foster, D.A., Ingersoll, R.V., Qing, Z., Xian-Qiang, Z., Xiao-Feng, W., Hanson, A., and Raza, A., 2002, Tectonic history of the Altyn Tagh fault system in northern Tibet inferred from Cenozoic sedimentation: Geological Society of America Bulletin, v. 114, p. 1257–1295, doi: 10.1130/0016-7606(2002)114<1257:THOTAT>2.0.CO;2.

Yin, A., Dang, Y.Q., Zhang, M., McRivette, M.W., Burgess, W.P., and Chen, X., 2007, Cenozoic tectonic evolution of Qaidam basin and its surrounding regions (part 2): Wedge tectonics in southern Qaidam basin and the Eastern Kunlun Range: Geological Society of America Special Papers, v. 433, p. 369–390, doi: 10.1130/2007.2433(18).

Yin, A., Dang, Y.Q., Wang, L.-C., Jiang, W.-M., Zhou, S.-P., Chen, X.-H., Gehrels, G.E., and McRivette, M.W., 2008, Cenozoic tectonic evolution of Qaidam basin and its surrounding regions (Part 1): The southern Qilian Shan-Nan Shan thrust belt and northern Qaidam basin: Geological Society of America Bulletin, v. 120, p. 813–846, doi: 10.1130/B26180.1.

Yin, J., Xu, J., Liu, C., and Li, H., 1988, The Tibetan plateau: regional stratigraphic context and previous work: Philosophical Transactions of the Royal Society of London. Series A, Mathematical and Physical Sciences, v. 327, p. 5–52.

York, D., 1968, Least squares fitting of a straight line with correlated errors: Earth and Planetary Science Letters, v. 5, p. 320–324.

Yuan, W., Dong, J., Shicheng, W., and Carter, A., 2006, Apatite fission track evidence for Neogene uplift in the eastern Kunlun Mountains, northern Qinghai–Tibet Plateau, China: Journal of Asian Earth Sciences, v. 27, p. 847–856, doi: 10.1016/j.jseaes.2005.09.002.

Zhang, P.-Z., Shen, Z., Wang, M., Gan, W., Bürgmann, R., Molnar, P., Wang, Q., Niu, Z., Sun, J., Wu, J., Hanrong, S., and Xinzhao, Y., 2004, Continuous deformation of the Tibetan Plateau from global positioning system data: Geology, v. 32, no. 9, p. 809–812, doi:

10.1130/G20554.1.

Zheng, D., Clark, M.K., Zhang, P., Zheng, W., and Farley, K. a., 2010, Erosion, fault initiation and topographic growth of the North Qilian Shan (northern Tibetan Plateau): Geosphere, v. 6, p. 937–941, doi: 10.1130/GES00523.1.

Zhong, X., 1989, Fenghuoshan Group geological era Tanggula Qinghai: Northwestern Geology, v. 6, p. 1–6.

Zhou, H., and Murphy, M. a., 2005, Tomographic evidence for wholesale underthrusting of India beneath the entire Tibetan plateau: Journal of Asian Earth Sciences, v. 25, p. 445–457, doi: 10.1016/j.jseaes.2004.04.007.

Zhuang, G., Hourigan, J.K., Ritts, B.D., and Kent-Corson, M.L., 2011, Cenozoic multiple-phase tectonic evolution of the northern Tibetan Plateau: Constraints from sedimentary records from Qaidam basin, Hexi Corridor, and Subei basin, northwest China: American Journal of Science, v. 311, p. 116–152, doi: 10.2475/02.2011.02.

Appendix A: Chapter III

Map units

Permian to Quaternary aged rocks are exposed throughout the Fenghuoshan Range and surrounding regions (QBGMR 1989a; 1989b). The marine Permian Wuli Group (P_2wl) is the oldest unit mapped in this region and is composed of dark grey lithic sandstone, siltstone and shale interbedded with bioclastic limestone, carbonaceous shale, and coal (QBGMR 1989b). It is roughly 830 m thick (QBGMR 1989b) and is exclusively exposed south of the Fenghuoshan Range along the south-directed Tuotuohe Thrust (TT; Figure 3.4a). The overlying Middle Triassic units, which are also only reported to the south of the Fenghuoshan Range, are divided into clastic (T_2^a) and carbonaceous (T_2^b) units and are ~500 m thick combined (QBGMR 1989b). The unconformable upper Triassic Jieza Group (T_3jz) ranges in stratigraphic thickness from ~3660 m north of the Fenghuoshan Range to as little as ~1930 m in the south (QBGMR 1989a; 1989b). It is composed of grey-green fine to coarse grained marine feldspathic sandstone interbedded with dark grey to black carbonaceous shale, siltstone, and bioclastic limestone (QBGMR 1989a; 1989b). North of the Fenghuoshan Range, the Triassic Batang (T_3bt) Group is deposited conformably over the Jieza Group and is composed of grey-green fine quartz to feldspathic sandstone, phyllite, dolomite, limestone, and chert interbedded with pillow basalts and basaltic breccia (QBGMR 1989a). It is not exposed within or south of the Fenghuoshan Range.

The Cenomanian – Ypresian Fenghuoshan Group ($E_{1\text{-}2}$fn, K_2fn^d, K_2fn^c, K_2fn^b, $K_{2fn}{}^a$) is the first record of terrestrial sedimentation and uplift above sea level in the Hoh Xil Basin (Staisch et al., 2014). In central Hoh Xil Basin, this unit is unconformably deposited on the Batang (T_3bt), Jieza (T_3jz), and Middle Triassic units (T_2^a, T_2^b) (QBGMR 1989a; 1989b). The Fenghuoshan Group is composed largely of fluvial to fan-delta mudstone, siltstone, fine to coarse sandstone, and conglomerate, with a minor component of lacustrine carbonate (Leeder et al., 1988; QBGMR 1989a; 1989b; Zhong, 1989; Ji, 1994; Liu et al., 2001; An et al., 2004). These sedimentary rocks are characteristically brick red to greyish purple in color, with occasional light green, copper-bearing layers (Yin et al., 1988; Li et al., 2005). Isopach maps suggest that the Fenghuoshan Group was deposited within the Fenghuoshan, Hantaishan, and Wudaoliang sub-basins, and that sedimentation

was thickest within the lenticular-shaped Fenghuoshan Sub-basin, near the town of Erdaguo (Figure 3.4c; Liu et al., 2001). The Fenghuoshan sub-basin depocenter migrated northwards with progressive infilling, such that the lowermost Fenghuoshan Group (K_{2fn}^{a}) is thickest in the south, and the middle and upper units (E_{1-2}fn, K_2fn^{d}, K_2fn^{c}, K_2fn^{b}) are thickest in the central Fenghuoshan Range (Figure 3.4c; Liu et al., 2001). Provenance analysis indicates that the Fenghuoshan Group strata was likely sourced from the central Qiangtang Terrane (Li et al., 2011; Staisch et al., 2014), possibly at the location of the modern Tanggula Shan. Following deposition of the Fenghuoshan Group, the Hoh Xil Basin experienced north-south oriented contraction and syntectonic deposition of the overlying and unconformable Tuotuohe and Yaxicuo Groups (Staisch et al., 2014).

The Eocene – early Oligocene Tuotuohe Group unconformably overlies the Fenghuoshan Group and is exposed along the Nan Fenghuoshan Thrust Fault (NFT) and in the Tuotuohe Sub-Basin, located to the south of the Fenghuoshan Range (QBGMR 1989a; Staisch et al., 2014). It is composed of beige to brick-red medium sandstone and conglomerate (QBGMR 1989a, 1989b; Staisch et al., 2014). The inclusion of Fenghuoshan Group clasts within the Tuotuohe Group strata indicates that it was, at least in part, sourced from the Fenghuoshan Range (Staisch et al., 2014). The Oligocene Yaxicuo Group overlies the Tuotuohe Group and, based on the overlap in biostratigraphically constrained depositional ages and previously reported field observations, may represent laterally variable deposition in early Oligocene time (Z. Duan et al., 2007; Q. Duan et al., 2007; 2008; Staisch et al., 2014). The Yaxicuo Group is moderately deformed to the north and south of the Fenghuoshan range, and is composed of beige to orange siltstone and sandstone with subordinate gypsum layers (Liu and Wang, 2001; Liu et al., 2001, 2003; Li et al., 2012). The overlying Miocene Wudaoliang Group unconformably overlaps many of the units in the region (QBGMR 1989a; 1989b; Z. Duan et al., 2007). It is composed of lacustrine carbonate and ranges from a few meters to 200 meters in thickness (QBGMR 1989a; 1989b). The Wudaoliang Group has only been mildly deformed in the northern Hoh Xil Basin, indicating that north-south oriented contraction in the Hoh Xil Basin ceased by Miocene time (Liu and Wang, 2001; Liu et al., 2001, 2003; Li et al., 2012). This is consistent with Late Oligocene sub-horizontal basalt flows that cap deformed Fenghuoshan Group strata are preserved in the Fenghuoshan Range (Staisch et al., 2014).

Appendix B: Chapter III

Sample Preparation

$^{40}Ar/^{39}Ar$ Fault Gouge Dating

Samples were dried under heat lamps and then pulverized to a fine powder via disc mill. Powered fault gouge was then suspended in deionized (DI) water, agitated for 30 minutes in an ultrasonic bath, and allowed to settle for 30 minutes – 1 hour. Gouge that remained suspended after this time was poured into casserole dishes and dried under heat lamps. Once dry, the gouge was placed into four 50 mL centrifuge tubes, suspended in DI water, and agitated once again in an ultrasonic bath. Samples were then gravitationally separated based on Stokes' Law using a ThermoFischer CL-2 centrifuge into coarse (1 – 2 μm), medium-coarse (0.5 – 1 μm), medium (0.2 – 0.5 μm), fine (0.05 – 0.2 μm), and ultrafine (<0.05 μm) size fractions. Finally, each size fraction was dried and powdered by hand in an agate mortar.

Low-Temperature Thermochronology

Samples were crushed and sieved using standard laboratory procedures. Apatite crystals were separated from the sample using standard density and magnetic techniques. Apatite crystals were handpicked at the University of Michigan to ensure grain quality using standard procedures (Farley and Stockli, 2002; Reiners et al., 2002) and analyzed for (U-Th)/He at the University of Michigan HeliUM Laboratory and University of Arizona Laserchron Center**.**

Appendix C: Chapter III

Bayesian linear regression

The Bayesian linear regression used in this study to obtain authigenic and detrital illite ages from fault gouge data is a statistical analysis of linear fit in the framework of Bayesian inference. The regression model requires three main inputs: aliquot $^{40}Ar/^{39}Ar$ ages and illite concentrations, associated uncertainties in age and illite concentration, and uniform prior bounds for slope and intercept values. The results of the regression model are posterior relative probability distributions of the slope and intercept parameters.

Prior bounds were chosen to effectively limit the model space searched without limiting the results. Once the posterior range was determined, we confirmed that prior bounds were non-informative and therefore not biasing posteriors by ensuring that prior bounds were outside the 5% bounds of the posterior range. For sample 12FHS12, the prior bounds selected were 0.025 to 0.065 and 0.015 to 0.035 for slope and intercept respectively. For sample 10UMT09, the prior bounds selected were 0.035 to 0.075 and 0.015 to 0.040 for slope and intercept, respectively. In this study, we chose to run 10^6 models for each fault gouge sample in order to obtain a well-distributed range in posterior parameter values and their associated likelihoods.

The model uniformly searches the prior bounds to test the likelihood of parameter combinations in fitting the measured fault gouge data. The likelihood of each trial was computed based on the assumption that uncertainties in x and y values of the measured data is Gaussian. Since we include uncertainty in illite concentrations and $^{40}Ar/^{39}Ar$ ages, the total model likelihood is a product of likelihood in fitting observed data:

$$L_x = e^{-\frac{(x-\mu_x)^2}{2\sigma_x^2}} \quad \text{(B1)}$$

$$L_y = e^{-\frac{(y-\mu_y)^2}{2\sigma_y^2}} \quad \text{(B2)}$$

$$L = L_x * L_y \quad \text{(B3)}$$

where values of x are the measured illite concentration, y are the measured $^{40}Ar/^{39}Ar$ age, μ_x and μ_y are the modeled values, and σ_x^2 and σ_y^2 are the variances in x and y, respectively. The likelihood of a trial fitting measured x and y values are L_x and $L_{y,}$ respectively and L is the total model likelihood. Thus, as the distance between measured and modeled x or y values increases, the model likelihood decreases. The trials were sampled from the posterior to return a normalized relative probability (NRP) distribution for slope and intercept values. We chose the linear fit with the highest calculated likelihood as our best fit model for each fault gouge sample. The posterior distributions for parameter values for both fault gouge samples are roughly Gaussian (Figure A3.5), such that the best fit, most likely, mean, and median values for slope and intercept are nearly indistinguishable.

The authigenic and detrital illite ages reported above and in Figure 3.7 are calculated from the best fit linear fit and each linear fit is colored by its value of normalized likelihood. The uncertainty reported for the authigenic illite age is taken to be the 95% confidence interval in the y-intercept posterior probability distribution. A NRP distribution for detrital illite ages was calculated from posterior parameter values, and the uncertainty was also taken to be the 95% confidence interval of the resulting probability distribution.

Appendix D: Chapter III

Shortening calculations and error propagation

To calculate original width (W_i), slight modifications were made to the equations presented in Judge and Allmendinger (2011) to account for a more complicated basal thrust geometry of our cross section. Instead of assuming that the undeformed area can be approximated by a simple four-sided polygon, we subdivided our total retrodeformed area (A) into three polygons (Figure 3.9b), with areas A^1, A^2 and A^3, such that

$$A = A^1 + A^2 + A^3 \tag{C1}$$

The area of subdivided polygons A^1 and A^2 can be calculated using equations C2 and C3, based values of the corresponding polygon widths, W_i^1 and W_i^2 (Figure 3.9b; Table 3.3), which are known by measuring the length of each polygon and the stratigraphic thicknesses measured at the area margins, T_a, T_b, T_c, and T_d (Figure 3.9b; Table 3.3). These quantities are known from stratigraphic columns from geologic maps (QBGMR, 1989a; 1989b) and isopach data from Liu et al. (2001) (Figure 3.4c).

$$A^1 = W_i^1 \left(\frac{T_a + T_b}{2}\right) \tag{C2}$$

$$A^2 = W_i^2 \left(\frac{T_b + T_c}{2}\right) \tag{C3}$$

Using the calculated values of A^1 and A^2 and the full area (A) (Table 3.3), which is known by measuring the area of the deformed section using the AreaErrorProp program presented in Judge and Allmendinger (2011), we can rearrange equation A1 to solve for A^3.

$$A^3 = A - (A^1 + A^2) \tag{C7}$$

From this, we can obtain the value of W_i^3 using the equation:

$$W_i^3 = \frac{2A_3}{T_a + T_b} \tag{C8}$$

The three widths of each polygon are now known and can be used to calculate the full initial width (W_i).

$$W_i = W_i^1 + W_i^2 + W_i^3 \tag{C9}$$

The magnitude of shortening can be calculated from the initial and final cross section transect widths, W_i and W_f, respectively, to obtain the magnitude of shortening:

$$S = W_i - W_f \tag{C10}$$

$$S\% = \frac{S}{W_i} \tag{C11}$$

To assess the uncertainty of our shortening estimate, we adapted the error analysis methods of Judge and Allmendinger (2011) to our cross section. The errors associated from our measured area (A) were obtained using the AreaErrorProp program (Judge and Allmendinger, 2011) into which we enter the uncertainty in measured stratigraphic thicknesses at the transect margins and the uncertainty in the location of polygon vertices. The uncertainty in stratigraphic thicknesses and the z-component of the polygon vertices were obtained from the range in reported stratigraphic thicknesses for each unit (Table 3.3; QBGMR, 1989a, 1989b; Liu et al., 2001). The uncertainty of the x-component of polygon vertices were set at an estimated value (0.25 km). The values of uncertainty in width measurements (W_i^1 and W_i^2) were also set at an estimated value of 5.0 km (Table 3.3).

The values of uncertainty in calculated variables were obtained by propagating errors in quadrature using the following system of equations:

$$\sigma_{A^1} = \sqrt{\left(\frac{\partial A^1}{\partial T_a}\right)\sigma T_a + \left(\frac{\partial A^1}{\partial T_b}\right)\sigma T_b + \left(\frac{\partial A^1}{\partial {W_i}^1}\right)\sigma {W_i}^1} \tag{C12}$$

$$\sigma_{A^2} = \sqrt{\left(\frac{\partial A^2}{\partial T_b}\right)\sigma T_b + \left(\frac{\partial A^2}{\partial T_c}\right)\sigma T_c + \left(\frac{\partial A^2}{\partial {W_i}^2}\right)\sigma {W_i}^2} \tag{C13}$$

$$\sigma_{A^3} = \sqrt{\left(\frac{\partial A^3}{\partial A}\right)\sigma A + \left(\frac{\partial A^3}{\partial A^1}\right)\sigma A^1 + \left(\frac{\partial A^3}{\partial A^2}\right)\sigma A^2} \tag{C14}$$

$$\sigma_{W^3} = \sqrt{\left(\frac{\partial W^3}{\partial A^3}\right)\sigma A^3 + \left(\frac{\partial W^3}{\partial T_c}\right)\sigma T_c + \left(\frac{\partial W^3}{\partial T_d}\right)\sigma T_d} \tag{C15}$$

$$\sigma_{W_i} = \sqrt{\left(\frac{\partial W_i}{\partial {W_i}^1}\right)\sigma {W_i}^1 + \left(\frac{\partial W_i}{\partial {W_i}^2}\right)\sigma {W_i}^2 + \left(\frac{\partial W_i}{\partial {W_i}^3}\right)\sigma {W_i}^3} \tag{C16}$$

$$\sigma_S = \sqrt{\left(\frac{\partial S}{\partial W_f}\right)\sigma W_f + \left(\frac{\partial S}{\partial W_i}\right)\sigma W_i} \tag{C17}$$

$$\sigma_{S\%} = \sqrt{\left(\frac{\partial S\%}{\partial S}\right)\sigma S + \left(\frac{\partial S\%}{\partial W_i}\right)\sigma W_i} \tag{C18}$$

Appendix E: Chapter III

Surface uplift due crustal thickening and mantle root loss

Assumptions

Our derived estimates of elevation depend strongly on the initial crustal and lithospheric thicknesses and elevations of the Hoh Xil Basin. The pre-deformational paleoelevation of Hoh Xil Basin has been estimated using stable isotope values from Paleocene - Eocene Fenghuoshan Group carbonates (Cyr et al., 2005), however lipid biomarker and thermochronologic data suggests that these carbonates may have been extensively thermally altered such that elevation estimates derived from these samples may not be reliable (Wang et al., 2008; Polissar et al., 2009; Staisch et al., 2014). Subaerial deposition of the Fenghuoshan Group indicates that the pre-deformational paleoelevation of the Hoh Xil Basin was above sea level since at least the late Cretaceous. We assume that prior to crustal shortening, the Hoh Xil Basin was similar to modern foreland basin systems and was thus at low elevation, likely less than 1 km above sea level (asl). This assumption is based on comparisons to modern foreland basins and palynological evidence from the Hoh Xil Basin that is suggestive of a warm, arid climate (Li and Yuan, 1990). We also assume that the initial crustal thickness was less than the average global crustal thickness (41 km; Christensen and Mooney, 1995) because the Songpan-Ganzi Terrane is likely underlain by oceanic lithosphere or extended continental lithosphere (Şengör and Hsü, 1984; Şengör, 1984; Burchfiel et al., 1995; Bruguier et al., 1997).

Parameters used and isostatic balance

We use a range of initial crustal and lithospheric thicknesses to explore a broad parameter space. We vary initial crustal thickness between 20 and 50 km, and initial lithospheric thickness between 20 and 140 km. The resulting combinations can therefore include conditions in which the lithosphere lacks a mantle root. The relative densities of the crust and mantle lithosphere vary depending on the thickness of the layers. The density of the underlying asthenosphere is invariant to lithospheric thickness. To calculate crustal, mantle lithospheric, and asthenospheric densities, we assume that the temperature at the base of the lithosphere is 1333°C, that the coefficient of thermal expansion is 3.4

$\times 10^{-5}$ K^{-1}, and that the crustal and mantle densities at 0°C are 2850 km m^{-3} and 3330 km m^{-3}, respectively. We also assume a linear geothermal gradient from the base of the lithosphere to the surface. Average densities of the crust and mantle lithosphere are then calculated based on the average temperature of each respective layer. We note that the amount of surface uplift and the range of crustal thicknesses for an initial elevation of 0 – 1 km are dependent on the chosen density structure of the lithosphere. The density of the asthenosphere is invariant to the crustal and lithospheric thicknesses. To calculate the elevation, we balance the continental lithospheric column to a mid-oceanic ridge column with water depth of 2.5 km and density of 1030 km m^{-3}, oceanic crust of 5 km and density 2850 km m^{-3} (Christensen and Wilkins, 1982), and asthenospheric density similar to the continental lithospheric column. We note that the range of initial crustal thickness and the amount of surface uplift is dependent upon the density structure of the lithosphere. By increasing the crustal density, the maximum allowable initial crustal thickness increases noticeably and the amount of surface uplift decreases slightly. Here, we match the majority of trials to the global average crustal density of 2830 kg m^{-3} (Christensen and Mooney, 1995). We consider the global average to be a best estimate for the purposes of our isostatic calculations, although we recognize that the paleo-density structure of the Hoh Xil Basin may have included denser crust, since the Songpan-Ganzi Terrane may be underlain by oceanic of extended continental crust, (Şengör and Hsü, 1984; Şengör, 1984; Burchfiel et al., 1995; Bruguier et al., 1997), and that the modern crustal density estimate from gravity anomalies is much less that our modeled range, possibly due to the heating effects of Neogene magmatism (He et al., 2014). Regardless of the crustal density, our calculations suggest ~28% shortening is not sufficient to attain modern values of crustal thickness in the Hoh Xil Basin.

Isostatic uplift in the absence of shortening

We quantify the amount of elevation gain due to lower crustal flow, preferential thickening of the lower crust and mantle lithosphere, and removal of the mantle lithosphere by calculating the isostatic response to thickening the crust from our post-shortening crustal thickness to the modern crustal thickness in Hoh Xil Basin and to removal of the mantle lithosphere. In all cases, we limit our final results to match the modern elevation (4.5 – 5.5 km), crustal thickness (65 – 75 km; Braitenberg et al., 2000; Vergne et al., 2002; Wittlinger et al., 2004; Karplus et al., 2011), and lithospheric thickness (80 – 120 km; Vozar et al., 2014) of the Hoh Xil Basin.

Lower crustal thickening

We consider two possible models of crustal thickening: (1) we test the effects of preferential shortening of the ductile mid-lower crust and mantle lithosphere by uniformly thickening the lithosphere below 15 km and (2) we test the effects of lower crustal flow by thickening only the crust while the mantle lithosphere retains its post-shortening thickness. In the first thickening scenario, we a value of 15 km as the depth of the brittle-ductile transition, at which point the upper and lower crust are decoupled and the lower crust can deform without leaving surficial evidence of strain (Gans, 1987; Zhang et al., 2011; Chamoli et al., 2014).

Mantle root loss

We calculate the surface uplift due to mantle root loss by removing mantle root material below a depth of 80 – 120 km, based on the a range of lithospheric thickness proposed for northern Tibet.

Results

Our results are plotted in Figure A3.6 and indicate that all proposed mechanisms of uplift in the absence of shortening are capable of reproducing the current dimensions of the northern Tibetan Plateau.

Appendix F: Chapter III

This appendix contains five figures and six tables.

Figure A3.1 contains XRD powder patterns for aliquots from sample 12FHS12, matched to WIDEFIRE© generated illite polytype powder patterns.

Figure A3.2 contains Argon age spectra for volcanic samples collected in the Fenghuoshan Fold and Thrust Belt.

Figure A3.3 contains XRD powder patterns for aliquots from sample 10UMT09, matched to WIDEFIRE© generated illite polytype powder patterns.

Figure A3.4 is an example of modeled Bayesian and York slope and intercept values as a comparison of statistical methods for linear regression.

Figure A3.5 shows modeled slope and intercept values for fault gouge samples from the Fenghuoshan Fold and Thrust Belt.

Figure A3.6 shows isostatic uplift results for mechanisms of uplift in the absence of upper crustal shortening.

Table A3.1 contains Argon isotopic data for fault gouge dating.

Table A3.2 contains apatite (U-Th)/He age data for samples from the Fenghuoshan Fold and Thrust Belt.

Table A3.3 contains apatite fission track age data for 11UMT16.

Table A3.4 contains apatite fission track age data for 11UMT22.

Table A3.5 contains apatite fission track length data for 11UMT16.

Table A3.6 contains apatite fission track age length for 11UMT22.

Table A3.7 contains measured bedding orientations from the Fenghuoshan Fold and Thrust Belt.

Table A3.8 contains a compilation of documented thrust fault activity within the Tibetan Plateau.

Figure A3.1. XRD powder patterns for various size fractions from sample 12FHS12 matched to standard illite polytype powder patterns from the $2M_1$ Owl Creek pegmatite (Wind Rivers Range, WY) and the 1Md IMt-1 standard (Silver Hills, MT). Black line indicates measured XRD pattern for each size fraction. Red line indicates modeled mixture of $2M_1$ and $1M_d$ illite polytypes.

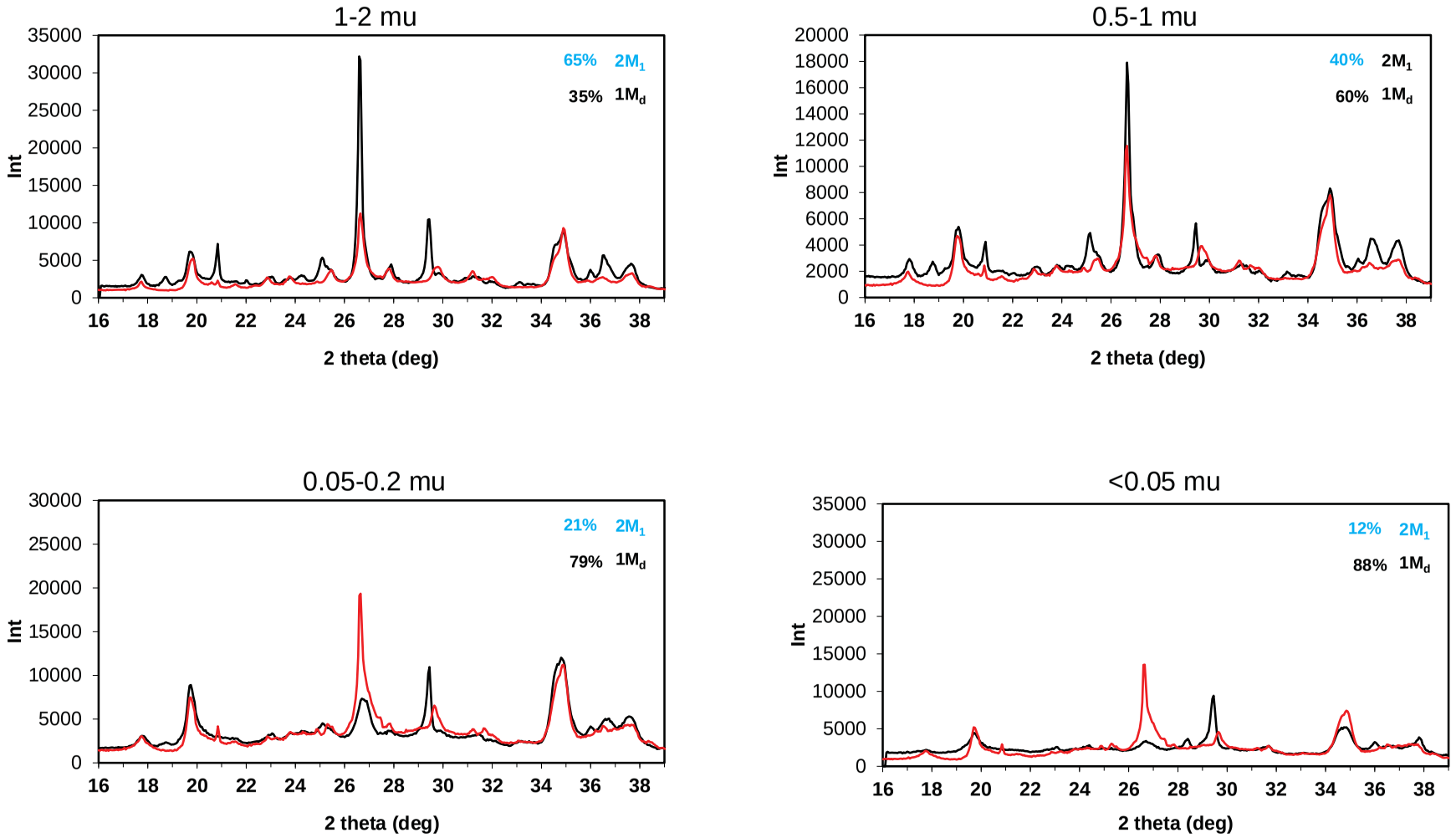

Figure A3.2. $^{40}Ar/^{39}Ar$ age spectra for fault gouge samples collected from the Fenghuoshan Range.

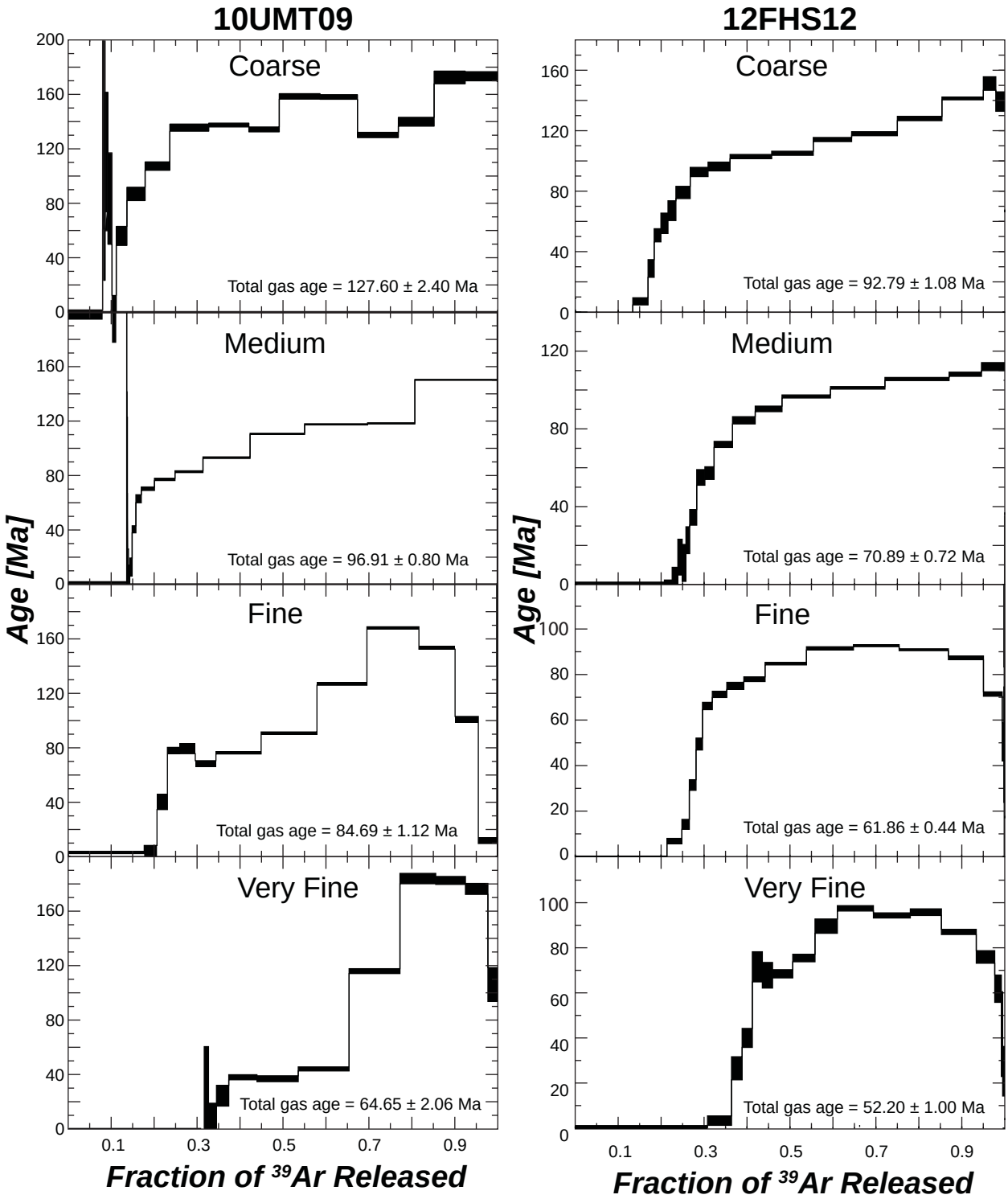

Figure A3.3. XRD powder patterns for various size fractions from sample 10UMT09 matched to standard illite polytype powder patterns from the $2M_1$ Owl Creek pegmatite (Wind Rivers Range, WY) and the 1Md IMt-1 standard (Silver Hills, MT). Black line indicates measured XRD pattern for each size fraction. Red line indicates modeled mixture of $2M_1$ and $1M_d$ illite polytypes.

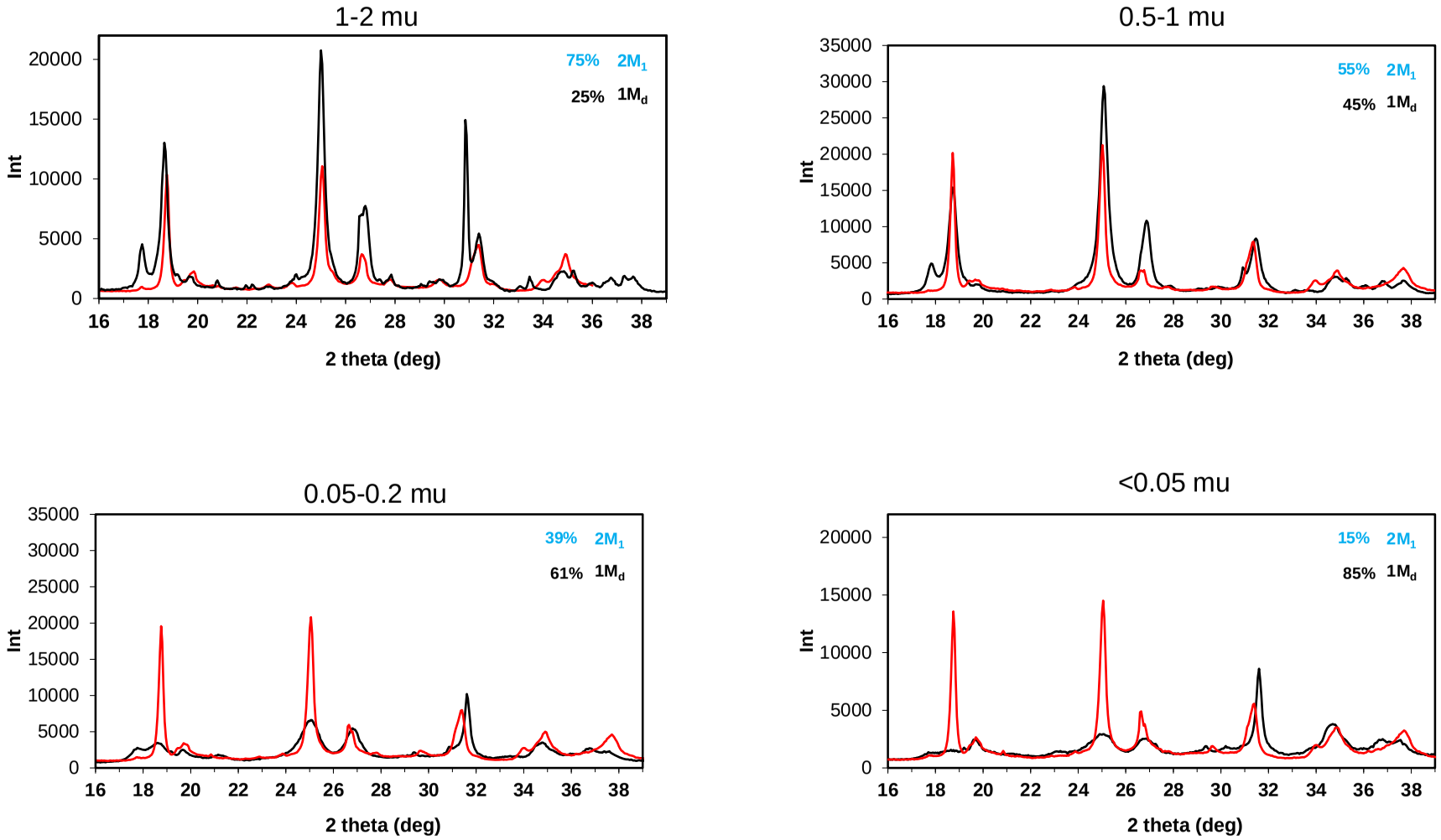

Figure A3.4. Example of Bayesian modeled slope and intercept values for fault gouge data compared to York least-squares linear regression. The mean slope and intercept values for both statistical methods should be similar and/or the same. However, the Bayesian method used in this study models and calculates the likelihood of linear fit through the data, and can resolve the correlation between slope and intercept. This leads to an uncertainty in linear fit that represents the variability within the data and the correlation between modeled parameters. In contrast, the York regression does not resolve the correlation between slope and intercept, such that the combinations of slope and intercept values lead to a range of linear regressions that do not actually fit the data (shown as shaded red regions). The small and large blue ellipses shown for the Bayesian regression represent 68% and 95% confidence intervals.

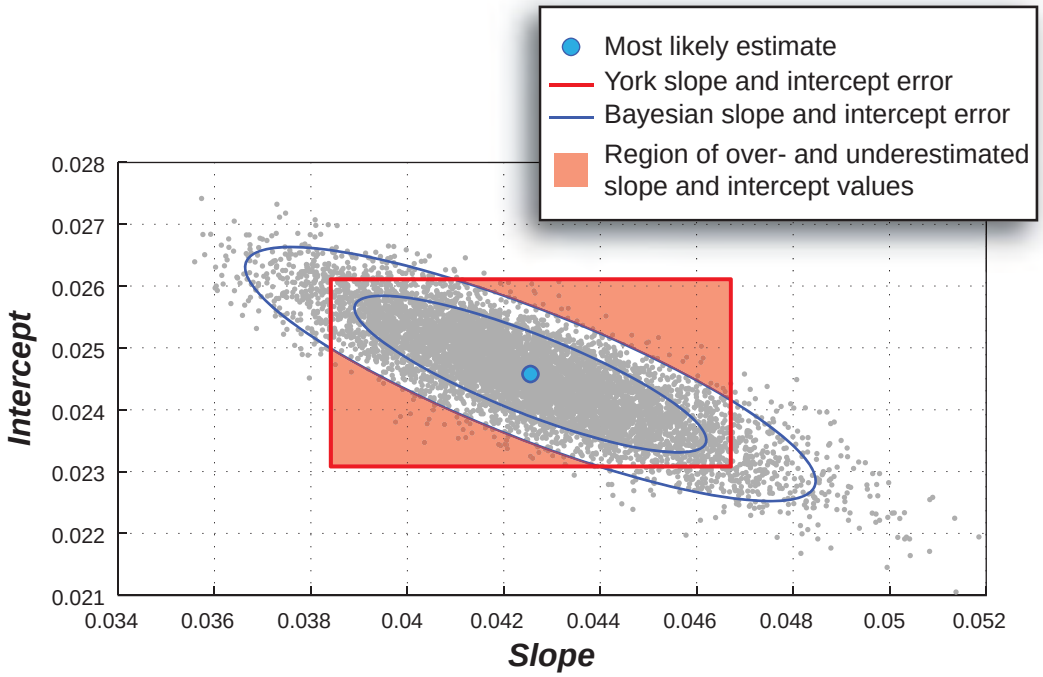

Figure A3.5. Modeled slope and intercept values for fault gouge samples 12FHS12 (top) and 10UMT09 (bottom).Grey dots are the modeled linear fits to fault gouge data, blue dot is the most likely model, and blue ellipses represent the 68% (smaller ellipse) and 95% (larger ellipse) confidence intervals. Marginal PDFs correlate to modeled data.

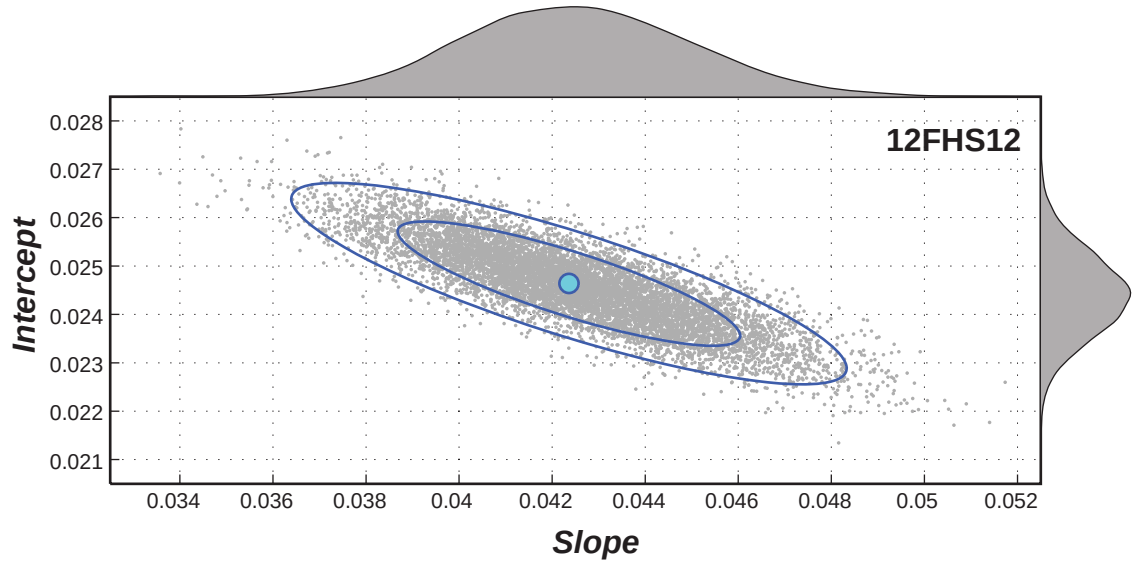

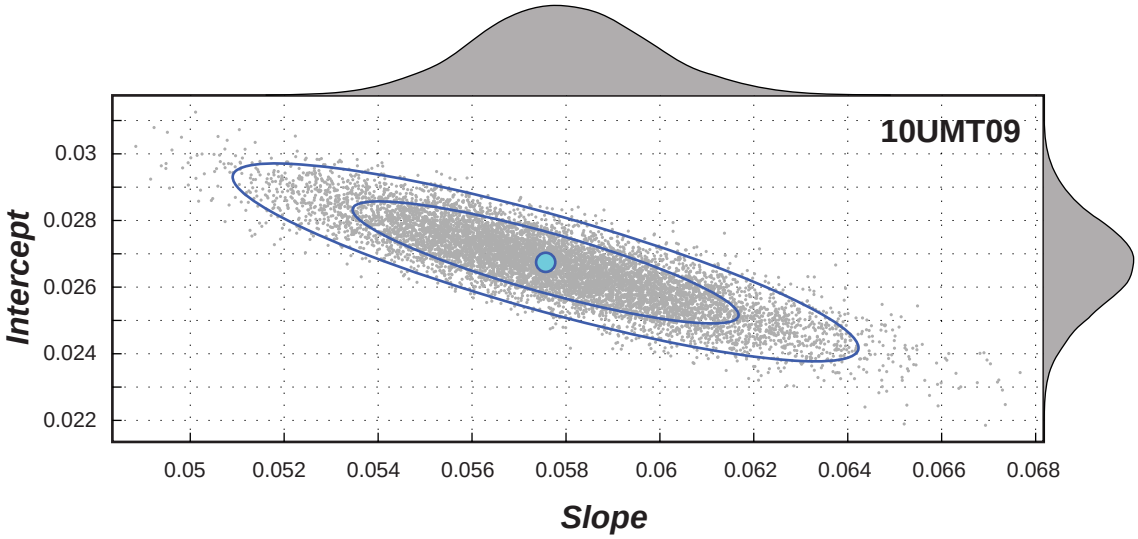

Figure A3.6. Results for isostatic calculations of (a) lower crustal and mantle lithospheric thickening, and (b) lower crustal thickening only. Initial crustal and lithospheric thicknesses are outlined in red, post-28% pure shear crustal and lithospheric thicknesses are outlined in purple, and final conditions following attainment of modern elevation and crustal and lithospheric thickness are outlined in cyan. The range of initial (subscript 0), intermediate (subscript m), and final (subscript f) values of crustal thickness (S), lithospheric thickness (L), and elevation (E) are printed to the right of each uplift scenario. ΔE_1 and ΔE_2 are the change in elevation between steps.

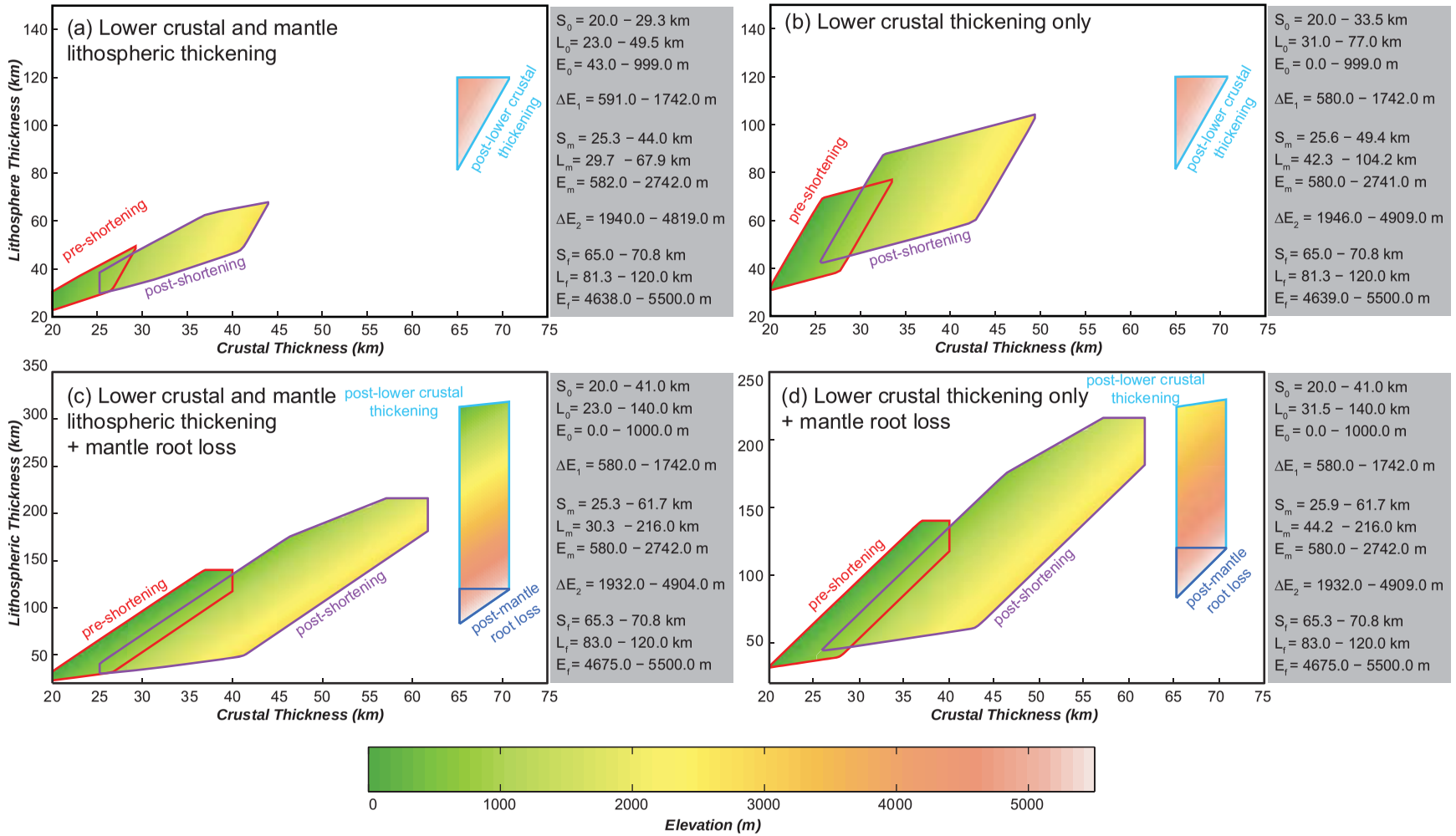

TABLE A3.1. ARGON ISOTOPIC DATA FOR $^{40}Ar/^{39}Ar$ FAULT GOUGE DATING

F39	Laser Power [mW]	Volume [ccSTP] ^{36}Ar	^{37}Ar	^{38}Ar	^{39}Ar	^{40}Ar	Age [Ma]
12FHS12 1 - 2 µm (mc4201) (J=0.00112753) Total gas age = 87.15 ± 1.12 Ma (34.6841° N, 92.6357° E, 4789.8 meters)							
0.134	0	176.346 ± 0.704	15.441 ± 0.236	33.412 ± 0.241	55.679 ± 0.382	50898.246 ± 44.620	-44.829 ± 7.976
0.170	100	0.503 ± 0.058	4.984 ± 0.122	0.590 ± 0.119	14.758 ± 0.168	200.262 ± 0.857	7.117 ± 2.359
0.184	150	0.278 ± 0.058	1.399 ± 0.089	0.055 ± 0.124	5.919 ± 0.141	166.678 ± 0.776	28.863 ± 5.839
0.199	200	0.252 ± 0.045	1.730 ± 0.155	0.167 ± 0.112	6.515 ± 0.200	239.488 ± 1.035	50.816 ± 4.339
0.216	250	0.364 ± 0.078	1.707 ± 0.198	-0.073 ± 0.119	6.853 ± 0.129	308.686 ± 0.911	58.743 ± 6.729
0.234	300	0.354 ± 0.086	1.974 ± 0.154	0.193 ± 0.046	7.667 ± 0.105	362.219 ± 1.234	67.106 ± 6.529
0.268	400	0.523 ± 0.095	3.865 ± 0.146	0.306 ± 0.092	13.825 ± 0.155	704.289 ± 1.075	79.141 ± 4.034
0.309	500	0.435 ± 0.087	4.856 ± 0.164	0.344 ± 0.063	17.281 ± 0.180	936.631 ± 2.454	92.700 ± 3.039
0.361	600	0.556 ± 0.089	7.164 ± 0.173	0.416 ± 0.095	21.308 ± 0.377	1200.523 ± 2.077	96.309 ± 2.906
0.457	800	0.827 ± 0.093	14.845 ± 0.223	0.714 ± 0.058	40.276 ± 0.175	2340.755 ± 2.618	102.882 ± 1.390
0.554	1000	0.945 ± 0.075	15.552 ± 0.281	0.691 ± 0.132	40.225 ± 0.316	2418.956 ± 3.176	105.078 ± 1.337
0.644	1200	0.762 ± 0.083	13.889 ± 0.281	0.638 ± 0.101	37.130 ± 0.165	2376.091 ± 2.410	114.150 ± 1.355
0.750	1600	1.286 ± 0.078	15.505 ± 0.204	0.620 ± 0.091	44.247 ± 0.331	3033.085 ± 2.271	118.023 ± 1.315
0.854	2000	1.138 ± 0.081	12.879 ± 0.232	0.460 ± 0.125	43.159 ± 0.332	3152.121 ± 2.096	128.066 ± 1.424
0.950	2600	1.067 ± 0.056	9.334 ± 0.143	0.628 ± 0.086	40.046 ± 0.141	3210.146 ± 2.522	141.355 ± 0.916
0.979	3200	0.546 ± 0.085	2.354 ± 0.114	0.134 ± 0.139	12.072 ± 0.179	1097.671 ± 2.097	151.228 ± 4.445
1.000	4000	0.356 ± 0.087	2.026 ± 0.176	0.049 ± 0.131	8.582 ± 0.194	716.047 ± 2.948	139.276 ± 6.424
12FHS12 0.5 - 1 µm (mc4202) (J=0.00112341) Total gas age = 70.891 ± 0.359 Ma (34.6841° N, 92.6357° E, 4789.8 meters)							
0.208	0	2.384 ± 0.085	18.820 ± 0.256	3.050 ± 0.169	123.026 ± 0.527	747.906 ± 1.532	0.713 ± 0.416
0.226	100	0.248 ± 0.053	2.101 ± 0.123	0.879 ± 0.109	10.752 ± 0.192	69.362 ± 1.165	-0.756 ± 2.968
0.239	150	0.241 ± 0.056	1.533 ± 0.141	0.389 ± 0.069	7.851 ± 0.145	88.597 ± 1.027	4.472 ± 4.285
0.249	200	0.181 ± 0.093	1.004 ± 0.132	0.170 ± 0.070	5.989 ± 0.137	95.157 ± 0.464	14.007 ± 9.204
0.258	250	0.241 ± 0.082	0.649 ± 0.140	0.223 ± 0.079	5.177 ± 0.093	99.495 ± 0.655	11.027 ± 9.488
0.267	300	0.217 ± 0.061	1.024 ± 0.180	0.222 ± 0.048	5.205 ± 0.111	122.680 ± 0.492	22.715 ± 6.902
0.283	400	0.419 ± 0.065	1.571 ± 0.170	0.286 ± 0.068	9.690 ± 0.223	290.109 ± 1.021	34.462 ± 4.006
0.302	500	0.344 ± 0.076	1.833 ± 0.175	0.578 ± 0.132	11.264 ± 0.171	412.229 ± 1.155	55.011 ± 4.014
0.323	600	0.560 ± 0.068	1.965 ± 0.203	0.369 ± 0.053	12.717 ± 0.227	530.287 ± 1.016	57.224 ± 3.266
0.366	800	0.874 ± 0.064	3.729 ± 0.199	0.680 ± 0.056	25.475 ± 0.188	1181.641 ± 0.988	71.999 ± 1.547
0.419	1000	0.860 ± 0.093	4.511 ± 0.244	0.541 ± 0.114	31.287 ± 0.283	1588.109 ± 2.299	84.406 ± 1.861
0.481	1200	0.957 ± 0.085	5.712 ± 0.093	0.541 ± 0.126	36.992 ± 0.229	1972.413 ± 2.023	90.273 ± 1.426
0.594	1600	1.714 ± 0.064	11.458 ± 0.194	0.957 ± 0.122	66.874 ± 0.398	3782.913 ± 2.282	96.660 ± 0.785
0.721	2000	1.679 ± 0.062	12.759 ± 0.283	0.833 ± 0.125	75.252 ± 0.338	4357.030 ± 2.427	101.099 ± 0.645
0.870	2600	1.886 ± 0.087	15.691 ± 0.246	1.089 ± 0.123	88.532 ± 0.487	5310.096 ± 3.285	105.648 ± 0.795
0.946	3200	0.771 ± 0.077	7.709 ± 0.157	0.624 ± 0.104	44.753 ± 0.177	2688.053 ± 2.279	108.106 ± 1.065
1.000	4000	0.566 ± 0.094	5.537 ± 0.239	0.537 ± 0.107	32.025 ± 0.367	1993.540 ± 1.901	112.017 ± 2.071

TABLE A3.1 CONTINUED. ARGON ISOTOPIC DATA FOR $^{40}Ar/^{39}Ar$ FAULT GOUGE DATING

F39	Laser Power [mW]	Volume [ccSTP] ^{36}Ar	^{37}Ar	^{38}Ar	^{39}Ar	^{40}Ar	Age [Ma]
12FHS12 0.05 - 0.2 µm (mc4203) (J=0.00111771) Total gas age = 61.865 ± 0.219 Ma (34.6841° N, 92.6357° E, 4789.8 meters)							
0.213	0	3.818 ± 0.081	26.379 ± 0.200	4.229 ± 0.162	253.592 ± 0.278	1134.300 ± 1.983	0.047 ± 0.190
0.248	100	0.520 ± 0.083	4.434 ± 0.167	1.564 ± 0.096	41.453 ± 0.205	294.201 ± 1.002	6.819 ± 1.195
0.266	150	0.538 ± 0.075	2.230 ± 0.107	0.464 ± 0.114	20.509 ± 0.197	304.025 ± 0.427	14.183 ± 2.179
0.281	200	0.551 ± 0.072	2.258 ± 0.151	0.363 ± 0.042	18.550 ± 0.246	454.855 ± 1.378	31.457 ± 2.326
0.296	250	0.664 ± 0.079	2.094 ± 0.177	0.345 ± 0.049	17.933 ± 0.192	642.223 ± 1.015	49.469 ± 2.616
0.319	300	0.880 ± 0.073	4.399 ± 0.193	0.575 ± 0.059	27.174 ± 0.178	1168.322 ± 1.931	66.170 ± 1.597
0.353	400	1.245 ± 0.093	6.587 ± 0.232	0.724 ± 0.077	40.023 ± 0.166	1810.917 ± 1.902	71.274 ± 1.372
0.393	500	1.099 ± 0.119	5.716 ± 0.170	0.671 ± 0.065	47.132 ± 0.374	2115.074 ± 2.386	75.010 ± 1.555
0.442	600	1.135 ± 0.097	7.401 ± 0.246	0.673 ± 0.055	58.737 ± 0.267	2655.566 ± 5.143	77.948 ± 1.019
0.538	800	1.695 ± 0.084	17.944 ± 0.210	1.124 ± 0.102	114.510 ± 0.498	5430.522 ± 2.691	84.783 ± 0.553
0.648	1000	1.866 ± 0.136	28.073 ± 0.169	1.216 ± 0.079	129.959 ± 0.548	6599.143 ± 9.241	91.476 ± 0.714
0.754	1200	1.690 ± 0.063	38.711 ± 0.337	0.933 ± 0.095	126.411 ± 0.440	6461.010 ± 7.675	92.674 ± 0.438
0.869	1600	1.790 ± 0.068	66.366 ± 0.496	1.266 ± 0.085	136.286 ± 0.381	6828.901 ± 10.177	90.885 ± 0.404
0.951	2000	1.381 ± 0.124	67.152 ± 0.478	0.950 ± 0.077	96.980 ± 0.365	4711.326 ± 7.312	87.326 ± 0.809
0.994	2600	1.041 ± 0.084	64.222 ± 0.434	0.771 ± 0.066	51.809 ± 0.173	2179.611 ± 2.532	71.424 ± 0.959
0.998	3200	0.275 ± 0.066	2.641 ± 0.141	0.238 ± 0.046	4.648 ± 0.089	199.140 ± 0.725	50.397 ± 8.347
1.000	4000	0.182 ± 0.096	0.390 ± 0.117	0.231 ± 0.060	2.198 ± 0.089	108.059 ± 0.533	49.193 ± 25.348
12FHS12 < 0.05 µm (mc4204) (J=0.00111189) Total gas age = 52.197 ± 0.502 Ma (34.6841° N, 92.6357° E, 4789.8 meters)							
0.308	0	5.414 ± 0.195	59.237 ± 0.338	14.194 ± 0.197	155.116 ± 0.533	1628.316 ± 1.535	0.367 ± 0.744
0.364	100	1.751 ± 0.099	12.466 ± 0.139	3.418 ± 0.073	28.136 ± 0.227	564.181 ± 2.429	3.321 ± 2.092
0.389	150	0.693 ± 0.108	5.315 ± 0.136	0.926 ± 0.109	12.436 ± 0.200	370.414 ± 1.091	26.540 ± 5.110
0.412	200	2.122 ± 0.085	5.015 ± 0.137	1.083 ± 0.077	11.950 ± 0.224	867.987 ± 1.708	40.011 ± 4.209
0.436	250	3.934 ± 0.136	6.289 ± 0.169	1.468 ± 0.087	11.719 ± 0.136	1588.817 ± 1.825	71.553 ± 6.678
0.459	300	3.690 ± 0.117	6.392 ± 0.175	1.696 ± 0.099	11.977 ± 0.159	1503.122 ± 1.446	67.807 ± 5.672
0.506	400	3.864 ± 0.072	11.875 ± 0.281	2.954 ± 0.118	23.678 ± 0.180	1965.384 ± 3.108	68.462 ± 1.818
0.558	500	1.155 ± 0.071	12.134 ± 0.221	1.431 ± 0.102	26.079 ± 0.209	1343.160 ± 1.315	75.459 ± 1.666
0.610	600	0.730 ± 0.140	17.351 ± 0.271	0.547 ± 0.074	26.179 ± 0.286	1414.517 ± 1.408	89.601 ± 3.171
0.694	800	1.044 ± 0.073	35.814 ± 0.435	0.715 ± 0.063	42.276 ± 0.298	2419.944 ± 2.619	97.506 ± 1.182
0.780	1000	1.266 ± 0.063	40.505 ± 0.155	0.860 ± 0.081	43.244 ± 0.365	2462.232 ± 2.591	94.354 ± 1.136
0.853	1200	1.154 ± 0.085	40.291 ± 0.359	0.781 ± 0.068	36.462 ± 0.249	2129.452 ± 2.181	95.806 ± 1.466
0.934	1600	2.133 ± 0.074	64.985 ± 0.472	1.369 ± 0.092	40.853 ± 0.224	2446.496 ± 4.202	87.037 ± 1.143
0.977	2000	1.691 ± 0.100	44.419 ± 0.244	1.066 ± 0.063	21.659 ± 0.248	1337.074 ± 2.387	75.927 ± 2.779
0.992	2600	0.962 ± 0.080	10.831 ± 0.255	0.491 ± 0.041	7.718 ± 0.145	526.421 ± 0.967	61.849 ± 6.055
0.995	3200	0.284 ± 0.051	0.773 ± 0.177	0.188 ± 0.094	1.581 ± 0.090	117.169 ± 0.651	41.691 ± 18.786
1.000	4000	0.163 ± 0.045	1.835 ± 0.190	0.100 ± 0.075	2.440 ± 0.098	78.967 ± 1.252	25.232 ± 10.985

TABLE A3.1 CONTINUED. ARGON ISOTOPIC DATA FOR $^{40}Ar/^{39}Ar$ FAULT GOUGE DATING

F39	Laser Power [mW]	Volume [ccSTP] ^{36}Ar	^{37}Ar	^{38}Ar	^{39}Ar	^{40}Ar	Age [Ma]
10UMT09 0.5 - 1 µm (mc3210) (J=0.0040476) Total gas age = 127.605 ± 1.201 Ma (34.5188° N, 92.7331° E, 4647 meters)							
0.080	0	3.490 ± 0.106	15.318 ± 0.373	1.860 ± 0.125	63.381 ± 0.366	1014.076 ± 1.589	-1.980 ± 3.604
0.082	100	-0.185 ± 0.144	0.176 ± 0.187	0.043 ± 0.067	1.986 ± 0.095	3.392 ± 0.534	201.893 ± 140.618
0.086	150	-0.135 ± 0.132	0.438 ± 0.190	0.056 ± 0.089	2.768 ± 0.117	6.980 ± 0.726	119.733 ± 96.322
0.092	200	-0.170 ± 0.130	0.699 ± 0.171	0.167 ± 0.077	5.170 ± 0.087	30.880 ± 0.694	110.988 ± 51.052
0.102	250	-0.116 ± 0.123	1.347 ± 0.226	0.271 ± 0.076	7.518 ± 0.164	54.008 ± 0.933	83.730 ± 33.726
0.112	300	0.315 ± 0.063	1.492 ± 0.195	-0.028 ± 0.061	7.774 ± 0.110	87.472 ± 0.838	-5.205 ± 17.429
0.137	400	0.301 ± 0.066	5.136 ± 0.278	0.242 ± 0.101	19.744 ± 0.233	243.182 ± 0.898	56.157 ± 7.007
0.179	500	0.325 ± 0.080	9.192 ± 0.196	0.488 ± 0.042	33.638 ± 0.219	507.351 ± 1.601	87.125 ± 4.903
0.237	600	0.459 ± 0.069	10.182 ± 0.207	0.521 ± 0.062	45.709 ± 0.181	829.829 ± 1.639	107.636 ± 3.092
0.327	800	0.635 ± 0.091	14.441 ± 0.287	0.701 ± 0.111	71.897 ± 0.326	1578.548 ± 2.919	136.004 ± 2.613
0.421	1000	0.495 ± 0.049	25.666 ± 0.276	0.951 ± 0.075	74.082 ± 0.245	1600.312 ± 1.723	137.912 ± 1.398
0.491	1200	0.442 ± 0.045	21.027 ± 0.140	0.840 ± 0.069	56.157 ± 0.288	1206.083 ± 3.015	134.676 ± 1.789
0.586	1600	0.590 ± 0.070	17.263 ± 0.168	0.811 ± 0.094	75.337 ± 0.325	1889.528 ± 4.234	159.026 ± 1.997
0.673	2000	0.814 ± 0.053	15.795 ± 0.211	0.819 ± 0.068	69.130 ± 0.320	1810.000 ± 2.183	158.594 ± 1.680
0.769	2600	0.874 ± 0.069	23.378 ± 0.252	1.166 ± 0.086	75.591 ± 0.335	1660.038 ± 2.651	130.581 ± 1.937
0.852	3200	0.724 ± 0.104	18.125 ± 0.311	0.756 ± 0.087	66.120 ± 0.356	1535.497 ± 2.128	140.335 ± 3.242
0.924	4000	0.895 ± 0.136	11.422 ± 0.162	0.685 ± 0.083	57.382 ± 0.171	1691.380 ± 1.981	172.999 ± 4.670
1.000	4001	0.663 ± 0.094	12.206 ± 0.330	0.695 ± 0.082	60.064 ± 0.491	1697.252 ± 3.116	173.879 ± 3.357
10UMT09 0.2 - 0.5 µm (mc3209) (J=0.00413512) Total gas age = 96.912 ± 0.405 Ma (34.5188° N, 92.7331° E, 4647 meters)							
0.136	0	8.041 ± 0.148	38.031 ± 0.303	18.757 ± 0.178	611.115 ± 0.793	2491.091 ± 2.278	1.405 ± 0.535
0.136	100	0.045 ± 0.068	0.280 ± 0.110	0.057 ± 0.062	-0.081 ± 0.077	1.441 ± 0.837	850.596 ± 1310.955
0.136	150	0.002 ± 0.080	0.302 ± 0.104	0.235 ± 0.051	1.136 ± 0.076	-1.573 ± 0.750	-14.010 ± 155.659
0.138	200	-0.275 ± 0.083	0.496 ± 0.104	0.942 ± 0.056	6.211 ± 0.140	-0.142 ± 0.803	94.785 ± 28.043
0.140	250	-0.084 ± 0.055	0.720 ± 0.121	0.872 ± 0.102	11.177 ± 0.128	-1.961 ± 0.891	15.237 ± 10.740
0.143	300	0.034 ± 0.064	0.917 ± 0.180	0.682 ± 0.088	13.439 ± 0.147	16.619 ± 0.884	3.647 ± 10.477
0.149	400	0.246 ± 0.076	1.488 ± 0.199	1.130 ± 0.091	24.987 ± 0.250	115.196 ± 0.629	12.681 ± 6.636
0.157	500	0.394 ± 0.047	2.475 ± 0.213	1.305 ± 0.088	39.179 ± 0.245	331.270 ± 0.938	40.446 ± 2.587
0.170	600	0.391 ± 0.077	3.529 ± 0.201	1.438 ± 0.134	56.195 ± 0.226	597.932 ± 1.471	62.918 ± 2.933
0.201	800	0.982 ± 0.082	8.753 ± 0.192	2.803 ± 0.122	137.903 ± 0.366	1615.434 ± 2.871	70.297 ± 1.280
0.248	1000	1.445 ± 0.080	13.611 ± 0.228	3.268 ± 0.136	214.468 ± 0.731	2692.530 ± 3.651	77.137 ± 0.836
0.314	1200	1.799 ± 0.089	18.726 ± 0.389	4.033 ± 0.130	292.837 ± 0.387	3857.701 ± 3.158	82.807 ± 0.654
0.423	1600	2.744 ± 0.124	30.445 ± 0.406	5.774 ± 0.191	492.727 ± 0.730	7122.296 ± 7.609	93.114 ± 0.555
0.550	2000	3.093 ± 0.113	34.212 ± 0.436	6.101 ± 0.191	570.068 ± 0.862	9628.936 ± 4.119	110.588 ± 0.443
0.697	2600	3.440 ± 0.119	39.141 ± 0.380	7.530 ± 0.105	658.700 ± 0.997	11747.344 ± 5.619	117.613 ± 0.415
0.807	3200	2.624 ± 0.080	29.675 ± 0.191	6.011 ± 0.072	494.592 ± 1.004	8882.963 ± 6.370	118.322 ± 0.418
1.000	4000	4.928 ± 0.122	48.855 ± 0.348	9.857 ± 0.167	866.218 ± 0.731	19657.645 ± 12.832	150.316 ± 0.326

TABLE A3.1 CONTINUED. ARGON ISOTOPIC DATA FOR $^{40}Ar/^{39}Ar$ FAULT GOUGE DATING

F39	Laser Power [mW]	Volume [ccSTP] ^{36}Ar	^{37}Ar	^{38}Ar	^{39}Ar	^{40}Ar	Age [Ma]
10UMT09 0.05 - 0.2 µm (mc3317) (J=0.0041400) Total gas age = 84.689 ± 0.556 Ma (34.5188° N, 92.7331° E, 4647 meters)							
0.177	0	2.511 ± 0.113	11.970 ± 0.159	3.527 ± 0.120	221.407 ± 0.532	832.706 ± 0.926	3.062 ± 1.127
0.207	100	0.243 ± 0.070	2.008 ± 0.246	1.241 ± 0.072	37.321 ± 0.332	90.656 ± 0.631	3.774 ± 4.140
0.231	150	0.350 ± 0.082	1.236 ± 0.260	0.600 ± 0.053	30.383 ± 0.275	268.766 ± 0.933	40.161 ± 5.825
0.260	200	0.354 ± 0.041	1.452 ± 0.191	0.655 ± 0.083	36.429 ± 0.281	491.628 ± 0.758	77.660 ± 2.449
0.296	250	0.365 ± 0.079	1.994 ± 0.187	0.803 ± 0.077	44.839 ± 0.186	593.937 ± 1.053	79.204 ± 3.730
0.344	300	0.527 ± 0.060	2.980 ± 0.165	0.875 ± 0.083	60.254 ± 0.276	716.269 ± 1.581	68.178 ± 2.132
0.449	400	0.742 ± 0.066	7.104 ± 0.241	1.616 ± 0.084	131.763 ± 0.312	1595.166 ± 1.837	76.352 ± 1.073
0.579	500	1.009 ± 0.069	8.264 ± 0.358	1.814 ± 0.123	162.769 ± 0.350	2321.843 ± 2.359	90.549 ± 0.916
0.696	600	0.839 ± 0.057	6.911 ± 0.187	1.429 ± 0.097	145.750 ± 0.671	2812.957 ± 4.225	126.873 ± 1.002
0.817	800	0.873 ± 0.053	6.748 ± 0.225	1.463 ± 0.099	151.629 ± 0.551	3831.483 ± 4.191	167.951 ± 0.935
0.901	1000	0.557 ± 0.050	4.609 ± 0.170	1.211 ± 0.101	105.402 ± 0.472	2427.428 ± 2.891	153.615 ± 1.184
0.955	1200	0.300 ± 0.073	3.425 ± 0.214	0.798 ± 0.059	67.779 ± 0.371	1027.302 ± 1.303	100.571 ± 2.302
0.998	1600	0.212 ± 0.051	2.803 ± 0.291	0.415 ± 0.078	53.955 ± 0.317	145.392 ± 0.607	11.421 ± 2.080
0.998	2000	-0.018 ± 0.045	-0.291 ± 0.203	0.077 ± 0.049	0.255 ± 0.087	43.597 ± 0.671	1055.293 ± 348.700
0.999	2600	0.313 ± 0.062	0.062 ± 0.190	0.108 ± 0.061	1.040 ± 0.084	93.970 ± 0.672	9.956 ± 130.020
0.999	3200	0.614 ± 0.068	-0.007 ± 0.190	0.133 ± 0.031	0.444 ± 0.094	142.583 ± 0.795	-809.014 ± 571.453
1.000	4000	0.982 ± 0.073	-0.015 ± 0.149	0.223 ± 0.029	0.736 ± 0.072	284.651 ± 0.940	-58.450 ± 226.841
10UMT09 < 0.05 µm (mc3207) (J=0.00419086) Total gas age = 64.646 ± 1.032 Ma (34.5188° N, 92.7331° E, 4647 meters)							
0.308	0	11.669 ± 0.172	13.065 ± 0.267	736.098 ± 1.148	251.357 ± 0.332	3419.918 ± 5.265	-0.850 ± 1.540
0.308	100	0.255 ± 0.072	0.109 ± 0.135	1.161 ± 0.079	0.029 ± 0.073	2.292 ± 0.615	-486444625.850 ± 5110.199
0.309	150	0.115 ± 0.072	0.059 ± 0.113	2.317 ± 0.072	0.035 ± 0.070	-3.718 ± 0.673	-3508028.958 ± 4821.052
0.309	200	0.207 ± 0.079	0.271 ± 0.108	6.194 ± 0.146	0.625 ± 0.072	-4.376 ± 0.831	-1044.035 ± 532.116
0.312	250	0.145 ± 0.076	0.267 ± 0.108	9.035 ± 0.146	2.167 ± 0.120	-3.168 ± 0.748	-167.805 ± 86.982
0.316	300	0.145 ± 0.070	0.366 ± 0.193	11.528 ± 0.120	2.975 ± 0.121	16.928 ± 0.834	-66.885 ± 54.618
0.326	400	0.100 ± 0.126	0.712 ± 0.122	24.906 ± 0.138	8.125 ± 0.180	58.011 ± 1.314	26.190 ± 34.284
0.344	500	0.306 ± 0.090	0.767 ± 0.177	25.877 ± 0.216	15.160 ± 0.144	101.944 ± 1.038	5.687 ± 13.164
0.373	600	0.358 ± 0.081	1.403 ± 0.121	18.542 ± 0.159	23.348 ± 0.174	181.689 ± 1.212	24.386 ± 7.624
0.439	800	0.710 ± 0.045	3.147 ± 0.171	18.361 ± 0.181	53.570 ± 0.434	481.476 ± 1.109	37.953 ± 1.858
0.535	1000	0.823 ± 0.077	4.399 ± 0.200	14.081 ± 0.162	78.479 ± 0.375	629.837 ± 1.001	36.860 ± 2.143
0.653	1200	0.766 ± 0.065	5.555 ± 0.140	12.610 ± 0.171	96.673 ± 0.339	797.049 ± 0.904	44.086 ± 1.471
0.772	1600	1.092 ± 0.080	8.698 ± 0.139	13.657 ± 0.159	96.646 ± 0.322	1854.143 ± 2.089	115.999 ± 1.783
0.856	2000	1.049 ± 0.126	10.075 ± 0.220	5.282 ± 0.085	68.017 ± 0.286	2053.122 ± 2.089	184.056 ± 3.805
0.925	2600	0.987 ± 0.078	10.764 ± 0.243	1.731 ± 0.111	56.451 ± 0.227	1726.959 ± 4.191	182.680 ± 2.914
0.977	3200	0.726 ± 0.081	9.088 ± 0.250	1.226 ± 0.098	42.734 ± 0.282	1262.418 ± 0.886	176.484 ± 4.005
1.000	4000	1.520 ± 0.109	2.236 ± 0.093	0.757 ± 0.102	18.547 ± 0.214	717.288 ± 1.176	106.133 ± 12.428

TABLE A3.2. APATITE (U-Th)/He AGE DATA FROM THE FENGHUOSHAN FOLD AND THRUST BELT

Sample	rep.	U [ppm]	Th [ppm]	Sm [ppm]	He [ppm]	mass [μg]	Ft[a]	width [μm]	length [μm]	ESR[b] [μm]	Raw Age [Ma]	Corrected Age [Ma]	Mean Age [Ma]	Std. Dev. [Ma]
11UMT16														
	a	46.66	115.56	100.00	0.0254	0.62	0.69	80	78	39.66	15.85	23.12	24.23	1.71
	† b	23.40	107.08	221.43	0.0214	0.78	0.66	71	83	37.30	20.16	30.63		
	c	4.99	28.64	86.83	0.0047	0.63	0.70	82	84	41.33	18.22	26.19		
	d	132.95	483.45	484.97	0.0871	1.00	0.70	78	112	43.39	16.25	23.36		
	† e	26.97	41.76	220.30	0.0133	0.53	0.63	62	99	35.41	16.66	26.57		
11UMT22														
	a	99.20	64.15	40.72	0.0492	0.85	0.70	80	99	42.73	19.91	28.56	28.16	1.33
	b	12.66	19.51	111.15	0.0067	0.64	0.67	76	77	38.17	17.93	26.68		
	c	7.39	18.27	131.83	0.0054	1.10	0.72	85	121	48.17	21.04	29.25		
	* d	13.64	29.90	109.78	0.0034	1.22	0.75	100	103	50.49	7.55	10.09		
	† e	16.54	40.90	116.11	0.0102	0.74	0.64	64	106	36.87	17.86	27.93		

[a] Ft correction (Farley et al., 1996)
[b] Equivalent spherical radius
*sample deemed outlier based on Dixon's q-test, and not used for mean age calculation or HeFTy modeling
†sample not used for mean age calculation or HeFTy modeling due to small grain radius

Table A3.3. Apatite fission track age data for sample 11UMT16. Samples marked by † and * were not included in analysis due to high U/Cation values (which may be indicate that an inclusion was hit by the laser) and LA-ICPMS failure, respectively.

Apatite Fission Track (age data)

Sample#	Grain #	N_s	Area (cm^2)	$^{238}U/^{43}Ca$	1σ	^{43}Ca	^{238}U	^{232}Th	^{147}Sm	FT Age (Ma)	1σ (Ma)	Etch	Dpar (μm)	Dper (μm)	U (ppm)	Th (ppm)	Sm (ppm)	Pit Depth (μm)	rmr0	Population
11UMT16	1	58	3.11E-05	0.606	0.053	38.6932	10.3765	0.0779	0.0215	25.42	4.03	4	2.07	0.51	101	1	169	19.0	0.757	
	2	6	1.75E-05	0.076	0.007	38.6859	1.9242	6.0377	0.0741	37.27	15.58	4	2.08	0.31	16	75	487	17.8	0.795	2
	3	3	1.75E-05	0.042	0.004	38.6785	1.0277	3.8678	0.0177	33.36	19.51	4	2.78	0.66	10	59	129	17.8	0.753	1
	4	21	1.94E-05	0.446	0.039	38.6711	9.8892	4.4351	0.0712	20.04	4.72	4	1.9	0.38	101	67	488	17.8	0.852	
	5*	1	1.75E-05	0.000	0.000	0.0000	0.0000	0.0000	0.0000	0.00	0.00	1	2.05	0.34	0	0	0	0.0	-	
	6	3	2.43E-05	0.008	0.001	38.6564	0.1898	0.2794	0.0026	121.57	71.14	2	2.37	0.48	2	4	18	17.2	0.848	
	7	15	3.88E-05	0.073	0.007	38.6490	1.1772	3.0495	0.0061	43.52	11.94	4	3.41	11.3	10	45	40	18.4	0.851	
	8	6	1.16E-05	0.057	0.005	38.6417	1.4306	0.6444	0.0184	73.80	30.90	3	1.85	0.32	14	9	117	17.8	0.859	
	9	3	1.94E-05	0.044	0.004	38.6343	1.1006	0.0125	0.0202	28.79	16.83	2	2.08	0.37	12	0	128	17.8	0.817	2
	10	36	1.75E-05	0.760	0.068	38.6270	13.0496	14.9243	0.0338	22.37	4.25	4	1.79	0.32	131	226	232	18.4	0.853	
	11	0	9.71E-06	0.020	0.002	38.6196	0.4540	0.2337	0.0504	0.00	0.00	1	2.14	0.26	5	5	294	18.4	0.770	2
	12	23	1.75E-05	0.455	0.040	38.6123	10.6906	0.6918	0.0193	23.87	5.42	4	2.11	0.31	112	11	146	17.8	0.856	
	13	4	1.36E-05	0.111	0.010	38.6049	2.0448	1.5239	0.0060	21.96	11.16	3	2.25	0.46	25	24	46	18.4	0.856	
	14	7	1.94E-05	0.062	0.005	38.5976	1.4797	3.0017	0.0308	48.30	18.78	3	2.18	0.44	14	49	222	18.4	0.729	1
	15	35	3.11E-05	0.406	0.035	38.5903	9.1202	3.5411	0.0001	22.90	4.37	4	1.85	0.39	80	50	1	17.8	0.863	
	16*	2	3.11E-05	0.000	0.000	0.0000	0.0000	0.0000	0.0000	0.00	0.00	1	1.92	0.4	0	0	0	0.0	-	
	17	3	1.16E-05	0.065	0.006	38.5756	1.4952	2.4691	0.0215	32.45	18.96	2	2.04	0.39	16	38	156	18.4	0.828	
	18	3	1.16E-05	0.002	0.000	38.5683	0.0715	40.6676	0.0953	845.37	513.60	2	1.95	0.32	1	702	891	18.4	0.638	1
	19*	1	1.21E-05	0.000	0.000	0.0000	0.0000	0.0000	0.0000	0.00	0.00	1	2.06	0.32	0	0	0	0.0	-	
	20	4	1.75E-05	0.104	0.009	38.5536	2.3497	6.5859	0.0195	18.11	9.21	2	2.45	0.49	27	113	144	18.4	0.857	
	21	1	1.75E-05	0.022	0.002	38.5463	0.4246	0.4699	0.0134	21.18	21.28	4	1.82	0.39	4	7	91	19.0	0.857	
	22	2	1.21E-05	0.041	0.004	38.5390	1.1986	0.4479	0.0052	33.39	23.80	2	1.86	0.41	11	6	36	19.0	0.851	
	23	2	1.46E-05	0.068	0.006	38.5317	1.4997	0.0713	0.0223	16.63	11.86	2	1.65	0.34	14	1	144	17.8	0.822	2
	24	1	1.21E-05	0.022	0.002	38.5244	0.4149	0.5299	0.0423	30.65	30.79	1	1.95	0.38	4	8	304	17.8	0.860	
	25	3	3.88E-05	0.012	0.001	38.5171	0.2677	0.6812	0.0220	53.72	31.44	2	1.85	0.3	2	11	151	18.4	0.823	2
	26†	34	9.71E-06	1.212	0.105	38.5098	27.8822	0.5435	0.0449	23.87	4.61	4	2.06	0.35	271	7	299	18.4	-	
	27	1	1.21E-05	0.003	0.000	38.5025	0.0561	0.0130	0.0035	239.25	241.91	1	2.01	0.4	1	20	40	18.4	0.856	
	28	4	4.85E-05	0.027	0.002	38.4952	0.6768	0.9917	0.0508	25.14	12.77	3	1.94	0.39	6	14	345	17.8	0.801	2
	29	2	9.71E-06	0.032	0.003	38.4879	0.6414	2.5356	0.0074	53.63	38.24	2	1.67	0.35	7	39	50	18.4	0.850	
	30	24	2.91E-05	0.261	0.023	38.4806	5.9604	0.0167	0.0394	26.10	5.81	4	2.04	0.27	56	0	272	16.1	0.828	2
	31	2	2.43E-05	0.018	0.002	38.4733	0.3472	0.7613	0.0405	38.45	27.48	4	1.87	0.34	3	12	243	18.4	0.806	2
	32	7	2.33E-05	0.085	0.008	38.4660	1.5272	0.6581	0.0525	29.34	11.42	4	2.38	0.42	15	10	387	19.0	0.000	1
	33†	25	1.21E-05	1.046	0.091	38.4587	23.0955	52.1735	0.0389	16.28	3.56	4	2.18	0.45	215	752	236	18.4	-	
	34	4	3.40E-05	0.014	0.002	38.4514	0.3653	0.5165	0.0125	70.14	35.92	2	1.76	0.3	4	8	104	19.0	0.786	2
	35	4	1.75E-05	0.128	0.011	38.4441	2.5511	4.1823	0.0881	14.82	7.53	3	1.97	0.31	24	65	528	18.4	0.834	
	36	7	1.75E-05	0.082	0.007	38.4369	1.8748	5.0048	0.0214	40.27	15.65	4	2.08	0.25	17	72	168	17.8	0.800	2
	37	1	1.21E-05	0.025	0.002	38.4296	0.4103	1.3331	0.0377	27.74	27.86	1	2.34	0.51	4	22	240	18.4	0.773	2
	38	2	1.46E-05	0.058	0.005	38.4223	1.2310	0.5692	0.0439	19.44	13.86	2	1.95	0.56	14	9	287	17.8	0.786	2
	39	1	1.75E-05	0.041	0.004	38.4150	0.9313	2.6404	0.0354	11.56	11.61	1	2.06	0.4	9	37	229	17.8	0.785	2
	40	19	2.91E-05	0.213	0.019	38.4078	4.3765	0.8661	0.0295	25.31	6.23	4	2.19	0.39	43	13	217	18.4	0.761	
Primary Zeta	8.2727	0.1407																		

All Data		**Population 1**	**Population 2**
Mean Dpar	2.08	2.32	1.99
Mean Dper	0.68	0.46	0.35
Mean rmr0	0.790	0.53	0.80
Mean track length	14.06 ± 1.26	14.24 ± 1.18	14.17 ± 1.28
# of grains	35	4	13
Reduced Chi-squared	2.22	0.41	0.79
Pooled Age (Ma)	26.18 ± 3.39	41.90 ± 9.7	31.00 ± 9.8

Table A3.4. Apatite fission track age data for sample 11UMT22. Samples marked by † and * were not included in analysis due to high U/Cation values (which may be indicate that an inclusion was hit by the laser) and LA-ICPMS failure, respectively.

Apatite Fission Track (age data)

Sample#	Grain #	N_s	Area (cm^2)	$^{238}U/^{43}Ca$	1σ	^{43}Ca	^{238}U	^{232}Th	^{147}Sm	FT Age (Ma)	1σ (Ma)	Etch	Dpar (µm)	Dper (µm)	U (ppm)	Th (ppm)	Sm (ppm)	Pit Depth (µm)	rmr0	Population
11UMT22	1†	10	1.16E-05	4.24E-01	7.95E-03	3.54E+01	1.50E+01	1.48E+01	7.61E-02	6.57	2.08	3	2.13	0.48	131	207	648	18.95	-	
	2	1	1.94E-05	1.45E-02	7.11E-04	3.71E+01	5.38E-01	1.04E-01	1.87E-02	17.42	17.44	2	1.66	0.24	6	2	151	17.80	0.852	
	3*	1	1.21E-05	1.02E-01	9.48E-03	1.14E+01	1.17E+00	1.31E+00	0.00E+00	0.00	5.03	1	1.89	0.3	58	90	0	17.80	-	
	4	5	9.71E-06	5.28E-02	2.11E-03	3.47E+01	1.83E+00	1.97E-01	1.02E-02	37.33	16.77	4	1.88	0.31	20	5	86	18.37	0.842	1
	5	2	1.16E-05	4.40E-03	2.85E-04	3.62E+01	1.59E-01	6.31E-01	9.77E-03	201.81	143.32	2	2.11	0.3	2	10	99	17.80	0.807	2
	6	1	2.43E-05	1.37E-02	4.55E-04	3.79E+01	5.18E-01	1.27E+00	2.42E-02	16.19	16.20	1	2.41	0.45	5	20	213	17.80	0.774	2
	7	5	7.28E-06	1.10E-01	2.83E-03	3.60E+01	3.95E+00	9.22E+00	1.05E-01	28.82	12.91	2	1.85	0.35	38	128	806	18.37	0.852	
	8*	3	7.77E-06	1.16E-01	3.22E-03	3.75E+01	4.34E+00	1.97E+00	1.04E-02	0.00	8.80	2	2	0.3	45	29	92	18.37	-	
	9	2	8.74E-06	3.34E-02	1.15E-03	3.67E+01	1.22E+00	4.86E+00	5.76E-02	35.98	25.47	3	2.22	0.36	12	85	522	18.37	0.788	2
	10*	2	7.77E-06	1.58E-01	3.03E-02	1.48E+01	2.34E+00	3.28E+00	2.15E-02	0.00	4.51	2	1.87	0.34	108	223	624	18.37	-	
	11	2	1.21E-05	2.47E-02	9.98E-04	3.80E+01	9.41E-01	3.41E+00	3.29E-02	28.48	20.17	2	1.91	0.35	10	52	247	18.37	0.830	1
	12	9	8.74E-06	1.74E-01	3.31E-03	3.93E+01	6.84E+00	8.49E-02	5.16E-02	32.91	10.99	3	1.7	0.4	64	1	394	17.80	0.809	
	13	2	9.71E-06	6.06E-02	1.65E-03	3.82E+01	2.32E+00	1.56E+00	1.77E-02	4.83	3.42	2	1.86	0.42	28	25	124	18.95	0.850	
	14	2	8.74E-06	6.19E-02	9.62E-03	4.77E+01	2.95E+00	7.10E+00	1.28E-02	24.04	17.41	2	1.79	0.37	24	86	85	18.95	0.648	
	15	1	9.71E-06	1.98E-02	9.89E-04	3.62E+01	7.14E-01	2.04E+00	3.57E-02	26.79	26.83	1	2.24	0.46	8	36	286	18.95	0.784	2
	16*	2	9.71E-06	0.00E+00	0.00E+00	2.17E+01	0.00E+00	8.97E-02	0.00E+00	0.00	0.00	2	1.86	0.3	0	10	9	17.80	-	
	17	12	1.21E-05	2.05E-01	4.41E-03	3.74E+01	7.67E+00	2.24E-01	1.80E-04	23.19	6.72	4	2.03	0.4	77	3	2	18.37	0.866	
	18*	0	8.74E-06	3.07E-03	2.41E-03	3.78E+01	1.16E-01	2.82E+00	0.00E+00	0.00	0.00	1	1.89	0.46	2	55	0	17.80	-	
	19	2	8.74E-06	4.66E-02	1.33E-03	3.62E+01	1.68E+00	2.84E+00	7.73E-03	28.79	20.38	2	2.32	0.37	17	41	70	18.37	0.841	1
	20*	0	5.82E-06	1.88E-02	9.91E-04	3.84E+01	7.22E-01	2.74E-02	2.77E-02	0.00	0.00	1	1.66	0.38	7	42	241	18.37	-	
	21	1	2.91E-05	2.17E-03	1.80E-04	3.85E+01	8.36E-02	2.57E-01	8.70E-03	99.57	99.91	1	1.71	0.43	1	4	69	18.37	0.855	
	22	0	5.82E-06	6.41E-03	7.73E-04	3.89E+01	2.49E-01	2.29E+01	3.04E-02	0.00	0.00	1	2.33	0.57	4	330	287	18.95	0.811	1
	23	6	7.77E-06	4.71E-03	2.04E-03	3.37E+00	1.59E-02	3.83E+00	5.18E-03	669.48	398.19	3	2.29	0.38	3	698	412	17.80	0.000	
	24*	0	7.28E-06	2.97E-02	7.73E-03	1.12E+01	3.34E-01	5.80E+00	3.51E-03	0.00	0.00	1	2.18	0.29	7	180	49	18.95	-	
	25	2	1.94E-05	1.25E-02	1.85E-03	3.91E+01	4.90E-01	9.92E-01	2.13E-02	26.48	19.13	2	2.58	0.46	16	76	237	18.37	0.795	2
	26*	1	1.46E-05	2.65E-01	7.15E-02	5.44E+00	1.44E+00	1.54E+00	0.00E+00	0.00	99.35	2	2.01	0.32	107	510	0	18.95	-	
	27*	7	1.75E-05	1.89E-03	2.48E-03	2.85E+01	5.40E-02	1.94E+00	3.24E-03	0.00	279.76	4	2.03	0.31	1	46	29	18.37	-	
	28	1	1.75E-05	2.18E-02	7.33E-04	3.85E+01	8.38E-01	2.48E+00	2.72E-02	11.80	11.81	1	1.68	0.28	7	44	214	18.95	0.796	2
	29*	3	1.21E-05	1.11E-01	1.38E-01	7.54E+00	8.36E-01	1.15E+00	0.00E+00	0.00	9.79	2	2.2	0.3	67	137	0	18.37	-	
	30	3	7.77E-06	7.77E-02	1.78E-03	3.82E+01	2.97E+00	2.25E+00	6.67E-03	25.58	14.78	2	1.79	0.36	29	37	55	17.80	0.856	
	31*	3	1.16E-05	0.00E+00	0.00E+00	0.00E+00	0.00E+00	0.00E+00	0.00E+00	0.00	0.00	1	1.9	0.42	0	0	0	0.00	-	
	32	1	7.77E-06	1.40E-02	7.07E-04	3.94E+01	5.51E-01	1.19E+00	5.08E-02	56.61	56.69	1	1.93	0.27	5	17	406	17.80	0.793	2
	33	6	9.71E-06	9.18E-02	8.22E-03	3.17E+01	2.91E+00	4.70E+00	6.12E-03	29.29	12.24	3	2.16	0.3	45	109	66	18.37	0.000	
	34	11	1.16E-05	1.03E-01	2.63E-03	4.15E+01	4.28E+00	1.16E+01	1.44E-02	39.05	11.82	4	2.15	0.41	40	230	143	18.37	0.610	
	35	0	1.21E-05	1.13E-02	4.68E-04	3.74E+01	4.21E-01	8.92E-01	1.02E-02	0.00	0.00	1	2.1	0.3	4	14	95	18.95	0.681	
	36*	2	1.21E-05	2.25E-01	1.38E-01	8.82E+00	1.99E+00	6.54E+00	1.54E-02	0.00	3.57	2	1.77	0.36	160	782	776	18.37	-	
	37	8	1.21E-05	1.23E-01	2.62E-03	3.85E+01	4.74E+00	6.24E-01	2.84E-02	26.85	9.51	3	1.78	0.3	47	9	217	17.80	0.844	1
	38	3	1.16E-05	4.07E-02	1.59E-03	3.71E+01	1.51E+00	1.74E+00	4.85E-02	26.79	15.50	2	1.85	0.34	15	29	387	18.37	0.848	1
	39	1	1.75E-05	1.89E-02	8.54E-04	4.08E+01	7.72E-01	1.58E+00	2.85E-02	11.94	11.95	1	2.02	0.35	8	28	261	18.37	0.851	
	40	1	9.71E-06	1.67E-02	6.37E-04	3.88E+01	6.48E-01	1.42E+00	1.26E-02	31.76	31.79	1	1.79	0.2	7	25	111	17.80	0.835	1
Primary Zeta	8.27	0.14																		

All Data		**Population 1**	**Population 2**
Mean Dpar	2.01	1.98	2.17
Mean Dper	0.36	0.35	0.37
Mean rmr0	0.745	0.836	0.791
Mean track length	13.95 ± 1.17	14.42 ± 0.98	14.1 ± 0.92
# of grains	27	7	7
χ^2_R	1.95	0.09	1.41
Pooled Age (Ma)	26.5 ± 5.77	30.4 ± 11.4	29.2 ± 9.3

Table A3.5. Apatite fission track length data for sample 11UMT16.

Apatite Fission Track (length data)

Sample#	Track #	Length (µm)	Etch	Dpar (µm)	Dper (µm)	Angle to c-axis (°)	rmr0
11UMT16	1	13.94	4	2.05	0.47	85.25	0.510
	2	12.05	4	2.05	0.47	64.75	0.510
	3	14.62	4	2.05	0.47	8.19	0.510
	4	11.04	4	2.05	0.47	67.20	0.510
	5	13.72	4	2.10	0.30	82.68	0.829
	6	14.62	4	2.10	0.30	37.94	0.829
	7	12.87	4	2.10	0.30	40.48	0.829
	8	12.99	4	2.10	0.30	64.67	0.829
	9	13.10	4	2.10	0.30	57.53	0.829
	10	12.61	4	2.10	0.30	65.27	0.829
	11	14.96	4	2.10	0.30	46.70	0.829
	12	14.96	4	2.14	0.81	55.11	0.767
	13	15.25	4	2.08	0.32	37.26	0.846
	14	14.02	4	2.08	0.32	51.08	0.846
	15	13.80	4	2.08	0.32	37.03	0.846
	16	14.13	4	2.07	0.37	68.44	0.000
	17	11.54	4	2.21	0.43	86.76	0.855
	18	12.68	4	2.21	0.43	45.45	0.855
	19	15.27	4	2.21	0.43	45.74	0.855
	20	11.89	4	2.21	0.43	46.20	0.855
	21	16.03	4	1.76	0.35	28.32	0.851
	22	14.09	4	1.76	0.35	40.08	0.851
	23	15.02	4	1.76	0.35	66.38	0.851
	24	14.20	4	1.76	0.35	55.33	0.851
	25	13.45	4	1.76	0.35	60.84	0.851
	26	14.56	4	1.76	0.35	27.20	0.851
	27	12.05	4	2.30	0.35	74.89	0.810
	28	12.81	4	2.30	0.35	61.47	0.810
	29	12.19	4	2.30	0.35	83.92	0.810
	30	16.17	4	3.85	0.68	39.10	0.856
	31	11.99	4	3.85	0.68	77.76	0.856
	32	15.79	4	3.85	0.68	72.27	0.856
	33	13.33	4	3.85	0.68	45.88	0.856
	34	14.37	4	3.85	0.68	80.52	0.856
	35	15.56	4	2.25	0.37	48.00	0.858
	36	14.57	4	2.25	0.37	35.85	0.858
	37	15.78	4	2.25	0.37	46.92	0.858
	38	14.04	4	2.25	0.37	73.77	0.858
	39	13.77	4	2.25	0.37	59.92	0.858
	40	15.33	4	2.25	0.37	50.36	0.858
	41	13.51	4	2.25	0.37	58.46	0.858
	42	13.05	4	2.25	0.37	45.79	0.858

Table A3.5 continued. Apatite fission track length data for sample 11UMT16.

Apatite Fission Track (length data)

Sample#	Track #	Length (µm)	Etch	Dpar (µm)	Dper (µm)	Angle to c-axis (°)	rmr0
11UMT16	43	15.10	4	2.01	0.40	63.78	0.852
	44	15.41	4	2.01	0.40	42.16	0.852
	45	10.90	4	2.12	0.38	86.22	0.853
	46	11.08	4	2.12	0.38	71.55	0.853
	47	14.10	4	2.12	0.38	78.17	0.853
	48	13.24	4	2.12	0.38	65.32	0.853
	49	13.82	4	2.04	0.33	50.41	0.856
	50	15.54	4	2.04	0.33	37.20	0.856
	51	14.86	4	2.04	0.33	38.54	0.856
	52	14.86	4	2.04	0.33	68.38	0.856
	53	15.25	4	2.04	0.33	32.42	0.856
	54	15.09	4	2.04	0.33	49.48	0.856
	55	14.16	4	2.04	0.33	45.75	0.856
	56	14.39	4	1.90	0.35	61.18	0.000
	57	12.03	4	2.31	0.40	72.27	0.803
	58	14.58	4	2.31	0.40	46.22	0.803
	59	12.59	4	2.31	0.40	65.48	0.803
	60	13.89	4	2.27	0.37	66.32	0.755
	61	12.79	4	2.27	0.37	53.20	0.755
	62	12.52	2	2.41	0.72	72.87	0.714
	63	15.67	4	2.03	0.37	67.24	0.860
	64	14.75	4	2.03	0.37	60.89	0.860
	65	15.08	4	2.15	0.34	59.33	0.864
	66	15.22	4	2.15	0.34	48.21	0.864
	67	15.42	4	2.15	0.34	80.66	0.864
	68	14.90	4	2.15	0.34	72.99	0.864
	69	11.38	4	2.15	0.34	74.71	0.864
	70	14.18	4	2.15	0.34	32.12	0.864
	71	13.34	4	2.15	0.34	74.38	0.864
	72	14.67	4	2.15	0.34	43.84	0.864
	73	14.93	4	2.03	0.30	35.36	0.807
	74	13.97	4	2.01	0.30	65.15	0.846
	75	13.99	4	2.01	0.30	57.96	0.846
	76	14.14	2	1.92	0.31	24.45	0.851
	77	15.06	3	1.91	0.51	65.69	0.852
	78	14.53	3	1.91	0.51	70.03	0.852
	79	15.66	4	2.23	0.40	68.02	0.735
	80	16.05	4	1.95	0.41	56.39	0.818
	81	14.78	4	1.95	0.41	28.08	0.818
	82	13.68	4	1.97	0.29	88.77	0.831
	83	14.61	4	1.97	0.29	64.51	0.831
	84	13.56	4	1.97	0.29	88.86	0.831
	85	13.29	4	1.97	0.29	55.58	0.831
	86	15.19	4	1.97	0.29	47.16	0.831
	87	14.98	4	2.62	0.48	81.13	0.821
	88	13.76	4	2.62	0.48	66.68	0.821

Table A3.5 continued. Apatite fission track length data for sample 11UMT16.

Apatite Fission Track (length data)

Sample#	Track #	Length (µm)	Etch	Dpar (µm)	Dper (µm)	Angle to c-axis (°)	rmr0
11UMT16	89	13.93	4	2.62	0.48	52.88	0.821
	90	14.44	4	2.25	0.47	29.19	0.786
	91	13.09	4	2.25	0.47	78.10	0.786
	92	14.33	4	2.20	0.51	70.22	0.824
	93	13.95	4	2.20	0.51	61.48	0.824
	94	15.91	4	2.19	0.36	50.56	0.690
	95	15.05	4	2.19	0.36	22.71	0.690
	96	14.02	4	2.19	0.36	53.70	0.690
	97	14.04	4	2.19	0.36	79.50	0.690
	98	14.72	4	2.19	0.36	38.82	0.690
	99	14.61	4	2.19	0.36	54.27	0.690
	100	14.84	4	2.19	0.36	42.86	0.690
	101	14.39	4	2.05	0.41	39.14	0.849
	102	11.45	4	2.05	0.41	71.95	0.849
	103	14.77	4	2.05	0.41	60.66	0.849
	104	12.26	4	2.05	0.41	66.27	0.849
	105	13.22	4	2.05	0.41	65.11	0.849
	106	15.13	4	2.05	0.41	39.34	0.849
	107	12.28	4	2.05	0.41	77.01	0.849
	108	14.50	4	2.05	0.41	73.03	0.849
	109	12.99	4	2.05	0.41	46.57	0.849
	110	13.17	4	2.05	0.41	78.54	0.849
	111	14.94	4	2.05	0.41	37.42	0.849
	112	15.89	4	2.05	0.41	8.63	0.849
	113	12.62	4	2.05	0.41	87.73	0.849
	114	14.79	4	2.05	0.41	54.09	0.849
	115	15.06	4	2.05	0.41	43.23	0.849
	116	13.56	4	1.93	0.37	67.83	0.000
	117	15.61	4	1.93	0.37	29.00	0.000
	118	13.38	4	1.93	0.37	89.55	0.000
	119	15.52	4	1.93	0.37	34.64	0.000
	120	14.75	4	1.93	0.37	45.63	0.000
	121	15.55	4	2.40	0.41	59.70	0.816
	122	15.09	4	2.40	0.41	30.87	0.816
	123	12.11	4	2.40	0.41	49.63	0.816
	124	13.42	4	2.40	0.41	44.97	0.816
	125	13.68	4	2.15	0.35	61.55	0.000
	126	14.10	4	3.32	0.83	79.29	0.676
	127	14.85	4	2.97	0.48	55.40	0.000
	128	14.63	4	2.97	0.48	75.39	0.000
	129	12.24	4	2.18	0.46	57.38	0.848
	130	11.22	4	2.18	0.46	69.82	0.848
	131	13.07	4	2.18	0.46	84.49	0.848
	132	13.45	4	2.18	0.46	46.60	0.848
	133	14.20	4	2.18	0.46	44.86	0.848
	134	13.40	4	2.18	0.46	80.39	0.848
	135	12.73	4	2.68	0.68	60.29	0.795
	136	12.99	4	2.00	0.34	70.44	0.853

Table A3.5 continued. Apatite fission track length data for sample 11UMT16.

Apatite Fission Track (length data)

Sample#	Track #	Length (µm)	Etch	Dpar (µm)	Dper (µm)	Angle to c-axis (°)	rmr0
11UMT16	137	13.66	4	2.00	0.34	72.84	0.853
	138	12.13	4	2.00	0.34	63.92	0.853
	139	15.47	4	2.31	0.46	52.93	0.793
	140	14.94	4	2.31	0.46	34.14	0.793
	141	16.69	4	2.68	0.35	50.35	0.775
	142	13.58	4	2.68	0.35	72.25	0.775
	143	17.24	4	2.68	0.35	36.28	0.775
	144	12.99	4	2.68	0.35	75.38	0.775
	145	13.08	4	2.68	0.35	71.78	0.775
	146	14.45	4	2.68	0.35	57.89	0.775
	147	14.64	4	2.68	0.35	34.93	0.775
	148	14.71	3	1.85	0.35	82.22	0.779
	149	13.29	3	1.85	0.35	65.55	0.779
	150	12.31	4	2.03	0.41	73.64	0.752
	151	13.97	4	2.03	0.41	69.26	0.752
	152	13.58	4	2.03	0.41	83.26	0.752
	153	12.90	4	2.03	0.41	42.56	0.752
	154	15.26	4	2.03	0.41	28.35	0.752
	155	16.35	4	2.03	0.41	36.94	0.752
	156	13.81	4	2.03	0.41	85.13	0.752
	157	13.93	4	2.03	0.41	74.17	0.752
	158	15.81	4	2.03	0.41	27.39	0.752
	159	14.15	4	2.03	0.41	57.99	0.752
	160	12.08	4	2.03	0.41	68.32	0.752
	161	15.57	4	2.03	0.41	36.95	0.752
	162	16.85	4	2.19	0.35	41.40	0.850
	163	14.95	4	2.38	0.54	75.47	0.790
	164	13.80	4	2.29	0.68	54.98	0.826
	165	13.53	4	2.29	0.68	76.40	0.826
	166	12.92	4	2.29	0.68	40.33	0.826
	167	15.36	4	2.29	0.68	45.86	0.826
	168	13.94	4	2.29	0.68	47.22	0.826
	169	13.53	4	2.29	0.68	49.64	0.826
	170	16.21	4	2.37	0.39	23.03	0.814
	171	15.36	4	2.20	0.36	33.85	0.798
	172	13.50	4	2.03	0.30	69.06	0.856
	173	12.81	4	2.03	0.30	72.73	0.856
	174	14.25	4	2.03	0.30	49.85	0.856
	174	11.78	4	2.03	0.30	88.20	0.856

Mean Dpar	2.2
Mean Dper	0.41
Mean Length (µm)	14.06
Std. Dev. (µm)	1.26
Skewness	-0.2561
Kurtosis	-0.3279

Table A3.6. Apatite fission track length data for sample 11UMT22

Apatite Fission Track (length data)

Sample#	Track #	Length (µm)	Etch	Dpar (µm)	Dper (µm)	Angle to c-axis (°)	rmr0
11UMT22	1	13.84	4	2.05	0.33	50.75	0.776
	2	15.17	4	2.05	0.33	37.68	0.776
	3	12.87	4	2.05	0.33	37.28	0.776
	4	14.45	4	2.05	0.33	83.34	0.776
	5	14.55	4	2.05	0.37	82.40	0.775
	6	15.48	4	2.05	0.37	10.07	0.775
	7	14.07	3	2.02	0.35	19.01	0.845
	8	13.79	3	2.02	0.35	66.68	0.845
	9	14.37	4	2.60	0.46	82.02	0.771
	10	14.27	4	2.60	0.46	75.34	0.771
	11	15.20	4	2.37	0.40	21.19	0.842
	12	12.93	4	2.37	0.40	79.73	0.842
	13	11.88	4	3.73	0.78	73.31	0.521
	14	12.02	2	2.09	0.36	46.31	0.851
	15	15.15	2	2.09	0.36	42.93	0.851
	16	13.29	4	2.08	0.37	56.42	0.777
	17	15.21	4	2.30	0.56	43.68	0.739
	18	14.80	2	1.94	0.22	54.01	0.000
	19	14.22	4	2.42	0.31	65.68	0.852
	20	12.71	4	2.42	0.31	55.52	0.852
	21	11.42	4	2.42	0.31	74.66	0.852
	22	14.20	3	2.28	0.46	69.06	0.871
	23	13.27	3	2.28	0.46	40.99	0.871
	24	13.68	4	1.81	0.36	76.58	0.000
	25	13.60	4	2.06	0.36	76.13	0.846
	26	14.82	4	1.94	0.32	56.93	0.854
	27	13.99	4	1.94	0.32	56.10	0.854
	28	14.16	4	2.26	0.36	56.43	0.734
	29	13.55	4	2.26	0.36	77.93	0.734
	30	13.37	4	2.26	0.36	82.55	0.734
	31	12.77	4	2.26	0.36	74.05	0.734
	32	11.97	4	2.26	0.36	87.55	0.734
	33	14.32	4	2.26	0.36	57.33	0.734
	34	15.28	4	2.27	0.36	19.90	0.821
	35	14.27	4	2.27	0.36	42.07	0.821
	36	14.59	4	2.27	0.36	39.51	0.821
	37	14.17	4	2.27	0.36	30.45	0.821
	38	12.70	4	2.17	0.54	35.79	0.794
	39	14.88	4	2.22	0.41	38.17	0.718
	40	12.16	4	2.22	0.41	79.13	0.718
	41	13.97	4	2.22	0.41	54.29	0.718
	42	16.58	4	2.35	0.41	49.98	0.848
	43	14.11	4	2.35	0.41	54.63	0.848
	44	15.19	2	2.65	0.69	80.69	0.704
	45	15.33	2	2.65	0.69	31.49	0.704
	46	16.19	4	2.07	0.35	62.54	0.000
	47	12.88	4	2.18	0.54	52.28	0.858
	48	11.97	4	2.18	0.54	43.06	0.858

Mean Dpar	2.25
Mean Dper	0.40
Mean Length (µm)	13.95
Std. Dev. (µm)	1.17
Skewness	6.45
Kurtosis	41.01

TABLE A3.7. MEASURED BEDDING ORIENTATIONS FROM THE FENGHUOSHAN FOLD AND THRUST BELT

Latitude	Longitude	Strike [°]	Dip [°]	Orientation	Unit	Elevation [m]
34.5833	92.6741	268	8	Upright	Fn	4563.7
34.5673	92.6921	114	45	Upright	Fn	4573.5
34.5402	92.7234	291	62	Upright	Fn	4579.8
34.5600	92.6971	325	40	Overturned	Fn	4588.2
34.5621	92.7002	301	34	Overturned	Fn	4588.4
34.5839	92.6631	277	86	Upright	Fn	4590.3
34.5353	92.7047	259	55	Upright	Fn	4590.4
34.5505	92.7373	281	19	Upright	Fn	4594.3
34.5790	92.6790	255	46	Overturned	Fn	4594.6
34.5818	92.6702	118	25	Upright	Fn	4598.9
34.5687	92.6856	279	85	Upright	Fn	4600.2
34.5411	92.6968	316	35	Upright	Fn	4602.6
34.5760	92.6761	312	86	Overturned	Fn	4603.5
34.5940	92.6292	081	85	Upright	Fn	4603.6
34.5400	92.7044	269	22	Upright	Fn	4604.1
34.5576	92.7411	045	22	Upright	Fn	4604.9
34.5541	92.6993	335	40	Upright	Fn	4604.9
34.5820	92.6556	289	57	Upright	Fn	4605.2
34.5931	92.6309	034	41	Upright	Fn	4605.4
34.5704	92.6784	058	56	Overturned	Fn	4605.8
34.5930	92.6251	074	24	Upright	Fn	4606.7
34.5369	92.6956	301	42	Upright	Fn	4606.9
34.5941	92.6259	039	44	Upright	Fn	4607.2
34.5941	92.6259	061	52	Upright	Fn	4607.2
34.5793	92.6622	218	89	Upright	Fn	4607.5
34.5294	92.6977	261	48	Upright	Fn	4607.6
34.5235	92.7171	261	41	Upright	Fn	4610.2
34.5405	92.7011	326	35	Upright	Fn	4610.2
34.5681	92.6855	100	75	Overturned	Fn	4611.6
34.5860	92.6725	264	19	Upright	Fn	4611.9
34.5830	92.6532	046	29	Upright	Fn	4612.3
34.5722	92.6767	040	80	Overturned	Fn	4613.7
34.5624	92.6916	021	59	Overturned	Fn	4614.3
34.5826	92.6529	261	14	Upright	Fn	4614.9
34.5338	92.6964	277	44	Upright	Fn	4615.0
34.5831	92.6539	024	26	Upright	Fn	4615.5
34.5447	92.6971	335	39	Upright	Fn	4615.5
34.5473	92.6975	359	50	Upright	Fn	4618.5
34.5766	92.6617	147	90	Vertical	Fn	4618.9
34.5824	92.6704	119	42	Upright	Fn	4619.3
34.3012	92.3304	240	55	Upright	Fn	4620.5
34.5960	92.7617	059	71	Upright	Fn	4621.2
34.5630	92.6891	013	54	Upright	Fn	4621.3
34.5964	92.7618	280	42	Upright	Fn	4621.4
34.8350	92.9231	204	70	Upright	Fn	4621.6
34.5637	92.6901	167	71	Overturned	Fn	4622.7
34.6072	92.6093	296	59	Upright	Fn	4624.6
34.5811	92.6666	270	90	Vertical	Fn	4625.2
34.5578	92.5173	321	55	Upright	Fn	4626.0
34.5883	92.7662	051	39	Upright	Fn	4626.2
34.5805	92.6670	038	60	Overturned	Fn	4626.7
34.5805	92.6670	080	36	Upright	Fn	4626.7
34.5816	92.6609	274	72	Upright	Fn	4629.3
34.5884	92.7622	344	24	Upright	Fn	4631.0
34.5791	92.6516	059	56	Upright	Fn	4631.1
34.5753	92.6570	334	43	Upright	Fn	4631.4
34.5789	92.6518	310	85	Upright	Fn	4632.1
34.5638	92.6844	341	14	Upright	Fn	4636.6
34.5518	92.6862	013	54	Upright	Fn	4637.9
34.5890	92.6775	224	46	Upright	Fn	4638.4
34.5738	92.6573	008	56	Upright	Fn	4638.8
34.5755	92.6550	159	65	Upright	Fn	4640.9
34.5805	92.6691	232	56	Upright	Fn	4643.7
34.5669	92.6885	113	15	Overturned	Fn	4646.1
34.5734	92.6572	005	33	Upright	Fn	4646.9
34.5805	92.6688	063	56	Overturned	Fn	4647.2
34.5474	92.6821	029	54	Upright	Fn	4652.5
34.5880	92.6750	060	55	Upright	Fn	4652.6
34.5915	92.6952	296	6	Upright	Fn	4654.6
34.5713	92.6471	069	76	Upright	Fn	4656.3
34.5713	92.6529	081	71	Upright	Fn	4657.0
34.5810	92.7557	279	27	Upright	Fn	4657.2
34.5281	92.6880	311	47	Upright	Fn	4657.2
34.6076	92.7671	056	72	Upright	Fn	4657.5

TABLE A3.7. CONTINUED. MEASURED BEDDING ORIENTATIONS FROM THE FENGHUOSHAN FOLD AND THRUST BELT

Latitude	Longitude	Strike [°]	Dip [°]	Orientation	Unit	Elevation [m]
34.6074	92.7677	094	44	Upright	Fn	4660.4
34.6003	92.6766	324	54	Upright	Fn	4663.2
34.7664	92.9004	117	65	Upright	Fn	4663.3
34.6083	92.7671	270	26	Upright	Fn	4665.4
34.6081	92.7669	101	81	Overturned	Fn	4666.3
34.6138	92.7978	249	35	Upright	Fn	4667.1
34.5798	92.6687	077	47	Upright	Fn	4667.3
34.5707	92.6513	065	85	Upright	Fn	4667.8
34.5842	92.7799	351	24	Upright	Fn	4669.2
34.5433	92.6771	006	41	Upright	Fn	4672.8
34.5691	92.6440	062	58	Upright	Fn	4675.2
34.6112	92.7624	098	69	Upright	Fn	4676.9
34.5793	92.6687	068	56	Upright	Fn	4677.0
34.5857	92.7809	064	41	Upright	Fn	4681.1
34.7509	92.8996	102	61	Upright	Fn	4681.3
34.5970	92.7370	250	50	Upright	Fn	4681.7
34.6536	92.6330	054	39	Upright	Fn	4681.8
34.5791	92.6676	082	60	Upright	Fn	4685.1
34.5791	92.6676	144	56	Upright	Fn	4685.1
34.5671	92.6411	029	39	Upright	Fn	4688.5
34.5298	92.6851	326	49	Upright	Fn	4689.3
34.7397	92.8953	094	62	Upright	Fn	4690.5
34.5955	92.7126	295	60	Upright	Fn	4691.0
34.5787	92.6669	266	86	Overturned	Fn	4692.7
34.5788	92.6670	276	36	Overturned	Fn	4692.9
34.5580	92.7487	211	85	Upright	Fn	4694.1
34.6118	92.7606	278	78	Overturned	Fn	4696.9
34.5334	92.6779	317	40	Upright	Fn	4697.9
34.5586	92.7485	064	30	Upright	Fn	4700.2
34.5619	92.6378	336	35	Upright	Fn	4702.4
34.6170	92.7856	104	74	Overturned	Fn	4702.6
34.5238	92.6856	256	6	Upright	Fn	4702.6
34.6129	92.7591	284	66	Overturned	Fn	4703.1
34.6016	92.6580	263	80	Overturned	Fn	4703.4
34.5869	92.9094	270	84	Overturned	Fn	4703.9
34.5634	92.6388	354	40	Upright	Fn	4704.3
34.5537	92.7475	321	46	Upright	Fn	4705.0
34.5931	92.9062	085	20	Overturned	Fn	4709.0
34.5900	92.9064	084	54	Upright	Fn	4709.3
34.6105	92.7975	101	19	Upright	Fn	4711.9
34.5614	92.6714	245	64	Upright	Fn	4713.0
34.5933	92.9060	234	42	Overturned	Fn	4716.4
34.5933	92.9060	315	36	Overturned	Fn	4716.4
34.6330	92.7878	124	60	Overturned	Fn	4719.1
34.5612	92.6396	326	21	Upright	Fn	4720.0
34.5608	92.6381	328	31	Upright	Fn	4723.8
34.5599	92.6378	311	47	Upright	Fn	4727.5
34.5602	92.6401	324	55	Upright	Fn	4733.6
34.6209	92.8825	077	54	Upright	Fn	4736.2
34.6202	92.8358	145	36	Upright	Fn	4737.6
34.6313	92.8823	027	46	Upright	Fn	4737.9
34.6174	92.7782	278	34	Upright	Fn	4741.5
34.6220	92.8410	291	41	Upright	Fn	4742.2
34.6151	92.7497	089	12	Overturned	Fn	4744.3
34.7865	92.8298	086	86	Upright	Fn	4745.6
34.6376	92.7807	105	62	Overturned	Fn	4745.6
34.6337	92.7887	164	46	Upright	Fn	4745.9
34.5672	92.6528	014	34	Upright	Fn	4746.9
34.6172	92.7473	019	61	Overturned	Fn	4747.3
34.6378	92.7795	131	53	Upright	Fn	4751.2
34.6366	92.8397	180	27	Upright	Fn	4752.3
34.7785	92.8889	102	31	Upright	Fn	4758.3
34.7119	92.8882	305	55	Upright	Fn	4762.3
34.5639	92.7686	299	47	Upright	Fn	4764.2
34.6004	92.9041	061	45	Overturned	Fn	4767.2
34.7089	92.8905	067	64	Upright	Fn	4768.8
34.6783	92.6328	013	56	Upright	Fn	4771.7
34.5554	92.6601	082	82	Overturned	Fn	4773.2
34.5631	92.6508	331	24	Upright	Fn	4773.2
34.4016	92.0364	040	56	Upright	Fn	4774.2
34.8411	92.9174	171	29	Upright	Fn	4778.3
34.6386	92.8244	074	50	Upright	Fn	4781.6
34.6841	92.6357	105	56	Upright	Fn	4786.8
34.6841	92.6357	357	25	Upright	Fn	4786.8

TABLE A3.7 CONTINUED. MEASURED BEDDING ORIENTATIONS FROM THE FENGHUOSHAN FOLD AND THRUST BELT

Latitude	Longitude	Strike [°]	Dip [°]	Orientation	Unit	Elevation [m]
34.6403	92.7759	097	65	Overturned	Fn	4796.7
34.6808	92.6315	278	74	Upright	Fn	4803.7
34.5550	92.6504	277	89	Upright	Fn	4807.7
34.7035	92.9044	238	75	Overturned	Fn	4808.4
34.6477	92.9269	086	56	Upright	Fn	4809.7
34.6473	92.8621	256	44	Upright	Fn	4810.4
34.6338	92.9217	257	43	Upright	Fn	4821.0
34.6534	92.8829	230	42	Upright	Fn	4837.0
34.6392	92.9074	065	29	Upright	Fn	4838.7
34.6957	92.9051	073	54	Upright	Fn	4838.7
34.6491	92.9429	321	37	Overturned	Fn	4839.1
34.6278	92.9232	077	51	Upright	Fn	4840.1
34.6497	92.9461	115	48	Upright	Fn	4843.4
34.5502	92.6584	277	18	Upright	Fn	4848.4
34.6463	92.7784	116	64	Overturned	Fn	4864.0
34.6514	92.9482	260	79	Overturned	Fn	4866.6
34.6689	92.8926	184	48	Upright	Fn	4871.6
34.6454	92.8418	061	61	Upright	Fn	4877.4
34.6462	92.8436	051	56	Upright	Fn	4885.0
34.6896	92.9023	245	88	Overturned	Fn	4886.7
34.6106	92.8544	081	71	Upright	Fn	4898.7
34.6192	92.9330	074	67	Upright	Fn	4927.1
34.6225	92.7866	015	76	Overturned	Fn	-
34.6186	92.7857	022	50	Overturned	Fn	-
34.6209	92.7861	024	50	Overturned	Fn	-
34.6259	92.7866	039	70	Overturned	Fn	-
34.6227	92.7865	045	64	Overturned	Fn	-
34.6259	92.7865	065	69	Overturned	Fn	-
34.7200	92.8825	072	32	Upright	Fn	-
34.6931	92.9069	089	70	Upright	Fn	-
34.6439	92.8045	092	52	Upright	Fn	-
34.6394	92.7983	092	55	Upright	Fn	-
34.6421	92.8044	096	52	Upright	Fn	-
34.6337	92.7944	096	50	Upright	Fn	-
34.6396	92.8038	098	65	Upright	Fn	-
34.6385	92.8036	102	42	Upright	Fn	-
34.6338	92.7999	105	41	Upright	Fn	-
34.6183	92.7851	120	56	Overturned	Fn	-
34.6279	92.7856	121	84	Overturned	Fn	-
34.6192	92.7853	121	71	Overturned	Fn	-
34.6295	92.8413	234	57	Upright	Fn	-
34.5253	92.7294	284	51	Upright	Fn	-
34.6219	92.7863	356	59	Overturned	Fn	-
34.3006	92.3309	241	60	Upright	Jz	4606.8
34.5208	92.7196	190	31	Upright	Tt	4582.9
34.5216	92.7183	225	86	Upright	Tt	4588.1
34.2814	92.2674	024	29	Upright	Tt	4604.2
34.3995	92.0684	247	29	Upright	Tt	4636.3
34.5490	92.6591	327	49	Upright	Tt	4798.4
34.5238	92.6772	010	25	Upright	Tt	4870.4
34.8019	92.9116	309	54	Upright	Yx	4611.8
34.8366	92.9220	141	31	Upright	Yx	4634.5
34.7926	92.8259	265	19	Upright	Yx	4694.5
34.7891	92.8274	356	50	Upright	Yx	4709.4
34.6296	92.7855	119	79	Overturned	Fn	-
34.6304	92.7859	120	70	Overturned	Fn	-
34.6405	92.8420	184	65	Upright	Fn	4788.0
34.8400	92.9166	299	87	Upright	Fn	4794.5
34.2956	92.2720	262	58	Upright	Fn	4706.3
34.6119	92.7590	082	40	Upright	Fn	4708.7
34.6303	92.6441	318	30	Upright	Fn	4657.7
34.5405	92.6791	338	41	Upright	Fn	4659.8
34.5310	92.6949	264	63	Upright	Fn	4616.4
34.5655	92.6901	086	76	Overturned	Fn	4617.9

TABLE A3.8. DOCUMENTED THRUST FAULT ACTIVITY WITHIN THE TIBETAN PLATEAU

Region	*Location/Fault*	*Timing*		*Source*
		Initiation	*Cessation*	
Himalaya				
	Main Central Thrust	23	13	Hubbard and Harrison (1989); Hodges et al. (1992); Metcalfe (1993); Hodges et al. (1996); Coleman (1998); Walker et al. (1999); Catlos et al. (2002a); Godin et al. (2001); Searle et al. (2003)
	Main Boundary Thrust	12	5	Meigs et al. (1995); Huyghe et al. (2001)
	Main Frontal Thrust	<5	0	DeCelles et al. (2001)
	Ramgarh Thrust	15	5	DeCelles et al. (2001); Peasron and DeCelles (2005)
Tethyan Himalaya				
	South Tibetan Detachment	23	<12	Herren (1987); Hodges et al. (1992); Hodges et al. (1996); Edwards and Harrison (1997); Dezes et al. (1999); Walker et al. (1999); Searle et al. (1999a); Murphy and Harrison (1999); Godin et al. (2001); Grujic et al. (2002); Daniel et al. (2003); Searle et al. (2003)
	Great Counter Thrust	25	13	Yin et al. (1999); Murphy et al. (2002); Ratschbacher et al. (1994); Quidelleur et al. (1997); Harrison et al. (2000)
	Tethyan Fold and Thrust Belt	56	44	Searle (1986); Ratschbacher et al. (1994); Pivnik and Wells (1996); Najman et al. (1997);DeCelles et al. (1998); Najman and Garzanti (2000); Klootwijk et al. (1985); Besse and Courtillot (1988); LePichon et al. (1992); Patzelt et al. (1996); DeCelles et al. (2002); Aikman et al. (2008); Wiesmayr and Grasemann, (2002)
Lhasa Terrane				
	Lhasa-Damxung Thrust	90	69	Kapp et al. (2007a)
	Gugu La Thrust		>99	Murphy et al. (1997)
	Shibaluo Thrust		>153	Murphy et al. (1997)
	Emei La Thrust		>113	Murphy et al. (1997)
	Narangjiapo Thrust	75	65	Kapp et al. (2003); Kapp et al. (2007a)
	Thrusts near Penbo	<43		Kapp et al. (2007a)
	Jaggang Thrust System	75	60	Kapp et al. (2003)
	Shiquanhe Thrust	~34	<22.6	Kapp et al. (2003)
	Zaduo Thrust	75	60	Kapp et al. (2003)
	Thrusts and anticlines in the Nyainquentanglha Range	96	53	Kapp et al. (2007b)
Bangong Nujiang Suture Zone	Gaize-Siling Co Backthrust	<99 26	97 25	Kapp et al. (2007b)
	Queri Malai Thrust	99 26	97 25	Kapp et al. (2007b)
	Zanggenong Thrust	Upper K	Tert	Kapp et al. (2007b)
	Muggar Thrust	108	99	Kapp et al. (2007a)
	Shiquanhe-Gaize-Amdo Thrust System (includes Puzuo and Zanggenong	<110 <43	- 22.6	Kapp et al., (2003; 2005; 2007b)
Qiangtang Terrane				
	Tanggula Shan Fold and Thrust Belt	85	45	Wang et al. (2008); Staisch et al. (2014)
	Lugu-Rongma Thrust System	>50 -	- <35	Kapp et al. (2005)
	Zadaona-Riganpei Co Thrust	~65	~65	Kapp et al. (2005)
	South Qiangtang Thrust	-	<31	Kapp et al. (2005)
	Zaduo Thrust	75	60	Kapp et al., (2003)
	Qiangtang Anticlinorium	130	100	Kapp et al., 2005
	Gangma Co-Shuang Hu Thrust	-	30	Kapp et al. (2005)
Jinsha Suture Zone				
	Fenghuoshan Fold and Thrust Belt	46	>27	Staisch et al. (in prep)
Kunlun Suture Zone				
	Qimen Tagh	28 - 24	-	Jolivet et al. (2003); Yin et al. (2007)
	Kunlun Shan Fold and Thrust Belt	35 - 25	-	Mock et al. (1999); Wang et al. (2004); Clark et al. (2010)
W. Qaidam				
	Dulan-Chaka Highland Fault system	17 - 12	-	Duvall et al. (2013)
	Jishi Shan	13	-	Lease et al. (2007; 2011)
	Laji Shan	22	-	Fang et al. (2005); Zheng et al. (2006); Lease et al. (2011); Hough et al. (2011)
	Qinghai Nan Shan Fault	11 - 9	-	Zhang et al. (2011); Craddock et al. (2011)

TABLE A3.8 CONT. DOCUMENTED THRUST FAULT ACTIVITY WITHIN THE TIBETAN PLATEAU

Region	*Location/Fault*	*Timing*		*Source*
		Initiation	*Cessation*	
Qilian Shan				
	Gong He Nan Shan Fault	10 - 7	-	Craddock et al. (2011)
	South Qilian Shan (overall)	65 - 50	-	Yin et al. (2008); Zhuang et al. (2011)
	Dasaibei Thrust	65 - 50	-	Yin et al. (2008)
	Xiaosabei Thrust	65 - 50	-	Yin et al. (2008)
	Qaidam Thrust	65 - 50	-	Yin et al. (2008)
	East Luliang Thrust	>33	-	Yin et al. (2008)
	Xitie Thrust	>33	-	Yin et al. (2008)
	West Lulian Thrust	~40	-	Yin et al. (2008)
	Sainan Thrust	~40	-	Yin et al. (2008)
	Olongbulak Thrust	10	-	Yin et al. (2008)
	Aimunik Thrust	10	-	Yin et al. (2008)
	Central Qilian Shan (overall)	>33	-	Yin et al. (2002; 2008)
	North Qilian Shan (overall)	16 - 10	0	Bovet et al. (2009); Zhuang et al. (2010)

Chapter IV

The timing of crustal shortening and the initiation of left-lateral shear within the central Kunlun Shan, northern Tibet: implications for the uplift history of the Tibetan Plateau[3]

Abstract

The timing of crustal shortening and strike-slip faulting along the Kunlun Shan, located in northern Tibet, provides insights for the history of surface uplift and may specifically constrain the time of high elevation attainment of the Tibetan Plateau. Here, we present new apatite and zircon (U-Th)/He thermochronologic dating and modeling and $^{40}Ar/^{39}Ar$ fault gouge dating along with structural observations from the central Kunlun Shan in order to put temporal constraints on the shift from crustal shortening to left-lateral shear. Fault gouge for $^{40}Ar/^{39}Ar$ illite analysis was sampled from two strike-slip and two thrust faults within the Dongdatan Valley to date the timing of faulting. Low-temperature thermochronologic ages were obtained from metaplutonic, plutonic, metasedimentary, and sedimentary rock units throughout the Dongdatan Valley, East Wenquan Basin, and East Deshuiwai Mountains in order to estimate the timing and rate of exhumation. Paired with structural observations, this data temporally constrains the tectonic history along the northern Tibetan Plateau. We investigated structures along the Xidatan Fault strand of the active Kunlun strike-slip fault. The eastern termination of this fault strand occurs in a small releasing bend, stepping over to the western termination of the Middle Kunlun (Alag Hu) Fault strand. Here, left-lateral, strike-slip faults cross-cut thrust faults, the latter of which place low-grade metamorphic rocks over terrestrial "red bed" sedimentary rocks. Because the eastern termination of the Xidatan Fault strand is extensional, we assume that the thrust faults in this area are likely related to an earlier phase of crustal shortening associated with the growth of the Kunlun Shan beginning by at least ~35 Ma, rather than to the active strike-slip faulting. Apatite helium ages (T_c = 60 – 70 °C) collected

[3] Citation: Staisch, L. M., N. A. Niemi, M. K. Clark, C. Hong, *in prep*, The timing of crustal shortening and the initiation of left-lateral shear along the central Kunlun Fault, northern Tibet: implications for the uplift history of the Tibetan Plateau.

from the lowest structural position in thrust faults range from 25 – 38 Ma, which suggests that Cenozoic exhumation due to thrust faulting may be preserved within these fault blocks. However, zircon helium ages (T_c = 200 – 210 °C) are on average much older (> 70 Ma), suggesting that the exhumation along thrust faults is less than ~ 4 km and that zircon helium ages are unrelated to Cenozoic tectonics. Therefore, we have difficulty fully resolving potential thrust fault-related cooling histories from our current dataset. New apatite fission-track ages (in progress) will provide information from a critical temperature window (T_c = ~100 – 120 °C). With this data, we expect to be able to distinguish between two end-member scenarios: (1) rapid cooling events related to crustal shortening sometime between 45 – 20 Ma, or (2) slow cooling until 20 Ma, which would suggest that thrust faulting postdates our youngest samples and that thrust fault related exhumation is less than 1 – 2 km. Fault gouge ages from the Dongdatan Valley are 47 and 113 Ma for thrust faults, and 90 Ma for a strike-slip fault. The 47 Ma thrust fault age is consistent with the available thermochronologic ages, but the Mesozoic ages are more difficult to understand given the lack of other regional data supporting tectonic activity at this time. We tentatively interpret these ages as low-grade metamorphic growth ages, rather than thrust or strike-slip fault motion. The transition from north-south oriented crustal shortening to left-lateral shear along the Kunlun Shan since 20 Ma, along with the onset of normal and strike-slip faulting in central and southern Tibet by 18 Ma, and the initiation of lower crustal flow in eastern Tibet by 13 Ma, suggests that east-west oriented extension and extrusion initiated in the mid-Miocene across the orogen. The plateau-wide shift in stress accommodation in the mid-Miocene implies that high gravitational potential energy, and likely high elevation, was attained at this time.

4.1. Introduction

The timing of onset of strike-slip faulting within the Kunlun Shan, located along the northern margin of the Tibetan Plateau, is an outstanding controversy with significant implications for the tectonic evolution of the Himalayan-Tibetan Orogen. Currently, the Kunlun Fault accommodates convergence between India and Eurasia via left-lateral shear at a rate of ~10 – 11 mm yr^{-1} (Avouac and Tapponnier, 1993; van der Woerd et al., 1998, 2000, 2002; Haibing et al., 2005; Kirby et al., 2007). However, the Kunlun Shan was previously the site of north-south oriented pure shear deformation, which is suggested to have initiated between 35 and 27 Ma (Mock et al., 1999; Jolivet et al., 2003; Wang et al., 2004; Yin et al., 2007; Wu et al., 2009; Clark et al., 2010). The transition in structural style, from crustal thickening to eastward extrusion, along the Kunlun Shan

indicates a shift in the orientation of principal stresses. This kinematic change may directly relate to the attainment of high elevation and associated high gravitational potential energy of the northern Tibetan Plateau (Burke and Şengör, 1986; Platt and England, 1994; Rey et al., 2001). Few constraints exist on the timing and forces involved in the switch from predominantly pure shear to simple shear deformation or on the timing of high elevation gain in northern Tibet, thus fueling the debate as to when and how the Tibetan Plateau was uplifted to modern elevation.

While most studies agree that left-lateral shear in the Kunlun Shan initiated in the Cenozoic, there is uncertainty in the exact timing of onset (Kidd and Molnar, 1988; Wu et al., 2001; Jolivet et al., 2003; Fu and Awata; 2007; Duvall et al., 2013). Several studies infer that strike-slip faulting initiated in Plio-Pleistocene time based on the offset of fluvial and glacial features (Kidd and Molnar, 1988; Wu et al., 2001), while others infer ~10 Ma initiation of shear based on fault displacement and extrapolation of the modern fault slip rate (Fu and Awata, 2007). However uncertainty in the timing of geomorphic feature development and in variations on the long-term slip history of the Kunlun Fault may lead to inaccurate estimates of the onset of shear. The timing of magmatism in extensional features near the Kunlun Fault has been used to infer shear onset at 15 Ma (Jolivet et al., 2003), which provides a minimum age for the onset of shear, and is contrary to the interpretations from offset features and fault displacement (Kidd and Molnar, 1988; Wu et al., 2001; Fu and Awata, 2007). The initiation of shear at 20 – 15 Ma, with a possible phase from 30 – 20 Ma, is inferred from the initiation of rapid cooling from thermochronology (Duvall et al., 2013), however difficulty in isolating the onset of strike-slip motion from the multi-phase deformation history of the northern plateau margin, particularly when using exhumation of discrete fault blocks as a proxy for the onset of lateral shear, may lead to overestimates in the timing of strike-slip fault onset. An additional complicating factor may be the heterogeneous onset of strike-slip faulting along the >1000 km length of the Kunlun Fault, as inferred by Duvall et al. (2013). To disentangle the convoluted kinematic history of the Kunlun Shan, detailed structural analyses of faulting style in concert with age constraints on exhumation from thrust and strike-slip motion are necessary.

Strike-slip motion within the Kunlun Shan has produced localized basin subsidence in en echelon rhombochasms and uplift along restraining bends, steps, and fault junctions (Figure 4.1; Fu and Awata, 2007; Duvall et al., 2013). The Dongdatan Valley, East Wenquan Basin, and East Deshuiwai Mountains are located within the central Kunlun Shan and along an active strand of the Kunlun Fault, locally named the Xidatan Fault or Xidatan-Dongdatan fault strand (Figure 4.1). The eastern termination of this fault strand occurs in an extensional step-over to the Middle Kunlun

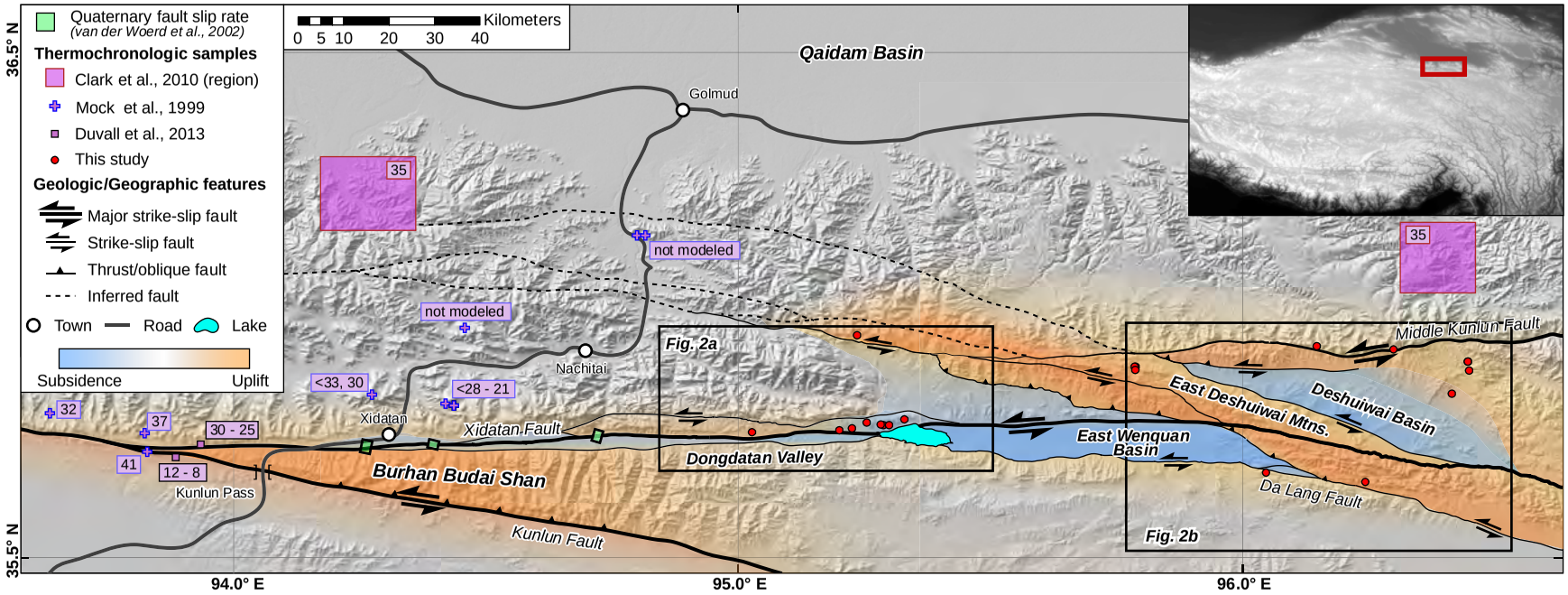

Figure 4.1. Hillshade map of the central Kunlun Shan with the general location marked in the inset map of the Tibetan Plateau. Active strike-slip faults and oblique-slip faults are shown. Thermochronologic and fault slip rate studies are denoted for reference. The modeled timing of initial rapid cooling, in millions of years, for samples from Mock et al. (1999), Clark et al. (2010), and Duvall et al. (2013) are outlined in blue, red, and black, respectively. Thermochronologic samples from this study are marked in red. The orange - blue gradient overlay qualitatively shows vertical uplift and subsidence related to recent strike-slip fault motion. The locations of geologic maps in Figure 4.2 are indicated.

(Alag Hu) Fault, which continues farther east (van der Woerd et al., 2002). Thrust faults are well exposed throughout the region and are commonly crosscut by major and subordinate strike-slip faults. Because these thrust faults are found within the extensional step-over region of the strike-slip fault, we assume that they are related to an earlier phase of mountain building in the Kunlun Shan since at least 35 Ma (Clark et al., 2010). The rock types throughout the central Kunlun Shan are heterogeneous and well suited for providing the mineral suites necessary for low-temperature thermochronologic analyses with exhumed Triassic greenschist metapelites, Triassic arkosic sandstone, small volume plutons and volcanic sequences, and Cenozoic red beds (Figures 4.2 and 4.3; Qinghai Bureau of Geology and Mineral Resources (QBGMR), 1980; 1981). Pervasive thrust and strike-slip fault zones also provide fault gouge for illite age analysis. In this study, we present new low-temperature thermochronologic data from along the length of the central Kunlun Fault Zone, $^{40}Ar/^{39}Ar$ fault gouge dating, and geochronologic ages from deformed sedimentary strata to assess the timing of thrust fault and strike-slip fault motion.

4.2. Geologic Setting

The Kunlun Shan form the boundary between the high-elevation, low-relief surfaces of the Tibetan Plateau to the south and the moderate to low elevation Tarim and Qaidam Basins to the north (Figure 4.1). As a Paleozoic suture between the Kunlun-Qaidam and Songpan-Ganzi Terranes, the Kunlun Shan is a long-lived tectonic boundary and has experienced multiple periods of tectonic reactivation, including Cretaceous shearing (Mock et al., 1999; Chen et al., 2002), Eocene – Oligocene crustal shortening (Yin et al., 2008; Wu et al., 2009; Clark et al., 2010), and modern left-lateral shear (van der Woerd et al., 1998; 2002). The multi-stage tectonic history of the Kunlun Shan has resulted in a structurally varied setting with a diverse assemblage of rock types. Perhaps the most complete exposure of rock types and tectonic structures is located within the central portion of the Kunlun Shan, where the Kunlun Fault and subordinate fault splays have produced a series of structurally-controlled basins and narrow, intervening ranges.

4.2.1. Map units

Within the Dongdatan Valley, East Wenquan Basin, and East Deshuiwai Mountains, sedimentary and metasedimentary rock units range from Proterozoic to Quaternary in age (QBGMR, 1980, 1981). The Proterozoic Wanbaoguo Group, which largely consists of limestone, dolomite and shale, is crosscut by mafic dikes and is exposed north of the Middle Kunlun Fault

(Figures 4.1 and 4.2b; QBGMR, 1980, 1981). The Carboniferous Haoteluowa Group is composed largely of marine carbonate with interbedded sandstone and shale and unconformably overlies the Wanbaoguo Group (QBGMR, 1980, 1981). Within our field area, it is exposed in fault contact with Mesozoic and Cenozoic strata (Figures 4.2a and 4.3; QBGMR, 1980, 1981). The Permian Ganjia and Maerzheng Groups consist of marine carbonate, often fossiliferous, and locally metamorphosed to marble (QBGMR, 1980, 1981). These units are spatially extensive and form the steep topography to the north of the Dongdatan Valley and in the southeastern East Deshuiwai Mountains (Figure 4.2). The Triassic Babaoshan and Naocangjiangou Groups are largely composed of shale, siltstone, and fine to coarse sandstone, with limited conglomerate, arkose, fossil-bearing coal layers, and interbedded volcanic flows (QBGMR, 1980, 1981). In most regions, these units have been metamorphosed to greenschist facies (Wu et al., 2009). In the east, the Jurassic – Cretaceous Yangqu Group is conformably deposited over the Babaoshan Group (QBGMR, 1980, 1981). It is relatively undeformed where exposed, and consists of siltstone and arkosic sandstone. Cenozoic strata are unconformably deposited over Triassic and Permian units and are exposed throughout the Dongdatan Valley and East Wenquan Basin, as well as to the south of the East Deshuiwai Mountains (Figures 4.2, 4.3, and 4.4a; QBGMR, 1980, 1981). The depositional age of Cenozoic strata are not well constrained. The Paleogene - Neogene red bed unit is composed of fluvial sandstone, lacustrine siltstone, and conglomerate (Figures 4.4b and 4.4c). The Neogene Quguo Group is composed of lacustrine carbonates and fine-grained siltstone and is exposed in the eastern East Wenquan Basin (QBGMR, 1980, 1981). This unit is characteristically light greyish-yellow to pistachio green in color (Figure 4.4d).

Igneous units are exposed throughout the central Kunlun Shan, and range from outcrop-sized plutonic bodies and volcanic flows to large intrusive and extrusive complexes. In the eastern portion of the field area (Figure 4.2b), Permian granite intrudes into the Paleozoic Wanbaoguo Group and is exposed in the high peaks to the north of the Middle Kunlun Fault (QBGMR, 1980, 1981). The Triassic Babaoshan and Yalixige Units are granitic and granodioritic intrusive complexes, respectively, over which the Babaoshan Group strata are unconformably deposited (Figure 4.4e; QBGMR, 1980, 1981). The Babaoshan Group is interbedded with a thick sequence of basalt flows (Figure 4.2b), which in some regions exhibits columnar jointing, and is exposed directly south of the Middle Kunlun Fault and in the eastern Deshuiwai Basin (QBGMR, 1980, 1981). Within the western portion of our field area (Figures 4.2a and 4.3), igneous units are sparse, small in volume, and generally intrude into the Triassic Naocangjiangou Group (QBGMR, 1980, 1981). The small

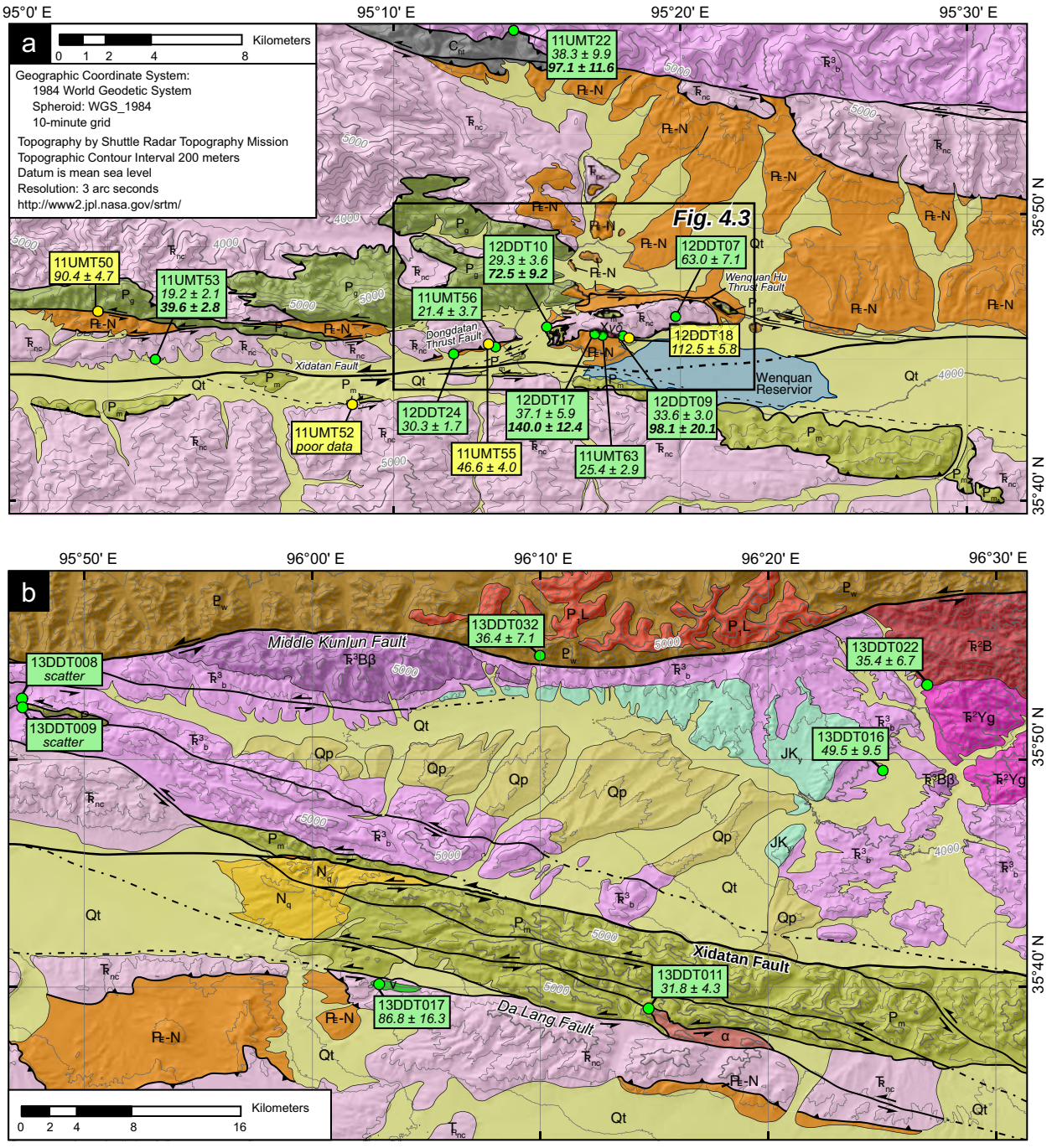

LEGEND

Samples
- apatite and zircon (U-Th)/He
- illite $^{40}Ar/^{39}Ar$

Geologic Features
- thrust fault
- strike-slip fault
- inferred fault
- contact

Sedimentary - Metasedimentary Units
- Qt — Quaternary alluvial - fluvial sandstone, siltstone, mudstone
- Qp — Quaternary coarse sandstone, and conglomerate
- N_q — Quguo Group: Neogene lacustrine mudstone, siltstone, carbonate
- Pε-N — Paleogene-Neogene sandstone, siltstone, conglomerate
- JK_y — Yangqu Group: Jurassic - Cretaceous arkosic sandstone, carbonaceous shale, pebble conglomerate
- T_3^3b — Babaoshan Group: greenschist - amphibolite facies, protolith: Triassic siltstone, mudstone, shale, sandstone
- T_nc — Naocangjiangou Group: greenschist - amphibolite facies, protolith: Triassic sandstone, conglomerate, shale, volcanic flows
- P_g — Ganjia Group: Permian marine limestone
- P_m — Maerzheng Group: Permian fossiliferous marine limestone, siltstone, interbedded pillow basalts
- C_h — Haoteluowa Group: Carboniferous limestone, sandstone, and shale
- P_w — Wanbaogou Group: Proterozoic limestone, dolomite, shale

Igneous Units
- T^2Yg — Yalixige Unit: Triassic granodiorite
- T^2B — Babaoshan Unit: Triassic biotite-rich granite
- $T^3B\beta$ — Basalt unit interbedded with Babaoshan Group
- T^3Bd — Triassic granite
- P'L — Longtong Unit: Permian biotite-rich granite
- Xyδ — granodioritic intrusions
- v — gabbro
- α — andesite

Figure 4.2. Geologic maps of (a) the Dongdatan Valley and East Wenquan Basin and (b) the East Deshuiwai Mountains and Deshuiwai Basin based on original mapping, published geologic maps (QBGMR, 1980; 1981), and satellite imagery. Hillshade and topographic contours are based on data from the Satellite Radar Topography Mission (SRTM). Fault gouge and thermochronologic samples are shown as yellow and green circles, respectively. Apatite (U-Th)/He ages are printed in italics, and zircon (U-Th)/He ages are printed in bold italics.

intrusions are generally rhyolitic to dacitic in composition, and have been moderately metamorphosed along with the host rock. Andesitic – dacitic flows are also present within the Triassic Naocangjiangou Group in the eastern portion of the field area (Figure 4.2b; QBGMR, 1980, 1981). These units tend to be thin, sub-meter to one meter in thickness. In the southern East Deshuiwai Mountains, a fairly thick sequence of andesitic lavas is faulted into place (Figure 4.2b; QBGMR, 1980, 1981). The structural complexity associated with the exposure of these andesitic rocks obscures the relationship with any specific sedimentary unit. South of the East Deshuiwai Mountains, small-volume andesitic intrusions are exposed within the Triassic Naocangjiangou Group (QBGMR, 1980, 1981).

4.2.2. Structural Geology

4.2.2.1. North-south oriented crustal shortening

In the central Kunlun Shan, the dominant style of modern deformation is left-lateral strike-slip faulting (Molnar and Tapponnier, 1978; Kidd and Molnar, 1988); however evidence for north-south contraction is also preserved (Wu et al., 2007, 2009). Throughout the study region, the Carboniferous Haoteluowa Group and the Permian Ganjia and Maerzheng Groups have been thrust over Triassic metapelites (Figures 4.2a and 4.3; QBGMR, 1980, 1981). This fault relationship is best exposed on either side of the Dongdatan Valley, along the northern East Wenquan Basin, and as a series of small klippen in a tectonic sliver immediately north of the Wenquan Reservoir (Figures 4.2a and 4.3). Deformed Triassic metapelites preserve tight east-west oriented folds and near-vertical axial planar cleavage (Figure 4.5a), suggesting that the greatest compressive stress was oriented north-south, in modern coordinates, and the least compressive stress was oriented vertically during the episode of deformation preserved in this strata. Based on field observations and the degree of tilting preserved in the strata, the contractional strain preserved in Cenozoic sedimentary units is far less than in Triassic metapelites, shortening of the Triassic strata took place prior to Cenozoic sedimentary deposition. In the central East Wenquan Basin, Cenozoic red beds are only mildly tilted

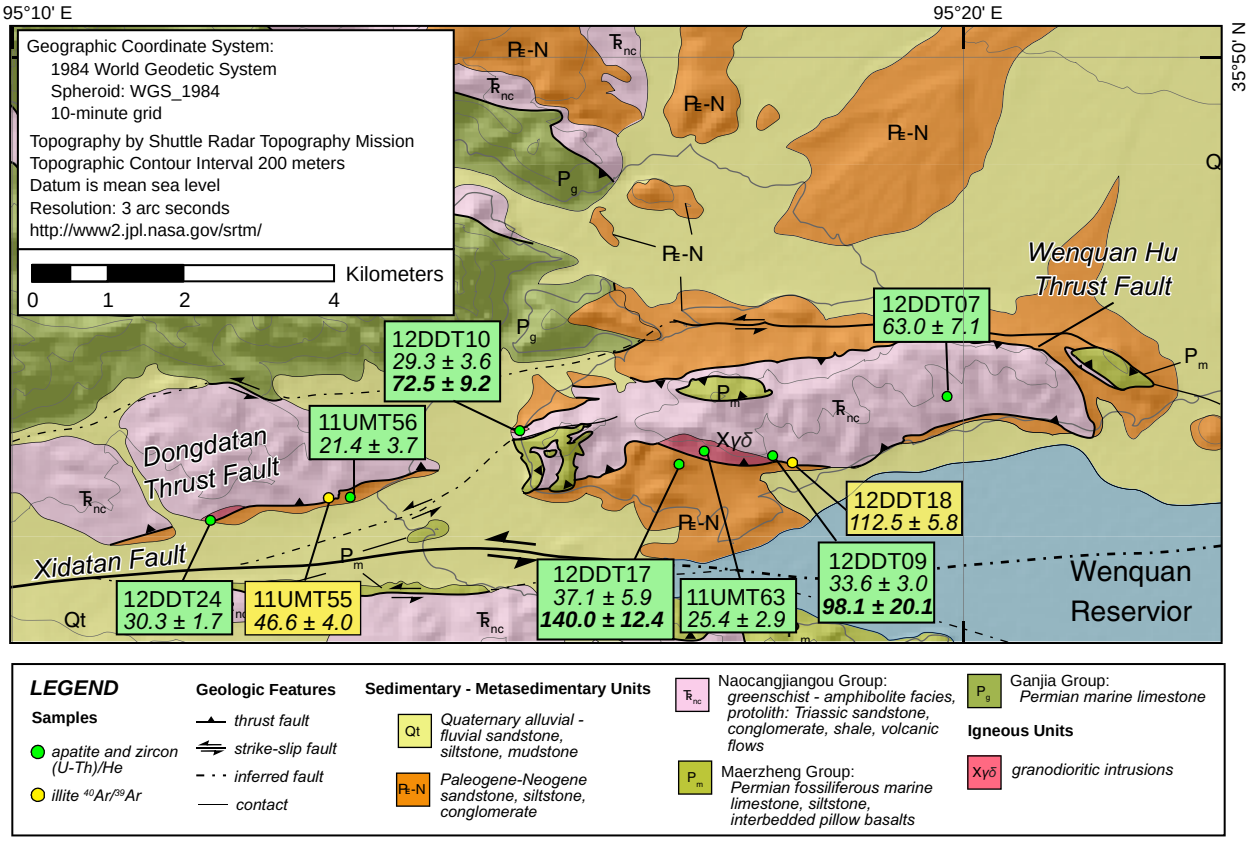

Figure 4.3. Geologic map of the Dongdatan Valley and East Wenquan Basin based on original mapping, published geologic maps (QBGMR, 1980; 1981), and satellite imagery. Hillshade and topographic contours are based on data from the Satellite Radar Topography Mission (SRTM). Fault gouge and thermochronologic samples are shown as yellow and green circles, respectively. Apatite (U-Th)/He ages are printed in italics, and zircon (U-Th)/He ages are printed in bold italics.

and overlie Triassic strata in angular unconformity (Figure 4.4a), however across the northern margin of the Dongdatan Valley and within East Wenquan Basin, red bed strata are more strongly deformed and the Dongdatan and Wenquan Hu Thrust Faults places Triassic metapelites and Paleozoic carbonate over Cenozoic red beds (Figures 4.2a, 4.3, and 4.5d). North of the Wenquan Reservoir, the Wenquan Hu Thrust Fault has been eroded on either side and is preserved as a klippe (Figures 4.2a and 4.3). The thrust fault relationship between Triassic strata and Cenozoic red beds is also well exposed south of the easternmost East Wenquan Basin in a fenster and south of the East Deshuiwai Mountains (Figure 4.2b).

4.2.2.2. Left-lateral shear

The Kunlun Fault Zone deforms a broad region within the central Kunlun Shan, such that left-lateral faulting is pervasive within the Dongdatan Valley, East Wenquan Basin, and East Deshuiwai Mountains. Major faults identified include the Xidatan Fault (the Xidatan-Dongdatan segment from van der Woerd et al (2002)), which is the main strand of the Kunlun Fault to the east of the Kunlun Pass, and the Middle Kunlun Fault (the Alag Hu strand from van der Woerd et al (2002)), which delineates a major lithological boundary between Proterozoic and younger strata in the eastern portion of the field area (Figures 4.1 and 4.2; QBGMR, 1980, 1981; Kidd et al., 1988). The mountainous terrane north of the Dongdatan Valley is crosscut by left-lateral faults that are subordinate to the main Xidatan Fault (Figure 4.2a). Subordinate faults offset Permian – Cenozoic strata, form well defined gouge and fault rock zones, and tend to form steep, near-vertical, topography when exposed in the Permian carbonate units (Figures 4.5b and 4.5c). Few minor strike-slip faults are exposed along the southern Dongdatan Valley (Figure 4.2a).

To the east, where the Xidatan Fault crosscuts the East Deshuiwai Mountains, it has created a wide fault gouge zone, up to 100s of meters in thickness, and forms a major structural discontinuity that separates Triassic metapelites to the north and Permian carbonate to the south (Figure 4.2b; QBGMR, 1980, 1981). Within the East Deshuiwai Mountains, left-lateral faulting is accommodated along many subordinate strike-slip faults. The Xidatan Fault and subordinate faults occasionally carry small fault bound blocks of allochthonous rock units that are isolated within an overall separate lithologic unit (QBGMR, 1980, 1981). The southern boundary of the East Deshuiwai Mountains a strike-slip fault, here named the Da Lang Fault, which continues to the west into the East Wenquan Basin and eventually converges with the Xidatan Fault (Figures 4.2a and 4.2b; QBGMR, 1980, 1981).

a
b
c
d
e

Figure 4.4. Field photographs of sedimentary features. (a) Flat-lying Cenozoic red bed strata are unconformably deposited over steeply dipping and tightly folded Triassic metapelites. (b) Fine sandstone of the Cenozoic red beds show well developed cross bedding, indicative of a medium-energy fluvial environment. (c) Pebble-cobble conglomerate of the Cenozoic red bed strata showing a heterogeneous source, generally dominated by Permian carbonate and Triassic metapelites. (d) Finely laminated lacustrine carbonate and carbonate-rich siltstone sequence of the Neogene Quoguo Group. (e) Panorama of the Triassic Babaoshan Group that is unconformably deposited on lower – mid Triassic plutonic rocks within the Deshuiwai Basin.

4.2.2.3. Modern fault activity

Offset Quaternary alluvial sediments along the Xidatan and Da Lang Faults, along with modern seismicity, suggests that strike-slip motion is actively accommodated within the central Kunlun Shan (seismic data courtesy of the US Geological Survey National Earthquake Information Center [USGS NEIC]). In the western and central portions of the field area, the surficial trace of the Xidatan Fault is evident from pressure ridges and offset Quaternary fluvial and alluvial features and is occasionally associated with hot springs and sag ponds. Terrestrial cosmogenic nuclide dating of offset river terraces in Dongdatan Valley suggests that the Xidatan Fault accommodates 10 – 11 mm yr^{-1} of left lateral motion (van der Woerd et al., 1998; 2002). Modern seismic data also suggest that faults within the East Deshuiwai Mountains are active (USGS NEIC). Slip rates along the Middle Kunlun and subordinate strike slip faults are not currently quantified. Seismic data does not provide evidence for modern fault activity along the Middle Kunlun Fault (USGS NEIC).

4.3. Low-temperature thermochronology

Low-temperature thermochronology provides a measure of the timing and rate of cooling as a rock is exhumed through the shallow crust by utilizing the temperature-dependent diffusion or annealing of radiogenic decay products within a host crystal. Under the assumption that tectonic activity causes an increase in the rate of erosion within an uplifted fault block, low-temperature thermochronology can be used to determine the onset of fault motion (Ehlers and Farley, 2003). In this study, we utilize the apatite and zircon (U-Th)/He thermochronometric system, hereafter referred to as AHe and ZHe, respectively. Both AHe and ZHe thermochronology are based on the quantification of the accumulated of radiogenically produced ^{4}He due to the decay of U, Th, and Sm (Ehlers and Farley, 2003). By measuring the elemental concentrations of radioactive parents and decay products, AHe and ZHe dating provides a measure of the time since a rock sample has passed

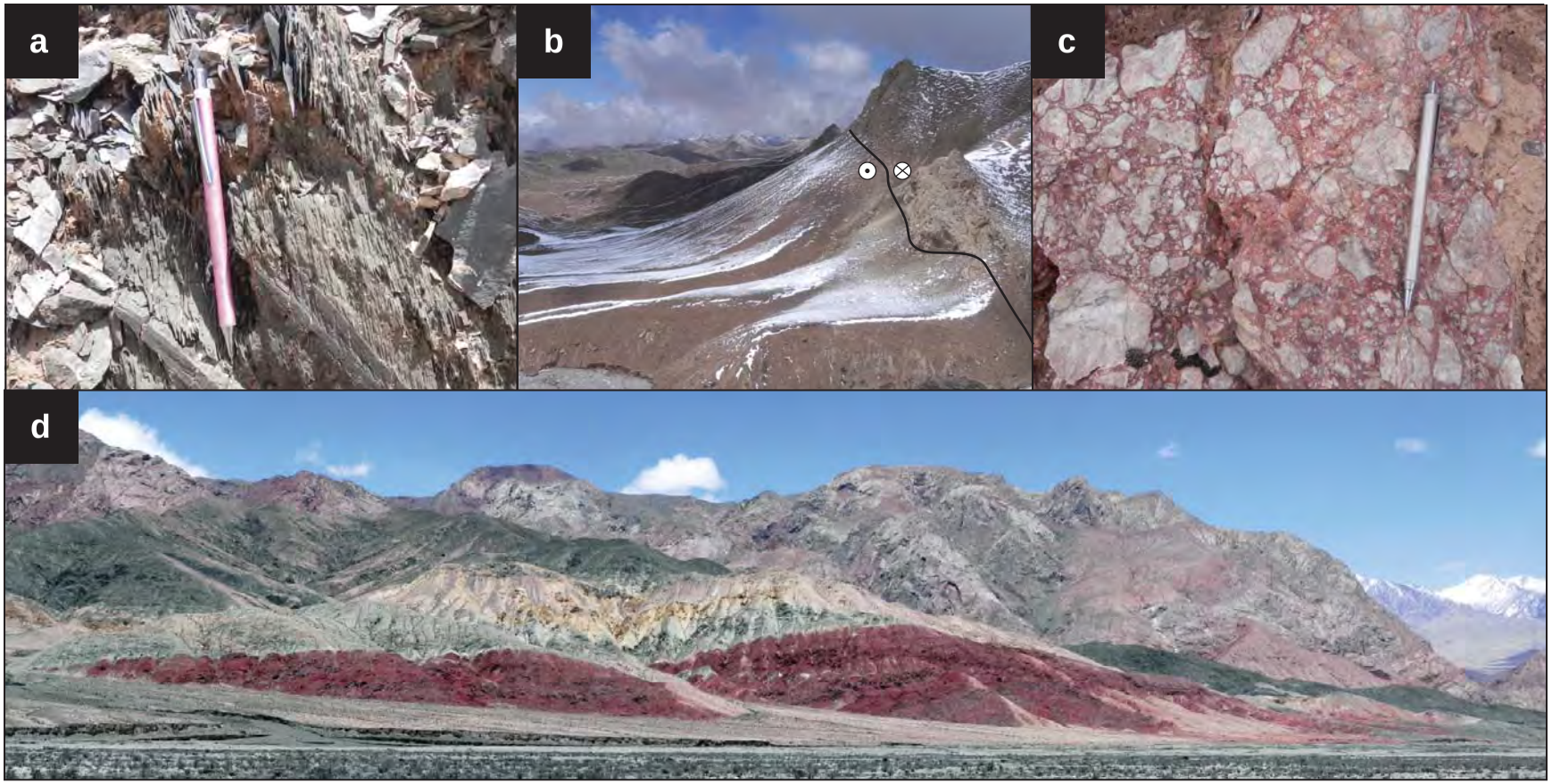

Figure 4.5. Field photographs of structural features observed. (a) shows axial planar cleavage developed in shale layers and tilted sandstone bedding within the Triassic Naocangjiangou Group. (b) is a westward-looking photo of a large strike-slip fault along the northern Dongdatan Valley, with poorly developed red bed strata to the south (left) and steep topography developed within the Permian carbonate units to the north (right). (c) shows a well developed breccia along the same fault shown in picture (b). (d) was taken looking roughly northeast and shows a well defined thrust fault with Triassic metapelites thrust over Cenozoic red bed strata. Both have been exhumed along the Xidatan Fault.

through an effective closure temperature after which ^{4}He is retained within the host crystal (Dodson, 1973; Warnock et al., 1997; Farley, 2000). For AHe thermochronology, the closure temperature is estimated at 60 – 75 °C (Wolf et al., 1996; Farley, 2000) and for ZHe thermochronology, the closure temperature is estimated at ~200 °C (Reiners et al., 2002). While geothermal gradients of continental interiors vary, a typical geothermal gradient for deformed continental crust of 25 – 35 °C km^{-1} suggests that the AHe and ZHe thermochronologic systems tend to record exhumation from 2 – 4 km and 6 – 8 km depth, which is ideal for understanding exhumation due to fault motion in the shallow crust (Ehlers and Farley, 2003; Braun, 2005; Ehlers, 2005).

4.3.1. Sample collection and preparation

The timing of fault initiation is typically determined from thermochronology in extensional or contractional deformation regimes, where tectonic activity generates topographic relief and a local increase in erosion rate (Ehlers and Farley, 2003; Braun, 2005). Conversely, thermochronologic studies along strike-slip faults are relatively few, since strike-slip faulting typically results in the lateral translation of fault blocks, rather than vertical exhumation. Certain strike-slip fault geometries, however, are also capable of producing vertical exhumation of sufficient magnitude to be recorded by low-temperature thermochronology, such as near fault junctions, terminations, and splays, as well as within restraining bends and along non-vertical fault planes (Spotila et al., 1998; 2001; 2007; Benowitz et al., 2011; Duvall et al., 2013; Niemi et al., 2014). We targeted these types of structural environments within the central Kunlun Shan in order to constrain the timing of strike-slip fault motion from low-temperature thermochronology. In order to constrain the timing of thrust faulting, on the other hand, we were required to avoid locations in which strike-slip related exhumation had caused considerable exhumation. We therefore also targeted sampling sites in which clear thrust fault relationships exist and where we expect strike-slip related exhumation to be absent or negligible (Figure 4.1).

Bedrock samples were collected from apatite and zircon bearing rock types, including volcanic and plutonic rocks of andesitic – dacitic composition (Table 4.1). We also collected medium – coarse grained sandstone rocks that we expected to experience sufficient burial to reset the apatite and zircon thermochronologic system prior to more recent fault-related exhumation. The limited topographic relief and heterogeneous geologic setting of our study site limited our ability to collect steep elevation transects, so we dated single samples to constrain the time of exhumation through the apatite and zircon effective closure temperatures. Sample locations and descriptions are available

Table 4.1. Sample locations, rock type, and mean apatite and zircon (U-Th)/He (AHe) ages for samples collected from the central Kunlun Shan. Age uncertainties are 1σ.

Sample	*Latitude [°]*	*Longitude [°]*	*Elevation [m]*	*Rock Type*	*AHe Age [Ma]*	*ZHe Age [Ma]*
11UMT53	35.749	95.028	4229	Gneiss	19.2 ± 2.1	39.6 ± 2.8
11UMT56	35.756	95.226	4030	Sandstone	21.4 ± 3.7	-
11UMT63	35.763	95.288	4091	Gneiss	25.4 ± 2.9	-
12DDT07‡	35.774	95.331	4026	Granitoid	63.0 ± 7.1	-
12DDT09	35.763	95.300	4068	Gneiss	33.6 ± 3.0	98.1 ± 20.1
12DDT10	35.768	95.256	3946	Gneiss	29.3 ± 3.6	72.5 ± 9.2
12DDT17	35.764	95.284	4084	Dacite-Andesite	37.1 ± 5.9	140.4 ± 12.4
12DDT22	35.940	95.236	4691	Sandstone	38.3 ± 9.9	97.1 ± 11.6
12DDT24	35.752	95.201	4063	Gneiss	30.3 ± 1.7	-
13DDT008†	35.878	95.787	4542	Metavolcanic	148.3 ± 47.3	-
13DDT009†	35.871	95.788	4558	Arkose	94.1 ± 55.3	-
13DDT011	35.632	96.246	4916	Metavolcanic	31.8 ± 4.1	-
13DDT016‡	35.825	96.417	3929	Arkose	49.5 ± 9.5	-
13DDT017‡	35.669	96.049	4373	Tonalite	86.8 ± 16.3	-
13DDT022	35.888	96.450	4123	Granodiorite	35.4 ± 6.7	-
13DDT023*	35.871	96.451	4053	Granodiorite	54.1 ± 15.6	-
13DDT032	35.909	96.166	4752	Andesitic dike	36.4 ± 7.1	-
13DDT036*	35.913	96.301	4538	Granite	73.1 ± 42.8	-

* samples omitted from analysis due to poor reproducibility (standard deviation > 25%)
† samples with broad age range and strong correlation between apatite age and crystal size
‡ samples have a strong correlation between age and effective Uranium content (eU)

in Table 4.1.

Once collected, samples were crushed and sieved using standard laboratory procedures. Apatite and zircon crystals were separated from the bulk sample using standard density and magnetic techniques. Crystals were handpicked at the University of Michigan to ensure grain quality using standard procedures (Farley and Stockli, 2002; Reiners et al., 2002). Apatite and zircon crystals were individually analyzed for He content at the University of Michigan HeliUM Laboratory. Apatites were analyzed for U, Th, and Sm content at the University of Arizona Laserchron Center, and zircons were analyzed for U and Th content at the University of Colorado Thermochronology Research and Instrumentation Laboratory.

4.3.2. Apatite (U-Th)/He age results

We collected and dated 18 bedrock samples for apatite (U-Th)/He thermochronology. A minimum of 4 apatite replicates were dated for each sample. Measured AHe ages range widely across the central Kunlun Shan, with mean ages between 20 and 87 Ma (Tables 4.1 and A4.1). Two samples, 13DDT23 and 13DDT36, were removed from further analysis because the standard deviation of replicate apatite ages exceeded 25%, indicating that the mean ages for these samples are not well constrained (Table 4.1). Five other samples exhibit correlations between age and effective Uranium content (eU) or grain size (samples 12DDT07, 13DDT008, 13DDT009, 13DDT016, 13DDT017), which afford the opportunity for thermal modeling. These samples are further discussed in section ***4.3.4*** and Appendix A. In the following paragraphs, we systematically describe the results and geologic setting for samples from west to east.

We collected nine bedrock samples along the Dongdatan Valley and East Wenquan Basin. The westernmost sample, 11UMT53, was collected from a small plutonic body that intruded the Triassic Naocangjiangou Group prior to metamorphism. This sample was dated at 19.2 ± 2.1 Ma (Figure 4.2a; Table 4.1). To the east, samples 12DDT24 and 11UMT56 were collected on either side of the Dongdatan Thrust Fault zone (Figures 4.2a, 4.3, and 4.5a). The hanging wall of the thrust fault is composed of the metamorphosed Triassic Naocangjiangou Group and small plutonic intrusions, from which 12DDT24 was sampled, and the footwall is composed of Cenozoic red beds, from which sample 11UMT56 was collected. The AHe ages of samples from the hanging and footwalls of the exposed thrust fault are 30.3 ± 1.7 and 21.4 ± 3.7 Ma, respectively (Figures 4.2a and 4.3; Table 4.1).

Immediately north of the Wenquan Reservoir, the Wenquan Hu Thrust Fault places Triassic

metapelites over Cenozoic red beds, similar to the Dongdatan Thrust Fault. We collected samples 12DDT10, 11UMT63, and 12DDT09, and 12DDT07 from small plutonic bodies within the hanging wall of the Wenquan Hu Thrust Fault (Figures 4.2a and 4.3; Table 4.1). The AHe ages for these samples range between 25 and 34 Ma, with the exception of 12DDT07 which has been dated at 63.0 ± 7.1 Ma (Table 4.1). Sample 12DDT07 shows a strong correlation between eU content and AHe age (Table A4.1), the implications of which are discussed below. From the footwall of the Wenquan Hu Thrust Fault, sample 12DDT17 was collected from a bed within the Cenozoic strata. The AHe age for this sample is older than the samples collected in the proximal hanging wall, at 37.1 ± 5.9 Ma (Figures 4.2a and 4.3; Table 4.1). In the northwestern corner of the East Wenquan Basin, sample 12DDT22 was collected from the upper Triassic Babaoshan Group and provides an AHe age of 38.3 ± 9.9 Ma (Figure 4.2a; Table 4.1). Sample 12DDT22 was collected ~2 km to the north of the surface exposure of the Middle Kunlun Fault (Figure 4.2a).

Within the East Deshuiwai Mountains, we collected samples 13DDT008 and 13DDT009 from interbedded volcanic and metamorphosed arkosic sandstone layers, respectively, of the Triassic Naocangjiangou Group. The replicate AHe ages from 13DDT008 range between 86 and 201 Ma, and the replicate ages from sample 13DDT009 range between 16 and 141 Ma (Figure 4.2b; Table 4.1). Apatite replicates for 13DDT008 and 13DDT009 show a strong correlation in AHe age and crystal width, which is elaborated on in section ***4.3.4*** and Appendix A. To the southeast of the East Deshuiwai Mountains, sample 13DDT017 similarly displays strong correlation between age and eU and was collected from a small plutonic body that intrudes into the Triassic Naocangjiangou Group. Within the East Deshuiwai Mountains, sample 13DDT011 was collected from a metamorphosed volcanic unit and provides an AHe age of 31.8 ± 4.1 Ma (Figure 4.2b; Table 4.1). This region of the East Deshuiwai Mountains is strongly deformed due to strike-slip motion and largely composed of Permian marine carbonate, such that exposed apatite bearing rock types are scarce.

To the north of the Deshuiwai Basin, we collected several igneous samples that intrude into the Proterozoic Wanbaoguo Group. Apatite quality was poor and only one sample (13DDT032) provided replicable AHe ages. Sample 13DDT032 was collected from an andesitic dike and provides a mean AHe age of 36.4 ± 7.1 (Figure 4.2b; Table 4.1). Within the center of the Deshuiwai Basin, the Triassic Babaoshan and Jurassic – Cretaceous Yangqu Group are fairly undeformed and well exposed. We collected a bedrock sample from an arkosic sandstone of the Babaoshan Group (13DDT016), which provided an AHe age of 49.5 ± 9.5 Ma (Figure 4.2b; Table 4.1). This sample shows a correlation between eU and replicate age, similar to samples 13DDT017 and 12DDT07.

Nearby, to the northeast, several plutonic units of lower Triassic age are exposed (Figure 4.2b; QBGMR, 1980; 1981). We collected two samples, 13DDT022 and 13DDT023, from these large intrusions of andesitic – dacitic composition. Sample 13DDT022 was dated using AHe analysis at 35.4 ± 6.7 Ma and 13DDT023 has very poor replicate agreement and was omitted from further analysis (Tables 4.1 and A4.1).

4.3.3. Zircon (U-Th)/He age results

To better resolve bedrock cooling histories from the Dongdatan Valley, we obtained zircon (U-Th)/He (ZHe) ages for 5 out of the 18 samples collected for thermochronologic analysis (Figures 4.2a and 4.3; Table 4.1). We dated a minimum of 3 zircon crystals per sample. All samples had reproducible ZHe ages with standard deviation of replicate apatite ages less than 25% of the mean age (Table 4.1). Below, we describe the results and geologic setting for samples from west to east.

The zircon (U-Th)/He age for the westernmost sample collected for thermochronologic analysis (11UMT53) provided an Eocene age of 39.6 ± 2.8 Ma (Figure 4.2; Table 4.1). This sample was collected from a small plutonic body near the trace of the Xidatan Fault (Figure 4.2). To the east, samples 12DDT09 and 12DDT10 were collected from the hanging wall of the Wenquan Hu Thrust Fault and have ZHe ages of 98.1 ± 20.1 Ma and 72.5 ± 9.2 Ma, respectively (Figures 4.2a and 4.3; Table 4.1). Sample 12DDT17 was collected from the footwall red bed strata of the Wenquan Hu Thrust Fault, and was dated using ZHe analysis at 140.0 ± 12.4 Ma (Figures 4.2a and 4.3; Table 4.1). We collected sample 12DDT22 from the northern East Wenquan Basin, from which we obtained a ZHe age of 97.1 ± 11.6 Ma (Figure 4.2; Table 4.1).

4.3.4. Thermal modeling results

Single apatite (U-Th)/He thermochronometric ages generally only constrain a time at which the sample passed through the effective closure temperature, but do not constrain the cooling rate, which is essential when seeking to constrain the onset of rapid cooling due to faulting. Thus, we only modeled the time-temperature histories samples for which we have both AHe and ZHe data, which include samples 11UMT53, 12DDT09, 12DDT10, 12DDT17, and 12DDT22, and for samples that show unique AHe data. For example, samples 12DDT07, 13DDT016, and 13DDT017 show a strong correlation between the apatite (U-Th)/He age and effective Uranium content (eU). In these cases, the helium diffusion kinetics within apatite crystals have been modified by

accumulated radiation damage, thus altering the effective closure temperature for each apatite (Flowers et al., 2009). The AHe age – eU correlation limits the acceptable modeled time-temperature histories and affords the possibility of constraining the time and rate of cooling with AHe data alone.

Similarly, correlations between age and grain size provide important insight into the thermal history of a rock. Typically, larger apatite crystals retain a greater fraction of radiogenic He than smaller crystal sizes, and therefore record older apparent (U-Th)/He ages (Farley, 2000). However, the thermal history of a rock has a strong influence on the magnitude of the age to crystal size relationship (Wolf et al., 1998; Reiners and Farley, 2001). For example, a moderate to fast cooling rate will render this relationship imperceptible because the rock will pass from conditions of complete He diffusion to He retention quickly relative to radiogenic He production. Conversely, for slow cooling rates, a rock may reside within the apatite PRZ for an extended period of time, at which point He is only partially retained within the crystal. The fraction of He retained, as a function of crystal size, will strongly influence the apparent apatite (U-Th)/He age (Wolf et al., 1998; Reiners and Farley, 2001). For samples with a strong age-crystal size correlation, the youngest crystal age provides a maximum time of exhumation (Reiners and Farley, 2001).

The methods and detailed results for thermal modeling of samples 11UMT53, 12DDT07, 12DDT09, 12DDT10, 12DDT17, 12DDT22, 13DDT008, 13DDT009, 13DDT016, and 13DDT017 are available in Appendix A an Figure A4.1. For samples with AHe and ZHe data, modeling results allow for several possible cooling histories. Modeling results indicate that samples may have monotonically cooled to near surface temperatures between Cretaceous to Cenozoic time, or that samples experienced an increase in cooling rate during Eocene – Oligocene time. Apatite fission-track dating for these samples, which is currently in progress, will be able to resolve the cooling history between the ~100 and 120 °C temperature window (Ketcham et al., 2007) and distinguish between current possible cooling scenarios.

For samples with only AHe data available, nearly all thermal modeling results, with the exception of 12DDT07, indicate that the rocks were isothermally held at shallow crustal levels from Mesozoic to Cenozoic time, which is consistent with thermal modeling in the northern Kunlun Shan (Figures A4.1 and A4.2; Clark et al., 2010). Modeling results for sample 12DDT007 do not clearly indicate whether these rocks were isothermally held but do not preclude the possibility (Figure A4.1). HeFTy modeling results for samples 12DDT007, 13DDT016, and 13DDT017 suggest that these rocks were rapidly exhumed no earlier than 65 Ma, 40 Ma, and 50 Ma, respectively (Figure

A4.1). The AHe ages and grain size correlations in samples 13DDT008 and 13DDT009 indicate that these rocks were exhumed rapidly after ~16 Ma (Figure A4.2). These samples were collected from a restraining bend along the Xidatan Fault (Fu and Awata, 2007).

4.4. $^{40}Ar/^{39}Ar$ fault gouge dating

Fault gouge is an unconsolidated material that is formed during discrete events of tectonic movement as wall rock undergoes brittle deformation and vertical or lateral transport. The grain size of fault gouge can vary, but is generally small and includes a considerable proportion of clay-sized material. Depending on the wall rock lithology and depth of fault gouge formation, clay-sized minerals can be well suited for age dating (van der Pluijm et al., 2001). Specifically, illite clay is a potassium-bearing micaceous mineral that is often found within fault gouge. Authigenically-grown illite (polytype $1M_d$) is a diagenetic product of tectonic activity and is the target for fault gouge dating. However, separation of pure authigenic illite from is not usually possible in fault gouge material because of the presence of detrital illite (polytype $2M_1$), and so the ages of authigenic and detrital illite are typically estimated from a two-end member mixing model between the two potassium-bearing clay phases (van der Pluijm et al., 2001). The authigenic illite age thus corresponds to the timing of faulting (van der Pluijm et al., 2001).

4.4.1. Sample collection and preparation

Fault gouge samples were collected from thrust and strike slip faults throughout the Dongdatan Valley, East Wenquan Basin, and East Deshuiwai Mountains by identifying fault zones with clay rich gouge material. Samples were initially prepared for illite age analysis by drying gouge under heat lamps and carefully pulverizing the material in an agate mortar. Powdered fault gouge was suspended in deionized water for 30 minutes and agitated in an ultrasonic bath for 30 – 60 minutes to ensure crystal disaggregation. The material that remained suspended after ultrasonic agitation was then poured off and further prepared for illite age analysis. Because authigenic illite crystals tends to be smaller than detrital illite crystals (Grathoff and Moore, 1996), the relative proportion of each illite polytype was varied by separating samples into several aliquots by gravitational separation in a centrifuge. Samples were separated using a ThermoFischer CL-2 centrifuge into coarse (1 – 2 μm), medium-coarse (0.5 – 1 μm), medium (0.2 – 0.5 μm), fine (0.05 – 0.2 μm), and ultrafine (<0.05 μm) size fractions. Finally, each size fraction was dried and powdered by hand in an agate mortar.

The presence of datable illite minerals, other clay phases, and evaporite mineral phases was determined using the Scintag X1 Powder X-Ray Diffractometer (PXRD) at the University of Michigan Electron Microbeam Analysis Laboratory (EMAL). Powder patterns were measured at a 0.05° step size for 30 seconds between 16 and 44 degrees (2Θ). For samples with clear illite abundance and a lack of other interfering mineral phases, such as potassium feldspar, which can influence the measured $^{40}Ar/^{39}Ar$ age, and halite, which can obscure illite PXRD patterns, we estimated the proportion of detrital to authigenic illite content and in each aliquot by comparing standard $2M_1$ and $1M_d$ powder patterns to each fault gouge sample aliquot. Measured standard powder patterns were combined in varying proportions and compared to measured sample aliquots. The error of polytype pattern matching is generally between 3 and 5 % (Haines and van der Pluijm, 2008), which we average to a 4% error for each aliquot.

Of the 34 samples of fault gouge collected and prepared for illite age analysis, we selected four samples for age dating based on abundant authigenic illite content and structural setting: two samples from thrust faults and two samples from strike-slip faults along the Dongdatan Valley (Figure 4.2a). Four aliquots from each sample were submitted for $^{40}Ar/^{39}Ar$ geochronology at the University of Michigan Argon Geochronology Laboratory. Clay samples were formed into small pellets and encapsulated into silica tubes at high vacuum to avoid recoil loss of argon during irradiation. Recoil argon gas was measured by cracking silica capsules under high vacuum. Aliquots were subsequently step heated with a Coherent Innova 5 W continuous argon-ion laser and argon isotopes were measured with a VG1200S mass spectrometer with a Daly detector. Fusion system blanks were run every five fusion steps and blank levels of ^{36}Ar through ^{40}Ar were subtracted from gas fractions. A zero-aged artificial glass sample was used for correction for interfering reactions that produce ^{40}Ar. The decay of ^{37}Ar and ^{39}Ar, K, Ca, and Cl interfering nucleogenic reactions and the production of ^{36}Ar from ^{36}Cl decay was corrected for. The argon age spectrum measured for each fault gouge aliquot does not exhibit typical age plateaus because aliquots are composed of a mixture between detrital and authigenic illite ages, and because of argon recoil during irradiation. For illite age analysis, the total gas ages are used to determine the age of the illite polytype mixtures present in each aliquot. We increased the error for each aliquot to 3% of the age in order to account for external errors (Renne et al., 1998; Karner and Renne, 1998; Dazé et al., 2003).

The authigenic and detrital ages are estimated using a Bayesian linear regression method through the plotted age and illite concentrations for each sample, in which the error in polytype concentration and geochronologic age are taken into account (Figure 4.6). This regressing technique

Table 4.2. Fault gouge data from thrust and strike-slip faults sampled in the Dongdatan Valley

Sample	***Size fraction*** *[μm]*	***$^{40}Ar/^{39}Ar$ age*** *[Ma]*	***Percent $2M_1$*** *[%]*	***F-recoil*** *[%]*
11UMT50				
	1.0 - 2.0	119.76 ± 0.52	37 ± 4	17.2
	0.5 - 1.0	117.62 ± 0.71	27 ± 4	15.0
	0.2 - 0.5	104.58 ± 0.39	15 ± 4	18.8
	0.05 - 0.2	93.75 ± 0.33	5 ± 4	21.9
11UMT52				
	1.0 - 2.0	168.77 ± 1.17	85 ± 4	10.1
	0.5 - 1.0	172.92 ± 0.78	78 ± 4	8.1
	0.2 - 0.5	163.05 ± 0.45	42 ± 4	10.1
	0.05 - 0.2	131.3 ± 0.41	36 ± 4	24.6
11UMT55				
	1.0 - 2.0	72.17 ± 0.4	55 ± 4	14.8
	0.5 - 1.0	80.09 ± 0.59	42 ± 4	13.0
	0.2 - 0.5	69.86 ± 0.61	30 ± 4	15.5
	0.05 - 0.2	54.65 ± 0.21	10 ± 4	21.7
12DDT18				
	1.0 - 2.0	142.39 ± 0.87	45 ± 4	20.3
	0.5 - 1.0	172.61 ± 0.64	37 ± 4	11.9
	0.05 - 0.2	132.52 ± 0.5	10 ± 4	21.6
	<0.05	117.35 ± 0.53	4 ± 4	23.7

estimates the likelihood of each linear regression to fitting the measured data and is able to resolve potential correlations between the regression slope and intercept values. Prior slope and intercept bounds were chosen to guide the regression without restricting the sampling of likely regression parameters by ensuring that posteriors were not within 5% of the prior slope and intercept bounds. The modeled linear regression with the highest likelihood of fitting the observed data was deemed the best-fit line, from which we calculated the estimated authigenic and detrital illite ages for each sample. We report errors in slope and intercept values at the 2σ level.

4.4.2. $^{40}Ar/^{39}Ar$ fault gouge dating results

The XRD powder patterns and modeled illite mixtures for each aliquot are available in Figures A4.3 – A4.6, $^{40}Ar/^{39}Ar$ age spectra are plotted in Figures A4.7 – A4.10, and Ar release data is available in Table A4.2. The simplified results for each sample aliquot are in Table 4.2 and plotted in Figure 4.6. In the following sections, we discuss the results and interpretations of fault gouge data.

4.4.2.1. Thrust faults

The two fault gouge samples (11UMT55 and 12DDT18) were collected from similar structural settings in which Triassic metapelites are thrust over Cenozoic red beds (Figure 4.2a). The age of authigenically-grown illite must be younger than the formation age of detrital illite within the surrounding wall rock, which suggests that an increase in the proportion of authigenic to detrital illite for each sample aliquot should correspond to a decrease in the $^{40}Ar/^{39}Ar$ age, assuming that there are only two age populations present (van der Pluijm et al., 2001). However, in the majority fault gouge samples collected from Dongdatan Valley, we do not see an entirely well-behaved relationship between the aliquot ages and authigenic illite proportions. For thrust fault gouge samples there is a linear age-illite concentration relationship in the three finest size fractions measured, but the coarsest size fraction in both samples deviates from this trend and is younger than the next coarsest size fraction (Figure 4.6; Table 4.2). There are several plausible explanations for non-linear trends in these samples. The first possibility is that, instead of a two-end member mixing problem, there are three or more illite populations with different ages. In this situation, the assumption that our sample ages reflect a linear mixing ratio is violated and an attempt to interpret the fault gouge data may run the risk of producing a geologically meaningless age. Another possibility is that the coarsest size fraction has undergone ^{40}Ar loss in nature, resulting in an erroneously young age. In this situation, we may be able to determine a geologically meaningful age

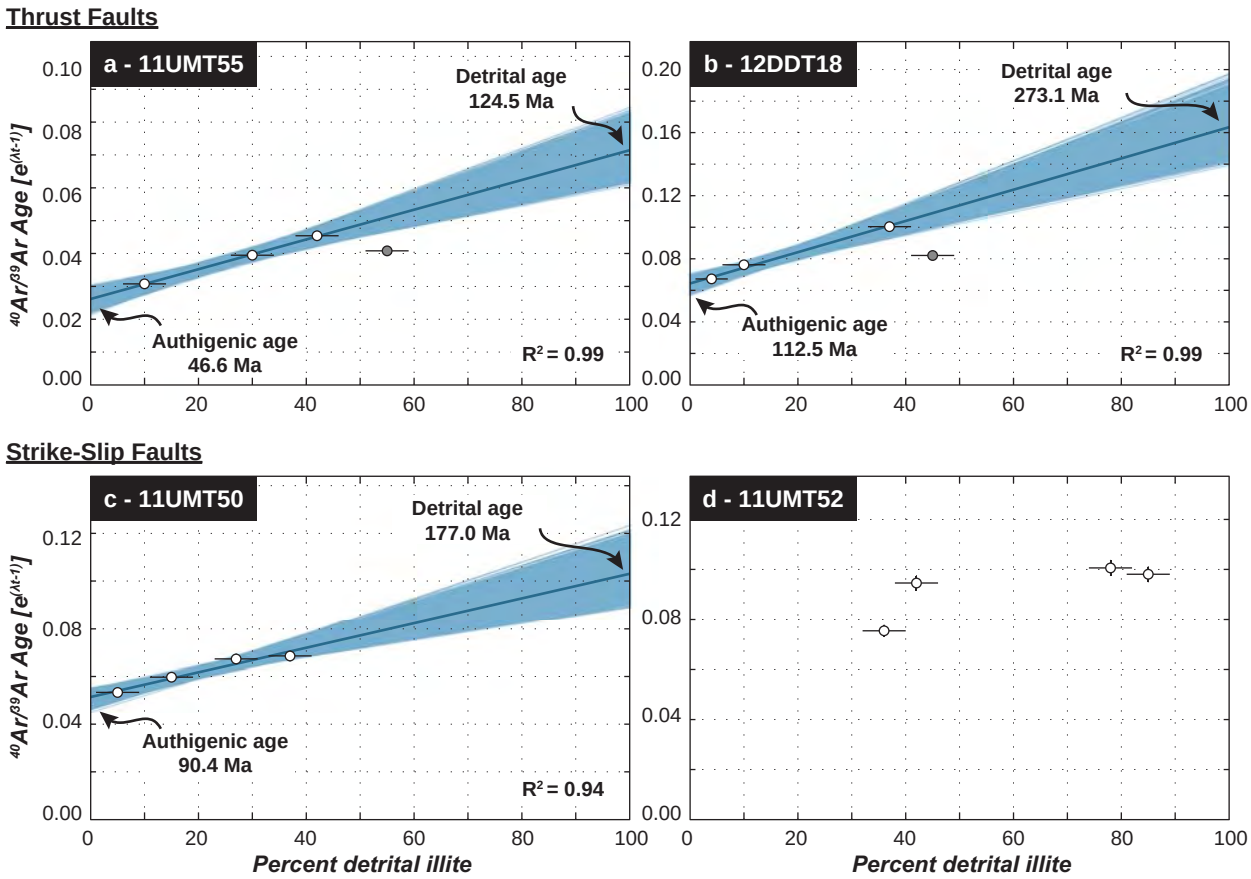

Figure 4.6. Results for fault gouge dating within the Dongdatan Valley. For each sample, size fraction aliquote age and illite concentrations are plotted as small dots. Age errors are present but hidden by the size of data points. Data points that are used for authigenic illite age estimation are shown as white dots and data points omitted are shown as grey dots. The best-fit results from Bayesian linear regression are shown as dark blue lines and other acceptible linear regression lines are shown in lighter blue. (a) shows thrust fault sample 11UMT55 with an estimated fault gouge age of 46.6 Ma. (b) shows thrust fault sample 12DDT18 with an estimated fault gouge age of 112.5 Ma. (c) shows strike-slip fault sample 11UMT50 with an estimated fault gouge age of 90.4 Ma. (d) shows strike-slip fault sample 11UMT52 with no estimate for the timing of fault motion due to lack of linear age-illite concentration trend.

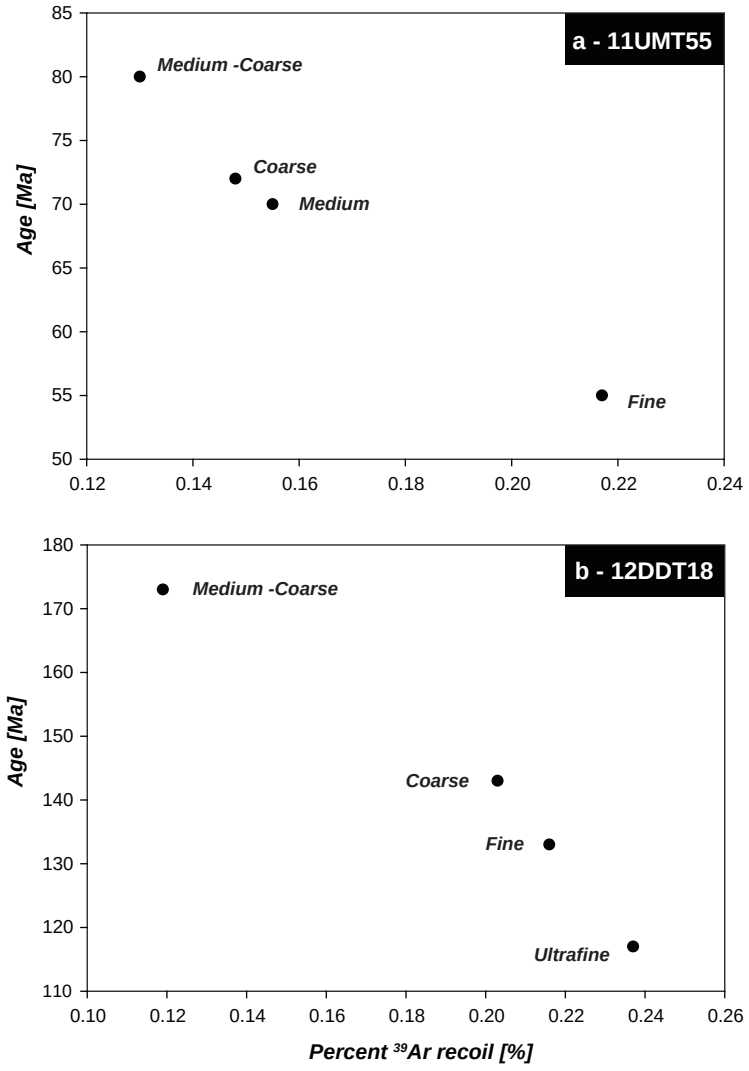

Figure 4.7. Fault gouge size fraction ages plotted against percent ^{39}Ar recoil (f-recoil) for thrust fault gouge samples 11UMT55 and 12DDT18. This plot shows the negative correlation between size fraction ^{40}Ar/^{39}Ar age and f-recoil, which is a proxy for illite crystallinity. In both samples, the coarsest size fraction has a younger age and higher f-recoil than the medium-coarse size fraction, which may relate to an increased potential for ^{40}Ar loss in nature and therefore an anomalously young ^{40}Ar/^{39}Ar age.

from the fault gouge data by omitting the coarsest size fraction from authigenic illite age analysis.

The natural loss of ^{40}Ar in the coarsest size fraction for samples 11UMT55 and 12DDT18 may be explained by examining the fraction of ^{39}Ar recoil during irradiation for each sample aliquot (f-recoil; Table 4.2). Studies of illite characteristics and f-recoil indicate that there is a strong correlation between the crystallinity of illite minerals and the amount of ^{39}Ar loss during irradiation (Dong et al., 1995). This relationship can be explained by increase in exposure of illite layers to crystal packet boundaries, voids, and dislocations, which correspond to pathways for ^{39}Ar recoil during irradiation. A decrease in illite crystallinity may also suggest that ^{40}K atoms are not entirely bound to the crystal structure, and since radiogenic ^{40}Ar is produced near the parent nuclei, this may result in an increased potential for ^{40}Ar loss in nature and thus a younging of the apparent $^{40}Ar/^{39}Ar$ age (Dong et al., 1995). Because the $2M_1$ detrital illite polytype has a lower crystallinity index (and therefore higher crystallinity) than the authigenic $1M_d$ polytype (Grubb et al., 1991), one expects to see an increase in illite crystallinity, and corresponding decrease in the fraction of ^{39}Ar recoil during irradiation (Dong et al., 1995), for increasing proportions of detrital illite. In both fault gouge samples collected from thrust faults, we see the expected negative correlation between relative detrital illite content and f-recoil in the three finest size fractions, but an increase in f-recoil measured in the coarsest size fraction, which likely corresponds to a decrease in illite crystallinity (Figure 4.7; Table 4.2; Dong et al., 1995). This may therefore suggest that the coarsest size fraction in samples 11UMT55 and 12DDT18 was more susceptible to ^{40}Ar loss in nature and that the apparent total gas age is erroneously young.

On this basis, we omit the coarsest size fraction for both thrust fault gouge samples and analyze the remaining three finest size fractions to determine an age of authigenic illite growth (Figure 4.6). The Bayesian linear regression for sample 11UMT55 produces an authigenic illite age of 46.6 ± 4.0 Ma, a detrital illite age of 124.5 ± 11.3 Ma, and an R^2 value of 0.99 (Figure 4.6a). Using a similar regression scheme, sample 12DDT18 produces a fault gouge age of 112.5 ± 5.8 Ma, a detrital illite age of 273.1 ± 27.4 Ma, and an R^2 of 0.99 (Figure 4.6b).

4.4.2.2. Strike-slip faults

Samples 11UMT50 and 11UMT52 were collected from recently or currently active strike-slip faults located to the north and south of the Dongdatan Valley, respectively. Only sample 11UMT50 provides an interpretable age-illite concentration pattern. Sample 11UMT52, on the other hand, has a non-linear relationship between illite concentration and $^{40}Ar/^{39}Ar$ age and the deviation from the

expected linear trend cannot be entirely explained by the measured f-recoil. In this sample, there is a younging of the coarsest size fraction that correlates with an increase in the measured ^{39}Ar recoil during irradiation and possibility of ^{40}Ar loss in nature (Table 4.2; Dong et al., 1995), however the other three size fractions do not produce a linear trend (Figure 4.6d). We therefore suggest that sample 11UMT52 is likely affected by three or more illite age populations and cannot be interpreted using a two end-member mixing model.

Fault gouge data from sample 11UMT50 do show an increase in ^{40}Ar/^{39}Ar age with an increase in the detrital illite component. The Bayesian linear regression through this fault gouge data suggests that the authigenic illite component was formed at 90.4 ± 4.7 Ma and that the detrital illite has an age of 177.0 ± 16.4 Ma. The best-fit regression has an R^2 value of 0.95 (Figure 4.6c).

4.5. Depositional age and provenance of terrestrial red bed strata

The depositional age and provenance of terrestrial red bed strata in the central Kunlun Shan provide important constraints for tectonic interpretations of the region. Red bed strata are present throughout the Dongdatan Valley, East Wenquan Basin, and East Deshuiwai Mountains and are exposed in the footwalls of the Dongdatan and Wenquan Hu Thrust Faults, as well as in the foot wall of a thrust fault in the central and eastern East Wenquan Basin, and unconformably overlying Triassic metapelites in the northern East Wenquan Basin (Figures 4.2a, 4.4a, and 4.5d; QBGMR 1980, 1981). Stratigraphic observations from red bed strata are suggestive of a nearby source terrane. Clasts within conglomeratic layers are sub-angular to sub-rounded and cobble to pebble sized (Fig. 4.4c). The clasts are composed of greenschist metapelites and marine carbonate. We suggest that the large size, moderate rounding, and composition of clasts indicate that the source rocks are from the proximally exposed Carboniferous Haoteluowa Group, the Permian Ganjia and Maerzheng Groups, and the Triassic Babaoshan and Naocangjiangou Groups. The timing of red bed strata deposition within the central Kunlun Shan may therefore relate to deformation and erosion of the proximal source terrane.

According to geologic maps from the central Kunlun Shan, red bed deposition occurred in Eocene to Miocene time (QBGMR, 1980, 1981). Wu et al. (2009) suggest that red bed strata within the Dongdatan Valley and East Wenquan Basin are of the Fenghuoshan Group. However, the timing of Fenghuoshan Group deposition is from late Cretaceous to Eocene time and the source terrane is likely the Tanggula Shan (Dai et al., 2012; Staisch et al., 2014), which are located 250 – 300 km to the south of the Dongdatan Valley. Based on the inference of a proximal source terrane for

conglomeratic strata in the Dongdatan Valley and East Wenquan Basin, we suggest that the deposition of red bed strata in the central Kunlun Shan is likely unrelated to Fenghuoshan Group deposition, and consider the mapped Eocene – Miocene depositional ages to be the most accurate age estimates available (Figures 4.2 and 4.3; QBGMR, 1980, 1981).

4.6. Discussion

Previous studies on the timing of rapid exhumation in the central Kunlun Shan have led to a variety of tectonic interpretations, including rapid unroofing between 41 and 21 Ma, the onset of crustal shortening at 35 Ma, and the onset of left-lateral shear between 20 and 15 Ma with a possible earlier history of shear between 30 and 20 Ma (Mock et al., 1999; Yuan et al., 2006; Clark et al., 2010; Duvall et al., 2013). The overlap in interpreted episodes and causes for deformation in the Kunlun Shan is largely due to the multi-stage tectonic history of the region and complexities involved in determining whether exhumation is caused by strike-slip or thrust fault deformation. According to experimental and field studies of transpressional environments, exhumation due to strike-slip faulting is of high magnitude and highly localized near the fault trace (Wilcox et al., 1973; Spotila et al., 2001; Niemi et al., 2014). On this basis, we suggest that the deformation history can be discerned by relating the timing of exhumation to strike-slip fault proximity and to key local structural observations. In the following section, we combine thermochronologic dating, field observations, and fault gouge dating to interpret the deformation history of the central Kunlun Shan.

4.6.1. The timing of crustal shortening

Thrust faults which place Triassic metapelites over Cenozoic red bed strata are preserved within an extensional step over between the Xidatan and Middle Kunlun Faults (Figures 4.1, 4.2, and 4.3). Because thrust faults are not likely due to the modern extensional tectonics within this locale, we infer that they are related to prior history of crustal shortening along the Kunlun Shan. Thermochronologic samples collected from metapelites in the hanging wall of the Dongdatan and Wenquan Hu Thrust Faults range between 25.4 and 33.6 Ma, with the exception of one sample, 12DDT07 which records an older age likely due to radiation damage effects (Figure 4.2a; Table 4.1). While the Dongdatan and Wenquan Hu Thrust Faults are located near the main strand of the Xidatan Fault, the AHe ages from both hanging wall blocks are similar to AHe data from the northern East Wenquan Basin, southern East Deshuiwai Mountains and Deshuiwai Basin, which are located farther from the strike-slip fault (Figure 4.8; Table 4.1). These ages are consistent with mid-

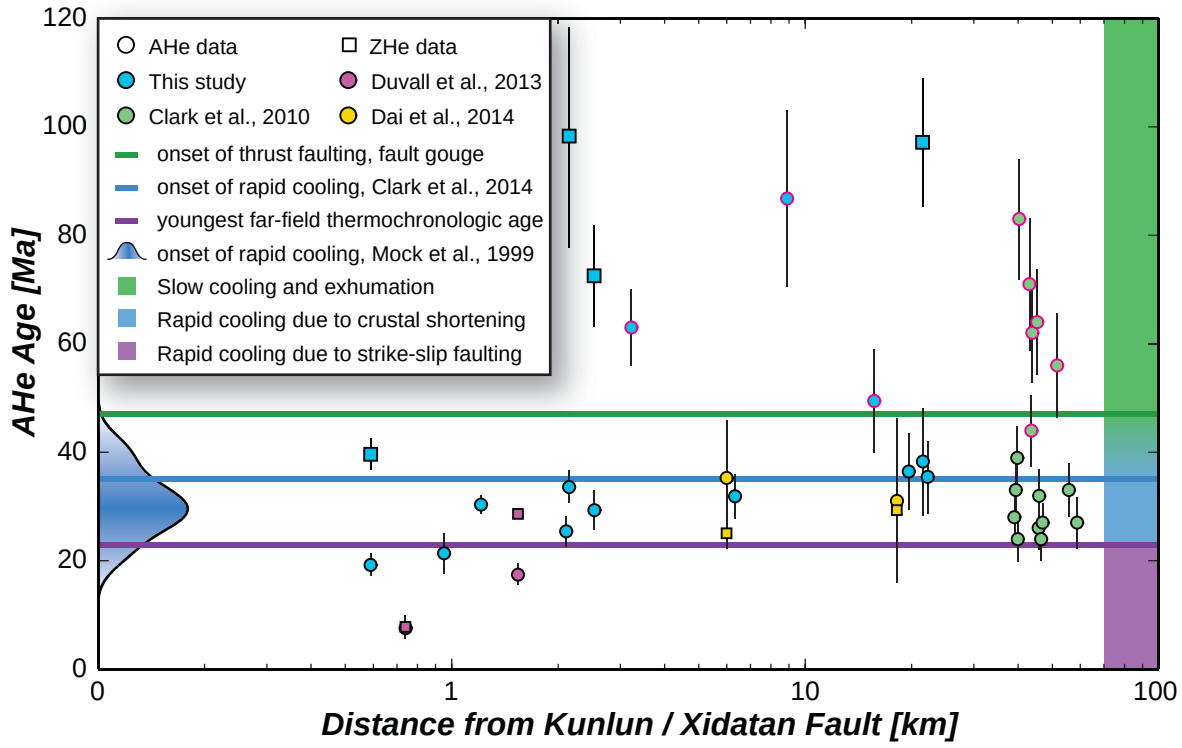

Figure 4.8. Thermochronologic ages from the central Kunlun Shan, plotted as a function of distance from the Kunlun Fault (or Xidatan Fault, as it is called near the Dongdatan Valley). The probability density function to the left is based on the timing of rapid cooling from Mock et al. (1999), and is shaded by probability. The green line represents the ~35 Ma onset of rapid cooling modeled by Clark et al. (2010). Mean apatite (U-Th)/He ages from Dai et al. (2014) were recalculated from raw data, so that the data treatment was uniform for all studies. Samples outlined in pink are older due to the effects of radiation damage or were not completeley reset prior to exhumation.

Eocene aged basin deposits in the footwall of the Wenquan Hu Thrust Fault that consist of locally-derived rocks, as well as with the timing of crustal shortening and rapid unroofing inferred from thermochronologic modeling elsewhere in the central Kunlun Shan (Mock et al., 1999; Clark et al., 2010). HeFTy modeling of thermochronologic data from the East Deshuiwai Mountains and Deshuiwai Basin permits rapid cooling events since ~45 Ma, however we have difficulty fully resolving potential Cenozoic thrust fault-related histories from the current dataset given that most of the zircon helium ages are older than 70 Ma. Apatite fission-track age analysis (in progress) will provide information from a critical temperature window (~ 100 – 120 °C; Ketcham et al., 2007) from which we expect to distinguish between two end-member scenarios: (1) thrust fault related rapid cooling sometime between 45 – 20 Ma, or (2) slow to moderate cooling until 20 Ma followed by crustal shortening, which would suggest that thrust faulting resulted in less than 1 – 2 km.

Since authigenic illite is formed at higher temperatures (~110 °C; Duvall et al., 2011) than the apatite helium effective closure temperature (~60 – 75 °C; Wolf et al., 1996; Farley, 2000), fault gouge dating is capable of resolving the earlier history of faulting. Illite age analysis of fault gouge collected from the Dongdatan and Wenquan Hu Thrust Faults gives authigenic illite ages of ~47 Ma and ~113 Ma, respectively. We suggest that the authigenic illite age from the Wenquan Hu Thrust Fault is due to ^{40}Ar loss during low-grade metamorphism, which may produce a similar age-size fraction relationship as expected for fault-related authigenic illite growth, and that the authigenic illite ages record a Cretaceous period of regional low grade metamorphism, rather than the onset of strike-slip faulting (Verdel et al., 2012). This is consistent with the timing of Cretaceous shear inferred from ^{40}Ar/^{39}Ar dating of shear zones near the Xidatan Fault (Arnaud et al., 2003). The Eocene fault gouge age determined for the Dongdatan Valley Thrust Fault, on the other hand, is compatible our thermochronologic data and prior studies along the northern plateau margin. Data from the Qimen Tagh and Qinling Shan, along the northern margin of the Tibetan Plateau, indicates that crustal shortening may have initiated in the early Eocene, at ~ 49 – 50 Ma (Yin et al., 2002; Clark et al., 2010; Duvall et al., 2011) and thermochronologic modeling in the central Kunlun Shan shows initial rapid exhumation as early as 41 Ma (Mock et al., 1999). Thus, we tentatively interpret the ~47 Ma fault gouge age to give the timing of tectonic motion along the Dongdatan Thrust Fault. Further thermochronometric analysis will allow us to test our interpretation of fault gouge data from the Dongdatan Valley.

Several structural observations indicate that there was a period of crustal shortening prior to the Eocene, however these thrust faults were likely active in the mid-Mesozoic. North of the

Wenquan Reservoir, the Wenquan Hu Thrust Fault dissects a thrust fault that place Permian carbonate strata over Triassic metapelites (Figure 4.2a). This relationship indicates that the latter fault initiated prior to the former. A similar thrust fault relationship exists in the northwestern corner of the East Wenquan Basin, where a thrust fault which places Carboniferous over Triassic strata is crosscut by a fault that places both Paleozoic and Mesozoic units over Cenozoic red beds (Figure 4.2a). Stratigraphic ages of the units involved indicate that deformation initiated after the Triassic, and HeFTy modeling of thermochronologic data suggests that there was a period of tectonic quiescence from immediately prior to the 47 Ma onset of shortening along the Dongdatan Thrust Fault. Therefore, we suggest that thrust faults that place Permian over Triassic strata are relatively old features that were active sometime between the late Triassic and early Cretaceous (Figure 4.9a).

The compiled thermochronologic and fault gouge data presented above, guided by structural observations, suggest that crustal shortening of the Kunlun Shan may have initiated by 47 Ma following a period of tectonic quiescence (Figure 4.9b; Clark et al., 2010). The younger thermochronologic ages preserved throughout the central Kunlun Shan suggest that exhumation continued into the Oligocene. The majority AHe data in moderate to distal locations relative to the Kunlun and Xidatan Faults suggest that the central Kunlun Shan underwent regional crustal shortening until the latest Oligocene (ca. 24 Ma; Figures 4.8 and 4.9c).

4.6.2. The onset of left-lateral shear

Thermochronologic data from the Dongdatan Valley and East Deshuiwai Mountains preserve the timing of strike-slip faulting and show that transpression-related exhumation is highly localized near the trace of the Xidatan Fault and within restraining bends. Eocene red bed strata in the footwall of the Dongdatan Thrust Fault have an apatite (U-Th)/He age of 21 Ma, which is younger than the exhumation age recorded in the hanging wall of the same fault. The younger exhumation age preserved in footwall strata is difficult to reconcile with the crustal shortening history of the central Kunlun Shan, and we suggest instead that this age reflects the timing of left-lateral shear along the Xidatan Fault, which is located within 1 km of the sampled footwall strata (Figures 4.8 and 4.9d). Several pop-up structures along the trace of the Xidatan Fault were identified proximal to the sampled footwall strata, suggesting that vertical exhumation is localized in this region. In the western Dongdatan Valley, sampled Triassic strata preserves a 19 Ma AHe age and was collected within 1 km of the Xidatan Fault (Figure 4.8). Near the Kunlun Pass, thermochronologic ages collected along the Kunlun Fault similarly younger than the crustal

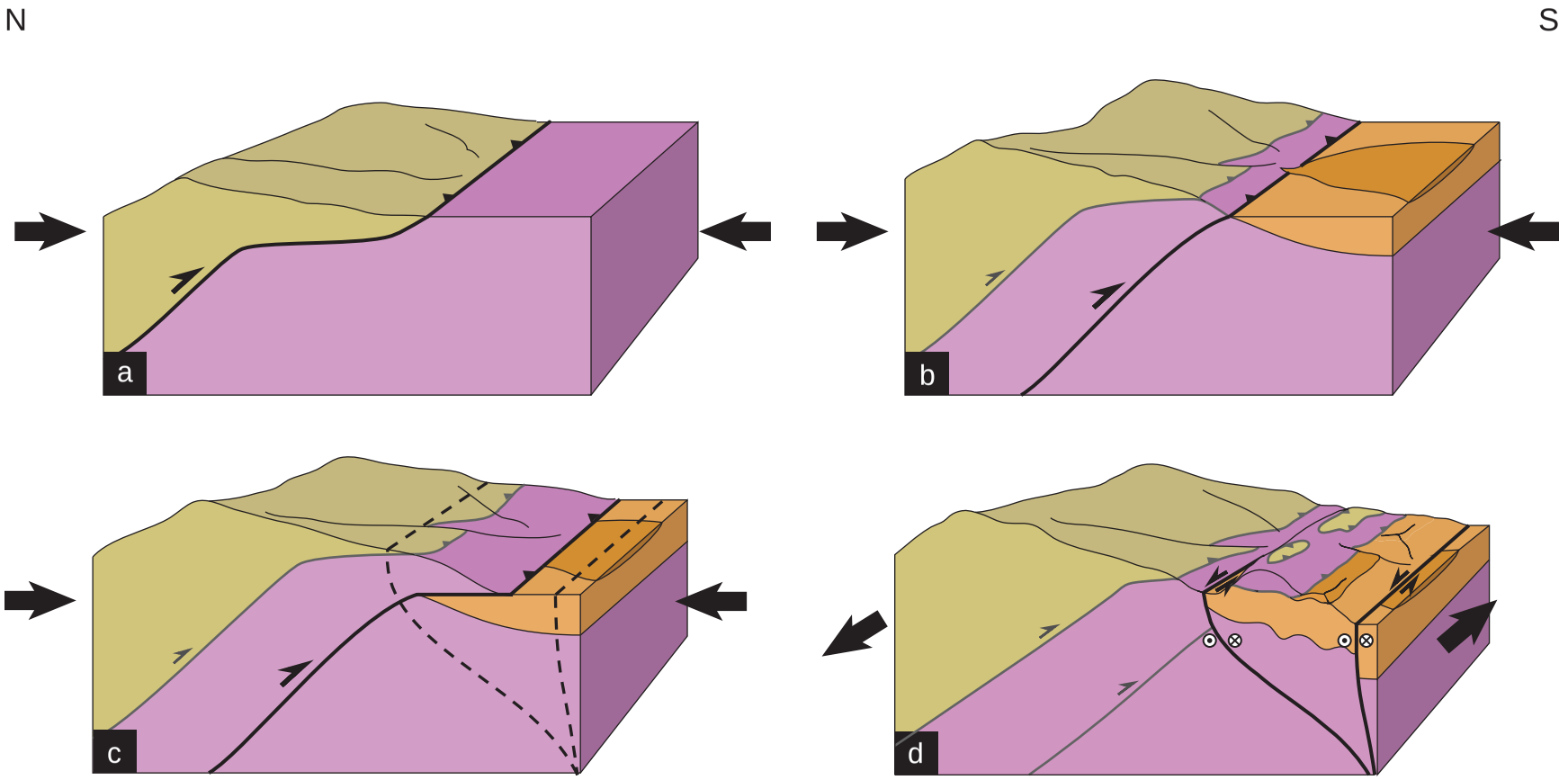

Figure 4.9. Schematic block diagrams showing the evolution of deformation within the Dongdatan Valley. (a) Late Triassic to early Cretaceous: north-south oriented compression results in thrust faulting of Permian carbonates over Triassic metapelites. (b) After a period of tectonic quiescence, thrust faulting initiates by 47 Ma, causing erosion of the hanging wall and mid Eocene aged basin deposits. (c) Late Eocene to early Miocene continued, and possibly increased, exhumation along thrust faults and burial of red bed strata. (d) East-west oriented strike-slip faulting locally causes exhumation and erosion. AHe dating of samples from the Cenozoic red bed strata suggest that strike-slip faulting initiated by ~20 Ma.

shortening history of the central Kunlun Shan (Figures 4.1 and 4.8; Duvall et al., 2013). The localization of transpressional exhumation in the Dongdatan Valley is similar to that observed along the San Andreas Fault in the United States, where young thermochronologic ages are concentrated within a few kilometers of the master fault (Spotila et al., 2001; Niemi et al., 2014).

Thermochronologic data from the East Deshuiwai Mountains, which is a restraining bend along the Xidatan Fault zone (Figure 4.1), similarly suggest post-early Miocene exhumation related to lateral shear. We interpret the age-grain size correlation of our thermochronologic data as evidence for an exhumed apatite (U-Th)/He partial retention zone. While thermal modeling of samples 13DDT008 and 13DDT009 is not able to clearly determine the cooling histories recorded in either sample, we can discern that these rocks were isothermally held for upwards of 100 Myr, and that cooling increased after ~16 Ma due to transpressional shear. Prolonged isothermal holding is in agreement with thermochronologic modeling of Clark et al. (2010) and HeFTy modeling of samples collected in the southern East Deshuiwai Mountains and Deshuiwai Basin.

Illite age analysis of fault gouge collected from a shear zone north of the Dongdatan Valley does not record Miocene strike-slip fault activity, but rather a Cretaceous authigenic illite age. This fault gouge age does not agree with thermal modeling of Cretaceous tectonic quiescence or the Miocene timing of lateral shear. Instead, we suggest that the correlation of illite age and size fraction is due to low-grade metamorphism and ^{40}Ar loss in nature (Verdel et al., 2012). Illite age analysis suggests that recent strike-slip motion did not result in sufficient exhumation along this shear structure to bring authigenic illite generated during faulting to the surface. Since the formation temperature of authigenic illite is ~110 °C (Duvall et al., 2011) and assuming a geothermal gradient of 25 – 35 °C km^{-1}, we suggest that vertical exhumation along the sampled strike-slip fault did not exceed ~3 km.

Based on thermochronologic ages and structural observations from the Dongdatan Valley and East Deshuiwai Mountains, we suggest that left-lateral motion within the Kunlun Shan initiated since ~20 Ma, although more precise timing may be resolved with pending apatite fission-track ages. This is in good agreement with an increase in the cooling rate between 20 – 15 Ma inferred from apatite (U-Th)/He and and zircon (U-Th)/He dating elsewhere along the strike of the Kunlun Fault (Duvall et al., 2013). We suggest that the earlier phase of cooling between 20 and 30 Ma recorded by Duvall et al. (2013) is likely due to crustal shortening in the central Kunlun Shan rather than transpression.

4.6.3. Comparison with deformation throughout Tibet

Our work in the central Kunlun Shan, along with other work along the northern margin of the Tibetan Plateau suggests that crustal shortening initiated during or soon after the onset of continental collision between India and Eurasia and continued into the early Miocene (Rowley, 1996; Yin et al., 2002; 2008; Molnar and Stock, 2009; Clark et al., 2010; Dupont-Nivet et al., 2010; Najman et al., 2010; Duvall et al., 2011). To the south, the timing of crustal shortening in the Hoh Xil Basin is quite similar, between 49 – 27 Ma (Staisch et al., *in prep*). Currently, however, convergence between India and Eurasia is not accommodated via crustal shortening within the Tibetan Plateau proper (Burg et al., 1983; England and Searle, 1986; Murphy et al., 1997; Kapp et al., 2005, 2007a, 2007b; Staisch et al., 2014). Rather, convergence is largely accommodated within Tibet along east-west oriented strike-slip faults and north-south oriented normal faults (Blisniuk et al., 2001; Murphy et al., 2000; Murphy et al., 2002; Garzione et al., 2003; Lee et al., 2003; Phillips et al., 2004; Taylor and Peltzer, 2006; Wang et al., 2009; Lee et al., 2011; Ratschbacher et al., 2011; McCallister et al., 2013; Sundell et al., 2013; Styron et al., 2013).

The onset of strike-slip and normal faulting throughout the orogen occurred in the early to mid-Miocene and continues today. Our interpretations of thermochronologic data, together with previous studies along the Kunlun Fault, suggest that left-lateral motion has been accommodated since 12 Ma (Duvall et al., 2013) and possibly as early as ~ 20 Ma (this paper) in the central Kunlun Shan, and may have propagated to the east and west by ~15 – 8 Ma (Figure 4.10; Jolivet et al., 2003; Duvall et al., 2013). In the Qilian Shan, located to the north of the Tibetan Plateau, left-lateral motion along the Haiyuan Fault initiated slightly after Kunlun Fault activity, ca. 17 Ma (Duvall et al., 2013). Since the Miocene, the zone of strike-slip dissipation between the Kunlun and Haiyuan Faults has resulted in counterclockwise block rotation accommodated along the Elashan and Riyueshan Faults (Duvall and Clark, 2010; Duvall et al., 2013).

Within central and southern Tibet, strike-slip faulting initiated by ~18 – 13 Ma (Figure 4.10; Murphy et al., 2000; Lee et al., 2003; Phillips et al., 2004; Taylor and Peltzer, 2006; Wang et al., 2009). While several studies infer that the Altyn Tagh Fault, which delineates the southern boundary of the Tarim Basin, may have accommodated lateral shear since the Eocene, pre-Miocene piercing points along the Altyn Tagh Fault show a common magnitude of offset, indicating that the inception of strike-slip likely occurred in late Oligocene – early Miocene time (Yue et al., 2001; 2003; Yin et al., 2002; Ritts et al., 2008).

The onset of normal faulting in southern Tibet is similar to the strike-slip history, with an

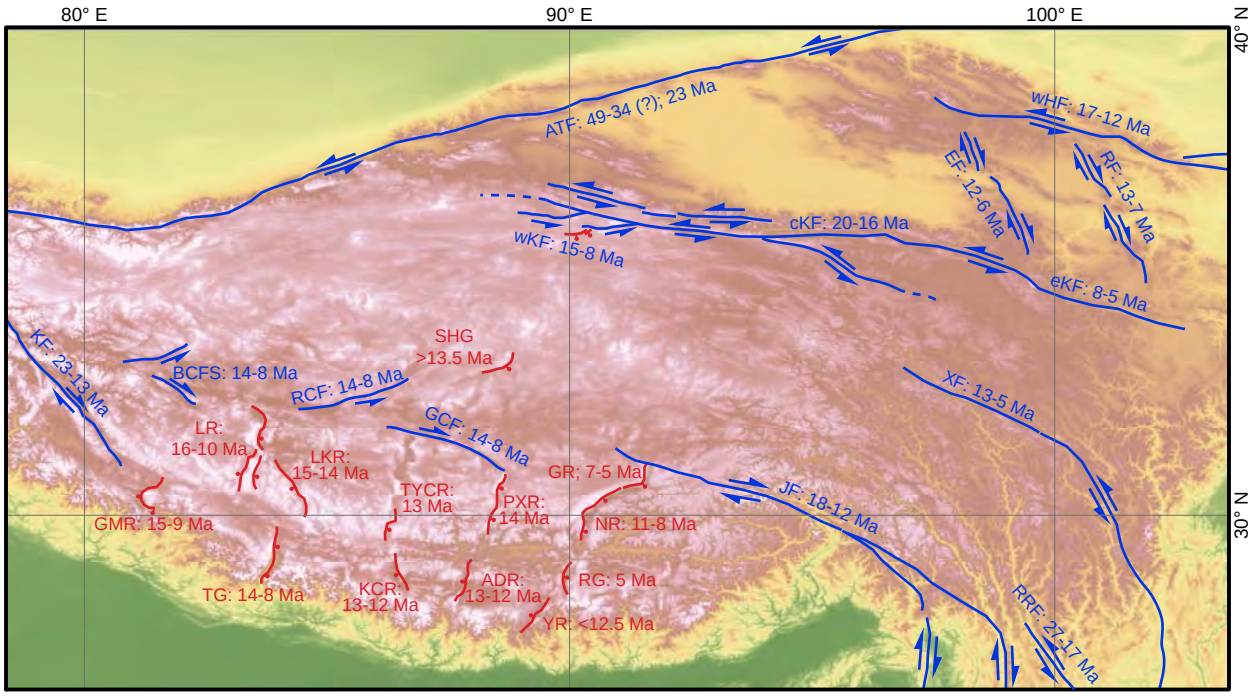

Figure 4.10. Map of major active strike-slip and normal faults in the Tibetan Plateau. The estimated initiation age of each fault system is denoted, along with abbreviated names. Abbreviations for strike-slip faults are as follows; cKF: central Kunlun Fault, eKF: east Kunlun Fault , wKF: west Kunlun Fault, wHF: west Haiyuan Fault, EF: Elashan Fault, RF: Riyueshan Fault, ATF: Altyn Tagh Fault, JF: Jiali Fault, RRF: Red River Fault; KF: Karakoram Fault, XF: Xianshuihe Fault, RCF: Riganpei Co Fault, GCF: Gyaring Co Fault, BCFS: Bue Co Fault System. Abbreviations for normal faults are as follows; TG: Thakkola Graben, ADR: Ama Drime Rift, KCR: Kung Co Rift, GMR: Gurla Mandhata Rift, RG: Ringbung Graben, YR: Yadong Rift, LR: Lunggar Rift, NR: Nyainqentanghlah Rift, LKR: Lopukangri Rift, TYCR: Tangra Yum Co Rift, PXR: Pumqu-Xainza Rift, GR: Gulu Rift, SHG: Shuang Hu Graben. Citations for the initiation of faulting are available in Tables A4.3 and A4.4.

onset by ~16 – 14 Ma (Figure 4.10; Blisniuk et al., 2001; Garzione et al., 2003; Murphy et al., 2002; Lee et al., 2011; Ratschbacher et al., 2011; McCallister et al., 2013; Sundell et al., 2013; Styron et al., 2013). The coeval onset of normal and strike-slip faulting may suggest that these processes are kinematically linked. This linkage is most prominently illustrated along the Bangong-Nujiang Suture zone and Karakoram Fault zone where, together, north-trending normal faults and conjugate strike slip faults accommodate east-west extension in an overall regime of north-south contraction (Armigo et al., 1986; 1989; Taylor et al., 2003).

4.6.4. Implications for the uplift history of the Tibetan Plateau

The cessation of crustal shortening in the Hoh Xil Basin by 27 Ma and along the Kunlun-Qaidam Basin margin by 24 Ma (Clark et al., 2010) and the onset of left-lateral shear along the Kunlun Fault since ~ 20 Ma are suggestive of a shift in the orientation of the least compressive stress from vertical to east-west, which may directly relate to the attainment of high elevation (Burke and Şengör, 1986; Staisch et al., *in prep*). Moreover, the mid-Miocene onset of normal and strike-slip faulting throughout the Tibetan Plateau implies a regional mechanistic cause, rather than of discrete local phenomena. In the following paragraphs, we outline a tectonic interpretation of the kinematic shift of the Kunlun Shan and of geologic events across the Tibetan Plateau, and discuss their implications for the evolution of surface uplift.

The northern plateau margin was established early in the Indo-Asian collision history and large-scale crustal shortening within the Lhasa and southern Qiangtang Terranes ceased by ~50 Ma, suggesting that post-collisional crustal shortening of the Tibetan Plateau proper was generally contained between the Tanggula Shan and the Kunlun Shan and that strong lithospheric blocks to the north of the Kunlun Shan have largely impeded northward plateau growth over the collision history (Burg et al., 1983; England and Searle, 1986; Murphy et al., 1997; Kapp et al., 2005, 2007a, 2007b; DeCelles et al., 2007a; Yin et al., 2008; Clark et al., 2010; Duvall et al., 2011; Hetzel et al., 2011; Clark, 2012; Rohrmann et al., 2012; Ding et al., 2014). The limiting boundaries of the Tibetan Plateau imply that lithospheric thickening and the increase in gravitational potential energy could not continue indefinitely. Evidence from the Hoh Xil Basin, along with data presented in this study, indicate that crustal shortening ceased by 27 – 24 Ma, however high elevation in northern Tibet was not yet attained (Duan et al., 2007; 2008; Polissar et al., 2009; Staisch et al., *in prep*). Thus, uplift to modern elevation likely occurred in the absence of upper crustal shortening.

The kinematic shift from crustal shortening to left-lateral shear along the Kunlun Fault, and

roughly uniform Miocene initiation of strike-slip and normal faulting throughout the Tibetan Plateau, indicates that high elevation and associated high gravitational potential energy throughout the Tibetan Plateau may have been attained by ~20 – 16 Ma. The attainment of near-modern elevation in the Lhasa and Qiangtang terranes may have preceded high elevation gain in northern Tibet, however the plateau-wide uplift to of high elevation by Miocene time is supported by paleoelevation and palynological data from across the plateau (Rowley and Currie, 2006; DeCelles et al., 2007a, 2007b; Wu et al., 2008; Polissar et al., 2009; Xu et al., 2013; Ding et al., 2014) as well as the onset of eastward plateau expansion via lower crustal flow (Royden et al., 1997; Clark and Royden, 2000; Clark et al., 2005b; Ouimet et al., 2010). Based on paleoelevation estimates in Hoh Xil Basin, the cessation of crustal shortening by 27 – 24 Ma, and the onset of strike-slip faulting along the Kunlun Shan by 20 Ma, we suggest that between 800 – 1600 meters of surface uplift in northern Tibet occurred in late Oligocene – early Miocene time. Paleoelevation estimates from the Hoh Xil Basin indicate that the northern Tibetan Plateau continued to rise to modern elevation in mid to late Miocene, and possibly Plio – Pleistocene, time (Polissar et al., 2009).

The mechanism of Miocene elevation gain in northern Tibet is debated, however post-Oligocene crustal thickening of the Hoh Xil Basin likely contributed to elevation gain in northern Tibet (Staisch et al., *in prep*). Alternatively, widespread post-20 Ma magmatism in the Hoh Xil Basin may be suggestive of mantle root loss, which could result in relatively rapid uplift of 1 – 3 km (England and Houseman, 1989; McKenna and Walker, 1990; Molnar et al., 1993; Ding et al., 2003; Lai et al., 2003; Williams et al., 2004; Chung et al., 2005; Wang et al., 2005; Guo et al., 2006; Jiang et al., 2006; Molnar and Stock, 2009; Chen et al., 2012). Regardless of the mechanism of post-Oligocene surface uplift, an increase in elevation in northern Tibet would affect the average of force per unit length throughout the orogen (Molar and Stock, 2009). We suggest that uplift to high elevation in northern Tibet by ~20 Ma resulted in the increase in average gravitational potential energy across the orogen and the plateau-wide inception of strike-slip and normal faulting activity.

4.7. Conclusions

Our data from the Dongdatan Valley, East Wenquan Basin, and East Deshuiwai Mountains, located in the central Kunlun Shan, provide needed clarification of the deformation history of the northern Tibetan Plateau margin. Results from thermochronologic and $^{40}Ar/^{39}Ar$ fault gouge dating tentatively suggest the timing of north-south oriented crustal shortening occurred between 47 and 24 Ma. Thermochronologic constraints suggest that left-lateral strike-slip faulting initiated possibly

as early as 20 Ma and that uplift due to transpression was highly localized near the main Xidatan Fault and within restraining bends.

The mid-Miocene transition from north-south oriented pure shear to east-west oriented simple shear was likely driven by shift in the orientation of the least compressive stress due to the increase in gravitational potential energy within the northern Tibetan Plateau. We infer that the early to mid-Miocene increase in gravitational potential energy signals the attainment of high elevation in northern Tibet. The roughly coeval onset of strike-slip and normal fault activity throughout the Tibetan Plateau (Blisniuk et al., 2001; Murphy et al., 2000; Murphy et al., 2002; Garzione et al., 2003; Lee et al., 2003; Phillips et al., 2004; Taylor and Peltzer, 2006; Wang et al., 2009; Lee et al., 2011; Ratschbacher et al., 2011; McCallister et al., 2013; Sundell et al., 2013; Styron et al., 2013) and eastward plateau expansion via lower crustal flow (Clark and Royden, 2000; Clark et al., 2005a; Clark et al., 2005b), suggests that post-Oligocene uplift of the northern Tibetan Plateau, whether by lower crustal thickening or mantle root loss, caused a plateau-wide increase in outward force per unit length.

4.8. References

Arnaud, N., Tapponnier, P., Roger, F., Brunel, M., Scharer, U., Wen, C., and Zhiqin, X., 2003, Evidence for Mesozoic shear along the western Kunlun and Altyn-Tagh fault, northern Tibet (China):, J. Geophys. Res., v. 108, doi:10.1029/2001JB000904, B1.

Armigo, R., Tapponnier, P., and Tonglin, H., 1989, Late Cenozoic Faulting in Southern Tibet: Journal of Geophysical Research, v. 94, p. 2787–2838.

Armijo, R., Tapponnier, P., Mercier, J.L., and Tonglin, H., 1986, Quaternary extension in southern Tibet: field observations and tectonic implications: Journal of Geophysical Research, v. 91, p. 13,803–13,872.

Avouac, J.-P., and Tapponnier, P., 1993, Kinematic model of active deformation in central Asia: Geophysical Research Letters, v. 20, p. 895–898.

Benowitz, J.A., Layer, P.W., Armstrong, P., Perry, S.E., Haeussler, P.J., Fitzgerald, P.G., and Van Laningham, S., 2011, Spatial variations in focused exhumation along a continental-scale strike-slip fault: The Denali fault of the eastern Alaska Range: Geosphere, v. 7, p. 455-467, doi:10.1130/GES00589.1

Blisniuk, P.M., Hacker, B.R., Glodny, J., Ratschbacher, L., Bi, S., Wu, Z., McWilliams, M.O., Calvert, A., and Geowissenschaften, È., 2001, Normal faulting in central Tibet since at least 13.5 Myr

ago: v. 412, p. 628–632.

Braun, J., 2005, Quantitative Constraints on the Rate of Landform Evolution Derived from Low-Temperature Thermochronology: Reviews in Mineralogy and Geochemistry, v. 58, p. 351–374, doi: 10.2138/rmg.2005.58.13.

Burg, J.P., Proust, F., Tapponnier, P., and Chen, G.M., 1983, Deformation phases and tectonic evolution of the Lhasa block: Eclogae Geol. Helv, v. 76, p. 643–683.

Burke, K., and Sengor, C., 1986, Tectonic escape in the evolution of the continental crust: Reflection Seismology: The Continental Crust, v. 14, p. 41–53.

Chen, W., Zhang, Y., Ji, Q., Wang, S., & Zhang, J., 2002, Magmatism and deformation times of the Xidatan rock series, East Kunlun Mountains: Science in China Series B: Chemistry, v. 45, no. 1, p. 20-27.

Chen, J.-L., Xu, J.-F., Wang, B.-D., and Kang, Z.-Q., 2012, Cenozoic Mg-rich potassic rocks in the Tibetan Plateau: Geochemical variations, heterogeneity of subcontinental lithospheric mantle and tectonic implications: Journal of Asian Earth Sciences, v. 53, p. 115–130, doi: 10.1016/j.jseaes.2012.03.003.

Chung, S.-L., Chu, M.-F., Zhang, Y., Xie, Y., Lo, C.-H., Lee, T.-Y., Lan, C.-Y., Li, X., Zhang, Q., and Wang, Y., 2005, Tibetan tectonic evolution inferred from spatial and temporal variations in post-collisional magmatism: Earth-Science Reviews, v. 68, p. 173–196, doi: 10.1016/j.earscirev.2004.05.001.

Clark, M.K., and Royden, L.H., 2000, Topographic ooze : Building the eastern margin of Tibet by lower crustal flow: Geology, v. 28, no. 8, p. 703–706.

Clark, M.K., Bush, J.W.M., and Royden, L.H., 2005a, Dynamic topography produced by lower crustal flow against rheological strength heterogeneities bordering the Tibetan Plateau: Geophysical Journal International, v. 162, no. 2, p. 575–590, doi: 10.1111/j.1365-246X.2005.02580.x.

Clark, M.K., House, M.A., Royden, L.H., Whipple, K., Burchfiel, B.C., Zhang, X., and Tang, W., 2005b, Late Cenozoic uplift of southeastern Tibet: Geology, v. 33, no. 6, p. 525–528, doi: 10.1130/G21265.1.

Clark, M.K., Farley, K.A., Zheng, D., Wang, Z., and Duvall, A.R., 2010, Early Cenozoic faulting of the northern Tibetan Plateau margin from apatite (U–Th)/He ages: Earth and Planetary Science Letters, v. 296, p. 78–88, doi: 10.1016/j.epsl.2010.04.051.

Clark, M.K., 2012, Continental collision slowing due to viscous mantle lithosphere rather than

topography: Nature, v. 483, p. 74–7, doi: 10.1038/nature10848.

Dai, J., X. Zhao, C. Wang, L. Zhu, Y. Li, and D. Finn (2012), The vast proto-Tibetan Plateau: New constraints from Paleogene Hoh Xil Basin, Gondwana Res.: v. 22, no. 2, p. 434–446, doi:10.1016/j.gr.2011.08.019.

Dazé, A., Lee, J.K.., and Villeneuve, M., 2003, An intercalibration study of the Fish Canyon sanidine and biotite 40Ar/39Ar standards and some comments on the age of the Fish Canyon Tuff: Chemical Geology, v. 199, p. 111–127, doi: 10.1016/S0009-2541(03)00079-2.

DeCelles, P.G., Quade, J., Kapp, P., Fan, M., Dettman, D.L., and Ding, L., 2007a, High and dry in central Tibet during the Late Oligocene: Earth and Planetary Science Letters, v. 253, no. 3-4, p. 389–401, doi: 10.1016/j.epsl.2006.11.001.

DeCelles, P.G., Kapp, P., Ding, L., and Gehrels, G.E., 2007b, Late Cretaceous to middle Tertiary basin evolution in the central Tibetan Plateau: Changing environments in response to tectonic partitioning, aridification, and regional elevation gain: Geological Society of America Bulletin, v. 119, no. 5-6, p. 654–680, doi: 10.1130/B26074.1.

Ding, L., Kapp, P., Zhong, D., Deng, W., 2003, Cenozoic Volcanism in Tibet: Evidence for a Transition from Oceanic to Continental Subduction: Journal of Petrology, v. 44, p. 1833–1865.

Ding, L., Xu, Q., Yue, Y., Wang, H., Cai, F., and Li, S., 2014, The Andean-type Gangdese Mountains: Paleoelevation record from the Paleocene–Eocene Linzhou Basin: Earth and Planetary Science Letters, v. 392, p. 250–264, doi: 10.1016/j.epsl.2014.01.045.

Dodson, M.H., 1973, Closure Temperature in Cooling Geochronological and Petrological Systems: Contr. Mineral. and Petrol., v. 40, p. 259–274.

Dong, H., Hall, C.M., Peacor, D.R., and Halliday, A.N., 1995, Mechanisms of argon retention in clays revealed by laster 40Ar/39Ar dating: Science, v. 267, p. 355–359.

Duan, Z., Li, Y., Shen, Z., Zhu, X., and Zhong, C., 2007, Analysis of the evolution of the Cenozoic ecological environment and process of plateau surface uplift in the Wenquan area in the interior of the Qinghai-Tibet Plateau: Geology in China, v. 34, no. 4, p. 688 – 696.

Duan, Q., Zhang, K., Wang, J., Yao, H., and Niu, Z., 2008, Oligocene Palynoflora, Paleovegetation and Paleoclimate in the Tanggula Mountains, northern Tibet: Acta Micropalaeontologica Sinica, v. 25, no. 2, p. 185–195Duvall, A.R., and Clark, M.K., 2010, Dissipation of fast strike-slip faulting within and beyond northeastern Tibet: Geology, v. 38, p. 223–226, doi: 10.1130/G30711.1.

Dupont-Nivet, G., P. C. Lippert, D. J. van Hinsbergen, M. J. Meijers, and P. Kapp (2010), Palaeolatitude and age of the Indo–Asia collision: Palaeomagnetic constraints, Geophys. J. Int., 182(3), 1189–1198.

Duvall, A.R., and Clark, M.K., 2010, Dissipation of fast strike-slip faulting within and beyond northeastern Tibet: Geology, v. 38, p. 223–226, doi: 10.1130/G30711.1.

Duvall, A.R., Clark, M.K., van der Pluijm, B. a., and Li, C., 2011, Direct dating of Eocene reverse faulting in northeastern Tibet using Ar-dating of fault clays and low-temperature thermochronometry: Earth and Planetary Science Letters, v. 304, p. 520–526, doi: 10.1016/j.epsl.2011.02.028.

Duvall, A.R., Clark, M.K., Kirby, E., Farley, K.A., Craddock, W.H., Li, C., and Yuan, D.-Y., 2013, Low-temperature thermochronometry along the Kunlun and Haiyuan Faults, NE Tibetan Plateau: Evidence for kinematic change during late-stage orogenesis: Tectonics, v. 32, p. 1190–1211, doi: 10.1002/tect.20072.

Ehlers, T.A., 2005, Crustal Thermal Processes and the Interpretation of Thermochronometer Data: Reviews in Mineralogy and Geochemistry, v. 58, p. 315–350, doi: 10.2138/rmg.2005.58.12.

Ehlers, T.A., and Farley, K.A., 2003, Apatite (U-Th)/He thermochronometry : methods and applications to problems in tectonic and surface processes: Earth and Planetary Science Letters, v. 206, p. 1–14.

England, P., and Houseman, G., 1989, Extension During Continental Convergence, With Application to the Tibetan Plateau: Journal of Geophysical Research, v. 94, no. B12, p. 17,561–17,579.

England, P., and Searle, M., 1986, The Cretaceous-tertiary deformation of the Lhasa Block and its implications for crustal thickening in Tibet: Tectonics, v. 5, p. 1–14.

Farley, K.A., 2000, Helium diffusion from apatite: General behavior as illustrated by Durango fluorapatite: Journal of Geophysical Research, v. 105, p. 2903–2914.

Farley, K.A., and Stockli, D.F., 2002, (U-Th)/He Dating of Phosphates: Apatite, Monazite, and Xenotime: Reviews in Mineralogy and Geochemistry, v. 48, p. 559–577, doi: 10.2138/rmg.2002.48.15.

Flowers, R.M., Ketcham, R. a., Shuster, D.L., and Farley, K. a., 2009, Apatite (U–Th)/He thermochronometry using a radiation damage accumulation and annealing model: Geochimica et Cosmochimica Acta, v. 73, p. 2347–2365, doi: 10.1016/j.gca.2009.01.015.

Fu, B., and Awata, Y., 2007, Displacement and timing of left-lateral faulting in the Kunlun Fault

Zone, northern Tibet, inferred from geologic and geomorphic features: Journal of Asian Earth Sciences, v. 29, p. 253–265, doi: 10.1016/j.jseaes.2006.03.004.

Garzione, C.N., DeCelles, P.G., Hodkinson, D.G., Ojha, T.P., and Upreti, B.N., 2003, East-west extension and Miocene environmental change in the southern Tibetan plateau: Thakkhola graben, central Nepal: Geological Society of America Bulletin, v. 115, p. 3–20, doi: 10.1130/0016-7606(2003)115<0003:EWEAME>2.0.CO;2.

Grubb, S.M.B., Peacor, D.R., and Jjang, W., 1991, Transmission electron microscope observations of illite polytypism: Clays and Clay Minerals, v. 39, p. 540–550.

Guo, Z., Wilson, M., Liu, J., and Mao, Q., 2006, Post-collisional, Potassic and Ultrapotassic Magmatism of the Northern Tibetan Plateau: Constraints on Characteristics of the Mantle Source, Geodynamic Setting and Uplift Mechanisms: Journal of Petrology, v. 47, p. 1177–1220, doi: 10.1093/petrology/egl007.

Haibing, L., Van der Woerd, J., Tapponnier, P., Klinger, Y., Xuexiang, Q., Jingsui, Y., and Yintang, Z., 2005, Slip rate on the Kunlun fault at Hongshui Gou, and recurrence time of great events comparable to the 14/11/2001, Mw~ 7.9 Kokoxili earthquake: Earth and Planetary Science Letters, v. 237, no. 1, p. 285-299.

Haines, S.H., and van der Pluijm, B.A., 2008, Clay quantification and Ar–Ar dating of synthetic and natural gouge: Application to the Miocene Sierra Mazatán detachment fault, Sonora, Mexico: Journal of Structural Geology, v. 30, no. 4, p. 525–538, doi: 10.1016/j.jsg.2007.11.012.

Hetzel, R., Dunkl, I., Haider, V., Strobl, M., Von Eynatten, H., Ding, L., and Frei, D., 2011, Peneplain formation in southern Tibet predates the India-Asia collision and plateau uplift: Geology, v. 39, no. 10, p. 983–986, doi: 10.1130/G32069.1.

Jiang, Y.-H., Jiang, S.-Y., Ling, H.-F., and Dai, B.-Z., 2006, Low-degree melting of a metasomatized lithospheric mantle for the origin of Cenozoic Yulong monzogranite-porphyry, east Tibet: Geochemical and Sr–Nd–Pb–Hf isotopic constraints: Earth and Planetary Science Letters, v. 241, p. 617–633, doi: 10.1016/j.epsl.2005.11.023.

Jolivet, M., Brunel, M., Seward, D., Xu, Z., Yang, J., Malavieille, J., Roger, F., Leyreloup, A., Arnaud, N., and Wu, C., 2003, Neogene extension and volcanism in the Kunlun Fault Zone, northern Tibet: New constraints on the age of the Kunlun Fault: Tectonics, v. 22, p. 1–23, doi: 10.1029/2002TC001428.

Kapp, P., DeCelles, P.G., Leier, A.L., Fabijanic, J.M., He, S., Pullen, A., and Gehrels, G.E., 2007a, The Gangdese retroarc thrust belt revealed: GSA Today, v. 17, p. 4–9.

Kapp, P., DeCelles, P.G., Gehrels, G.E., Heizler, M., and Ding, L., 2007b, Geological records of the Lhasa-Qiangtang and Indo-Asian collisions in the Nima area of central Tibet: Geological Society of America Bulletin, v. 119, p. 917–933, doi: 10.1130/B26033.1.

Kapp, P., Yin, A., Harrison, T.M., and Ding, L., 2005, Cretaceous-Tertiary shortening, basin development, and volcanism in central Tibet: Geological Society of America Bulletin, v. 117, p. 865–878, doi: 10.1130/B25595.1.

Karner, D.B., and Renne, P.R., 1998, 40Ar/39Ar geochronology of Roman volcanic province tephra in the Tiber River valley : Age calibration of middle Pleistocene sea-level changes: Geological Society of America Bulletin, v. 110, p. 740–747, doi: 10.1130/0016-7606(1998)110<0740.

Ketcham, R.A., 2005, Forward and Inverse Modeling of Low-Temperature Thermochronometry Data: Reviews in Mineralogy and Geochemistry, v. 58, p. 275–314, doi: 10.2138/rmg.2005.58.11.

Ketcham, R.A., Carter, A., Donelick, R.A., Barbarand, J., and Hurford, A.J., 2007, Improved modeling of fission-track annealing in apatite: American Mineralogist, v. 92, p. 799–810, doi: 10.2138/am.2007.2281.

Kidd, W.S., and Molnar, P., 1988, Quaternary and active faulting observed on the 1985 Academia Sinica- Royal Society Geotraverse of Tibet: Philosophical Transactions of the Royal Society of London. Series A, Mathematical and Physical Sciences, v. 327, p. 337–363.

Kidd, W.S., Pan, Y., Chang, C., Coward, M.P., Dewey, J.F., Gansser, A., Molnar, P., Shackleton, R.M., and Yiyin, S., 1988, Geological mapping of the 1985 Chinese-British Tibetan (Xizang-Qinghai) Plateau Geotraverse route: Philosophical Transactions of the Royal Society of London. Series A, Mathematical and Physical Sciences, v. 327, p. 287–305.

Kirby, E., Harkins, N., Wang, E., Shi, X., Fan, C., and Burbank, D., 2007, Slip rate gradients along the eastern Kunlun fault: Tectonics, v. 26, TC2010, doi:10.1029/2006TC002033.

Lai, S.-C., Liu, C.-Y., and Yi, H.-S., 2003, Geochemistry and Petrogenesis of Cenozoic Andesite-Dacite Associations from the Hoh Xil Region, Tibetan Plateau: International Geology Review, v. 45, p. 998–1019, doi: 10.2747/0020-6814.45.11.998.

Lee, H.-Y., Chung, S.-L., Wang, J.-R., Wen, D.-J., Lo, C.-H., Yang, T.F., Zhang, Y., Xie, Y., Lee, T.-Y., Wu, G., and Ji, J., 2003, Miocene Jiali faulting and its implications for Tibetan tectonic evolution: Earth and Planetary Science Letters, v. 205, p. 185–194, doi: 10.1016/S0012-821X(02)01040-3.

Lee, J., Hager, C., Wallis, S.R., Stockli, D.F., Whitehouse, M.J., Aoya, M., and Wang, Y., 2011,

Middle to late Miocene extremely rapid exhumation and thermal reequilibration in the Kung Co rift, southern Tibet: Tectonics, v. 30, p. n/a–n/a, doi: 10.1029/2010TC002745.

McCallister, A.T., Taylor, M.H., Murphy, M.A., Styron, R.H., & Stockli, D.F., 2013, Thermochronologic constraints on the late Cenozoic exhumation history of the Gurla Mandhata metamorphic core complex, Southwestern Tibet: Tectonics, v. 33, p. 27–52.

McKenna, L.W., and Walker, J.D., 1990, Geochemistry of Crustally Derived Leucocratic Igneous Rocks From the Ulugh Muztagh Area, Northern Tibet and Their Implications for the Formation of the Tibetan Plateau: Journal of Geophysical Research, v. 95, p. 21483 – 21502.

Mock, C., Arnaud, N.O., and Cantagrel, J., 1999, An early unroofing in northeastern Tibet ? Constraints from 40Ar/39Ar thermochronology on granitoids from the eastern Kunlun range: Earth and Planetary Science Letters, v. 171, p. 107–122.

Molnar, P., and Stock, J.M., 2009, Slowing of India's convergence with Eurasia since 20 Ma and its implications for Tibetan mantle dynamics: Tectonics, v. 28, p. 1–11, doi: 10.1029/2008TC002271.

Molnar, P., and Tapponnier, P., 1978. Active faulting in Tibet: J. Geophys. Res, v. 83, p. 5361-5375.

Molnar, P., England, P., and Martinod, J., 1993, Mantle dynamics, uplift of the Tibetan Plateau, and the Indian Monsoon: Reviews in Geophysics, v. 31, no. 4, p. 357–396.

Murphy, M.A., Yin, A., Harrison, T.M., Dürr, S.B., Z, C., Ryerson, F.J., Kidd, W.S.F., X, W., and X, Z., 1997, Did the Indo-Asian collision alone create the Tibetan plateau?: Geology, v. 25, p. 719–722, doi: 10.1130/0091-7613(1997)025<0719:DTIACA>2.3.CO;2.

Murphy, M.A., Yin, A., Kapp, P., Harrison, T.M., Ding, L., and Jinghui, G., 2000, Southward propagation of the Karakoram fault system , southwest Tibet : Timing and magnitude of slip: Geology, v. 28, p. 451–454.

Murphy, M.A., Manning, C.E., Ryerson, F.J., and Lin, D., 2002, Structural evolution of the Gurla Mandhata detachment system, southwest Tibet : Implications for the eastward extent of the Karakoram fault system: , p. 428–447.

Najman, Y., Appel, E., Boudagher-Fadel, M., Bown, P., Carter, A., Garzanti, E., Godin, L., Han, J., Liebke, U., Oliver, G., Parrish, R., and Vezzoli, G., 2010, Timing of India-Asia collision: Geological, biostratigraphic, and palaeomagnetic constraints: Journal of Geophysical Research, v. 115, no. B12, p. 1–18, doi: 10.1029/2010JB007673.

Niemi, N.A., Buscher, J.T., Spotila, J.A., House, M.A., and Kelley, S.A., 2013, Insights from low-temperature thermochronometry into transpressional deformation and crustal exhumation

along the San Andreas fault in the western Transverse Ranges, California: Tectonics, v. 32, p. 1602–1622, doi: 10.1002/2013TC003377.

Ouimet, W., Whipple, K., Royden, L., Reiners, P., Hodges, K., and Pringle, M., 2010, Regional incision of the eastern margin of the Tibetan Plateau: Lithosphere, v. 2, p. 50–63, doi: 10.1130/L57.1.Polissar, P.J., Freeman, K.H., Rowley, D.B., McInerney, F.A., and Currie, B.S., 2009, Paleoaltimetry of the Tibetan Plateau from D/H ratios of lipid biomarkers: Earth and Planetary Science Letters, v. 287, p. 64–76, doi: 10.1016/j.epsl.2009.07.037.

Platt, J. P., and England, P. C., 1994, Convective removal of lithosphere beneath mountain belts; thermal and mechanical consequences: American Journal of Science, v. 294, no. 3, p. 307-336.

Phillips, R.J., Parrish, R.R., and Searle, M.P., 2004, Age constraints on ductile deformation and long-term slip rates along the Karakoram fault zone, Ladakh: v. 226, p. 305–319, doi: 10.1016/j.epsl.2004.07.037.

van der Pluijm, B.A, Hall, C.M., Vrolijk, P.J., Pevear, D.R., and Covey, M.C., 2001, The dating of shallow faults in the Earth's crust.: Nature, v. 412, p. 172–175, doi: 10.1038/35084053.

Polissar, P.J., Freeman, K.H., Rowley, D.B., McInerney, F.A., and Currie, B.S., 2009, Paleoaltimetry of the Tibetan Plateau from D/H ratios of lipid biomarkers: Earth and Planetary Science Letters, v. 287, p. 64–76, doi: 10.1016/j.epsl.2009.07.037.

QBGMR (Qinghai Bureau of Geology and Mineral Resources), 1980, Geologic map of the Dongwenquan region, scale 1:200,000.

QBGMR (Qinghai Bureau of Geology and Mineral Resources), 1981, Geologic map of the Aikendelesite region, scale 1:200,000.

Ratschbacher, L., Krumrei, I., lumenwitz, M., Staiger, M., Gloaguen, R., Miller, B.V., Samson, S.D., Edwards, M.A., Appel, E., 2011, Rifting and strike-slip shear in central Tibet and the geometry, age and kinematics of upper crustal extension in Tibet: Geol. Soc. Spec. Publ., v. 353, no. 1, p. 127–163, doi:10.1144/SP353.8.

Reiners, P.W., and Farley, K.A., 2001, Influence of crystal size on apatite (U-Th)/He thermochronology and example from the Bighorn Mountains, Wyoming: Earth and Planetary Science Letters, v. 188, p. 413–420.

Renne, P.R., Swisher, C.C., Deino, A.L., Karner, D.B., Owens, T.L., and Depaolo, D.J., 1998, Intercalibration of standards, absolute ages and uncertainties in $^{40}Ar/^{39}Ar$ dating: Chemical Geology, v. 145, p. 117–152.

Rey, P., Vanderhaeghe, O., and Teyssier, C., 2001, Gravitational collapse of the continental crust: definition, regimes and modes: Tectonophysics, v. 342, no. 3, p. 435-449.

Ritts, B.D., Yue, Y., Graham, S. a., Sobel, E.R., Abbink, O. a., and Stockli, D., 2008, From sea level to high elevation in 15 million years:Uplift history of the northern Tibetan Plateau margin in the Altun Shan: American Journal of Science, v. 308, no. 5, p. 657–678, doi: 10.2475/05.2008.01.

Rohrmann, A., Kapp, P., Carrapa, B., Reiners, P.W., Guynn, J., Ding, L., and Heizler, M., 2012, Thermochronologic evidence for plateau formation in central Tibet by 45 Ma: Geology, v. 40, no. 2, p. 187–190, doi: 10.1130/G32530.1.

Rowley, D.B., 1996, Age of initiation of collision between India and Asia: A review of stratigraphic data: Earth and Planetary Science Letters, v. 145, p. 1–13.

Rowley, D.B., and Currie, B.S., 2006, Palaeo-altimetry of the late Eocene to Miocene Lunpola basin, central Tibet: Nature, v. 439, p. 677–81, doi: 10.1038/nature04506.

Royden, L., Burchfiel, B., King, R., Wang, E., Chen, Z., Shen, F., and Liu, Y., 1997, Surface Deformation and Lower Crustal Flow in Eastern Tibet: Science, v. 276, p. 788–790.

Spotila, J., Farley, K.A., and Sich, K., 1998, Uplift and erosion of the San Bernardino Mountains associated with transpression along the San Andreas fault, California, as constrained by radiogenic helium thermochronometry: Tectonics, v. 17, p. 360–378.

Spotila, J. A., Farley, K. A., Yule, J.D., and Reiners, P.W., 2001, Near-field transpressive deformation along the San Andreas fault zone in southern California, based on exhumation constrained by (U-Th)/He dating: Journal of Geophysical Research, v. 106, p. 30909, doi: 10.1029/2001JB000348.

Spotila, J. A., Niemi, N., Brady, R., House, M., Buscher, J., and Oskin, M., 2007, Long-term continental deformation associated with transpressive plate motion: The San Andreas fault: Geology, v. 35, p. 967, doi: 10.1130/G23816A.1.

Srodon, J., and Eberl, D.D., 1984, Illite: Reviews in Mineralogy and Geochemistry1, v. 13, p. 495–544.

Staisch, L.M., Niemi, N.A., Chang, H., Clark, M.K., Rowley, D.B., and Currie, B.S., 2014, A Cretaceous-Eocene depositional age for the Fenghuoshan Group, Hoh Xil Basin: Implications for the tectonic evolution of the northern Tibet Plateau: Tectonics, v. 33, p. 281–301, doi: 10.1002/2013TC003367.

Staisch, L. M., N. A. Niemi, M. K. Clark, C. Hong, *in prep*, Eocene – late Oligocene history of crustal

shortening within the Hoh Xil Basin, north-central Tibetan Plateau.

Styron, R.H., Taylor, M.H., Sundell, K.E., Stockli, D.F., Oalmann, J. a. G., Möller, A., McCallister, A.T., Liu, D., and Ding, L., 2013, Miocene initiation and acceleration of extension in the South Lunggar rift, western Tibet: Evolution of an active detachment system from structural mapping and (U-Th)/He thermochronology: Tectonics, v. 32, p. 880–907, doi: 10.1002/tect.20053.

Sundell, K.E., Taylor, M.H., Styron, R.H., Stockli, D.F., Kapp, P., Hager, C., Liu, D., Ding, L., 2013, Evidence for constriction and Pliocene acceleration of east-west extension in the North Lunggar rift region of west central Tibet: Tectonics, v. 32, no. 5, p. 1454–1479.

Taylor, M., Yin, A., Ryerson, F.J., Kapp, P., and Ding, L., 2003, Conjugate strike-slip faulting along the Bangong-Nujiang suture zone accommodates coeval east-west extension and north-south shortening in the interior of the Tibetan Plateau: Tectonics, v. 22, p. 1–16, doi: 10.1029/2002TC001361.

Taylor, M., and Peltzer, G., 2006, Current slip rates on conjugate strike-slip faults in central Tibet using synthetic aperture radar interferometry: Journal of Geophysical Research, v. 111, B12402, doi: 10.1029/2005JB004014.

Teyssier, C., Tikoff, B., and Markley, M., 1995, Oblique plate motion and continental tectonics: Geology, v. 23, p. 447–450, doi: 10.1130/0091-7613(1995)023<0447:OPMACT>2.3.CO;2.

Tikoff, B., and Teyssier, C., 1994, Strain modeling of displacement-field partitioning in transpressional orogens: Journal of Structural Geology, v. 16, p. 1575–1588.

Verdel, C., van der Pluijm, B.A., and Niemi, N.A., 2012, Variation of illite/muscovite $^{40}Ar/^{39}Ar$ age spectra during progressive low-grade metamorphism: an example from the US Cordillera: Contributions to Mineralogy and Petrology, v. 164, p. 521–536, doi: 10.1007/s00410-012-0751-7.

Wang, F., Lo, C.-H., Li, Q., Yeh, M.-W., Wan, J., Zheng, D., and Wang, E., 2004, Onset timing of significant unroofing around Qaidam basin, northern Tibet, China: constraints from $^{40}Ar/^{39}Ar$ and FT thermochronology on granitoids: Journal of Asian Earth Sciences, v. 24, p. 59–69, doi: 10.1016/j.jseaes.2003.07.004.

Wang, Q., McDermott, F., Xu, J., Bellon, H., and Zhu, Y., 2005, Cenozoic K-rich adakitic volcanic rocks in the Hohxil area, northern Tibet: Lower-crustal melting in an intracontinental setting: Geology, v. 33, p. 465–468, doi: 10.1130/G21522.1.

Wang, C.S., Zhao, X., Liu, Z., Lippert, P.C., Graham, S.A, Coe, R.S., Yi, H., Zhu, L., Liu, S., and Li,

Y., 2008, Constraints on the early uplift history of the Tibetan Plateau.: Proceedings of the National Academy of Sciences of the United States of America, v. 105, no. 13, p. 4987–4992, doi: 10.1073/pnas.0703595105.

Wang, S., Fang, X., Zheng, D., and Wang, E., 2009, Initiation of slip along the Xianshuihe fault zone, eastern Tibet, constrained by K/Ar and fission-track ages: International Geology Review, v. 51, p. 1121–1131, doi: 10.1080/00206810902945132.

Warnock, A.C., Zeitler, P.K., Wolf, R.A., and Bergman, S.C., 1997, An evaluation of low-temperature apatite U-Th/He thermochronometry: Geochimica et Cosmochimica Acta, v. 61, p. 5371–5377, doi: 10.1016/S0016-7037(97)00302-5.

Wilcox, R.E., Harding, T.T., and Seely, D.R., 1973, Basic wrench tectonics: AAPG Bulletin, v. 57, p. 74–96.

Williams, H.M., Turner, S.P., Pearce, J.A., Kelley, S.P., and Harris, N.B.W., 2004, Nature of the Source Regions for Post-collisional, Potassic Magmatism in Southern and Northern Tibet from Geochemical Variations and Inverse Trace Element Modelling: Journal of Petrology, v. 45, p. 555–607, doi: 10.1093/petrology/egg094.

van der Woerd, J., Tapponnier, P., Ryerson, F.J., Meriaux, A., Meyer, B., Gaudemer, Y., Finkel, R.C., Caffee, M.W., Guoguang, Z., and Zhiqin, X., 2002, Uniform postglacial slip-rate along the central 600 km of the Kunlun Fault (Tibet), from ^{26}Al, ^{10}Be, ^{14}C dating of riser offsets, and climatic orogin of the regional morphology: Geophysical Journal International, v. 148, p. 356–388.

van der Woerd, J., Ryerson, F.J., Tapponnier, P., Meriaux A.S., Gaudemer Y., Meyer, B., Finkel, R.C., Caffee, M.W., Zhao, G., and Xu, Z., 2000, Uniform slip-rate along the Kunlun Fault: Implications for seismic behaviour and large-scale tectonics: Geophysical Research Letters, v. 27, no. 16, p. 2353-2356.

van der Woerd, J., Ryerson, F.J., Tapponnier, P., Gaudemer, Y., Finkel, R.C., Meriaux, A.-S., Caffee, M.W., Zhao, G., and He, Q., 1998, Holocene left-slip rate determined by cosmogenic surface dating on the Xidatan segment of the Kunlun fault (Qinghai, China): Geology, v. 26, p. 695–698, doi: 10.1130/0091-7613(1998)026<0695.

Wolf, R.A., Farley, K.A., and Kass, D.M., 1998, Modeling of the temperature sensitivity of the apatite (U-Th)/He thermochronometer: Chemical Geology, v. 148, p. 105–114.

Wolf, R.A., Farley, K.A., Silver, L.T., Geological, D., Sciences, P., and Stop, M., 1996, Helium diffusion and low-temperature thermochronometry of apatite: Geochemica et

Cosmochemica Acta, v. 60, p. 4231–4240.

Wu, Y., Cui, Z., Liu, G., Ge, D., Yin, J., Xi, Q., and Pang, Q., 2001, Quaternary geomorphological evolution of the Kunlun Pass area and uplift of the Qinghai-Xizang, Tibet Plateau: Geomorphology, v. 36, p. 203–216.

Wu, Z. H., Ye, P. S., Zhao, W. J., et al., 2007, Late Cenozoic Overthrust System in the Southern East Kunlun Mountains, China: Geological Bulletin of China, v. 26, no. 4, p. 448–456 (in Chinese with English Abstract).

Wu, Z., Barosh, P.J., Wu, Z., Hu, D., Zhao, X., and Ye, P., 2008, Vast early Miocene lakes of the central Tibetan Plateau: Geological Society of America Bulletin, v. 120, no. 9-10, p. 1326–1337, doi: 10.1130/B26043.1.

Wu, Z., Ye, P., Patrick, B.J., Hu, D., Zhao, W., and Wu, Z., 2009, Late Oligocene-Early Miocene thrusting in southern East Kunlun Mountains, northern Tibetan plateau: Journal of Earth Science, v. 20, p. 381–390, doi: 10.1007/s12583-009-0031-2.

Xia, L., Li, X., Ma, Z., Xu, X., and Xia, Z., 2011, Cenozoic volcanism and tectonic evolution of the Tibetan plateau: Gondwana Research, v. 19, p. 850–866, doi: 10.1016/j.gr.2010.09.005.

Xu, Q., Ding, L., Zhang, L., Cai, F., Lai, Q., Yang, D., and Liu-Zeng, J., 2013, Paleogene high elevations in the Qiangtang Terrane, central Tibetan Plateau: Earth and Planetary Science Letters, v. 362, p. 31–42, doi: 10.1016/j.epsl.2012.11.058.

Yin, A., Rumelhart, P.E., Butler, R., Cowgill, E., Harrison, T.M., Foster, D.A., Ingersoll, R.V., Qing, Z., Xian-Qiang, Z., Xiao-Feng, W., Hanson, A., and Raza, A., 2002, Tectonic history of the Altyn Tagh fault system in northern Tibet inferred from Cenozoic sedimentation: Geological Society of America Bulletin, v. 114, p. 1257–1295, doi: 10.1130/0016-7606(2002)114<1257:THOTAT>2.0.CO;2.

Yin, A., Dang, Y.-Q., Wang, L.-C., Jiang, W.-M., Zhou, S.-P., Chen, X.-H., Gehrels, G.E., and McRivette, M.W., 2008, Cenozoic tectonic evolution of Qaidam basin and its surrounding regions (Part 1): The southern Qilian Shan-Nan Shan thrust belt and northern Qaidam basin: Geological Society of America Bulletin, v. 120, p. 813–846, doi: 10.1130/B26180.1.

Yin, A., Dang, Y., Zhang, M., McRivette, M.W., Burgess, W.P., and Chen, X., 2007, Cenozoic tectonic evolution of Qaidam basin and its surrounding regions (part 2): Wedge tectonics in southern Qaidam basin and the Eastern Kunlun Range: Geological Society of America Special Papers, v. 433, p. 369–390, doi: 10.1130/2007.2433(18).

Yuan, W., Dong, J., Shicheng, W., and Carter, A., 2006, Apatite fission track evidence for Neogene

uplift in the eastern Kunlun Mountains, northern Qinghai–Tibet Plateau, China: Journal of Asian Earth Sciences, v. 27, p. 847–856, doi: 10.1016/j.jseaes.2005.09.002.

Yue, Y., Ritts, B.D., and Graham, S. a., 2001, Initiation and Long-Term Slip History of the Altyn Tagh Fault: International Geology Review, v. 43, no. 12, p. 1087–1093, doi: 10.1080/00206810109465062.

Yue, Y., Ritts, B.D., Graham, S. a., Wooden, J.L., Gehrels, G.E., and Zhang, Z., 2004, Slowing extrusion tectonics: lowered estimate of post-Early Miocene slip rate for the Altyn Tagh fault: Earth and Planetary Science Letters, v. 217, no. 1-2, p. 111–122, doi: 10.1016/S0012-821X(03)00544-2.

Appendix A: Chapter IV

Thermochronologic modeling

HeFTy modeling

We inversely modeled the time-temperature histories for thermochronologic samples using HeFTy software (Ketcham, 2005). Model inputs include single grain apatite and zircon (U-Th)/He ages and data were modeled using the helium diffusion properties of Flowers et al. (2009) for apatite and Reiners et al. (2004) for zircon. Models were guided using broad geologic constraints specific to the geologic setting of each particular sample. All models were required to reach modern surface temperatures of 0 – 20 °C by 0 Ma. Goodness of fit for each time-temperature history model was determined by comparing modeled and observed AHe and ZHe ages (Ketcham, 2005). We use standard goodness of fit thresholds values 0.05 and 0.5 to determine which thermal models are considered "acceptable" and "good", respectively. Models were run until a minimum of 100 good paths were generated or, in the case of no good paths, 500 acceptable paths were generated. The results for each modeled sample are plotted in Figure A4.1.

Samples 11UMT53 was collected from a small plutonic body intruded into Triassic metapelites (Figures 4.2a) near the trace of the Xidatan Fault. Samples 12DDT09 and 12DDT10 were collected also from intrusions into the Triassic metapelites, however these sample locations were located within the hanging wall of the Wenquan Hu Thrust Fault (Figures 4.2a and 4.3). Sample 12DDT17 was collected from the footwall of the Wenquan Hu Thrust Fault (Figures 4.2a and 4.3) and sample 12DDT22 was collected from Triassic metapelites in the northern East Wenquan Basin (Figure 4.2a). The geologic constraints used to guide the aforementioned samples include residence at temperatures in excess of the ~200 °C ZHe closure temperature (Reiners et al., 2002) until mid-Cretaceous time, and exhumation to surface temperatures (0 – 20 °C) by 5 Ma.

Sample 12DDT07 was sampled from a small plutonic body that intruded into Triassic metapelites (Figures 4.2a and 4.3). The geologic constraints used to guide the model include post-early Triassic origin at depth (>40 °C) and exhumation to the surface (0 – 20 °C) between 0 and 65 Ma, based on the assumption that the sample cooled to surface temperature after the time recorded

by the mean AHe age. For sample 12DDT07, the HeFTy model results do not constrain the onset of rapid cooling as hoped, only the time at which the sample passed through the nominal closure temperature at ~65 – 60 Ma. We suggest the range in measured AHe age and eU content for sample replicates was not sufficiently broad to further constrain the cooling history. However, while this sample does not provide much illumination to the cooling history of the sampled hanging wall, the range of modeled cooling paths are compatible with other thermochronologic samples collected from the hanging wall of the Wenquan Hu Thrust Fault (11UMT63, 12DDT09, 12DDT10).

Sample 13DDT016 was collected from a Triassic sandstone, so the geologic constraints include deposition at the surface between 240 and 200 Ma, followed by burial to temperatures in excess of 40 °C, and exhumation to the surface sometime between 60 and 0 Ma. While the modeling results show a fairly broad range of possible early Mesozoic cooling paths, the good model fits tightly constrain slow, monotonic cooling between 80 to 50 °C after 100 Ma followed by rapid exhumation to the surface (Figure A4.1). The onset of rapid exhumation may have occurred between 50 and 10 Ma, which is consistent with the ~35 – 36 Ma AHe ages recorded from nearby samples 13DDT022 and 13DDT032 (Figure 4.2b; Table 4.1).

Sample 13DDT017 was collected from a small intrusion into Triassic metapelites located in the southern East Deshuiwai Mountains (Figure 4.2), thus HeFTy modeling included geologic constraints of post-early Triassic origin at depth (>40 °C) and exhumation to surface temperature (0 – 20 °C) after 80 Ma. No good fit models could be resolved with AHe data from this sample, however acceptable fit models resolve slow monotonic cooling between ~90 and 50 Ma, followed by rapid exhumation to surface temperatures sometime after 50 Ma, consistent with the ~31 Ma AHe ages from nearby sample 13DDT011 (Figure 4.2b; Table 4.1).

Modeling AHe data with correlated age and crystal size

Two samples collected in close proximity to each other from the East Deshuiwai Mountains show a strong correlation between replicate age and radius (samples 13DDT008 and 13DDT009; Figure A4.2a, Table A4.1). The correlation between age and crystal size provides important constraints on the timing and magnitude of exhumation within this region. In an attempt to model the thermal history of the East Deshuiwai Mountains, we used equations of He diffusion to match the observed age – crystal size distribution from our samples, similar to the methods of Reiners and Farley (2001). Without independent knowledge of the specific kinetic parameters of our sampled

apatite crystals, we used the coefficient of diffusion and activation energy measured for the Durango apatite standard (Farley, 2000). Because these samples are from the Triassic metapelites, we modeled the early thermal history to include Triassic deposition (250 – 200 Ma) and subsequent burial to a minimum temperature of 300 °C, which is in agreement with the metamorphic grade of the sampled rock. Following burial to high temperatures, we varied the possible rate and timing of exhumation to near-surface depths (correlated to temperatures between 10 °C and 80 °C) and isothermal holding. The modeled isothermal holding time was varied between 10 and 240 million years, and the time of subsequent exhumation was varied between 0 and 100 Ma. We determined the best-fit model to each sample by calculating the χ^2 value for observed and predicted AHe ages for measured apatite crystal radii (Figures A4.2b and A4.2c).

Our numerical modeling was not able to reproduce the observed age to crystal size variation in either sample particularly well, however both suggest similar exhumation histories (Figures A4.2b and A4.2c). The modeled histories suggest that samples from the East Deshuiwai Mountains were held isothermally between 48 and 80 °C for 236 – 238 Myr and rapidly exhumed to the surface. The onset of rapid exhumation is 2 – 4 Ma. The difficulty in modeling the thermal histories of the East Deshuiwai samples may be due to the unknown diffusion kinetics of our particular samples. Modeled temperature sensitivities of apatite crystals suggest that the diffusion coefficient specific to each sample may have a strong influence on the range of apparent AHe ages, particularly for rocks that have a prolonged residence within the partial retention zone (Wolf et al., 1998). We therefore suggest that the diffusion parameters used are not appropriate for the East Deshuiwai Mountain samples and may be the cause for our inability to replicate the observed age – crystal size correlation.

Despite our inability to precisely model the thermal history of the East Deshuiwai Mountains, qualitative observations of the observed age – crystal size relationship, as well as the structural and stratigraphic setting of sample 13DDT008 and 13DDT009, offer important insight into the burial and exhumation history of the region. As mentioned above, the geologic age and greenschist metamorphic grade of the samples suggests that the rocks were deposited in the Triassic and were buried to temperatures in excess of 300 °C. Additionally, the broad range of AHe ages measured for samples 13DDT008 – 009 suggests these rocks likely experience an extended residence time in the PRZ, perhaps upwards of 100 Myr. Together, this indicates that samples 13DDT008 – 009 were deposited in the Triassic, moderately to rapidly buried to reach greenschist metamorphic conditions (300 – 450 °C, and exhumed to shallow crustal depths soon thereafter to allow for a long residence within the apatite PRZ. Additionally, the youngest apatite age within this

sample suite is 16.1 ± 0.34 Ma (Figure A4.2; Table A4.1), suggesting that renewed exhumation of the East Deshuiwai Mountains initiated after ~16 Ma. Assuming a PRZ between 40 °C and 80 °C and a geothermal gradient of 25 – 35 °C km^{-1}, this suggests that there has been between 1.1 and 3.2 km of overburden eroded from the East Deshuiwai Mountains since the Neogene.

Appendix B: Chapter IV

This appendix contains eight figures and four tables.

Figure A4.1 contains HeFTy modeling results for thermochronologic samples.

Figure A4.2 contains thermochronologic modeling results for age – grain size correlations.

Figure A4.3 contains XRD powder patterns matches for aliquots from sample 11UMT50.

Figure A4.4 contains XRD powder patterns matches for aliquots from sample 11UMT52.

Figure A4.5 contains XRD powder patterns matches for aliquots from sample 11UMT55.

Figure A4.6 contains XRD powder patterns matches for aliquots from sample 12DDT18.

Figure A4.7 contains argon age spectra for sample 11UMT50.

Figure A4.8 contains argon age spectra for sample 11UMT52.

Figure A4.9 contains argon age spectra for sample 11UMT55.

Figure A4.10 contains argon age spectra for sample 12DDT18.

Table A4.1 contains apatite (U-Th)/He age data for samples from the central Kunlun Shan.

Table A4.2 contains zircon (U-Th)/He age data for samples from the central Kunlun Shan.

Table A4.3 contains Argon isotopic data for fault gouge dating.

Table A4.4 contains compiled ages for the initiation of strike-slip faulting in Tibet.

Table A4.5 contains compiled ages for the initiation of normal faulting in Tibet.

Figure A4.1. Modeled time-temperature histories for low-temperature thermochronology using HeFTy modeling software. Geologic constraints on each model are shown as red boxes. Blue and grey lines represent good fit, and acceptable fit modeled thermal, respectively.

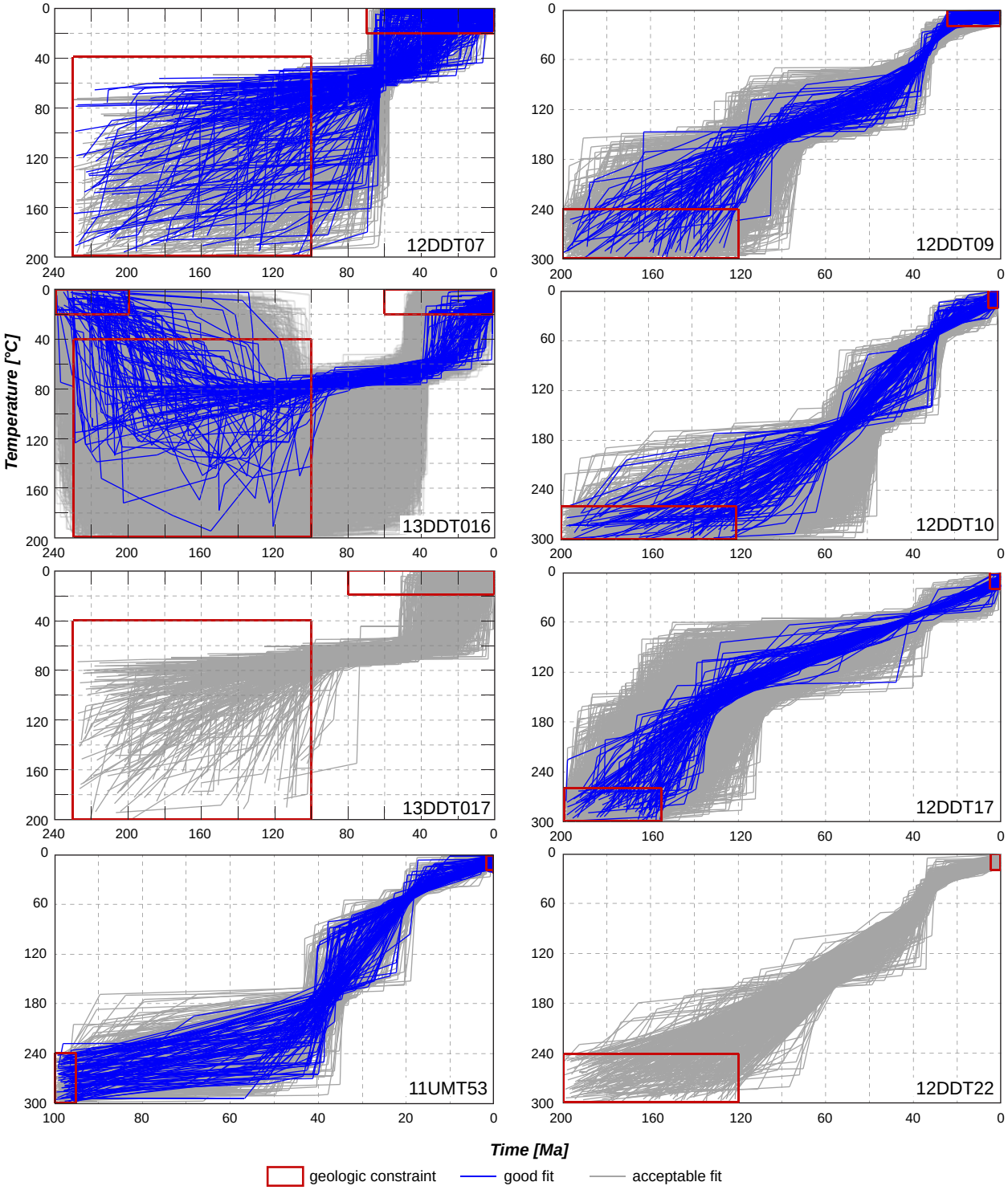

Figure A4.2. (a) Apatite (U-Th)/He ages for replicates of samples 13DDT008 and 13DDT009, plotted against the spherical equivalent radius. The positive relationship may suggest isothermal holding for a prolonged period of time. (b) Best fit thermal history model for sample 13DDT009. (c) Best fit thermal history model for sample 13DDT009.

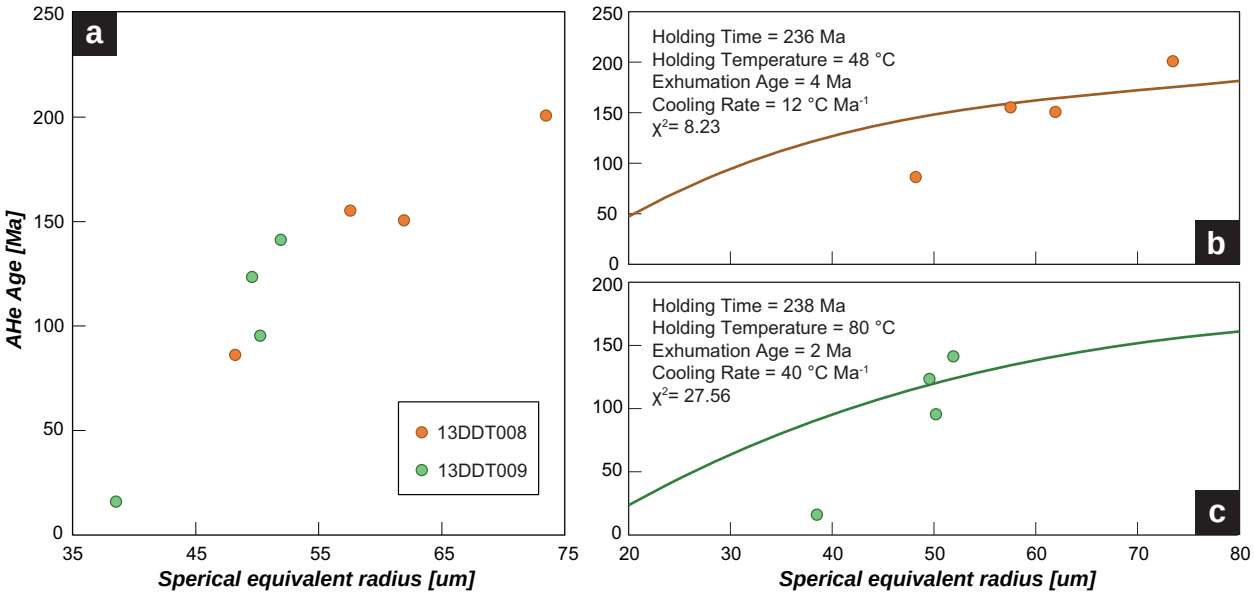

Figure A4.3. Illite powder pattern matching results for sample 11UMT50. The measured XRD pattern is in black, the modeled in red.

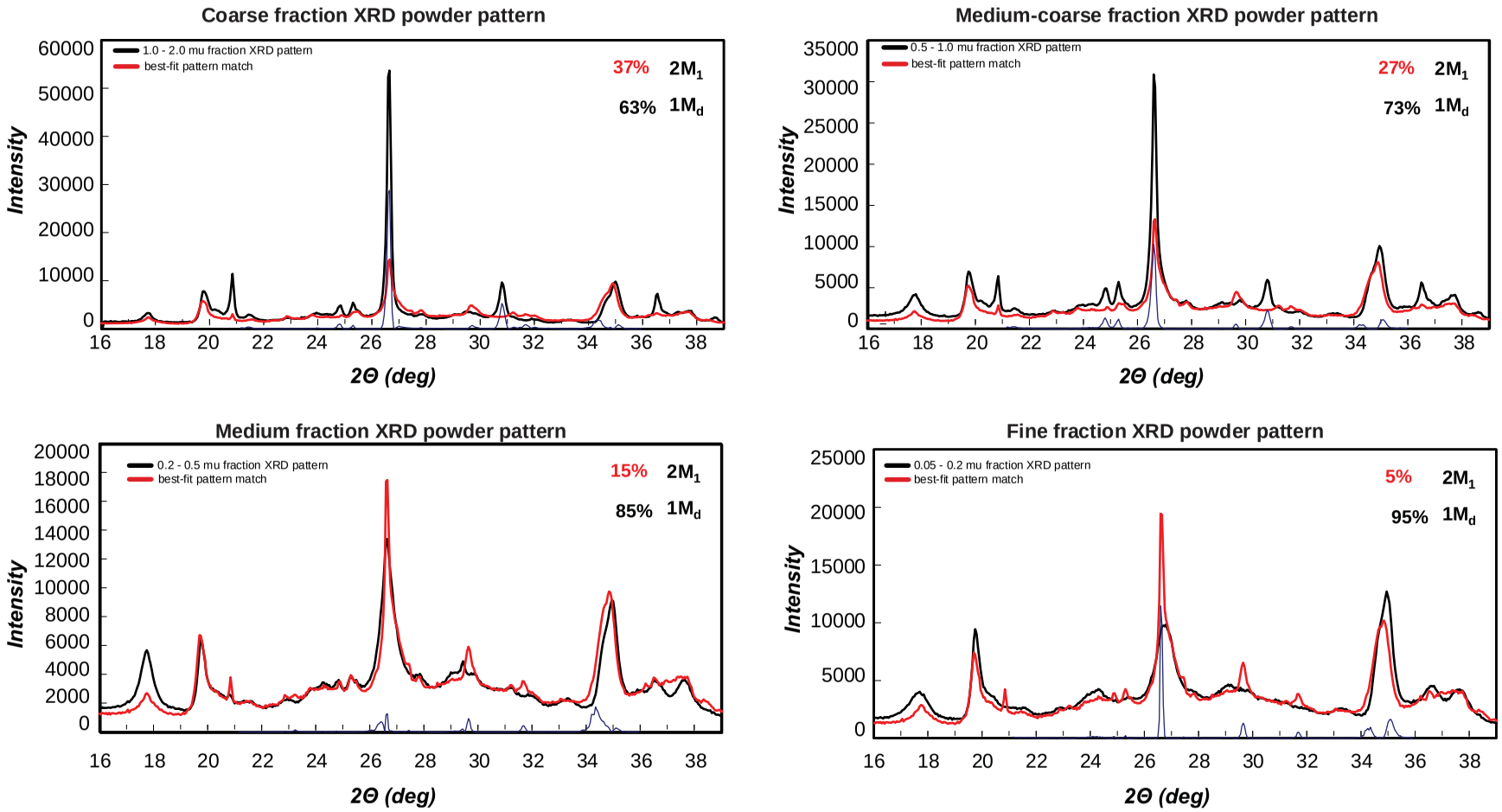

Figure A4.4. Illite powder pattern matching results for sample 11UMT52. The measured XRD pattern is in black, the modeled in red.

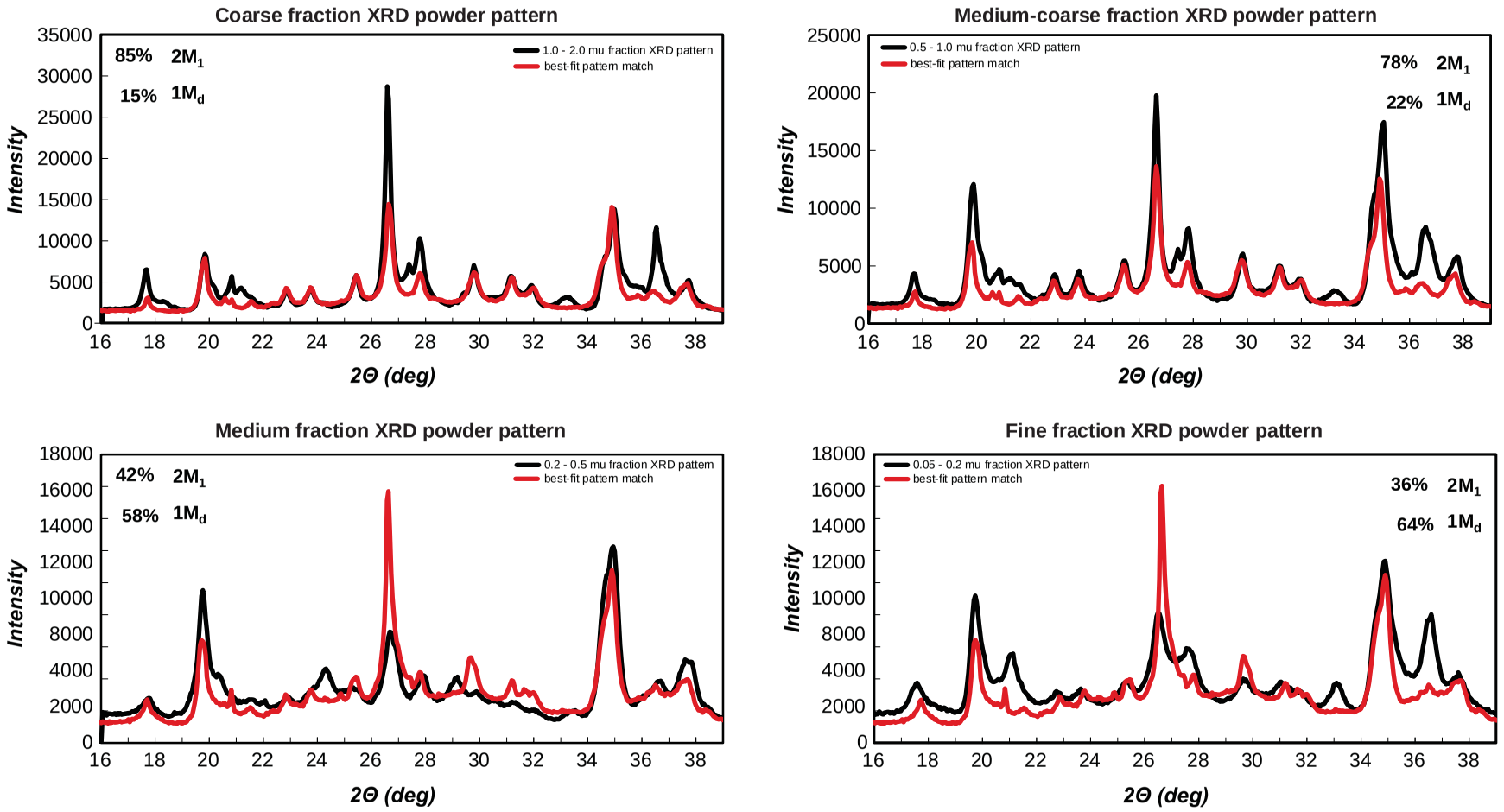

Figure A4.5. Illite powder pattern matching results for sample 11UMT55. The measured XRD pattern is in black, the modeled in red.

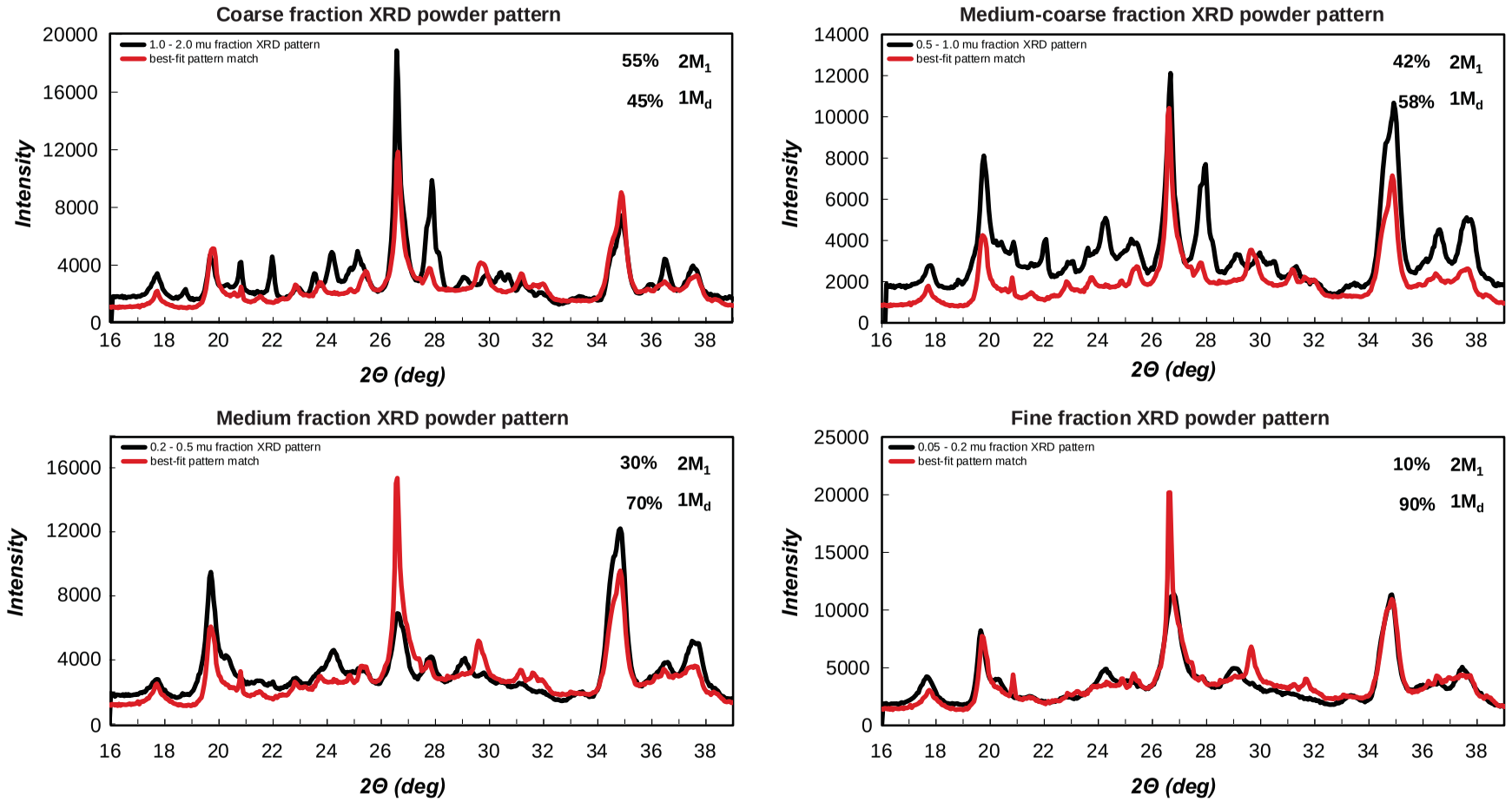

Figure A4.6. Illite powder pattern matching results for sample 12DDT18. The measured XRD pattern is in black, the modeled in red.

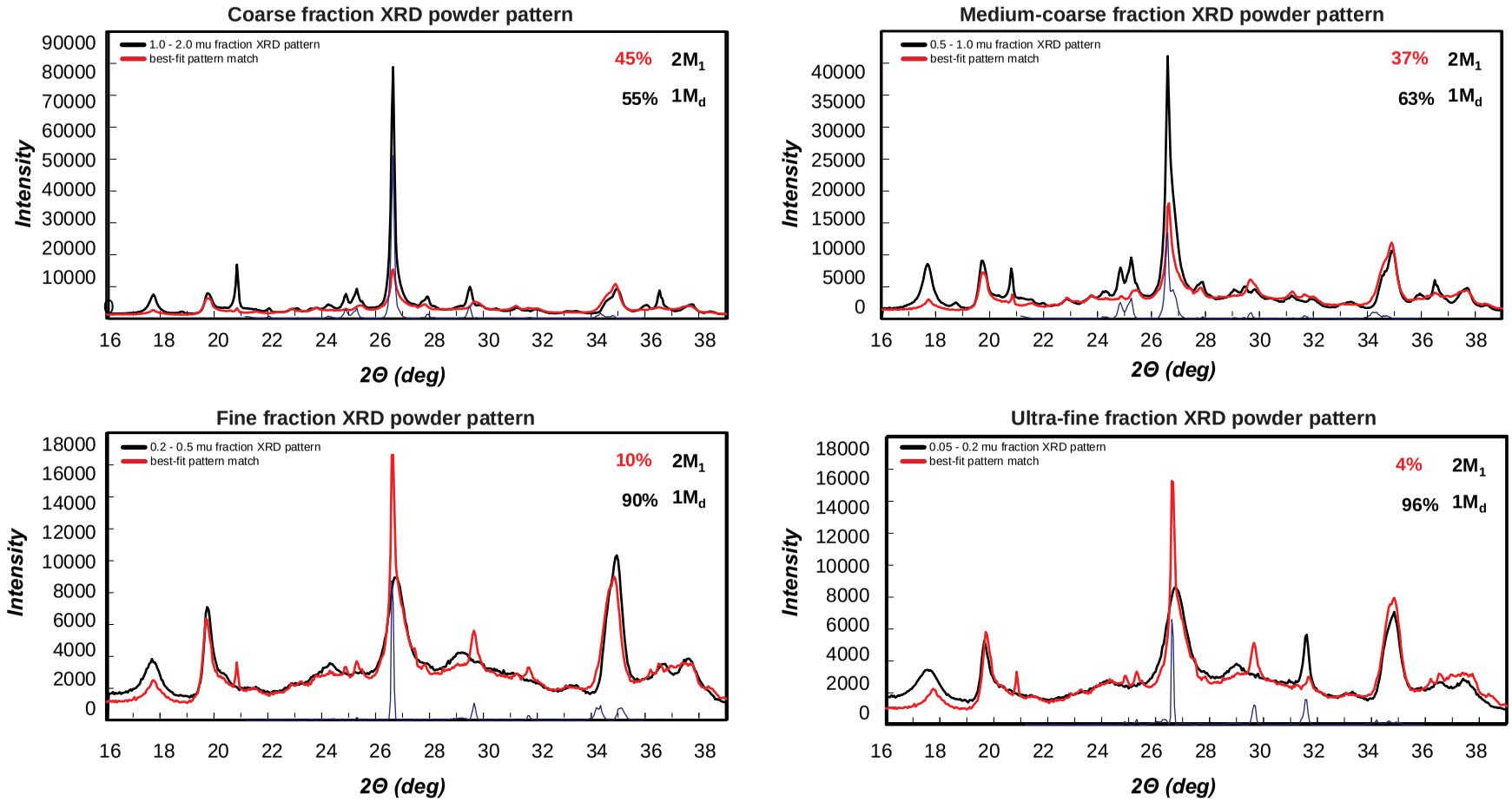

Figure A4.7. Argon release spectra for fault gouge sample 11UMT50.

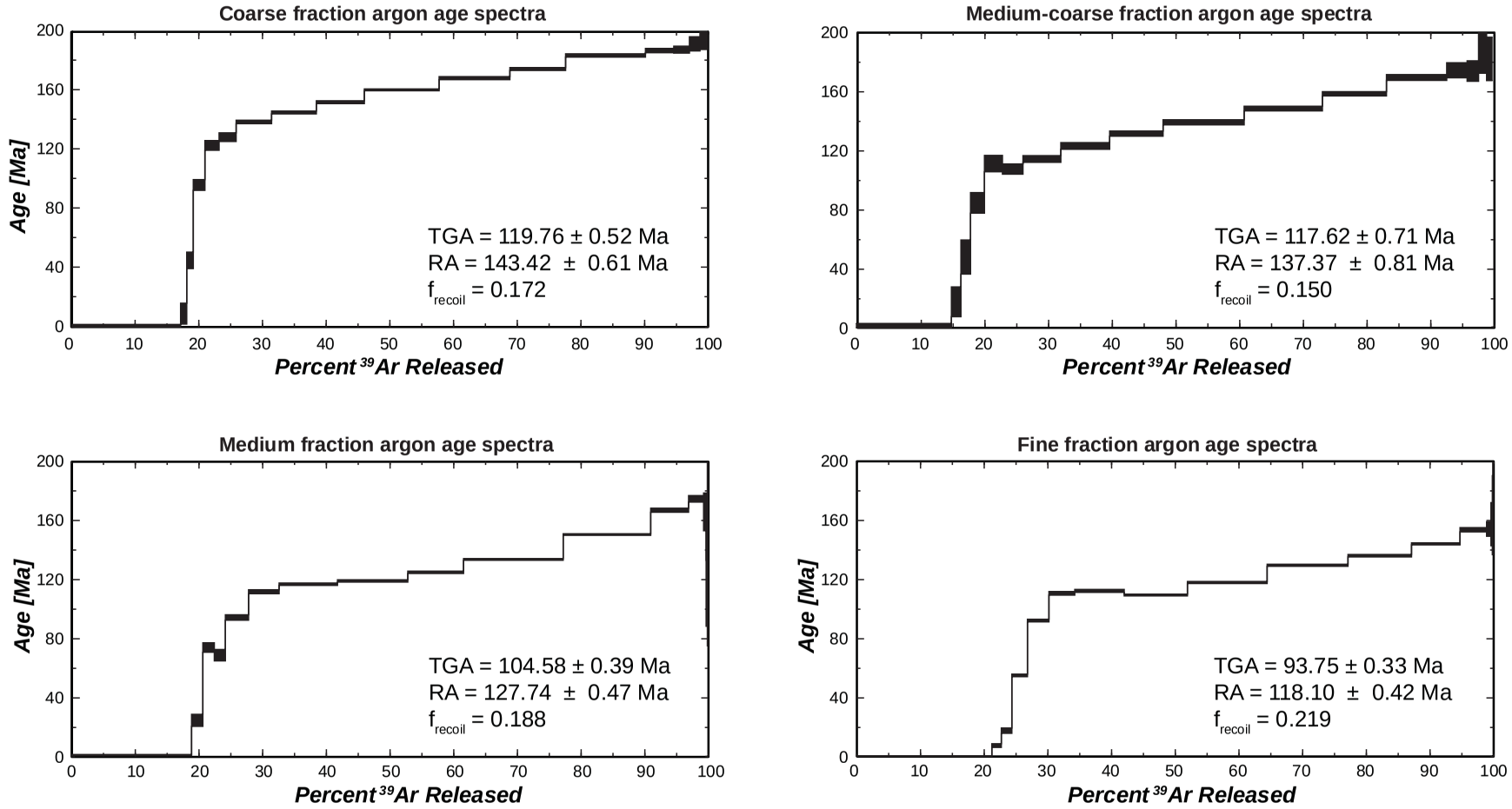

Figure A4.8. Argon release spectra for fault gouge sample 11UMT52.

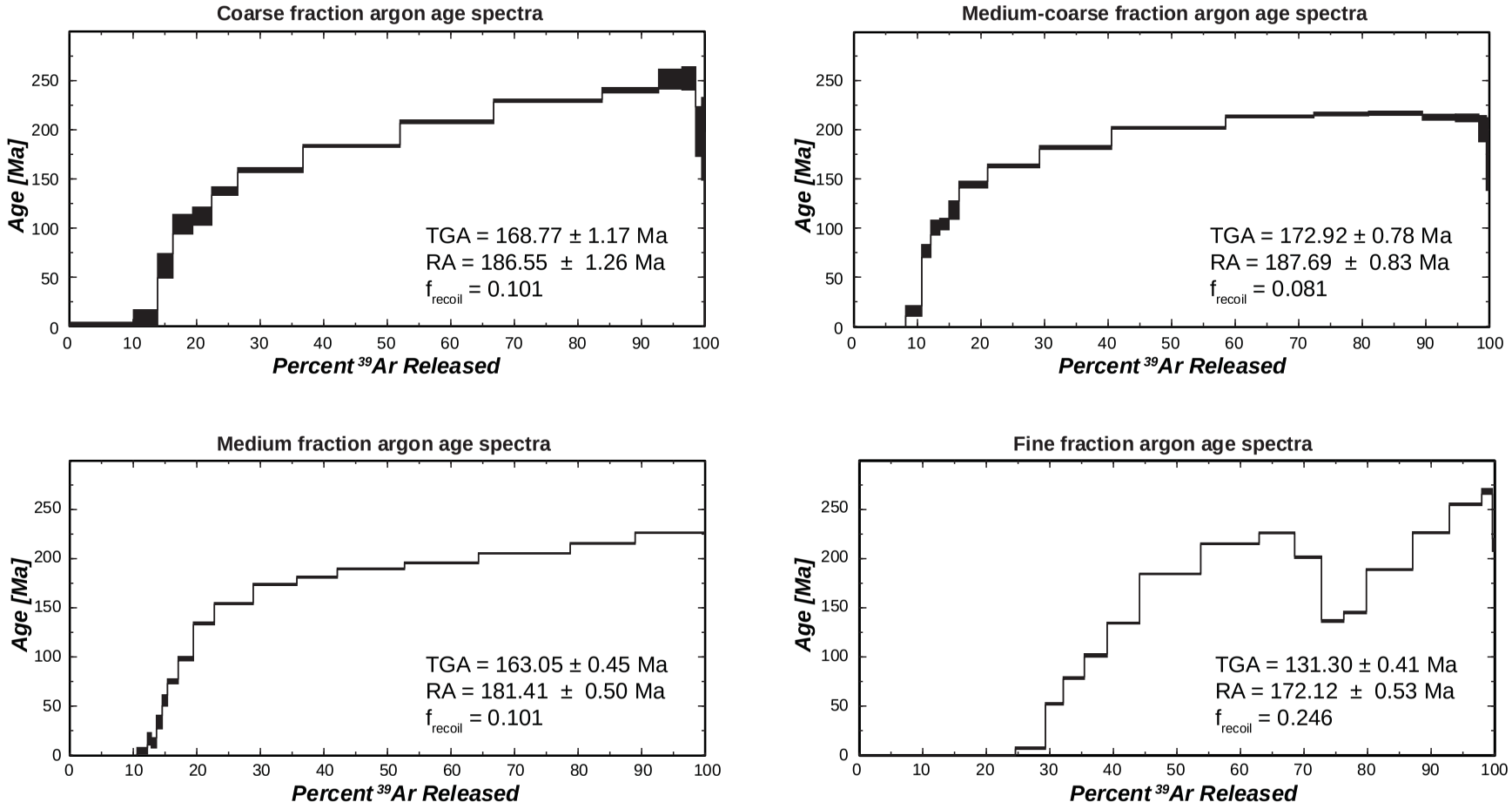

Figure A4.9. Argon release spectra for fault gouge sample 11UMT55.

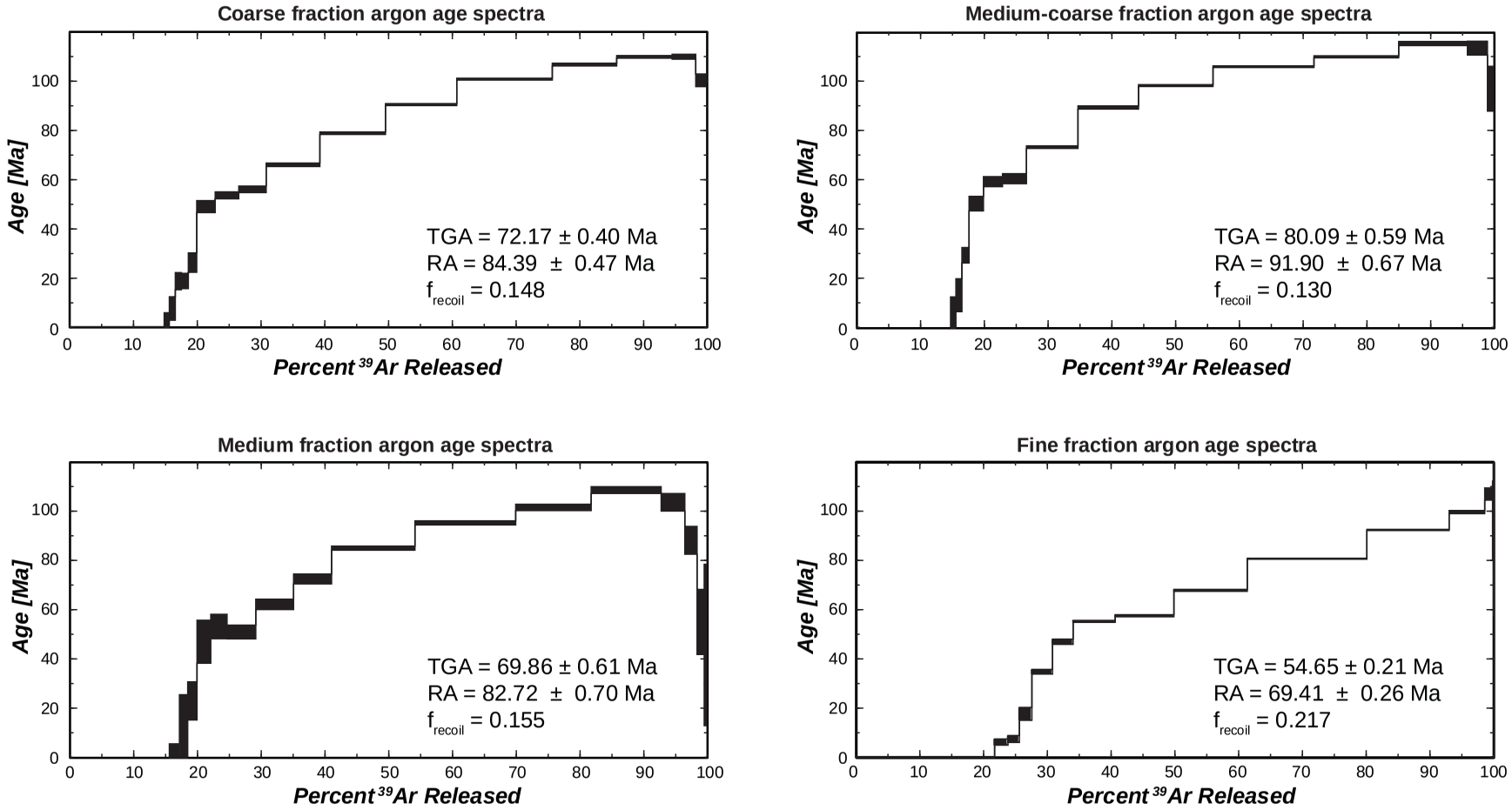

Figure A4.10. Argon release spectra for fault gouge sample 12DDT18.

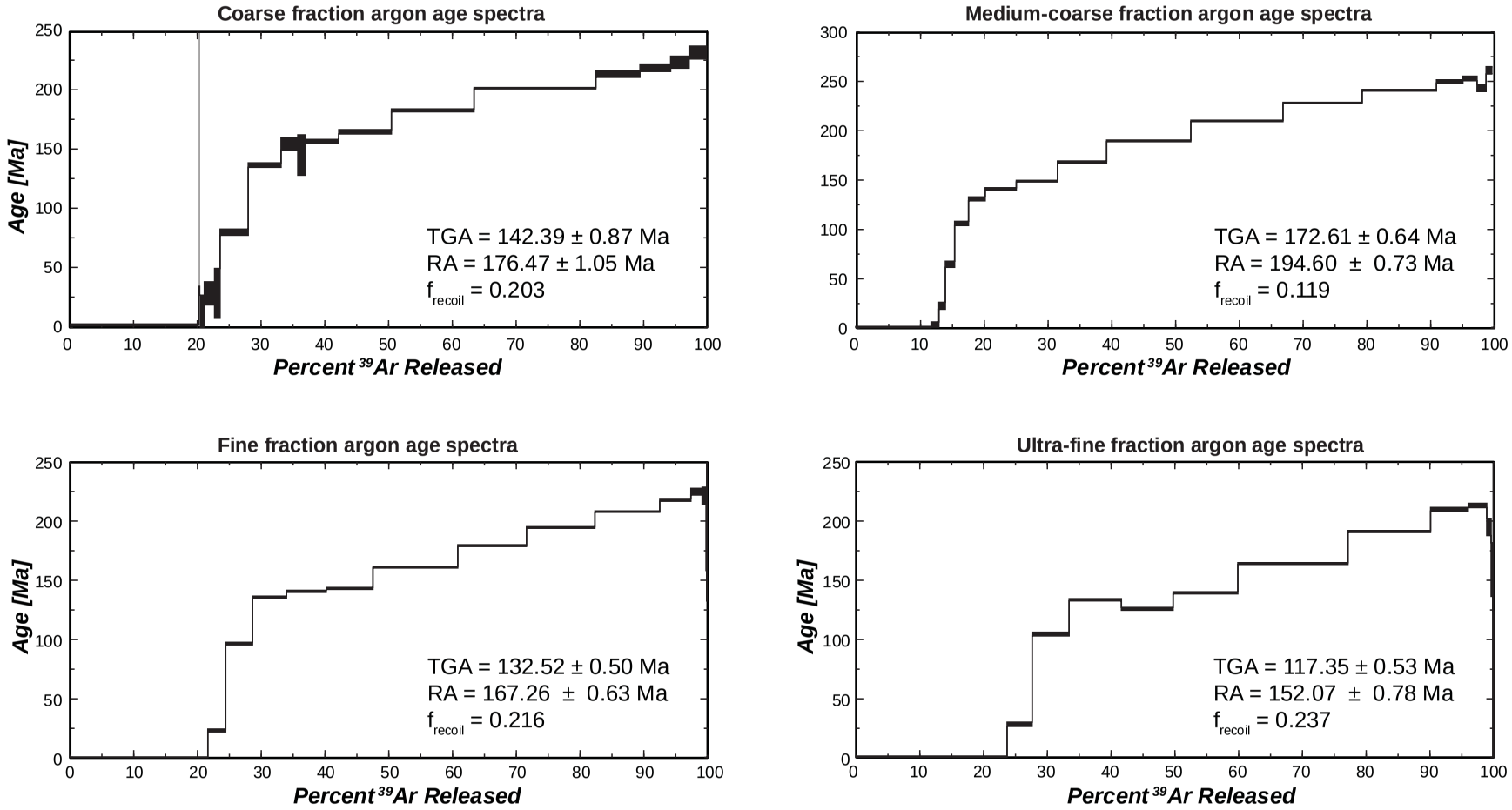

Table A4.1. Apatite (U-Th)/He age data for samples collected throughout the central Kunlun Shan.

Sample	Replicate	eU [ppm]	He [nmol/g]	U [ppm]	Th [ppm]	Sm [ppm]	radius [μm]	F_T	Age [Ma]	Error [Ma]
11UMT53	a	25.15	1.67	23.41	7.41	122.99	48.81	0.75	20.05	0.33
	b	29.53	1.49	24.32	22.14	207.26	47.41	0.72	16.77	0.56
	c	10.67	0.53	9.71	4.07	161.33	48.80	0.73	18.52	0.29
	d*	15.24	1.27	13.76	6.29	150.33	45.53	0.72	32.76	1.26
	e	82.79	5.19	80.67	9.01	34.78	57.11	0.76	21.55	0.30
11UMT56	a	23.56	0.98	10.46	55.71	183.22	58.53	0.80	25.40	0.28
	b	34.06	1.30	17.03	72.45	340.03	51.11	0.76	20.51	0.23
	c	31.72	1.74	18.77	55.11	92.25	51.20	0.75	22.88	0.27
	d	12.71	0.45	3.19	40.52	49.65	43.43	0.74	16.68	0.25
11UMT63	a	78.67	5.38	62.08	70.60	235.46	45.64	0.73	23.89	0.28
	b	51.42	3.07	38.90	53.25	221.44	46.47	0.71	22.43	0.49
	c	44.06	2.89	34.74	39.67	135.09	52.85	0.75	26.48	0.31
	d	67.59	4.71	54.35	56.31	166.84	50.20	0.75	28.88	0.41
12DDT07	a	11.25	2.55	10.43	3.48	145.60	65.01	0.79	61.50	2.50
	b	16.25	3.26	15.27	4.15	156.15	65.76	0.80	72.88	1.07
	c	8.00	1.28	7.32	2.90	206.78	82.41	0.84	56.08	1.92
	d	10.98	1.65	9.95	4.41	162.69	65.32	0.80	61.61	0.91
12DDT09	a	22.52	2.21	16.33	26.33	123.49	46.41	0.71	33.94	0.41
	b	26.81	1.60	18.27	36.33	181.61	45.56	0.71	29.92	1.14
	c	14.83	1.14	10.85	16.97	76.83	43.80	0.71	33.20	0.42
	d	9.14	1.00	7.24	8.08	25.99	45.56	0.73	37.27	1.46
12DDT10	a	29.46	2.25	19.54	42.23	137.42	53.32	0.75	31.46	1.40
	b	34.85	3.23	24.61	43.57	115.28	43.93	0.70	32.09	0.42
	c	35.62	2.21	23.32	52.34	157.22	53.61	0.75	24.09	0.69
	e	30.94	2.24	19.44	48.93	139.03	55.95	0.76	29.64	1.06
12DDT17	a	17.29	1.46	9.48	33.24	161.84	50.84	0.74	28.84	0.31
	b	15.37	1.32	6.60	37.29	310.67	52.77	0.75	40.18	0.43
	d	15.16	1.42	9.29	25.00	174.86	52.42	0.74	42.35	0.46
	e	16.93	1.41	7.83	38.73	195.34	51.83	0.74	36.95	0.44
12DDT22	a	10.68	1.32	4.07	28.11	106.33	74.06	0.83	48.72	0.51
	b	46.02	5.25	18.28	118.03	224.25	76.39	0.83	33.43	0.35
	c	44.79	3.18	36.79	34.02	156.12	44.28	0.71	26.86	0.33
	d	3.84	0.47	1.34	10.61	48.87	61.69	0.79	44.06	0.55
12DDT24	a	33.52	3.95	21.74	50.12	111.89	46.86	0.71	30.43	0.33
	b	36.57	4.24	27.43	38.91	88.33	44.96	0.71	30.22	0.36
	c	27.93	3.37	20.02	33.70	67.88	55.21	0.76	29.17	0.33
	d	34.86	4.56	25.23	41.01	91.77	49.71	0.73	33.08	0.37
	e	22.84	2.80	15.36	31.81	80.41	59.99	0.78	28.76	0.31
13DDT008	a	5.55	1.53	2.44	13.22	284.55	61.92	0.79	150.66	1.74
	b	10.85	2.12	4.73	26.03	357.08	48.20	0.72	86.23	0.96
	c	7.91	3.28	3.50	18.76	284.58	57.54	0.78	155.37	1.62
	d	5.30	2.23	2.42	12.23	256.47	73.46	0.82	200.81	2.03

Table A4.1 continued. Apatite (U-Th)/He age data for samples collected throughout the central Kunlun Shan.

Sample	Replicate	eU [ppm]	He [nmol/g]	U [ppm]	Th [ppm]	Sm [ppm]	radius [μm]	F_T	Age [Ma]	Error [Ma]
13DDT009	a	11.93	3.22	5.19	28.70	294.54	51.89	0.74	141.31	1.48
	c	19.48	4.37	8.76	45.64	400.12	50.22	0.73	95.43	1.00
	d†	17.85	2.56	6.82	46.94	375.72	73.40	0.83	309.32	3.46
	e	16.28	3.46	6.95	39.71	343.87	38.51	0.68	16.07	0.17
	f	14.91	5.02	5.63	39.47	378.38	49.56	0.72	123.55	1.36
13DDT011	a	8.13	0.46	5.36	11.79	103.72	59.96	0.78	28.95	0.43
	b	4.04	0.27	3.02	4.35	20.12	44.30	0.72	36.33	0.89
	c	5.94	0.41	4.76	4.99	69.81	56.22	0.77	36.31	0.53
	d	5.65	0.32	3.95	7.24	22.87	57.48	0.77	28.00	0.37
	e	6.62	0.38	3.63	12.71	29.12	47.21	0.72	29.60	0.55
13DDT016	a	46.52	7.44	28.62	76.16	273.98	72.59	0.81	58.04	0.61
	b	25.26	2.19	11.51	58.51	335.82	76.74	0.82	35.07	0.38
	c	28.22	3.15	23.74	19.07	282.79	88.82	0.85	44.88	0.55
	d	37.38	4.44	15.42	93.41	483.46	54.69	0.75	52.89	0.55
	e	33.68	4.32	12.56	89.88	340.68	58.13	0.77	56.50	0.62
13DDT017	a	43.22	6.76	31.94	47.99	63.68	61.83	0.78	68.43	0.78
	b	46.98	10.86	34.43	53.42	64.05	54.92	0.75	92.48	1.01
	c	43.67	5.66	33.82	41.94	17.63	52.74	0.75	42.72	0.49
	d	49.41	12.64	35.90	57.48	58.04	64.61	0.79	99.43	1.09
13DDT021‡	a	9.37	0.84	3.72	24.03	453.62	59.07	0.77	41.71	0.48
	b	13.59	1.53	5.33	35.16	521.67	75.50	0.82	50.48	0.55
	c	10.74	1.28	4.50	26.52	487.17	61.06	0.79	51.92	0.58
	d	8.06	1.35	3.27	20.39	388.97	52.06	0.75	58.88	0.68
13DDT022	a	9.56	0.49	3.79	24.52	349.40	42.46	0.70	28.51	0.55
	b	12.99	1.19	5.52	31.77	385.34	44.87	0.73	44.18	0.57
	c*	17.67	2.21	7.53	43.14	391.44	39.52	0.67	58.66	0.85
	d	10.10	0.82	4.27	24.79	371.16	39.68	0.67	32.58	0.48
	e	17.75	1.35	7.61	43.17	379.73	41.79	0.70	36.43	0.50
13DDT023	a	9.58	1.21	3.51	25.86	483.66	61.78	0.78	51.85	0.62
	b	7.79	1.10	3.20	19.51	438.74	48.00	0.73	51.23	0.66
	c	9.19	1.70	4.25	21.01	420.69	57.49	0.78	75.51	0.78
	d	9.31	0.89	3.81	23.40	465.99	52.97	0.74	37.93	0.41
13DDT032	a	11.08	0.55	5.80	22.49	156.58	44.42	0.70	30.50	0.52
	b	19.43	1.52	8.91	44.80	231.58	43.60	0.70	41.42	0.46
	c	18.13	0.83	8.38	41.51	243.75	46.69	0.72	29.39	0.39
	d	12.18	1.17	5.80	27.16	141.50	45.75	0.70	34.97	0.43
	e	15.06	1.55	7.59	31.78	152.21	50.15	0.73	45.82	0.52
13DDT036	a	18.51	5.21	8.77	41.42	434.46	49.54	0.72	132.95	1.39
	b	15.10	2.02	7.39	32.81	290.19	46.90	0.72	74.81	0.91
	c	17.57	2.07	8.86	37.07	164.20	60.74	0.80	44.68	0.48
	d	8.84	1.27	4.71	17.55	234.77	46.57	0.71	40.08	0.47

* replicate is omitted from further analysis on the basis of Dixon's Q-test for outlier identification.
† replicate is omitted from further analysis on the basis that the AHe age is older than the depositional age of the unit.
‡ sample not used in analysis it was because collected as float.

Table A4.2. Zircon (U-Th)/He age data for samples collected throughout the central Kunlun Shan.

Sample	Replicate	He (ncc)	Radius (um)	F_T	Mass (ug)	U (ppm)	Th (ppm)	He (ppm)	Age (Ma)
11UMT53									
	a(z)	10.91	50.85	0.76	6.39	443.50	232.41	76.20	37.11
	b(z)	11.78	50.66	0.77	5.76	533.29	120.85	91.26	39.23
	c(z)	4.78	46.47	0.74	3.83	286.40	168.45	55.65	42.55
12DDT09									
	a(z)	13.12	48.81	0.75	4.78	226.85	236.58	122.49	106.46
	b(z)	4.96	43.43	0.73	3.10	214.89	110.85	71.33	75.26
	c(z)	8.20	46.60	0.74	3.94	174.36	128.70	92.84	112.71
12DDT10									
	a(z)	2.26	47.99	0.75	4.71	57.64	44.82	21.44	77.58
	b(z)	1.77	43.39	0.73	3.15	91.21	51.10	25.07	61.84
	c(z)	5.77	63.68	0.81	10.36	64.58	34.73	24.86	78.08
12DDT17									
	a(z)	5.15	50.67	0.76	5.12	70.32	58.81	44.88	129.19
	b(z)	34.42	51.95	0.77	6.17	344.47	185.12	249.02	153.60
	c(z)	41.80	52.59	0.77	7.10	413.69	180.12	262.82	137.32
12DDT22									
	b(z)	5.09	43.26	0.73	3.06	171.52	77.31	74.21	99.33
	c(z)	5.23	56.56	0.79	7.21	81.78	34.29	32.34	84.46
	d(z)	4.35	47.17	0.75	4.31	96.82	26.47	45.05	107.37

Table A4.3. Argon isotopic data for $^{40}Ar/^{39}Ar$ fault gouge dating

F39	Laser Power [mW]	Volume [ccSTP] ^{36}Ar	^{37}Ar	^{38}Ar	^{39}Ar	^{40}Ar	Age [Ma]
11UMT55 0.05 - 0.2 µm (mc4017) (J=0.00249439) Total gas age = 54.66 ± 0.21 Ma (35.757478 N, 95.224211° E)							
0.21696	0	5.938 ± 0.117	12.090 ± 0.388	14.802 ± 0.212	809.063 ± 1.436	1824.395 ± 2.386	0.387 ± 0.192
0.23800	100	0.229 ± 0.075	1.303 ± 0.228	1.923 ± 0.122	78.442 ± 0.452	180.799 ± 0.865	6.475 ± 1.263
0.25583	150	0.489 ± 0.071	0.969 ± 0.257	0.988 ± 0.111	66.509 ± 0.410	258.843 ± 0.894	7.722 ± 1.408
0.27545	200	0.748 ± 0.145	1.239 ± 0.219	1.078 ± 0.120	73.138 ± 0.181	513.481 ± 0.905	17.901 ± 2.618
0.30781	250	1.927 ± 0.087	1.242 ± 0.349	1.418 ± 0.134	120.664 ± 0.490	1516.479 ± 1.760	34.978 ± 0.948
0.34006	300	2.886 ± 0.097	1.864 ± 0.277	1.235 ± 0.091	120.285 ± 0.517	2129.560 ± 2.453	47.141 ± 1.071
0.40599	400	5.104 ± 0.067	4.103 ± 0.320	1.960 ± 0.086	245.833 ± 0.757	4581.160 ± 3.408	55.393 ± 0.396
0.49798	500	5.097 ± 0.104	5.572 ± 0.262	1.993 ± 0.087	343.053 ± 0.868	5974.310 ± 4.729	57.678 ± 0.419
0.61303	600	4.203 ± 0.128	6.785 ± 0.306	1.707 ± 0.137	429.006 ± 0.678	7845.011 ± 4.420	67.967 ± 0.398
0.80046	800	4.571 ± 0.077	9.913 ± 0.265	1.504 ± 0.143	698.926 ± 1.131	14183.254 ± 10.416	80.787 ± 0.200
0.92935	1000	1.954 ± 0.070	6.837 ± 0.269	0.774 ± 0.069	480.661 ± 0.742	10710.137 ± 5.730	92.455 ± 0.237
0.98514	1200	0.882 ± 0.088	3.172 ± 0.266	0.322 ± 0.118	208.045 ± 0.742	4999.114 ± 4.724	99.691 ± 0.643
0.99739	1600	0.439 ± 0.085	0.313 ± 0.290	0.175 ± 0.082	45.669 ± 0.326	1248.413 ± 1.243	107.003 ± 2.463
0.99904	2000	0.444 ± 0.078	-0.081 ± 0.345	0.049 ± 0.071	6.161 ± 0.134	266.387 ± 1.054	96.224 ± 16.059
0.99957	2600	0.511 ± 0.064	-0.080 ± 0.299	0.134 ± 0.069	1.978 ± 0.127	195.496 ± 0.823	98.771 ± 41.115
0.99982	3200	0.460 ± 0.053	-0.564 ± 0.156	0.133 ± 0.101	0.919 ± 0.099	141.467 ± 1.186	26.355 ± 76.368
1.00000	4000	0.677 ± 0.063	-0.310 ± 0.236	0.205 ± 0.084	0.671 ± 0.109	217.742 ± 1.034	114.375 ± 119.327
11UMT55 0.2 - 0.5 µm (mc4018) (J=0.00248541) Total gas age = 69.86 ± 0.61 Ma (35.757478 N, 95.224211° E)							
0.15513	0	1.542 ± 0.068	1.429 ± 0.251	4.054 ± 0.193	110.088 ± 0.417	411.999 ± 1.062	-1.784 ± 0.824
0.17200	100	0.089 ± 0.061	0.307 ± 0.228	0.598 ± 0.069	11.968 ± 0.145	23.989 ± 0.428	-0.845 ± 6.764
0.18499	150	0.058 ± 0.111	0.191 ± 0.331	0.268 ± 0.068	9.220 ± 0.177	37.120 ± 0.582	9.723 ± 15.892
0.19959	200	0.076 ± 0.061	0.314 ± 0.202	0.163 ± 0.070	10.358 ± 0.212	76.260 ± 0.677	23.087 ± 7.745
0.22115	250	0.113 ± 0.103	0.347 ± 0.252	0.198 ± 0.078	15.300 ± 0.185	196.240 ± 0.602	47.131 ± 8.729
0.24668	300	0.284 ± 0.070	0.198 ± 0.197	0.233 ± 0.062	18.122 ± 0.144	302.512 ± 0.715	53.323 ± 4.957
0.29173	400	0.502 ± 0.069	0.526 ± 0.190	0.098 ± 0.078	31.966 ± 0.225	517.914 ± 1.387	51.095 ± 2.797
0.35102	500	0.302 ± 0.069	0.566 ± 0.378	0.114 ± 0.089	42.071 ± 0.204	684.258 ± 0.784	62.323 ± 2.112
0.41060	600	0.253 ± 0.065	0.614 ± 0.208	0.058 ± 0.078	42.285 ± 0.183	773.645 ± 1.477	72.641 ± 2.000
0.54135	800	0.323 ± 0.056	1.087 ± 0.227	0.049 ± 0.077	92.780 ± 0.334	1899.985 ± 1.422	85.165 ± 0.828
0.69936	1000	0.428 ± 0.064	1.415 ± 0.386	0.044 ± 0.056	112.131 ± 0.490	2576.923 ± 3.547	95.422 ± 0.836
0.81772	1200	0.403 ± 0.076	1.437 ± 0.207	0.059 ± 0.089	83.991 ± 0.505	2079.204 ± 3.782	101.712 ± 1.290
0.92744	1600	0.440 ± 0.081	1.345 ± 0.298	0.043 ± 0.052	77.867 ± 0.302	2076.925 ± 2.196	108.758 ± 1.373
0.96458	2000	0.305 ± 0.074	0.278 ± 0.262	0.120 ± 0.066	26.356 ± 0.153	718.190 ± 1.037	103.784 ± 3.558
0.98378	2600	0.443 ± 0.060	0.489 ± 0.234	0.229 ± 0.047	13.624 ± 0.123	405.890 ± 1.325	88.343 ± 5.648
0.99497	3200	0.634 ± 0.081	0.429 ± 0.218	0.070 ± 0.043	7.936 ± 0.218	286.491 ± 0.806	55.174 ± 13.218
1.00000	4000	0.614 ± 0.091	-0.090 ± 0.241	0.182 ± 0.063	3.573 ± 0.111	218.441 ± 0.931	45.828 ± 32.787
11UMT55 1.0 - 2.0 µm (mc4031) (J=0.00230862) Total gas age = 72.17 ± 0.40 Ma (35.757478 N, 95.224211° E)							
0.14811	0	2.422 ± 0.082	18.733 ± 0.340	8.038 ± 0.220	347.318 ± 1.056	734.298 ± 1.694	0.224 ± 0.292
0.15625	100	0.099 ± 0.083	1.165 ± 0.148	1.044 ± 0.073	19.085 ± 0.252	31.619 ± 0.823	0.544 ± 5.372
0.16563	150	0.101 ± 0.085	1.299 ± 0.150	0.728 ± 0.097	21.982 ± 0.320	70.216 ± 0.704	7.650 ± 4.765
0.17512	200	0.040 ± 0.063	0.942 ± 0.172	0.440 ± 0.070	22.270 ± 0.223	112.574 ± 0.946	18.751 ± 3.479
0.18607	250	0.251 ± 0.065	0.846 ± 0.194	0.331 ± 0.079	25.658 ± 0.242	190.670 ± 0.610	18.825 ± 3.099
0.19923	300	0.528 ± 0.100	1.510 ± 0.137	0.515 ± 0.086	30.870 ± 0.189	352.293 ± 1.107	26.299 ± 3.944
0.22819	400	1.065 ± 0.137	3.017 ± 0.228	0.979 ± 0.130	67.909 ± 0.371	1125.074 ± 1.649	49.036 ± 2.436
0.26520	500	1.570 ± 0.101	4.437 ± 0.203	0.985 ± 0.114	86.781 ± 0.374	1598.032 ± 2.727	53.619 ± 1.412
0.30821	600	1.403 ± 0.110	5.247 ± 0.208	0.872 ± 0.110	100.855 ± 0.427	1793.098 ± 2.958	56.051 ± 1.325
0.39247	800	1.873 ± 0.116	12.159 ± 0.257	0.928 ± 0.151	197.587 ± 0.423	3744.094 ± 1.260	66.032 ± 0.708
0.49540	1000	1.406 ± 0.095	18.484 ± 0.296	0.951 ± 0.110	241.379 ± 0.641	5087.409 ± 2.261	78.864 ± 0.508
0.60727	1200	1.028 ± 0.076	21.911 ± 0.182	0.396 ± 0.108	262.316 ± 0.628	6148.003 ± 3.950	90.486 ± 0.404
0.75716	1600	0.935 ± 0.061	30.955 ± 0.444	0.768 ± 0.136	351.480 ± 1.086	9027.454 ± 4.117	100.827 ± 0.368
0.85819	2000	0.673 ± 0.087	19.745 ± 0.294	0.449 ± 0.088	236.918 ± 0.849	6454.920 ± 2.629	106.754 ± 0.568
0.94521	2600	0.818 ± 0.080	12.162 ± 0.252	0.656 ± 0.129	204.047 ± 0.499	5792.247 ± 5.209	109.877 ± 0.531
0.98228	3200	0.593 ± 0.063	5.925 ± 0.231	0.118 ± 0.097	86.932 ± 0.416	2541.351 ± 3.132	109.938 ± 0.998
1.00000	4000	0.778 ± 0.087	4.805 ± 0.130	0.166 ± 0.107	41.556 ± 0.340	1259.513 ± 2.059	100.357 ± 2.568

Table A4.3 continued. Argon isotopic data for $^{40}Ar/^{39}Ar$ fault gouge dating

F39	Laser Power [mW]	Volume [ccSTP] ^{36}Ar	^{37}Ar	^{38}Ar	^{39}Ar	^{40}Ar	Age [Ma]
11UMT55 0.1=5 - 1.0 µm (mc4032) (J=0.00226897) Total gas age = 80.09 ± 0.59 Ma (35.757478 N, 95.224211° E)							
0.12984	0	2.023 ± 0.089	4.342 ± 0.217	2.584 ± 0.137	210.377 ± 0.438	538.692 ± 1.678	-1.149 ± 0.516
0.14029	100	0.374 ± 0.087	0.214 ± 0.194	0.448 ± 0.105	16.933 ± 0.116	65.846 ± 0.432	-10.806 ± 6.273
0.14926	150	0.567 ± 0.104	0.445 ± 0.235	0.317 ± 0.106	14.538 ± 0.103	119.149 ± 0.532	-13.650 ± 8.682
0.15761	200	0.429 ± 0.088	0.269 ± 0.291	0.214 ± 0.094	13.524 ± 0.116	142.704 ± 0.687	4.800 ± 7.881
0.16703	250	0.493 ± 0.085	0.227 ± 0.244	0.321 ± 0.092	15.268 ± 0.101	195.846 ± 1.039	13.371 ± 6.689
0.17820	300	0.491 ± 0.047	0.314 ± 0.203	0.234 ± 0.071	18.093 ± 0.209	276.918 ± 1.187	29.612 ± 3.133
0.20072	400	0.716 ± 0.091	0.416 ± 0.234	0.246 ± 0.077	36.486 ± 0.249	668.953 ± 1.767	50.583 ± 2.961
0.23053	500	0.711 ± 0.084	0.156 ± 0.277	0.278 ± 0.096	48.310 ± 0.120	924.265 ± 1.436	59.516 ± 2.039
0.26803	600	0.800 ± 0.105	1.164 ± 0.272	0.494 ± 0.087	60.746 ± 0.175	1152.874 ± 1.779	60.726 ± 2.032
0.34863	800	1.141 ± 0.054	2.010 ± 0.193	0.293 ± 0.091	130.600 ± 0.376	2731.841 ± 0.781	73.534 ± 0.525
0.44333	1000	0.751 ± 0.074	2.628 ± 0.213	0.229 ± 0.087	153.443 ± 0.572	3667.044 ± 2.582	89.644 ± 0.648
0.55991	1200	0.684 ± 0.049	3.323 ± 0.206	0.259 ± 0.096	188.895 ± 0.427	4875.986 ± 3.761	98.544 ± 0.377
0.71787	1600	0.684 ± 0.054	3.937 ± 0.193	0.169 ± 0.146	255.934 ± 0.535	7043.148 ± 5.484	106.227 ± 0.334
0.85043	2000	0.776 ± 0.047	3.366 ± 0.150	0.201 ± 0.081	214.776 ± 0.654	6193.689 ± 4.663	110.235 ± 0.419
0.95794	2600	0.520 ± 0.104	2.838 ± 0.171	0.327 ± 0.099	174.210 ± 0.733	5235.752 ± 5.845	115.629 ± 0.837
0.98931	3200	0.180 ± 0.120	1.103 ± 0.269	0.107 ± 0.127	50.822 ± 0.390	1511.239 ± 1.651	113.769 ± 2.804
1.00000	4000	0.549 ± 0.136	0.832 ± 0.176	0.072 ± 0.075	17.320 ± 0.266	585.021 ± 1.567	97.264 ± 9.103
11UMT50 1.0 - 2.0 µm (mc4305) (J=00.00135112) Total gas age = 119.76 ± 0.52 Ma (35.776855 N, 94.995011° E)							
0.17159	0	4.925 ± 0.170	34.954 ± 0.242	3.086 ± 0.149	160.085 ± 0.586	1519.694 ± 2.246	0.981 ± 0.767
0.18123	100	0.058 ± 0.079	2.863 ± 0.099	0.408 ± 0.061	8.991 ± 0.140	47.738 ± 1.574	8.311 ± 6.312
0.19152	150	0.026 ± 0.067	2.143 ± 0.189	0.217 ± 0.073	9.606 ± 0.183	169.494 ± 1.490	40.592 ± 4.973
0.20978	200	0.023 ± 0.077	3.526 ± 0.207	0.087 ± 0.063	17.034 ± 0.180	624.303 ± 1.512	86.259 ± 3.253
0.23204	250	0.038 ± 0.073	4.202 ± 0.224	0.178 ± 0.062	20.768 ± 0.331	979.537 ± 2.204	110.221 ± 2.930
0.25881	300	0.239 ± 0.094	5.771 ± 0.133	0.319 ± 0.119	24.972 ± 0.125	1289.596 ± 2.746	115.216 ± 2.611
0.31449	400	0.243 ± 0.059	14.639 ± 0.188	0.244 ± 0.096	51.946 ± 0.300	2817.313 ± 4.087	124.439 ± 1.047
0.38475	500	0.552 ± 0.066	21.076 ± 0.280	0.373 ± 0.082	65.550 ± 0.204	3793.378 ± 9.494	130.182 ± 0.848
0.46014	600	0.544 ± 0.063	24.184 ± 0.234	0.272 ± 0.093	70.337 ± 0.329	4249.508 ± 1.600	136.405 ± 0.862
0.57758	800	0.805 ± 0.086	40.692 ± 0.366	0.461 ± 0.091	109.563 ± 0.127	6970.128 ± 3.640	143.885 ± 0.549
0.68870	1000	0.641 ± 0.063	43.607 ± 0.421	0.351 ± 0.115	103.671 ± 0.579	6887.258 ± 5.035	150.983 ± 0.909
0.77618	1200	0.686 ± 0.081	35.089 ± 0.231	0.330 ± 0.104	81.612 ± 0.302	5676.801 ± 4.421	156.509 ± 0.866
0.90158	1600	0.857 ± 0.117	41.531 ± 0.389	0.536 ± 0.079	116.993 ± 0.545	8531.075 ± 5.795	164.716 ± 0.990
0.94605	2000	0.389 ± 0.058	12.036 ± 0.250	0.285 ± 0.101	41.486 ± 0.232	3105.864 ± 3.078	167.690 ± 1.293
0.97065	2600	0.198 ± 0.056	6.313 ± 0.145	0.181 ± 0.092	22.952 ± 0.186	1719.028 ± 2.264	168.255 ± 2.085
0.98718	3200	0.153 ± 0.090	4.364 ± 0.187	0.060 ± 0.073	15.422 ± 0.179	1185.253 ± 1.544	171.754 ± 4.287
1.00000	4000	0.132 ± 0.087	3.541 ± 0.161	0.104 ± 0.066	11.960 ± 0.162	933.727 ± 5.167	173.690 ± 5.337
11UMT50 0.5 - 0.2 µm (mc4306) (J=0.00135186) Total gas age = 104.58 ± 0.39 Ma (35.776855 N, 94.995011° E)							
0.18822	0	2.476 ± 0.126	8.260 ± 0.279	2.067 ± 0.116	209.641 ± 0.797	827.282 ± 2.761	1.111 ± 0.432
0.20594	100	0.002 ± 0.113	0.772 ± 0.151	0.443 ± 0.084	19.731 ± 0.188	202.022 ± 1.517	24.731 ± 4.066
0.22393	150	-0.162 ± 0.085	0.839 ± 0.125	0.193 ± 0.102	20.037 ± 0.279	573.637 ± 6.060	74.104 ± 3.194
0.24131	200	-0.027 ± 0.104	0.737 ± 0.112	0.185 ± 0.100	19.362 ± 0.287	549.743 ± 1.676	68.902 ± 3.858
0.27774	250	0.025 ± 0.103	1.656 ± 0.180	0.166 ± 0.074	40.570 ± 0.257	1620.660 ± 2.607	94.462 ± 1.831
0.32571	300	0.416 ± 0.087	2.227 ± 0.149	0.291 ± 0.089	53.434 ± 0.361	2653.015 ± 2.917	111.935 ± 1.330
0.41743	400	0.662 ± 0.097	4.312 ± 0.175	0.466 ± 0.080	102.147 ± 0.313	5259.415 ± 13.745	117.022 ± 0.792
0.52787	500	0.758 ± 0.079	5.301 ± 0.200	0.594 ± 0.094	123.010 ± 0.641	6441.747 ± 12.158	119.246 ± 0.776
0.61547	600	0.670 ± 0.095	3.919 ± 0.202	0.291 ± 0.093	97.570 ± 0.325	5380.180 ± 5.321	125.093 ± 0.778
0.77198	800	1.167 ± 0.089	7.611 ± 0.223	0.322 ± 0.078	174.316 ± 0.599	10274.376 ± 9.257	133.833 ± 0.572
0.90950	1000	0.674 ± 0.082	8.727 ± 0.262	0.396 ± 0.101	153.169 ± 0.405	10070.087 ± 5.150	150.698 ± 0.528
0.96899	1200	0.521 ± 0.056	4.019 ± 0.169	0.134 ± 0.065	66.254 ± 0.512	4912.823 ± 4.558	167.188 ± 1.361
0.99257	1600	0.503 ± 0.071	1.313 ± 0.140	0.038 ± 0.072	26.267 ± 0.205	2126.722 ± 2.926	174.904 ± 2.205
0.99654	2000	0.158 ± 0.082	0.146 ± 0.139	0.016 ± 0.095	4.423 ± 0.104	362.032 ± 1.744	166.073 ± 12.777
0.99847	2600	0.207 ± 0.069	-0.051 ± 0.133	-0.028 ± 0.062	2.146 ± 0.099	161.836 ± 1.454	110.891 ± 22.361
0.99940	3200	0.084 ± 0.119	-0.291 ± 0.192	-0.200 ± 0.070	1.039 ± 0.063	92.260 ± 1.000	151.860 ± 76.573
1.00000	4000	-0.009 ± 0.095	-0.090 ± 0.144	-0.095 ± 0.054	0.669 ± 0.074	63.536 ± 0.838	226.001 ± 93.196

Table A4.3 continued. Argon isotopic data for $^{40}Ar/^{39}Ar$ fault gouge dating

F39	Laser Power [mW]	Volume [ccSTP] ^{36}Ar	^{37}Ar	^{38}Ar	^{39}Ar	^{40}Ar	Age [Ma]
11UMT50 0.05 - 0.2 µm (mc4307) (J=0.00135077) Total gas age = 93.75 ± 0.33 Ma (35.776855 N, 94.995011° E)							
0.21186	0	3.473 ± 0.047	9.559 ± 0.226	3.534 ± 0.082	316.237 ± 0.595	1046.853 ± 3.038	0.160 ± 0.110
0.22674	100	-0.068 ± 0.038	0.683 ± 0.095	0.985 ± 0.058	22.217 ± 0.168	46.902 ± 1.068	7.339 ± 1.236
0.24328	150	0.216 ± 0.062	0.764 ± 0.095	0.201 ± 0.076	24.679 ± 0.156	241.415 ± 1.159	17.444 ± 1.785
0.26779	200	0.233 ± 0.043	1.276 ± 0.125	0.219 ± 0.082	36.596 ± 0.128	905.953 ± 1.862	54.906 ± 0.854
0.30156	250	0.353 ± 0.036	1.404 ± 0.124	0.199 ± 0.090	50.402 ± 0.415	2058.578 ± 1.970	92.092 ± 0.891
0.34212	300	0.560 ± 0.097	1.763 ± 0.126	0.352 ± 0.046	60.542 ± 0.315	2998.371 ± 4.463	110.563 ± 1.229
0.41977	400	1.043 ± 0.160	3.359 ± 0.101	0.636 ± 0.050	115.908 ± 0.305	5814.251 ± 6.188	112.201 ± 0.987
0.51910	500	6.904 ± 0.122	4.428 ± 0.110	1.573 ± 0.097	148.268 ± 0.202	8902.727 ± 9.353	109.406 ± 0.594
0.64433	600	7.149 ± 0.162	5.577 ± 0.146	1.551 ± 0.141	186.931 ± 0.560	11458.546 ± 8.211	117.898 ± 0.685
0.77135	800	4.001 ± 0.102	5.323 ± 0.135	1.252 ± 0.115	189.591 ± 0.807	11634.673 ± 20.651	129.583 ± 0.688
0.87114	1000	0.096 ± 0.104	4.091 ± 0.172	0.400 ± 0.063	148.966 ± 0.658	8667.600 ± 21.733	136.063 ± 0.814
0.94733	1200	-0.380 ± 0.083	3.050 ± 0.153	0.130 ± 0.127	113.717 ± 0.366	6887.183 ± 5.100	144.085 ± 0.667
0.98907	1600	-0.709 ± 0.123	1.680 ± 0.136	0.170 ± 0.091	62.313 ± 0.238	3891.952 ± 5.939	153.666 ± 1.432
0.99594	2000	-1.031 ± 0.073	0.211 ± 0.137	-0.115 ± 0.085	10.243 ± 0.089	371.846 ± 2.299	154.182 ± 4.923
0.99809	2600	-1.044 ± 0.064	-0.047 ± 0.139	-0.074 ± 0.050	3.220 ± 0.131	-91.244 ± 2.249	157.437 ± 14.607
0.99920	3200	0.063 ± 0.065	0.066 ± 0.227	-0.084 ± 0.110	1.653 ± 0.077	134.655 ± 0.914	163.523 ± 26.771
1.00000	4000	-0.115 ± 0.055	-0.238 ± 0.224	-0.031 ± 0.105	1.194 ± 0.069	100.799 ± 1.020	256.166 ± 32.131
11UMT50 0.5 - 1.0 µm (mc4308) (J=0.00134778) Total gas age = 117.62 ± 0.71 Ma (35.776855 N, 94.995011° E)							
0.15009	0	2.797 ± 0.124	7.182 ± 0.152	1.424 ± 0.130	61.441 ± 0.400	864.873 ± 2.935	1.516 ± 1.452
0.16504	100	-0.085 ± 0.086	0.715 ± 0.133	0.129 ± 0.072	6.122 ± 0.140	19.330 ± 1.144	17.532 ± 9.999
0.18013	150	-0.095 ± 0.101	0.702 ± 0.150	0.113 ± 0.066	6.174 ± 0.111	94.338 ± 1.277	47.605 ± 11.448
0.20198	200	-0.052 ± 0.086	0.886 ± 0.154	0.015 ± 0.085	8.947 ± 0.227	301.016 ± 1.277	83.983 ± 6.901
0.23021	250	-0.140 ± 0.090	1.009 ± 0.202	-0.004 ± 0.071	11.554 ± 0.162	499.318 ± 1.275	110.365 ± 5.485
0.26245	300	0.197 ± 0.063	1.193 ± 0.142	-0.030 ± 0.080	13.201 ± 0.147	654.867 ± 1.063	106.684 ± 3.413
0.32190	400	0.200 ± 0.066	2.808 ± 0.099	0.003 ± 0.058	24.334 ± 0.282	1231.086 ± 1.882	113.465 ± 2.239
0.39861	500	0.200 ± 0.085	3.740 ± 0.175	0.107 ± 0.079	31.405 ± 0.338	1692.353 ± 2.370	122.220 ± 2.229
0.48245	600	0.190 ± 0.083	4.398 ± 0.137	-0.048 ± 0.125	34.317 ± 0.155	1966.075 ± 2.190	130.496 ± 1.723
0.60978	800	0.351 ± 0.109	7.104 ± 0.157	-0.008 ± 0.077	52.127 ± 0.379	3180.339 ± 3.322	138.089 ± 1.701
0.73265	1000	0.327 ± 0.085	6.703 ± 0.192	-0.046 ± 0.077	50.296 ± 0.383	3271.733 ± 3.228	147.321 ± 1.558
0.83325	1200	0.396 ± 0.075	5.373 ± 0.209	0.103 ± 0.083	41.182 ± 0.207	2899.628 ± 2.598	157.240 ± 1.427
0.92786	1600	0.500 ± 0.069	4.724 ± 0.201	0.308 ± 0.108	38.730 ± 0.369	2955.673 ± 4.684	168.197 ± 1.942
0.95993	2000	0.285 ± 0.085	1.439 ± 0.219	0.062 ± 0.058	13.127 ± 0.218	1064.690 ± 1.098	173.049 ± 5.043
0.97787	2600	0.275 ± 0.071	0.744 ± 0.155	-0.026 ± 0.050	7.344 ± 0.116	628.068 ± 1.351	172.525 ± 6.862
0.99051	3200	-0.036 ± 0.094	0.566 ± 0.159	0.218 ± 0.068	5.177 ± 0.198	403.500 ± 1.427	184.692 ± 13.618
1.00000	4000	0.023 ± 0.069	0.521 ± 0.149	0.106 ± 0.062	3.883 ± 0.199	310.318 ± 0.950	180.683 ± 14.544
12DDT18 1.0- 2.0 µm (mc4309) (J=0.00141847) Total gas age = 142.93 ± 0.1 Ma (35.761694 N, 95.302° E)							
0.20281	0	2.712 ± 0.112	9.670 ± 0.335	16.753 ± 0.163	84.091 ± 0.466	861.723 ± 1.753	1.839 ± 1.007
0.20387	100	-0.186 ± 0.087	0.250 ± 0.253	0.374 ± 0.060	0.437 ± 0.066	-23.896 ± 1.111	173.442 ± 138.745
0.21109	150	-0.055 ± 0.116	0.851 ± 0.236	2.344 ± 0.133	2.995 ± 0.080	-18.900 ± 1.058	-2.251 ± 29.448
0.22721	200	-0.167 ± 0.088	1.098 ± 0.204	1.912 ± 0.059	6.685 ± 0.147	26.299 ± 1.107	28.727 ± 9.785
0.23584	250	-0.115 ± 0.101	0.646 ± 0.176	0.438 ± 0.060	3.577 ± 0.125	6.655 ± 1.167	28.753 ± 21.076
0.28002	300	0.014 ± 0.063	1.852 ± 0.116	0.925 ± 0.057	18.318 ± 0.197	593.597 ± 1.432	80.511 ± 2.623
0.33154	400	-0.008 ± 0.050	2.080 ± 0.149	0.717 ± 0.063	21.361 ± 0.154	1188.564 ± 1.770	137.311 ± 1.906
0.35777	500	-0.024 ± 0.057	1.251 ± 0.109	0.313 ± 0.044	10.877 ± 0.275	681.982 ± 0.816	155.251 ± 5.219
0.36971	600	0.103 ± 0.120	0.592 ± 0.116	0.045 ± 0.054	4.953 ± 0.098	324.457 ± 0.629	145.810 ± 17.090
0.42206	800	0.063 ± 0.041	2.773 ± 0.115	0.307 ± 0.071	21.704 ± 0.165	1412.262 ± 2.343	157.257 ± 1.764
0.50470	1000	0.319 ± 0.057	4.375 ± 0.202	0.402 ± 0.064	34.267 ± 0.305	2415.217 ± 2.128	165.494 ± 1.822
0.63436	1200	0.357 ± 0.057	6.123 ± 0.169	0.401 ± 0.056	53.759 ± 0.301	4166.276 ± 3.041	183.629 ± 1.223
0.82548	1600	0.567 ± 0.036	8.112 ± 0.170	0.447 ± 0.072	79.244 ± 0.183	6800.451 ± 4.411	202.408 ± 0.551
0.89469	2000	0.307 ± 0.087	2.398 ± 0.212	0.088 ± 0.058	28.697 ± 0.252	2642.326 ± 1.735	214.293 ± 2.699
0.94288	2600	0.210 ± 0.079	1.715 ± 0.147	0.074 ± 0.074	19.979 ± 0.166	1885.912 ± 2.291	219.691 ± 3.163
0.97188	3200	0.056 ± 0.072	1.149 ± 0.217	0.221 ± 0.109	12.026 ± 0.178	1139.669 ± 1.109	224.435 ± 5.075
1.00000	4000	0.036 ± 0.061	1.404 ± 0.222	0.047 ± 0.155	11.658 ± 0.222	1141.471 ± 2.951	232.561 ± 5.431

Table A4.3 continued. Argon isotopic data for $^{40}Ar/^{39}Ar$ fault gouge dating

F39	Laser Power [mW]	Volume [ccSTP] ^{36}Ar	^{37}Ar	^{38}Ar	^{39}Ar	^{40}Ar	Age [Ma]
12DDT18 0.5 - 1.0 µm (mc4310) (J=0.00141657) Total gas age = 172.61 ± 0.64 Ma (35.761694° N, 95.302° E)							
0.11914	0	2.146 ± 0.144	9.224 ± 0.214	3.789 ± 0.090	178.552 ± 0.541	711.135 ± 1.916	1.100 ± 0.610
0.13138	100	-0.040 ± 0.065	1.280 ± 0.108	1.702 ± 0.095	18.356 ± 0.142	14.341 ± 1.249	3.646 ± 2.668
0.14149	150	-0.003 ± 0.071	0.441 ± 0.094	0.351 ± 0.091	15.151 ± 0.251	134.716 ± 1.321	22.712 ± 3.534
0.15601	200	0.040 ± 0.091	0.891 ± 0.148	0.272 ± 0.136	21.759 ± 0.226	573.964 ± 1.316	64.844 ± 3.109
0.17782	250	0.176 ± 0.089	1.206 ± 0.127	0.362 ± 0.099	32.683 ± 0.298	1452.381 ± 2.193	106.310 ± 2.164
0.20400	300	0.028 ± 0.107	1.727 ± 0.120	0.229 ± 0.079	39.246 ± 0.147	2100.038 ± 1.682	131.309 ± 1.981
0.25277	400	0.172 ± 0.104	2.896 ± 0.158	0.435 ± 0.075	73.084 ± 0.366	4256.286 ± 4.507	141.367 ± 1.216
0.31737	500	0.318 ± 0.095	3.832 ± 0.095	0.211 ± 0.085	96.816 ± 0.255	5989.871 ± 5.205	149.280 ± 0.790
0.39458	600	0.285 ± 0.125	4.673 ± 0.129	0.457 ± 0.093	115.717 ± 0.558	8090.343 ± 4.895	168.677 ± 1.081
0.52665	800	0.684 ± 0.123	8.260 ± 0.260	0.420 ± 0.068	197.946 ± 0.712	15738.268 ± 20.597	190.192 ± 0.811
0.67129	1000	0.972 ± 0.069	9.251 ± 0.154	0.410 ± 0.076	216.770 ± 0.709	19224.147 ± 6.698	210.484 ± 0.687
0.79548	1200	0.901 ± 0.097	9.083 ± 0.146	0.435 ± 0.115	186.137 ± 0.472	18023.696 ± 16.434	228.677 ± 0.676
0.91212	1600	0.941 ± 0.088	8.819 ± 0.211	0.543 ± 0.082	174.801 ± 0.577	17960.485 ± 15.389	241.595 ± 0.841
0.95359	2000	0.404 ± 0.049	3.541 ± 0.134	0.179 ± 0.093	62.153 ± 0.395	6657.499 ± 5.751	250.592 ± 1.590
0.97580	2600	0.154 ± 0.072	1.863 ± 0.131	-0.083 ± 0.103	33.291 ± 0.253	3592.855 ± 2.444	253.620 ± 2.298
0.98999	3200	0.220 ± 0.076	1.197 ± 0.201	0.112 ± 0.048	21.271 ± 0.253	2238.673 ± 4.109	243.911 ± 3.615
1.00000	4000	0.037 ± 0.057	1.031 ± 0.125	0.037 ± 0.093	14.999 ± 0.166	1665.075 ± 2.351	261.856 ± 3.691
12DDT18 0.05 - 0.2 µm (mc4311) (J=0.0014073) Total gas age = 132.52 ± 0.50 Ma (35.761694° N, 95.302° E)							
0.21607	0	1.887 ± 0.077	8.612 ± 0.169	1.743 ± 0.125	293.940 ± 0.784	607.012 ± 2.227	0.426 ± 0.196
0.24413	100	0.206 ± 0.060	0.810 ± 0.187	0.682 ± 0.131	38.173 ± 0.161	410.752 ± 1.199	23.114 ± 1.174
0.28625	150	0.515 ± 0.071	1.590 ± 0.158	0.147 ± 0.131	57.297 ± 0.337	2392.452 ± 2.437	96.637 ± 1.048
0.33956	200	0.807 ± 0.075	1.767 ± 0.174	0.124 ± 0.129	72.522 ± 0.372	4266.621 ± 3.997	135.783 ± 0.996
0.40189	250	0.839 ± 0.079	2.160 ± 0.129	0.323 ± 0.152	84.796 ± 0.370	5141.705 ± 3.384	140.879 ± 0.881
0.47520	300	1.169 ± 0.090	3.115 ± 0.223	0.235 ± 0.102	99.726 ± 0.366	6205.384 ± 5.131	143.339 ± 0.813
0.60828	400	1.581 ± 0.097	4.791 ± 0.215	0.323 ± 0.117	181.045 ± 0.645	12498.805 ± 12.700	161.296 ± 0.682
0.71608	500	1.081 ± 0.080	4.224 ± 0.218	0.402 ± 0.103	146.650 ± 0.548	11224.766 ± 7.191	179.559 ± 0.748
0.82349	600	0.921 ± 0.069	4.368 ± 0.211	0.471 ± 0.121	146.119 ± 0.407	12118.151 ± 18.931	194.911 ± 0.673
0.92522	800	0.875 ± 0.064	4.390 ± 0.209	0.271 ± 0.087	138.390 ± 0.319	12297.198 ± 8.696	208.352 ± 0.567
0.97411	1000	0.552 ± 0.053	2.481 ± 0.173	0.193 ± 0.111	66.509 ± 0.329	6241.110 ± 5.838	218.267 ± 1.164
0.99172	1200	0.242 ± 0.058	1.100 ± 0.152	0.069 ± 0.132	23.955 ± 0.258	2334.830 ± 3.862	225.205 ± 2.821
0.99783	1600	0.102 ± 0.066	0.398 ± 0.138	0.097 ± 0.100	8.316 ± 0.189	803.317 ± 1.130	221.866 ± 7.117
0.99889	2000	0.167 ± 0.066	-0.120 ± 0.128	0.002 ± 0.099	1.440 ± 0.085	163.900 ± 0.956	191.305 ± 32.773
0.99941	2600	0.057 ± 0.072	0.020 ± 0.073	0.022 ± 0.091	0.715 ± 0.087	77.499 ± 0.761	203.798 ± 71.166
0.99973	3200	-0.089 ± 0.098	-0.086 ± 0.128	0.051 ± 0.068	0.430 ± 0.063	52.366 ± 0.658	413.508 ± 146.031
1.00000	4000	-0.099 ± 0.090	-0.015 ± 0.167	-0.084 ± 0.071	0.368 ± 0.084	39.865 ± 0.570	422.794 ± 168.887
12DDT18 <0.05 µm (mc4312) (J=0.00139415) Total gas age = 117.35 ± 0.53 Ma (35.761694° N, 95.302° E)							
0.23670	0	1.834 ± 0.128	6.419 ± 0.147	91.752 ± 0.354	220.614 ± 0.653	595.950 ± 1.903	0.617 ± 0.433
0.27597	100	0.203 ± 0.088	1.060 ± 0.166	9.990 ± 0.199	36.598 ± 0.318	469.939 ± 1.176	27.961 ± 1.785
0.33404	150	0.631 ± 0.103	1.613 ± 0.191	6.630 ± 0.116	54.120 ± 0.443	2497.741 ± 2.266	104.343 ± 1.578
0.41608	200	1.286 ± 0.086	2.113 ± 0.180	7.807 ± 0.098	76.467 ± 0.306	4587.191 ± 4.220	133.337 ± 0.937
0.49719	250	1.258 ± 0.096	2.147 ± 0.193	4.518 ± 0.131	75.600 ± 0.493	4284.351 ± 2.606	125.685 ± 1.186
0.59876	300	1.443 ± 0.110	2.666 ± 0.167	3.078 ± 0.137	94.665 ± 0.238	5874.618 ± 8.897	139.237 ± 0.896
0.77164	400	1.941 ± 0.125	4.699 ± 0.153	2.827 ± 0.138	161.128 ± 0.534	11572.779 ± 4.122	164.009 ± 0.742
0.90123	500	1.397 ± 0.069	3.717 ± 0.125	1.366 ± 0.091	120.784 ± 0.485	10096.061 ± 9.430	191.149 ± 0.841
0.96031	600	0.666 ± 0.090	1.374 ± 0.099	0.425 ± 0.079	55.065 ± 0.278	5072.696 ± 7.760	209.998 ± 1.504
0.98935	800	0.473 ± 0.066	0.786 ± 0.113	0.414 ± 0.075	27.066 ± 0.107	2574.916 ± 4.382	213.182 ± 1.832
0.99624	1000	0.237 ± 0.057	0.188 ± 0.214	0.225 ± 0.070	6.420 ± 0.144	595.833 ± 0.927	195.003 ± 7.274
0.99878	1200	0.318 ± 0.074	0.028 ± 0.216	0.080 ± 0.079	2.374 ± 0.126	250.950 ± 0.818	158.944 ± 22.678
0.99977	1600	0.395 ± 0.084	0.040 ± 0.215	0.121 ± 0.055	0.918 ± 0.089	138.028 ± 0.563	57.665 ± 66.066
0.99995	2000	0.314 ± 0.104	0.043 ± 0.241	0.055 ± 0.065	0.166 ± 0.068	59.632 ± 0.726	-588.076 ± 704.552
0.99999	2600	0.185 ± 0.066	-0.113 ± 0.222	0.103 ± 0.067	0.042 ± 0.079	35.675 ± 0.351	-1808.328 ± 6806.437
0.99996	3200	0.171 ± 0.057	0.301 ± 0.111	-0.234 ± 0.094	-0.026 ± 0.081	20.782 ± 0.453	1719.977 ± 3508.120
1.00000	4000	0.181 ± 0.052	0.220 ± 0.117	-0.041 ± 0.115	0.034 ± 0.088	27.911 ± 0.505	-5069.310 ± 90902.894

Table A4.3 continued. Argon isotopic data for $^{40}Ar/^{39}Ar$ fault gouge dating

F39	Laser Power [mW]	Volume [ccSTP] ^{36}Ar	^{37}Ar	^{38}Ar	^{39}Ar	^{40}Ar	Age [Ma]
11UMT52 0.05 - 0.2 µm (mc4013) (J=0.00238948) Total gas age = 131.30 ± 0.41 Ma (35.725018° N, 95.143533° E)							
0.24562	0	3.766 ± 0.138	53.274 ± 0.696	10.827 ± 0.163	698.188 ± 1.560	1082.005 ± 1.941	-0.191 ± 0.251
0.29289	100	1.762 ± 0.117	11.785 ± 0.320	3.465 ± 0.115	134.351 ± 0.423	758.676 ± 2.920	7.624 ± 1.111
0.32094	150	1.706 ± 0.070	6.585 ± 0.337	1.211 ± 0.131	79.743 ± 0.328	1493.328 ± 2.542	52.693 ± 1.108
0.35404	200	1.855 ± 0.091	6.934 ± 0.231	1.251 ± 0.117	94.078 ± 0.384	2308.215 ± 1.670	78.903 ± 1.227
0.38992	250	1.573 ± 0.133	7.646 ± 0.250	0.911 ± 0.103	102.011 ± 0.453	2945.314 ± 3.397	101.886 ± 1.636
0.44107	300	1.445 ± 0.070	10.175 ± 0.442	0.503 ± 0.087	145.402 ± 0.583	5145.808 ± 5.022	134.742 ± 0.785
0.53725	400	1.569 ± 0.087	19.940 ± 0.280	0.629 ± 0.123	273.374 ± 0.738	12799.379 ± 7.219	184.731 ± 0.607
0.62913	500	1.193 ± 0.092	17.621 ± 0.454	0.606 ± 0.131	261.187 ± 0.810	14213.453 ± 7.093	215.383 ± 0.753
0.68507	600	0.961 ± 0.080	10.494 ± 0.324	0.334 ± 0.070	159.003 ± 0.399	9182.564 ± 4.006	226.430 ± 0.784
0.72735	800	1.559 ± 0.076	8.018 ± 0.245	0.619 ± 0.085	120.173 ± 0.516	6410.596 ± 4.513	201.722 ± 1.104
0.76223	1000	1.896 ± 0.095	7.375 ± 0.367	0.595 ± 0.091	99.150 ± 0.485	3831.492 ± 3.773	136.899 ± 1.315
0.79779	1200	1.541 ± 0.092	7.063 ± 0.288	0.375 ± 0.075	101.092 ± 0.330	4008.480 ± 3.966	145.482 ± 1.176
0.87062	1600	1.938 ± 0.128	14.777 ± 0.314	0.388 ± 0.142	207.035 ± 0.382	10148.981 ± 9.003	189.126 ± 0.800
0.92854	2000	1.232 ± 0.076	11.740 ± 0.305	0.286 ± 0.099	164.638 ± 0.466	9586.144 ± 16.820	226.616 ± 0.884
0.97947	2600	1.616 ± 0.101	10.035 ± 0.385	0.366 ± 0.102	144.763 ± 0.501	9693.580 ± 12.173	255.464 ± 1.171
0.99621	3200	1.538 ± 0.068	3.211 ± 0.253	0.122 ± 0.121	47.586 ± 0.449	3651.182 ± 3.262	268.571 ± 2.835
1.00000	4000	3.905 ± 0.052	1.215 ± 0.276	0.614 ± 0.116	10.769 ± 0.178	1722.085 ± 2.746	214.170 ± 6.463
11UMT52 0.2 - 0.5 µm (mc4014) (J=0.00237312) Total gas age = 163.05 ± 0.45 Ma (35.725018° N, 95.143533° E)							
0.10584	0	4967.467 ± 9.82078	5.034 ± 0.298	923.54869 ± 1.823	196.440 ± 0.513	1429828.468 ± 3626.621	-1108.985 ± 187.427
0.12221	100	1.643 ± 0.0784	1.345 ± 0.285	1.73722 ± 0.135	30.388 ± 0.248	519.062 ± 3.572	4.742 ± 3.294
0.12825	150	-0.081 ± 0.05453	0.424 ± 0.340	0.13142 ± 0.130	11.220 ± 0.090	20.688 ± 3.322	16.998 ± 6.221
0.13636	200	0.045 ± 0.06028	0.673 ± 0.229	0.19149 ± 0.114	15.045 ± 0.150	58.759 ± 3.293	12.907 ± 5.120
0.14548	250	0.077 ± 0.09243	0.802 ± 0.242	0.1184 ± 0.108	16.940 ± 0.100	158.784 ± 3.362	34.032 ± 6.828
0.15373	300	0.139 ± 0.06981	0.625 ± 0.227	0.18145 ± 0.043	15.303 ± 0.189	244.260 ± 1.163	56.004 ± 5.645
0.17056	400	0.442 ± 0.06122	0.589 ± 0.269	0.30399 ± 0.084	31.239 ± 0.176	692.777 ± 1.533	75.455 ± 2.422
0.19462	500	0.578 ± 0.07673	0.797 ± 0.173	0.28784 ± 0.080	44.657 ± 0.214	1226.790 ± 1.596	98.496 ± 2.114
0.22760	600	0.373 ± 0.05422	1.262 ± 0.174	0.40072 ± 0.128	61.222 ± 0.387	2104.353 ± 3.390	134.332 ± 1.342
0.28861	800	0.680 ± 0.05872	2.238 ± 0.317	0.27847 ± 0.058	113.239 ± 0.532	4467.603 ± 4.043	154.508 ± 0.931
0.35749	1000	0.437 ± 0.06677	2.423 ± 0.327	0.28716 ± 0.089	127.836 ± 0.559	5582.784 ± 7.551	173.979 ± 0.970
0.42110	1200	0.681 ± 0.08337	2.596 ± 0.302	0.174 ± 0.088	118.077 ± 0.311	5463.976 ± 3.989	181.387 ± 0.936
0.52687	1600	0.905 ± 0.09512	3.986 ± 0.264	0.4077 ± 0.082	196.305 ± 0.553	9444.153 ± 6.663	189.795 ± 0.761
0.64337	2000	0.858 ± 0.08049	4.097 ± 0.262	0.35945 ± 0.099	216.248 ± 0.789	10704.581 ± 7.705	195.879 ± 0.810
0.78785	2600	1.140 ± 0.0745	6.073 ± 0.257	0.04589 ± 0.084	268.159 ± 0.536	13974.315 ± 8.043	205.562 ± 0.512
0.88997	3200	0.941 ± 0.05427	3.654 ± 0.232	0.10534 ± 0.096	189.541 ± 0.640	10421.449 ± 6.703	215.692 ± 0.770
1.00000	4000	5.036 ± 0.07174	4.114 ± 0.297	1.34461 ± 0.138	204.231 ± 0.278	13003.127 ± 17.810	226.551 ± 0.588
11UMT52 0.5 - 0.1 µm (mc4015) (J=0.00234757) Total gas age = 172.61 ± 0.64 Ma (35.725018° N, 95.143533° E)							
0.08132	0	1.855 ± 0.09213	0.649 ± 0.260	9.1935 ± 0.218	50.722 ± 0.358	513.890 ± 0.854	-2.869 ± 2.278
0.10667	100	0.469 ± 0.06712	0.134 ± 0.279	1.3012 ± 0.059	15.816 ± 0.205	199.712 ± 0.603	16.3 ± 5.270
0.12092	150	0.188 ± 0.0466	-0.159 ± 0.250	0.12101 ± 0.055	8.886 ± 0.186	220.983 ± 0.979	77.113 ± 6.501
0.13498	200	0.375 ± 0.05367	0.187 ± 0.178	0.20865 ± 0.050	8.769 ± 0.163	325.769 ± 0.657	100.9 ± 7.476
0.14951	250	0.244 ± 0.04246	0.009 ± 0.164	0.17373 ± 0.034	9.063 ± 0.113	302.280 ± 0.963	104.483 ± 5.693
0.16529	300	0.210 ± 0.07626	0.386 ± 0.352	0.06032 ± 0.051	9.845 ± 0.137	347.378 ± 1.098	118.722 ± 9.227
0.21031	400	0.207 ± 0.07729	0.302 ± 0.404	0.12025 ± 0.054	28.081 ± 0.197	1059.273 ± 1.347	144.596 ± 3.331
0.29212	500	0.252 ± 0.06971	1.019 ± 0.321	0.1955 ± 0.082	51.030 ± 0.272	2137.358 ± 1.856	163.555 ± 1.775
0.40544	600	0.200 ± 0.08849	1.147 ± 0.340	0.04879 ± 0.051	70.684 ± 0.495	3260.234 ± 2.150	182.275 ± 1.869
0.58506	800	0.438 ± 0.08242	1.172 ± 0.385	0.12578 ± 0.069	112.042 ± 0.528	5789.804 ± 3.409	202.194 ± 1.226
0.72396	1000	0.432 ± 0.05688	0.275 ± 0.200	0.20034 ± 0.080	86.641 ± 0.443	4771.031 ± 4.969	213.795 ± 1.281
0.81003	1200	0.433 ± 0.06673	0.079 ± 0.251	0.17335 ± 0.092	53.684 ± 0.277	3040.440 ± 4.185	216.268 ± 1.761
0.89485	1600	0.691 ± 0.06149	-0.501 ± 0.164	0.17066 ± 0.081	52.905 ± 0.392	3085.511 ± 2.817	217.049 ± 2.001
0.94702	2000	0.747 ± 0.06235	0.090 ± 0.199	0.16811 ± 0.057	32.545 ± 0.312	1958.090 ± 2.952	213.011 ± 2.892
0.98363	2600	0.846 ± 0.06664	-0.311 ± 0.241	0.30464 ± 0.091	22.837 ± 0.223	1464.843 ± 1.971	212.315 ± 3.807
0.99548	3200	0.711 ± 0.08409	0.483 ± 0.263	0.01816 ± 0.085	7.387 ± 0.129	581.574 ± 1.227	201.339 ± 13.183
1.00000	4000	1.290 ± 0.09036	-0.011 ± 0.259	0.18199 ± 0.064	2.822 ± 0.093	504.118 ± 1.043	175.586 ± 36.798

Table A4.3 continued. Argon isotopic data for $^{40}Ar/^{39}Ar$ fault gouge dating

F39	Laser Power [mW]	Volume [ccSTP] ^{36}Ar	^{37}Ar	^{38}Ar	^{39}Ar	^{40}Ar	Age [Ma]
11UMT52 1.0 - 2.0 µm (mc4013) (J=0.00232016) Total gas age = 168.77 ± 1.17 Ma (35.725018° N, 95.143533° E)							
0.10065	0	0.900 ± 0.06126	0.987 ± 0.282	1.31332 ± 0.136	31.477 ± 0.234	278.116 ± 1.051	1.63 ± 2.409
0.13862	100	0.107 ± 0.07868	1.301 ± 0.439	0.48691 ± 0.057	11.876 ± 0.212	55.971 ± 0.678	8.592 ± 8.160
0.16262	150	0.078 ± 0.07754	0.882 ± 0.472	0.09625 ± 0.052	7.506 ± 0.126	135.318 ± 0.556	61.576 ± 12.395
0.19382	200	0.019 ± 0.08128	0.357 ± 0.467	0.09367 ± 0.054	9.759 ± 0.166	255.080 ± 0.776	103.895 ± 9.881
0.22380	250	0.069 ± 0.07235	0.828 ± 0.442	0.07041 ± 0.040	9.377 ± 0.135	279.508 ± 0.740	112.107 ± 9.109
0.26476	300	0.040 ± 0.04442	0.280 ± 0.289	0.09102 ± 0.065	12.810 ± 0.131	449.397 ± 1.018	137.63 ± 4.212
0.36743	400	0.033 ± 0.06375	0.929 ± 0.272	0.17957 ± 0.072	32.111 ± 0.162	1284.870 ± 1.418	158.996 ± 2.381
0.52003	500	0.118 ± 0.03934	1.540 ± 0.404	-0.03742 ± 0.080	47.725 ± 0.247	2238.326 ± 1.939	183.597 ± 1.299
0.66741	600	0.010 ± 0.05961	0.933 ± 0.266	-0.09171 ± 0.089	46.094 ± 0.238	2432.401 ± 2.790	208.143 ± 1.764
0.83801	800	0.144 ± 0.04633	1.241 ± 0.241	0.03014 ± 0.065	53.357 ± 0.304	3163.368 ± 2.323	229.571 ± 1.560
0.92698	1000	-0.066 ± 0.06372	1.130 ± 0.220	0.05295 ± 0.069	27.824 ± 0.101	1688.808 ± 1.402	240.274 ± 2.616
0.96371	1200	-0.016 ± 0.10537	0.130 ± 0.190	-0.09865 ± 0.073	11.489 ± 0.076	736.157 ± 0.862	251.585 ± 9.994
0.98531	1600	0.123 ± 0.06516	0.561 ± 0.208	0.10426 ± 0.085	6.753 ± 0.155	473.387 ± 0.932	252.34 ± 11.705
0.99485	2000	0.330 ± 0.06675	0.284 ± 0.244	0.10803 ± 0.096	2.986 ± 0.075	246.886 ± 0.525	198.239 ± 25.223
0.99899	2600	0.363 ± 0.04745	0.067 ± 0.259	0.01199 ± 0.080	1.294 ± 0.068	169.591 ± 0.709	190.838 ± 41.974
0.99978	3200	0.546 ± 0.05621	-0.107 ± 0.231	0.05632 ± 0.077	0.246 ± 0.085	155.270 ± 0.572	-104.499 ± 301.611
1.00000	4000	0.665 ± 0.05917	-0.130 ± 0.151	0.08057 ± 0.078	0.070 ± 0.071	199.565 ± 0.764	167.462 ± 968.906

TABLE A4.4. DOCUMENTED STRIKE-SLIP FAULT ACTIVITY WITHIN THE TIBETAN PLATEAU

Region	*Location/Fault*	*Timing*		*Source*
		Initiation	*Cessation*	
Northern Tibet				
	Kunlun Fault (central)	20 - 15	0	Duvall et al. (2013)
	Kunlun Fault (east)	8 - 5	0	Duvall et al. (2013)
	Kunlun Fault (west)	15 - 8	0	Jolivet et al. (2003); Duvall et al. (2013)
	Haiyuan Fault (west)	17 - 12	0	Duvall et al. (2013)
	Haiyuan Fault (central/east)	10 - 8	0	Zheng et al. (2003); X. Wang et al. (2011); W. Wang et al. (2011); Lin et al. (2011)
	Elashan Fault	12 - 6	0	Yuan et al. (2011)
	Riyueshan Fault	13 - 7	0	Yuan et al. (2011)
	Altyn Tagh	49 - ~34	0	Yue et al. (2001); Yin et al., (2002); Ritts et al. (2008)
Central Tibet				
	Jiali Fault	18 - 12	0	Lee et al. (2003)
	Ailao Shan -Red River Shear Zone	27 - 17	0	Harrison et al. (1992; 1996); Wang et al. (1998)
	Karakoram	~23 - 13	0	Murphy et al. (2000); Phillips et al. (2004); Valli et al. (2008)
	Xianshuihe Fault	13 - 5	0	Wang et al. (2009)
	Bue Co Fault System	> 8	0	Taylor and Peltzer (2006)
	Dong Co Fault System: Riganpei Co Fault, Gyaring Co Fault	> 8	0	Taylor and Peltzer (2006)

TABLE A4.5. DOCUMENTED NORMAL FAULT ACTIVITY WITHIN THE TIBETAN PLATEAU

Region	*Location/Fault*	*Timing*		*Source*
		Initiation	*Cessation*	
Tethyan Himalaya				
	Thakkhola Graben	14 - 8	0	Garzione et al. (2000)
	Ama Drime Rift	13 - 12	0	Kali et al. (2010)
	Kung Co Rift	13 - 12	0	Lee et al. (2007)
	Gurla Mandhata Rift	15 - 9	0	Murphy et al. (2002); McCallister et al. (2013)
	Leo Pargil Dome	23 - 15	0	Thiede et al. (2006); Langille et al. (2012)
	Ringbung Graben	5	0	Ratschbacher et al. (2011)
	Yadong rift	<12.5	0	Edwards and Harrison (1997)
Lhasa Terrane				
	Lunggar Rift	16 - 10	0	Styron et al. (2013); Sundell et al. (2013)
	Nyainqentanghlah Rift	11 - 8	0	Harrison et al. (1995); J. Kapp et al. (2005)
	Lopukangri Rift	15 - 14	0	Murphy et al. (2010); Sanchez et al. (2010)
	Tangra Yum Co Rift	13	0	Dewane et al. (2006)
	Pumqu-Xainza Rift	14	0	Hager et al. (2009)
	Gulu Rift	7 - 5	0	Stockli et al. (2002)
Qiangtang Terrane				
	Shuang Hu Graben	>13.5	0	Blisniuk et al. (2001)

Chapter V

Synthesis and conclusions

5.1. Principal findings

The integration of new data and tectonic interpretations from this thesis is aimed towards understanding the history of deformation and topographic development of the Tibetan Plateau, and find that there is much needed revision of the timing and mechanisms responsible for surface uplift and crustal thickening of Tibetan lithosphere. Chapters II and III are focused on the paleo-foreland basin of the Tibetan "proto-plateau" and reveal the northern limit of pre-collisional deformation and the timing of retro-arc foreland basin sedimentation and crustal shortening. Chapter IV is directed towards untangling the history of crustal shortening and strike-slip faulting with the goal of relating the shift in primary stress orientations along the northern plateau margin to the Cenozoic evolution of high topography within the Tibetan Plateau. I interpret the synthesized results from these chapters in the framework of the broader Mesozoic and Cenozoic tectonic history of southern and central Tibet to discern the pre- and post-collisional deformation and uplift history of the orogen.

5.1.1. Chapter II

Here I revise the depositional history and stratigraphy of the Hoh Xil Basin, located in north-central Tibet, based on the analysis of compiled biostratigraphic data, U-Pb and $^{40}Ar/^{39}Ar$ geochronologic dating of volcanic units, and reinterpreted magnetostratigraphic data (Liu et al., 2001, 2003). Results from this study demonstrate that the Fenghuoshan Group, which is the first evidence of terrestrial sedimentation in the Hoh Xil Basin, was deposited from late Cretaceous to earliest Eocene time, which is ~30 Myr earlier than previously interpreted (Liu et al., 2001, 2003). Furthermore, we determine that the sediment source for the Hoh Xil Basin was likely the Tanggula Shan, located directly to the south. This indicates that the deformation, erosion, and uplift of the Tanggula Shan occurred prior to the ~50 Ma Indo-Asian collision (Molnar and Stock, 2009; Dupont-Nivet et al., 2010; Najman et al., 2010). The sedimentary history of the Hoh Xil Basin, along

with radiometric dating of variably deformed volcanic rocks, suggest that deformation progressed into the Hoh Xil Basin after the ~50 Ma onset of the Indo-Asian collision and ceased between 34 and 27 Ma. Along with previous work in southern and central Tibet, these results show that a pre-collisional deformation belt spanned from the Gangdese Fold and Thrust Belt in the south to the Tanggula Shan in the north (Burg et al., 1983; England and Searle, 1986; Murphy et al., 1997; Kapp et al., 2005, 2007a, 2007b; DeCelles et al., 2007a; Molnar and Stock, 2009; Dupont-Nivet et al., 2010; Najman et al., 2010). The northern limit of pre-collisional deformation defined by this study allows for direct comparison of the extent of pre-50 Ma thickened and elevated Tibetan lithosphere to possible present-day analogues. The modern Altiplano-Puna Plateau in South America serves as the most appropriate analogue to the pre-collisional Tibetan Plateau.

5.1.2. Chapter III

In this work, I focus on the timing and magnitude of crustal shortening of the Fenghuoshan Fold and Thrust Belt, located in the central Hoh Xil Basin, and calculations of isostatic uplift to understand how and when the Tibetan Plateau evolved from an Andean-type margin to its current dimensions. I use geochronologic dating presented in Chapter II, new apatite fission-track and (U-Th)/He thermochronologic dating, and new $^{40}Ar/^{39}Ar$ illite age analysis of fault gouge to constrain the timing of upper crustal shortening between Eocene and late Oligocene time. These results, along the previous constraints on the timing of deformation, suggest that crustal shortening initiated across much of northern and northeastern Tibet within 10 Myr of the onset of Indo-Asian collision and was distributed over a broad region (Horton et al., 2002; Yin et al., 2002; Spurlin et al., 2005; Clark et al., 2010; Duvall et al., 2011).

To determine the magnitude of Eocene – late Oligocene shortening, I construct and retrodeform a cross section of the Fenghuoshan Fold and Thrust Belt and find 28.0 ± 7.2 % shortening. The magnitude of post-collisional crustal shortening compiled north of the Tanggula Shan (~25%; Yakovlev and Clark, 2014), suggesting that our measurements from the Hoh Xil Basin are representative of shortening within northern Tibet. On this basis, I calculate the isostatic response to distributed ~28% shortening in northern Tibet for a broad range of reasonable initial crustal thickness values, and determine that the measured shortening magnitude cannot account for high elevation in the Hoh Xil Basin nor can it account for the modern 65 – 75 km thick crust (Braitenberg et al., 2000; Vergne et al., 2002; Wittlinger et al., 2004; Karplus et al., 2011). These results indicate that other mechanisms of crustal thickening and surface uplift are required to attain

the modern crustal thickness and elevation of the northern Tibetan Plateau, and that these mechanisms must occur in the absence of upper crustal shortening. Previously proposed thickening and/or uplift mechanisms include lower crustal flow (Clark et al., 2005b; Karplus et al., 2011), preferential shortening and thickening of the lower crust and mantle lithosphere (Isacks, 1988; Gubbels et al., 1993), and possibly removal of the dense mantle lithospheric root (Molnar et al., 1993).

5.1.3. Chapter IV

Low-temperature thermochronologic dating, illite age analysis of fault gouge, and structural observations are used to constrain the timing and style of faulting within the Kunlun Shan, located along the northern margin of the Tibetan Plateau. Analytical results and structural observations indicate that north-south oriented crustal shortening may have initiated as early as 47 Ma and likely continued until 24 Ma, which is fairly similar to the history of crustal shortening of the Hoh Xil Basin (Chapter III) and suggests that crustal shortening in northern Tibet was distributed over a broad region. Data presented in Chapter IV also shows that left-lateral shear, which is the modern style of deformation across the northern plateau margin, initiated as early as 20 Ma. Based on thermochronologic data, I show that vertical exhumation due to strike-slip faulting within the Kunlun Shan is concentrated within one – two kilometers of large-scale faults and within restraining bends. The mid-Miocene onset of strike-slip faulting within the Kunlun Shan may slightly precede, but is roughly synchronous with, the initiation of normal and strike-slip faulting in the southern and central Tibetan Plateau (Blisniuk et al., 2001; Murphy et al., 2000, 2002; Garzione et al., 2003; Jolivet et al., 2003; Lee et al., 2003; Phillips et al., 2004; Taylor and Peltzer, 2006; Wang et al., 2009; Lee et al., 2011; Ratschbacher et al., 2011; Duvall et al., 2013; McCallister et al., 2013; Sundell et al., 2013; Styron et al., 2013). I infer that the shift from north-south oriented contraction to east-west oriented shear along the northern plateau margin was caused by late Oligocene – mid Miocene surface uplift in northern Tibet and an associated increase in the average gravitational potential energy of the Tibetan Plateau. The interpretations from my data within the Kunlun Shan suggest that high elevation of the northern Tibetan Plateau was attained by the early to mid-Miocene, which is consistent with paleoelevation data from the Hoh Xil Basin (Polissar et al., 2009).

5.2. Integration of the Cenozoic deformation history of northern Tibet

The analytical results and interpretations presented in Chapters II through IV of this thesis

provide a comprehensive tectonic history of the northern Tibetan Plateau. Previous work in southern and central Tibet has shown that north-south oriented crustal shortening occurred largely prior to the ~50 Ma collision between India and Eurasia (Burg et al., 1983; England and Searle, 1986; Murphy et al., 1997; Kapp et al., 2005, 2007a, 2007b; DeCelles et al., 2007a; Molnar and Stock, 2009; Dupont-Nivet et al., 2010; Najman et al., 2010), however the northern extent of pre-collisional deformation was not well established, which is critical for understanding the elevation history of the plateau and for interpreting the geodynamic response to collision. My work on the depositional age and provenance of the Fenghuoshan Group of the Hoh Xil Basin indicates that crustal shortening in central Tibet extended as far north as the Tanggula Shan prior to the Indo-Asian collision and resulted in retroarc foreland basin sedimentation within the Hoh Xil Basin (Figure 5.1a; Wang et al., 2008). The cessation of Fenghuoshan Group deposition within the Hoh Xil Basin indicates that crustal shortening progressed north of the Tanggula Shan after 51 Ma.

Chapters III and IV further resolve the history of crustal shortening within the northern Tibetan Plateau. Crustal shortening initiated within the Hoh Xil Basin between 49 and 44 Ma and in the Kunlun Shan by ~47 Ma. This, and along with previous work on deformation in northern Tibet, indicates that crustal shortening was distributed over a large region (Figure 5.1b), rather than progressing northward as proposed by conceptual models of step-wise block uplift and continuum models of thin viscous sheet deformation (England and Houseman, 1986; Tapponnier et al., 2001; Yin et al., 2002, 2008; Horton et al., 2002; Spurlin et al., 2005; Clark et al., 2010; Duvall et al., 2011). Geochronologic dating of variably deformed volcanic rocks and low-temperature thermochronology indicate that crustal shortening within the Hoh Xil Basin and Kunlun Shan ceased by 27 Ma and 24 Ma, respectively (Figures 5.1b and 5.1c). Meanwhile in the Lhasa and southern-central Qiangtang Terranes, little to no crustal shortening is observed after ~50 Ma aside from minor thrust reactivation along the Bangong-Nujiang Suture zone (Figure 5.1b; Burg et al., 1983; England and Searle, 1986; Murphy et al., 1997; DeCelles et al., 2007b; Kapp et al., 2007a, 2007b). South of the Gangdese Fold and Thrust Belt, the convergence between India and Eurasia resulted in major shortening within the Tethyan Himalaya and southward migration of forearc deposition (Figure 5.1b; Ratschbacher et al., 1994; DeCelles et al., 2001; Searle et al., 2003; Murphy and Yin, 2003; Yin et al., 2005; Aikman et al., 2008, DeCelles et al., 2014).

Thermochronologic dating and structural observations presented in Chapter IV indicate that left-lateral shear initiated in the central Kunlun Shan as early as 20 Ma, subsequent to the late Oligocene cessation of crustal shortening in northern Tibet (Figure 5.1d). The mid-Miocene onset of

Figure 5.1. A schematic diagram on the history of Tibetan Plateau deformation and surface uplift. (a) Crustal shortening of the Tibetan Plateau is limited between the Gangdese and the Tanggula Shan Fold and Thrust Belts (FTB) (Burg et al., 1983; England and Searle, 1986; Murphy et al., 1997; Kapp et al., 2007a; 2007b; Staisch et al., 2014). Arc magmatism due to northward subduction of the Indian Plate produces the Gangdese Batholith and Linzizong volcanic sequence (Ding et al., 2003). Marine sedimentation occurs in the Xigaze Forearc (Orme et al., 2014), and terrestrial sedimentation occurs along the Bangong-Nujiang Suture zone and north of the Tanggula Shan, in the Hoh Xil Basin (Liu et al., 2001; 2003; DeCelles et al., 2007b). (b) Following the onset of Indo-Asian collision, deformation within the central Tibetan Plateau proper is largely absent (Burg et al., 1983; England and Searle, 1986; Murphy et al., 1997; Kapp et al., 2007a; 2007b), and initiates within the Tethyan Himalaya (Ratschbacher et al., 1994; DeCelles et al., 2001; Searle et al., 2003; Murphy and Yin, 2003; Yin et al., 2005; Aikman et al., 2008), Hoh Xil Basin (Chapter III), and along the modern northern plateau boundary (Yin et al., 2008; Clark et al., 2010; Duvall et al., 2011; Chapter IV). Linzizong volcanism continues in the early Eocene (Ding et al., 2003). Surface uplift within the Lhasa Terrane may have occurred due to northward underplating of the Greater Indian lithosphere (DeCelles et al., 2007b). Moderate surface uplift (0.6 – 1.6 km) due to crustal thickening occurs in the Hoh Xil Basin (Chapter III). (c) Crustal shortening along the southern margin of the orogen continues (DeCelles et al., 2001) but ceases in the Hoh Xil Basin and Kunlun Shan (Chapters III and IV). Surface uplift of the northern Tibetan Plateau may have been driven by lower crustal thickening. (d) Onset of left-lateral shear along the Kunlun Shan may have been driven by the attainment of high elevation in the early – mid-Miocene. Normal and strike slip faulting initiates in the southern and central Tibetan Plateau, coincident with the onset of volcanism in northern Tibet and eastward plateau expansion via lower crustal flow (Clark and Royden, 2000; Murphy et al., 2000; 2002; Blisniuk et al., 2001; Garzione et al., 2003; Lee et al., 2003; Phillips et al., 2004; Clark et al., 2005b; Taylor and Peltzer, 2006; Wang et al., 2009; Lee et al., 2011; Ratschbacher et al., 2011; McCallister et al., 2013; Sundell et al., 2013; Styron et al., 2013). Acronyms include BNS: Bangong-Nujiang Stuture, JS: Jinsha Suture, AKMS: Ayimaqin-Kunlun-Mutztagh Suture, IYS: Indus-Yarlung Suture. Blue arrows represent surface uplift, mauve arrows represent lower crustal flow, squiggly red arrows represent dewatering of the subducting slab.

lateral shear presented in this work is similar to the interpretations of Duvall et al. (2013), and suggest an earlier onset of left-lateral motion than previously resolved (Jolivet et al., 2003). Additional studies along the Kunlun Shan indicate that left-lateral motion progressed to the east and west of the central Kunlun Fault in the mid-Miocene, and strike-slip faulting initiated at this time to the north in the Qilian Shan and Dulan-Chaka Highland (Jolivet et al., 2003; Duvall et al., 2013). The mid-Miocene onset of strike- slip and normal faulting throughout the Tibetan Plateau suggests a large-scale geodynamic shift of the orogen in mid-Miocene time (Figure 5.1d; Blisniuk et al., 2001; Murphy et al., 2000; Murphy et al., 2002; Garzione et al., 2003; Lee et al., 2003; Phillips et al., 2004;

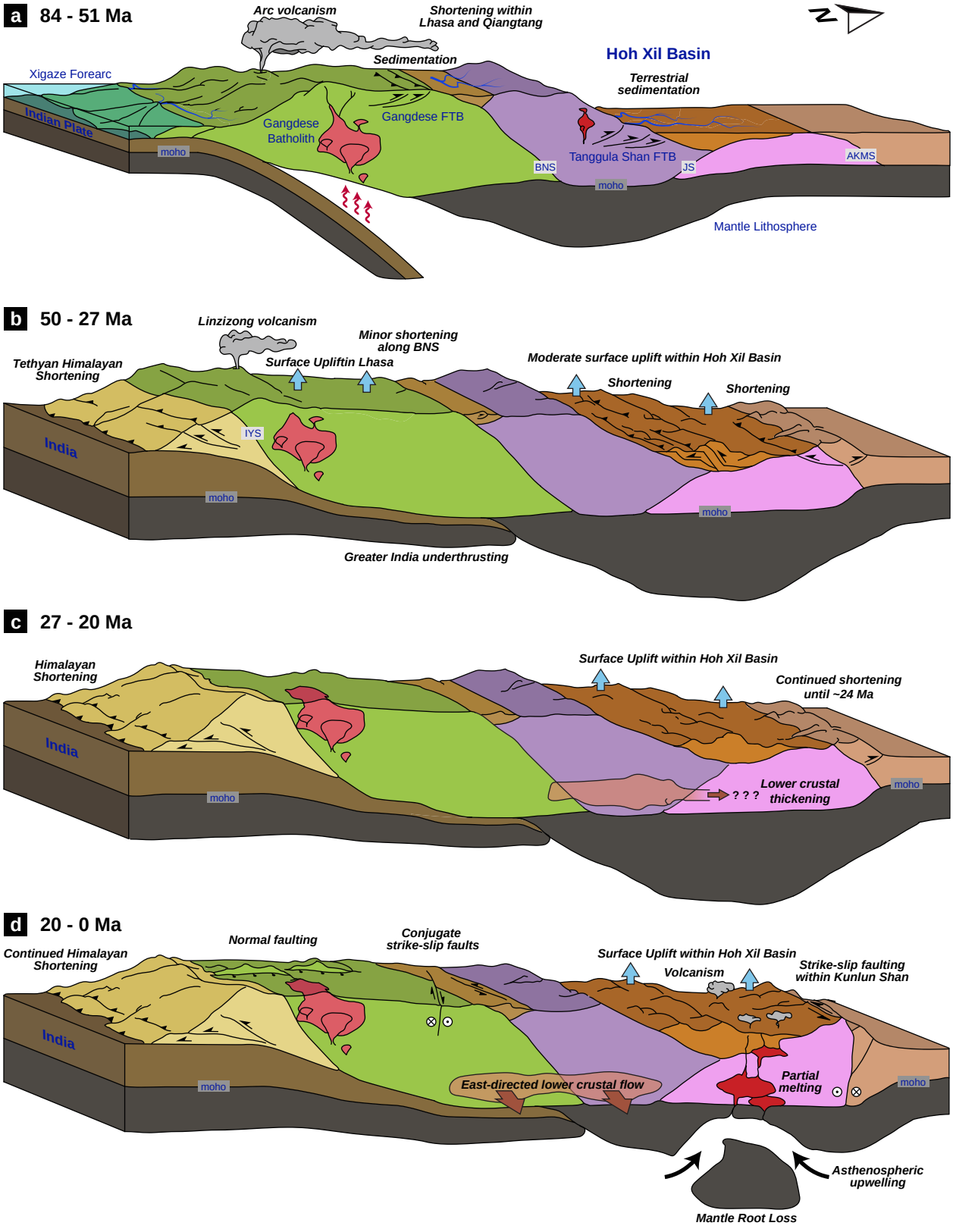
a 84 - 51 Ma
Arc volcanism
Shortening within Lhasa and Qiangtang
Sedimentation
Hoh Xil Basin
Terrestrial sedimentation
Xigaze Forearc
Indian Plate
Gangdese Batholith
Gangdese FTB
moho
BNS
Tanggula Shan FTB
JS
AKMS
moho
Mantle Lithosphere
b 50 - 27 Ma
Linzizong volcanism
Minor shortening along BNS
Tethyan Himalayan Shortening
Surface Upliftin Lhasa
Moderate surface uplift within Hoh Xil Basin
Shortening
Shortening
India
IYS
moho
moho
Greater India underthrusting
c 27 - 20 Ma
Himalayan Shortening
Surface Uplift within Hoh Xil Basin
Continued shortening until ~24 Ma
India
moho
Lower crustal thickening
? ? ?
moho
d 20 - 0 Ma
Normal faulting
Conjugate strike-slip faults
Continued Himalayan Shortening
Surface Uplift within Hoh Xil Basin
Volcanism
Strike-slip faulting within Kunlun Shan
India
moho
East-directed lower crustal flow
Partial melting
moho
Asthenospheric upwelling
Mantle Root Loss
Indian Plate
Himalaya
Lhasa Terrane
Qiangtang Terrane
Songpan-Ganzi Terrane
Kunlun-Qaidam Terrane
Hoh Xil Basin
Nima Basin
Mantle Lithosphere
Partially molten lower crust
Arc magmatism
Intracontinental magmatism

Taylor and Peltzer, 2006; Wang et al., 2009; Lee et al., 2011; Ratschbacher et al., 2011; McCallister et al., 2013; Sundell et al., 2013; Styron et al., 2013). The contemporaneous volcanism in Hoh Xil Basin may suggest that lower crustal melting due to mantle root loss may be dynamically linked to the onset of orogen-wide east-west extension (Figure 5.1d; McKenna and Walker, 1990; Ding et al., 2003; Lai et al., 2003; Williams et al., 2004; Chung et al., 2005; Wang et al., 2005; Guo et al., 2006; Jiang et al., 2006; Chen et al., 2012).

5.3. Implications for the uplift history of the Tibetan Plateau

The history of deformation within the northern Tibetan Plateau provides key insights into the evolution of surface uplift throughout the orogen. The lack of pre-collisional deformation north of the Tanggula Shan implies that crustal thickening-related surface uplift of the Tibetan "proto-plateau" was confined south of this boundary prior to ~50 Ma and that the Cretaceous – early Eocene elevation of the Hoh Xil Basin was likely low (Figure 5.1a). Palynological data from the Fenghuoshan Group suggests that climatic conditions within the Hoh Xil Basin were warm and arid, and thus provides support for low elevation in northern Tibet during late Cretaceous – early Eocene time (Li and Yuan, 1990). Studies on the paleoelevation of the Lhasa and Qiangtang Terranes indicate that high elevation may have been attained prior to the Indo-Asian collision, however post-collisional uplift due to underplating of the Greater Indian lithosphere is also possible (Figures 5.1a and 5.1b; Rowley and Currie, 2006; DeCelles et al., 2007a, 2007b; Polissar et al., 2009; Xu et al., 2013; Ding et al., 2014).

Following collision, crustal shortening and thickening in the Hoh Xil Basin and Kunlun Shan likely resulted in surface uplift in northern Tibet. The isostatic calculations I present in Chapter III for shortening-related surface uplift within the Hoh Xil Basin indicate that ~28% shortening may have produced between 0.6 and 1.6 km of surface uplift, which does not account for high plateau elevations. Moreover, the achievement of modern crustal thickness via 28% shortening is not likely. Oligocene flora in the Hoh Xil Basin includes mixed vegetation that may be indicative of moderate, but not high, elevation (Duan et al., 2008). Together, these data indicate that crustal shortening resulted in moderate surface uplift in northern Tibet (Figure 5.1b), and that uplift to high elevation occurred after the late Oligocene in the absence of upper crustal shortening. Proposed mechanisms for uplift in the absence of crustal shortening include distributed thickening of the lower crust and mantle lithosphere, lower crustal flow, and removal of the mantle lithosphere (Isacks, 1988; Gubbels et al., 1993; Molnar et al., 1993; Clark et al., 2005a; Karplus et al., 2011). Geophysical observations

from the Hoh Xil Basin may indicate that lower crustal thickening was accomplished via lower crustal flow (Figure 5.1c; Owens and Zandt, 1997; Klemplerer, 2006; Karplus et al., 2011). To the south, several studies in the Lhasa and Qiangtang Terranes indicate that post-collisional surface uplift may have occurred until in Eocene – Oligocene time due to northward underthrusting of the Greater Indian lithosphere and that high elevations were achieved throughout southern and central Tibet by the late Oligocene (Figure 5.1b; Rowley and Currie, 2006; DeCelles et al., 2007a, 2007b; Xu et al., 2013).

In Chapter IV, I show that the transition from crustal shortening to left-lateral shear occurred in the early to mid-Miocene and infer that the shift in the least compressive stress from vertical to east-west is related to the achievement of high elevation in northern Tibet. This interpretation is compatible with palynological and paleoelevation data from northern Tibet, which show a major shift to cold- and drought-tolerate species by the mid-Miocene and estimate elevation between 3.4 and 4.2 km (Duan et al., 2007, 2008; Wu et al., 2008; Polissar et al., 2009). Lower crustal thickening and mantle root loss are both proposed mechanisms for surface uplift in the absence of shortening (Isacks, 1988; Gubbels et al., 1993; Molnar et al., 1993; Clark et al., 2005a; Karplus et al., 2011). However, it is predicted that the latter process is accompanied by an increase in volcanism, which is not observed in northern Tibet until after ~20 Ma (McKenna and Walker, 1990; Ding et al., 2003; Lai et al., 2003; Williams et al., 2004; Chung et al., 2005; Wang et al., 2005; Guo et al., 2006; Jiang et al., 2006; Chen et al., 2012). Therefore, I suggest that late Oligocene – early Miocene (27 – 20 Ma) surface uplift was caused by lower crustal thickening, rather than mantle root loss (Figure 5.1c). Alternatively, the 27 Ma small-volume basaltic eruption in the Fenghuoshan Range may indicate that mantle root loss occurred earlier, and the major magmatism did not initiate until after ~20 Ma due to delayed magma migration to the surface.

After the mid-Miocene, there was likely between 0.8 and 1.6 km of surface uplift in northern Tibet (Polissar et al., 2009) which may have been caused, at least in part, by mantle root loss (Molnar et al., 1993). The primary evidence for Miocene mantle root loss is the ca. 20 Ma onset of intracontinental volcanism in the Hoh Xil Basin and the wide range of magma compositions, which are compatible with proposed compositions due to mantle root loss (McKenna and Walker, 1990; Ding et al., 2003; Lai et al., 2003; Williams et al., 2004; Chung et al., 2005; Wang et al., 2005; Guo et al., 2006; Jiang et al., 2006; Chen et al., 2012). Additionally, the increase in the surface elevation and buoyancy of the crustal column in northern Tibet due to convective removal of the mantle lithosphere would lead to an increase in the average potential energy per unit area of the entire

Tibetan Plateau, as well as the force per unit length exerted along the plateau margins (Houseman et al., 1981; England and Molnar, 1990; Molnar et al., 1993; Molnar and Stock, 2009). The coincidence between the timing of northern Tibetan volcanism, the onset strike-slip and normal faulting throughout the Tibetan Plateau, and rapid river incision and plateau expansion in eastern Tibet may indicate that Tibetan mantle root loss in the mid-Miocene triggered a large-scale shift in the dynamics of the orogen (Figure 5.1d; McKenna and Walker, 1990; Clark and Royden, 2000; Blisniuk et al., 2001; Murphy et al., 2000; Murphy et al., 2002; Garzione et al., 2003; Jolivet et al., 2003; Lee et al., 2003; Ding et al., 2003; Lai et al., 2003; Phillips et al., 2004; Williams et al., 2004; Chung et al., 2005; Clark et al., 2005a, 2005b; Wang et al., 2005; Guo et al., 2006; Taylor and Peltzer, 2006; Theide et al., 2006; Jiang et al., 2006; Molnar and Stock, 2009; Wang et al., 2009; Lee et al., 2011; Ratschbacher et al., 2011; Chen et al., 2012; McCallister et al., 2013; Sundell et al., 2013; Styron et al., 2013; Duvall et al., 2013). Mid-Miocene mantle root loss is further supported by the argument that the marked slowing of the Indo-Asian convergence rate between 20 and 10 Ma was caused by an increase in the outward force per unit length and resistance to plate motion due to contemporaneous, and possibly rapid, uplift of the Tibetan Plateau (Molnar and Stock, 2009). It bears mention that recent work argues for an exponentially decreasing rate of Indo-Asian convergence since collision that is not sensitive to the development of topography (Clark, 2012). Regardless, both arguments of the deceasing plate convergence rate between India and Eurasia are compatible with the interpretation of surface uplift presented above.

5.4. Epilogue

The amount of data on the timing and magnitude of deformation throughout the Tibetan Plateau has significantly increased within the past several decades. Recent data have provided key constraints towards the understanding of large-scale lithospheric deformation and a needed departure from the classic understanding of how the Tibetan Plateau formed. The analyses and interpretations presented in this dissertation clarify the tectonic evolution of the northern Tibetan Plateau, which previously constituted a geographic gap in our knowledge of the orogen's history. The primary findings of this thesis, integrated with previous work across the Tibetan Plateau, provide a comprehensive history of lithospheric deformation and the development of high topography. Importantly, this work shows that the development of high topography and the structural evolution of the Tibetan Plateau, while unquestionably linked, are not equivalent and require careful inspection.

Due to the scarcity of suitable material for paleoelevation analysis and of tight age control, the detailed history of elevation gain throughout the Tibetan Plateau has remained enigmatic. Here we provide the most comprehensive analysis of the evolution of topography in the northern Tibetan Plateau to date by integrating the limited paleoelevation constraints with structural and geodynamic arguments. However, future work towards absolute measurement of paleoelevation in northern Tibet is required in order to test the interpretations and conclusions presented in this thesis. The vast, and largely unexplored, extent of the northern Tibetan Plateau affords the opportunity for discovery and analysis of suitable material for paleoelevation analysis.

5.5. References

Aikman, A.B., Harrison, T.M., and Lin, D., 2008, Evidence for Early (>44 Ma) Himalayan Crustal Thickening, Tethyan Himalaya, southeastern Tibet: Earth and Planetary Science Letters, v. 274, no. 1-2, p. 14–23, doi: 10.1016/j.epsl.2008.06.038.

Blisniuk, P.M., Hacker, B.R., Glodny, J., Ratschbacher, L., Bi, S., Wu, Z., Mcwilliams, M.O., Calvert, A., and Geowissenschaften, È., 2001, Normal faulting in central Tibet since at least 13 . 5 Myr ago: v. 412, p. 628–632.

Braitenberg, C., Zadro, M., Fang, J., Wang, Y., and Hsu, H.T., 2000, The gravity and isostatic Moho undulations in Qinghai–Tibet plateau: Journal of Geodynamics, v. 30, no. 5, p. 489–505, doi: 10.1016/S0264-3707(00)00004-1.

Burg, J.P., Proust, F., Tapponnier, P., and Chen, G.M., 1983, Deformation phases and tectonic evolution of the Lhasa block: Eclogae Geol. Helv, v. 76, p. 643–683.

Chen, J.-L., Xu, J.-F., Wang, B.-D., and Kang, Z.-Q., 2012, Cenozoic Mg-rich potassic rocks in the Tibetan Plateau: Geochemical variations, heterogeneity of subcontinental lithospheric mantle and tectonic implications: Journal of Asian Earth Sciences, v. 53, p. 115–130, doi: 10.1016/j.jseaes.2012.03.003.

Chung, S.-L., Chu, M.-F., Zhang, Y., Xie, Y., Lo, C.-H., Lee, T.-Y., Lan, C.-Y., Li, X., Zhang, Q., and Wang, Y., 2005, Tibetan tectonic evolution inferred from spatial and temporal variations in post-collisional magmatism: Earth-Science Reviews, v. 68, p. 173–196, doi: 10.1016/j.earscirev.2004.05.001.

Clark, M.K., and Royden, L.H., 2000, Topographic ooze : Building the eastern margin of Tibet by lower crustal flow: Geology, v. 28, no. 8, p. 703–706.

Clark, M.K., Bush, J.W.M., and Royden, L.H., 2005a, Dynamic topography produced by lower

crustal flow against rheological strength heterogeneities bordering the Tibetan Plateau: Geophysical Journal International, v. 162, no. 2, p. 575–590, doi: 10.1111/j.1365-246X.2005.02580.x.

Clark, M.K., House, M.A., Royden, L.H., Whipple, K., Burchfiel, B.C., Zhang, X., and Tang, W., 2005b, Late Cenozoic uplift of southeastern Tibet: Geology, v. 33, no. 6, p. 525, doi: 10.1130/G21265.1.

Clark, M.K., Farley, K. a., Zheng, D., Wang, Z., and Duvall, A.R., 2010, Early Cenozoic faulting of the northern Tibetan Plateau margin from apatite (U–Th)/He ages: Earth and Planetary Science Letters, v. 296, p. 78–88, doi: 10.1016/j.epsl.2010.04.051

Clark, M.K., 2012, Continental collision slowing due to viscous mantle lithosphere rather than topography: Nature, v. 483, p. 74–7, doi: 10.1038/nature10848.

DeCelles, P.G., Robinson, D.M., Quade, J., Ojha, T.P., Garzione, C.N., Copeland, P., and Upreti, B.N., 2001, Himalayan fold-thrust belt in western Nepal: Tectonics, v. 20, no. 4, p. 487–509.

DeCelles, P.G., Quade, J., Kapp, P., Fan, M., Dettman, D.L., and Ding, L., 2007a, High and dry in central Tibet during the Late Oligocene: Earth and Planetary Science Letters, v. 253, no. 3-4, p. 389–401, doi: 10.1016/j.epsl.2006.11.001.

DeCelles, P.G., Kapp, P., Ding, L., and Gehrels, G.E., 2007b, Late Cretaceous to middle Tertiary basin evolution in the central Tibetan Plateau: Changing environments in response to tectonic partitioning, aridification, and regional elevation gain: Geological Society of America Bulletin, v. 119, no. 5-6, p. 654–680, doi: 10.1130/B26074.1.

DeCelles, P.G., Kapp, P., Gehrels, G.E., and Ding, L., 2014, Paleocene-Eocene foreland basin evolution in the Himalaya of southern Tibet and Nepal: implications for the age of initial India-Asia collision: Tectonics, in press, doi: 10.1002/2014TC003522.

Ding, L., Kapp, P., Zhong, D., Deng, W., 2003, Cenozoic Volcanism in Tibet: Evidence for a Transition from Oceanic to Continental Subduction: Journal of Petrology, v. 44, p. 1833–1865.

Ding, L., Xu, Q., Yue, Y., Wang, H., Cai, F., and Li, S., 2014, The Andean-type Gangdese Mountains: Paleoelevation record from the Paleocene–Eocene Linzhou Basin: Earth and Planetary Science Letters, v. 392, p. 250–264, doi: 10.1016/j.epsl.2014.01.045.

Duan, Z., Li, Y., Shen, Z., Zhu, X., and Zhong, C., 2007, Analysis of the evolution of the Cenozoic ecological environment and process of plateau surface uplift in the Wenquan area in the interior of the Qinghai-Tibet Plateau: Geology in China, v. 34, no. 4, p. 688 – 696.

Duan, Q., Zhang, K., Wang, J., Yao, H., and Niu, Z., 2008, Oligocene Palynoflora, Paleovegetation and Paleoclimate in the Tanggula Mountains, northern Tibet: Acta Micropalaeontologica Sinica, v. 25, no. 2, p. 185–195Duvall, A.R., and Clark, M.K., 2010, Dissipation of fast strike-slip faulting within and beyond northeastern Tibet: Geology, v. 38, p. 223–226, doi: 10.1130/G30711.1.

Dupont-Nivet, G., Lippert, P.C., Van Hinsbergen, D.J.J., Meijers, M.J.M., and Kapp, P., 2010, Palaeolatitude and age of the Indo-Asia collision: palaeomagnetic constraints: Geophysical Journal International, v. 182, no. 3, p. 1189–1198, doi: 10.1111/j.1365-246X.2010.04697.x.

Duvall, A.R., Clark, M.K., van der Pluijm, B.A., and Li, C., 2011, Direct dating of Eocene reverse faulting in northeastern Tibet using Ar-dating of fault clays and low-temperature thermochronometry: Earth and Planetary Science Letters, v. 304, p. 520–526, doi: 10.1016/j.epsl.2011.02.028.

Duvall, A.R., Clark, M.K., Kirby, E., Farley, K.A., Craddock, W.H., Li, C., and Yuan, D.-Y., 2013, Low-temperature thermochronometry along the Kunlun and Haiyuan Faults, NE Tibetan Plateau: Evidence for kinematic change during late-stage orogenesis: Tectonics, v. 32, p. 1190–1211, doi: 10.1002/tect.20072.

England, P., and Houseman, G., 1986, Finite strain calculations of continental deformation: 2. Comparison with the India-Asia Collision Zone: Journal of Geophysical Research: Solid Earth, v. 91, p. 3664–3676.

England, P., and Molnar, P., 1990, Surface uplift, uplift of rocks, and exhumation of rocks: Geology, v. 18, p. 1173–1177.

England, P., and Searle, M., 1986, The Cretaceous-tertiary deformation of the Lhasa Block and its implications for crustal thickening in Tibet: Tectonics, v. 5, p. 1–14.

Garzione, C.N., DeCelles, P.G., Hodkinson, D.G., Ojha, T.P., and Upreti, B.N., 2003, East-west extension and Miocene environmental change in the southern Tibetan plateau: Thakkhola graben, central Nepal: Geological Society of America Bulletin, v. 115, no. 1, p. 3–20, doi: 10.1130/0016-7606(2003)115<0003:EWEAME>2.0.CO;2.

Gubbels, T.L., Isacks, B.L., and Farrar, E., 1993, High-level surfaces, plateau uplift, and foreland development, Bolivian central Andes: Geology, v. 21, p. 695 – 698. 177–1220, doi: 10.1093/petrology/egl007.

Guo, Z., Wilson, M., Liu, J., and Mao, Q., 2006, Post-collisional, Potassic and Ultrapotassic Magmatism of the Northern Tibetan Plateau: Constraints on Characteristics of the Mantle

Source, Geodynamic Setting and Uplift Mechanisms: Journal of Petrology, v. 47, p. 1

Horton, B.K., Yin, A., Spurlin, M.S., Zhou, J., and Wang, J., 2002, Paleocene – Eocene syncontractional sedimentation in narrow , lacustrine-dominated basins of east-central Tibet: Geological Society of America Bulletin, v. 114, no. 7, p. 771–786, doi: 10.1130/0016-7606(2002)114<0771.

Houseman, G.A., McKenzie, D.P., and Molnar, P., 1981, Convective instability of a thickened boundary layer and its relevance for the thermal evolution of continental convergence belts: Journal of Geophysical Research: Solid Earth, v. 86, no. B7, p. 6115–6132.

Isacks, B.L., 1988, Uplift of the central Andean plateau and bending of the Bolivian orocline: Journal of Geophysical Research, v. 93, p. 3211-3231.

Jiang, Y.-H., Jiang, S.-Y., Ling, H.-F., and Dai, B.-Z., 2006, Low-degree melting of a metasomatized lithospheric mantle for the origin of Cenozoic Yulong monzogranite-porphyry, east Tibet: Geochemical and Sr–Nd–Pb–Hf isotopic constraints: Earth and Planetary Science Letters, v. 241, p. 617–633, doi: 10.1016/j.epsl.2005.11.023.

Jolivet, M., Brunel, M., Seward, D., Xu, Z., Yang, J., Malavieille, J., Roger, F., Leyreloup, A., Arnaud, N., and Wu, C., 2003, Neogene extension and volcanism in the Kunlun Fault Zone, northern Tibet: New constraints on the age of the Kunlun Fault: Tectonics, v. 22, p. 1–23, doi: 10.1029/2002TC001428.

Kapp, P., DeCelles, P.G., Leier, A.L., Fabijanic, J.M., He, S., Pullen, A., and Gehrels, G.E., 2007a, The Gangdese retroarc thrust belt revealed: GSA Today, v. 17, p. 4–9.

Kapp, P., DeCelles, P.G., Gehrels, G.E., Heizler, M., and Ding, L., 2007b, Geological records of the Lhasa-Qiangtang and Indo-Asian collisions in the Nima area of central Tibet: Geological Society of America Bulletin, v. 119, p. 917–933, doi: 10.1130/B26033.1.

Kapp, P., Yin, A., Harrison, T.M., and Ding, L., 2005, Cretaceous-Tertiary shortening, basin development, and volcanism in central Tibet: Geological Society of America Bulletin, v. 117, p. 865, doi: 10.1130/B25595.1.

Karplus, M.S., Zhao, W., Klemperer, S.L., Wu, Z., Mechie, J., Shi, D., Brown, L.D., and Chen, C., 2011, Injection of Tibetan crust beneath the south Qaidam Basin: Evidence from INDEPTH IV wide-angle seismic data: Journal of Geophysical Research, v. 116, p. 1–23, doi: 10.1029/2010JB007911.

Klemperer, S.L., 2006, Crustal flow in Tibet: geophysical evidence for the physical state of Tibetan lithosphere, and inferred patterns of active flow: Geological Society, London, Special

Publications, v. 268, p. 39–70, doi: 10.1144/GSL.SP.2006.268.01.03.

Lai, S.-C., Liu, C.-Y., and Yi, H.-S., 2003, Geochemistry and Petrogenesis of Cenozoic Andesite-Dacite Associations from the Hoh Xil Region, Tibetan Plateau: International Geology Review, v. 45, p. 998–1019, doi: 10.2747/0020-6814.45.11.998.

Lee, H.-Y., Chung, S.-L., Wang, J.-R., Wen, D.-J., Lo, C.-H., Yang, T.F., Zhang, Y., Xie, Y., Lee, T.-Y., Wu, G., and Ji, J., 2003, Miocene Jiali faulting and its implications for Tibetan tectonic evolution: Earth and Planetary Science Letters, v. 205, p. 185–194, doi: 10.1016/S0012-821X(02)01040-3.

Lee, J., Hager, C., Wallis, S.R., Stockli, D.F., Whitehouse, M.J., Aoya, M., and Wang, Y., 2011, Middle to late Miocene extremely rapid exhumation and thermal reequilibration in the Kung Co rift, southern Tibet: Tectonics, v. 30, TC2007, doi: 10.1029/2010TC002745.

Li, P., and Yuan, L., 1990, The Fenghuoshan Group of palynological assemblages and their meaning: Northwestern Geology, v. 4, p. 7–9.

Liu, Z., Wang, C., and Yi, H., 2001, Evolution and mass accumulation of the Cenozoic Hoh Xil Basin, Northern Tibet: Journal of Sedimentary Research, v. 71, no. 6, p. 971–984.

Liu, Z., Zhao, X., Wang, C., Liu, S., and Yi, H., 2003, Magnetostratigraphy of Tertiary sediments from the Hoh Xil Basin: implications for the Cenozoic tectonic history of the Tibetan Plateau: Geophysical Journal International, v. 154, no. 2, p. 233–252, doi: 10.1046/j.1365-246X.2003.01986.x.

McCallister, A.T., Taylor, M.H., Murphy, M.A., Styron, R.H., & Stockli, D.F., 2013, Thermochronologic constraints on the late Cenozoic exhumation history of the Gurla Mandhata metamorphic core complex, Southwestern Tibet: Tectonics, v. 33, p. 27-52.

McKenna, L.W., and Walker, J.D., 1990, Geochemistry of Crustally Derived Leucocratic Igneous Rocks From the Ulugh Muztagh Area, Northern Tibet and Their Implications for the Formation of the Tibetan Plateau: Journal of Geophysical Research, v. 95, p. 21,483–21,502.

Molnar, P., and Stock, J.M., 2009, Slowing of India's convergence with Eurasia since 20 Ma and its implications for Tibetan mantle dynamics: Tectonics, v. 28, p. 1–11, doi: 10.1029/2008TC002271.

Molnar, P., England, P., and Martinod, J., 1993, Mantle dynamics, uplift of the Tibetan Plateau, and the Indian Monsoon: Reviews in Geophysics, v. 31, no. 4, p. 357–396.

Murphy, M.A., and Yin, A., 2003, Structural evolution and sequence of thrusting in the Tethyan fold-thrust belt and Indus-Yalu suture zone, southwest Tibet: Geological Society of America

Bulletin, v. 115, p. 21–34, doi: 10.1130/0016-7606(2003)115<0021.

Murphy, M.A., Yin, A., Harrison, T.M., Dürr, S.B., Z, C., Ryerson, F.J., Kidd, W.S.F., X, W., and X, Z., 1997, Did the Indo-Asian collision alone create the Tibetan plateau?: Geology, v. 25, p. 719–722, doi: 10.1130/0091-7613(1997)025<0719:DTIACA>2.3.CO;2.

Murphy, M.A., Yin, A., Kapp, P., Harrison, T.M., Ding, L., and Jinghui, G., 2000, Southward propagation of the Karakoram fault system , southwest Tibet : Timing and magnitude of slip: Geology, v. 28, p. 451–454.

Murphy, M. a., Yin, A., Kapp, P., Harrison, T.M., Manning, C.E., Ryerson, F.J., Lin, D., and Jinghui, G., 2002, Structural evolution of the Gurla Mandhata detachment system, southwest Tibet: Implications for the eastward extent of the Karakoram fault system: Geological Society of America Bulletin, v. 114, no. 4, p. 428–447, doi: 10.1130/0016-7606(2002)114<0428:SEOTGM>2.0.CO;2.

Najman, Y., Appel, E., Boudagher-Fadel, M., Bown, P., Carter, A., Garzanti, E., Godin, L., Han, J., Liebke, U., Oliver, G., Parrish, R., and Vezzoli, G., 2010, Timing of India-Asia collision: Geological, biostratigraphic, and palaeomagnetic constraints: Journal of Geophysical Research, v. 115, no. B12, doi: 10.1029/2010JB007673.

Owens, T.J., and Zandt, G., 1997, Implications of crustal property variations for models of Tibetan plateau evolution: Nature, v. 387, p. 37–43.

Phillips, R.J., Parrish, R.R., and Searle, M.P., 2004, Age constraints on ductile deformation and long-term slip rates along the Karakoram fault zone , Ladakh: v. 226, p. 305–319, doi: 10.1016/j.epsl.2004.07.037.

Polissar, P.J., Freeman, K.H., Rowley, D.B., McInerney, F.A., and Currie, B.S., 2009, Paleoaltimetry of the Tibetan Plateau from D/H ratios of lipid biomarkers: Earth and Planetary Science Letters, v. 287, p. 64–76, doi: 10.1016/j.epsl.2009.07.037.

Ratschbacher, L., Frisch, W., and Liu, G., 1994, Distributed deformation in southern and western Tibet during and after the India-Asian collision: Journal of Geophysical Research, v. 99, p. 19,917–19,945.

Ratschbacher, L., Krumrei, I., lumenwitz, M., Staiger, M., Gloaguen, R., Miller, B.V., Samson, S.D., Edwards, M.A., Appel, E., 2011, Rifting and strike-slip shear in central Tibet and the geometry, age and kinematics of upper crustal extension in Tibet: Geol. Soc. Spec. Publ., v. 353, no. 1, p. 127–163, doi:10.1144/SP353.8.

Rowley, D.B., and Currie, B.S., 2006, Palaeo-altimetry of the late Eocene to Miocene Lunpola basin,

central Tibet: Nature, v. 439, p. 677–81, doi: 10.1038/nature04506.

Searle, M.P., Simpson, R.L., Law, R.D., Parrish, R.R., and Waters, D.J., 2003, The structural geometry, metamorphic and magmatic evolution of the Everest massif, High Himalaya of Nepal-South Tibet: Journal of the Geological Society of London, v. 160, p. 345–366.

Spurlin, M.S., Yin, A., Horton, B.K., Zhou, J., and Wang, J., 2005, Structural evolution of the Yushu-Nangqian region and its relationship to syncollisional igneous activity, east-central Tibet: Geological Society of America Bulletin, v. 117, no. 9-10, p. 1293–1317, doi: 10.1130/B25572.1.

Staisch, L.M., Niemi, N.A., Chang, H., Clark, M.K., Rowley, D.B., and Currie, B.S., 2014, A Cretaceous-Eocene depositional age for the Fenghuoshan Group, Hoh Xil Basin: Implications for the tectonic evolution of the northern Tibet Plateau: Tectonics, v. 33, p. 281–301, doi: 10.1002/2013TC003367.Received.

Styron, R.H., Taylor, M.H., Sundell, K.E., Stockli, D.F., Oalmann, J. a. G., Möller, A., McCallister, A.T., Liu, D., and Ding, L., 2013, Miocene initiation and acceleration of extension in the South Lunggar rift, western Tibet: Evolution of an active detachment system from structural mapping and (U-Th)/He thermochronology: Tectonics, v. 32, p. 880–907, doi: 10.1002/tect.20053.

Sundell, K.E., Taylor, M.H., Styron, R.H., Stockli, D.F., Kapp, P., Hager, C., Liu, D., Ding, L., 2013, Evidence for constriction and Pliocene acceleration of east-west extension in the North Lunggar rift region of west central Tibet: Tectonics, v. 32, no. 5, p. 1454–1479.

Tapponnier, P., Shu, Z., Roger, F., Meyer, B., Arnaud, N., Wittlinger, G., and Jingsui, Y., 2001, Oblique stepwise rise and growth of the Tibet plateau: Science, v. 294, p. 1671–1677, doi: 10.1126/science.105978.

Taylor, M., and Peltzer, G., 2006, Current slip rates on conjugate strike-slip faults in central Tibet using synthetic aperture radar interferometry: Journal of Geophysical Research, v. 111, p. B12402, doi: 10.1029/2005JB004014.

Vergne, J., Wittlinger, G., Hui, Q., Tapponnier, P., Poupinet, G., Mei, J., Herquel, G., and Paul, A., 2002, Seismic evidence for stepwise thickening of the crust across the NE Tibetan plateau: Earth and Planetary Science Letters, v. 203, p. 25–33, doi: 10.1016/S0012-821X(02)00853-1.

Wang, Q., McDermott, F., Xu, J., Bellon, H., and Zhu, Y., 2005, Cenozoic K-rich adakitic volcanic rocks in the Hohxil area, northern Tibet: Lower-crustal melting in an intracontinental setting: Geology, v. 33, p. 465–468, doi: 10.1130/G21522.1.

Wang, C.S., Zhao, X., Liu, Z., Lippert, P.C., Graham, S.A, Coe, R.S., Yi, H., Zhu, L., Liu, S., and Li, Y., 2008, Constraints on the early uplift history of the Tibetan Plateau.: Proceedings of the National Academy of Sciences of the United States of America, v. 105, no. 13, p. 4987–4992, doi: 10.1073/pnas.0703595105.

Wang, S., Fang, X., Zheng, D., and Wang, E., 2009, Initiation of slip along the Xianshuihe fault zone, eastern Tibet, constrained by K/Ar and fission-track ages: International Geology Review, v. 51, p. 1121–1131, doi: 10.1080/00206810902945132.

Williams, H.M., Turner, S.P., Pearce, J.A., Kelley, S.P., and Harris, N.B.W., 2004, Nature of the Source Regions for Post-collisional, Potassic Magmatism in Southern and Northern Tibet from Geochemical Variations and Inverse Trace Element Modelling: Journal of Petrology, v. 45, p. 555–607, doi: 10.1093/petrology/egg094.

Wittlinger, G., Vergne, J., Tapponnier, P., Farra, V., Poupinet, G., Jiang, M., Su, H., Herquel, G., and Paul, a, 2004, Teleseismic imaging of subducting lithosphere and Moho offsets beneath western Tibet: Earth and Planetary Science Letters, v. 221, p. 117–130, doi: 10.1016/S0012-821X(03)00723-4.

Wu, Z., Barosh, P.J., Wu, Z., Hu, D., Zhao, X., and Ye, P., 2008, Vast early Miocene lakes of the central Tibetan Plateau: Geological Society of America Bulletin, v. 120, no. 9-10, p. 1326–1337, doi: 10.1130/B26043.1.

Xu, Q., Ding, L., Zhang, L., Cai, F., Lai, Q., Yang, D., and Liu-Zeng, J., 2013, Paleogene high elevations in the Qiangtang Terrane, central Tibetan Plateau: Earth and Planetary Science Letters, v. 362, p. 31–42, doi: 10.1016/j.epsl.2012.11.058.

Yakovlev, P. V., Clark, M. K., 2014, Conservation and redistribution of crust during the Indo-Asian collision: Tectonics, v. 33, no. 6, p. 1016–1027, doi: 10.1002/2013TC003469.

Yin, A., Rumelhart, P.E., Butler, R., Cowgill, E., Harrison, T.M., Foster, D. A., Ingersoll, R.V., Qing, Z., Xian-Qiang, Z., Xiao-Feng, W., Hanson, A., and Raza, A., 2002, Tectonic history of the Altyn Tagh fault system in northern Tibet inferred from Cenozoic sedimentation: Geological Society of America Bulletin, v. 114, no. 10, p. 1257–1295, doi: 10.1130/0016-7606(2002)114<1257:THOTAT>2.0.CO;2.

Yin, A., 2005, Cenozoic tectonic evolution of the Himalayan orogen as constrained by along-strike variation of structural geometry, exhumation history, and foreland sedimentation: Earth-Science Reviews, v. 76, p. 1–131, doi: 10.1016/j.earscirev.2005.05.004.

Yin, A., Dang, Y.-Q., Wang, L.-C., Jiang, W.-M., Zhou, S.-P., Chen, X.-H., Gehrels, G.E., and

McRivette, M.W., 2008, Cenozoic tectonic evolution of Qaidam basin and its surrounding regions (Part 1): The southern Qilian Shan-Nan Shan thrust belt and northern Qaidam basin: Geological Society of America Bulletin, v. 120, p. 813–846, doi: 10.1130/B26180.1.